Lecture Notes in Mechanical Engineering

Leijun Li
Dilip Kumar Pratihar
Suman Chakrabarty
Purna Chandra Mishra *Editors*

Advances in Materials and Manufacturing Engineering

Proceedings of ICAMME 2019

Springer

Lecture Notes in Mechanical Engineering

Lecture Notes in Mechanical Engineering (LNME) publishes the latest developments in Mechanical Engineering—quickly, informally and with high quality. Original research reported in proceedings and post-proceedings represents the core of LNME. Volumes published in LNME embrace all aspects, subfields and new challenges of mechanical engineering. Topics in the series include:

- Engineering Design
- Machinery and Machine Elements
- Mechanical Structures and Stress Analysis
- Automotive Engineering
- Engine Technology
- Aerospace Technology and Astronautics
- Nanotechnology and Microengineering
- Control, Robotics, Mechatronics
- MEMS
- Theoretical and Applied Mechanics
- Dynamical Systems, Control
- Fluid Mechanics
- Engineering Thermodynamics, Heat and Mass Transfer
- Manufacturing
- Precision Engineering, Instrumentation, Measurement
- Materials Engineering
- Tribology and Surface Technology

To submit a proposal or request further information, please contact the Springer Editor in your country:

China: Li Shen at li.shen@springer.com
India: Dr. Akash Chakraborty at akash.chakraborty@springernature.com
Rest of Asia, Australia, New Zealand: Swati Meherishi at swati.meherishi@springer.com
All other countries: Dr. Leontina Di Cecco at Leontina.dicecco@springer.com

To submit a proposal for a monograph, please check our Springer Tracts in Mechanical Engineering at http://www.springer.com/series/11693 or contact Leontina.dicecco@springer.com

Indexed by SCOPUS. The books of the series are submitted for indexing to Web of Science.

More information about this series at http://www.springer.com/series/11236

Leijun Li · Dilip Kumar Pratihar ·
Suman Chakrabarty · Purna Chandra Mishra
Editors

Advances in Materials and Manufacturing Engineering

Proceedings of ICAMME 2019

Springer

Editors
Leijun Li
Department of Chemical and Materials Engineering
University of Alberta
Alberta, AB, Canada

Suman Chakrabarty
Department of Mechanical Engineering
Indian Institute of Technology Kharagpur
Kharagpur, West Bengal, India

Dilip Kumar Pratihar
Department of Mechanical Engineering
Indian Institute of Technology Kharagpur
Kharagpur, West Bengal, India

Purna Chandra Mishra
School of Mechanical Engineering
KIIT Deemed to be University
Bhubaneswar, Odisha, India

ISSN 2195-4356 ISSN 2195-4364 (electronic)
Lecture Notes in Mechanical Engineering
ISBN 978-981-15-1306-0 ISBN 978-981-15-1307-7 (eBook)
https://doi.org/10.1007/978-981-15-1307-7

This Springer imprint is published by the registered company Springer Nature Singapore Pte Ltd.
The registered company address is: 152 Beach Road, #21-01/04 Gateway East, Singapore 189721, Singapore

Preface

This International Conference on Advances in Materials and Manufacturing Engineering (ICAMME-2019) held in the School of Mechanical Engineering inside the beautiful campus of KIIT Deemed to be University, Bhubaneswar, Odisha, India, during 15–17 March 2019. With the pure flame of education, visionary educationalist Dr. Achyuta Samanta established KIIT Deemed to be University, formerly Kalinga Institute of Industrial Technology, which is a co-educational autonomous university located at Bhubaneswar in the eastern state of Odisha, India. It was established in 1992 as an Industrial Training Institution which was developed to KIIT Deemed to be University in 2004. It was one of the youngest institutions to be awarded the Deemed University status in India and then the University status in 2004 and is recognized by Limca Book of Records. All the academic programmes are accredited by NAAC of UGC and NBA as per Washington Accord of AICTE, which are benchmarks of excellence. NAAC (government agency to evaluate universities) has awarded KIIT the highest grade of "A" with a CGPA of 3.36/4. KIIT Deemed to be University recently achieved the tag of Institution of Eminence (IoE) by MHRD, Government of India. The School of Mechanical Engineering, established in the year 1997, produces graduates who can meet the rapidly changing needs of the industry which demand new skills. Current consultancy and research and development areas of the school include residual stresses in fusion-welded structure, surface finish optimization by high-pressure impingement cooling and CAD modelling. Material processing technology, cleaner manufacturing technology, renewable energy, automotive engineering and quality engineering and management are the other areas of interest. Research and development efforts of the school are supported by bodies like ARDB, BRNS, AICTE and DST, Government of India.

The International Conference on Advances in Materials and Manufacturing Engineering (ICAMME-2019) provided an ideal platform and brought together the researchers, scientists, engineers, industrial experts, scholars and students to share and widen their knowledge on theoretical, numerical and experimental developments in the fields of processing, manufacturing and characterization of materials. This conference offered excellent opportunities for the participants to have a direct

exchange of ideas and experiences, to mine potential research problems and to forge research relations alongside finding partners for future collaborations. The conference has invited eminent speakers from the industry and academia for delivering keynote lectures and plenary talks. Given the gamut of engineering challenges pertaining to mechanical engineering and materials that the modern society is currently faced with, a holistic effort involving and transcending various disciplines of mechanical engineering is essential. ICAMME proceedings spans over created 50 topical tracks, which are well balanced in content and manageable in terms of number of contributions and create an adequate discussion space for trendy topics. There were 80 oral presentations and about 40 poster presentations by participants which brought great opportunity to share their recent research work knowledge among each other graciously.

Efforts taken by peer reviewers contributed to improve the quality of manuscripts, provided constructive critical comments, improvements and corrections to the authors are gratefully appreciated. We are very much grateful to the International/National Advisory Committee, session chairs, student volunteers and administrative assistants from the institute management who selflessly contributed to the success of this conference. Also, we are thankful to all the authors who submitted papers, because of which the conference became a history of success. It was the quality of their presentations and their passion to communicate with the other participants that really made this conference a great success.

Last but not least, we are thankful for the enormous support of Springer for supporting us in every step of our journey towards success. Their cooperation was not only the strength but also an inspiration for the organizers.

Edited by:

Prof. Purna Chandra Mishra
Prof. Leijun Li
Prof. Dilip Kumar Pratihar
Prof. Suman Chakraborty

Bhubaneswar, India

Prof. (Dr.) Purna Chandra Mishra
Conference Co-chair-ICAMME 2019
pcmishrafme@kiit.ac.in

Contents

About the Editors

Leijun Li received his B.S. degree in Welding Engineering from Huazhong University of Science and Technology, China and his M.S. degree in Mechanical Engineering from Xi'an Jiaotong University, China. He subsequently completed his Ph.D. in Materials Engineering at the Warren "Doc" Savage Materials Joining Lab at Rensselaer Polytechnic Institute (RPI). His Materials Processing and Testing Lab has become a respected research group in the United States. In 2013, he relocated from Utah to Alberta and took up his present position at the University of Alberta.

Dilip Kumar Pratihar completed his B.E. (Hons.) and M.Tech. in Mechanical Engineering at the REC Durgapur in 1988 and 1995, respectively. Presently, he is a Professor at the IIT Kharagpur, India. His research interests include robotics, soft computing, and manufacturing science. He has made significant contributions to the development of intelligent autonomous systems in various fields, including robotics and manufacturing science. He has published more than 200 papers, and serves on the editorial boards of 12 international journals. He is also a member of the expert committee on Advanced Manufacturing Technology, DST, Government of India.

Suman Chakrabarty is Associate Dean of SIRC, a Professor of Mechanical Engineering, and the Head of Medical Science and Technology at the IIT Kharagpur. His research interests include microfluidics and nanofluidics, interfacial phenomena and phase changes, and computational fluid dynamics. He received the Shanti Swaroop Bhatnagar Prize in 2013, INAE Chair Professorship in 2014, and the K.N. Seetharamu Medal and Prize from the Indian Society of Heat and Mass Transfer in 2011. He is a member of many academic and professional bodies, including the ASME, ISHMT, and APS. He serves on the editorial boards of various journals, and has published many papers in international journals and conference proceedings.

Purna Chandra Mishra is a Professor and Dean (Research) of the School of Mechanical Engineering, Kalinga Institute of Industrial Technology, India. He received his B.E. in Mechanical Engineering from Berhampur University in 2001, and his M.E. and Ph.D. in Engineering from Jadavpur University, Kolkata, in 2006 and 2011, respectively. He is a member of many professional and academic bodies, and author of the book "Heat and Mass Transfer," as well as numerous book chapters and papers in international journals and conference proceedings. In addition, he holds more than 10 Indian and international patents.

Fused Deposition Modelling and Parametric Optimization of ABS-M30

Hemant Cherkia, Sasmita Kar, Sudhansu Sekhar Singh and Ashutosh Satpathy

Abstract In the current development of generative manufacturing industries, 3D printing technologies have a significant impact in the production of complex geometry with least time and the absence of human intercession, tools, fixtures and dies. Presently in engineering application, fused deposition modelling (FDM) has better demand in additive manufacturing. The improvement in design quality and manufacturing in FDM is based on the proper selection of principal operational parameters. This paper experimentally describes the influence of stereotypical operational variables, i.e. layer thickness, raster angle, raster width, part build orientation and their reciprocation on the precision of change in length, width, thickness, hole diameter and angle orientation of test part of acrylonitrile butadiene styrene-M30 (ABS-M30) after generated by FDM approach. It was profound that shrinkage predominates along the diameter of hole but an increase in dimension of length, width, thickness and angle of inclination is more than the thirst value of the fabricated specimen. The most favourable parametric combination is followed to optimize the precise responses just as a change in length, width, thickness, hole diameter and angle orientation of build part by using a parametric design of Taguchi's L_9 orthogonal array. As Taguchi's methodology is not much satisfactory for steady optimal factor amalgamation of each response Grey-Taguchi methods used to investigate the influence of FDM parameters on multi-performance characteristics, combining all the responses into a single response. The correlative effect of significant factors is determined by Analysis of Variance (ANOVA). Finally, the ANOVA on Grey relational grade indicates layer thickness, part build orientation and raster width which are significant. Layer thickness is the most influencing factor for part build. The percentage errors are

H. Cherkia · S. Kar (✉) · S. S. Singh · A. Satpathy
CAPGS, Biju Patnaik University of Technology, Rourkela, India
e-mail: sasmitakarom@gmail.com

H. Cherkia
e-mail: hemantcherkia@gmail.com

S. S. Singh
e-mail: singhsudhansu16@yah.com

A. Satpathy
e-mail: ashutoshsatpathy2017@gmail.com

L. Li et al. (eds.), *Advances in Materials and Manufacturing Engineering*, Lecture Notes in Mechanical Engineering, https://doi.org/10.1007/978-981-15-1307-7_1

12.05, 4.55, 2.45, 3.4, 5.07 and 0.74 for change in length, width, thickness, diameter, angle and Grey relational grade, respectively.

Keywords Fused deposition modelling (FDM) · 3D printing · Acrylonitrile butadiene styrene-M30 (ABS-M30) · Analysis of Variance (ANOVA)

1 Introduction

FDM is one among the extrusion-based additive machining process. Most significantly, the part build occurs by continuous heating and extruding the filament through a small regulated nozzle. Both the semi-molten filaments are deposited for part and support structure simultaneously according to the specific design of CAD model. Mostly, it assigns with ABS thermoplastics and polymer composites also. Any critical complicated parts with precise dimension can be manufactured by FDM technology for different field of application, i.e. medical science, robotics, electronic items, aerospace models, investment casting moulds and patterns. CAD model is converted to the format of stereolithography (STL) file, and the material deposition starts from the outer periphery towards the inner zone by controlling the speed with temperature of nozzle. Gradually, the subsequent layers are generated till the completion of the build part by controlling the process parameters. Fused deposition modelling (FDM) operation is based on Taguchi design of experiments to optimize the number of experiments, followed by ANOVA analysis and Grey relation analysis, respectively, to determine the relative influence of factors with effect of FDM parameters in a single response rather than individual response for dimensional precision. The important operation parameters such as density of layer, direction of parts, raster angle and raster width depend upon length, width, thickness of the ABSP 400 parts which are assembled by FDM method. The contraction prevailed along the direction of the length and width, whereas the thickness increased from the desired value of the fabricated part is defined by Padhi et al. [1]. Kaveh et al. investigated that optimized printing parameters (PPs) of fabricated part had insignificant internal cavity having least deviation in part dimensions, hole dimension and thickness [2]. Sahu et al. proposed that the dimensional precision of ABSP 400 parts is manufactured by FDM techniques and conducted the minimum experiments with Taguchi philosophy and further focused on single and multi-performance characteristics of responses [3].

Mahapatra and Sood proposed that they adopted Bayesian regularization to collect optimum network architecture due to its ability to fix sum of network constants not according to the consideration of network size and trained ANN model using Levenberg–Marquardt algorithm [4]. Sood et al. studied that the process parameters that are affecting the compressive stress significantly affect the test specimen geometry. They used quantum-behaved particle swarm optimization (QPSO) to obtain optimal parameters [5]. Equbal et al. focused on the five important process parameters of FDM process which is depending upon the tensile, flexural and impact strength of test specimen. They used bacterial foraging technique [6]. Senthilkumaran et al. studied

the five effective process parameter interaction calculated by Taguchi's L_{27} orthogonal array [7]. Panda et al. defined the impact of build orientation effect, thickness of layer and feed rate on the mechanical achievement of 3D printed PLA samples with a low cost. Mechanical response of the printed specimens is obtained by tensile and three-point bending tests [8]. According to Sood et al., the distortion data obtained by SL processed part is simulated by finite element method. Two significant factors liable for part in accuracy were volumetric shrinkage and curl distortion [9]. Taguchi method defined that the raster thickness width depends upon the layer of distortion, and the measured dimensions are presented by the LOM, FDM and SLS process [10, 11]. According to Companelli et al., the surface roughness is significantly affected by thickness and orientation of ABSP 400 plastic layer which is produced by an FDM 1650 machine [12]. Chacon et al. observed that the part orientation and part alignment depend upon the direction of the deposition [13].

2 Critical Literature Review

The immense review of the performance characteristics of FDM process is elaborately discussed, and the critical evaluation of significant research findings are explained. The poor surface finish leads least attention in FDM technology and which can be improved by controlling different parameters for dimensional precision [14–17]. It is concluded that for the different dimensional part generation or any critical contour, the significance of influencing factor combination varies and accordingly change in process parameters occurs. It also found after each performance response parameter is giving different results so to overcome this problem different optimization techniques are adopted [18, 19]. Mechanical performance development is another point which can be improved by specific control of extrusion temperature, design and inclination angle of nozzle, ambient temperature, etc [20, 21]. Though many researchers have tried to optimize the parameters to obtain dimensional accuracy from the enervative review of the literature, less attention has been paid for optimizing the inclination angle of test specimen if any. So there is an opportunity to optimize the process parameters by introducing the inclination angle for a standard specimen having one central hole with specific diameter. The design of the experiment is done based on Taguchi methodology to minimize the number of experiments as it is robust design technology [22].

3 Experimental Methodology

The FDM process is stipulated here due to its least cost and ease of manufacturing with less time and without the influence of laser in the academic field of research. The experiment is done by FDM process because in this process, high strength, isotropic, tailored properties of multi-materials parts are produced which can be directly used

for making functional prototype also uniform fine-grained microstructure is produced. In the FDM process ABSP 400 used as the specimen, it contains 90–100% ABS resin, (0–2%) mineral oil, (0–2%) tallow and (0–2%) wax. ABS is manufactured by polymerization of styrene and acrylonitrile in process of poly-butadiene (Table 1).

Fused deposition modelling (FDM) method mostly influenced by the input parameters which are used in this process are part orientation, layer thickness, raster angle and raster width to find the measuring process parameters length (L), width (W), thickness (T), diameter (D) and inclination angle (θ). In this experiment, two types of input parameters are used: one is fixed parameter and another is control parameter which are defined in Tables 2 and 3. The input parameters and their levels are represented in Table 3. Fixed parameters depend upon specific FDM machine set-up. The part build generation is along the vertical direction z-axis, as x- and y-axis are horizontally placed on build platform.

The experimental study for four control parameters mostly necessitates 81 (3^4) experiments in classical DOE but similar statistical result can be obtained by adopting Taguchi DOE methods. Considering four factors with 3-level, there are 8 degrees of freedom, and a suitable orthogonal array L_9 (3^4) is established. The designed array builds up with four columns for assigning factors and nine rows designating the trial or experiment conditions. The L_9 orthogonal array can contain a maximum no. of four factors and each factor at three levels. The experimental set-up having four

Table 1 Mechanical properties of ABSP 400 material

Mechanical properties	Unit	Extruded	Moulded
Density	g/cm^3	0.350–1.26	1.02–1.17
Rockwell hardness	HRC	90.0–121	68.00–115
UTS	MPa	27.00–52.00	28.00–49.00
Yield strength	MPa	20.0–62.0	13.00–65.00
Modulus of elasticity	GPa	1.52–6.10	1.00–2.65
Elongation yield	% (percentage)	0.620–30.0	1.70–6.00

Table 2 Fixed parameters

Parameter	Value	Unit
Style of part fill	Perimeter/style	–
Width of counter	0.4064	mm
Style of interior part	Normal solid	–
Visible surface	Normal raster	–
Shrink factor in XY and Z	1.0038	–
Air gap of perimeter/raster	0	mm

Table 3 Control parameters and their level

Parameters	Symbols	Levels		
		1	2	3
Thickness of layer	*A*	0.127	0.178	0.254
Orientation	*B*	0	15	30
Raster angle	*C*	0	30	60
Raster width	*D*	0.4064	0.4654	0.5064

factors without any interactions, then factors can be placed arbitrarily in any column. Therefore, in this case layer thickness (*A*) is assigned to first column, orientation (*B*) is assigned to column 2, raster angle (*C*) is assigned to column 3 and raster width (*D*) is assigned to column 4. After fabricating the model (ABS-M30) by Fortus 400mc machine set-up, the measurement of each dimension is obtained. Horizontal, vertical and hole dimensions are measured using Mitutoyo digital Vernier calliper having least count of 0.01 mm where external and internal distances can be precisely determined. Internal jaws are used for measuring internal dimensions of holes and cavities, i.e. length (*L*), width (*W*) and thickness (*T*). For measuring hole diameter (*d*), internal jaws are adjusted carefully until they touch the internal surface of hole. Angle of inclination of the specimen is measured by optical profile projector, an optical device with enlarge image. It contains a light source, condenser lens, projection lens and screen. A beam of light from the light source is passed through the condenser lens and projection lens and falls on the screen. The work piece will be placed in between the light source and condenser lens. A shadow image of the work piece will be created, while the work piece is placed (Figs. 1 and 2, Table 4).

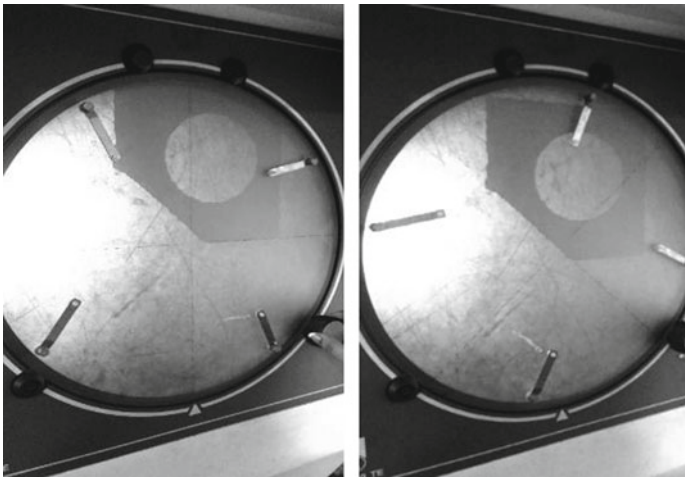

Fig. 1 Enlarged views of specimen on optical profile projector screen

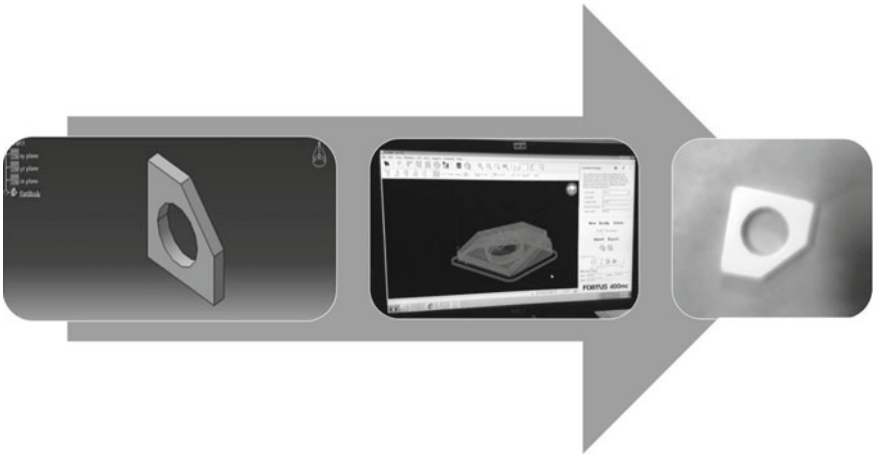

Fig. 2 Fabrication of FDM processed part

Table 4 L_9 OA (*S/N* ratio)

No of exp	Aspects				*S/N* ratio				
	A	*B*	*C*	*D*	ΔL	ΔW	ΔT	ΔD	$\Delta\theta$
1	1	1	1	1	22.3078	32.6404	16.4781	20.9151	7.3508
2	1	2	1	2	26.6198	23.9673	11.9261	13.4188	13.4732
3	1	3	1	3	22.6939	33.9794	15.5630	12.2759	10.2289
4	2	1	2	2	23.9673	21.9382	15.2223	18.9128	12.2878
5	2	2	2	3	13.8358	22.6939	11.0568	13.6945	11.2767
6	2	3	2	1	12.6404	23.9673	9.9879	12.0411	13.4324
7	3	1	3	3	16.2872	17.0774	12.2759	9.0363	11.1191
8	3	2	3	1	20.5992	19.7151	11.1608	10.1727	5.1927
9	3	3	3	2	13.9794	17.2867	8.8739	10.6527	1.1004

Relative change in dimensions of the measuring process parameters is calculated as per the following equation

$$\Delta X = |X - X_{\mathrm{CAD}}| \tag{1}$$

In Taguchi methodology, the significant use of *S/N* ratio is to find the required values of differences between the performance characteristics. The inspection of *S/N* ratio is based on three categories: (i) the lower the better, (ii) the higher the better and (iii) the more nominal the better. Objective of experiment plan is to reduce the relative change in length (ΔL), width (ΔW), thickness (ΔT), diameter (ΔD) and angle ($\Delta\theta$) as small as possible. Therefore, "smaller the better" quality characteristic is considered. For

"smaller the better" quality characteristic, *S*/*N* ratio (η) is expressed by Eq. (2) [23].

$$[S/N]_{\mathrm{SB}} = -10\log(\mathrm{MSD}_{\mathrm{SB}}) \tag{2}$$

where $\mathrm{MSD}_{\mathrm{SB}} = [y1 + 2y2 + 2y3 + 2 \ldots yn2]/n$

4 Grey Relational Analysis

Grey relational analysis (GRA) is an impacting measurement method in Grey theory that analyses uncertain relations among factors and interactions in a given system. The aim is to determine the optimum factor setting to satisfy all the five performance characteristics simultaneously. It is actually a measurement of the absolute value of the data difference between sequences, and it could be used to measure the approximate correlation between sequences. The Taguchi method is best suited for optimization of a single performance characteristic, whereas Grey-based Taguchi (Grey-Taguchi) combines all performance characteristics (objectives) considered in the study into a single value that can be used as the single characteristic in optimization problems. In Grey relational analysis (GRA), the experimental results of responses are normalized at first in the range between 0 and 1 due to different measurement units.

5 Analysis of Variance (ANOVA)

The analysis of data is done by using Minitab R17 software at 95% level of confidence value and the relation between the factors are resolved by the ANOVA technique. This technique is used to analyse the difference between group mean also used apportioning the variance of an output to a different input. The total degrees of freedom of four parameters and each contain three levels of eight which is equivalent to the experimental DF. The ANOVA results of ΔL, ΔW, ΔT, ΔD and $\Delta\theta$ are shown in Tables 5, 6, 7 and 8, respectively, and also using this value, main effect plots are prepared which show the minimizing response and *S*/*N* ratio.

6 Results and Discussions

In this section, there will be an analysis result obtained from the experiment done through FDM process, and all the resulting values show that there is a shrinkage occur in diameter of hole, but length, width, thickness and angle of inclination value is consistently greater than the model value those prepared by CAD software. Shrinkage along the diameter of hole may be obtained due to the progress of closer stresses in material deposition time. To minimize this error of part dimension, Grey-Taguchi

Table 5 ANOVA table for ΔL (change in length)

Sources	DF	Sum of squares	Variance	*F*-value	*P*-value	*P* (%)
A	2	97.72	48.86	3.88	0.025	46.72
B	2	35.07	17.54	1.39	0.418	16.76
*C**		25.21	12.60			
D	2	51.15	25.57	2.03	0.330	24.45
Error	2	25.21	12.60			12.05
Total	8	209.15				

*Signifies the pulled out parameter based on Grey Taguchi method

Table 6 ANOVA table for ΔW (change in width)

Sources	DF	Sum of squares	Variance	*F*-value	*P*-value	*P* (%)
A	2	225.24	112.618	17.02	0.056	77.47
*B**		13.24	6.618			
C	2	32.28	16.140	2.44	0.291	11.10
D	2	19.97	9.987	1.51	0.399	6.86
Error	2	13.24	6.618			4.5
Total	8	290.72				

*Signifies the pulled out parameter based on Grey Taguchi method

Table 7 ANOVA table for ΔT (change in thickness)

Sources	DF	Sum of squares	Variance	*F*-value	*P*-value	*P* (%)
A	2	23.425	11.7123	16.95	0.056	41.58
B	2	20.888	10.4440	15.11	0.062	37.07
*C**		1.382	0.6912			
D	2	10.638	5.3191	7.70	0.115	18.88
Error	2	1.382	0.6912			2.45
Total	8	56.333				

*Signifies the pulled out parameter based on Grey Taguchi method

Table 8 ANOVA table for ΔD (change in diameter)

Sources	DF	Sum of squares	Variance	*F*-value	*P*-value	*P* (%)
A	2	55.89	27.944	3.8	0.205	43.99
B	2	36.94	18.471	2.56	0.281	29.07
C		14.46	7.202			
D	2	19.81	9.903	1.38	0.421	15.59
Error	2	14.40	7.202			11.33
Total	8	127.04				

Table 9 ANOVA table for $\Delta\theta$ (change in inclination angle)

Sources	DF	Sum of squares	Variance	*F*-value	*P*-value	*P* (%)
A	2	67.218	33.690	9.53	0.095	48.33
*B**		7.051	3.525			
C	2	8.690	4.345	1.23	0.448	6.24
D	2	56.097	28.049	7.96	0.112	40.34
Error	2	7.051	3.525			5.07
Total	8	139.056				

*Signifies the pulled out parameter based on Grey Taguchi method

method is used because this is an effective method for determining the effectiveness of experimental design by relating the effect of the input parameters with that to the output parameters. Taguchi method uses a statistical tool to measure performance known as signal-to-noise ratio (*S*/*N*). *S*/*N* ratio consists of both mean and variability of performance characteristics. The main objective of this paper is to reduce the value of change in length (ΔL), width (ΔW), thickness (ΔT), diameter (ΔD) and angle ($\Delta\theta$), and those things are discussed.

Tables 5, 6, 7, 8 and 9 show the observed significant factors for different responses are different.

7 Main Effect Plot for *S*/*N* Ratios

These plots are shown the relation between input of FDM parameter and signal-to-noise ratio which obtain by the help of Minitab software. It responses mean for each factor level connected by a line and indicates the response in a different way with varying levels and factors independently (Figs. 3, 4, 5, 6 and 7).

From the plot, the most significant factors of combination on process parameters are obtained *A*, *B*, *D* for ΔL, *A*, *C*, *D* for ΔW, *A*, *B*, *D* for ΔT and ΔD, *A*, *C*, *D* for $\Delta\theta$, respectively.

8 Grey Relational Analysis for Dimensional Accuracy

For improvement in part dimensional accuracy, Grey-Taguchi method is used. In Grey-Taguchi method, the five input parameters are ΔL, ΔW, ΔT, ΔD and $\Delta\theta$, and smaller is the better type response which is considered. It represents a combination of all the response into a single response (Fig. 8).

Exclusive experimental investigation was carried out using Taguchi's method for different responses individually. Grey relational optimization was to find the significant factors affecting FDM processed part at different levels, and ANOVA

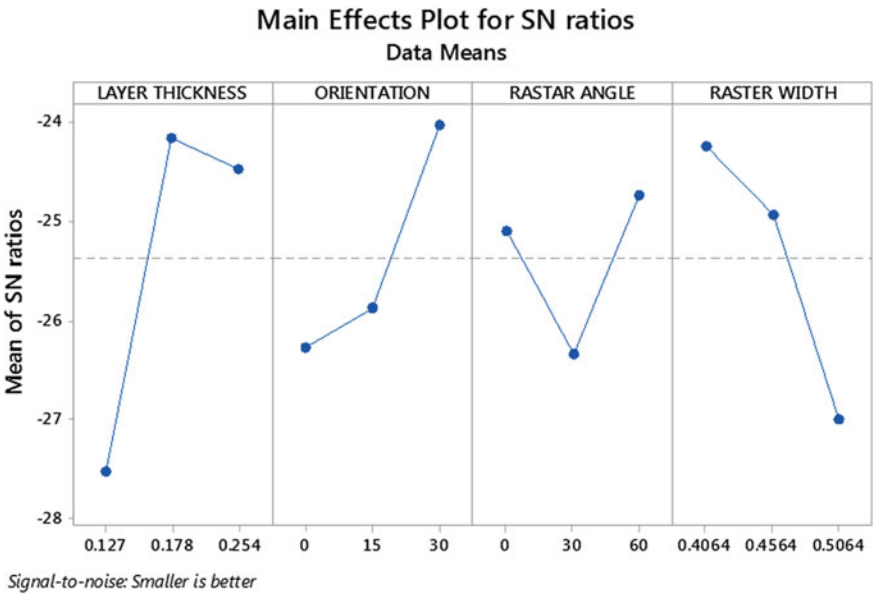

Fig. 3 Main effect plot for *S*/*N* ratios (ΔL)

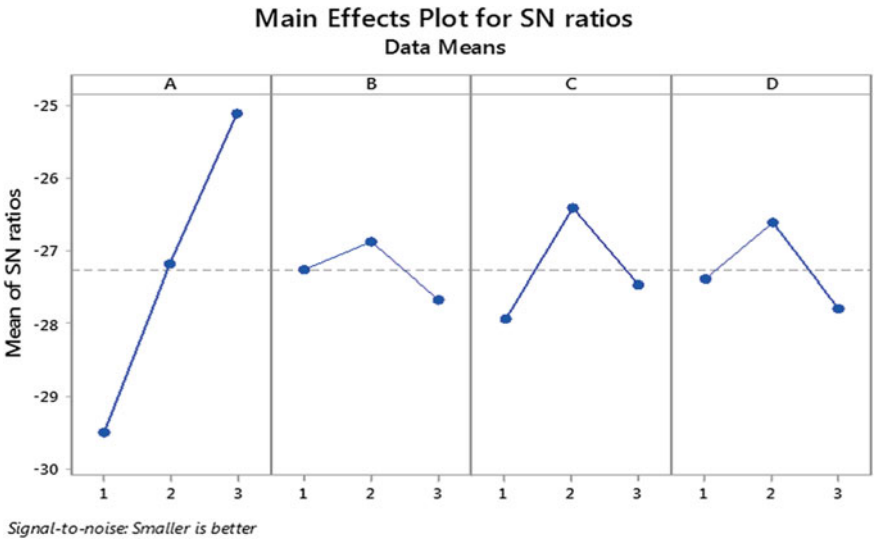

Fig. 4 Main effect plot for *S*/*N* ratios (ΔW)

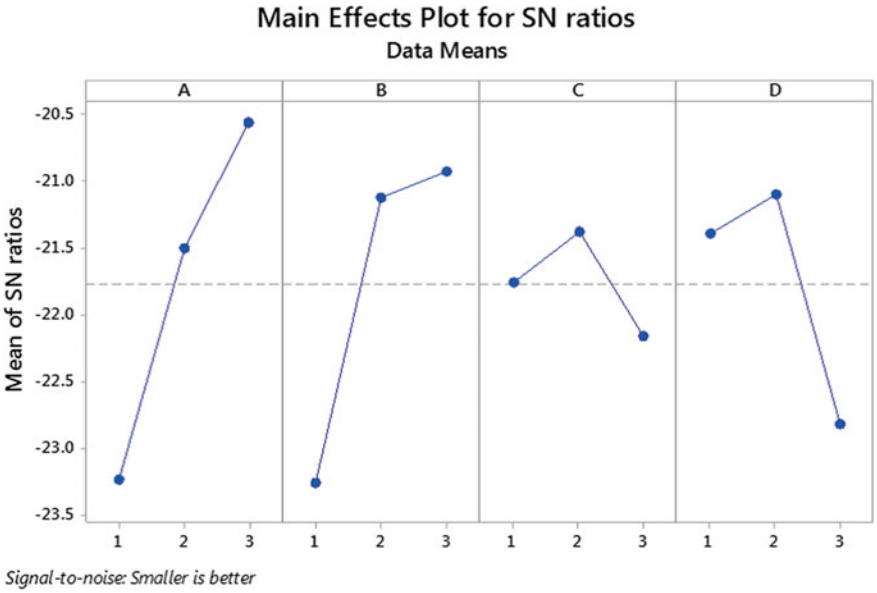

Fig. 5 Main effect plot for *S*/*N* ratios (ΔT)

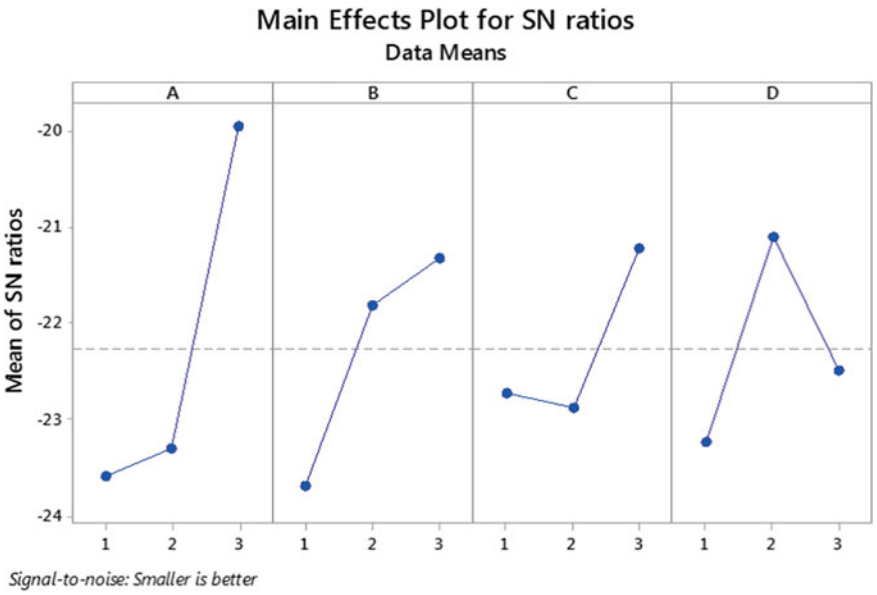

Fig. 6 Main effect plot for *S*/*N* ratios (ΔD)

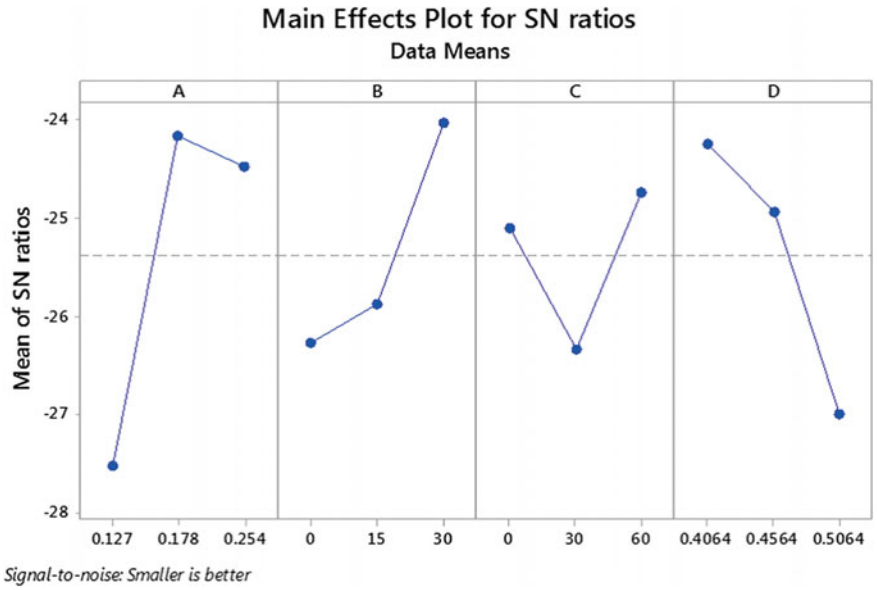

Fig. 7 Main effect plot for *S*/*N* ratios ($\Delta\theta$)

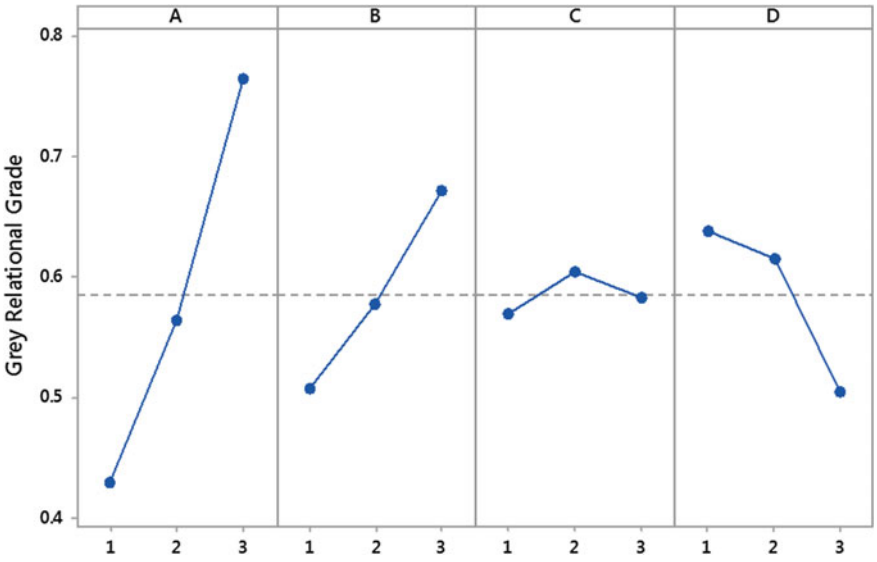

Fig. 8 Effects of FDM parameters on the multi-performance characteristics

Table 10 Contribution percentage

Factors	Contribution (%)					
	ΔL	ΔW	ΔT	ΔD	$\Delta\theta$	Grey relational grade
Layer thickness (A)	46.72	77.47	41.58	43.99	48.33	70.08
Orientation (B)	16.76	–	37.07	29.07	–	16.66
Raster angle (C)	–	11.10	–		6.24	–
Raster width (D)	24.45	6.86	18.88	15.59	40.34	12.49
Error (%)	12.05	4.55	2.45	3.4	5.07	0.74

was calculated to predict the percentage contribution of different factors at different levels. The percentage error for the difference in length, width, thickness and angle by Grey relational analysis is obtained: 12.05, 4.55, 2.45, 3.4, 5.07 and 0.74, respectively. This result shows that all the responses are combining into a single response using Grey-Taguchi method. It is more effective than considering the responses individually by the Taguchi method (Table 10).

9 Conclusions

In this current work, the FDM technique was used to fabricate acrylonitrile butadiene styrene (ABS-M30) parts. The process parameters were optimized at a common level setting using Grey-based Taguchi with DOE of Taguchi's philosophy to obtain the minimum changes in length, width, hole diameter, angle of orientation and thickness from the desired values simultaneously. Based on experimental studies carried out for optimization of the FDM process parameters, some of the important findings are obtained.

The height of the part considered in this work at maximum orientation of 30 will be 13.031 mm. If it is sliced with minimum thickness of 0.127 mm, a total of 102.60 slices will be required by simple arithmetic. It is found that shrinkage is dominant along the diameter of hole and of test part whereas the length, width, thickness and angle orientation are always more than the desired value. Ultimately, thickness of layer 0.255 mm, orientation of part 30°, raster angle of 30° and raster width of 0.4046 mm are optimal factor settings for developing all characteristics of performance concurrently. The contribution of layer thickness is more compared to all other measured constants for governing the change in dimension of FDM built part. Effect of process parameters on dimensional accuracy is studied on flat and circular profiles only.

References

1. Padhi, S.K., Sahu, R.K., Mahapatra, S.S., Das, H.C., Sood, A.K., Patro, B., Mondal, A.K.: Optimization of fused deposition modeling process parameters using a fuzzy inference system coupled with Taguchi philosophy. Adv. Manuf. **5**(3), 231–242 (2017)
2. Kaveh, M., Etefagh, A.H., Badrossamay, M.: Optimization of the printing parameters affecting dimensional accuracy and internal cavity for HIPS material used in fused deposition modeling processes. J. Mater. Process. Technol. **226**, 280–286 (2015)
3. Sahu, R.K., Mahapatra, S.S., Sood, A.K.: A study on dimensional accuracy of fused deposition modelling (FDM) processed parts using fuzzy logic. J. Manuf. Sci. Prod. **13**(3), 183–197 (2013)
4. Mahapatra, S.S., Sood, A.K.: Bayesian regularization-based Levenberg–Marquardt neural model combined with BFOA for improving surface finish of FDM processed part. Int. J. Adv. Manuf. Technol. **60**, 1223–1235 (2012)
5. Sood, A.K., Ohdar, R.K., Mahapatra, S.S.: Experimental investigation and empirical modelling of FDM process for compressive strength improvement. J. Adv. Res. **3**, 81–90 (2012)
6. Equbal, A., Sood, A.K., Toppo, V., Ohdar, R.K., Mahapatra, S.S.: Prediction and analysis of sliding wear performance of fused deposition modelling-processed ABS plastic parts. J. Eng. Tribol. **224**, 70–80 (2010)
7. Senthilkumaran, K., Pandey, P.M., Rao, P.V.M.: Influence of building strategies on the accuracy of parts in selective laser sintering. Mater. Des. **30**, 2946–2954 (2009)
8. Panda, S.K., Padhee, S., Sood, A.K., Mahapatra, S.S.: Optimization of fused deposition modelling (FDM) process parameters using bacterial foraging technique. Intell. Inf. Manage. **1**, 89–97 (2009)
9. Sood, A.K., Ohdar, R.K., Mahapatra, S.S.: Parametric appraisal of fused deposition modelling process using the grey Taguchi method. J. Eng. Manuf. **224** (2009)
10. Wang, R.J., Wang, L., Zhao, L., Liu, Z.: Influence of process parameters on part shrinkage in SLS. Int. J. Adv. Manuf. Technol. **33**, 498–504 (2007)
11. Pandey, P., Raghunath, N.: Improving accuracy through shrinkage modelling by using Taguchi method in selective laser sintering. Int. J. Mach. Tools Manuf. **47**, 985–995 (2007)
12. Campanelli, S.L., Cardano, G., Giannoccaro, R., Ludovic, A.D., Bohez, E.L.J.: Statistical analysis of stereolithographic process to improve the accuracy. Comput. Aided Des. **39**(1), 80–86 (2007)
13. Chacon, J.M., Caminero, M.A., Garcıa-Plaza, E., Nunez, P.J.: Additive manufacturing of PLA structures using fused deposition modelling: effect of process parameters on mechanical properties and their optimal selection. Mater. Des. **124**, 143–157 (2007)
14. Nizam, A., Gopal, R.N., Naing, L., Hakim, A.B., Samsudin, A.R.: Dimensional accuracy of the skull models produced by rapid prototyping technology using stereo lithography apparatus. Arch. Orofac. Sci. **32**, 60–66 (2006)
15. Zhu, H.H., Lu, L., Fuh, J.Y.H.: Study on shrinkage behavior of direct laser sintering metallic powder. Proc. Inst. Mech. Eng. J. Eng. Manuf. **220**, 183–190 (2006)
16. Huang, Y., Lan, H.: Dynamic reverse compensation to increase the accuracy of the rapid prototyping system. J. Mater. Process. Technol. **167**, 167–176 (2005)
17. Lehtihet, E., Tong, K., Joshi, S.: Software compensation of rapid prototyping machines. Precis. Eng. **28**, 280–292 (2004)
18. Xu, F., Wong, Y.S., Loh, H.T.: Toward generic models for comparative rapid prototyping and manufacturing. J. Manuf. Syst. **19**, 283–296 (2000)
19. Zhou, J., Herscovici, D., Chen, C.C.: Parametric process optimization to improve the accuracy of rapid prototyped stereo lithography parts. Int. J. Mach. Tools Manuf. **40**, 363–379 (2000)
20. Vasudevarao, B., Natarajan, D.P., Razdan, A., Mark, H.: Sensitivity of RP surface finish to process parameter variation. In: Solid Free Form Fabrication Proceedings, pp. 252–258. The University of Texas, Austin (2000)
21. Es-Said, O.S., Foyos, J., Noorani, R., Mendelson, M., Marloth, R., Pregger, B.A.: Effect of layer orientation on mechanical properties of rapid prototyped samples. Mater. Manuf. Processes **15**(1), 107–122 (2000)

22. Dao, Q., Frimodig, J.C., Le, H.N., Li, X., Putnam, S.B., Golda, K., Foyos, J., Noorani, R., Fritz, B.: Calculation of shrinkage compensation factors for rapid prototyping (FDM 1650). Comput. Appl. Eng. Educ. **7**(3), 186–195 (1999)
23. Anitha, R., Arunachalam, S., Radhakrishnan, P.: Critical parameters influencing the quality of prototypes in fused deposition modelling. J. Mater. Process. Technol. **118**, 385–388 (2001)

Performance of Laminated Composite Turbomachinery Blades Using Finite Element Method with Delamination

Sai Mouli Makineni, P. V. Satyanarayana Yalamachili, P. Phani Prasanthi, K. Sivaji Babu and M. Mounika

Abstract The aim of the present study is to analyze the composite twisted blades with pre-existed cracks as these are the key parts in the power unit such as turbomachinery. The composite 16-layered twisted blade is analyzed by varying the twisting angle (θ), stacking sequence $[0/90/90/0]_{2s}$, $[0/45/-45/0]_{2s}$, $[0/60/-60/0]_{2s}$ and type of composite lamina (glass/epoxy, Kevlar/epoxy and carbon AS4/epoxy) in the laminate. The structural performance of the composite twisted blade with the presence of debond at the center of the composite laminate is explored with finite element method. The changes in the structural response of the composite blade in terms of deformations, and normal and shear stresses are evaluated. The FE models are validated with published results. The present work is used for the effective design of turbomachinery blades with pre-existed cracks.

Keywords Composite blades · Finite element method · Normal and shear stresses · ANSYS

1 Introduction

Fiber-reinforced composite laminates are widely used in aircraft, aerospace, turbines and in other industries as a main load carrying member. These composite material behavior will be decreased by some defects such as matrix cracking, delamination between the laminas of the laminate and hygrothermal stresses [1–6]. Delamination means separation of laminas from the laminate due to the concentration of high interfacial stress between the laminas. Delamination within the composite structure

S. M. Makineni · P. V. Satyanarayana Yalamachili · P. Phani Prasanthi (✉) · K. Sivaji Babu · M. Mounika
Department of Mechanical Engineering, Prasad.V. Potluri Siddhartha Institute of Technology, Vijayawada, Kanuru, India
e-mail: pprasanthi.parvathaneni@gmail.com; saimouli121@gmail.com

L. Li et al. (eds.), *Advances in Materials and Manufacturing Engineering*, Lecture Notes in Mechanical Engineering, https://doi.org/10.1007/978-981-15-1307-7_2

is not clearly visible or hardly visible to the normal inspection methods. With existing powerful non-destructive methods, one can visualize the location of delamination in the laminate [7]. Delamination in the composite laminate increases the stress concentration factor and reduces the overall performance in terms of strength and stiffness [8].

On the other side, composite twisted plates are used in turbine blades, compressor blades, marine propellers and helicopter blades, and it is required to understand the stresses, deformation of these blades with flaws such as delamination and voids. Analysis of twisted plates with delamination has been studied extensively by many researchers. Analysis of thin rectangular plates under tension and twisting load was studied by Crispino and Benson [9]. Kar and Neogy [10] were studied the pre-twisted tapered and rotated cantilever beam to explore the effect of thermal gradient on the strength of the structure. The progress in the delamination with the local buckling of composite plates was studied using three-dimensional finite element methods [11].

A composite laminate is modeled using finite element method to understand the interaction of each layer of the laminate [12]. The dynamic behavior of a composite helicopter blade with crack was simulated by using extended finite element method. Natural frequency along with their mode shapes of the cracked composite blade is analyzed [13]. A thin ribbon flexible helicopter rotor blade is analyzed using Euler–Bernoulli beam theory, and the static and dynamic aeroelastic behavior is evaluated [14].

The one-dimensional beam analysis is replaced by a three-dimensional model using ANSYS with the application of static force. The authors identified [15] the ways to strengthen the structural performance of the three-dimensional rotor blade. The velocity gradient and probability of air vortexes in the rotor case are studied by selecting an arc-shaped rotor blade [16].

Two different positions of the mixed flow pump impeller blades (forward and trapezoidal) in the meridional annulus are studied to highlight the Von Misses stress distribution among different blade positions [17]. The fluid–structure interaction analysis of the blade, structural design loads and the blade structure was studied using the finite element method [18]. A numerical simulation of two types of axial composite impellers studied for fatigue life using finite element method and fluid dynamic method and using suitable experiments [19, 20]. From the above observations, it is observed that the finite element method is an effective tool to address the composite twisted plate subjected to different loads.

The objective of the present work is to identify the overall deformations and stresses of the twisted composite plate with delamination. The effect of stacking sequence, type of lamina in the laminate and influence of twisting angle on the overall performance of composite blade are identified.

2 Twisted Composite Laminate Blades with a Delamination

The composite twisted blade with a dimension of 100 mm × 100 mm is modeled by varying the twisting angle from 10° to 40°. The twisted composite blade with dimensions is shown in Fig. 1a. Finite element model of twisted plate with twisting angle of 30° is shown in Fig. 1b. The composite plate is made with unidirectional fiber-reinforced composite laminas of 16 layers with different layups with different materials. The material properties of each ply are given in Table 1.

The laminate is made with carbon/epoxy laminas. Each layer in a laminate is maintained to a thickness of 0.125 mm [22]. The composite twisted plate is made of 16 plies and these layers are arranged in XY plane with different stacking sequences such as $[0/90/90/0]_{2s}$, $[0/45/-45/0]_{2s}$ and $[0/60/-60/0]_{2s}$. The thickness of each ply is 0.125 mm. The composite plate is fixed at one end and a uniform pressure load of

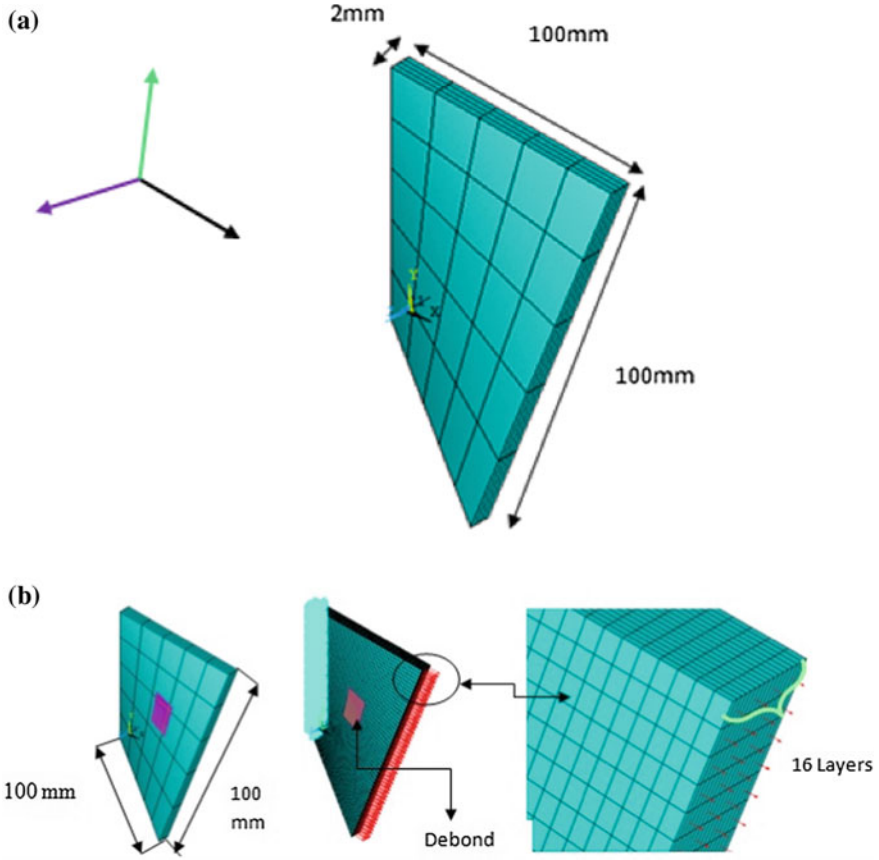

Fig. 1 **a** Composite twisted plate with debond, **b** geometry and finite element model of twisted composite laminate ($\theta = 30^0$)

Table 1 Material properties of a ply of S-glass/epoxy, Kevlar/epoxy and carbon/epoxy unidirectional layer of thickness 0.125 mm at fiber volume fraction 50% [21]

Name of the property	S-glass/epoxy	Kevlar/epoxy	Carbon/epoxy
Longitudinal elastic modulus (E_z) [GPa]	45	75	140
Transverse elastic modulus (E_x) or (E_y) [GPa]	11	5.5	10.3
In plane shear modulus (G_{XY}) [GPa]	4.5	2.2	7
Major poisson's ratio	0.29	0.34	0.27
Minor poisson's ratio	0.06	0.02	0.02

1 MPa is applied at the opposite end of the fixed support. The boundary conditions of a twisted blade are shown in Fig. 1b. The twisting angle of composite laminate varies from 10° to 40° with an interval of 10°. A delamination of 20 mm × 20 mm is created at the geometric center of the plate and in between the 8th and 9th layer of the laminate.

The objective of the present work is to study the effect of delamination of composite twisted plate on deformation, stresses by varying the twisting angle of the blade, stacking sequence, type of material using finite element method.

3 Fe Modeling of the Twisted Composite Blade with Embedded Delamination

Finite element-based software ANSYS has been used to evaluate the deformations and stresses of the delaminated composite blade. These stresses are responsible for the growth and propagation of the embedded delamination. The three-dimensional FE mesh of the twisted plate with the number of layers is shown in Fig. 1b. The twisted plate is modeled based on assumptions that the cross-section of the blade is constant and the material behavior is elastic. The composite plate is twisted with respect to the XY plane. Four key points are generated in ANSYS software; for example, first key point position is (0, 0), second key point location is (100, 0) and third and fourth key points are determined based on the twisting angle. These key points are connected through line option, and later, these lines are connected to generate area and the area is extruded in *Z*-direction. A 20-node layered volume element designated as SOLID 191 has been used to generate finite element mesh. Using the material properties in Table 1, the analysis is performed.

The mesh density of the finite elements has been increased (other than through-thickness direction, *Z*-direction) to ensure the convergence of the solution. SOLID 191 elements with 16 layers are generated, and each layer thickness is maintained at 0.125 mm. For the total layers, the thickness of the blade becomes 2 mm (16*0.125). This is indicated in Fig. 1b. The delamination of 20 mm is located at the geometric center and in between 8th and 9th ply of the laminate. To simulate the delamination,

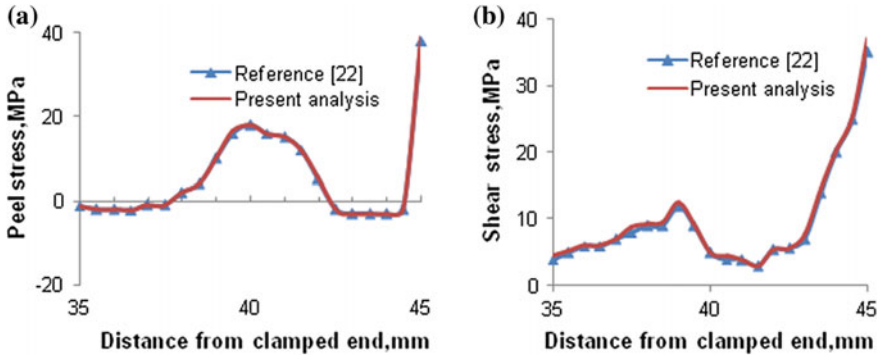

Fig. 2 **a** Variation of peel stresses, **b** variation of shear stresses

TARGET 170 and CONTACT 191 element with a contact algorithm of augment and contact behavior of standard were used [22].

3.1 Validation of Finite Element Procedure

The present finite element models are validated with the published results [22]. The authors studied an adhesive-strap lap joint with delamination of 10 mm using three-dimensional finite element method and evaluated peel stresses and shear stresses at the interface. Using the same data, the variation of peel stresses and shear stresses is computed using finite element-based software ANSYS and results are presented in Fig. 2a, b, which show close agreement between the published results and present results.

4 Results and Discussion

Variation of twisted composite blade overall deformation U_X, U_Y and U_Z in X-, Y- and Z-directions, respectively, and maximum normal stresses (σ_X, σ_Y and σ_Z directions) and interlaminar shear stresses in the τ_{XY}, τ_{YZ} and τ_{XZ} planes are evaluated from the simulated models.

(a) Deformation in X-direction (U_X) (Fig. 3).

1. The magnitude of deformation decreases with increase in twisting angle of the composite laminate.
2. The magnitude of this deformation is less for $[0/90/90/0]_{2s}$ layup, compared to other stacking arrangements, because the transverse stiffness is increased

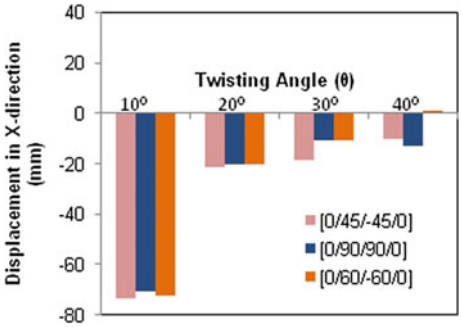

Fig. 3 U_X with respect to θ

by arranging the fiber parallel to the transverse direction of the laminate (*Y*-direction).

(b) Deformation in *Y*-direction (U_Y) and *Z*-direction (U_Z) (Figs. 4 and 5).

1. The magnitude of deformation in *Y*-direction (U_Y) is less compared to *X*-directional deformation (U_X). The pressure load is applied to the blade in *X*-direction; as a result, the resulting deformation will be more in *X*-direction (U_X), and compared to *X*- and *Y*-directional deformations, the *Z*-directional

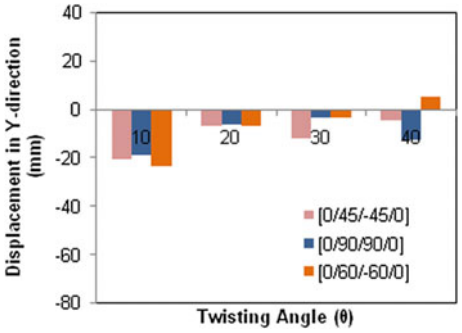

Fig. 4 U_Y with respect to θ

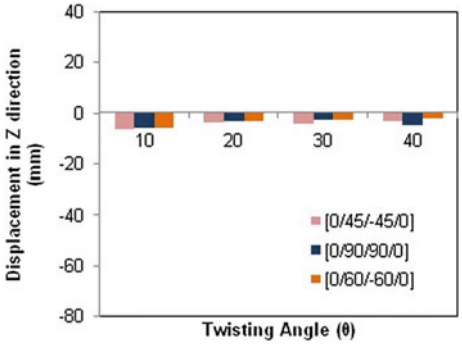

Fig. 5 Variation of deformation in *Z*-direction with respect to θ

deformation is less (U_z). The composite laminate is prepared by arranging layers in XY plane, and in the through-thickness direction (*Z*-direction), the deformation is less.

(c) Normal stresses in *X*-direction (σ_X) (Figs. 6).

1. The composite plate is fixed at one end and a uniform pressure of 1 MPa is applied to the other end of the plate. Due to this condition, the stresses are more in direction parallel to loading.
2. Magnitude of σ_X increases with the increase in twisting angle of the composite plate. The stress developed in the composite is more with $[0/60/60/0]_{2s}$ stacking sequence.
3. The minimum magnitude of these stresses is observed for $[0/45/-45/0]_{2s}$ layup. The delamination at the center of the plate increases the shearing effect. These effects will be decreased by arranging the laminate in $[0/45/-45/0]_{2s}$ stacking sequence.

(d) Normal stresses in *Y*- and *Z*-direction (σ_Y) (Figs. 8 and 10).

1. Magnitude of σ_Y and σ_Z increases with the increase in twisting angle of the composite plate.
2. Compared to normal directional stresses in *X*-direction, normal stress in *Y*- and *Z*-directions is less. The stress developed in the composite is more in σ_Y with $[0/90/90/0]_{2s}$ stacking sequence.

(e) Shear stresses (τ_{XY}, τ_{YZ} and τ_{XZ}) (Figs. 7, 9 and 11).

1. Compared to normal stresses, the magnitude of shear stresses is less with delamination.
2. Slight increment in theses stresses is observed with twisting angle of the plate.

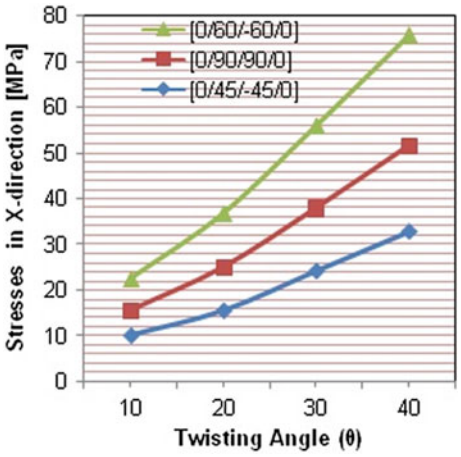

Fig. 6 Variation of σ_X w.r.t (θ)

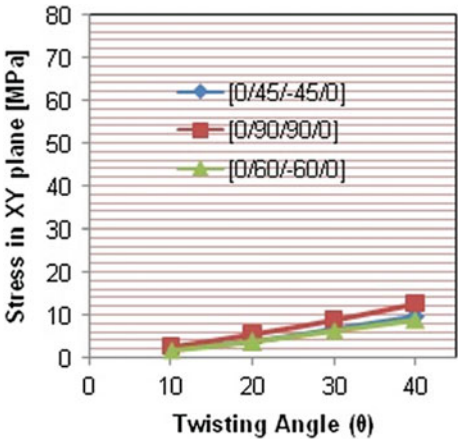

Fig. 7 Variation of τ_{XY} w.r.t (θ)

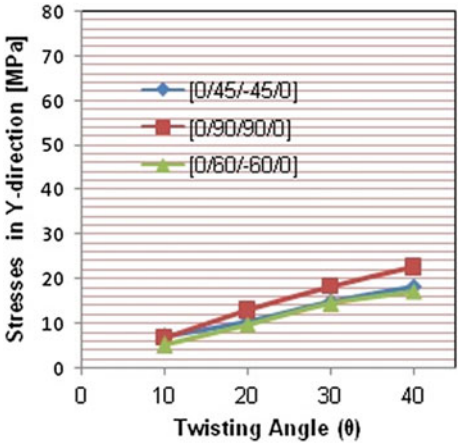

Fig. 8 Variation of σ_Y w.r.t (θ)

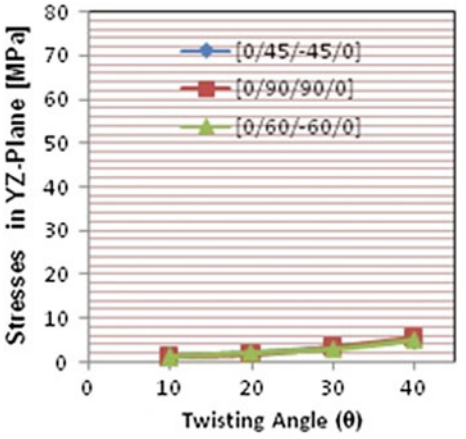

Fig. 9 Variation of τ_{YZ} w.r.t (θ)

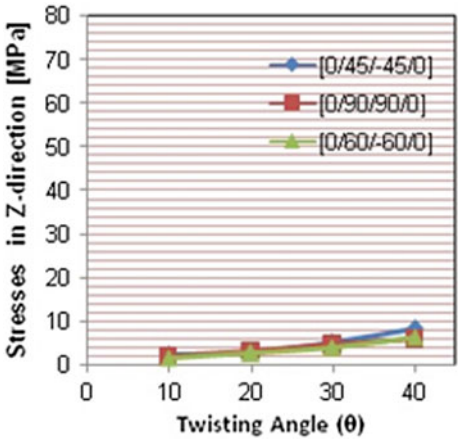

Fig. 10 Variation of σ_Z w.r.t (θ)

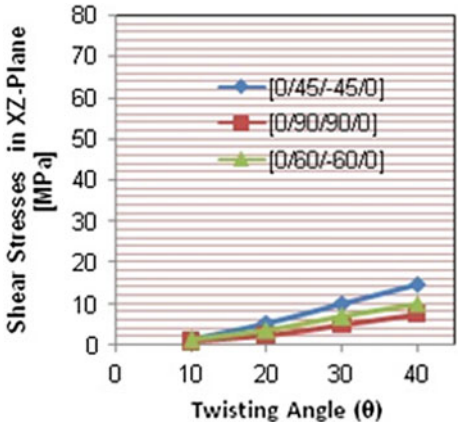

Fig. 11 Variation of i_{XZ} w.r.t (θ)

3. The influence of fiber stacking sequence has insignificant effect on shear stress of the composite plate with delamination.

(f) Normal stress (σ_X) for different materials (Fig. 12).

1. From the above results, it is observed that the normal stress σ_x magnitude is very high due to delamination for $[0/60/\text{-}60/0]_{2s}$ stacking sequence. The effect of material on the delamination is studied by selecting Kevlar/epoxy and AS4-carbon/epoxy composite for same stacking sequence.
2. It is observed that the AS4-carbon/epoxy laminate showed good response to withstand high normal stress (σ_X). Kevlar/epoxy performance is very less in the same point of view. Compared to glass/epoxy, the Kevlar/epoxy composite has high longitudinal strength, but Kevlar/epoxy composite transverse modulus is very less compared to other two laminates (glass/epoxy

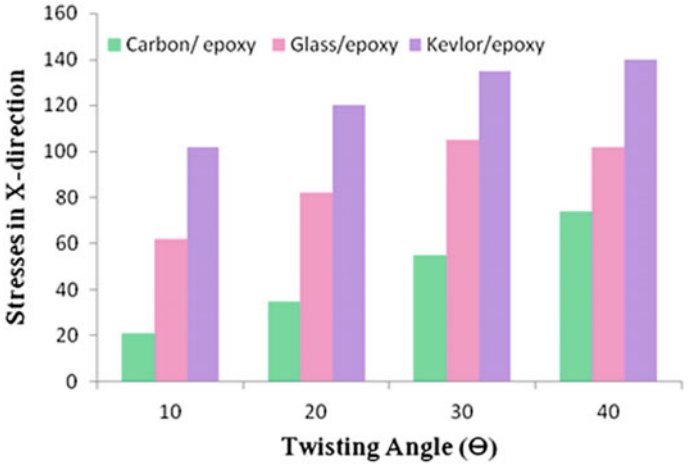

Fig. 12 Variation of σ_X with respect to (θ) and material

and AS4-carbon/epoxy). Because of this reason, the normal stress (σ_X) is very high for Kevlar/epoxy composite.

5 Conclusion

Three-dimensional finite element method is used to explore the twisted composite blade behavior in the presence of debond by varying the stacking sequence and the type of laminas in the laminate. The following conclusions are obtained from the present method.

- The magnitude of compressive deformations in *X*-direction (U_X) is more than other directional deformations (U_Y and U_Z) for various twisting angles under considered boundary conditions.
- The composite plate shows less deformation in *Z*-direction (U_Z) than other directional deformations (U_X and U_Y).
- The magnitude of normal stress (σ_X) is more compared to other directional stresses, and these stresses are increasing with increase in the twisting angle of the composite blade. Care should be taken while selecting a twisting angle of the composite blade in this regard.
- The selection of stacking sequence is one of the important aspects in the design of twisted composite blades. From the present work, it is observed that $[0/60/\text{-}60/0]_{2s}$ layup showed very higher stresses (σ_X) than other stacking sequences considered for the study.
- The effect of material on the (σ_X) for $[0/60/\text{-}60/0]_{2s}$ is studied. From these studies, it is observed that the normal stress (σ_X) is very high for Kevlar/epoxy composite.

References

1. Kumar, S.K., Ganguli, R., Harursampath, D.: Delamination detection in rotorcraft flex beams using fractal dimensions. In: The 19th International Conference on Composite Materials, Canada, 1–11 2013
2. Della, C.N., Shu, D.: Vibration of delaminated composite laminates: a review. Appl. Mech. Rev. **6**, 1–20 (2007). https://doi.org/10.1115/1.2375141
3. Gayathri, P., Umesh, K., Ganguli, R.: Effect of matrix cracking and material uncertainty on composite plates. Reliab Eng Syst Safe **95 716-28**, 716–728 (2010). https://doi.org/10.1016/j.ress.2010.02.004
4. Umesh, K., Ganguli, R.: Shape and vibration control of a smart composite plate with matrix cracks. Smart Mater. Struct. **18**, 025002 (2009)
5. Zou, Y., Tong, L., Steven, G.: Vibration-based model dependent damage (delamination) identification and health monitoring for composite structures-a review. J. Sound Vib. **230**, 357–378 (2000). https://doi.org/10.1006/jsvi.1999.2624
6. Pawar, P.M., Ganguli, R.: Genetic fuzzy system for damage detection in beams and helicopter rotor blades. Comput. Methods in Appl. Mech. Eng **192**, 2031–2057 (2003)
7. Smith, R.A.: Composite defects and their detection. Mater. Sci. Eng. **3**, Encyclopedia of Life Support Systems
8. Prasanthi, P., Rao, G.S., Gowd, B.U.: Mechanical performance of Buckminster fullerene-reinforced composite with interface defects using finite element method through homogenization techniques. Compos Interface **29**, 214–299 (2015). https://doi.org/10.1080/09276440.2015.1021223
9. Crispino, D.J., Benson, R.C.: Stability of twisted orthotropic plates. Int. J. Mech. Sci. **28,** 371–379 (1986). https://doi.org/10.1016/0020-7403(86)90056-1
10. Kar, R.C., Neogy, S.: Stability of a rotating, pre twisted non uniform cantilever beam with tip mass and thermal gradient subjected to a non-conservative forces. Comput. Struct. **33**, 499–507 (1989)
11. Whitcomb, J.D.: Three-Dimensional analysis of a post buckled embedded delamination. J Compos Mater, **23**, 862–889 (1989). https://doi.org/10.1177/002199838902300901
12. Kumar, J., Wurm, F.H.: Bi-directional fluid–structure interaction for large deformation of layered composite propeller blades. J. Fluids Struct. **57**, 32–48 (2015). https://doi.org/10.1016/j.jfluidstructs.2015.04.007
13. Nour, A., Gherbi, M.T., Tawfiq, I.: Analysis of the Bauschinger effect on a multilayer helicopter blade by XFEM simulation. Aerosp. Sci. Technol. **69**, 97–113 (2017). https://doi.org/10.1016/j.ast.2017.05.039
14. Sicard, J., Sirohi, J.: Aeroelastic stability of a flexible ribbon rotor blade. J. Fluids Struct. **67**, 106–123 (2016). https://doi.org/10.1016/j.jfluidstructs.2016.09.010
15. Vu, N.A., Lee, J.W., Le, T.P.N., Nguyen, S.T.T.: A fully automated framework for helicopter rotor blades design and analysis including aerodynamics, structure, and manufacturing. Chin. J. Aeronaut. **29**, 1602–1617 (2016)
16. Ren, W., Liu, J., Yu, Y.: Design of a rotor cage with non-radial arc blades for turbo air classifiers. Powder Technol. **292**, 46–53 (2016)
17. Srivastava, S., Roy, A.K., Kumar, K.: Design of a mixed flow pump impeller blade and its validation using stress analysis. Procedia Mat Sci **6**, 417–424 (2014). https://doi.org/10.1016/j.mspro.2014.07.053
18. Park, H.: Advanced turboprop composite propeller design and analysis using fluid structure interaction method. Compos Part B **97**, 111–119 (2016). https://doi.org/10.1016/j.compositesb.2016.04.054
19. Li, Q., Piechna, J., Mueller, N.: Simulation of fatigue failure in composite axial compressor blades. Mater. Des. **32**, 2058–2065 (2011). https://doi.org/10.1016/j.matdes.2010.11.051
20. Zhang, M., Liu, Y., Wang, W., Wanga, P., Li, J.: The fatigue of impellers and blades. Eng. Fail. Anal. **62**, 208–231 (2016). https://doi.org/10.1016/j.engfailanal.2016.02.001

21. Danial, I.M., Ishai, O.: Engineering mechanics of composite materials, 2nd edn. Oxford University Press, New York (2006)
22. Parida, S.K., Pradhan, A.K.: Influence of curvature geometry of laminated FRP composite panels on delamination damage in adhesively bonded lap shear joints. Int. J. Adhes. Adhes. **54**, 57–66 (2014). https://doi.org/10.1016/j.ijadhadh.2014.05.003

Numerical Simulation of Back-Extrusion Process

Ch. Bhanu Vardhan and K. Prakash Marimuthu

Abstract Finite element analysis has long been used to research the underlying phenomenon in different processes. It has helped researches to study the different processes in the microscopic level. The present work is a study on the back-extrusion process using finite element analysis using commercially available software. In the back-extrusion process, the workpiece undergoes large deformation. Large deformation subsequently affects the performance of the components when they are put into working condition. The aim of the present work is to determine the stress and strain distribution in the workpiece that undergoes back extrusion. Commercially available software Abaqus has been used in the analysis. A 2D axisymmetric model has been developed to do the studies. The results obtained are promising and can be used for further research.

Keywords Back extrusion · Stress and strain analysis · Finite element analysis

1 Introduction

Forming is a manufacturing process of making use of suitable stresses which cause plastic deformation to produce desired shapes or components. The essence of forming is abruptly increasing mechanical advantages though it is a tedious job. Analysis software programs like Abaqus and Ansys have reduced the cost of experimenting with all kinds of forming or any other processes. It is well known that the materials, which undergo high plastic deformation, produce better results in properties like improved grain, structure, strength and so on [1]. By extrusion methods, different shapes like cylinders and shafts are produced with better outputs than other methods. However, friction between die and workpiece improves the grain structure [2] and density of the material. It is also claimed that friction between the die and plunger can also change the flow parameters and properties of the material present between them [3, 4]. Strain hardening improves the strength of the workpiece and porosity

Ch. B. Vardhan · K. P. Marimuthu (✉)
Department of Mechanical Engineering, Amrita School of Engineering, Bengaluru, Amrita Vishwa Vidyapeetham, Bengaluru, India
e-mail: k_prakash@blr.amrita.edu

L. Li et al. (eds.), *Advances in Materials and Manufacturing Engineering*, Lecture Notes in Mechanical Engineering, https://doi.org/10.1007/978-981-15-1307-7_3

of the workpiece can be completely eliminated [5]. The cylindrical die helps in compaction of metal in confined space. Performance of the component improves after extrusion while there is a compromise with surface finish leading to surface defects like cracking and piping [6]; however, they have good weldability, excellent corrosion resistance and relatively good cold formability.

Extrusion is a compressive deformation process in which material is squeezed through an orifice in order to obtain a reduction in cross section of the material. Whereas back extrusion is a process in which a plunger moves against the material in the die, this makes the material in the die to move in the opposite direction to the plunger from the left-out region between die and plunger as shown in the figure. The authors in this paper tried to study the stresses involved after the extrusion process using a finite element model. The chosen thematic medium was dynamic, explicit step [7, 8].

2 Finite Element Model

The software used for this analysis is Abaqus 6.13 because it is basically designed to study the behaviour of solids and structures in a smooth and accurate manner under externally applied loads [9].

Adding to the earlier mentioned points, this model is designed as a 2D axisymmetric. The approximate global size of the mesh is 1.0 with maximum deviation factor of 0.1. The model has meshed with CAX3T elements. A linear triangular mesh has been used as a mesh type with standard size as mentioned above. The chosen mesh is so fine that the mesh does not distort during the extrusion process. Figure 1 shows the meshed model of the complete assembly in a 2D view, and Fig. 2 shows the constraints and loading regions. A 270-degree revolved model is shown in Fig. 3. The dimensions that were considered to make the model are shown in Fig. 4.

The properties which are used in the analysis were taken from Abaqus Simulia library [10], and they are provided in Tables 1 and 2.

3 Loads on Work and Boundary Conditions

Amount of load on the work depends on the type of loading and the type of material which includes flowability of the work. In this simulation, regardless of the amount of force required for the extrusion to happen, boundary condition velocity term has been included so as to analyse the number of stresses induced in the material using von Mises stress theory. The outer boundary of the die is grounded, and the plunger moves towards the inner diameter of the die with the uniform velocity of 30 mm/s. The bottom surface of the material has been constrained to move as shown in Fig. 2 for effective extrusion to happen and to avoid slip between die and material. The extrusion happens between the die and the plunger.

Fig. 1 Meshed model

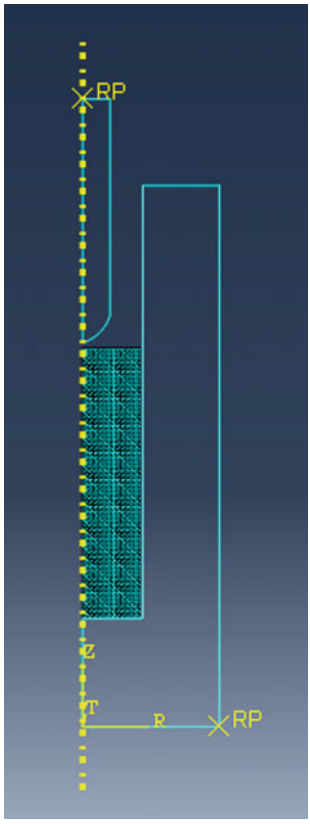

4 Simulation Results

The results are shown below for the given boundary conditions. The stress analysis and strain analysis are done for the considered plunging rate of 30 mm/s. Figure 5 shows the workpiece before, and Fig. 6 shows the workpiece after the extrusion.

4.1 Stress Analysis

This shows the plastic stress distribution thought out the workpiece. It is observed that the stress values vary from 18.88 to 32.5 MPa as shown in Fig. 7.

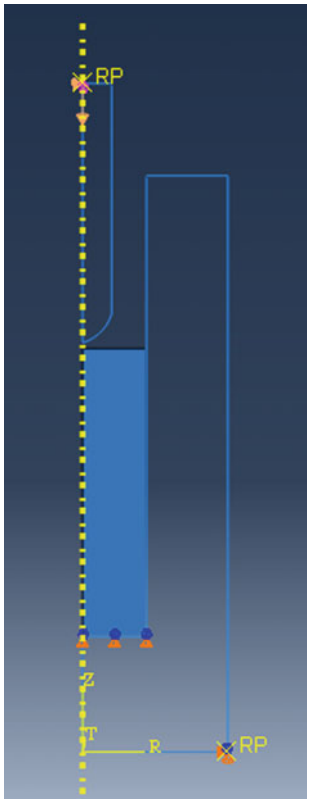

Fig. 2 Finite element boundary conditions

4.2 Strain Analysis

Figure 8 shows the strain values at different points in the form of bands after the extrusion process is complete. It is noted that the maximum value of the strain is 20.48. It also shows that elongation happened only in the region between the plunger and the work and there was no significant amount of strain values on the outer surface of the material.

5 Conclusion

A 2D axisymmetric model of the back-extrusion process was modelled using commercially available software. The aim of the present work was to analyse the stresses and strain in the aluminium back-extrusion process. The maximum plastic stress

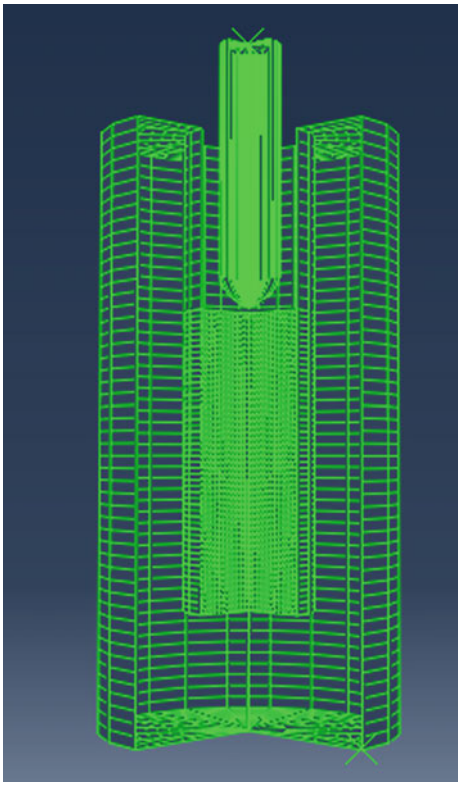

Fig. 3 Revolved model

recorded was 32.5 MPa in the simulated results. The presented results are preliminary with respect to the application of heat and stir friction processes, and further study will be continued in the future.

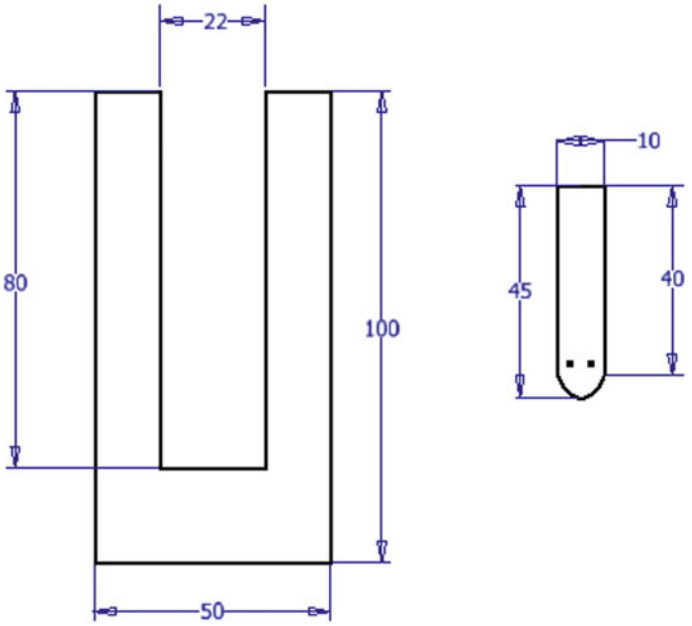

Fig. 4 Dimensions involved in the model (in mm)

Table 1 Material properties of aluminium

Parameter	Value
Density	2672 kg/m^3
Young's modulus	68.0 GPa
Poisons ratio	0.33
Specific heat	0.9 J/g K

Table 2 Stress values versus plastic strain

Plastic stress (MPa)	Plastic strain
27.0	0
31.0	0.25
32.5	0.5

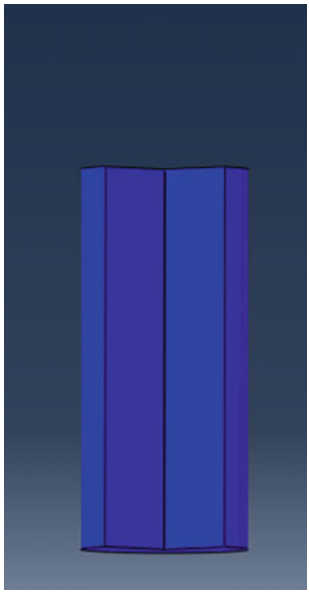

Fig. 5 Workpiece before extrusion

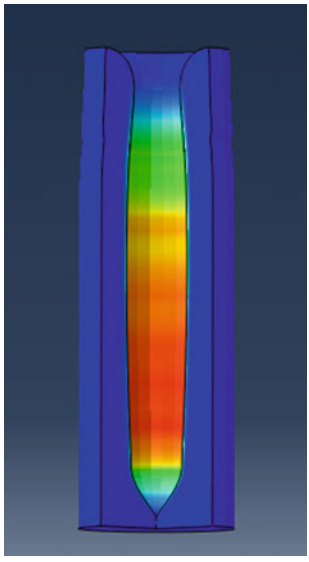

Fig. 6 Workpiece after extrusion

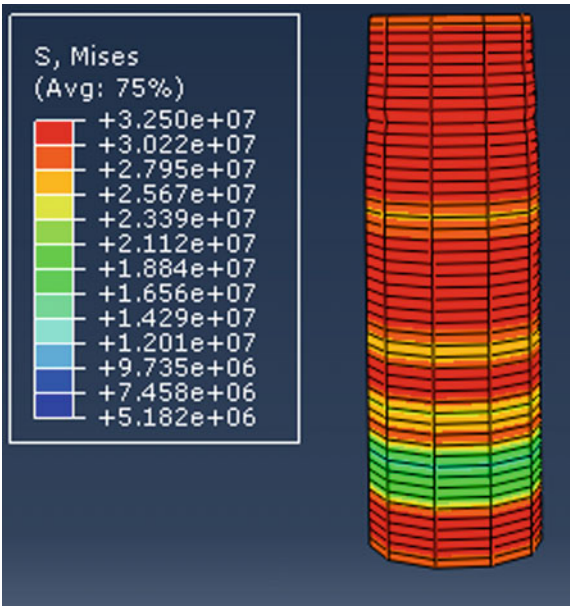

Fig. 7 von Mises stress distribution in the extruded tube

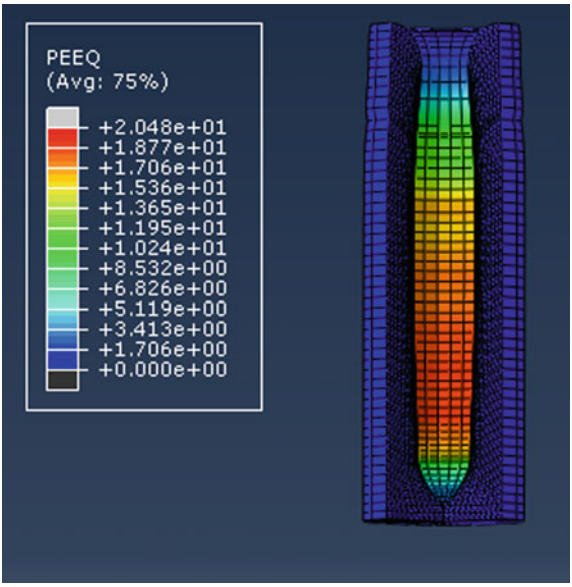

Fig. 8 Variation of strain values on the workpiece

References

1. Balokhonov, R., Romanova, V., Batukhtina, E., Sergeev, M., Emelianova, E.: A numerical study of the microscale plastic strain localization in friction stir weld zones. Facta Univ. Ser. Mech. Eng. **16**, 77–86 (2018)
2. Alihosseini, H., Faraji, G., Dizaji, A.F., Dehghani, K.: Characterization of ultra-fine-grained aluminum produced by accumulative back extrusion (ABE). Mater. Charact. **68**, 14–21 (2012)
3. Kathirgamanathan, P., Neitzert, T.: Modelling of metal extrusion using ABAQUS (2015)
4. Farhoumand, A., Ebrahimi, R.: Experimental investigation and numerical simulation of plastic flow behavior during forward-backward-radial extrusion process. Prog. Nat. Sci. Mater. Int. **26**, 650–656 (2016)
5. Fatemi-Varzaneh, S.M., Zarei-Hanzaki, A.: Accumulative back extrusion (ABE) processing as a novel bulk deformation method. Mater. Sci. Eng. A **504**, 104–106 (2006)
6. Sheikh, A.K., Qamar, S.Z., Raza, M.K.: Product defects in aluminum extrusion and their impact on operational cost. In: 6th Saudi Engineering Conference, vol. 5, p. 137 (2002)
7. Marimuthu, K.P., Prasada, H.P.T., Kumar, C.S.C.: 3D finite element model to predict machining induced residual stresses using arbitrary Lagrangian Eulerian approach. J. Eng. Sci. Technol. **13** (2018)
8. Marimuthu, P.K., Thirtha, P.H.P., Chethan, K.C.S.: Force, stress prediction in drilling of AISI 1045 steel using finite element modelling. IOP Conf. Ser. Mater. Sci. Eng. **225**, 12030 (2017)
9. Milutinovi, M., Viloti, D., Pepelnjak, T., Plancak, M.: Stress-strain state of combined backward—radial extrusion process of can-flanged part. J. Technol. Plast. **31**, 1–8 (2006)
10. Systèmes, D.: Simulia Problems Manual (2018)

Effect of Two Different Dielectrics on the Machining Performance and Their Parametric Optimization Through Response Surface Methodology

Deepak Kumar, Shakti Kumar, Dheeraj Kumar and Nirmal Kumar Singh

Abstract The present experimental work addresses a comparative analysis of machining performance in two different dielectrics fluid, i.e., EDM oil and deionized water on Nimonic (grade C-263) alloy. The performance measures specifically MRR, TWR, and SR were analyzed and optimized through response surface methodology. Furthermore, regression models were established to study the inter-relationship between the input variables and performance outcomes. Different values for the T_{ON} (20, 60 and 100 μs), duty factor (0.2, 0.5, 0.8), and I_p (4, 10, 16 A) were selected to perform the experiments. The experimental results revealed the fact that the machining condition significantly influenced the MRR, TWR, and SR. The competency of the developed model has been verified through analysis of variance (ANOVA). The outcomes of the analysis of variance indicate that the proposed regression models are well suited. Meanwhile, the predicted results were validated by performing a confirmation test, and error was found within the acceptable level.

Keywords Die-sink EDM · Nimonic alloy · EDM oil · Deionized water · Response surface methodology (RSM) · ANOVA · Surface topography

1 Introduction

Nowadays, due to a drastic increase in the application of superalloys such as Nimonic alloys, Inconel, titanium alloys, DC 53 die steel, SKD11 [1–3], etc. a comparative study of processing these superalloys is an active field for research [4]. These superalloys are coming in the category of difficult to cut material and poses superior physical and mechanical properties, for example, high oxidation resistance and corrosive resistance at high temperature and pressure compared to other materials. Nimonic C-263 superalloy is a very concerned material [5, 6] among these and poses a wide area of implementation in avionics industries, biomedical implants, gas turbine, and automotive engines [7, 8].

D. Kumar (✉) · S. Kumar · D. Kumar · N. K. Singh
Indian Institute of Technology (Indian School of Mines), Dhanbad, Dhanbad 826004, India
e-mail: deepakme521@gmail.com

L. Li et al. (eds.), *Advances in Materials and Manufacturing Engineering*, Lecture Notes in Mechanical Engineering, https://doi.org/10.1007/978-981-15-1307-7_4

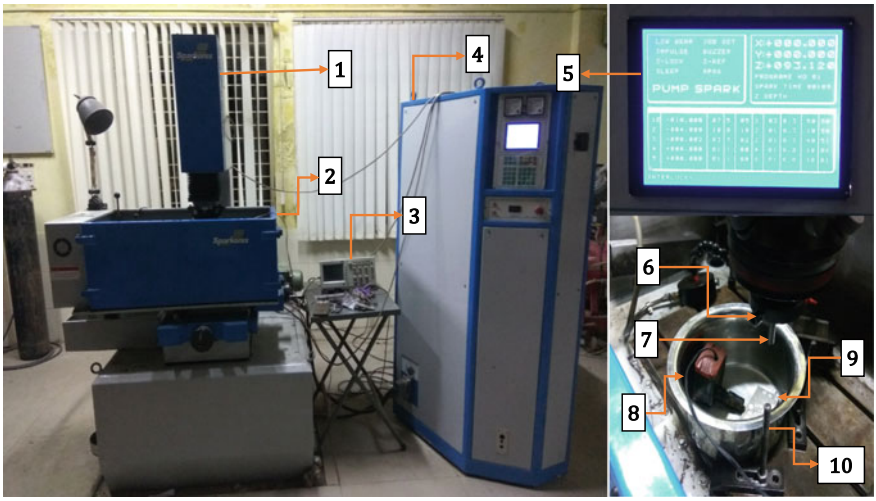

1. EDM Servo control 2. Dielectric tank 3 .Oscilloscope 4. Control unit 5. Control panel 6. Tool holder 7. Tool 8. Flushing nozzle 9. Workpiece 10. Holding stand

Fig. 1 Pictorial representation of experimental setup along with their key components

2 Method and Materials

2.1 Experimental Setup and Material Used

The present experimental works were completed on ZNC EDM (SPARKONIX-ENC35) machine setup as illustrated in Fig. 1. A Nimonic alloy (grade C-263) of size 94 mm × 50 mm × 5 mm plate was selected as workpiece material. A copper tool of diameter 10 mm (cylindrical shape) and length 60 mm with a rectangular cross-section (13 mm × 6 mm) was used as tool electrode. The tool material poses high melting (1080 °C) and boiling point with greater thermal conductivity (385 W/m K). A separate small container along with auxiliary pump was installed for the effective utilization of dielectric fluid and for better flushing. A set of first 15 data were collected using plane EDM oil while another 15 data were collected by using deionized water. Servo control with self-retraction mechanism was used to retain an appropriate gap between the tool and the workpiece.

2.2 Design of Experiment

In the present work, a Box–Behnken method based on RSM modeling approach was implemented for the design of the experiment. It comprises 2^k or 2^{k-1} factorial points, while 'k' denotes the total number of factors. This experimental design contains a

total of 15 combinations along with 8 corner points, 1 center point, and 6 star points. Three parameters with three levels were considered for experimental design.

3 Response Surface Modeling

Response surface regression (EDM oil): MRR versus current, duty factor, pulse-on time

$$\begin{aligned}\text{MRR (EDM oil)} = {} & -15.8 + 6.88\, I_p + 1.368\, \tau + 0.871\, T_{\text{on}} - 0.1436\, I_p * I_p \\ & - 0.00586\, \tau * \tau - 0.00072\, T_{\text{on}} * T_{\text{on}} + 0.0007\, I_p * \tau \\ & - 0.04008\, I_p * T_{\text{on}} - 0.00542\, \tau * T_{\text{on}} \end{aligned} \quad (1)$$

$$\begin{aligned}\text{TWR (EDM oil)} = {} & -7.62 + 1.859\, I_p + 0.0467\, \tau + 0.1053\, T_{\text{on}} - 0.0580\, I_p * I_p \\ & + 0.000350\, \tau * \tau - 0.000533\, T_{\text{on}} * T_{\text{on}} - 0.00087\, I_p * \tau \\ & + 0.00275\, I_p * T_{\text{on}} - 0.000650\, \tau * T_{\text{on}} \end{aligned} \quad (2)$$

$$\begin{aligned}\text{SR (EDM oil)} = {} & 1.38 + 0.606\, I_p - 0.0328\, \tau + 0.0670\, T_{\text{on}} - 0.01883\, I_p * I_p \\ & - 0.000059\, \tau * \tau - 0.000375\, T_{\text{on}} * T_{\text{on}} + 0.001670\, I_p * \tau \\ & - 0.001670\, I_p * T_{\text{on}} + 0.000548\, \tau * T_{\text{on}} \end{aligned} \quad (3)$$

Response surface regression (deionized water): MRR versus current, duty factor, pulse-on time

$$\begin{aligned}\text{MRR2 (deionized water)} = {} & -49.2 + 3.56\, I_p + 0.856\, \tau + 0.851\, T_{\text{on}} \\ & - 0.1793\, I_p * I_p - 0.00660\, \tau * \tau - 0.00164\, T_{\text{on}} * T_{\text{on}} \\ & + 0.0599\, I_p * \tau - 0.0236\, I_p * T_{\text{on}} - 0.00606\, \tau * T_{\text{on}} \end{aligned} \quad (4)$$

$$\begin{aligned}\text{TWR2 (deionized water)} = {} & -9.42 + 2.2332\, I_p + 0.122\, \tau + 0.661\, T_{\text{on}} \\ & - 0.0622\, I_p * I_p + 0.00108\, \tau * \tau - 0.000537\, T_{\text{on}} * T_{\text{on}} \\ & - 0.01480\, I_p * \tau + 0.00532\, I_p * T_{\text{on}} - 0.000298\, \tau * T_{\text{on}} \end{aligned} \quad (5)$$

$$\begin{aligned}\text{SR2 (deionized water)} = {} & -1.156 + 0.2255\, I_p + 0.0395\, \tau + 0.0540\, T_{\text{on}} \\ & - 0.00058\, I_p * I_p - 0.000237\, \tau * \tau - 0.000290\, T_{\text{on}} * T_{\text{on}} \\ & - 0.001790\, I_p * \tau - 0.001020\, I_p * T_{\text{on}} + 0.000225\, \tau * T_{\text{on}} \end{aligned} \quad (6)$$

4 Results and Discussion

4.1 Impact of Process Variables on MRR

MRR is one which is highly related to machining efficiency. The amount of deviation in the MRR was predicted by the parameter R^2 and is clarified by the input factors. $R^2 = 93.30\%$ in case of EDM oil and $R^2 = 81.21\%$ in case of deionized water reveal that the model is capable to predict the response with their corresponding accuracy. Figure 2 illustrates the normal probability graph for MRR in case of (a) EDM oil and (b) deionized water and influence of current, duty factor, and pulse-on time on MRR in case of (c) EDM oil and (d) deionized water. With the increase of current from 4 to 16 A, the discharge energy increases. Due to this sufficient energy, material removal of the Nimonic alloy was found more; consequently, MRR was found to be more in EDM oil as compared to deionized water. This was due to the fact that the fire point of EDM oil is less, so it deionizes quickly which leads to higher discharge energy and causes more material removal rate. Whereas in deionized water, the fire point was more, so it deionizes at a slower rate which leads to low discharge energy, and as a result, low MRR was found. Similarly, the same pattern was found in case of duty factor. In the case of deionized water, as pulse-on time rises from 20 to 100 μs, MRR increases, and the slope becomes steeper.

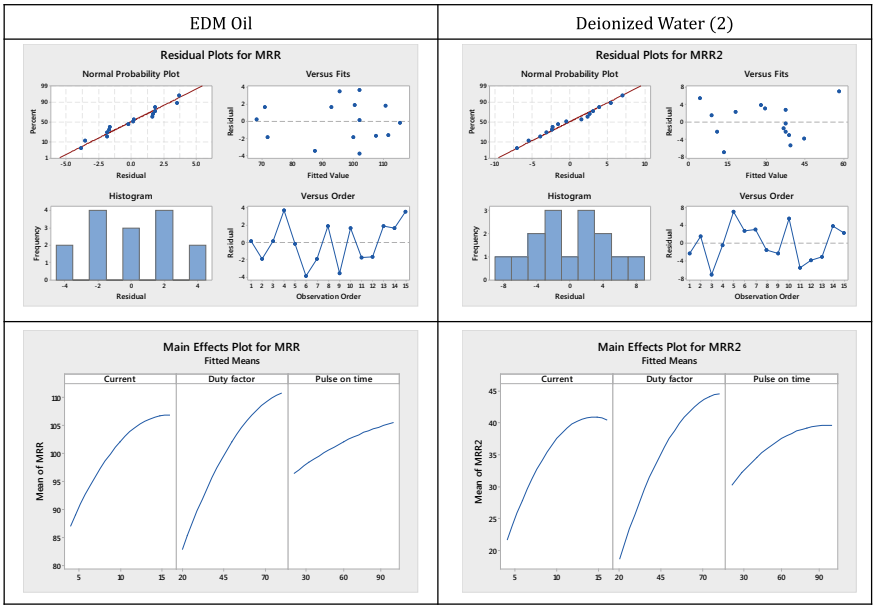

Fig. 2 Normal probability graph for MRR in case of **a** EDM oil and **b** deionized water, and influence of current, duty factor, and pulse-on time on MRR in case of **c** EDM oil and **d** deionized water

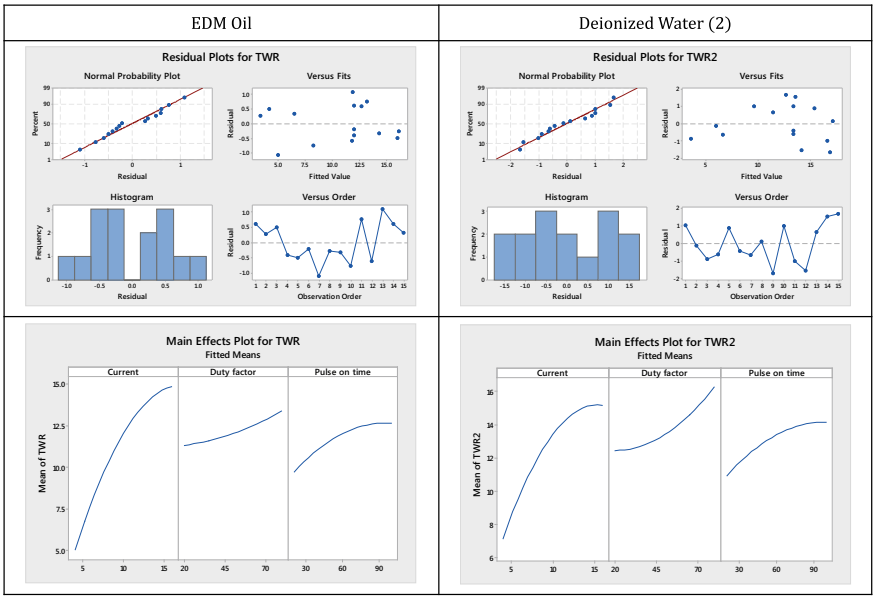

Fig. 3 Normal probability plot for TWR in case of **a** EDM oil and **b** deionized water and influence of current, duty factor, and pulse-on time on TWR in case of **c** EDM oil and **d** deionized water

4.2 Impact of Process Variables on TWR

TWR helps to define the machining efficiency in any EDM system. $R^2 = 93.57\%$ in case of EDM oil and $R^2 = 81.96\%$ in case of deionized water reveal that the model is capable to predict the response and their corresponding accuracy. It was perceived that by raising the value of all three parameters, surface roughness increases. Normal probability plot for TWR in case of (a) EDM oil and (b) deionized water is displayed in Fig. 3. TWR is found to be more in the case of deionized water due to the formation of some compounds.

4.3 Impact of Process Variables on SR

Surface roughness defines the durability and functionality of the surface in the actual area of work. In the present experimental work, the effort was made to investigate the impact of process variables on the machining outputs via response surface methodology (RSM) with two critical dielectrics, i.e., EDM oil and deionized water. $R^2 = 94.52\%$ in case of EDM oil and $R^2 = 92.06\%$ in case of deionized water reveal that the model is capable to predict the response with high accuracy. It was perceived that by raising the value of all three parameters, surface roughness increases due to crater

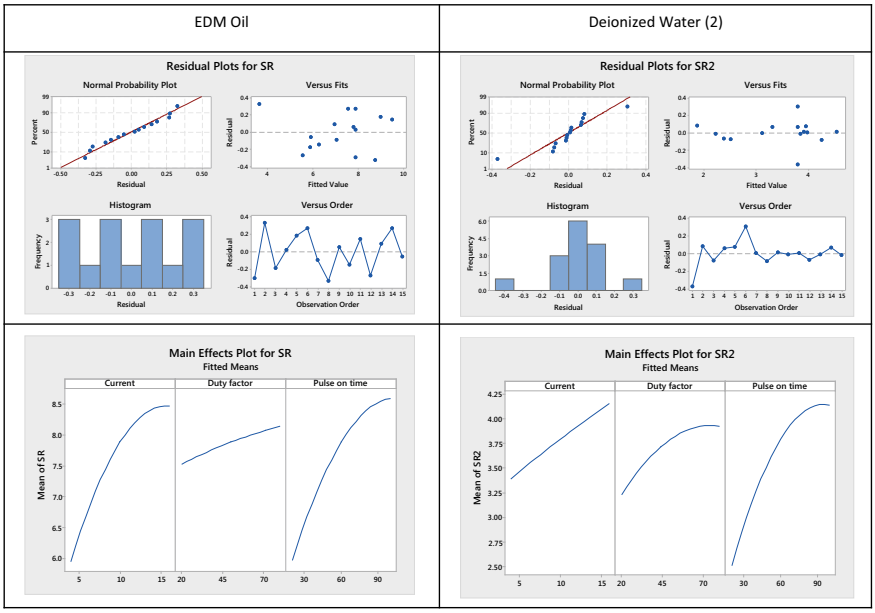

Fig. 4 Normal probability plot for SR in **a** EDM oil and **b** deionized water and influence of current, duty factor, and pulse-on time on SR in case of **c** EDM oil and **d** deionized water

formation. The better surface was seen in the case of deionized water due to better flushing condition and a broader gap between electrodes. SR is majorly influenced by all the three factors peak current, pulse-on time, and pulse-off time. Figure 4 illustrates the normal probability graph for SR in (a) EDM oil and (b) deionized water and effect of current, duty factor, and pulse-on time on SR in case of (c) EDM oil and (d) deionized water. In order to attain a better surface finish, set peak current and pulse-on time at low levels.

4.4 Surface Topography

Conducting the experiment on various parameters to set up the lower surface roughness images is obtained at a magnification of (10× and 20×) as presented in Fig. 5. In the inspected images, holes and cracks were found more in EDM oil whereas lesser holes and cracks are perceived in deionized water. In EDM oil, the SR obtained was more showing uneven deposition of molten material. It had been justified that the material removal was less irregular and micro-cracks and micro-holes were fewer in number as compared to EDM oil.

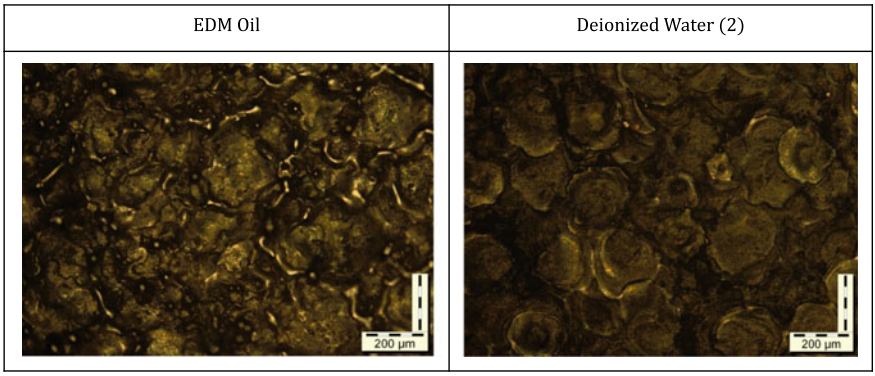

Fig. 5 Optical images of the finished surface in case of **a** EDM oil and **b** deionized water at 10× and 20× magnification

4.5 Optimization and Analysis of the Process Parameters

The variation in the output parameters such as surface roughness, tool wear rate, and material removal rate with respect to the variation in current, pulse-on time, and duty factor is shown in Fig. 6. The figure shows the minimum surface roughness and wear rate and maximum MRR trends. Meanwhile, Fig. 7 shows optimization through RSM. The optimum input parameter with EDM oil is found to be current 4.11 A, duty factor 80%, and pulse on time 31.313 µs, and optimum output values are 3.9 µm, 6.2 mm^3/min, and 90.13 mm^3/min (SR, TWR, and MRR). In case of deionized water, current 16.0 A, duty factor 80%, and pulse-on time 20 µs were the optimum condition while optimum output values were 2.6 µm, 12.0 mm^3/min, and 63.9 mm^3/min (SR, TWR, and MRR).

5 Conclusions

The machining of Nimonic C-263 using two different dielectrics (EDM oil and deionized water) has been successfully examined. The major conclusions drawn from the above investigation are as follows.

1. The developed regression models were well suited with the experimental data having confidence level approx. 95%. The statistical investigation of experimental data results indicate the significant influence of process variables on MRR, TWR, and SR. MRR increases with rising in pulse-on time, duty factor, and peak current; however, the current was the most influential parameter as compared to other two. Maximum and Minimum values of MRR obtained were 115.45 and 68.28 mg/min in case of EDM oil and 66.6 and 65.2857 mg/min in case of deionized water. MRR was found to be more in EDM oil as compared to deionized

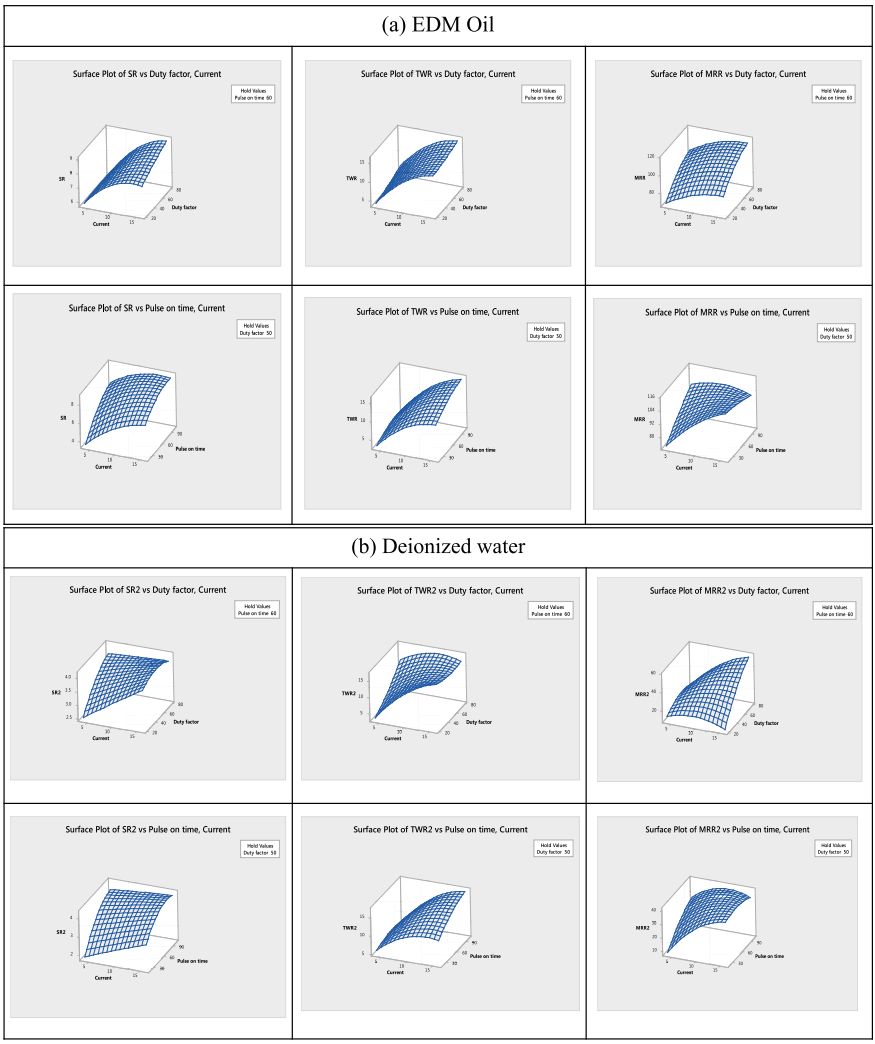

Fig. 6 Surface plot of the response output with input parameter in **a** EDM oil and **b** deionized water

water. This may be due to the fire point of EDM oil which is less, so it deionizes quickly which leads to higher discharge energy and causes more material removal rate.

2. TWR significantly influences the machining efficiency. Maximum and Minimum values of TWR obtained are 15.87 and 3.66 mg/min in case of EDM oil and 14.32 and 2.66 mg/min in case of deionized water. TWR was found a little bit more in case of deionized water as compared to EDM oil.

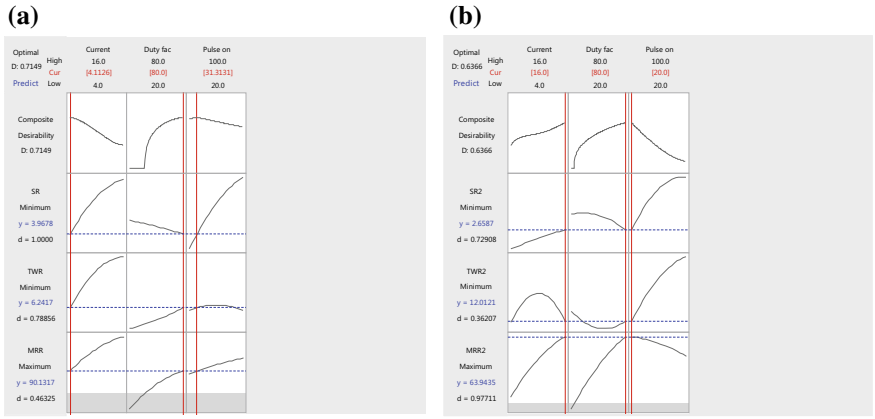

Fig. 7 Optimization plot of **a** EDM oil and **b** deionized water

3. SR was majorly affected by the factors peak current, pulse-on time, and pulse-off time during machining of Nimonic alloy. Maximum and Minimum values of SR obtained were 9.6504 and 3.968 μm in case of EDM oil and 4.551 and 1.9556 μm in the case of deionized water. Better SR was obtained in case of deionized water compared to EDM oil.
4. If the material removal rate is concerned, then EDM oil is more preferred than deionized water while deionized water is more preferred as dielectric than EDM oil in case of surface alloying.

Acknowledgements Special thanks to Dr. A. R. Dixit and Dr. Amitava Mandal for providing the experimental setup and support.

References

1. Wang, F., Liu, Y., Shen, Y., Ji, R., Tang, Z., Zhang, Y.: Machining performance of Inconel 718 using high current density electrical discharge milling. Mater. Manuf. Process. **28**, 1147–1152 (2013). https://doi.org/10.1080/10426914.2013.822985
2. Kanlayasiri, K., Boonmung, S.: Effects of wire-EDM machining variables on surface roughness of newly developed DC 53 die steel: design of experiments and regression model. J. Mater. Process. Technol. **192–193**, 459–464 (2007). https://doi.org/10.1016/j.jmatprotec.2007.04.085
3. Zhang, G., Zhang, Z., Guo, J., Ming, W., Li, M., Huang, Y.: Modeling and optimization of medium-speed WEDM process parameters for machining SKD11. Mater. Manuf. Process. **28**, 1124–1132 (2013). https://doi.org/10.1080/10426914.2013.773024
4. Rajesha, S., Sharma, A.K., Kumar, P.: On electro discharge machining of Inconel 718 with hollow tool. J. Mater. Eng. Perform. **21**, 882–891 (2012). https://doi.org/10.1007/s11665-011-9962-8
5. Pramanik, A., Arsecularatne, J.A., Zhang, L.C.: Machining of particulate-reinforced metal matrix composites. Mach. Fundam. Recent Adv., 127–166 (2008). https://doi.org/10.1007/978-1-84800-213-5_5

6. Boswell, B., Islam, M., Pramanik, A.: Sustainable machining of aerospace material. In: World Congress on Engineering—WCE 2013, vol. III (2013)
7. Ulutan, D., Ozel, T.: Machining induced surface integrity in titanium and nickel alloys: a review. Int. J. Mach. Tools Manuf. **51**, 250–280 (2011). https://doi.org/10.1016/j.ijmachtools.2010.11.003
8. Jawahir, I.S., Brinksmeier, E., M'Saoubi, R., Aspinwall, D.K., Outeiro, J.C., Meyer, D., Umbrello, D., Jayal, A.D.: Surface integrity in material removal processes: recent advances. CIRP Ann. Manuf. Technol. **60**, 603–626 (2011). https://doi.org/10.1016/j.cirp.2011.05.002

Optimized Path Planning for Three-Wheeled Autonomous Robot Using Teaching–Learning-Based Optimization Technique

Abhishek K. Kashyap and Anish Pandey

Abstract Path planning is a leading topic in the field of the wheeled robot (WR). Three basic characteristic path planning should have when the WR is traveling toward the goal: (1) obtain information about the given working space conditions, (2) location of itself, and (3) optimize the decision to reach the target. The current research paper focuses on obtaining an efficient and robust technique to guide the WR. Teaching–learning-based optimization technique is the centerpiece of the present research work. Fitness function has been presented to optimize the path planning and reaching target. Parameters selected for the proposed technique are (1) distance between robot, start point, goal, and obstacles and (2) turning angle while avoiding obstacles. The technique is examined in various environments with the different level of difficulties. The WR efficiently reaches the target by avoiding collision with the obstacles. In addition, the proposed technique is compared with the previously used technique. The obtained simulated results justified that the teaching–learning-based optimization technique selects better travel path and have shorter travel length.

Keywords Wheeled robot · Path planning · Obstacle avoidance · Teaching–learning-based optimization · Static obstacles

1 Introduction

To obtain an efficacious path planning, researchers put the deep attention on navigational strategies. Path planning is defined as obtaining an optimal path to guide the WR from the start point to the target by avoiding collision with the obstacles. Path planning becomes a broad topic for researchers. Figure 1 describes the wheeled robot embedded with an efficient and robust technique gives us optimum, shortest, and collision-free path planning. Algabri et al. [1] have used particle swarm optimization (PSO) to optimize the fuzzy logic controller by adjusting the membership function automatically. Real Khepera III platform was the main focus, and the

A. K. Kashyap · A. Pandey (✉)
School of Mechanical Engineering, KIIT Deemed to be University, Patia, Bhubaneswar 751024, India
e-mail: anish06353@gmail.com

L. Li et al. (eds.), *Advances in Materials and Manufacturing Engineering*, Lecture Notes in Mechanical Engineering, https://doi.org/10.1007/978-981-15-1307-7_5

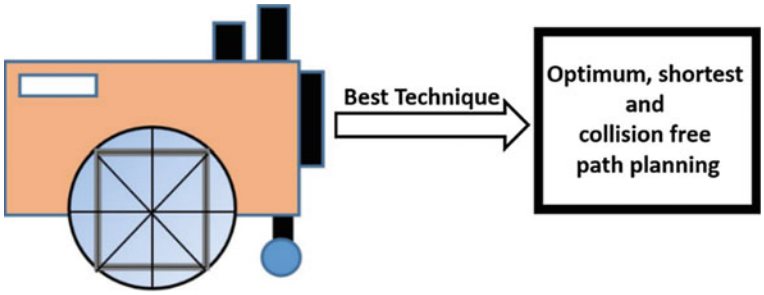

Fig. 1 Result of best technique on implementation in the wheeled robot

proposed technique was compared with it. Liu et al. [2] outlined the genetic fuzzy controller. Authors implemented a genetic algorithm so that enhanced parameters of membership function and scaling factor can be obtained. The neuro-fuzzy technique has been proposed in [3] for the path planning of autonomous mobile robot (AMR). Weighing factor is determined to minimize the count of fuzzy rules. Korkmaz and Durdu [4] have concluded that A* and PRM technique is efficient in terms of travel length and elapsed time, respectively. Lu and Gong [5] experimented in an unknown environment with AMR embedded with PSO. They implemented PSO to obtain the best path, but it lacks in modifying the control parameters. Li and Chen [6] have carefully used a five-order polynomial to design smooth trajectory based on PSO and adaptive neural network control. Parhi et al. [7] have simulated and experimented the theory to find the behavior of swarm intelligence techniques. Using the proposed technique, authors try to obtain the optimized path for autonomous wheeled robot.

2 Kinematics of Wheeled Robot

Kinematics defines the geometry of motion. It describes the initial conditions and portrays the positions of the WR. Steering of the WR is retrieved by utilizing various conditions, which are listed below in equations. Different property of wheels should be attained; these are (1) non-deformable, (2) pure rolling ($v = 0$ at contact points), and (3) no slip, skid, or slide. a is the radius of wheels; x is the distance between powered wheels. R is the point which is used to estimate the position and motion of the WR. It is pointed at the intersection of the axis of the powered wheel and a straight line passing through the center of mass of the system. Figure 2 describes the schematic diagram of the WR in (X_0, Y_0) plane. (X_N, Y_N, α) is the location and the orientation of the WR. The axes (X_0, Y_0) indicate inertial global reference frame with origin O. α is the angular difference between the global and reference frames. The global reference frame is denoted by point R on the robot chassis specified by coordinates (X, Y). Center of mass is represented by C.

Description of kinematic model is shown by following equations:

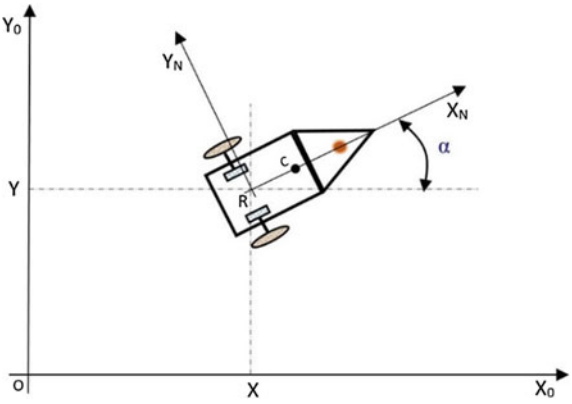

Fig. 2 Schematic diagram of wheeled robot in X_0–Y_0 plane

$$\dot{x} = (W_\mathrm{l} + W_\mathrm{r}) \cos \alpha/2 \tag{1}$$

$$\dot{y} = (W_\mathrm{l} + W_\mathrm{r}) \sin \alpha/2 \tag{2}$$

$$\dot{\alpha} = (W_\mathrm{l} - W_\mathrm{r})/b \tag{3}$$

where W_l = velocity of the left wheel, W_r = velocity of the right wheel, and b = track width between two wheels.

Following conditions are used for the orientation of the WR:

1. $W_\mathrm{l} = W_\mathrm{r}$, Robot travel straight.
2. $W_\mathrm{l} < W_\mathrm{r}$, Robot turns left.
3. $W_\mathrm{l} > W_\mathrm{r}$, Robot turns right.

3 Navigational Algorithm

Teaching–learning-based optimization technique is the centerpiece of this research paper. It is applied to optimize the path planning for an autonomous, obtain a shortest and collision-free path. TLBO is a nature-based technique that depends upon the teaching and learning skill of teacher and learner, respectively. The ability of the teacher to teach decides the strength of optimized result because at last teacher (best learner) is described as the best solution. TLBO optimizes the problem for two times in a single run, one after teacher phase and second after the learner phase. This process optimizes the path planning of the robot better than other optimization technique [9] and provides the shortest and collision-free path.

Rao et al. [8] have proposed TLBO, and in this paper, it is inserted in path planning. Researchers observed the behavior of learning the skill of learner from teachers and other learner and proposed this technique. Implemented technique mainly contains

two phases: One is teacher phase described in Fig. 3a, and second is the learner phase described in Fig. 3b. Teacher phase represents the first optimization of skill of leaner, in which learner observed and grabs the knowledge of the teacher. In the second phase, i.e., learner phase, learners interact among themselves and further optimize their skills. Figure 4 shows the steps for obtaining the optimized path.

Fitness function of TLBO:

Optimization of any technique very much depends upon its selected fitness function. Therefore, the fitness function of any technique should be decided precisely. TLBO mainly revolves around the ability to gain knowledge by the learner, and it decreases the path length by optimizing the turning angle of the WR. Therefore, two fitness functions which are picked for TLBO technique are:

(1) **The distance between wheeled robot, start point, target, and obstacles:**

The command given to the WR is to move in Euclidean distance. TLBO embedded WR always follows the same path to reach the target until any obstacles come in between its path. When such things occur, the WR takes a turn with the sufficient and optimum angle and again follows the same shortest path.

$$f_1 = \sqrt{(\text{Tarm} - m(i))^2 + (\text{Tarn} - n(i))^2} \tag{4}$$

where f_1 is the first fitness function of the proposed technique. Coordinate of the start point in ith iteration is $(m(i), n(i))$, and coordinate of the target is given by (Tarm, Tarn).

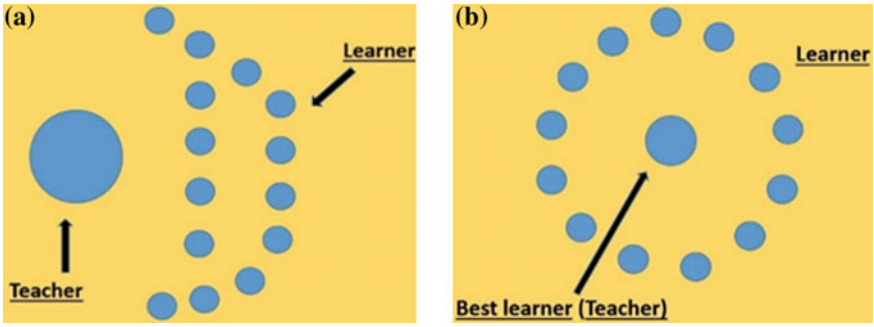

Fig. 3 Representation of different phases

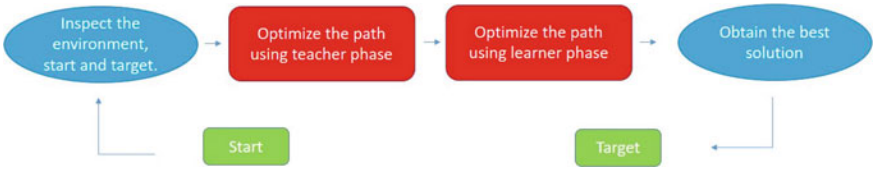

Fig. 4 Steps to obtain an optimized path

(2) **Turning angle while avoiding obstacles:**

Turning angle should not be too less that; it fails to avoid the collision. In addition, it should not be too large that it increases the path length. It should be selected after many iterations so that it satisfies the need of the problem. Optimality of the solution depends upon the optimality of the turning angle, and it is represented as follow:

$$f_2 = \begin{cases} \text{optimum}(i), & x < \text{safe distance} \\ \tan^{-1}\frac{y(i)}{x(i)}, & x \geq \text{safe distance} \end{cases} \tag{5}$$

where f_2 is the second fitness function of the proposed technique. optimum(i) is the best turning angle when the WR comes in front of obstacles. $(x(i), y(i))$ is the coordinate of the WR at ith iteration.

4 Simulation Results

MATLAB graphical user interphase (GUI) has been taken into consideration to obtain the simulation results. Three different types of environments have been considered to find out the stableness of the proposed technique. Environments have one obstacle, two obstacles, and multi-obstacles which have been preferred as shown in Figs. 5, 6, and 7. The complexity of the environment is gradually increased to retrieve the strength of TLBO technique. In each environment, WR embedded with TLBO technique is reaching the target by avoiding the obstacles. In every environment, sufficient

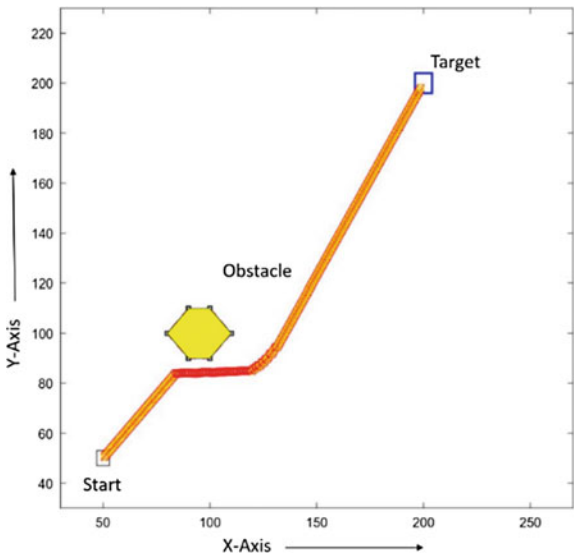

Fig. 5 Application of TLBO technique in environment having one obstacle

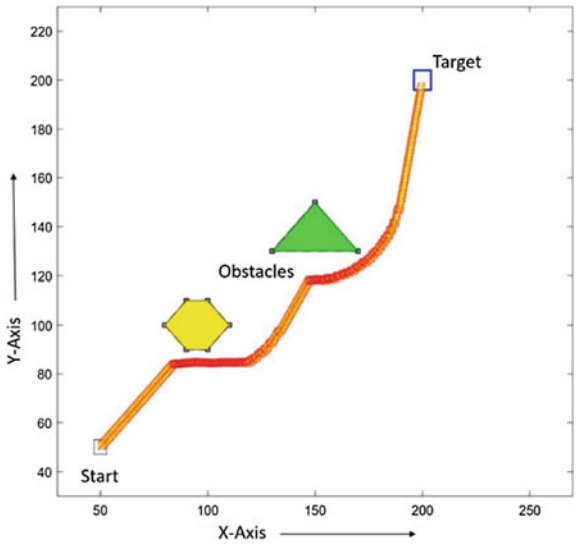

Fig. 6 Application of TLBO technique in environment having two obstacles

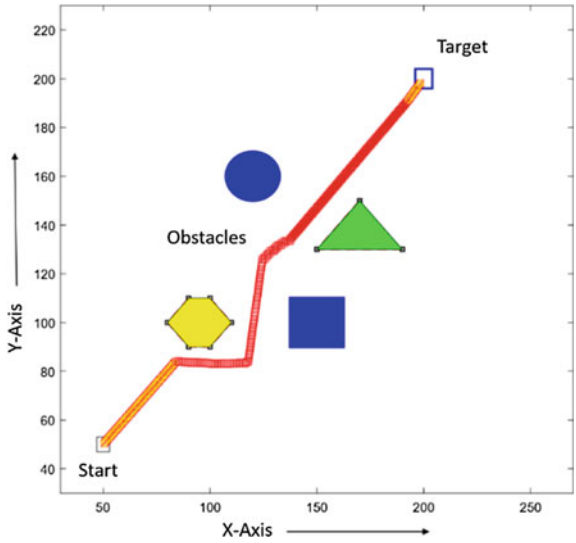

Fig. 7 Application of TLBO technique in environment having many obstacles

numbers of iterations are carried out, and it is about 10–30, and sometimes it reaches up to 40, depending upon the complexity of the environments. A sufficient number of iterations results in optimum path selection by avoiding the collision with the obstacles. Figure 5 makes evident that WR reached the target by avoiding the single pentagon-shaped obstacle. In the process, 12 iterations were carried out to obtain the optimized result. Sometimes the WR reached the target without avoiding collision with the obstacle, reached the target, avoided the obstacle, but the travel length is

high. Finally, after 12 iterations, following result has been obtained which is optimum. In Fig. 6, WR is simulated in the environment having two obstacles, one having pentagon shape and other triangular shape. The complexity of this environment is in more than the previous environment because of the shape and number of obstacles. As the complexity is increased, subsequently the number of iterations to obtain the optimum result has been increased. 23 iterations were carried out, and different problems arise in each run. Different results have been gathered, and the optimum result is selected as shown in Fig. 6. Now, the complexity of the environment is tossed to the top, so that the stability, effectuality, robustness, and efficiency of the technique can be gathered. Multiple obstacles having different shape increased the difficulty to the peak. After 28 iterations, we picked the best result which is completing all the need of the WR as shown in Fig. 7. So finally, it can be understood from the results (Figs. 5, 6, and 7) the selected technique is robust and efficient enough to successfully work in any environment.

5 Comparison with Previously Opted Technique

Performing simulation experiment of any technique in the various environment is not enough to claim that it is best. It should give some evident that it is better by comparing it with previously implemented techniques. The current technique is compared with previously opted technique to find out the response in the environment selected by them. To get the best possible result, the previously designed environment is replicated. In addition, during replication, it is strictly taken care to obtain the best possible result. Deepak and Parhi [9] observed the result as shown in Fig. 8a after implementing PSO technique. Figure 8b is describing the best result which is obtained by embedding the TLBO technique. It took more number of iteration to improve the result. At last, the result we obtained is far better than the previously

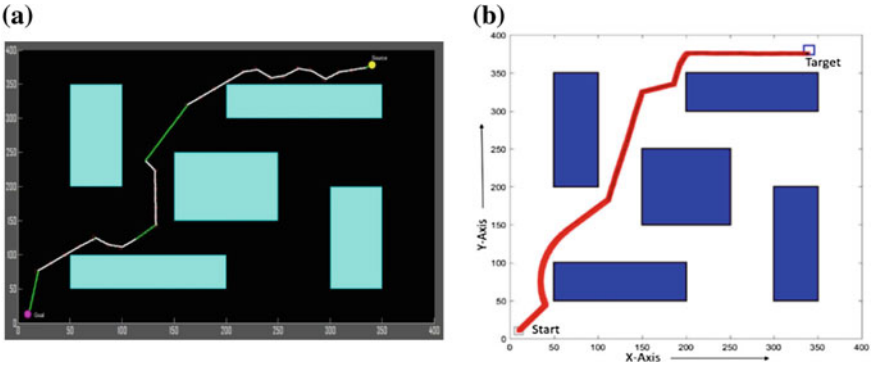

Fig. 8 **a** Route selected by PSO technique [9]. **b** Route selected by currently proposed TLBO technique

Table 1 Results gathered from Fig. 8a and b

Figure no.	Travel path length (cm)	No. of iteration
8a	675.2	20
8b	623.78	25

used technique. Table 1 is sufficient to find out the best technique. Travel length in the current technique is lesser than the travel length obtained in previously opted technique. It is effortlessly winning the race of obtaining the shortest travel length.

6 Conclusion

The current paper is making evident of the shortest path length after selecting TLBO technique. The current technique is demonstrated in the various environment by gradually increasing the difficulty. Every time the current technique comes out as the winner with the optimum and best possible result. The technique is extremely robust and efficient that irrespective of the complexity of the environment, it provides the best possible results. The current technique is compared with the previously opted technique, and the result is favorable. TLBO reached the target by traveling the shortest path. Finally, it can be accepted the TLBO technique can work in any environment and give the optimized result. It is also better than the previously opted technique in their selected environment. Future studies could investigate the mutation of TLBO with different algorithms to obtain more efficient results.

References

1. Algabri, M., Ramdane, H., Mathkour, H., Al-Mutib, K., Alsulaiman, M.: Optimization of fuzzy logic controller using PSO for mobile robot navigation in an unknown environment. Appl. Mech. Mater. **541**, 1053–1061 (2014)
2. Liu, Q., Lu, Y.G., Xie, C.X.: Optimal genetic fuzzy obstacle avoidance controller of autonomous mobile robot based on ultrasonic sensors. In: IEEE International Conference on Robotics and Biomimetics ROBIO'06, pp. 125–129. IEEE Press, Kunming, China (2006)
3. Tahboub, K.K., Al-Din, M.S.: A neuro-fuzzy reasoning system for mobile robot navigation. JJMIE **3**(1), 77–88 (2009)
4. Korkmaz, M., Durdu, A.: Comparison of optimal path planning algorithms. In: 14th IEEE International Conference on Advanced Trends in Radio Electronics Telecommunications and Computer Engineering (TCSET), pp. 255–258. IEEE Press, Lviv-Slavske, Ukraine (2018)
5. Lu, L., Gong, D.: Robot path planning in unknown environments using particle swarm optimization. In: Fourth IEEE International Conference on Natural Computation ICNC'08, pp. 422–426. IEEE Press, Jinan, China (2008)
6. Li, Y., Chen, X.: A new stochastic PSO technique for neural network training. In: International Symposium on Neural Networks 2006. LNCS, vol. 3971, pp. 564–569. Springer, Berlin, Heidelberg (2006)

7. Parhi, D.R., Pothal, J.K., Singh, M.K.: Navigation of multiple mobile robots using swarm intelligence. In: World Congress on Nature & Biologically Inspired Computing NaBIC, pp. 1145–1149. IEEE Press, Coimbatore, India (2009)
8. Rao, R.V., Savsani, V.J., Vakharia, D.P.: Teaching–learning-based optimization: a novel method for constrained mechanical design optimization problems. Comput. Aided Des. **43**(3), 303–315 (2011)
9. Deepak, B.B.V.L., Parhi, D.R.: PSO based path planner of an autonomous mobile robot. Open Comput. Sci. **2**(2), 152–168 (2012)

An Efficient Robotic Manipulator Trajectory Planning Using Modified Firefly Algorithm

Pradip Kumar Sahu, Gunji Bala Murali, Bijaya Kumar Khamari, Surya Narayan Panda and Bibhuti Bhusan Biswal

Abstract A novel modified firefly algorithm (MFA) for optimal and accurate robotic trajectory planning has been proposed in this paper. In order to demonstrate the entire trajectory planning problem, an industrial 4-DOF SCARA robot manipulator has been chosen. An error function which is a combination of both error in position and error in orientation coordinates is defined as total objective function for the trajectory optimization assignment. In order to accomplish an efficient optimal trajectory, the best cost of the error objective fitness function, algorithm convergence speed, the error in positions and orientations are chosen as performance parameters. The objective function has been executed using bat algorithm (BA), cuckoo-search algorithm (CS), firefly algorithm (FA), artificial bee colony (ABC) algorithm and the proposed MFA. The effectiveness of the proposed MFA is validated by carrying out a comparative review of the acquired trajectory results from the MFA against the other considered existing algorithms. The ranks of the algorithms have been evaluated by conducting Friedman test for the mean solutions of error in positions and orientation. The comparative study of the implemented algorithms shows that MFA executes superior to the other algorithms with less computational effort for the same boundary conditions.

P. K. Sahu (✉)
Oriental University, Indore, Madhya Pradesh 453555, India
e-mail: pradipsahu2@gmail.com

G. B. Murali · B. K. Khamari
National Institute of Technology Rourkela, Rourkela, Odisha, India
e-mail: bmgunji@gmail.com

B. K. Khamari
e-mail: bijayaa.khamari@gmail.com

S. N. Panda
Birsa Institute of Technology Sindri, Dhanbad, India
e-mail: suryanarayan.uce@gmail.com

B. B. Biswal
National Institute of Technology Meghalaya, Shillong, Meghalaya, India
e-mail: bibhuti.biswal@gmail.com

L. Li et al. (eds.), *Advances in Materials and Manufacturing Engineering*, Lecture Notes in Mechanical Engineering, https://doi.org/10.1007/978-981-15-1307-7_6

Keywords Manipulator trajectory planning · Optimization · Heuristic optimization methods · Modified firefly algorithm (MFA) · Graphical simulation · Motion analysis

1 Introduction

Robots are greatly being engaged for various applications in so many fields due to its flexibility, repeatability, preciseness and accuracy of performing the assigned task. The application area mostly includes the industrial robot manipulator operations such as assembly, machining, spray painting, machine loading/unloading, welding, material handling, etc. The smoothness and accuracy of the assigned trajectory to perform the whole operation affects the final end product preciseness and accuracy. So, in the context of trajectory planning and robot motion planning, the execution time must be minimized in order to increase total productivity. In order to acquire smooth and accurate manipulation of the considered manipulators for the intended task, its joints parameters or variables also must be optimized. The trajectory planning problem of robot manipulators involves inverse kinematics (IK) problems which result in multiple solutions and that has to be optimized. And this nature multiple solutions make the mathematical computation more complex and difficult. The current generation researchers mostly implement the metaheuristic techniques and algorithms for faster execution of trajectory planning problem. In the following sections, some of the earlier conducted research works have been highlighted.

Ayyıldız and Çetinkaya [1] have employed the heuristic algorithms such as GA, GSA, PSO and quantum particle swarm optimization (QPSO) algorithm for a fabricated 4-DOF serial manipulator trajectory optimization problem. Gigras et al. [2] have implemented the artificial bee colony (ABC) algorithm and PSO to solve the path planning problem of a robot. Kazem et al. [3] have accomplished the motion planning of a serial 3R robot manipulator by using the GA. Savsani et al. [4] conducted the same optimization performed by Kazem et al. [3] using teaching–learning-based optimization (TLBO) and ABC. In an extended and comprehensive research of the previous work, Savsani et al. [5] have been implemented seven heuristic techniques such as FA, BA, TLBO, CS, ABC, biogeography-based optimization (BBO) and GSA so as to compute the optimal solution of the 3R manipulator trajectory. The comparative assessment of trajectory results of all algorithms reveals that TLBO, ABC and CS trajectory results perform superior to the other adopted methods. Aghajarian and Kiani [6] have used an adaptive neuro-fuzzy inference system (ANFIS) model for the optimal trajectory planning problem of a PUMA 560 manipulator. Rokbani et al. [7] have applied FA to solve trajectory optimization assignment of a revolute manipulator. Sahu et al. [8] have adopted BA, FA, TLBO and PSO for optimal trajectory planning of a SCARA manipulator. Their results of simulation show that TLBO method performance is better than other algorithms.

This paper proposes a novel method for the robotic manipulator trajectory planning and optimization problem using a modified firefly algorithm (MFA). In earlier

works, the orientation error function has not been considered in the total objective fitness function of the algorithm. In this paper, the orientation error function of the robotic manipulator has been included in the total objective function as the orientation of manipulator end-effector is as important as its position.

2 Problem Definition and Objective Function

The main aim of the IK-based trajectory planning assignment is to generate an efficient and optimal trajectory by considering best cost, minimum error in positions and orientations as the performance parameters. The trajectory planning using metaheuristic optimization methods is accomplished with a 4-DOF SCARA manipulator.

The kinematic diagram of a SCARA manipulator is presented in Fig. 1. The SCARA manipulator end-effector forward kinematics position is obtained as given in the following Eqs. (1–3);

$$P_x = a_1 c_1 + a_2 c_{12} \tag{1}$$

$$P_y = a_1 s_1 + a_2 s_{12} \tag{2}$$

$$P_z = -d_3 - d_4 \tag{3}$$

The target point has been defined in terms of position coordinates and orientation values. Let the position coordinates be (a, b, c). Similarly, the orientation values of

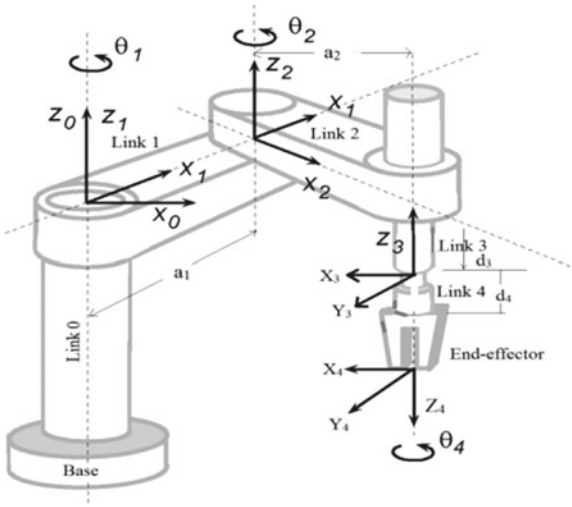

Fig. 1 Kinematic model with DH parameters of Quest SCARA robot manipulator

n_s vector say (d, e). Here, only n_s vector is chosen for orientation control. Because if we can compute the n_s value, it indirectly provides the o_s and a_s value as all (n, o, a) are function of θ_1, θ_2, d_3 and θ_4. In order to evaluate the optimal trajectory, a combined error function of position and orientation between the computed value and the desired value of the parameters is defined as the objective fitness function. The error objective function for the position and orientation is determined by Eqs. (4) and (5), respectively.

$$f_1 = \sqrt{(P_x - a)^2 + (P_y - b)^2 + (P_z - c)^2} \tag{4}$$

$$f_2 = \sqrt{(n_x - d)^2 + (n_y - e)^2} \tag{5}$$

The total objective function (f) can be formulated by adding Eqs. (4) and (5),

$$f = w_1 \times f_1 + w_2 \times f_2 \tag{6}$$

where weighing factor, $w_1 = w_2 = 0.5$ (equal weightage to end-effector position and orientation).

Here, θ_1, θ_2, d_3 and θ_4 are the design variables for function optimizations by using optimization algorithms. In order to find the IK solution through heuristic optimization procedures, the sample population configuration for the objective function as presented in Eq. (6) is given as,

$$S = \begin{bmatrix} \theta_{1,i} & \theta_{2,i} & d_{3,i} & \theta_{4,i} \\ \dots & \dots & \dots & \dots \\ \theta_{1,n} & \theta_{2,n} & d_{3,n} & \theta_{4,n} \end{bmatrix} \tag{7}$$

where S signifies the population configuration for the IK trajectory planning problem and n defines size of the population ($i = 1, 2, \dots n$).

3 Proposed Modified Firefly Algorithm (MFA)

In the existing basic FA, the local best solution is attained through general random search. The general random search often trapped the solution to local optima. In order to avoid being trapped to local optima and refine/improve the solution accuracy, adaptive random search algorithm has been implemented in the MFA instead of general random search of the existing FA. The proposed modification in the MFA avoids being confined to local optima and in so doing increases the solution accuracy. The entire process of evaluating optimal solution for the defined trajectory planning problem of 4-DOF SCARA robotic manipulator using the MFA optimization model has been described in Fig. 2.

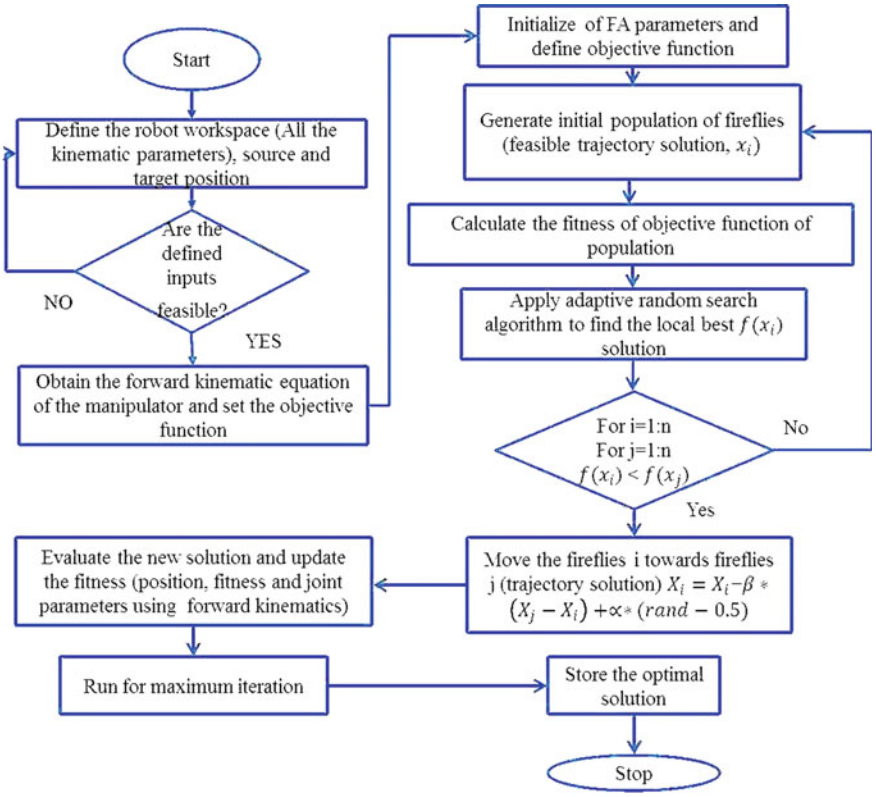

Fig. 2 Flowchart for the optimal trajectory planning using the MFA

4 Results and Discussion

The comparison of best cost plot of MFA algorithm against the other adopted existing algorithms is presented in Fig. 3a. It can be observed from the figure that the MFA

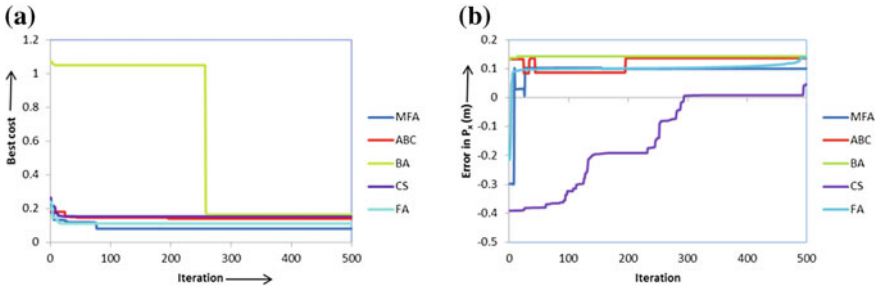

Fig. 3 **a** Best cost plot with iteration, **b** error in *X*-positions obtained from all algorithms

method is providing the best cost for the objective fitness functions for the current optimization problem and the next best algorithm being the FA. The standard BA and CS algorithm has the worst optimal fitness values as compared to other algorithms. So, the proposed modification to basic FA by performing adaptive random search as done in MFA efficiently enhances the MFA performance in terms of accuracy. The improvement is due to the wider global search ability of MFA algorithm and also its feature of avoiding local optima. The error in positions (X, Y and Z) in reaching the target points obtained using different algorithms are represented in Figs. 3b and 4a, b, respectively. It can be seen from the figures that least or minimum error is attained with MFA. The CS, ABC and FA are providing higher error and thus become worst performers.

The error in orientation values (n_x, n_y) attained through different algorithms has been shown in Fig. 5a, b, respectively. These figures also reveal the capability of the MFA in achieving least error in orientation values relative to other algorithms. On the other hand, the CS and FA offer higher error in orientation values. Therefore, the proposed MFA can be successfully employed for achieving optimal and accurate solutions of robotic trajectory. The computational or execution time of all algorithms for achieving the optimal trajectory solutions has been presented in Table 1. The table shows that the computational time needed by MFA for execution of the current trajectory optimization task is very less as compared to basic FA and ABC algorithms.

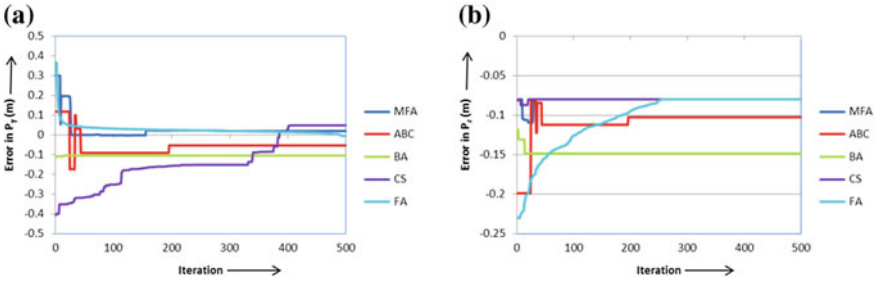

Fig. 4 Error in **a** Y-positions, **b** Z-positions obtained from all algorithms

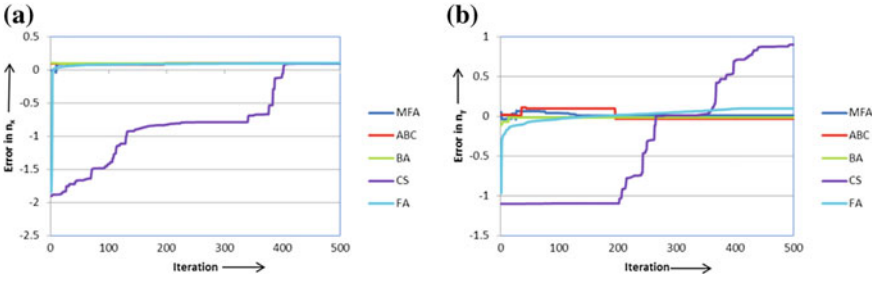

Fig. 5 Error in **a** X-orientation, **b** Y-orientation value obtained from all algorithms

Table 1 Friedman rank test result and computational time of the executed algorithms

Algorithms	Rank	Mean rank	Friedman rank	Computational time
MFA	1	1	10	1.22
ABC	4	6.6	66	2.21
BA	5	7.6	76	0.98
CS	3	6.3	63	1.25
FA	2	4.8	48	5.14

In the post-optimization analysis part, the Friedman rank test is conducted in OriginPro 2016 software for MFA and other adopted algorithms with the results of 10 runs. The confidence interval is kept at $\alpha = 0.05$ for the rank test. The Friedman rank test result for the best fitness values of the employed algorithms along with MFA is presented in Table 1.

It can be observed from Table 1 that the MFA is ranked 1st with Friedman rank 10 and mean rank 1 followed by FA and CS with 2nd and 3rd rank, respectively. Hence, best results of trajectory optimization are achieved with the proposed MFA algorithm.

5 Conclusions

This paper presents a new and efficient modified firefly algorithm (MFA) to solve the optimal trajectory planning problem of a 4-DOF SCARA manipulator. A combined objective function of error in position and orientation has been defined for the optimization problem, and it has been executed with all the adopted algorithms, viz. CS, BA, FA, ABC and the proposed MFA. The comparisons are established in terms of performance parameters such as best cost, error in positions and orientations, and the output results have been presented. The results of simulation confirm that MFA is providing superior optimal trajectories with minimum error in positions and orientations with minimum execution time. The Friedman rank test also confirms that the MFA is ranked first among all algorithms. Therefore, the aforementioned evaluation commends that an efficient, optimal, precise and accurate trajectory planning of industrial robotic manipulator can be performed with the proposed MFA in less time. In future work, the developed MFA will be employed for the trajectory planning of higher DOF robots and also for the path planning of the mobile robots.

References

1. Ayyıldız, M., Çetinkaya, K.: Comparison of four different heuristic optimization algorithms for the inverse kinematics solution of a real 4-DOF serial robot manipulator. Neural Comput. Appl. **27**(4), 825–836 (2016). https://doi.org/10.1007/s00521-015-1898-8
2. Gigras, Y., Jora, N., Dhull, A.: Comparison between different meta-heuristic algorithms for path planning in robotics. Int. J. Comput. Appl. **142**(3) (2016). https://doi.org/10.5120/ijca2016909705
3. Kazem, B.I., Mahdi, A.I., Oudah, A.T.: Motion planning for a robot arm by using genetic algorithm. JJMIE **2**(3) (2008)
4. Savsani, P., Jhala, R.L., Savsani, V.J.: Optimized trajectory planning of a robotic arm using teaching learning based optimization (TLBO) and artificial bee colony (ABC) optimization techniques. In: 2013 IEEE International on Systems Conference (SysCon), April 2013, pp. 381–386. IEEE. https://doi.org/10.1109/SysCon.2013.6549910
5. Savsani, P., Jhala, R.L., Savsani, V.J.: Comparative study of different metaheuristics for the trajectory planning of a robotic arm. IEEE Syst. J. **10**(2), 697–708 (2016). https://doi.org/10.1109/JSYST.2014.2342292
6. Aghajarian, M., Kiani, K.: Inverse kinematics solution of PUMA 560 robot arm using ANFIS. In: International Conference on Ubiquitous Robots and Ambient Intelligence (URAI), Nov 2011, pp. 574–578. IEEE. https://doi.org/10.1109/URAI.2011.6145885
7. Rokbani, N., Casals, A., Alimi, A.M.: IK-FA, a new heuristic inverse kinematics solver using firefly algorithm. In: Computational Intelligence Applications in Modeling and Control, pp. 369–395. Springer (2015). https://doi.org/10.1007/978-3-319-11017-2_15
8. Sahu, P.K., Balamurali, G., Mahanta, G.B., Biswal, B.B.: A heuristic comparison of optimization algorithms for the trajectory planning of a 4-axis SCARA robot manipulator. In: Computational Intelligence in Data Mining, pp. 569–582. Springer, Singapore (2019). https://doi.org/10.1007/978-981-10-8055-5_51

2D Computational Fluid Dynamics Analysis into Rotational Magnetorheological Abrasive Flow Finishing (R-MRAFF) Process

Atul Singh Rajput, Deokant Prasad, Arpan Kumar Mondal and Dipankar Bose

Abstract Rotational magnetorheological abrasive flow finishing is a nano-finishing technique used to finish hard and complex materials. By R-MRAFF, high grade surface finish can be achieved with close tolerances and without damaging surface topography. R-MRAFF works on the comparative movement among the magnetorheological fluid, and the workpiece surface attends the high surface quality. This article deals with the finite element analysis on behavior of magnetorheological fluid on workpiece in the influence of the magnetic field. In this work, a 2D computational fluid dynamics simulation in ANSYS FLUENT is performed to analyze the stresses generated due to magnetorheological fluid on workpiece and effect of concentration of carbonyl iron particles on surface roughness.

Keywords Nano-finishing · Magnetorheological fluid · R-MRAFF

1 Introduction

In rotational magnetorheological fluid flow finishing process with the help of magnetorheological fluid (MR fluid) which works as a finishing material, surface finish up to nano-level can be acquired [1]. Magnetorheological fluid is a non-Newtonian fluid which is comprised of carbonyl iron particles (CIP), and carrier fluid abrasive changes its viscosity when it comes under the influence of some external field and behaves as Bingham fluid [2]. MR fluid forms a columnar structure in external magnetic field as shown in Fig. 1. In this article, 2D computational fluid dynamics simulation in ANSYS FLUENT is performed to analyze the velocity profile of MR fluid to analyze axial and radial stress generated by abrasive particles on the workpiece. By implementing magnetohydrodynamics in ANSYS, magnetic field of magnitude 0.4 T is applied. With the variation of composition of carbonyl iron particle in the MR fluid, its effect on surface roughness is also determined. MR fluid consists of carbonyl iron particles of size 18 μm, SiC is used as abrasive of diameter 19 μm, AP3 grease is

A. S. Rajput · D. Prasad · A. K. Mondal (✉) · D. Bose
National Institute of Technical Teachers Training and Research, Kolkata 700106, India
e-mail: arpan@nitttrkol.ac.in

L. Li et al. (eds.), *Advances in Materials and Manufacturing Engineering*, Lecture Notes in Mechanical Engineering, https://doi.org/10.1007/978-981-15-1307-7_7

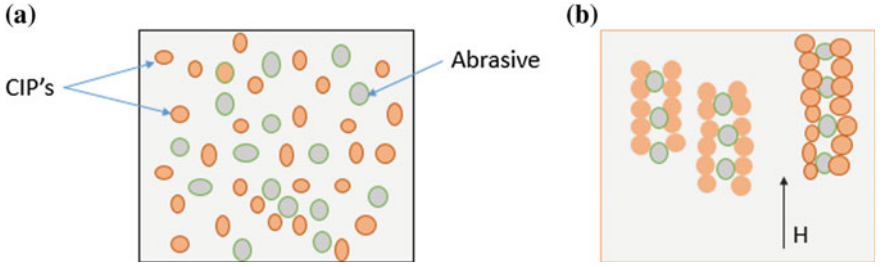

Fig. 1 Rearrangement of carbonyl iron particles and abrasives **a** in absenteeism of magnetic field, **b** in the occurrence of magnetic field

used as surfactant to improve the fluid stability, and rest are paraffin oil which is used as carrier fluid.

2 Computational Flow Dynamics Simulation of Magnetorheological Fluid Movement

The purpose of this segment is to analyze the fluid flow variation with change in compositions of CIP by calculating the axial stresses and radial stresses due to the impact of abrasive on surface of the workpiece with numerical analysis. Shear stress of the Bingham fluid is defined as in Eq. (1) [4].

$$\overline{\overline{\tau}} = \overline{\overline{\tau}}_0 + \eta \overline{\overline{D}} \tag{1}$$

where τ_0 is the yield shear stress and D is a tensor which denotes the rate of deformation. Viscosity and shear stress of Bingham fluid K and τ_0, respectively, is contingent on the concentration of MR fluid and magnitude of magnetic field described in Eqs. (2) and (3) [3].

$$\begin{aligned} K = {} & -202.64 + 11.09A + 9.54B + 5C - 110.23D - 0.38AB \\ & - 0.53AC + 19.23CD \end{aligned} \tag{2}$$

$$\begin{aligned} \tau_0 = {} & -176.13 + 9.11A + 14.58B + 2.19C - 218.46D - 0.34AB \\ & - 0.4AC - 0.57BC + 17.15CD + 0.39C^2 + 170.42H^2 \end{aligned} \tag{3}$$

where A is concentration of CIP, B is concentration of SiC, C is concentration of AP3 grease in MR fluid, and D is magnitude of magnetic field.

Magnetohydrodynamics is implemented in fluent to achieve the required magnetic field. The link among the external magnetic field and fluid stream field depends upon the two basic concepts: the first one is the electric field produced due to the movement

of electrons in conductive materials in the influence of some external magnetic field, and the second one is Lorentz force produced by the electric and magnetic field. From Ohm's law and Maxwell's equation, the induction equation can be derived as in Eq. (4) [4].

$$\frac{\partial B}{\partial t} + (U \cdot \nabla)B = \frac{1}{\mu\sigma}\nabla^2 B + (B \cdot \nabla)U \tag{4}$$

where magnetic field is defined by B, fluid velocity field is defined by U, and magnetic permeability and electric permittivity are defined by μ and σ, respectively.

Graphical illustration of the symmetrical flow domain is represented in figure where the domain is divided into two zones: first one is zone 1, and the second one is zone 2 as shown in Fig. 2.

In zone 1, external magnetic field is not applied, and hence, MR fluid behaved like Newtonian fluid. In zone 2, magnetic field of magnitude 0.4 T is applied and its viscosity and yield shear stress are defined as Eqs. (2) and (3) which are calculated in Table 1. As in the experimental setup, the back and forth motion of piston is controlled by crank of diameter 120 mm; hence, the velocity of MR fluid varies in the cosine form. To justify the velocity of MR fluid, a UDF is developed.

Modeling of surface texture is carried out after investigating the surface roughness profile data obtained from the surface irregularity evaluating device. Ra value of the surface roughness was found to be 0.6 μm. It is considered that the diameter of the abrasive particle is greater than the gap between the two successive crests of surface

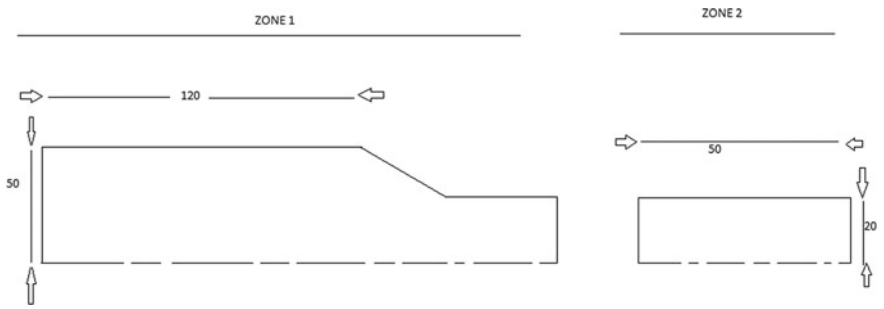

Fig. 2 Schematic diagram of flow domain (all dimensions are in mm)

Table 1 Properties of MR fluid with different compositions

CIP (% VOL)	SiC (% VOL)	Magnetic field (T)	Zone 1		Zone 1	
			Yield stress (Pa)	Viscosity (Pa s)	Yield stress (Pa)	Viscosity (Pa s)
10	10	0.4	41.494	0.780	15.013	13.904
15	10	0.4	55.760	1.588	19.560	18.554
20	10	0.4	69.200	2.350	24.110	23.204

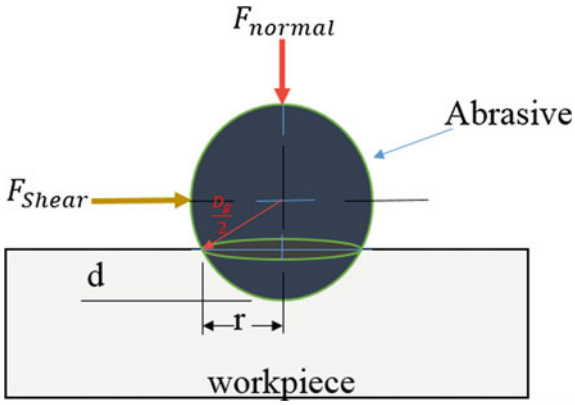

Fig. 3 Indentation by abrasive on workpiece

roughness. Normal force required for indenting the abrasives into the workpiece is obtained from the simulation. Using this normal force and by knowing the BHN of the workpiece material, we can find out the diameter of indentation by using Eq. (5) [2] as shown in Fig. 3.

$$d = \frac{D_g}{2} - \frac{1}{2}\sqrt{D_g^2 - D_i^2} \tag{5}$$

The following steps are considered for simulating the surface roughness model.

Step 1. The initial surface roughness statistics obtained from the surface irregularity evaluating device are stockpiled in an array.
Step 2. It is essential that all the crests identified should undergo cutting action at each stroke.
Step 3. After several strokes, the position of the mean line changes ΔY, and after each recapitulation, new mean line of the updated surface texture is evaluated, and consequently, all the data $Y_{i,n}$ are updated and given in Eq. (6).

$$Y_{i,n+1} = Y_i - \Delta Y \tag{6}$$

Step 4. The centerline average surface roughness value R_a of the surface texture can be evaluated using surface texture data points Y_i from Eq. (7).

$$R_a = \frac{\sum_{i=1}^{n} |Y_i|}{n} \tag{7}$$

where n is the data point's number.

The formation of velocity circulation in zone 1 is shown in Fig. 4. The axial velocity profile plot in Zone 2 is shown in Fig. 5 specifies that nearby axis of work piece fixture there is a compact core section where the MR fluid flows with highest velocity and the reduction in velocity is non-linearly, in the radial direction from the

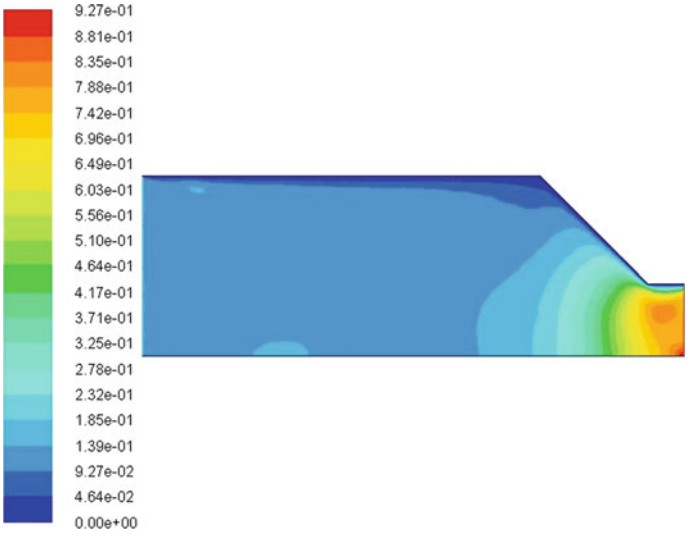

Fig. 4 Velocity profile (m/s) for zone 1 (15% CIP with 10% SiC)

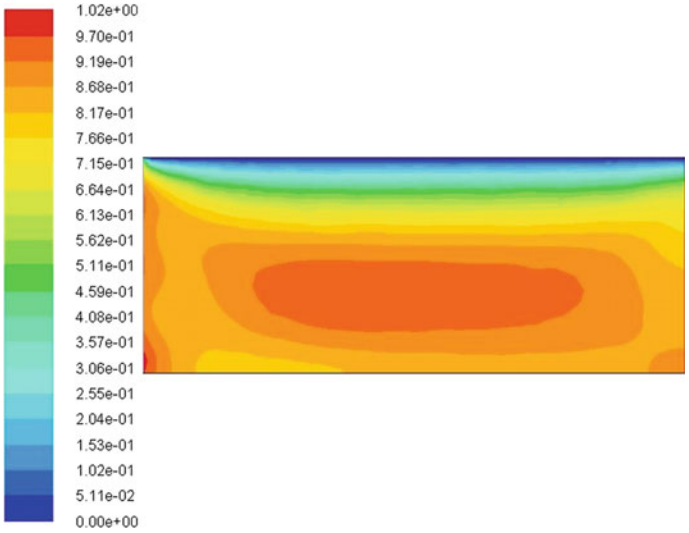

Fig. 5 Velocity profile (m/s) for zone 2 (15% CIP with 10% SiC)

center of the work piece fixture where velocity becomes zero. This approves the MR fluid flow circulation of the non-Newtonian Bingham plastic fluid [3].

Due to an upsurge in the CIP concentration in the MR fluid, the persuaded strength of magnetic field also increased. The induced magnetic field simulation with the help

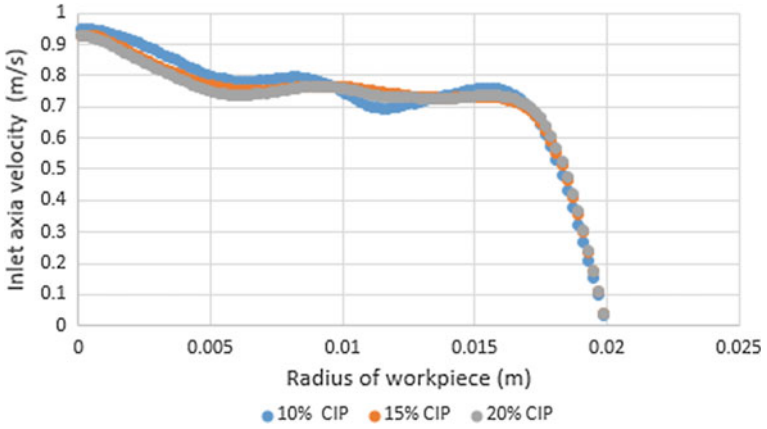

Fig. 6 Radial variation of inlet axial velocity in zone 2

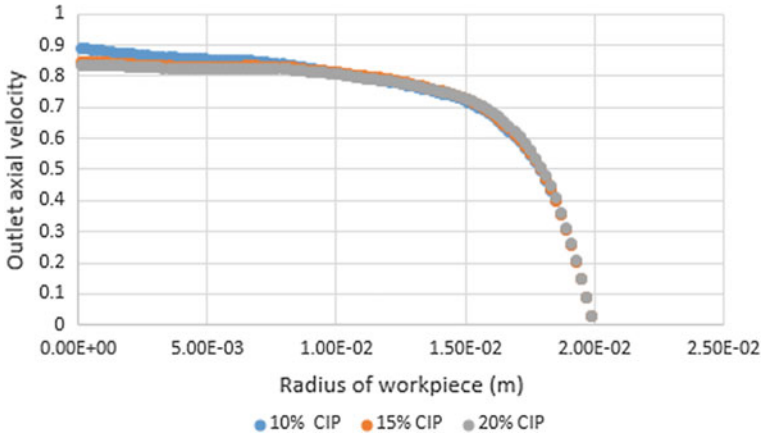

Fig. 7 Radial variation of outlet axial velocity in zone 2

of magneto hydrodynamics. The radial variation of inlet velocity and outlet velocity of different compositions of CIP in MR fluid in zone 2 is shown in Figs. 6 and 7, respectively.

3 Conclusion

The average values of axial and radial stresses generated by the action of single abrasive over different compositions of CIP are listed in Table 2. It can be observed that with increase in composition of CIP, radial and axial stresses also get increased.

Table 2 Final surface roughness variation by different CIP concentration

CIP (%VOL)	Axial stress (kPa)	Radial stress (Pa)	Radial force (nN)	Final surface roughness (μm)
10	12.498	15.889	4.494	0.032
15	14.978	23.782	6.729	0.027
20	21.229	41.658	11.795	0.019

The cause for this kind of behavior is described below. CIP is the key constituent of the MR fluid and offers a noteworthy influence to the physical characteristic of MR fluid. In Table 2, it is observed that with increase in the concentration of CIP axial velocity in zone 2 as shown in Fig. 6 gets decreased likewise, as the volume fraction of increases, body-centered tetragonal crystal structure is predicted because of that large yield stress was noticed. For the similar cause, the MR fluid imposes higher radial and axial stresses near the wall if fixture with increase in composition of CIP as shown in Table 2.

References

1. Chhabra, R.P., Richardson, J.F.: Non-Newtonian Flow and Applied Rheology: Engineering Applications. Butterworth-Heinemann (2011)
2. Das, M., Jain, V.K., Ghoshdastidar, P.: The out-of-roundness of the internal surfaces of stainless steel tubes finished by the rotational magnetorheological abrasive flow finishing process. Mater. Manuf. Processes **26**(8), 1073–1084 (2011)
3. Das, M., Jain, V.K., Ghoshdastidar, P.S.: Computational fluid dynamics simulation and experimental investigations into the magnetic-field-assisted nano-finishing process. Proc. Inst. Mech. Eng. Part B J. Eng. Manuf. **226**(7), 1143–1158 (2012)
4. Gedik, E., Kurt, H., Recebli, Z., Balan, C.: Two-dimensional CFD simulation of magnetorheological fluid between two fixed parallel plates applied external magnetic field. Comput. Fluids **63**, 128–134 (2012)
5. Jha, S., Jain, V.K.: Design and development of the magnetorheological abrasive flow finishing (MRAFF) process. Int. J. Mach. Tools Manuf. **44**(10), 1019–1029 (2004)

Effect of Red Mud on Mechanical and Microstructural Characteristics of Aluminum Matrix Composites

Priyaranjan Samal, Rishu Raj, Ravi Kumar Mandava and Pandu R. Vundavilli

Abstract The aim of the present paper is to study the effect of red mud on the characterization and mechanical behavior of aluminum alloy AA6082 composites reinforced with red mud. Four different volume fractions (0, 2, 4, and 6%) have been considered to fabricate the composites by stir casting route. The effect of heat treatment on mechanical properties is also investigated. Vickers micro-hardness testing and tensile testing were carried out to measure mechanical properties. Compared to the base alloy, a significant enhancement in the hardness and tensile strength is observed in the case of the red mud-reinforced composites. Furthermore, field emission scanning electron microscope analysis (FESEM) and energy-dispersive spectroscopy (EDX) were also employed to study the microstructural evolution and elemental analysis of the composites. The tensile fractography study revealed a ductile nature of failure in terms of dimple, micro-voids, and cracks.

Keywords AA6082 · Red mud · Stir casting · Microstructure · Mechanical properties

1 Introduction

Metal matrix composites are the combination of metal (matrix) and particle/ceramic (reinforcement) to achieve superior properties than the base metal. The aluminum

P. Samal (✉) · R. Raj · P. R. Vundavilli
Indian Institute of Technology Bhubaneswar, Bhubaneswar, Odisha 752050, India
e-mail: ps23@iitbbs.ac.in

R. Raj
e-mail: rr15@iitbbs.ac.in

P. R. Vundavilli
e-mail: pandu@iitbbs.ac.in

R. K. Mandava
Vignan's Foundation for Science, Technology and Research, Guntur, Andhra Pradesh 522213, India
e-mail: rm19@iitbbs.ac.in

L. Li et al. (eds.), *Advances in Materials and Manufacturing Engineering*, Lecture Notes in Mechanical Engineering, https://doi.org/10.1007/978-981-15-1307-7_8

metal matrix composites (AMMCs) are considered for the use in automotive applications as they manifest good properties in terms of high wear resistance, specific weight, strength, and thermal stability at high temperature [1, 2]. Lightweight AMMCs have been developed by many investigators and revealed the above properties. The attempt to further enhance the properties of aluminum alloys continued in the last few decades. Different types of material such as oxides, carbides of silicon, aluminum, zircon, boron [3–6] were used as reinforcement for the fabrication of aluminum metal matrix composites. There are a lot of fabrication techniques developed for the preparation of MMCs. Liquid metallurgy, i.e., stir casting is the most common, economical, and highly productive method used to produce metal matrix composites [7]. This method involves melting of aluminum alloy in a graphite crucible followed by the addition of the required amount of reinforcement. Constant stirring takes place to achieve a homogenous mixture of reinforcement particles with the molten matrix element with the help of a mechanical stirrer.

In the present work, AA6082/red mud MMCs are prepared by stir casting route with varying weight % of red mud. The composites are subjected to heat treatment to enhance the properties. The mechanical properties such as micro-hardness, tensile strength are tested for the composites both for heat-treated and as-casted condition. The microstructural analysis is also studied for the composites.

2 Materials and Methods

The main challenge in the fabrication of AMMCs is the selection of suitable matrix and reinforcement material. In this work, commercially available AA6082 material was selected as base alloy and supplied by Venuka Engineering Pvt. Ltd., Hyderabad, India, in ingot form. Aluminum 6000 series is the combination of Al–Mg–Si family. The melting point temperature of AA6082 is 555 °C (1031 °K), and it yields higher strength after undergoing heat treatment. The detailed composition of this alloy is given in Table 1. Red mud was used as reinforcement for the fabrication of aluminum MMC. The red mud is a corrosive, solid waste residue obtained from the production of aluminum from the bauxite ore. It has been noticed that for each ton of production of alumina, more than one ton of red mud is produced [8] and is dumped to the atmosphere and causes serious environmental pollution. Many attempts were made to successfully utilize red mud for ceramic and construction materials. The chemical composition of red mud used in this paper is presented in Table 2. As red mud contains various metal oxides such as alumina, silica, and ferric, it may be used as a

Table 1 Chemical composition of AA6082

Element	Si	Mg	Cr	Fe	Zn	Mn	Ti	Al
wt%	1.20	1.05	0.02	0.15	0.02	0.75	0.08	Remainder

Table 2 Chemical composition of red mud

Element	Fe_2O_3	Al_2O_3	SiO_2	TiO_2	Na_2O	CaO
wt%	24.5–54.8	14.8–24.3	6.2–7.3	13.5–18	3.5–5.3	2–5

suitable reinforcement for the synthesis of MMCs. Red mud used as reinforcement in this work was procured from NALCO Damanjodi, India.

AA6082/red mud composites were fabricated through stir casting route. Commercially available AA6082 alloy ingots were cut into a convenient size so as to fit in the graphite crucible and heated to 800 °C which is beyond the liquidus temperature of the aluminum alloy. The prerequisite amount of red mud was preheated to 400 °C in another furnace to remove any kind of moisture present in the particles which might create casting defects. The red mud wrapped in an aluminum foil was then mixed into the molten metal. Granules of hexachloroethane (C_2Cl_6) as degasser were then added into the melt to remove the hydrogen gas present in it. The temperature of the furnace was raised up to 1000 °C and then maintained there for 30 min. The mixture was stirred intermittently for every 10 min with the help of mechanical stirrer for homogenous mixing of red mud with the aluminum melt. After complete mixing occurred, the molten metal was poured into a preheated die to get the casted product for further investigation. Before that, the dross has to be removed from the melt before pouring into the die to avoid the formation of defects. The muffle furnace and casted composites were shown in Fig. 1. To compare the variation of different mechanical and wear properties of the alloy with the composites, the specimens were undergone solutionizing and artificial age-hardening heat treatment (T_6 temper) in a muffle furnace. The casted specimens were subjected to solutionizing heat treatment at a temperature of 540 °C for 30 min, followed by quenching at an artificial aging temperature of 170 °C for 8 h. The solutionizing treatment is required to completely dissolve the solute elements in the aluminum solid solution. The solution-treated samples are then quenched in water. This rapid cooling results in the prevention of

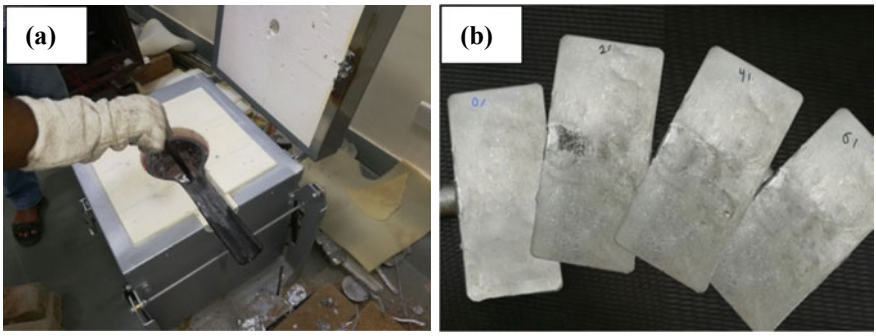

Fig. 1 **a** Electric muffle furnace, **b** Al-red mud casted composites (0, 2, 4, 6%)

formation of precipitates of the solute elements. In order to further improve the properties, artificial aging is also done to get hardened composite products. Then both the casted and heat-treated specimens are subjected to various tests to evaluate the properties.

2.1 Experimentation

The micro-hardness tests were carried out on the polished specimens of the composites after following the standard procedure. The tests were conducted in an OMNITECH Vickers micro-hardness tester with a load and dwell time of 500 g and 10 s, respectively. Three readings were taken at three different locations of both as-casted and heat-treated composites to avoid any undesirable effect of the indenter on the non-homogeneity distribution of reinforcement particles. Tensile specimens were prepared as per the ASTM E8 standard and tested in a universal testing machine (TUE-C-200) at room temperature. Two samples were tested for both the as-casted and heat-treated composites, and a comparison has been done to study the effect of heat treatment on the tensile strength of the composites.

2.2 Characterization

Microstructural characterization was conducted by ZEISS Merlin Compact Gemini, a FESEM machine. Highly polished samples were prepared using necessary emery paper and Keller's etchant. Energy-dispersive X-ray spectroscopy (EDX) was used to identify the elements present in the composites. The SEM micrographs for the aluminum alloy with red mud composites are shown in Fig. 2. The EDX analysis was also carried out to find out the element composition present in the composites shown in Fig. 3. For this study, the samples were cut from the fabricated composites and polished using different grit of emery paper followed by cloth polishing as per standard manual polishing method. The specimens were then subjected to standard Keller's etchant for further microstructural study.

3 Results and Discussion

A fair homogenous distribution of red mud particles was observed in the AA6082 alloy which leads to microstructural advantage. The SEM micrographs show that continuous stirring is required in the case of red mud-reinforced composites because of the tendency of red mud particles to form agglomeration at higher reinforcement content. It was also observed that the composites are free from any type of defect in casting. A clean interface is required for good interfacial strength in the composites,

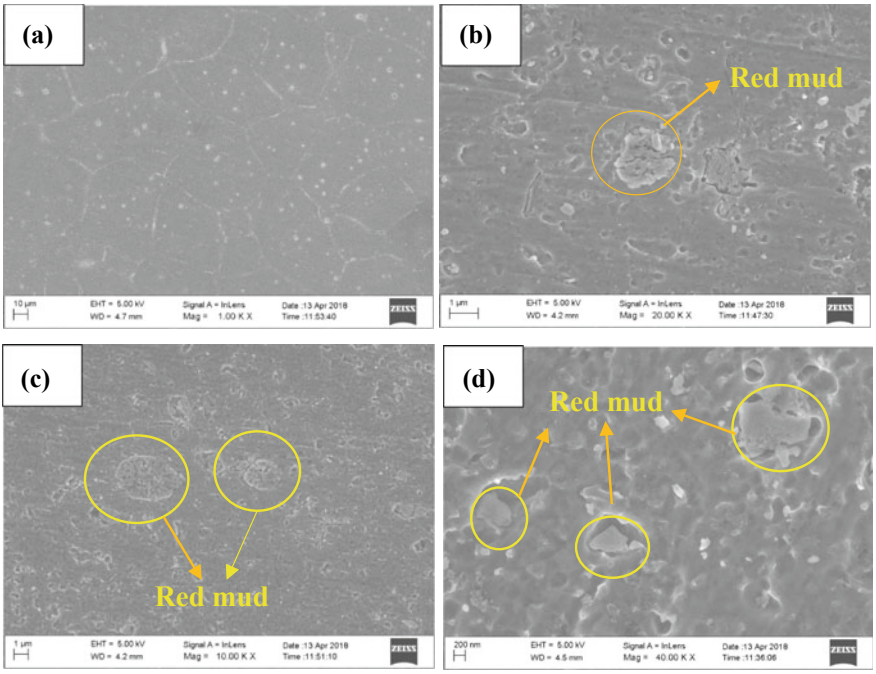

Fig. 2 SEM images of Al-red mud composites **a** Al alloy, **b** 2% red mud, **c** 4% red mud, **d** 6% red mud

which yields higher tensile properties of the composites compared to the base alloy. Furthermore, the presence of every element of red mud and aluminum alloy 6082 can be confirmed from the EDX analysis. Figure 4a, b show the comparison of micro-hardness and ultimate tensile strength, respectively, for both the as-casted and heat-treated specimens. It is observed that hardness of the AA6082/red mud composites increases with the increase in weight percentage of reinforcement due to the resistance provided to the indentation by hard red mud particles. Compared to the base alloy, the hardness of the 6% red mud as-casted composites increased by 15%, whereas 18% increase can be noted in the case of heat-treated specimens shown in Fig. 4a. Influence of red mud particles on the ultimate tensile strength of aluminum composites for both the as-casted and heat-treated samples presented in Fig. 4b. It can be noted that the ultimate tensile strength increases with the increase in weight percentage of red mud particles. UTS increases a maximum of 17 and 13% for as-casted and heat-treated specimens, respectively. The increase in tensile strength indicates a better interfacial bonding of red mud in the soft aluminum matrix. Increase in tensile strength can also be attributed to the absence of pores in the casting. Similar trends can be found by other research works considering different reinforcements with aluminum matrix [1, 4, 9].

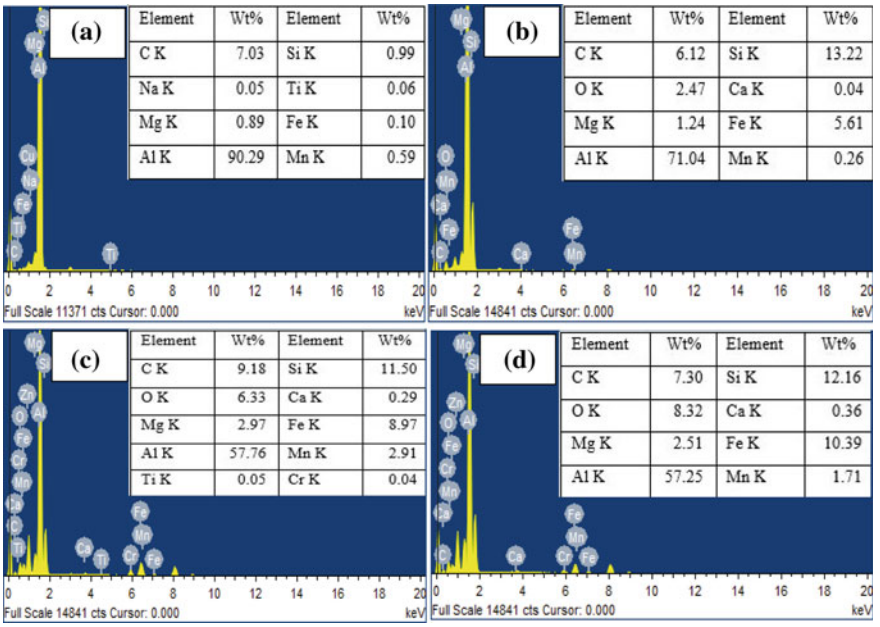

Fig. 3 EDX elemental analysis of the composites, **a** base alloy, **b** 2% red mud, **c** 4% red mud, **d** 6% red mud

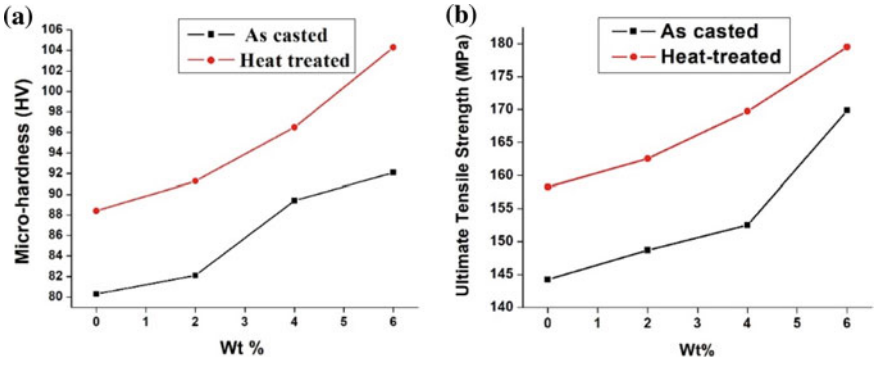

Fig. 4 Comparison of micro-hardness and UTS for as-casted and heat-treated samples

3.1 Fractography

The tensile fractured surface of AA6082/red mud composite is shown in Fig. 5 as scanning electron micrographs. Some equiaxed dimples are observed in case of aluminum 6082 alloy indicating the failure due to plastic deformation. This phenomenon is attributed to a ductile nature of fracture for the base alloy initiated by the cracking

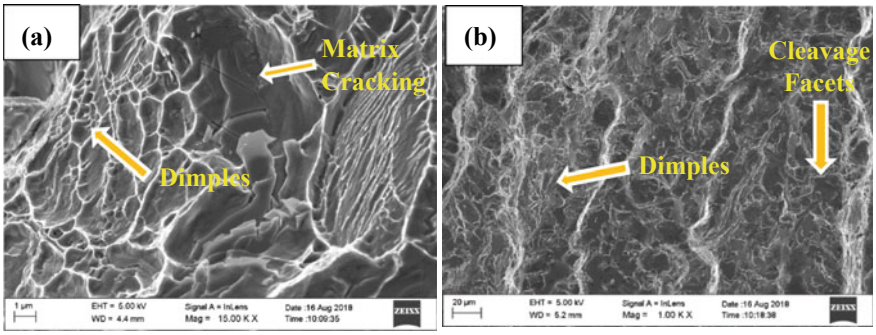

Fig. 5 Tensile fractography of Al-red mud composite; **a** base alloy, **b** red mud composite

of the matrix. The agglomeration of red mud particles can be seen in case of higher volume percentage composites as it is practically difficult to distribute homogenously for a large amount of reinforcement by stirring. The micro-voids are the major reason for the crack initiation which resulted in the tensile fracture of the specimens. The cleavage facets and the dimples are the indications that the composites have undergone brittle as well as ductile nature of fracture, respectively.

4 Conclusions

AA6082/red mud composites were successfully manufactured and the effect of heat treatment on the mechanical properties was also investigated. The microstructure of fabricated MMCs was characterized by SEM and XRD, and it revealed the existence of red mud particle in the composites with uniform dispersion. The micro-hardness of the composites was enhanced from 80.3 to 92.1 HV with respect to the variation of red mud particles in as-casted condition and 88.4 to 104.3 HV in heat-treated condition. Addition of red mud particles increased the tensile strength both in as-casted and heat-treated condition from 144.23 to 169.87 MPa and 158.25 to 179.5 MPa, respectively. The fracture mode of the composite was found to be a mixed mode in nature.

References

1. Sharifitabar, M., Sarani, A., Khorshahian, S., Sharfiee Afarani, M.: Fabrication of 5052Al/Al_2O_3 nanoceramic particle reinforced composite via friction stir processing route. Mater. Des. **32**, 4164–4172 (2011)
2. Nieto, A., Yang, H., Jiang, L., Schoenung, J.M.: Reinforcement size effects on the abrasive wear of boron carbide reinforced aluminum composites. Wear **390–391**, 228–235 (2017)

3. Deepak Kumar, S., Vundavilli, P.R., Mandal, A., Mantry, S., Chakraborty, M.: Erosion response of thixoformed A356-5TiB_2 in-situ composite using taguchi's experimental design. Tribol. Trans. **60**, 39–46 (2017)
4. Kumar, N., Gautam, R.K., Mohan, S.: In-situ development of ZrB_2 particles and their effect on microstructure and mechanical properties of AA5052 metal-matrix composites. Mater. Des. **80**, 129–136 (2015)
5. Lijay, K.J., Rajaselvam, J.D., Dinaharan, I., Vijay, S.: Microstructure and mechanical properties characterization of AA6061/TiC aluminum matrix composites synthesized by in-situ reaction of silicon carbide and potassium fluotitanate. Trans. Nonferrous Met. Soc. China **26**, 1791–1800 (2016)
6. Suryakumari, T.S.A., Ranganathan, S.: Preparation and study the wear behaviour of aluminum hybrid composite. Mater. Today Proc. **5**, 8104–8111 (2018)
7. Chawla, N., Chawla, K.K.: Metal Matrix Composites, 2nd edn. Springer-Verlag, New York (2013)
8. Samal, S., Ray, A., Bandopadhyay, A.: Proposal for resources, utilization and processes of red mud in India—a review. Int. J. Miner. Process. **118**, 43–55 (2013)
9. Ravikumar, K., Kiran, K., Sreebalaji, V.S.: Characterization of mechanical properties of aluminum/tungsten carbide composites. Measurement **102**, 142–149 (2017)

Performance Measurement in Incremental Deformation of Brass Cu67Zn33 Through Soft Computing Tool

Manish Oraon, Vinay Sharma and Soumen Mandal

Abstract Incremental deformation is an innovative manufacturing process. Commonly, it is known as incremental sheet forming (ISF). The deformation of sheet to a single point tool therefore it is called the single-point incremental forming (SPIF). The surface finish is the common issue in SPIF which is increased with the processing of hard materials. In the present study, the brass Cu67Zn33 is formed through SPIF, and nano-scale surface roughness is measured through atomic force microscopy (AFM). A soft computing tool, i.e., artificial neural network (ANN), a second-order mathematical prediction model, is established due to variability in experimental outputs. The SPIF is successfully done on brass Cu67Zn33, and the error found in predicted R_a is in the range of -6.813-73.04.

Keywords SPIF · Surface roughness · Input variables · ANN

1 Introduction

The making of die for producing few parts or prototyping in sheet metal industries is a complex situation as it consumes huge materials, labor, machining time, etc. As a whole, the manufacturing cost is high enough. To overcome this situation, SPIF is developed in the last decade. In SPIF, the part is finished without the use of dedicated dies. So, it can be a solution for the rapid prototyping and low batch production of sheet metal products. SPIF is precisely conducted in computer numerical control (CNC) machine.

An extensive research is done in the past years to understand the SPIF. Various models are proposed by the authors for the optimization of SPIF, but yet, no optimized

M. Oraon (✉) · S. Mandal
Birla Institute of Technology, Patna, Off Campus, Patna, Bihar 800014, India
e-mail: moraon@bitmesra.ac.in

S. Mandal
e-mail: soumenbhu@gmail.com

V. Sharma
Birla Institute of Technology, Deoghar, Off Campus, Deoghar, Jharkhand 814142, India
e-mail: vinay@bitmesra.ac.in

L. Li et al. (eds.), *Advances in Materials and Manufacturing Engineering*, Lecture Notes in Mechanical Engineering, https://doi.org/10.1007/978-981-15-1307-7_9

condition for SPIF is proposed for surface roughness, formability and tool path. Surface roughness is the major response which decides the process capability of SPIF.

The present study is a soft computing of experimental data for the prediction of results and error. The experiments are conducted on brass Cu67Zn33 alloy, Further the measured surface roughness is used as inputs for soft computing. The rate of deformation which includes step down size and feed rate of tool (longitudinal and transverse) are the significant input variables in SPIF [1–5]. A prediction model was developed by considering maximum and average roughness evaluation of surface finishing [6]. In the succession, an effect spindle speed and feed rate of tool are investigated in SPIF of aluminum grade Al3003 (H14) by considering the non-contact (orange peel effect) surface roughness, sectional microstructure and thickness distribution [7]. The initial roughness is investigated by the researchers during the manufacturing of medical implants (femoral condylar surface of the knee) by SPIF technique. It was observed that the non-contact surface of titanium sheet has better finishing in low friction condition [8]. The authors investigated the effects of SPIF on two carbon steel grades DC01 and 304 and an aluminum grade A1050 to analyze the surface roughness [9]. The results indicated that surface roughness and wall thickness were affected 17.23% by wall angle and 64.19% by step depth increment [10].

Presently, some SPIF research moves toward the soft computing-based solution like artificial intelligence-based model development which incorporates neural network training [11], data-mining model [12] and artificial neural network [13, 14].

2 Surface Roughness Model

SPIF is affected by several input variables but it is very difficult to consider all at a time. For that, only the major input variables are chosen on the basis of preliminary experiments. The considered input variables for the present study are wall angle (θ), feed rate (f), spindle speed/RPM (R), step depth (Δz), density of lubricant (L) and sheet thickness (T). The dimension of square pyramid and adopted step depth for SPIF are shown in Fig. 1. The mechanical properties of Cu67Zn33 alloy are shown in Table 1.

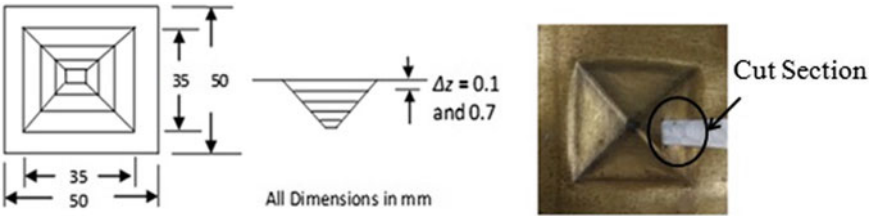

Fig. 1 The dimensions of square pyramid and finished part with cut section for test

Table 1 The mechanical properties of Cu67Zn33 alloy

Material	Tensile strength	Elongation	Density	Modulus of elasticity
Cu67Zn33	336 MPa	4%	8.44 kg/m^3	103.4 GPa

Table 2 Orthogonal array L8 and measured R_a

Test	Δz (mm)	f (mm/min)	R	θ (°)	T (mm)	L (kg/m^3)	$\boldsymbol{R_a}$
1	0.1	20	500	15	0.2	1.5	134.86
2	0.1	20	500	45	0.4	4.9	268.29
3	0.1	100	2000	15	0.2	4.9	156.10
4	0.1	100	2000	45	0.4	1.5	269.83
5	0.7	20	2000	15	0.4	1.5	362.94
6	0.7	20	2000	45	0.2	4.9	378.63
7	0.7	100	500	15	0.4	4.9	360.95
8	0.7	100	500	45	0.2	1.5	369.63

3 Experimental Investigation

The experiment is performed on CNC machine DT-110 (Mikrotools Pvt. Ltd.). The 50 mm * 50 mm sheet is cut for experiment. The hemispherical end tool of 6 mm diameter is used to form deformation. The suitable orthogonal array (OA), i.e., L8, is used for experiment run preparation. The numeric value of input variables (low and high) for experiment set and measured output response R_a is shown in Table 2.

4 Surface Roughness Measurement

The section of 25 mm^2 from each formed part is measured at its base side (Fig. 1) through a digital caliper and cut for measuring the surface roughness. The surface roughnesses of samples are measured through atomic force measurement (AFM) technique. The roughness is measured in NT-MDT machine at 5× magnification. The pictorial image (2D and 3D) measured area along with average surface roughness (R_a), ten-point height (R_z), peak to peak (R_y) and root mean square (R_q) is generated. The microscopic image of each sample is presented in Fig. 2.

5 Modeling R_a Through Soft Computing Tool

Artificial neural network (ANN) is a soft computing tool used for optimization. Various types of network algorithms such as feed-forward back propagation (FFBP),

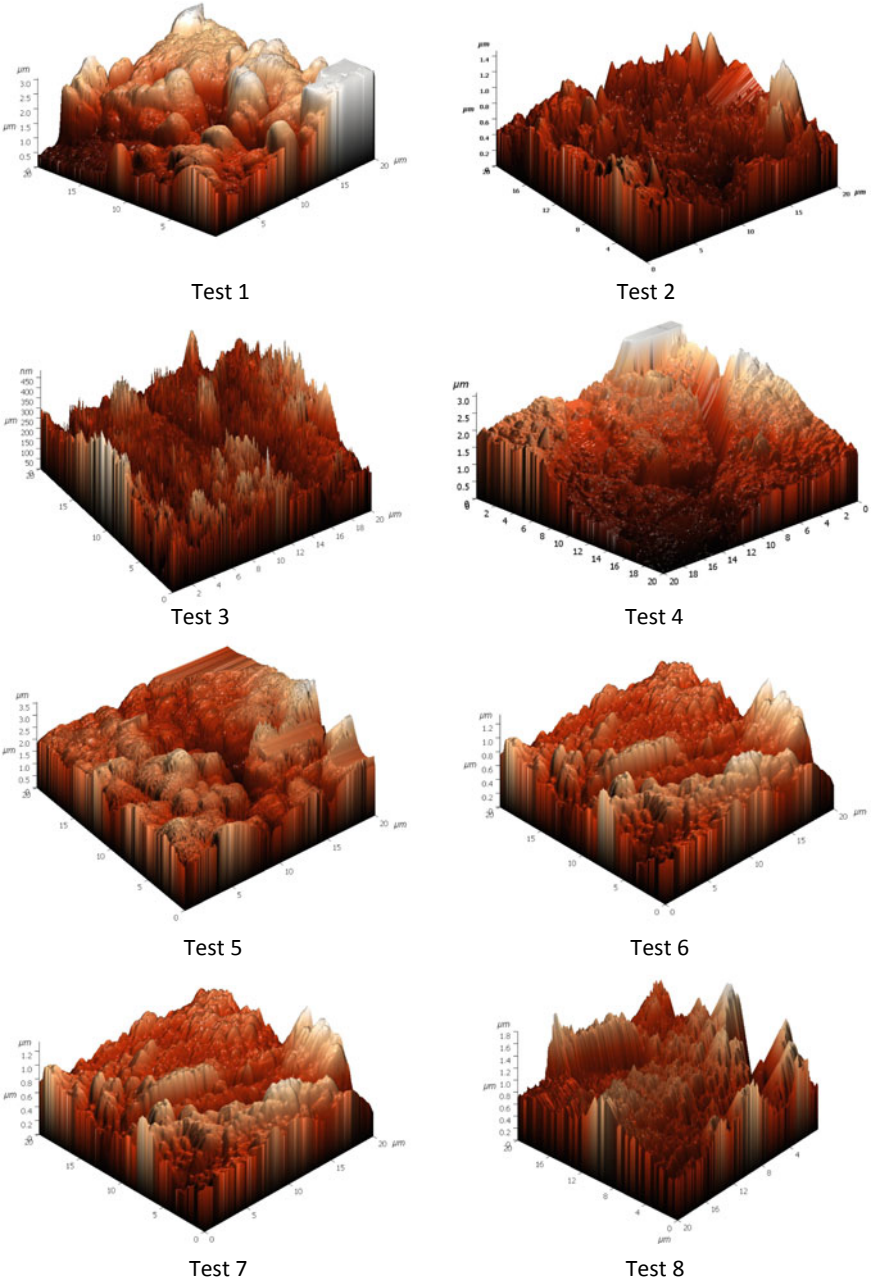

Fig. 2 3D microscopic image of individual test sample

Elman back propagation (EBP), time-delay back propagation (TDBP), Cascade forward back propagation (CFBP) and self-organizing map (SOM) are implemented by authors for modeling. Mostly, the FFBP algorithm [15–18] is widely utilized for predicting output responses in SPIF.

For the present research work, FFBP neural network structure 6-6-1 is developed (Fig. 3). The sigmoid transfer function is used at hidden layer, and at output layer, linear activation function is used.

The input variables and output response, i.e. R_a obtained from each experiment are taken are considered as inputs for the prediction of average surface roughness through ANN. Randomly, 60% of experimental data are used for training, whereas 20% data are used for testing and rest 20% are used for validation of the BP model without normalizing the input data. The simulated R_a from the ANN for the test condition and mean error is presented in Table 3.

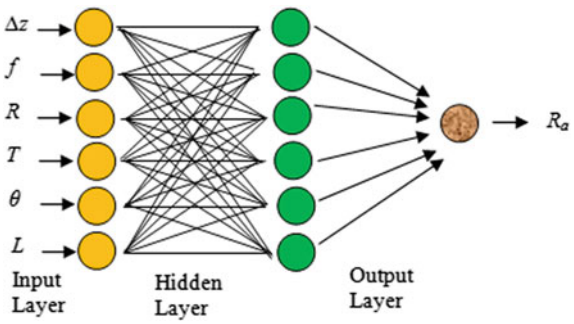

Fig. 3 Feed forward neural network system

Table 3 Predicted R_a with its mean error

Test	R_a (Experiment)	R_a (Predicted)	Error	Error (%)	Mean error
1	134.863	176.497	41.63	30.871	0.71
2	268.29	272.376	4.086	1.522	
3	156.102	149.289	−6.813	−4.364	
4	269.831	270.174	0.343	0.127	
5	362.943	348.148	14.795	−4.076	
6	378.637	377.619	1.018	−0.268	
7	360.951	287.911	73.04	−20.23	
8	369.637	377.594	7.957	2.152	

6 Result and Discussion

The data form experiments yielding a very good agreement with predicted results of ANN for the considered parameters. Besides, the percentage error of predicted R_a is in the range of −0.286 to 30.871. Minimum error, i.e., 0.343 nm, is found in experiment 4, whereas maximum error, i.e. 73.04, in experiment 7.

7 Conclusion

ANN is a user-friendly tool which can be used in manufacturing processes too. The capability of this tool is to forecast the output responses without doing pivot experiment only on the basis of past records. The output is predicted only on few steps which reduces both cost and time. In the present study, the ANN is used to predict the output response, i.e. R_a, and compared with experimental R_a to find the error in results. The prediction results show that ANN could be used as a soft computing tool in manufacturing industries too.

References

1. Ambrogio, G., Cozza, V., Filice, L., Micari, F.: An analytical model for improving precision in single point incremental forming. J. Mater. Process. Technol. **191**, 92–95 (2007)
2. Pohlak, M., Majak, J., Kuttner, R.: Manufacturability and limitations in incremental sheet forming. Proc. Est. Acad. Sci. Eng. **13**(2), 129–139 (2007)
3. Bahoul, R., Arfa, H., Belhadj, H.S.: A study on optimal design of process parameters in single point incremental forming of sheet metal by combining Box-Behnken design of experiments, response surface methods and genetic algorithms. Int. J. Adv. Manuf. Technol. **74**, 163–185 (2014)
4. Oraon, M., Sharma, V.: Sheet metal micro forming: future research potentials. Int. J. Prod. Ind. Eng. **1**(1), 31–35 (2010)
5. Park, J.J., Kim, Y.H.: Fundamental studies on the incremental sheet metal forming technique. J. Mater. Process. Technol. **140**, 447–453 (2003)
6. Hamilton, K., Jeswiet, J.: Single point incremental forming at high feed rates and rotational speeds: surface and structural consequence. CIRP Ann. Manuf. Technol. **59**, 311–314 (2010)
7. Hamilton, K.A.S.: Friction and external surface roughness in single point incremental forming: a study of surface friction, contact area and the 'orange peel' effect. M.Sc. dissertation, Department of Mechanical and Materials Engineering, Queen's University, Canada (2010)
8. Oleksik, V., Pascu, A., Deac, R., Fleaca, R., Bologa, O., Racz, G.: Experimental study on the surface quality of the medical implants obtained by single point incremental forming. Int. J. Mater. Form. **3**, 935–938 (2010)
9. Radu, M.C., Cristea, I.: Processing metal sheets by SPIF and analysis of parts quality. Mater. Manuf. Processes **28**, 287–293 (2013)
10. Uttarwar, P.B., Raini, S.K., Malwad, D.S.: Optimization of process parameter on surface roughness (Ra) and wall thickness on SPIF using Taguchi method. Int. Res. J. Eng. Technol. **2**(9), 781–784 (2015)

11. Liew, K.M., Tan, H., Ray, T., Tan, M.: Optimal process design of sheet metal forming for minimum spring back via an integrated neural network evolutionary algorithm. Int. J. Adv. Manuf. Technol. **26**(3–4), 284–294 (2004)
12. Xu, J., Zhang, Z., Wu, Y.: Application of data mining method to improve the accuracy of spring back prediction in sheet metal forming. Int. J. Adv. Manuf. Technol. **8**(3), 348–353 (2004)
13. Wang, L., Lee, T.C.: Prediction of limiting dome height using neural network and finite element method. J. Shanghai Univ. (Eng. Ed.) **27**, 1082–1088 (2006)
14. Oraon, M., Sharma, V.: Predicting force in single point incremental forming by using artificial neural network. Int. J. Eng. Trans. A **31**(1), 88–95 (2018)
15. Ambrogio, G., Filice, L., Guerriero, F., Guido, R., Umbrello, D.: Prediction of incremental sheet forming process performance by using a neural network approach. Int. J. Adv. Manuf. Technol. (2010)
16. Vahdati, M., Sedighi, M., Mahdavinejad, R.: Prediction of applied forces in incremental sheet metal forming (ISMF) process by means of artificial neural network (ANN). J. Automot. Appl. Mech. **2**(2) (2014)
17. Varthini, R., Gandhinathan, R., Pandivelan, C., Jeevanantham, A.K.: Modelling and optimization of process parameters of the single point incremental forming of aluminium 5052 alloy sheet using genetic algorithm-back propagation neural network. Int. J. Mech. Prod. Eng. **2**(5), 55–62 (2014)
18. Oraon, M., Sharma, V.: Prediction of surface roughness in single point incremental forming of AA3003-O alloy using artificial neural network. Int. J. Mater. Eng. Innov. **9**(1), 1–19 (2018)

Parametric Analysis on Surface Roughness of Micro-channel by Fiber Laser Milling on Zirconia (ZrO_2)

O. F. Biswas, A. Sen, G. Kibria, Biswanath Doloi and B. Bhattacharyya

Abstract In the present days, the requirement of micro-machining has seen a rapid growth for the fabrication of precision machining of complex parts in automobile, shipbuilding, aerospace, electronics, medical industries, etc. Surface finish of these types of components is one of the most important criteria for fabricating better quality and to avoid failure caused by surface defects. The paper addresses the experimental investigation for the variation of surface roughness of micro-channel milling on flat zirconia (ZrO_2) ceramics by using a pulsed fiber laser system. In this work, considered parameters are laser power, pulse frequency, laser scan speed, and the number of scan while responses considered are surface roughness parameters, i.e., R_a and R_z. The experimental results show that aforesaid factors revealed huge influences on surface finish criteria on machined micro-channel on zirconia ceramics.

Keywords Fiber laser · Micro-channel milling · Zirconia · Surface roughness

1 Introduction

Nowadays, micro-machining of engineering materials has become very popular for the production of miniaturized components to fulfill the demands of various industries. Zirconia (ZrO_2) is one of the most promising ceramic materials for the replacement of other advanced hard-to-machine materials, due to its several advantages

O. F. Biswas (✉)
Department of Mechanical Engineering, Bankura Unnayani Institute of Engineering, Bankura 722146, India
e-mail: faruk.au91@gmail.com

A. Sen
Department of Mechanical Engineering, Calcutta Institute of Technology, Howrah 711316, India

G. Kibria
Department of Mechanical Engineering, Aliah University, Kolkata 700156, India

B. Doloi · B. Bhattacharyya
Department of Production Engineering, Jadavpur University, Kolkata 700032, India

L. Li et al. (eds.), *Advances in Materials and Manufacturing Engineering*, Lecture Notes in Mechanical Engineering, https://doi.org/10.1007/978-981-15-1307-7_10

such as high strength, fracture toughness, very low thermal conductivity, and excellent wear properties. It is widely applied in medical industries, mainly for orthopedic application for the fabrication of crown, bridge restorations, implant abutments, etc. [1–6]. Therefore, the machining of these types of material is one of the challenging tasks for the manufacturer. Laser micro-channel milling process is one of the recently developed material removal techniques which is widely employed for micro-fabrication on metal and nonmetals [7, 8]. In this study, a high-intensity laser beam is utilized for producing micro-channel on the work sample zirconia (ZrO_2) ceramic. To explore the influence of considered factors on performance criteria, one factor at a time was varied.

2 Experimental Planning

A multi-diode-pumped 50 W fiber laser system is employed to carry out laser micro-channel milling on zirconia (ZrO_2) ceramic. 43 μm of laser beam spot diameter (at focused condition) is utilized in the present research work. One factor at a time (OFAT) strategy has been utilized for conducting the experiments. Process variables which are taken for this research work are laser average power, pulse frequency, scanning speed, and the number of pass. The values of surface roughness (R_a and R_z) have been measured after performing each experiment.

Some of the process variables are kept constant during the experiment such as pulse width as 80% of duty cycle and air pressure of nozzle at 4 kgf/cm^2. MITUTOYO SJ410 roughness measuring instrument is utilized for the measurement of the micro-milling surfaces. Using this instrument, the responses (R_a and R_z) are measured along workpiece length. The values of R_a and R_z are measured at five different locations, and the average of these values is taken for analysis. During laser micro-channel milling operation, overlap factors such as spot overlap and transverse overlap of the laser beam are considered. The values of process parameters are chosen in such a manner that these two overlap factors are more than 85% for each set of the experiment which ensures that good quality of surface finish has been achieved.

3 Results and Discussions

Based on the experimental results, various plots are drawn for surface roughness values, i.e., R_a and R_z at various ranges of process variables in combination with the focused condition and analyzed subsequently.

In Fig. 1, the effect of laser power on surface roughness (R_a and R_z) is shown. The plot shows that lower setting of laser average power results in smooth micro-channel profiles compared to higher laser power. The reason behind the fact is that the low amount of material is melted at lower values of average power which yields into low pulse energy. As a result, the material removal rate is lowered which in turn produces

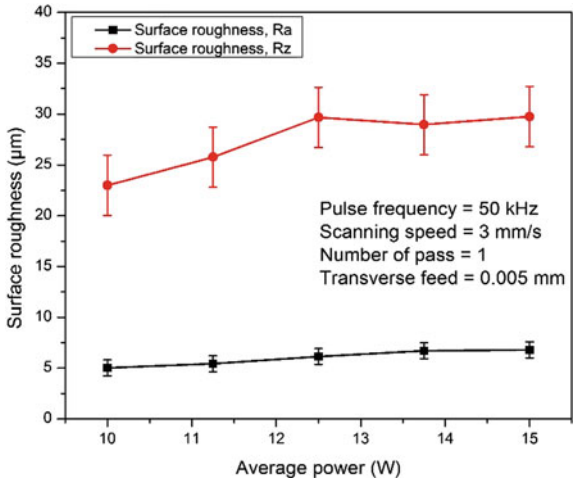

Fig. 1 Effect plot of laser average power on surface roughness

a uniform surface. Thus, lower values of R_a are observed at low beam power. Micro-channel surface roughness increases with the increment of average power due to high material removal rate. According to Eq. (1) [9], the peak power of the laser beam is directly proportional to the average power, while other parameters are as kept constants. The graph also revealed that surface roughness (R_z) increases with average power. When the laser beam peak power increases significantly, high pulse energy is irradiated in the machining zone. Thus, the machining zone is subjected to melt and vaporize, which causes re-solidification of melt material on machined surface. Thus, micro-peaks are formed on the machining zone surface.

$$\text{Peak power} = \frac{\text{Average power}}{\text{Pulse frequency} \times \text{Pulse duration}} \tag{1}$$

In Fig. 2, the variation of surface roughness due to an increase in pulse frequency is shown. With the increment of pulse frequency, the surface roughness values have increased (R_a) subsequently. It is observed from Eq. (1) that laser peak power is inversely proportional to the pulse frequency or pulse repetition rate. On the contrary, with increase in pulse frequency, the time duration for irradiation of two laser pulses decreases. Thus, the machining zone does not get adequate time for the removal of the excess material which produces rough surface. From Fig. 2, it can be observed that surface roughness (R_z) has also increased with the increment of pulse frequency. The more irregularities on the surface have occurred at higher values of pulse frequency which causes an increment of crater size.

In Fig. 3, the variation of surface roughness due to an increase in scanning speed is shown. It is already known that laser spot overlap is governed by the combined effect of laser scan speed and pulse frequency. The plot shows that with scanning speed, surface roughness values decrease. However, the rate of decrement of R_a value is lesser than the values of R_z. Spot overlap factor drops significantly with

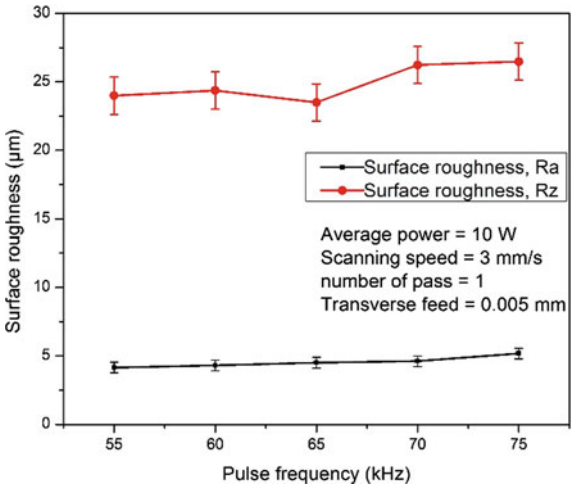

Fig. 2 Effect plot of pulse frequency on surface roughness

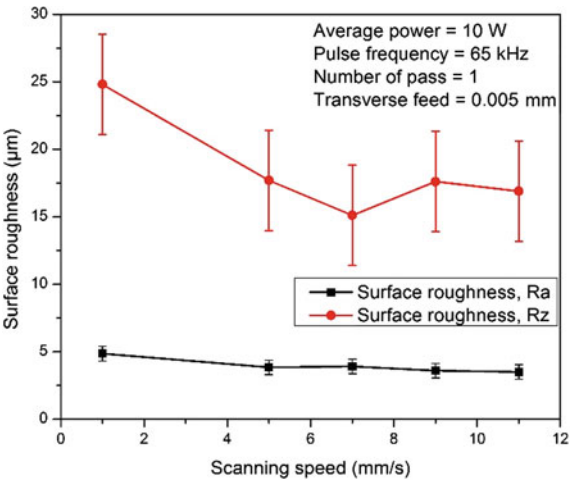

Fig. 3 Effect plot of scanning speed on surface roughness

the increment of scanning speed. With scanning speed, laser-material interaction decreases. Therefore, cutting zone gets sufficient time for the removal of the molten particles. Thus, the number of micro-peaks generated on the surface is less.

Figure 4 represents the variation of surface roughness with number of pass. This figure reveals that the values of surface roughness (R_a and R_z) decrease with the repeated movement of the laser beam along the machining zone. With the number of pass, both width and depth of machined micro-channel increase. Here, with the interaction of material and laser beam, the material from the heat radiated zone is removed in layer by layer. The applied assist air jet helps in removing the molten material from machining zone. Due to this, a decrement of the uneven peaks on

micro-channel machined surface is observed, which further causes smooth finished surface at a higher number of pass settings.

Optical microscopic images are taken at various parametric combinations to examine the micro-channel milling surface qualitatively. Figure 5a and b depict optical microscopic images of surface of micro-channel milling on zirconia at various parametric settings. Comparing these microscopic views of machined micro-channels, it is obvious that laser average power, pulse frequency, scanning speed, and the number of passes have contributed immensely in order to achieve desired laser micro-channel milling surface. The values of surface roughness (R_a) are 4.86 μm and 2.48 μm, respectively. The values of surface roughness (R_z) are 24.81 μm and 14.22 μm.

4 Conclusions

From the set of experimentation and optical microscopic views of machined micro-channels during laser micro-channel milling on zirconia ceramics, it can be concluded that the considered process parameters have huge influences in generating accurate micro-channel of desired shapes and surface finish. From the experimental result and discussion, the following conclusions can be drawn:

(a) Surface roughness (R_a and R_z) value increases with the increment in laser average power. More micro-peaks and valleys are generated at higher values of average power. The lowest values of R_a and R_z are obtained as 5.02 μm and 22.99 μm, respectively.
(b) Higher values of pulse frequency produce rough micro-milled surfaces. The lowest values of R_a and R_z are obtained as 4.15 μm and 23.99 μm, respectively.

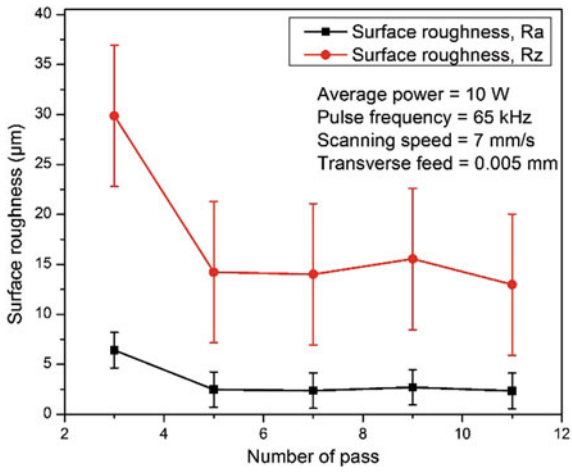

Fig. 4 Effect plot of number of pass on surface roughness

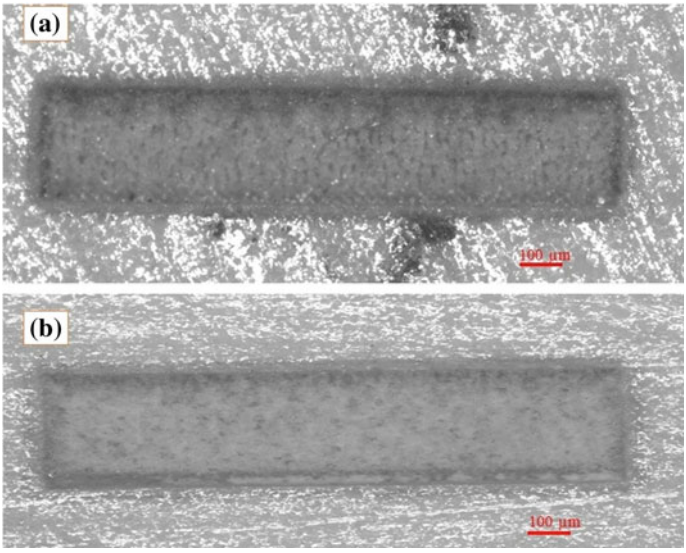

Fig. 5 Optical microscopic images of surface of micro-channel milling on zirconia at settings of **a** average power of 10 W, pulse frequency at 65 kHz, scanning speed of 1 mm/s, number of pass 1, and transverse feed at 0.005 mm, **b** average power of 10 W, pulse frequency at 65 kHz, scanning speed at 7 mm/s, number of pass 5, and transverse feed at 0.005 mm

(c) Surface finish of the micro-channel improves with the increment of scanning speed. The rate of decrement of R_a value is lesser than the values of R_z. The lowest values of R_a and R_z are obtained as 3.5 µm and 15.11 µm, respectively.
(d) A gradual decrement of surface roughness is observed while the number of pass increases. The lowest values of R_a and R_z are obtained as 2.34 µm and 12.98 µm, respectively.

The present set of experimental results will be beneficial for further research work in the area of laser micro-milling of difficult-to-machine material and also for analyzing other various characteristics such as skewness and waviness in order to achieve better quality of micro-channel on ceramics.

References

1. Madfa, A.A., Al-Sanabani, F.A., Al-Qudami, N.H., Al-Sanabani, J.S., Amran, A.G.: Use of zirconia in dentistry: an overview. Open Biomater. J. **5**, 1–9 (2014)
2. Manicone, P.F., Iommetti, P.R., Raffaelli, L.: An overview of zirconia ceramics: basic properties and clinical applications. J. Dent. **35**, 819–826 (2007)
3. Rizvi, N.H., Apte, P.: Developments in laser micro-machining techniques. J. Mater. Process. Technol. **127**(2), 206–210 (2002)
4. Meijer, J.: Laser beam machining (LBM), state of the art and new opportunities. J. Mater. Process. Technol. **149**(1–3), 2–17 (2004)

5. Majumdar, J.D., Manna, I.: Laser processing of materials. Sadhana **28**(3–4), 495–562 (2003)
6. Mishra, S., Yadava, V.: Laser beam micro machining (LBMM)—a review. Opt. Lasers Eng. **73**, 89–122 (2015)
7. Campanelli, S.L., Casalino, G., Ludovico, A.D., Bonserio, C.: An artificial neural network approach for the control of the laser milling process. Int. J. Adv. Manuf. Technol. **66**(9–12), 1777–1784 (2013)
8. Leone, C., Genna, S., Tagliaferri, F., Palumbo, B., Dix, M.: Experimental investigation on laser milling of aluminium oxide using a 30 W Q-switched Yb:YAG fiber laser. Opt. Laser Technol. **76**, 127–137 (2016)
9. Kibria, G., Doloi, B., Bhattacharyya, B.: Experimental investigation and multi objective optimization of Nd:YAG laser micro-turning process of alumina ceramic using orthogonal array and grey relational analysis. Opt. Laser Technol. **48**, 16–27 (2013)

Characterization of High-Frequency Thermal Sensor for Transient Temperature Measurement

Anil Kumar Rout, Niranjan Sahoo and Pankaj Kalita

Abstract A thermal probe has been fabricated in-house from an E-type thermocouple (Chromel-constantan) for transient temperature measurements during the studies related to groundbased high speedflow phenomena. The thermo elements of the thermocouple are coupled in the format of coaxial sensor called as coaxial surface junction thermocouple (CSJT). The junction properties have been analysed qualitatively and quantitatively through field emission scanning electron microscopy (FESEM) technique and the configuration of the thermo elements have been observed through energy dispersive X-ray (EDX) technique. The thermal probe is then calibrated by using a fluid bath and used to study the shock wave phenomena in a shock tube, which produces shock waves in a laboratory scale. The thermal probe response is captured and compared with a standardized highsensitive pressure sensor signal. The in-housefabricated thermal probe response is quite fast and can be used to replace the highcost pressure sensor.

Keywords Surface junction thermocouple · Calibration · Characterization · Shock tube · Sensitivity

1 Introduction

Phenomenon of aerodynamic heating is an important aspect in every aero vehicle, re-entry bodies and space vehicles moving with supersonic and hypersonic speeds. The real-time constraint to carry out the experiments has put down the studies to ground-based evaluation with the help of shock tubes and shock tunnels, which generate shock waves at laboratory and industrialscale. There are few gauges which

A. K. Rout (✉) · N. Sahoo · P. Kalita
Indian Institute of Technology Guwahati, Guwahati, Assam, India
e-mail: anil.rout@iitg.ac.in

N. Sahoo
e-mail: shock@iitg.ac.in

P. Kalita
e-mail: pankajk@iitg.ac.in

L. Li et al. (eds.), *Advances in Materials and Manufacturing Engineering*, Lecture Notes in Mechanical Engineering, https://doi.org/10.1007/978-981-15-1307-7_11

can respond to those high speed flows. As a common practice, standardized high-frequency pressure gauges are used in those devices for the measurement of pressure. Thin-film gauges, slug gauges, temperature-sensitive paint, thermography are some of the options for measurements of transient temperature and heat flux values. Each of the sensors has their own advantages and disadvantages in terms of response, fabrication, cost, applicability, durability, etc. So, in the search of a low cost, durable, and fast-response thermal sensor, coaxial surface junction thermocouple (CSJT) has been found to be one option for such studies. Thermocouples are measuring probes, governed by Seebeck effect and are used to measure temperatures in various experiments with accuracy. Presently, coaxial surface junction thermocouple (CSJT) has been evolved as a potential tool for transient temperature measurement and from the temperature history, surface heat flux can be predicted with suitable modelling of the sensor. Using CSJT, few researchers have calculated heat flux values for K type and also for E-type thermocouple [1–4]. The design technique, fabrication process, and junction formation of such probes require much parametric involvement [5–7]. The response time is one among the features of CSJT which helps in prediction of highly transient flow parameters [8, 9]. Though there are some studies carried out based on this, still there is a requirement for in-depth study in the aspects related to fabrication and application. For the present case, an E-type CSJT has been fabricated and the junction properties have been studied through optical techniques. The probe is calibrated and used in a high speed-flow environment to capture the shock effects.

2 Fabrication of the Sensor

Chromel and constantan are the thermo elements for E-type thermocouple. Chromel element of 3.25 mm diameter coaxially forms an outer jacket over 0.91 mm constantan wire with a very small (few μm) insulation thickness in between them as depicted in Fig. 1a. The length of the sensor is taken as 10 mm. The junction is prepared at the surface through abrasion technique, which forms plastic deformation in between two thermo elements through some cold welds. The fabrication process requires some precision work and hand-on practice. After fabrication, the sensor is packaged in a BS4 standard mounting for fitting in the shock tube. The realized schematic in Fig. 1b shows a packaged probe with chromel and constantan lead wires for measurement.

3 Characterization of the Sensor

The formation of junction is a tricky task which requires a lot of practice and technique even though; there is a requirement for checking of every sensor junction for detecting junction defect and junction thickness. The surface texture and insulation thickness are observed through field emission scanning electron microscopy (FESEM). The plots from Fig. 2 represent different types of junctions and defects

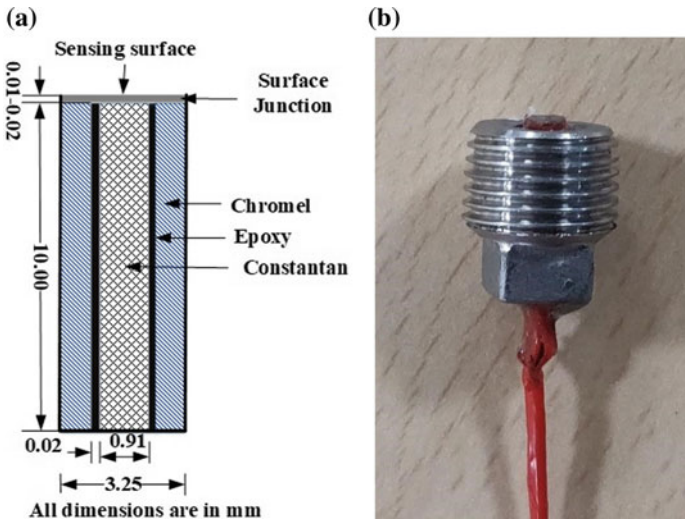

Fig. 1 Fabrication and packaging of the sensor: **a** schematic of the sensor, **b** realization of packaged sensor (thermal probe)

generally encountered during preparation of junction. A proper junction will lead to proper exposure of real sensing part of sensor to heat and hence, accurate estimation of heat fluxes at a later part. For the present case, a bid-type surface, prepared through sanding is considered for study.

The surface junction characteristics are directly related to its response. The junction characteristics also depend on the composition of the thermo elements. So, the thermo elements used for fabrication of sensor are examined through electron discharge X-ray (EDX) technique for configuration of material composition and compared with literature [5, 9]. The chromel element is having a composition of 87.1% Ni, 10.1% Cr and 2.8% Si, while copper (51.5%) and nickel (35.4%) are dominant elements for constantan (Fig. 3).

4 Calibration of Sensor

The output from the thermocouple is measured in terms of voltage. In order to infer change in surface temperatures, the voltage values need to be calibrated against a known temperature. Here, a fluid bath is used for the calibration purpose. The thermocouple along with a thermometer is inserted into the glycerine bath to sense the similar environment. The thermocouple is connected to a data acquisition system for voltage measurement. Before placing the thermometer, it is checked for ice point and steam point. The temperature is noted from the thermometer and at the same time, the voltage is noted from the data acquisition system for the same rise and fall of

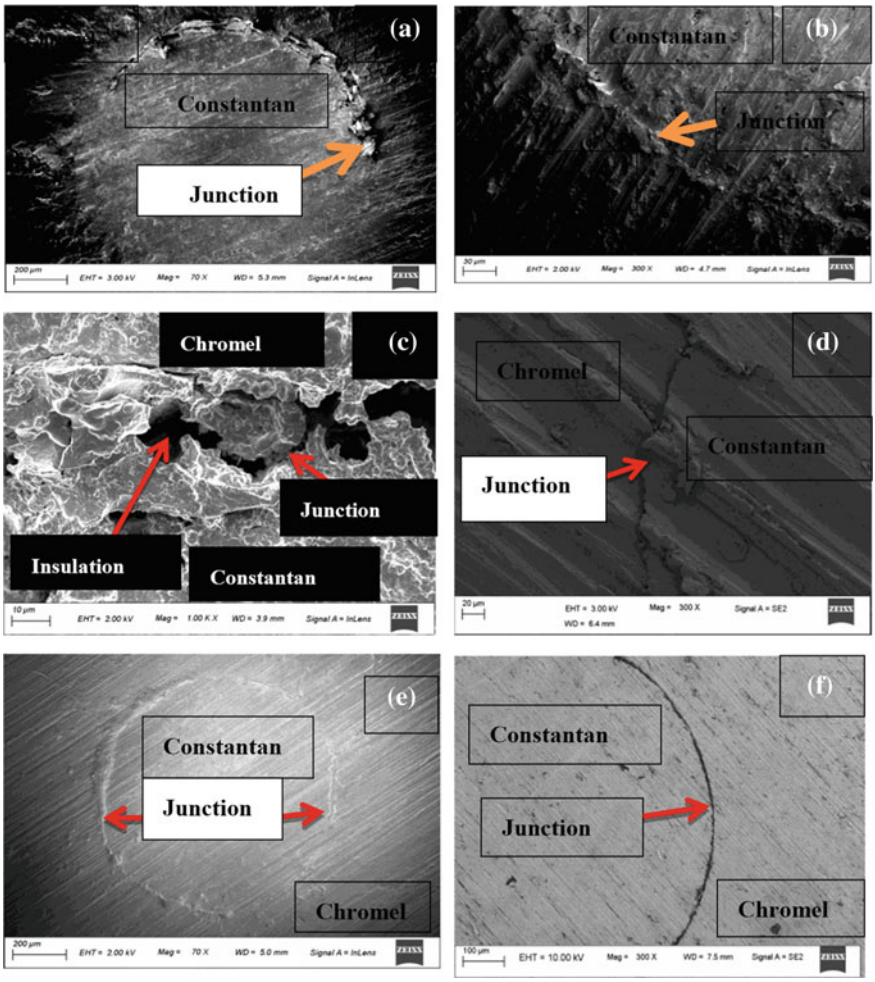

Fig. 2 Surface junction characteristics. **a** A defective junction, **b** partial linkage, **c** butt type junction, **d** a lap-type junction, **e** a bid-type junction, **f** polished sensing surface

temperature and plotted in Fig. 4a. The sensitivity of the thermocouple is calculated from Fig. 4b as 59 μV/°C.

5 Real-Time Experiment

To check the feasibility of the sensor, it is tested in a shock tube facility installed at IIT Guwahati. A shock tube is a device that produces shock waves due to sudden rupture of diaphragm separating a high pressure driver gas to a low pressure driven

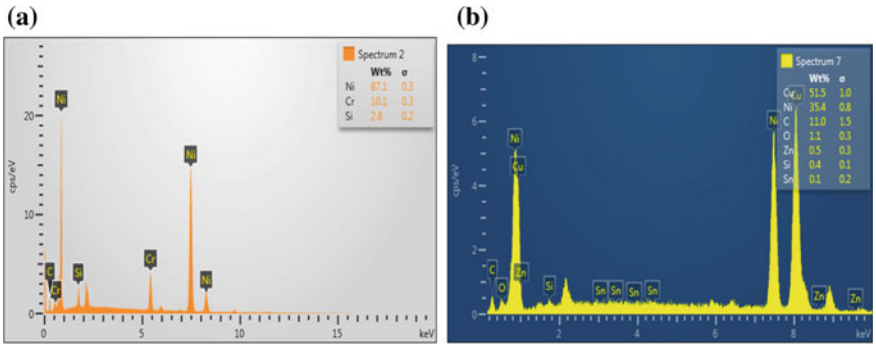

Fig. 3 Configuration of thermo elements **a** chromel, **b** constantan

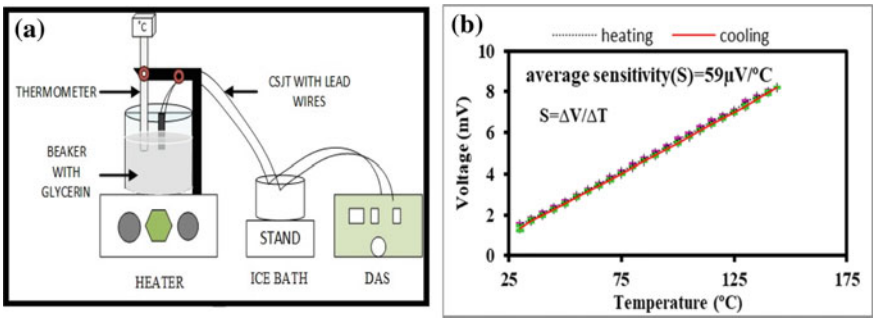

Fig. 4 **a** Calibration set-up, **b** calibration plot

gas. The shock tube, made from a constant area duct mainly used for laboratory scale experiments related to aerodynamic ground-based studies. When nitrogen gas in the driver section is pressurized against atmospheric air in the driven section, the diaphragm bursts suddenly, creating a series of compression waves which travel towards the driven section (Fig. 5). The compression waves combine to form a normal shock wave. After reaching at the end of the tube, the shock wave is reflected and travel as reflected shock wave towards driver section. Any aerodynamic body placed in the flow field or at the end flange can experience the effect of shock wave and hence, the parametric variations impacted due to shock wave can be investigated. The duration of test is few milliseconds so; there is requirement of sensors that can respond very fast.

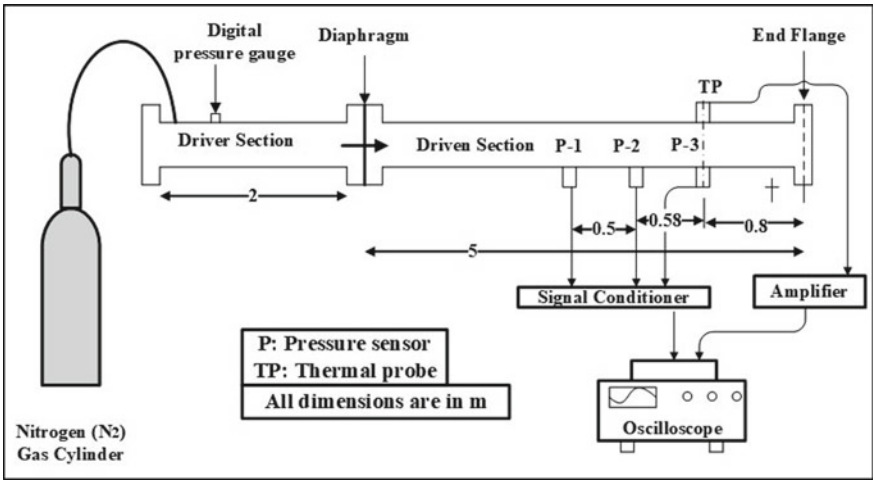

Fig. 5 Schematic of shock tube facility at IIT Guwahati

5.1 Instrumentation for the Experiment

The driver section of the shock tube is fitted with a digital pressure gauge to measure the pressure of driver gas and high-frequency pressure sensors (PCB Piezotronics, USA) are mounted at the driven section. Two pressure sensors (P1 and P2) are placed at a known distance apart to calculate Mach number. These pressure sensors are standardized pressure sensors with very fast response time. So, by taking measurements from these pressure sensors as reference, response behaviour of the thermal probe is checked for which, the thermal probe (TP) is placed exactly opposite to a third pressure sensor (P3). Output from all the sensors is in terms of voltage which is to be recorded with an oscilloscope. The output from the thermal probe is in terms of few millivolt which need to be amplified for recording in the oscilloscope. So, the signal is suitably amplified before recording. With the passage of shock wave over pressure sensors, a step change in the signal is recorded corresponding to a pressure jump across the shock wave in the oscilloscope (Make: Yokogawa, having a bandwidth of 200 MHz and a sampling rate of 2.5 GS/s). Along with P3, the thermal probe also responded to the incident shock wave. The pressure sensors underwent a step change where the thermal probe shown a parabolic growth obeying the basic fundamentals of heat transfer, i.e. the temperature profile to a step input is parabolic. On return from the end flange, the reflected shock wave is sensed by P3 and again at the same time, it also sensed by the thermal probe. Hence, it can be concluded from the figure that, the thermal probe is showing a fast response (Fig. 6). From the plot, it can also be observed that the thermal probe is having a rise time of 236.04 μs in comparison to pressure sensor, with a rise time of 196.012 μs.

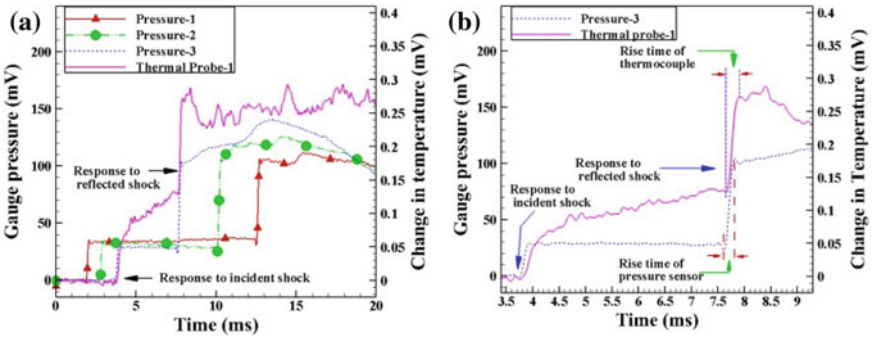

Fig. 6 Transient responses from thermal probe during shock tube experiments

6 Conclusion

A thermal sensor is fabricated in-house from a thermocouple (E-type) and packaged successfully for application in diagnosis of high-speed phenomena in shock tube-based studies. The junction and surface characteristics are diagnosed under optically zoomed environment using FESEM technique and the configuration of the elements through EDX technique. The junction defects, junction types are observed. The sensor is calibrated using a glycerine bath and mounted in the shock tube for flow diagnosis against a standardized pressure sensor. The shock phenomenon in terms of thermal response is captured by the thermal probe along with pressure sensor. It is observed that the thermal probe is quite efficient in capturing the shock phenomena. From the response of the thermal sensor, it can be concluded that the low-cost thermal sensor can be used in lieu of high-cost pressure sensor.

Acknowledgements The authors are very much grateful to "Defence Research and Development Organization (DRDO), New Delhi (India)" for financial support for this experimental work.

References

1. Agarwal, S., Sahoo, N., Singh, R.K.: Experimental techniques for thermal product determination of coaxial surface junction thermocouples during short duration transient measurements. Int. J. Heat Mass Transf. **103**, 327–335 (2016)
2. Kumar, R., Sahoo, N., Kulkarni, V.: Design, fabrication and calibration of heat transfer gauges for transient measurement. In: Proceedings of the ASME 2010 International Mechanical Engineering Congress & Exposition, pp. 1–7. ASME, Canada (2010)
3. Kumar, R., Sahoo, N.: Dynamic calibration of a coaxial thermocouples for short duration transient measurements. J. Heat Transfer **135**(12), 124502 (1–7) (2013)
4. Sanderson, S., Sturtevant, B.: Transient heat flux measurement using a surface junction thermocouple. Rev. Sci. Instrum. **73**(2), 2781–2787 (2002)

5. Mohammed, H., Salleh, H., Yusoff, M.Z.: Design and fabrication of coaxial surface junction thermocouples for transient heat transfer measurements. Int. Commun. Heat Mass Transfer **35**, 853–859 (2008)
6. Mohammed, H., Salleh, H., Yusoff, M.Z.: The effect of scratch technique on the thermal-product value of temperature sensors. Thermophys. Aeromech. **18**(1), 51–64 (2011)
7. Sahoo, N., Peetala, R.K.: Transient surface heating rates from a nickel film sensor using inverse analysis. Int. J. Heat Mass Transf. **54**, 12971302 (2011)
8. Sahoo, N., Kumar, R.: Performance assessment of thermal sensors during short-duration convective surface heating measurements. Heat Mass Transfer **52**, 20052013 (2016)
9. Caldwell, F.R.: Applied methods and instrument. In: Herzfeld, C.W. (ed.) Temperature: Its Measurement and Control in Science and Industry, vol. 3, no. 2, pp. 81–134. Reinhold, New York (1962)

Experimental Investigation of Waste Heat Recovery from Exhaust of Four-Stroke Diesel Engine Using Specifically Manufactured Heat Exchanger

Ram Thakar, Santosh Bhosle and Subhash Lahane

Abstract This paper is concerned with means for performance improvement and reducing exhaust emissions of four-stroke single-cylinder diesel engines by heating inlet air passed to the cylinder by using specifically designed and manufactured heat exchanger. A diesel generating set having a cylinder, 5 horse power (HP), water cooled, Kirloskar Make diesel engine was selected as base engine and the experiments were conducted at part load conditions. The diesel generating setup was modified to run with incorporation of heat exchanger and blower. The exhaust heat is used by specifically designed heat exchanger to heat inlet air passed to the cylinder. The blower is used to increase the volumetric efficiency of the engine which tends to reduce due to heating of the inlet air passed to the cylinder. The experiments were conducted for three setups viz. i. Basic diesel engine setup, ii. Modified setup with heat exchanger and iii. Modified setup with heat exchanger and blower. The experimental results obtained with incorporation of waste heat recovery system were compared with base line data. The rectangular-type shell and tube heat exchanger is designed based on the potential heat savings available at the diesel engine exhaust and manufactured. The due attention is paid while selecting the material for manufacturing heat exchanger. The shell is made of cold-rolled carbon steel and tubes used were copper tubes. The results indicate improved performance and reduced emission levels for modified engine, i.e. using specifically designed heat exchanger for heating the inlet air passed to the engine. The results obtained indicate that there is potential in the exhaust gases and heat of exhaust gases can be utilized using specifically designed and manufactured rectangular-type shell and tube heat exchanger to heat inlet air passed to the engine cylinder.

Keywords Diesel engine · Exhaust heat recovery · Heat exchanger

R. Thakar (✉) · S. Lahane
Marathwada Institute of Technology, Aurangabad 431010, India
e-mail: thakar_ram@ycmou.digitaluniversity.ac

S. Bhosle
Maharashtra Institute of Technology, Aurangabad, India

L. Li et al. (eds.), *Advances in Materials and Manufacturing Engineering*, Lecture Notes in Mechanical Engineering, https://doi.org/10.1007/978-981-15-1307-7_12

1 Introduction

Efficiency is major parameter related to any diesel engine which is always measured for checking its performance. There are many losses concerned with diesel generating (DG) set that tends to reduce the performance of the engine. Among all losses, the exhaust gas loss or exhaust flue gas loss contribute major loss that badly affects on the performance of the engine. The high temperature available in the exhaust gases attributes toward the decline in performance and increasing the exhaust emissions of the engine. Many techniques had been tried to make use of this exhaust heat of gases for improving efficiency and minimizing the emission level.

Abd-Alla investigated on the use of exhaust gas recirculation (EGR) technique to check its potential of recovering exhaust heat from engine exhaust and reducing the NO_x emissions. They suggested to make optimum use of EGR by using it in airflow path rather than displacing part of inlet air. The use of EGR by this method substantially reduces NO_x emissions [1]. Shi et al. made use of both internal and exhaust gas recirculation on HCCI engine and found reduction in NO_x and smoke emissions due to use of homogeneous charged compression ignition system [2]. Hountals et al. verified effect of using cooled EGR gas temperature on turbocharged DI heavy duty diesel engine using multizone combustion model and shown its positive effect on brake-specific fuel consumption and lowering the soot values [3]. Aranguren et al. experimented, validated and developed computational model for thermoelectric generation which predicts results with an accuracy of 12% [4]. Many other researchers investigated on diesel engine with biodiesel blend with diesel fuel. They used waste rice **bran** oil, vegetable cooking oil, pongamia, Pungam methyl esters to prepare biodiesels [5]. In recent years, the new technique of preparation of homogeneous charged compression ignition (HCCI) is becoming familiar where homogeneous charge is prepared by mixing fuel and air which is compressed and allowed to self-ignite [6]. The organic Rankine cycle (ORC) is proven technique to recover low grade heat at 90 °C from industrial excess heat. Lemmens and Lecompte investigation suggested practical and financial suitability of using ORC systems for flue gas heat recovery for electricity generation under certain conditions [7]. The researchers investigated on different technologies for recovery of the exhaust heat from IC Engines. The techniques such as thermoelectric generation, bottoming Rankine cycle, six-stroke cycle found opportunities for potential energy savings and improvement in the performance [8]. Yang et al. designed organic Rankine cycle having low-temperature and high-temperature loops. They used R245fa as refrigerant which extracts heat from coolant and released heat from turbocharged air to recover waste heat from six cylinder diesel engine. The experimentation resulted into an increase in efficiency by 13%. It is also seen there is maximum reduction of 4% in brake specific fuel consumption when diesel engine working in the part of higher load [9]. The new technique introduces the concept of use of light weight material and alternative refrigerant for heat exchangers considering their environmental concerns. Mastrullo et al. optimized geometrical model for a shell and louvered fin mini–tubes heat exchanger with organic Rankine cycles (ORCs) and suggested

low-weight and compact-size heat exchanger to be used for producing considerable amount of work and thermal efficiency [10]. Many researchers investigated to use organic Rankine cycle (ORC) for recovery of exhaust heat and emphasized that the design of evaporator is critical and the success of recovery system entirely depends on its design. Zhang et al. developed mathematical model of evaporator based on its designed dimensions and specified ORC working conditions for exhaust waste heat recovery from diesel engine. They showed as speed and load increase, evaporator outlet exhaust temperature increases. To achieve this, careful selection of heat transfer area for finned tube is required which is based on engine's operating range [11]. Hossian and Bari experimented for waste heat recovery on 40 kW DG set using two of the shelf-type heat exchangers for superheated steam generation. They simulated design of heat exchanger with available data after experimentation and compared it with effectiveness of optimized heat exchanger. They reported less effectiveness of heat exchanger compared to optimized heat exchanger. It is also observed that effectiveness was more for parallel arrangement [12]. Researchers have been trying to improve thermal efficiency of diesel engines by applying different techniques. The effect of high injection pressure and cylindrical air pressure have been investigated on combustion and heat release rate for DI diesel engines shown improved brake thermal efficiency [13]. Bari and Hossain designed and simulated pancake-shaped type heat exchanger by using CFD software and concluded generating additional power of 10.5 kW due to pancake-shaped heat exchanger as compared to heat exchanger of round-shaped-type which was able to produce power 9.5 kW [14]. Meng et al. shown fuel consumption efficiency can be improved by using thermoelectric generators by developing multiphysics model applied in a automobile exhaust wherein exhaust is modeled and reported improvement in system performance at the cost of less thermoelectric material consumption [15]. Kim et al. experimentally investigated on a direct contact thermoelectric generator (DCTEG) for recovery of heat from exhaust of diesel engine to improve performance. They adopted the method of varying coolant temperature, engine load and rotation speed during experimentation. Their result showed improved energy conversion efficiency of DCTEG which was in between 1 and 2%. Their results also show that maximum thermal energy is extracted by DCTEG and about 20% energy wasted to the environment irrespective of load conditions [16]. Shixue et al. used thermoelectric generator (TEG) for recovery of heat from gasoline engine exhaust for which they optimized geometrically sandwich heat exchanger of plate type using finite element analysis and suggested key parameters flow velocity and TEG module area for optimization of TEG [17]. Thakar et al. designed counter flow shell and tube heat exchanger and reported heating of inlet air up to 150 °C [18]. The present paper is the result of experimentation on single cylinder, four-stoke diesel engine with the incorporation of waste heat recovery with use of specifically designed and manufactured heat exchanger and blower. The rectangular-type counter flow shell and tube heat exchanger is designed based on the potential heat savings available at the diesel engine exhaust and then manufactured. The due attention is paid while selecting the material for manufacturing heat exchanger. The shell is made of cold-rolled carbon steel and tubes used were copper tubes. The use of CRC sheet for shell and copper material for tube acts as

thermal storage and heat exchanging device. The result shows substantial savings in the exhaust heat and thereby showing improved performance and reduction in emissions of the engine by waste heat recovery using the heat exchanger between outlet and inlet duct of the diesel engine.

2 Experimentation, Instrumentation and Methodology

The present experimentation is completed on vertical, water cooled, single cylinder, four stroke, vertical, 5 HP, diesel engine. The fuel used for experimentation is high speed (HS) diesel oil. The designed heat exchanger is manufactured with attention to recover maximum heat potential from exhaust gas of diesel engine. The details of the material used for manufacturing of heat exchanger are given in Table 1. The modified experimental setup with manufactured heat exchanger is shown in Fig. 1.

Thermocouples connected to control panels are used to measure the temperatures at various locations. The volumetric type of method is used for measuring the fuel consumption. Hartridge smokemeter is used for measurement of smoke in the exhaust. Following three trials were conducted to determine volumetric efficiency, brake thermal efficiency, brake-specific fuel consumption and smoke density. The three experimentations have been conducted on stationary diesel for measurement of the performance and emissions of the engine viz. i: Experimentation on basic diesel engine running at normal conditions at injection timing 26° BEFORE TDC at atmospheric temperature, ii. Experimentation with modified engine setup with heat exchanger at injection timing 23° BEFORE TDC and iii. Experimentation with modified engine setup with heat exchanger and blower at injection timing 23° BEFORE TDC.

Table 1 Details of material used for manufacturing heat exchanger

Description	Quantity	Material
1. Tubes: O.D = 9.54 mm, I.D = 9.94 mm, length = 4.2 m	14	Copper
2. Shell: (For end closure) Width = 105 m, height = 90 mm, thickness = 2 mm	2	Carbon rolled carbon steel (CRC)
Shell: (For end connectors) Top width = 110 mm, base width = 60 mm, height = 90 mm thickness = 2 mm	8	
3. Baffles: Width = 92 mm, height = 90 mm, thickness = 2 mm	4	Carbon rolled carbon steel (CRC)

Fig. 1 Modified experimental setup with heat exchanger

2.1 Experimental Trial 1: Experimentation on Basic Diesel Engine Running at Normal Conditions at Injection Timing 26° BEFORE TDC at Atmospheric Temperature

Initially, the cooling water supply is started. The engine allowed to run on no load till steady state has been reached. At no load, the cooling flow rate is adjusted. After the steady state has been reached, the time for outlet water temperature, manometer reading is noted. The exhaust gas sample drawn in smoke meter is analyzed for measuring the percent smoke density. Then, the engine is loaded in step of six, twelve, eighteen and twenty kilograms and the procedure is repeated again.

2.2 Experimental Trial 2: Experimentation with Modified Engine Setup with Heat Exchanger at Injection Timing 23° BEFORE TDC

The heat exchanger on the basis of availability of heat potential at the exhaust was designed and manufactured. This heat exchanger was placed just near the inlet and outlet ducts of the engine. The inlet air was passed through rectangular shell tube type heat exchanger. In this, the inlet air was passed through the number of tubes and the exhaust gases were passed over these tubes. Efficiencies and emissions of stationary diesel engine for experimentation with modified engine setup with heat exchanger at injection timing 23° BTDC were evaluated. The trial on diesel engine with heat exchanger is conducted at no load to gradually increasing to full load.

2.3 Experimental Trial 3: Experimentation with Modified Engine Setup with Heat Exchanger and Blower at Injection Timing 23° BEFORE TDC

In this, the blower was placed between the air box and heat exchanger. Proper care was taken for the placement, since the blower is driven by pulley which is driven by camshaft of the engine. Efficiencies and emissions of stationary diesel engine for experimentation with modified engine setup with heat exchanger and blower at injection timing 23° BTDC were evaluated. The trial on diesel engine with heat exchanger and blower is conducted at no load to gradually increasing to full load.

3 Results and Discussion

The performance of 3.7 kW capacity four-stroke single-cylinder stationary diesel engine was evaluated for inlet air temperature 30 °C and injection timing 26° before TDC. The rectangular-type counter flow shell and tube heat exchanger were fabricated and placed upstream of inlet and outlet duct of the engine. In this, inlet air is passed through tubes and the exhaust gases are passed over the tubes. The previous work reports inlet air heating up to 150 °C at the injection timings 23°, before TDC yields best engine performance. The test conducted on same diesel engine with modified engine setup with heat exchanger shows the temperature of air gradually raises with load. At no load, inlet air heating achieved upto temperature of 100 °C when exhaust temperature was 190 °C. At 50% load, inlet air heating achieved upto temperature of 145 °C when exhaust temperature was 235 °C.

The improved performance in terms of thermal efficiency of engine found for setup with heat exchanger is due to heating of inlet air using heat of exhaust gases which also lowers the emission level of the engine. The various performance parameters and emissions of the engine for these three kinds of experimentation were measured and the effect of these experimentation on the performance parameters and emissions of the engine elaborated in details in the following section.

3.1 Thermal Efficiency

The brake thermal efficiency variations for the three experimental setups at different outputs are shown in Fig. 2. The graph plotted for brake thermal efficiency verses percentage brake power for engine operating at (i) normal condition, (ii) with heat exchanger and (iii) with heat exchanger and blower. The thermal efficiency increases during early part of brake power and it reaches to maximum during full load condition. The trend of decrease in thermal efficiency is observed beyond full load for the engine running at normal conditions. The similar trend is observed for engine operating with

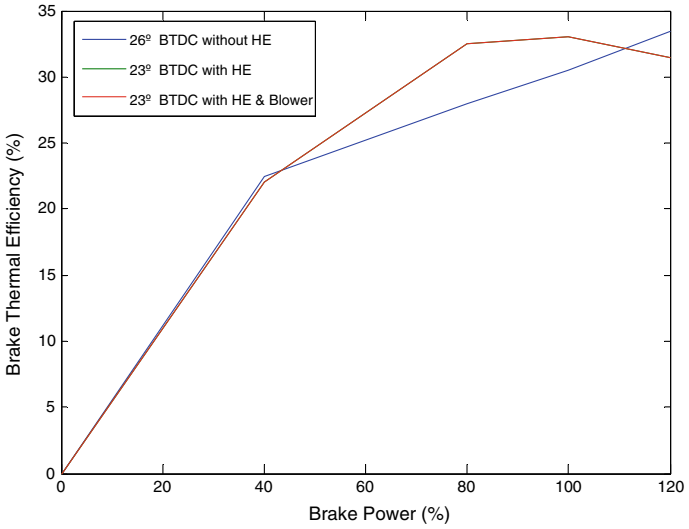

Fig. 2 Comparison of brake thermal efficiency for three engine setups

heat exchanger where at full load thermal efficiency reaches to maximum value and it **starts** decreasing when engine is operating beyond full load. This is the effect of inlet air heating which improves the engine combustion resulted into improvement in the performance when engine is running at full load. The same effect of inlet air heating does not observed when the engine is running beyond full load and it shows decline in the performance beyond full load. The increase in inlet air temperature helps in proper mixing of fuel at full load which benefited in vaporization and combustion of injected fuel. The values of brake thermal efficiencies at full load and at 120% load are 32.5 and 28.9, respectively. There is no change observed in thermal efficiency when blower is connected to the heat exchanger. The gain in performance in terms of thermal efficiency is lesser as compared to the power consumed by the blower. Due to this no change in thermal efficiency is observed after connecting the blower.

3.2 Volumetric Efficiency

The variation volumetric efficiency verses percentage of brake power at various operating conditions shown in Fig. 3 for engine operating at (i) normal condition, (ii) with heat exchanger and (iii) with heat exchanger and blower. The graph shows volumetric efficiency remains more or less same with respect to load for engine running at normal condition. The volumetric efficiency variation for normal engine lies between 84 and 85%. The graph also indicates that the engine running with heat exchanger shows decrease in volumetric efficiency as the load increases. This is due to the arrangement of heating inlet air by heat exchanger tends to reduce the volumetric

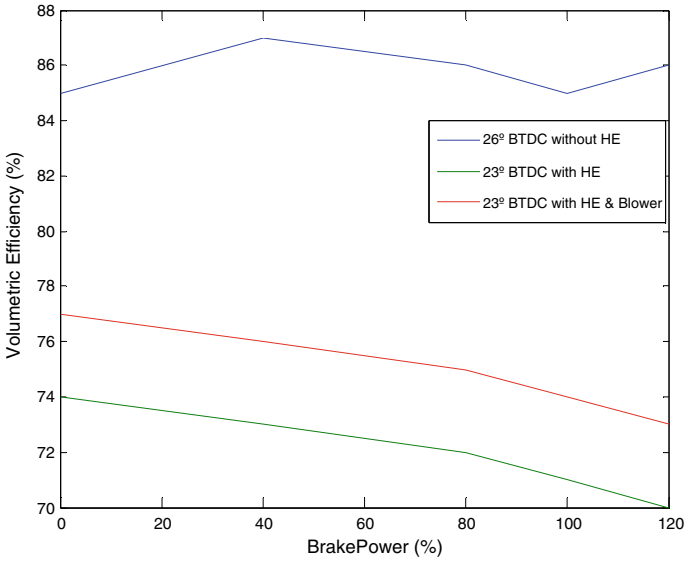

Fig. 3 Comparison of volumetric efficiency for three engine setups

efficiencies as compared to values of efficiencies obtained for engine running with basic experimental setup. This is due to decrease in density of inlet air passed to the engine. After connecting blower to the heat exchanger, the values of volumetric efficiency are found to be increased than the heat exchanger without blower. The loss in volumetric efficiency due to heating of inlet air can be compensated with use of blower.

3.3 Brake Specific Fuel Consumption

The effect of brake power on brake-specific fuel consumption (BSFC) at 50, 100 and 110% of brake power calculated and plotted as shown in Fig. 4. The BSFC values corresponding to these load are 0.335, 0.2625, 0.25 kg/kW h, respectively, for engine running at normal conditions. This show reduced values of BSFC as there is increase in load on engine. The graph for engine operating with heat exchanger clearly show that the BSFC is improved for test compared to normal operating conditions. This is due to improved combustion temperature as the temperature of inlet air passed is more than the temperature of inlet air operating under normal operating condition. The values of BSFC obtained for this test are 0.34, 0.2542, 0.25 and 0.2650 kg/kW h at 50, 75, 100 and 110% of brake power, respectively. These values also show that BSFC with heat exchanger is better compared to the normal operating condition between 0.3738 and 0.2650. There is no significant change in BSFC with additional blower.

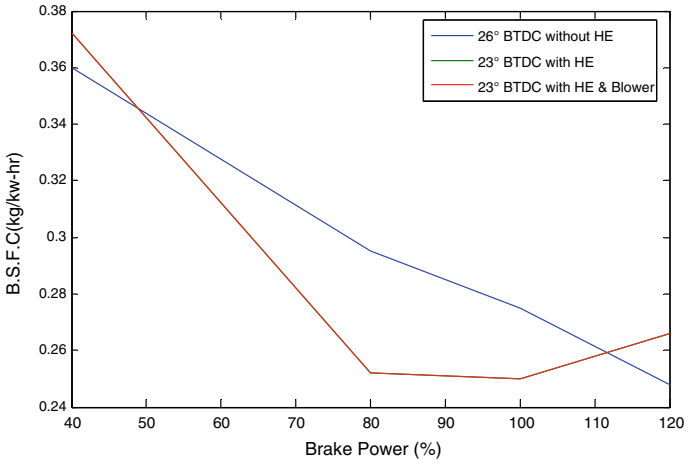

Fig. 4 Comparison of brake specific fuel consumption for three engine setups

3.4 Smoke Density

A comparison of the percentage of smoke density from the diesel engine setup equipped with heat exchanger and blower are presented in Fig. 5. The smoke density values measured were 15 and 29% at full load and at overload conditions, respectively, for basic engine setup running at normal conditions. There is reduction in smoke density values to 14 and 22% at full load and overload conditions, respectively, for

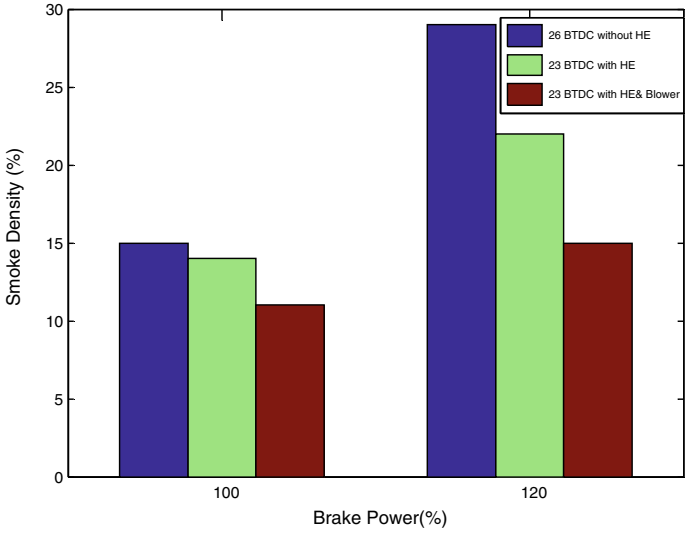

Fig. 5 Comparison of smoke density for three engine setups

modified experimental setup heat exchanger at injection timing of 23° before TDC. It shows that inlet air heating lowers down the emission level of the stationary diesel engine. It is also seen that use of the blower in the suction line further reduces the emission level. There is 6.66% reduction in the smoke density at full load by inlet air heating and 26.66% reduction in smoke density at full load with inlet air heating assisted by blower. Similarly, reduction in smoke density is observed at part load and overload with modified engine setup with heat exchanger and blower.

4 Conclusions

The experimentation on diesel engine with technique of using specifically manufactured heat exchanger for exhaust heat recovery has shown improved performance of the engine due to inlet air heating. Performance improvement is depicted by improved values of thermal efficiency. The decrease in volumetric efficiency due to heating of inlet air is compensated by use of blower. It is also seen that specific fuel consumption value improves by inlet air heating and it lowers down the emission level of the stationary engine.

References

1. Abd-Alla, G.H.: Using exhaust gas recirculation in internal combustion engine: a review. Energy Convers. Manage. **43**, 1027–1042 (2002)
2. Shi, L., Cui, Y., Deng, K., Peng, H., Chen, Y.: Study of low emission homogeneous charge compression ignition (HCCI) engine using combined internal and external exhaust gas recirculation (EGR). Energy **31**, 2665–2676 (2006)
3. Hountals, D.T., Mavropoulos, G.C., Binder, K.B.: Effect of exhaust gas recirculation (EGR) temperature for various EGR rates on heavy duty DI diesel engine performance and emissions. Energy **33**, 272–283 (2008)
4. Aranguren, P., Araiz, M., Astrain, D., Martinez, A.: Thermoelectric generators for waste heat harvesting: a computational and experimental approach. Energy Convers. Manage. **148**, 680–691 (2012)
5. Ghobadian, B., Rahimi, H., Nikbakht, A.M., Najafi, G., Yusaf, T.Y.: Diesel engine performance and exhaust emission analysis using waste cooking biodiesel fuel with an artificial neural network. Renew. Energy **34**, 976–982 (2009)
6. Swami Nathan, S., Mallikarjuna, J.M., Ramesh, A.: Effects of charge temperature and exhaust gas re-circulation on combustion and emission characteristics of an acetylene fuelled HCCI engine. Fuel **89**, 515–521 (2010)
7. Lemmens, S., Lecompte, S.: Case study of an organic Rankine cycle applied for excess heat recovery: technical, economical and policy matters. Energy Convers. Manage. **138**, 670–685 (2012)
8. Saidur, R., Rezaei, M., Muzammil, W.K., Hassan, M.H., Paria, S., Hasanuzzaman, M.: Technologies to recover exhaust heat from internal combustion engines. Renew. Sustain. Energy Rev. **16**, 5649–5659 (2012)
9. Yang, F., Dong, X., Zhang, H., Wang, Z., Yang, K., Zhang, J., Wang, E., Liu, H., Zhao, G.: Performance analysis of waste heat recovery with a dual loop organic Rankine cycle (ORC)

system for diesel engine under various operating conditions. Energy Convers. Manage. **80**, 243–255 (2014)
10. Mastrullo, R., Mauro, A.W., Revellin, R., Viscito, L.: Modeling and optimization of a shell and louvered fin mini-tubes heat exchanger in an ORC powered by an internal combustion engine. Energy Convers. Manage. **101**, 697–712 (2015)
11. Zhang, H.G., Wang, E.H., Fan, B.Y.: Heat transfer analysis of a finned tube evaporator for engine exhaust heat recovery. Energy Convers. Manage. **65**, 438–447 (2013)
12. Hossian, S.N., Bari, S.: Waste heat recovery from the exhaust of a diesel generator using Rankine cycle. Energy Convers. Manage. **75**, 141–151 (2013)
13. Yuksek, L., Sandalci, T., Ozener, O., Ergenc, A.T.: Modelling the effect of injection pressure on heat release parameters and nitrogen oxides in direct injection diesel engines. Therm. Sci. **18**, 155–168 (2014)
14. Bari, S., Hossain, S.N.: Design and optimization of compact heat exchanger to be retrofitted into a vehicle for waste heat recovery from a diesel engine. Procedia Eng. **105**, 472–479 (2015)
15. Meng, J.-H., Wang, X.-D., Chen, W.-H.: Performance investigation and design optimization of a thermoelectric generator applied in automobile exhaust waste heat recovery. Energy Convers. Manage. **120**, 71–80 (2016)
16. Kim, T.Y., Negash, A., Cho, G.: Experimental and numerical study of waste heat recovery characteristics of direct contact thermoelectric generator. Energy Convers. Manage. **140**, 273–280 (2017)
17. He, W., Wang, S., Yang, Y.: Peak power evaluation and optimal dimension design of exhaust heat exchanger for different gas parameters in automobile thermoelectric generator. Energy Convers. Manage. **151**, 661–669 (2017)
18. Thakar, R., Bhosle, S., Lahane, S.: Design of heat exchanger for waste heat recovery from exhaust gas of diesel engine. Procedia Manuf. **20**, 372–376 (2018)

Influences of Feed Rate and Machining Length in Micro-milling of P-20 Steel

Priyabrata Sahoo and Karali Patra

Abstract This study is focused on the influences of feed rate and machining length upon the significant machining parameters such as cutting force, surface roughness, burr size and microhardness. For this case study, micro-milling operation has been carried out for the combination of TiAlN-coated 0.5-mm flat end mill and P-20 steel in dry environment. To avoid the ploughing effect, experiments have been performed in shearing dominated region for three feed rates, viz. 1, 2 and 3 μm/tooth up to a machining length of 350 mm, each. The experimental results revealed that with increase in feed rate and machining length, the magnitude of machining parameters increases. The magnitude of cutting force and surface roughness increases with machining length due to tool wear effect, and microhardness value increases due to strain hardening. The magnitude of burr width also increases with increase in feed rate and machining length due to more chip load and deterioration of sharpness of the tool, respectively.

Keywords Micro-milling · Machining length · Burr width · Surface roughness · Microhardness · Cutting force

1 Introduction

Micro-milling is a preferred micro-fabrication technique due to its enhanced performance in terms of higher material removal rate, capable of fabrication for 3-D complex shape and applicable for a wide range of engineering materials [1–3]. Micro-milling is a conventional micro-fabrication process where machining is done by submillimeter range micro-end mill. However, due to downscaling in dimension of the tool, some inherent mechanics such as ploughing, elastic recovery and tool run-out come into picture which limits the performance of the process [4]. Especially, stringent surface quality and dimensional accuracy are the major concerns for functionally required micro-features [5]. However, due to the effect of elastic recovery, ploughing and tool run-out, surface quality becomes worse and the tool

P. Sahoo (✉) · K. Patra
Mechanical Engineering Department, Indian Institute of Technology, 801103 Patna, India
e-mail: priyabrata.pme16@iitp.ac.in

L. Li et al. (eds.), *Advances in Materials and Manufacturing Engineering*, Lecture Notes in Mechanical Engineering, https://doi.org/10.1007/978-981-15-1307-7_13

is prone to wear and breakage which again causes the deterioration of the surface quality. Further, tool wear, tool breakage and surface quality become more critical during fabrication of micro-features from hard materials such as nickel-based super-alloy, titanium alloy, ceramics and hardened die steel [6]. Some of the literature those are based on the effect of process parameters on machining performances in micro-milling are discussed in this section as follows:

Hassanpour et al. [7] investigated the effects of process parameters on surface roughness, burr width, microhardness and cutting force. They reported that spindle speed is the most effective parameter for surface roughness; whereas, the feed rate is the most effective parameter for burr formation. Kiswanto et al. [8] reported the effects of feed rate, cutting speed and machining time on burr formation and surface roughness. They observed that lower feed rate is suitable for better surface quality and burr width rises with machining time due to tool wear. Lekkala et al. [9] studied various types of burr formation in micro-milling and reported that depth of cut and tool diameter contributed significantly on burr formation. Ucun et al. [10, 11] reported the improvement of micro-milling performance by using coated tool.

Considering the aforesaid literature, it can be realized that surface quality is the major concern for micro-features. Further, material such as hard die steel which has wide applications for the fabrication of micro-die using micro-milling has not studied very much by the researchers. By considering author's earlier work [12] on P-20 steel, it was observed that lowest feed value in shearing dominant region gives good surface quality and lower cutting force values which are indeed helpful to avoid catastrophic tool breakage. However, the influence of machining length at different feed values has not been reported in that analysis. Therefore, the objective of this work is to investigate the influences of feed rate and machining length on surface roughness, microhardness, burr formation and cutting forces for micro-milling of P-20 steel.

2 Materials and Methods

Hardened 30 HRC P-20 steel and TiAlN coated flat carbide end mill cutter (SECO, 905005-MEGA-T) having diameter 500 μm tool were used for the experiment. The geometrical properties of the micro-end mill cutter are illustrated in Table 1. Micro-milling experiment was performed on a 3-axis CNC micro-machining centre (DT-110, micro-tools) as shown in Fig. 1. The investigation which was carried out at

Table 1 Geometrical properties of end mill cutter

Helix length, (mm)	Shank diameter, (mm)	Tool diameter, (mm)	Helix angle, (°)	Rake angle, (°)	Edge radius, (μm)
1.4	3	0.5	30	12	3

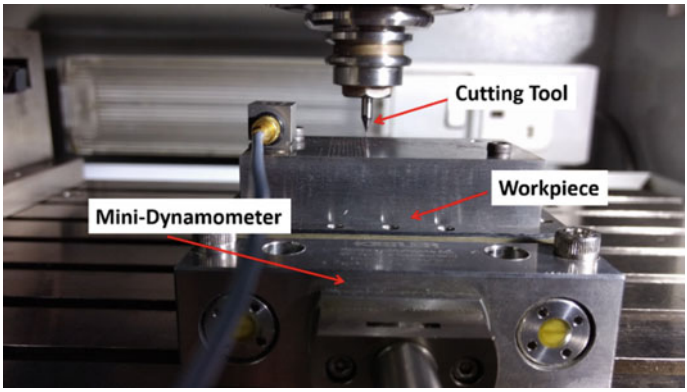

Fig. 1 Micro-milling set up

spindle speed (N) 20,000 RPM, axial depth of cut (a_d) 30 μm and three levels of feed rate (f) (1, 2 and 3 μm/tooth) with ten numbers of machining cut was performed having length 35 mm each. The cutting forces were measured in x and y directions by mini-dynamometer (9256C2, Kistler). The surface roughness of the specimen was measured by a contact-type profilometer (SJ-400, Mitotoyo) by setting the cut-off length 2.5 mm in feed direction. Burr width on the top surface of the channel was measured by scanning electron microscope (Zeiss, Gemini 500). Subsurface microhardness of the channel was measured by microhardness tester (Leco, LM-248AT).

3 Results and Discussion

3.1 Analysis of Cutting Forces

For the analysis of cutting forces, RMS values of force signal have been considered. Based on Fig. 2, cutting force increases with increase in feed per tooth and progression of cutting length in both x and y directions. In shearing dominant region with increase in feed per tooth, chip load increases subsequently cutting force increases. Meanwhile, with progression of machining length, tool wear increases and tool geometry abruptly changes which results in an increase in cutting force as shown in Fig. 2.

3.2 Analysis of Surface Roughness

The variation of surface roughness with feed per tooth and machining length is shown in Fig. 3. Surface roughness is directly proportional to the square of the feed per

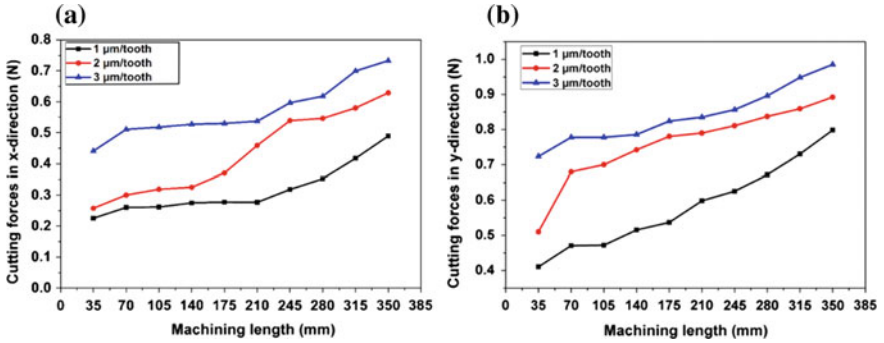

Fig. 2 Variation of cutting force with feed/tooth and machining length

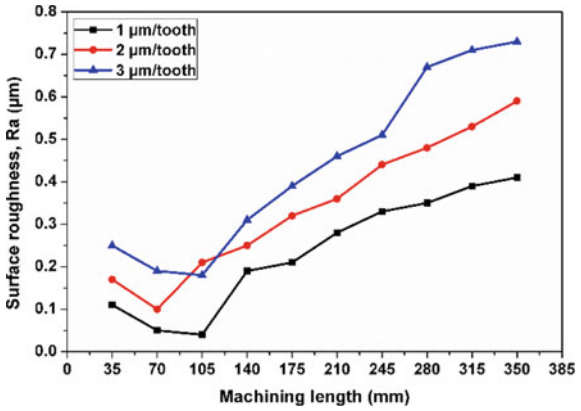

Fig. 3 Variation of surface roughness with feed/tooth and machining length

tooth which can be termed as undeformed chip thickness. In addition, with increase in feed per tooth, vibration raises which deteriorates surface quality by enhancing waviness [13]. From Fig. 3, it can be noticed that with increase in cutting length, surface roughness increases; meanwhile, a peculiar trend was observed after 70 and 105 mm machining length. The drop of surface roughness value can be assumed due to rounding of edge radius after the first cut. Aslantas et al. [10] suggested that tool wear in micro-end milling is bi-directional. That means tool wear occurs both in peripheral and in frontal sides. The lower roughness value is observed due to increase in edge radius; again tool wear increases in frontal face up to a certain value of edge radius. The increase of tool wear in frontal face leads to reduction edge radius which contributes to the rise of surface roughness [11].

3.3 *Analysis of Burr Width*

By analysing the burrs as shown in Fig. 4a, the size of burr in down milling side is observed to be bigger as compared to up milling side. For the current analysis, burr width on the top surface of the channel is considered by taking the average value of the burr width from both sides. As depicted in Fig. 5, burr width increases with increase in feed per tooth due to increase in magnitude of uncut chip thickness as more materials peel out in front of the cutting edge. Again, burr width increases with the progress in cutting length. This is because the sharpness of the cutting tool deteriorates due to tool wear [10].

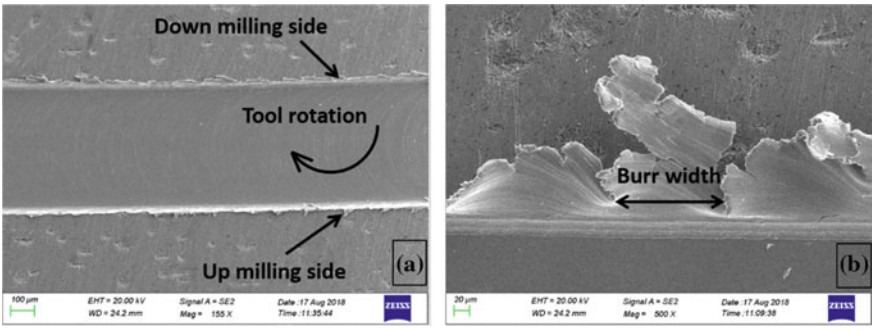

Fig. 4 **a** Burr formation in both up milling and down milling sides with tool rotation; **b** Enlarged view of the burrs

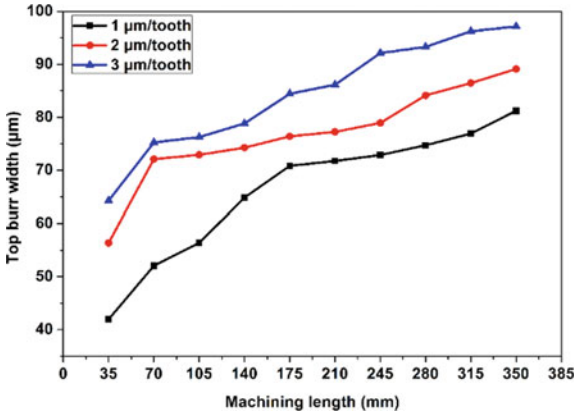

Fig. 5 Effect of feed/tooth and machining length with burr width

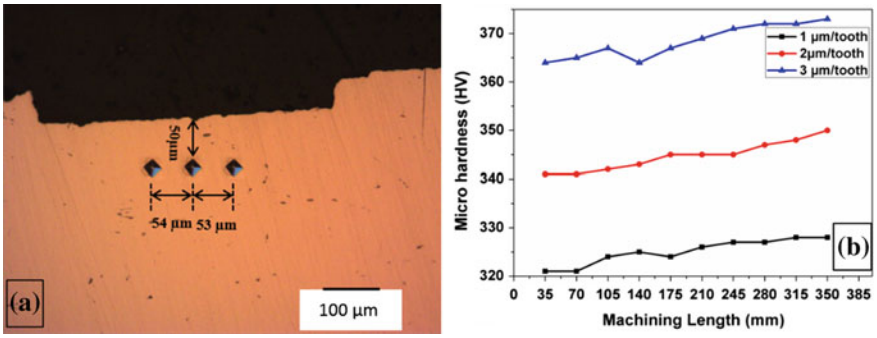

Fig. 6 **a** Pattern of micro-indentation; **b** Variation of microhardness value with feed rate and machining length

3.4 Analysis of Microhardness

As shown in Fig. 6a, indentations were performed beneath the machined channel having a gap of around 50 µm and the average value has been considered. With increase in feed per tooth, hardness values rise as given in Fig. 6b. At higher feed rate, strain rate increases owing to work hardening as a result workpiece hardness grows up [7]. Further, the variation of hardness values with cutting length has been shown in Fig. 6b. It reveals that hardness value increases with machining length. The increase of hardness values with machining length may be due to wear of cutting tool which favours the work hardening process.

4 Conclusion

The aforementioned experimental work unveils the causes and effects of feed per tooth and machining length on machinability parameters such as surface roughness, burr width, cutting force and microhardness. The experimental results showed that the feed rate 1 µm/tooth is desirable as compared to 3 µm/tooth to obtain the micro-features with good surface quality and less cutting force. With increase in feed rate, surface roughness and cutting force, burr width and microhardness increased due to rise in chip load. With the progression of machining length, cutting force and surface roughness increase due to tool wear and vibration. Burr width increases with machining length and is due to deterioration of sharpness of the tool which hampers the cutting and separation of the chips from the work material. Microhardness value rises due to strain hardening with increase in machining length. This study will be helpful for the micro-die industries to find the suitable parameters according to their desired quality requirement.

References

1. Aramcharoen, A., Mativenga, P.T.: Size effect and tool geometry in micromilling of tool steel. Precis. Eng. **33**, 402–407 (2009)
2. Sahoo, P., Pratap, T., Patra, K.: A hybrid modelling approach towards prediction of cutting forces in micro end milling of Ti-6Al-4 V titanium alloy. Int. J. Mech. Sci. **150**, 495–509 (2018)
3. Sahoo, P., Pratap, T., Patra, K.: Prediction of cutting forces in micro milling of P-20 steel by TiAlN coated WC tool : an analytical approach. In: 7th International & 28th All India Manufacturing Technology, Design and Research (AIMTDR) Conference, Chennai, 2018
4. Sahoo, P., Patra, K.: Mechanistic modeling of cutting forces in micro- end-milling considering tool run out, minimum chip thickness and tooth overlapping effects. Mach. Sci. Technol. 0344, (2018). https://doi.org/10.1080/10910344.2018.1486423
5. Pratap, T., Sahoo, P., Patra, K.: Fabrication of circular end micro slots using micro ball-end milling. IOP Conf. Ser. Mater. Sci. Eng **377**, (2018)
6. Lu, X., Hu, X., Jia, Z., Liu, M., Gao, S., Qu, C., Liang, S.Y.: Model for the prediction of 3D surface topography and surface roughness in micro-milling Inconel 718. Int. J. Adv. Manuf. Technol. **94**, 2043–2056 (2018)
7. Hassanpour, H., Sadeghi, M.H., Rezaei, H., Rasti, A.: Experimental study of cutting force, microhardness, surface roughness, and burr size on micromilling of Ti6Al4 V in minimum quantity lubrication. Mater. Manuf. Process **31**, 1654–1662 (2016)
8. Kiswanto, G., Zariatin, D.L., Ko, T.J.L.: The effect of spindle speed, feed-rate and machining time to the surface roughness and burr formation of aluminum alloy 1100 in micro-milling operation. J. Manuf. Process. **16**, 435–450 (2015)
9. Lekkala, R., Bajpai, V., Singh, R.K., Joshi, S.S.: Characterization and modeling of burr formation in micro-end milling. Precis. Eng. **35**, 625–637 (2011)
10. Aslantas, K., Hopa, H.E., Percin, M., Ucun, I., Çicek, A.: Cutting performance of nano-crystalline diamond (NCD) coating in micro-milling of Ti6Al4 V alloy. Precis. Eng. **45**, 55–66 (2015)
11. Ucun, I., Aslantas, K., Bedir, F.: An experimental investigation of the effect of coating material on tool wear in micro milling of Inconel 718 super alloy. Wear **300**, 8–19 (2013)
12. Sahoo, P., Pratap, T., Patra, K., Dyakonov, A.A.: Size effects in micro end-milling of hardened P-20 steel. Mater. Today Proc. **5**, 23726–23732 (2018)
13. Ucun, I., Aslantas, K., Bedir, F.: The performance of DLC-coated and uncoated ultra-fine carbide tools in micromilling of Inconel 718. Precis. Eng. **41**, 135–144 (2015)

Order Tracking: Angular Domain Features Extraction Method for Condition Monitoring of Variable Speed

A. Dhal, I. Panigrahi, C. Mishra and A. K. Samantaray

Abstract Most of the rotating machines operate at variable speed/cyclo-stationary due to fluctuation of power, load etc. It is difficult to monitor the condition of rotating machines in conventional time/frequency analysis when the fluctuation of speed of rotor is more than 0.5 Hz. In such circumstances, angle/time cyclo-stationary analysis of a machine signal is a fundamental procedure for condition monitoring of rotating machine operating at variable speed. Rolling element bearing is widely used in rotating machines starting from bicycle to more sophisticated machines like cryogenic engines. In the present paper, a hybrid diagnosis scheme based on computed order tracking and envelope analysis is used as diagnosis scheme for condition monitoring of rolling element bearing operating at a fluctuating speed of approximately 5–15 Hz. Experiments were conducted using Spectraquest machine faults simulator. Rolling element bearing with fault in the outer race is taken to show the effectiveness of the diagnosis scheme.

Keywords Order tracking · Cyclo-stationary · Condition monitoring · Rolling element bearing · Rotor dynamics

1 Introduction

Rotating machine signal is generally periodic and/or cyclo-stationary due to the nature of operation of machine. Therefore, it can be modelled by a cyclo-stationary process [1]. Whenever a rolling element encounters a defect in its path it excites systems that includes the housing in which it is mounted [2]. The excitation stays for a small time and dies out after the rotating element passes the discontinuity. As the

A. Dhal · I. Panigrahi
Kalinga Institute of Industrial Technology, Bhubaneswar, Odisha, India

C. Mishra (✉)
National Institute of Technology Durgapur, Durgapur, West Bengal, India
e-mail: chintamani.mishra@me.nitdgp.ac.in

A. K. Samantaray
IIT, Kharagpur, WB, India

L. Li et al. (eds.), *Advances in Materials and Manufacturing Engineering*, Lecture Notes in Mechanical Engineering, https://doi.org/10.1007/978-981-15-1307-7_14

process of cyclo-stationary repeats itself at interval it can be classified and searched for the fault symptoms from the original signal if there is any.

Rolling element bearing is widely used in rotating machines due to its low friction characteristics and its adaptability to operate at wide range of load and speed. The most common types of faults that can be observed in the bearing are the fault in the ball and/or outer race and/or inner race. These discontinuities in bearing can lead to the excitation as the rolling element/ball passes the fault and it dies out at bearing characteristic frequencies (BCFs). The nature of signal in different speed is shown in Fig. 1. It can be easily inferred from figure that time interval of fault induced signal is not constant when the speed is variable or slow. However, it is constant angularly spaced. It is also evident from figure that amplitude level of fault induced signal is more when the bearing operates at high speed compared to constant and/low speed. In such situation the bearing characteristics frequencies are replaced by bearing characteristics order [3]. The corresponding bearing characteristics order assuming the outer race of bearing stationary can be written as

$$O_{\mathrm{BPO}} = \frac{n}{2}\left(1 - \frac{d}{D}\cos\beta\right) \tag{1}$$

$$O_{\mathrm{BPI}} = \frac{n}{2}\left(1 + \frac{d}{D}\cos\beta\right) \tag{2}$$

$$O_{\mathrm{BS}} = \frac{D}{2d}\left(1 - \frac{d}{D}\cos\beta\right)^2 \tag{3}$$

where, O_{BPO}, O_{BPI} and O_{BS} are the orders of ball pass for fault in the outer race, ball pass for fault in the inner and ball spin for fault in ball or roller, respectively. The order of element defect is twice that of order of ball spin. The shaft order/one complete rotation of shaft is defined by O_{S}. The other terms in the expression n,d, D

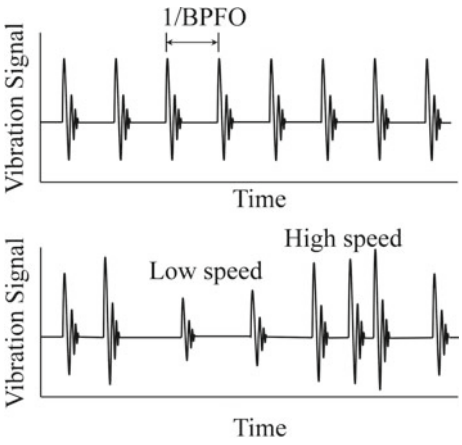

Fig. 1 Bearing signal at different speed assuming a fault in the outer race

and β represents number of balls, diameter of ball, pitch diameter and phase angle, respectively.

For non-uniform/variable speed/cyclo-stationary shaft rotation the conventional diagnosis scheme are not suitable to diagnose faults in bearing. There are ample literatures available which gives a pointer to signal processing steps/scheme used to diagnose faults in the bearing under variable speed operation. Some of the important contributions are, wavelet denoising coupled with order tracking [3], EMD based denoising coupled with order tracking [2], computed order tracking coupled with square envelope spectrum [4], transient signal analysis based on angular sampling [5], angular domain features instantaneous power spectrum [6], cepstrum pre-whitening and order tracking [7], method based on rotating speed isolation [8], techoless envelope order analysis [9] and so on.

2 Experimental Setup

The experimental setup [Fig. 2] consists of an induction motor with rotor, connecting shaft, a jaw coupling, two pedestals, an encoder arrangement, a loader and two bearings as its main part. The jaw coupling is used to connect the rotor shaft to connecting shaft. The pedestal nearer to the induction motor supports the good bearing whereas the farther one supports the faulty bearing. Bearing with outer race fault is used to investigate the effectiveness of the diagnosis scheme. The MFS system has an inbuilt keyphasor which gives one pulse per revolution. It is used for calculating shaft speed whose average value is displayed by the machine. However, it is not good for measuring speed variation within one shaft revolution. So, a new encoder was developed for this work. The encoder used in the rotary machine sensor-encoder system for calculating the instantaneous speed consists of 30 reflecting and the same number of non-reflecting surfaces. An infrared (IR) sensor is used to measure encoder pulses. This sensor has an IR emitter and an IR sensor. The output is a pulse signal with maximum value when the light is reflected and minimum when the light is not reflected. The instantaneous angular speed is computed from the data collected from the sensor-encoder system based on the principle of zero crossing time. Ploytec

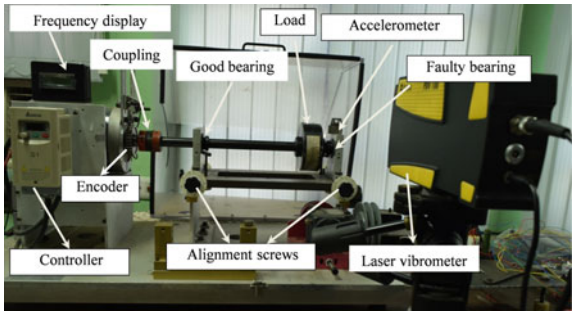

Fig. 2 Machine fault simulator

laser vibrometer is used to get the velocity of vibration of pedestal and USB type NI DAC-6311 is used as data collector.

3 Computed Order Tracking

Signal smearing is caused due to fluctuation of speed of the rotor. To avoid this difficulty order tracking is used. From the different order tracking method computed order tracking and Volt Kalman filter based order tracking is widely used. In computed order tracking the resampling of data/signal is done in angular domain whereas in Volt-Kalman filter signal is resampled in time domain to find out the order of interest.

Computed order tracking is a frequency analysis method that considers multiples of running speed (order) instead of absolute frequency as frequency base [10]. The data is re-sampled at desired angular increment of shaft angle or angular resolution $\Delta\theta$. The keyphasor pulse angle, i.e., angle between consecutive key-phasor encounter is taken as $\Delta\phi$. Fyfe and Munck [10] calculated the re-sampling time assuming that the shaft undergoes constant angular acceleration by following formulations. They described shaft angle θ in the form of quadratic equation,

$$\theta(t) = b_o + b_1(t) + b_2 t^2 \tag{4}$$

where, b_o, b_1 and b_2 are three unknown coefficients and it can be found by fitting three consecutive key phasor arrival time t_o, t_1 and t_2 as shown in Fig. 3. Thus for $\theta(0) = 0$ the following expression can be written,

$$\begin{pmatrix} 0 \\ \Delta\phi \\ 2\Delta\phi \end{pmatrix} = \begin{bmatrix} 1 & t_1 & t_1^2 \\ 1 & t_2 & t_2^2 \\ 1 & t_3 & t_3^2 \end{bmatrix} \begin{Bmatrix} b_1 \\ b_2 \\ b_3 \end{Bmatrix} \tag{5}$$

For any desired shaft angle θ, the time at which the re-sampling need to be performed is given by

$$t = \frac{1}{2b_2}\left[\sqrt{4b_2(\theta - b_0) + b_1^2} - b_1\right] \tag{6}$$

Constant numbers of samples are usually taken between two key phasor pulses, with $\frac{\Delta\phi}{\Delta\theta} \gg 1$ as an integral value. To avoid overlap in sampling, Fyfe and Munck [10], considered $\theta = k\Delta\theta$ with following condition,

$$\frac{\Delta\phi}{2\Delta\theta} \leq k < \frac{\Delta\phi}{3\Delta\theta} \tag{7}$$

where, k is a positive integer. So, the Eq. (5) can be written as

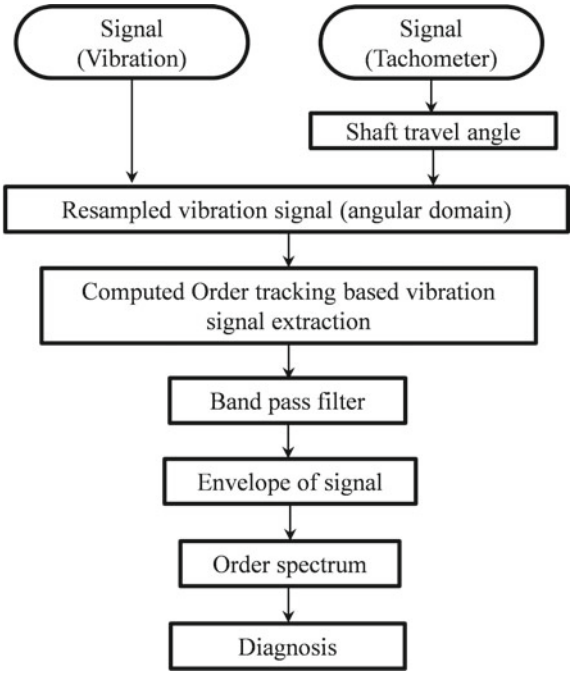

Fig. 3 Flow chart of diagnosis scheme based on computed order tracking and envelope analysis

$$t = \frac{1}{2b_2}\left[\sqrt{4b_2(k\Delta\theta - b_0) + b_1^2} - b_1\right] \tag{8}$$

where, $t(k)$ is the time when k^{th} sample is taken.

To avoid singularity, $t(k) = \frac{k\Delta\theta - b_0}{b_1}$ when $b_2 \cong 0$ and $t_2 - t_1 \cong t_3 - t_2$ with $b_0 = -\frac{t_1\Delta\phi}{t_2 - t_1}$ and $b_1 = -\frac{\Delta\phi}{t_2 - t_1}$.

Diagnosis scheme: The flow chart of diagnosis scheme is shown in Fig. 3. The procedure can be summarized as follows:

- Collect a large number of data to observe several orders of fundamental order.
- Apply computed order tacking technique to get the re-sampling time and corresponding vibration signal.
- Filter the vibration signal through a band pass filter with frequency in the range of structural resonance.
- The vibration signal is modulated by Hilbert transform to keep only the envelope.
- Finally, compute the frequency spectrum of the envelope by applying FFT (Fast Fourier Transform), called envelope order spectrum, to identify fault in the demodulated signal. All the above signal processing steps are performed with the help of Matlab®.

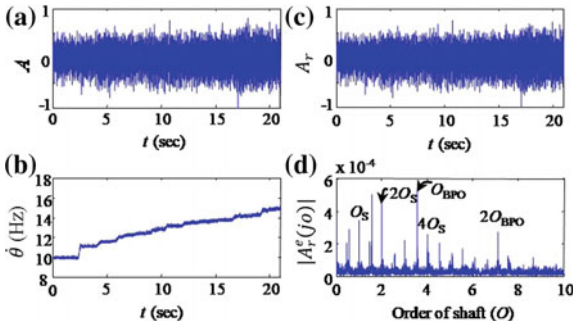

Fig. 4 Signal processing steps for vibration signal acquired from bearing with outer race fault

4 Results and Discussion

Experiments are conducted using machine fault simulator developed by "Spectra Quest" where the rotor shaft is supported on 1″ bearings. This bearing used here (MB ER16 K) is a single row deep groove ball bearing with following geometric parameters: ball diameter 7.94 mm, pitch diameter 39.32 mm, inner race diameter 31.38 mm and outer race diameter 47.32 mm. Substituting these data in the kinematic relations (Eqs. 1, 2 and 3), we get OBPO 3.591 O_S, OBPI as 5.408 O_S, and OBS as 2.375 O_S. Intentional outer raceways faults of 3 mm width and 1 mm depth are prefabricated in faulty bearings.

Signal processing steps proposed in the previous section is applied to the signal collected by the data collector (NI DAC-6311). The VFD is used to achieve a rotor variation of 5–15 Hz. The experimental result for faulty bearing with outer race fault is shown in Fig. 4. The notation used in figure $A, \dot{\theta}$(Hz), A_r and $\left|A_r^e(jo)\right|$ respectively represents the signal, angular speed of shaft rotation, resampled envelope signal and absolute value of envelope order spectrum. From the envelope order spectrum it can be observed that the shaft order $O_S = 1$ and its harmonics, O_{BPO} and its harmonics and some side bands are present. Thus, it reveals the presence of outer race fault.

5 Conclusion

With Under variable/oscillating speed operation of rotor there is a possibility of smearing of signal in the frequency domain. Therefore, the signal processing steps generally used in constant or uniform speed rotation is not applicable. A signal processing steps based on computed order tracking and envelope analysis is proposed in this article to find out the order envelope spectrum. Using the instantaneous angular speed measurement the signal is resampled in angular domain with the help of computed order tacking technique. The envelope of signal is then computed to find out the order spectrum. The proposed diagnosis scheme is explained in details and the effectiveness of the proposed diagnosis scheme is established using the experimental result.

References

1. Antoni, J., Xin, G., Hamzaoui, N.: Fast computation of the spectral correlation. Mech. Syst. Sig. Process. **92**, 248–277 (2017)
2. Mishra, C., Samantaray, A.K., Chakraborty, G.: Bond graph modelling and experimental verification of a novel scheme for fault diagnosis of rolling element bearings in special operating conditions. J. Sound Vib. **377**, 302–330 (2016)
3. Mishra, C., Samantaray, A.K., Chakraborty, G.: Rolling element bearing defect diagnosis under variable speed operation through angle synchronous averaging of wavelet de-noised estimate. Mech. Syst. Signal Process. **72–73**, 206–222 (2016)
4. Borghesani, P., Ricci, R., Chatterton, S., Pennacchi, P.: A new procedure for using envelope analysis for rolling element bearing diagnostics in variable operating conditions. Mech. Syst. Signal Process. **38**(1), 23–35 (2013)
5. Lu, S., Wang, X., Hi, Q., Liu, F., Liu, Y.: Fault diagnosis of motor bearing with speed fluctuation via angular resampling of transient sound signals. J. Sound Vib. **377**, 302–330 (2016)
6. Urbanek, J., Barszcz, T., Antoni, J.: Time–frequency approach to extraction of selected second-order cyclostationary vibration components for varying operational conditions. Measurement **46**(4), 1454–1463 (2013)
7. Borghesani, P., Pennacchi, P., Randall, R.B., Sawalhi, N., Ricci, R.: Application of cepstrum pre-whitening for the diagnosis of bearing faults under variable speed conditions. Mech. Syst. Signal Process. **36**(2), 370–384 (2013)
8. Wang, Y., Xu, G., Zhang, Q., Liu, D., Jiang, K.: Rotating speed isolation and its application to rolling element bearing fault diagnosis under large speed variation conditions. J. Sound Vib. **348**, 381–396 (2015)
9. Zhao, M., Lin, J., Xu, X.Q., Lei, Y.: Tacholess envelope order analysis and its application to fault detection of rolling element bearings with varying speeds. Sensors **13**, 10856–10875 (2013)
10. Fyfe, K.R., Munck, E.D.S.: Analysis of computed order tracking. Mech. Syst. Signal Process. **11**(2), 187–205 (1997)

Surface Roughness Characteristics of MS Rod Using Different Cutting Fluids During Turning Operation

Pradip Mondal and Samiran Samanta

Abstract During any machining process, there exists an essential criterion to determine the surface characteristics to achieve the desired product quality. Considering this fact as a primary objective, the present study is carried out to determine the average surface roughness (Ra), root mean square (Rq), and average maximum height of the profile (Rz) values of surfaces generated during the machining of MS rod. Plain turning operation is carried out in a lathe considering different machining parameter, viz. cutting speed and depth of cut and using different cutting fluids, viz. mustard oil, kerosene oil, olive oil and water as well as in dry condition (without coolant) via MQL technique. Single-point cutting tool, made of high-speed steel (HSS) has been used in this experimentation work. The study shows that higher spindle sped and depth of cut result in higher surface roughness, irrespective of cutting fluid used. Furthermore, it is experienced that if low viscous cutting fluids (e.g., kerosene and water) are used as cutting fluids, the machined surface becomes rougher.

Keywords Surface roughness · Turning · MS rod · Cutting fluids · Machining parameters

1 Introduction

Among the different machining process carried out in mechanical workshop, turning operation is widely used now and then. In this process, the material is removed from the upper surface of the workpiece using a single point cutting tool. During this operation, high normal and shear stresses are generated on the cutting tool as the chip slides over the rake face of the tool. At the same time, the chip slides against a high frictional resistance. Due to this phenomenon, high-temperature zones are

P. Mondal
Department of Mechanical Engineering, National Institute of Technology, Ravangla, South Sikkim 737139, Sikkim, India

S. Samanta (✉)
School of Mechanical Engineering, Kalinga Institute of Industrial Technology, Deemed to Be University, Bhubaneswar 24, India
e-mail: samirankgec@gmail.com

L. Li et al. (eds.), *Advances in Materials and Manufacturing Engineering*, Lecture Notes in Mechanical Engineering, https://doi.org/10.1007/978-981-15-1307-7_15

created both at the cutting point and thus both get heated. As the tool temperature becomes higher the tool wear expedites and surface finish of the job gets affected. To overcome this problem, cutting fluids are used during any machining processes. Cutting fluids serve the purpose of a lubricant as well as a coolant. It helps in lowering the temperature of cutting zone and lowering the frictional resistance [1–3]. Thus, the usage of cutting fluid enhances the tool life as well as improves the surface characteristics of workpiece.

Cutting fluid is a type of liquid that is used as coolant and as well as lubricant, in general practice, during metal cutting or machining processes. Different types of oils, oil-water emulsions, pastes, gels, aerosols (mists), air or other gases are commonly used as cutting fluids. Use of cutting fluids influences the productivity and quality of the finished product. It is one of the key parameters that indicate the quality of the finished job. Surface roughness is nothing but the measurement of geometrical regularity of texture on any surface. It is generally measured via three components, viz. roughness, waviness, and form. All of these three parameters are measured to examine the surface of any machined job, in practice.

Several research works based on the surface roughness parameters and using different work metals have been carried out by many group of researchers and reported in literature [4–7]. Optimization studies on different cutting parameters and their effect on the surface roughness characteristics have also been emphasized in the literature [8–10]. The premier objective of this present study is to understand and examine the characteristics of surface produced while the turning operation of MS rod, in lathe. MS is taken as work material due to its wide usability in any kind of machining process. In this experimentation work, turning is carried out using mustard oil, kerosene oil and without any cutting fluid at 248, 375, and 556 rpm. Furthermore, olive oil and water are used as a coolant at 250, 350, and 481 rpm. Three different depths of cut values (0.25, 0.5, and 0.75 mm) are considered during all these operations. Finally, an attempt has been made to reveal the best suitable machining condition which offers the best surface characteristics.

2 Experimental Setup and Procedure

Turning operation has been carried out using three depth (0.25, 0.5, and 0.75 mm) cuts through 20 mm individually. MS rod is used as the study material. The surface roughness of the workpiece is measured by using Talysurf apparatus and respective surface roughness parameters (Ra, Rq, and Rz) values are noted corresponding to different depth cuts. Specifications of the lathe and the Talysurf apparatus are shown in Table 1. Firstly, the turning operation is carried out using mustard oil, kerosene oil and without any cutting fluid at spindle speed values of 248, 375, and 556 rpm. Then the experimentations are repeated using olive oil and water as cutting fluids at 250, 350, and 481 rpm, respectively. Ra, Rq, and Rz values are noted for all of these machining conditions. Properties of the cutting fluids are shown in Table 2.

Table 1 Specifications of the lathe and the Talysurf used during experiment

Lathe	Talysurf
Overbed-14 in.	Make-Mitutoyo
Overcariage-8 in.	Model: SJ-120
Height of centers-7 in.	Set No: 178-560-02
Swing gap-22 in.	
Max. rpm-1425	
Maximum length-41/2 ft.	

Table 2 Properties of cutting fluids

Fluid properties	Kerosene oil	Mustard oil	Olive oil	Water
Density (kg/m^3)	820.1	900	930	997
Viscosity (Ns/m^2)	1.64	70	84	1

3 Results and Discussions

The results, noted during this study, are plotted and discussed in this section. All of these surface parameters values are measured in μm.

From Fig. 1, it is observed that for 0.25–0.5 mm depth of cut, Ra, Rq, and Rz values increase, reaches an optimum value. Then from 0.5 to 0.75 mm depth of cut, values of these surface parameter decrease at spindle speed of 248 and 375 rpm. But in case of 556 rpm, it is examined that values of Ra and Rq increase linearly along with increase depth of cut. However, the Rz value of increases from 0.25 to 0.5 mm and decreases from 0.55 to 0.75 mm depth of cut.

Figure 2 shows that from 0.25 to 0.5 mm depth of cut, Ra, Rq, and Rz values first increase, then reach an optimum value and then for 0.75 mm depth of cut, these values decrease for 248 and 375 rpm. But in the case of 556 rpm, it is observed that values of Ra, Rq, and Rz decrease from 0.25 to 0.5 mm, attains a minimal value and then increase from 0.5 to 0.75 mm depth of cut value.

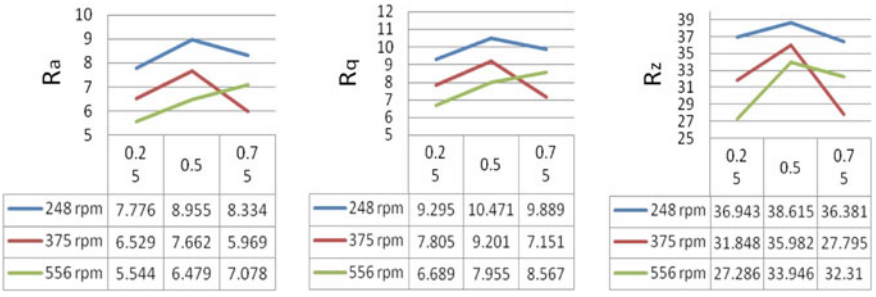

Fig. 1 Variation of surface roughness parameters without *any fluid*

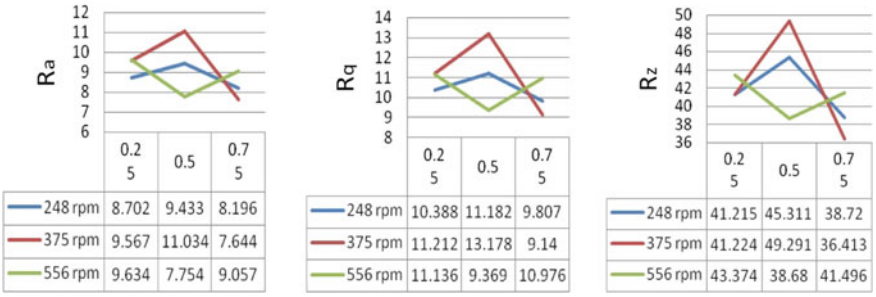

Fig. 2 Variation of surface roughness parameters using *kerosene oil*

A variation of surface roughness parameters using mustard oil as cutting fluid is shown in Fig. 3. It is seen that at 248 rpm, the values of Ra and Rq decrease from 0.25 to 0.55 mm, whereas they increase at 0.75 mm depth of cut. But Rz decreases along with depth of cut (range 0.25–0.5 mm). At 375 rpm, the values of Ra, Rq and Rz increase along with depth of cut. At 556 rpm, the values of Ra and Rz decrease from 0.25 to 0.5 mm and then increase from 0.5 to 0.75 mm depth of cut, whereas Rq decreases along with depth of cut.

Figure 4 depicts the surface roughness characteristics when olive oil is used as a cutting fluid. From the graph, it is observed that all of these three surface parametric plots are quite similar to the previous surface roughness plots. At 250 rpm, the values of Ra, Rq, and Rz decrease along with increase in depth of cut. At 350 and 481 rpm, the values of Ra, Rq, and Rz decrease from 0.25 to 0.5 mm and then increase from 0.5 to 0.75 mm.

Figure 5 presents the surface roughness characteristics of the workpiece using water as cutting fluid. From the graph, it is experienced that all these parameters for this case follow the same trend as observed in the earlier cases. At 250 rpm, the values of Ra, Rq, and Rz increase linearly along with increase in the depth of cut. At 350 and 481 rpm, the value of Ra, Rq, and Rq increase from 0.25 to 0.5 mm,

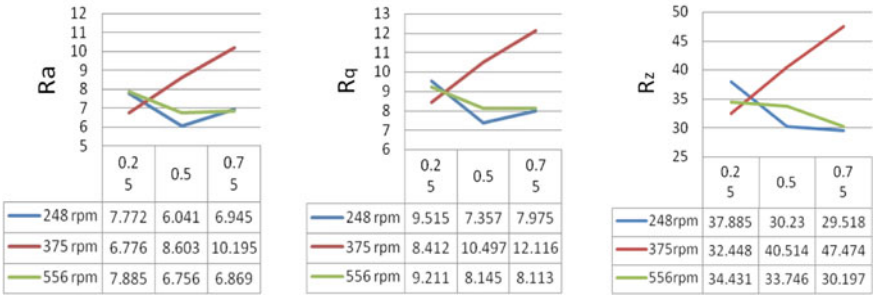

Fig. 3 Variation of surface roughness parameters using *mustard oil*

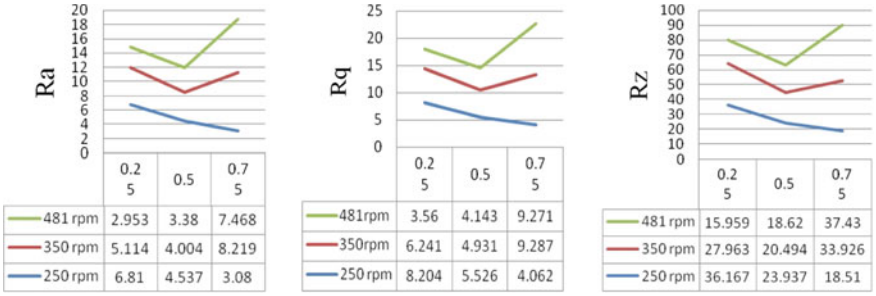

Fig. 4 Variation of surface roughness parameters using *olive oil*

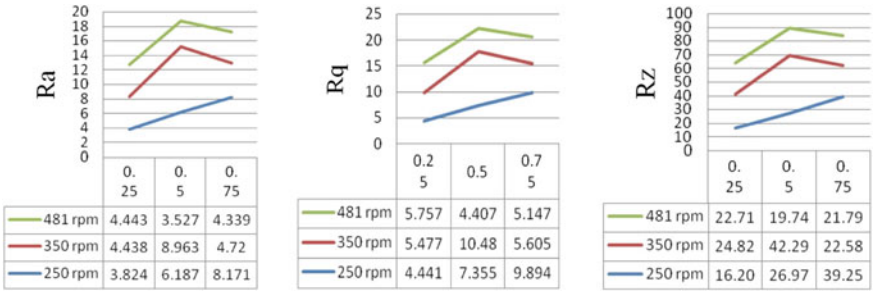

Fig. 5 Variation of surface roughness parameters using *water*

reaches an optimum value and then increase from 0.5 to 0.75 mm which are beyond the values obtained for 0.25 mm depth of cut.

As seen from Table 2, both water and kerosene oil having very lower viscosity among the other. Due to lower viscosity, chip removal rate from the finished surface is also higher for these two fluids. Due to this fact, the surface roughness parameter values are higher for these two fluids at all spindle speed and depth of cut values, as seen from Fig. 6.

4 Conclusions

The present study reports the effect of spindle speed and depth of cut on surface roughness during plain turning operation of mild steel rod using different cutting fluids. These results can be beneficial for the selection of cutting parameters for producing better surface quality of product made of mild steel. It is observed that to produce better surface cutting fluids need to be applied during the machining process for machining conditions. Therefore, a better combination of cutting speed and depth of cut with cutting fluids need to be selected to have a better quality of surface finish during turning operation of MS rod. Figure 6 shows the relation

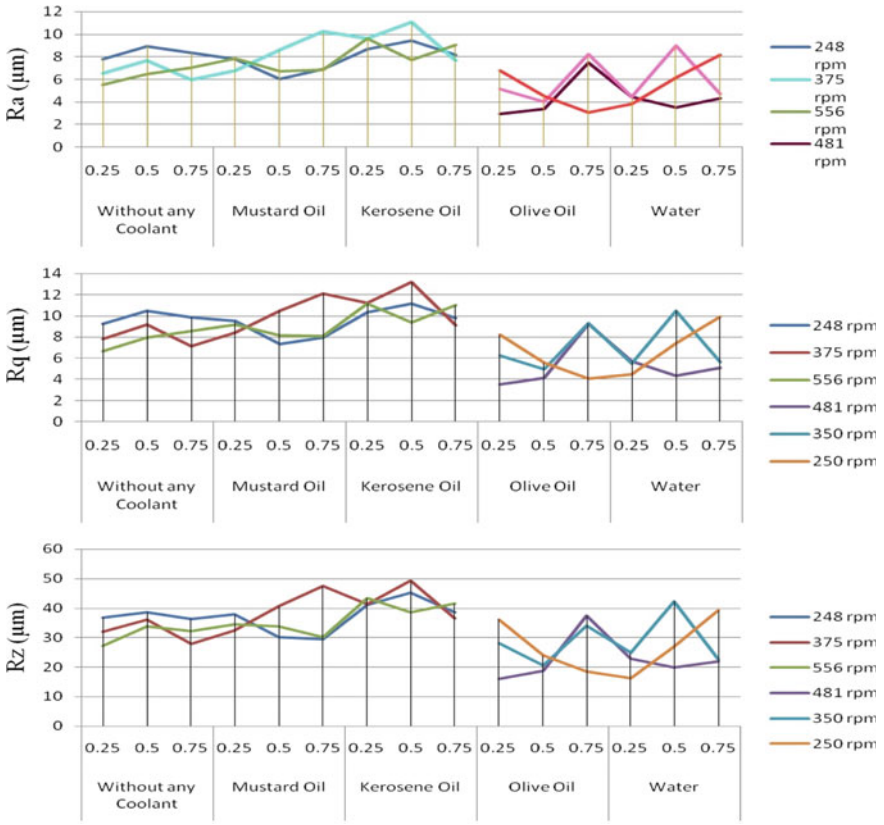

Fig. 6 Variation of different surface roughness parameters for all the cutting fluids

between the surface parameters versus depth of cut for different coolants at different speeds. The study concludes that obtained surface roughness parameter values are higher when kerosene is used as cutting fluid with higher depth of cut and higher cutting speeds. Also, surface roughness parameters are lower for higher viscous cutting fluids. Furthermore, lower rpm and lower depth of cut offer better surface finish when higher viscous fluids are used as cutting fluid.

References

1. Davim, J.P., Gaitonde, V.N., Karnik, S.R.: Investigations into the effect of cutting conditions on surface roughness in turning of free machining steel by ANN models. J. Mater. Process. Technol. **205**, 16–23 (2008)
2. Rech, J., Moisa, A.: Surface integrity in finish hard turning of case-hardened steels. Int. J. Mach. Tools Manuf. **43**, 543–550 (2003)

3. Sharman, A.R.C., Aspinwall, D.K., Dewes, R.C., Bowen, P.: Work piece surface integrity considerations when finish turning gamma titanium aluminide. Wear **249**, 473–481 (2001)
4. Asilturk, I., Akkus, H.: Determining the effect of cutting parameters on surface roughness in hard turning using the Taguchi method. Measurement **44**, 1697–1704 (2011)
5. Ahmed, S.G.: Development of a prediction model for surface roughness in finish turning of aluminum. Sudan Eng. Soc. J. **52**(45), 1–5 (2006)
6. Abburi, N.R., Dixit, U.S.: A knowledge-based system for the prediction of surface roughness in turning process. Robot. Comp Integr. Manuf. **22**, 363–372 (2006)
7. Al-Ahmari, A.M.A.: Predictive machinability models for a selected hard material in turning operations. J. Mater. Process. Technol. **190**, 305–311 (2007)
8. Abdallah, A., Rajamony, B., Embark, A.: Optimization of cutting parameters for surface roughness in CNC turning machining with aluminum alloy 6061 material. IOSR J. Eng. (IOSRJEN) **4**(10), 01–10 (2014)
9. Abhang, L.B., Hameedullah, M.: Optimization of machining parameters in steel turning operation by taguchi method. International conference on modeling Optimization and computing. Procedia Eng. **38**, 40–48 (2012)
10. Kohli, A., Dixit, U.S.: A neural-network-based methodology for the prediction of surface roughness in a turning process. Int. J. Adv. Manuf. Technol. **25**, 118–129 (2005)

Low Velocity Impact Behavior of Closed-Cell Aluminum Foam Considering Effect of Foam Skin

Y. M. Chordiya and M. D. Goel

Abstract Drop weight impact is the preferable choice for studying the impact behavior of material due to its low to medium strain rates of loading. So, herein, a finite element model is developed using LS-DYNA® for numerical simulation of drop weight test. For this investigation, closed-cell aluminum foam (Alulight foam) is used for test simulation. These foams are available with and without skin and in the present investigation, foam with skin is analyzed. Three different impact velocities are used to consider the effect of impact velocities and skin on impact behavior for the foam considered herein. In the present study, material model used for hammer and skin is plastic kinematic, and Deshpande–Fleck material model is used to model the aluminum foam. Based on the developed FE-model, energy absorption by each drop impact test is calculated using the force–displacement relation for the impact velocities considered in the present study.

Keyword Drop impact test · Numerical simulation · LS-DYNA® · Alulight foam · Foam with skin

1 Introduction

Total number of accidents occurred and passengers killed/injured in India in last decade have been substantially increased as evident from the report published by Government of India [1]. From the report "Road Safety in India-2017," it is observed that people are willing to pay more for the improved safety features for their vehicles to safeguard their life in the event of crash [2]. Vehicular occupant safety should be the prime concern while designing the vehicle. So, a lot of research is being carried out in this sector on how one can increase the crashworthiness of the vehicle? The main component for such vehicles is crash box, attached to front end of the cars.

Y. M. Chordiya · M. D. Goel (✉)
Department of Applied Mechanics, Visvesvaraya National Institute of Technology (VNIT), Nagpur 440 010, India
e-mail: mdgoel@apm.vnit.ac.in

Y. M. Chordiya
e-mail: chordiyaymoo7@gmail.com

L. Li et al. (eds.), *Advances in Materials and Manufacturing Engineering*, Lecture Notes in Mechanical Engineering, https://doi.org/10.1007/978-981-15-1307-7_16

These boxes are the parts in the vehicles which are designed purposely for impact energy absorption. With the materials research advancement, these crash boxes are packed with different types of foams to increase the energy absorption of the vehicle under impact. The materials best suited for such circumstances are metal foams because of their impact-resistant properties and light weight in comparison with the solid metals. Further, these foams are also used in packaging, blast lining materials, helmets, knee, and elbow guards [3–6].

In the past, several researchers carried out drop weight testing on different materials. These tests were carried out mostly for metal foams, concrete, graphite–fiber-reinforced composite, hybrid fiber engineered cementitious composite [7–10]. Based on the literature review, it is observed that very few numerical simulation investigations are carried out to study the impact behavior of metal foams. In addition, effect of foam skin has not been considered in most of the previous studies. Hence, present investigation is carried out with an aim to numerically simulate the drop weight impact of closed-cell aluminum foam. For this purpose, commercially available Alulight foam under three different impact velocities for is considered as the test material. To understand the effect of presence of foam skin, investigation is carried out for foam with and without skin on the basis of reaction force, displacement—time history, and energy absorption capacity.

2 FE Modeling and Material Properties

In the present study, dimensions of foam are 80 mm diameter and 100 mm length, whereas hammer has diameter of 155 and 720 mm in length. For validation of present FE-scheme, results reported by Rajendran et al. [5] are chosen and a similar model is prepared in LS-DYNA® as suggested by author and it can be concluded from Fig. 1 that numerical simulation is validated [5], for further details about validation of present FE-scheme, author's earlier investigation can be referred [11]. Based on the mesh convergence study, a converged mesh size of 20 mm for hammer and 10 mm for foam is chosen which results in a total of 18,400 elements for hammer and 1050 elements for the foam. Clamped boundary condition is applied at bottom of foam and automatic surface to surface contact is given between top of foam and bottom of hammer. Figure 2 shows stress–strain curve for Alulight foam for a density of 300 kg/m^3 [6]. In the present study, Alulight foam is modeled using MAT_154 (MAT _DESHPANDE_ FLECK_ FOAM) of LS-DYNA® material library. Foam has density of 300 kg/m^3, modulus of elasticity as 5000 MPa, Poisson's Ratio as 0.005, and plateau stress of 3 MPa. Other properties are shown in Fig. 2 for the MAT_154 used herein. In the present study, effect of skin is also taken, as lot of research has been carried out in the field of foam materials but inclusion of skin during analysis is scarce. Skin helps to increase the impact resistance of the material and it also increases the energy absorption of the material. In the present study, skin is modeled around the foam using cylinder shell element and the bilinear material model is used for skin using MAT_003 (MAT _PLATIC _KINEMATIC) of LS-DYNA® material

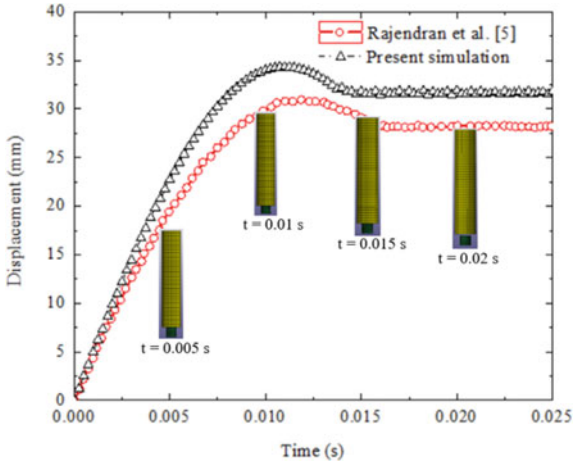

Fig. 1 Validation of present FE-scheme with the results reported by Rajendran et al. [5]

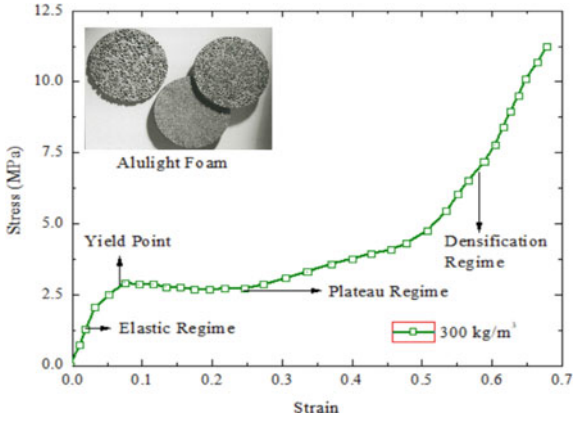

Fig. 2 Quasi-static stress-strain curve for Alulight foam for density of 300 kg/m^3 [6]

library [12]. The mesh size of foam as well as skin is kept the same (Fig. 3) because when the skin is modeled over the foam then there are chances of numerical instability to occur in the finite element model. The skin material has density (ρ), modulus of elasticity (E), Poisson's ratio (μ), yield stress (σ_y), and tangent modulus (E_t) as 2700 kg/m^3, 70 GPa, 0.3, 364 MPa, and 700 MPa, respectively. In the present study, simulation is carried out for three different drop velocities which as 3.13, 4.42, and 6.26 m/s which corresponds to a drop height of 0.5, 1, 2 m, respectively.

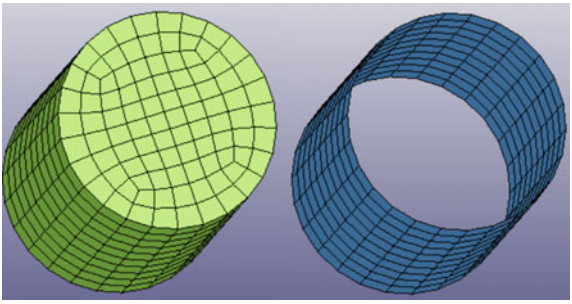

Fig. 3 FE-model of foam and skin in LS-DYNA®

3 Results and Discussions

Figure 4a shows displacement–time history for all the models considered in the present study for foam density of 300 kg/m^3. From this figure, it is clear that inclusion of skin has significant effect on the impact behavior of the foam. It is evident from Fig. 4a that increased in velocity results in increased displacement for model with skin as well as without skin. The peak displacement value obtained for model with skin is almost half of that obtained for the model without skin. This type of variation is observed while comparing both the models for a particular velocity considered in the present study. It is interesting to note that time required for model without skin to achieve peak displacement is almost same irrespective of drop velocities considered in the present investigation. Wherein, such type of behavior is not observed in model with skin. It is evident from the displacement–time history that the peak displacement, for models with skin, under an impact velocity of 6.26 m/s is 213.77 and 75.1% higher than for velocities 3.13 and 4.42 m/s, respectively. Whereas,

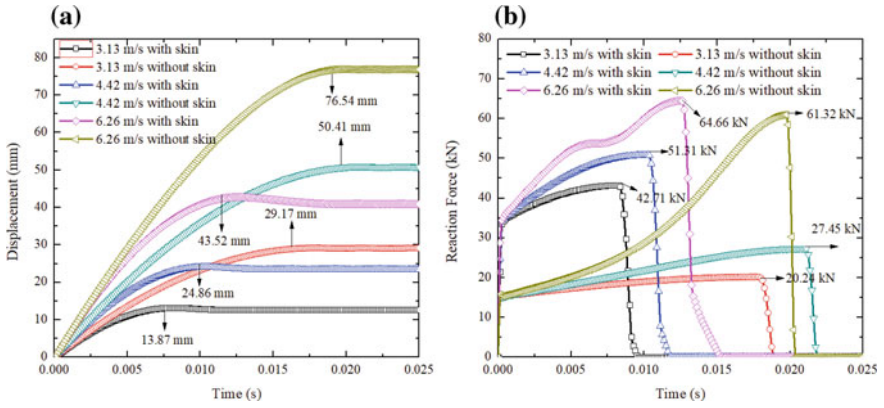

Fig. 4 **a** Displacement–time history under different drop velocities for model with skin and without skin for Alulight foam of density 300 kg/m^3, **b** Reaction-force time history under different drop velocities for model with skin and without skin for Alulight foam of density 300 kg/m^3

for models without skin, the peak displacement under impact velocity of 6.26 m/s is 162.39 and 51.83% higher than for velocities 3.13 and 4.42 m/s, respectively. If both models for a particular velocity are compared then, under an impact velocity of 4.42 m/s, model with skin results in 102.8% lower displacement in comparison with model without skin. Figure 4b shows the reaction-force time history of all the models considered, i.e., with skin and without skin for three different velocities for density of 300 kg/m^3. It is evident from figure that increase in velocity gives increased value of reaction force for model with skin as well as without skin. The reaction force increases up to a certain time then a sudden reduction is observed. If we consider model with skin under an impact velocity of 4.42 m/s and concentrate on its corresponding value from Fig. 4a and b, then we can observe that the time after which displacement becomes constant is the same time at which force becomes zero. The peak reaction-force obtained for model without skin is almost half of that obtained for the model with skin. This type of variation is observed while comparing both the models for a particular velocity considered in the present study, except for the models under an impact velocity of 6.26 m/s. They have peak reaction-force value in the same range. Further, it is evident from the reaction-force time history that the peak reaction-force, for models with skin, under an impact velocity of 6.26 m/s is 51.39 and 26.02% higher than for velocities 3.13 and 4.42 m/s, respectively. Whereas, for models without skin the peak reaction-force under impact velocity of 6.26 m/s is 202.96 and 123.4% higher than for velocities 3.13 and 4.42 m/s, respectively. If both models for a particular velocity are compared then under an impact velocity of 4.42 m/s the model with skin results 46.5% higher reaction force in comparison with model without skin.

Figure 5 shows force–displacement variation for the different impact velocities considered along with quasi-static force displacement curve for Alulight foam. Energy absorption by foam for a given velocity can be computed by finding area under the force displacement curve. From Fig. 5, it can be observed that maximum

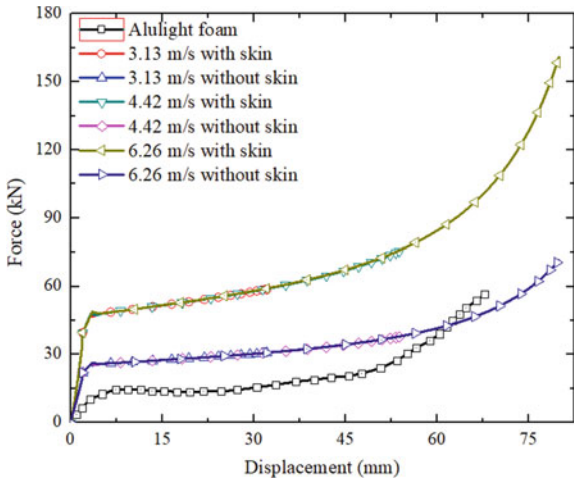

Fig. 5 Variation of force with displacement under different drop velocities for foam with skin and without skin for Alulight foam of density 300 kg/m^3

displacement is 68 mm, whereas for the velocity 3.13 and 4.42 m/s lower displacement is observed. So, a common displacement of 30 mm is chosen for comparison. The trend followed for different velocities for a particular model is same. Considering foam with skin model, displacement observed for impact velocity 6.26 m/s is greater than 3.13 and 4.42 m/s, so it superimposes them and only a single curve is observed. Foam without skin also shows the same variation in displacement and only single curve is observed. The energy absorbed by the foam with skin under velocities of 3.13, 4.42 and 6.26 m/s are 1498.94, 1526, and 1529 J, respectively. Further, energy absorbed by the foam without skin under velocities of 3.13, 4.42 and 6.26 m/s is 800, 814.56, and 816 J, respectively. The energy absorption from quasi-static curve is 396.26 J. It can be observed that energy absorption of foam with skin model is 286.11 and 87.38% higher in comparison with quasi-static curve for Alulight and foam without skin material model, respectively.

4 Conclusions

The basic aim of this study was numerical simulation of drop weight impact for Alulight foam for different impact velocities, considering the effect of skin on foam. Based on the study conducted, following conclusions can be deduced,

1. There is an increase in displacement as well as reaction force for an increase in drop height for all the foam models considered in the present investigation.
2. The time required for peak displacement and peak reaction-force is same for all models considered in the present investigation.
3. The energy absorbed by foam is drop-velocity independent.
4. If the effect of skin is considered, then the impact resistance of the material increases.

References

1. Ministry of Road Transport and Highways Transport Research Wing (2016) Road accidents in India. 2–7
2. SaveLIFEFoundation (2017) Road safety in India. 4–15
3. Barr, B., Bouamrata, A.: Development of a repeated dropweight impact testing apparatus for studying fibre reinforced concrete materials. Composites **19**, 453–466 (1988). https://doi.org/10.1016/0010-4361(88)90703-3
4. Bowles, K.: The correlation of low-velocity impact resistance of graphite-fiber-reinforced composites with matrix properties. In: Composite Materials: Testing and Design (Eighth Conference). ASTM International, 100 Barr Harbor Drive, PO Box C700, West Conshohocken, PA 19428-2959, 124–149 1988
5. Rajendran, R., Moorthi, A., Basu, S.: Numerical simulation of drop weight impact behaviour of closed cell aluminium foam. Mater. Des. **30**, 2823–2830 (2009). https://doi.org/10.1016/j.matdes.2009.01.026

6. Pinnoji, P.K., Mahajan, P., Bourdet, N., et al.: Impact dynamics of metal foam shells for motorcycle helmets: experiments and numerical modeling. Int. J. Impact Eng. **37**, 274–284 (2009). https://doi.org/10.1016/j.ijimpeng.2009.05.013
7. Banthia, N., Mindess, S., Bentur, A., Pigeon, M.: Impact testing of concrete using a drop-weight impact machine. Exp. Mech. **29**, 63–69 (1989). https://doi.org/10.1007/BF02327783
8. Zhang, W., Chen, S., Liu, Y.: Effect of weight and drop height of hammer on the flexural impact performance of fiber-reinforced concrete. Constr. Build. Mater. **140**, 31–35 (2017). https://doi.org/10.1016/j.conbuildmat.2017.02.098
9. Zhang, J., Maalej, M., Quek, S.T.: Performance of hybrid-fiber ECC blast/shelter panels subjected to drop weight impact. J. Mater. Civ. Eng. **19**(10), 855–863 (2007). https://doi.org/10.1061/(ASCE)0899-1561
10. Roesset, J.M., Kausel, E., Cuellar, V., Monte, J.L., Valerio, J.: Impact of weight falling onto the ground. J. Geotech. Eng. **120**(8), 1394–1412 (1994). https://doi.org/10.1061/(ASCE)0733-9410
11. Chordiya, Y.M., Goel, M.D.: Study of impact behavior of polymeric foams using numerical simulation of drop weight impact. In: Proceedings of National Conference: Advanced Structures, Materials and Methodology in Civil Engineering (ASMMCE—2018), (2019)
12. LS-DYNA®: keyword user's manual, 2nd edn. Livermore Software Technology Corporation, Livermore, California, U.S.A

Design of Optimal State Observer-Based Controller for 4-DOF Planar Manipulator Using PSO

Jishnu AK, Ravi Kumar Mandava and Pandu R. Vundavilli

Abstract The present paper aims at developing state observer-based controller for a 4-DOF planar serial manipulator. The kinematics of the manipulator has been achieved through D-H convention, and dynamics of the same has been derived after utilizing Lagrange–Euler formulation. The nonlinear dynamic equations have been linearized and expressed in state-space representation. Based on the arbitrarily chosen pole values, pole placement has been done and then observer is designed to evaluate the state variables. Further, PSO algorithm is also used to optimize the pole values and to minimize steady-state error. Once the optimal controller is designed, its performances have been tested in simulations.

Keywords 4-DOF planar manipulator · State observer-based controller · Optimization · PSO

1 Introduction

Serial robotic manipulators consist of a number of links connected together serially by joints. This has found diverse applications both in industry and laboratory in accomplishing tasks like welding, pick and place, automotive assembly, dealing with hazardous radioactive substances, so on and so forth. The degree of freedom (DOF) of a serial manipulator is the number of independent variables required to fully define its configuration and it is equal to the number of links present in the serial manipulator. The crucial step in robotics is establishing the kinematics of the manipulator which

J. AK · P. R. Vundavilli
School of Mechanical Sciences, Indian Institute of Technology, Bhubaneswar 752050, Odisha, India
e-mail: jak10@iitbbs.ac.in

P. R. Vundavilli
e-mail: pandu@iitbbs.ac.in

R. K. Mandava (✉)
Department of Mechanical Engineering, Vignan's Foundation for Science Technology and Research, Guntur 522213, Andhra Pradesh, India
e-mail: rm19@iitbbs.ac.in

L. Li et al. (eds.), *Advances in Materials and Manufacturing Engineering*, Lecture Notes in Mechanical Engineering, https://doi.org/10.1007/978-981-15-1307-7_17

consists of forward and inverse kinematics. The former involves locating the end effector when joint variables are provided. Contrary, the latter predicts the joint parameters to achieve a particular end effector position or path. Forward kinematic equations of a 4-DOF serial manipulator have been developed by Mohammed et al. [1] after using D-H convention and product of exponential formulae. It is important to note that the solution methodology for the inverse kinematics of the manipulator is not as easy as the forward kinematics and it might not involve a unique solution. The inverse kinematic equations of a 2- and 4-DOF manipulators were derived by Mustafa et al. [2] and Ravi et al. [3], respectively. The inverse kinematics equation obtained in [3] was nonlinear; thus, linearization techniques are adopted. Description of linearization is given in [4]. The authors had utilized the multivariable calculus chain rule to linearize about the operating point as given in [2]. On linearizing, the system was expressed in terms of state-space representation. A survey of prevailing control strategies used for controlling the robotic manipulator was given by Khan et al. [5]. This paper focuses on developing a state observer-based controller for a 4-DOF robotic manipulator. After expressing the system in its state-space representation, the poles of the system were placed at a specific predetermined location. This was achieved by introducing a feedback gain matrix in such a way that the Eigenvalues of A-BK will be placed at the desired pole locations. The algorithms to determine the gain matrix were discussed in [6]. Further, the pole placement methods for the multivariable control of robotic manipulator were given by Norcross et al. [7]. This pole placement approach was done by assuming the state variables on a real-time basis. But in practice, implementing this using sensor could make the system more complex and expensive. To avoid this, an attempt was made to introduce a feature called observation, where we approximately estimate the unmeasured state variables. This was theoretically done by designing an observer which works in tandem with the controlled system whose output was a matrix of state variables. A step response for such a controller was discussed in [8]. Designing of observer primarily involves determining the observer gain matrix (Ke) such that the Eigenvalues of A-KeC will attain the desired value [6]. The poles for the controlled system have to be chosen through the trial and error method, but this might not give the best result. Thus, it necessitates the use of optimization algorithms. Mandava et al. [9] had used genetic algorithm (GA) and particle swarm optimization (PSO) algorithm to optimize the parameters of 3-DOF robotic manipulator. In the present manuscript, an attempt is made to develop the state observer-based controller to control the motion of end effector of a 4-DOF manipulator. Further, the poles of the observer-based controller have also been optimized with the help of PSO algorithm. Finally, the performances of the developed algorithms are compared in computer simulations.

2 Mathematical Formulation

The system of interest in the present study is a 4-DOF serial manipulator (ref. to Fig. 1) having link lengths equal to L_1, L_2, L_3, and L_4 with an including angles of θ_1,

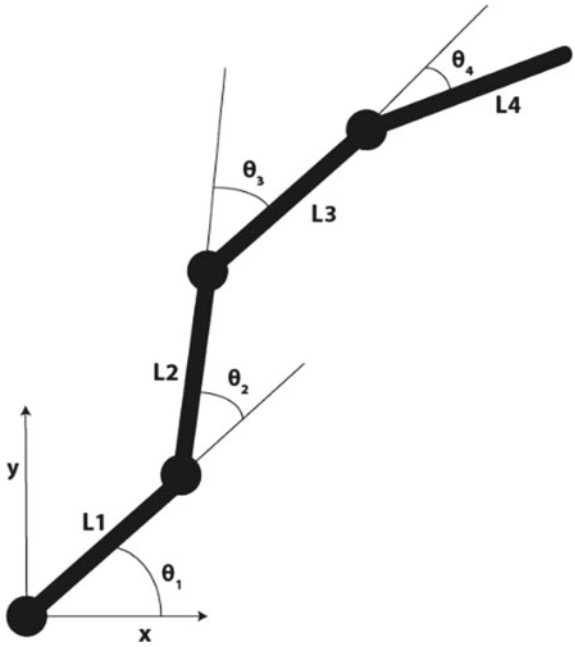

Fig. 1 Four DOF planar manipulator configuration

θ_2, θ_3, and θ_4, respectively between the consecutive links. Mathematical modeling of serial manipulator mainly involves two steps, namely forward and inverse kinematics. Forward kinematics involves locating the position and orientation of end effector when system parameters (link length and angles) are given. D-H convention is utilized for kinematic analysis. Coordinate system is allocated to each joint with four D-H parameters associated with each link. Further, these parameters are employed to generate D-H table (ref. to Table 1). Utilizing the D-H parameters given in Table 1, the transformation matrix between the end effector and the base of the manipulator ($^0T_4$) is given by Eq. (1).

Table 1 The D-H parameters of DOF manipulator are as follows

Link (i)	a_i	α_i	d_i	θ_i
1	L_1	0	0	θ_1
2	L_2	0	0	θ_2
3	L_3	0	0	θ_3
4	L_4	0	0	θ_4

$$ {}^{0}T_4 = \begin{bmatrix} C_{1234} & -S_{1234} & 0 & L_1C_1 + L_2C_2 + L_3C_{123} + L_4C_{1234} \\ S_{1234} & C_{1234} & 0 & L_1S_1 + L_2S_2 + L_3S_{123} + L_4S_{1234} \\ 0 & 0 & 1 & 0 \\ 0 & 0 & 0 & 1 \end{bmatrix} \tag{1} $$

where the notations are referring to $C_1 = \cos(\theta_1)$, $S_1 = \sin(\theta_1)$, $C_{12} = \cos(\theta_1 + \theta_2)$, $S_{12} = \sin(\theta_1 + \theta_2)$, $C_{123} = \cos(\theta_1 + \theta_2 + \theta_3)$, $S_{123} = \sin(\theta_1 + \theta_2 + \theta_3)$, $C_{1234} = \cos(\theta_1 + \theta_2 + \theta_3 + \theta_4)$, and $S_{1234} = \sin(\theta_1 + \theta_2 + \theta_3 + \theta_4)$. Once the kinematics of the manipulator is derived, the next step is to derive the dynamic model of robotic manipulator, where we establish the relationship for the torque to be applied at the joint actuators to achieve the desired position, velocity, and acceleration of the end effector. This is accomplished by using Lagrange–Euler formulation and is given by Eq. (2).

$$ F = M(q)\ddot{q} + h(\dot{q}, \ddot{q}) + G(q) $$

$$ \ddot{q} = M(q)^{-1}[-h(\dot{q}, q) - G(q)] + M(q)^{-1} * F \tag{2} $$

where F is the torque matrix, M, G, and h represent inertia matrix, gravity matrix, and centrifugal matrix, respectively. Further q is a 4×1 matrix with elements containing the terms related to $\theta_1, \theta_2, \theta_3$, and θ_4. The above equations that describe the dynamics of the system are nonlinear in nature. This could be assumed to be linear in nature about its operational point within a short operating range. Therefore, let us define the state variables of the system as follows:

$$ \begin{aligned} x_1 &= \theta_1 \quad x_2 = \theta_2 \quad x_3 = \theta_3 \quad x_4 = \theta_4 \\ x_5 &= \dot{\theta}_1 \quad x_6 = \dot{\theta}_2 \quad x_7 = \dot{\theta}_3 \quad x_8 = \dot{\theta}_4 \end{aligned} \tag{3} $$

Hence, on differentiating state variables with time, we obtain the velocities as given by Eq. (4).

$$ \begin{aligned} \dot{x}_1 &= x_5 \quad \dot{x}_2 = x_6 \quad \dot{x}_3 = x_7 \quad \dot{x}_4 = x_8 \\ \dot{x}_5 &= \ddot{\theta}_1 \quad \dot{x}_6 = \ddot{\theta}_2 \quad \dot{x}_7 = \ddot{\theta}_3 \quad \dot{x}_8 = \ddot{\theta}_4 \end{aligned} \tag{4} $$

after substituting state variables in Eq. (2), the equation is linearized as mentioned in Eq. (5) and is expressed in terms of state-space representation as follows,

$$ \dot{x}(t) = A(t)x(t) + B(t)u(t) \tag{5} $$

$$ y(t) = C(t)x(t) + D(t)u(t) \tag{6} $$

where A, B, C, and D represent the control matrix, input matrix, output matrix, and feed-forward matrix, respectively.

3 Controller Design

Designing the state observer-based controller for a serial manipulator involves two steps, namely pole placement and designing the observer. Former involves placing the poles of the controlled system at the desired pole location by means of the state gain matrix. The pole location was taken on a trial and error basis which gives the best result. Let us assume that no reference input is given, and all the state variables are measurable. We shall choose our control signal to be

$$u = -Kx \tag{7}$$

where K is the control gain matrix. Thus, the newly obtained system is given by Eq. (8).

$$\dot{x}(t) = (A - BK)x(t) \tag{8}$$

whose solution is given by Eq. (9).

$$x(t) = e^{(A-BK)t}x(0) \tag{9}$$

The Eigenvalues of the matrix $[A-BK]$ will determine the stability and transient response of the system. So, if the values of K were chosen with care, $A-BK$ could create an asymptotically stable response such that $x(t)$ approaches zero when time goes infinity (steady-state). This is achieved by placing the Eigenvalues of $A-BK$ which are called regulator poles in the desired locations in left-half plane. If the system is controllable, the determination of K could be done using several algorithms as given in [6]. This could be easily implemented using 'place' command in MATLAB. However, for the K matrix to exist, the sufficient and necessary condition is that the system should be controllable. This is possible if the controllability matrix is of order 'n' (here 8). The above method is done by assuming that all the state variables can be measured in real time. However, in practice, state variables would not be always available for feedback. This necessitates the need of an observer which is usually a computer program which estimates the value of state variables approximately. This process of estimating unknown state variables is called observation. Here, an attempt is made to use a full state observer which estimates all state variables regardless of whether they are available for direct measurement or not. The block diagram showing the observer-based controller is given in Fig. 2.

The mathematical model of observer is almost the same as that of the system with an additional term accounting for the measured output ($y = Cx$) and observed output ($y = C\tilde{x}$). The expression for $\dot{\tilde{x}}$ is given by Eq. (10).

$$\dot{\tilde{x}} = (A - K_eC)\tilde{x} + Bu + K_ey \tag{10}$$

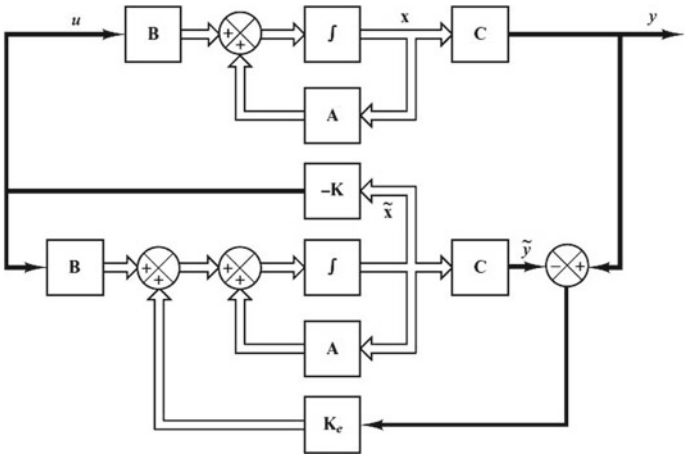

Fig. 2 Block diagram showing the state observer-based controller [5]

where $\tilde{x}$ is the estimated state matrix. Combining the above equation with (Eq. 2), we get

$$\dot{x} - \dot{\tilde{x}} = (A - K_e C)(x - \tilde{x})$$

Let $e = x - \tilde{x}$

$$\dot{e} = (A - K_e C)e \tag{11}$$

Further, the state equations of the combined model are given by Eq. (12).

$$\begin{bmatrix} \dot{x} \\ \dot{e} \end{bmatrix} = \begin{bmatrix} A - BK & BK \\ 0 & A - K_e C \end{bmatrix} \begin{bmatrix} x \\ e \end{bmatrix} \tag{12}$$

Now, let us introduce nonzero reference input which is the final angle that the system needs to trace. Let R be reference input.

$$P = \begin{bmatrix} A - BK & BK \\ 0 & A - K_e C \end{bmatrix}$$

Now, the system could be expressed as

$$\dot{z}(t) = Pz - PR \tag{13}$$

where $z = \begin{bmatrix} x \\ e \end{bmatrix}$

On solving this differential equation by providing initial condition and R being the final boundary condition, the response of the system can be determined.

4 PSO Algorithm for Optimizing Pole Values

Particle swarm optimization (PSO) is an optimization algorithm motivated by the sociological behavior of a group of individuals such as flocks of bird. This was formerly introduced by Kennedy and Eberhart [10]. Each particle constituting the population (swarm) represents a solution which is denoted as its position $X_i = (x_{i1}, x_{i2}, \ldots x_{iD})$ in search space. The position of the particle is modified in each iteration based on P_{best} and P_g, where P_{best} represents a particle's previous best position and P_g represents solution with the best fitness among the entire population. Both P_{best} and P_g are untiled to alter the velocity $V_i = (v_{i1}, v_{i2}, \ldots v_{iD})$ assigned to the particle. The particles position and velocity are manipulated as given by Eqs. (14) and (15), respectively.

$$V_{i,D}(t+1) = wV_{i,D}(t) + C_1R_1(P_{iD} - x_{iD}(t)) + C_2R_2\big(P_{gD} - x_{iD}(t)\big) \tag{14}$$

$$x_{iD}(t+1) = x_{iD}(t) + V_{i,D}(t+1) \tag{15}$$

where w, C_1, and C_2 are inertia weight, cognitive parameter, and social parameter, respectively. R_1 and R_2 represent the random numbers between 0 and 1. PSO algorithm is implemented to determine the optimal pole values of the controlled system which are four conjugate pairs as the position of the swarm. The search space constitutes of possible pole values. The squared sum of errors of all four angles has been chosen as the cost function which is to be minimized. The optimization problem is formulated as given below.

Minimize $E = \sqrt{\sum e(\theta_i)^2}$ $i = 1, 2, 3, 4$

Subjected to the condition,

$$\begin{aligned}
&-22.99 < \text{Re}(P_1) < -2.09 \quad 2.19 < \text{Im}(P_1) < 17.19\\
&-25.60 < \text{Re}(P_2) < -0.60 \quad -2.44 < \text{Im}(P_2) < 12.55\\
&-2.08 < \text{Re}(P_3) < -27.08 \quad -7.22 < \text{Im}(P_3) < 7.22\\
&-4.08 < \text{Re}(P_4) < -29.08 \quad -6.72 < \text{Im}(P_4) < 8.27
\end{aligned}$$

where P_1, P_2, P_3, and P_4 are the pole values and Re (z) and Im (z) represent the real and imaginary part of z, respectively.

5 Result and Discussion

5.1 Design of State Observer-Based Controller

This research aims at designing and developing a state observer-based controller for the 4-DOF robotic manipulator. The dynamic equation obtained through Lagrange–Euler formulation has been linearized with respect to the operating point $\left(\theta_1 = \frac{3}{8}\pi, \theta_2 = \frac{1}{4}\pi, \theta_3 = \frac{1}{8}\pi, \theta_4 = \frac{1}{6}\pi\right)$. The control matrix ($A$), input matrix ($B$), output matrix ($C$), and feed-forward matrix (D) obtained are given below. It is to mention that D is a zero matrix.

$$A = \begin{bmatrix} 0 & 0 & 0 & 0 & 1\,0\,0\,0 \\ 0 & 0 & 0 & 0 & 0\,1\,0\,0 \\ 0 & 0 & 0 & 0 & 0\,0\,1\,0 \\ 0 & 0 & 0 & 0 & 0\,0\,0\,1 \\ -1.7844 & 0.7560 & -3.2725 & 1.2826 & 0\,0\,0\,0 \\ -5.8387 & -9.3687 & 18.5190 & -13.7950 & 0\,0\,0\,0 \\ 6.4004 & 11.2720 & -38.6070 & 29.7921 & 0\,0\,0\,0 \\ 0.7169 & -0.0955 & 31.8188 & -27.5377 & 0\,0\,0\,0 \end{bmatrix} \quad B = \begin{bmatrix} 0 & 0 & 0 & 0 \\ 0 & 0 & 0 & 0 \\ 0 & 0 & 0 & 0 \\ 0 & 0 & 0 & 0 \\ 0.2572 & -0.5225 & 0.3646 & 0.0097 \\ -0.5725 & 1.9730 & -2.4778 & 1.0829 \\ 0.4915 & -2.6646 & 4.9229 & -3.7441 \\ -0.1033 & 1.3143 & -3.9090 & 5.2835 \end{bmatrix}$$

$$C = \begin{bmatrix} 1\,0\,0\,0\,0\,0\,0\,0 \\ 0\,1\,0\,0\,0\,0\,0\,0 \\ 0\,0\,1\,0\,0\,0\,0\,0 \\ 0\,0\,0\,1\,0\,0\,0\,0 \end{bmatrix}$$

After expressing the system in state-space representation, the next step involves determination of state gain matrix. Prior to this, the controllability of the system has been verified with the aid of MATLAB. Determination of K matrix has been done with the pole values (which has been chosen through trial and error method) $-10.89 \pm 15.49i$, $-21.81 \pm 10.65i$, $-13.77 \pm 2.7i$, $-24.67 \pm 2.20i$. In order to make the response of observer to be quicker, the pole values have been chosen 10 times the present values. Thus, the obtained K and Ke matrices are given below.

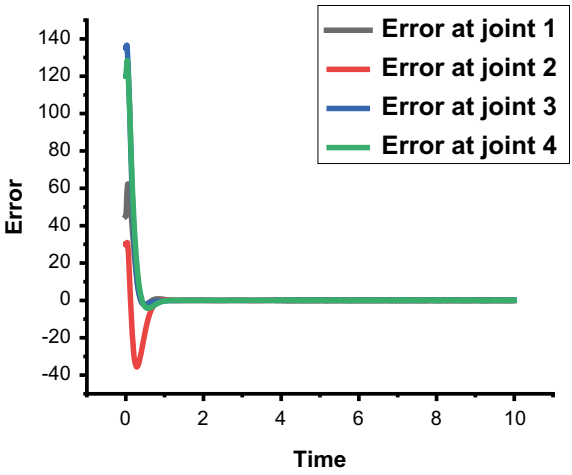

Fig. 3 Convergence plot for all the joints

$$K = \begin{bmatrix} 11,007 & 580 & -2917 & 3835 & 951 & 359 & 151 & 207 \\ 8001 & 1209 & 1023 & 3296 & 645 & 314 & 186 & 183 \\ 4379 & 827 & -103 & 2039 & 339 & 179 & 138 & 118 \\ 1456 & 298 & 114 & 822 & 108 & 60 & 59 & 53 \end{bmatrix} \quad Ke = \begin{bmatrix} 351 & 58 & 34 & 75 \\ 72 & 368 & 53 & -11 \\ 15 & -22 & 382 & 30 \\ -97 & -5 & -33 & 321 \\ 32,158 & 16,679 & 8402 & 25,528 \\ -16,922 & 32,756 & 9529 & 936 \\ -8444 & -3144 & 42,331 & 3051 \\ -20,367 & -2358 & 2719 & 31,082 \end{bmatrix}$$

Both K and Ke clubbed with the state-space matrixes substituted in differential equation by the reference input $\left[\pi/2 \; \pi/3 \; \pi/2 \; \pi/2 \; 0 \; 0 \; 0 \; 0 \; 0 \; 0 \; 0 \; 0 \; 0 \; 0 \; 0 \; 0\right]^T$ and initial condition $\left[\pi/4 \; \pi/6 \; -\pi/4 \; -\pi/6 \; 0 \; 0 \; 0 \; 0 \; 0.5 \; 0.5 \; 0.5 \; 0.5 \; 0.5 \; 0.5 \; 0.5 \; 0.5\right]^T$, the trajectory of robotic manipulator is solved by using the state-space approach. The error convergence plot obtained by the controller for all the four joints is given in Fig. 3.

5.2 Optimization of Pole Values Using PSO

Particle swarm optimization has been utilized to reduce the steady-state error associated with each angle by optimizing the pole values. Parameter study has been

conducted to identify the PSO parameters which give the best performance. Figures 4 and 5 show the parametric study related to the population size and maximum number of generations, respectively.

The optimal values of population size and number of generations are seen to be equal to 25 and 20, respectively. Further, the optimal values of four pole conditions are found to be equal to $-5.55 \pm 6.61i$, $-6.80 \pm 3.56i$, $-18.13 \pm 2.57i$, $-18.61 \pm 0.61i$, respectively. Once the controllers are designed, the performances of both the approaches are tested in simulation. Figure 6 shows the path followed by the end effector between the start and goal points by the state observer-based controller and PSO optimized state observer-based controller.

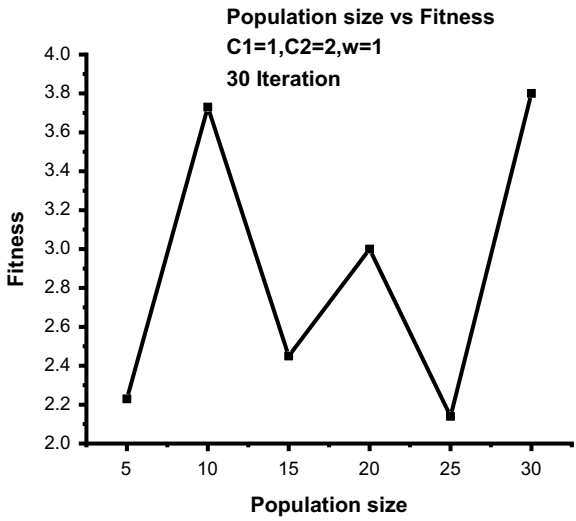

Fig. 4 Population size versus fitness

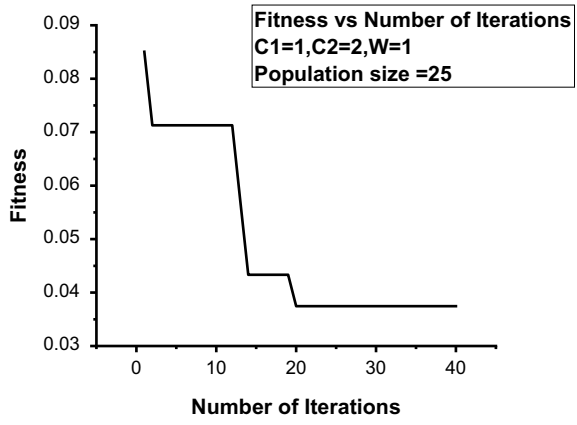

Fig. 5 Number of iterations versus fitness

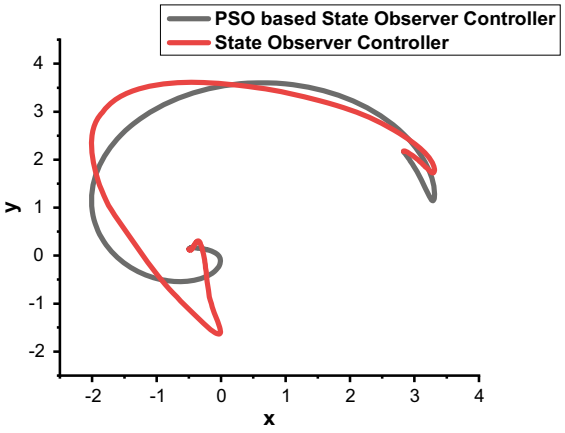

Fig. 6 Schematic diagram showing the path traced by the end effector

It has been observed that PSO optimized state observer-based controller has traced the path in a more circular fashion when compared with the normal observer-based controller. This might be due to the global optimal solution obtained for the four pole positions when compared with the random initial solution chosen for the poles in the conventional observer-based controller.

6 Conclusion

In this paper, the authors have successfully developed a traditional state observer-based controller and a PSO optimized state observer-based controller for a 4-DOF serial planar manipulator. As part of the controller design, the equation of motion that represents the torques required at various joints of the manipulator is derived by following the L-E formulations. The performances of the developed algorithms are tested in a computer simulation. The cumulative error value for all the joints of traditional state observer-based controller and PSO-based state observer controller is seen to be equal to 0.26 and 0.037 radians, respectively. This might have happened due to the global searching capability of PSO algorithm when compared with the traditional state observer-based controller.

References

1. Mohammed, A.A., Sunar, M.: Kinematics modeling of a 4-DOF robotic arm. In: International Conference on Control, Automation and Robotics, 87–91(2015)
2. Mustafa, A.M, Al-Saif, A.: Modeling, simulation and control of 2-R robot. Glob. J. Res. Eng. **14**(1), (2014)

3. Mandava, R.K., Vundavilli, P.R.: Design 4-DOF PID controller for 4-DOF planar and spacial manipulators. In: International Conference on Robotics Automation and Control and Embedded systems, (2015)
4. Cardoso, G.S., Schnitman, L.: Analysis of exact linearization and approximate feedback linearization techniques. Math. Probl. Eng. **2011**, (2011)
5. Khan, M.F., Islam, R.Ul., Iqbal, J.: Control strategies for robotic manipulators. In: International Conference of Robotics and Artificial Intelligence. ICRAI 2012, 26–33 2012
6. Ogata, K.: Modern Control Engineering, 5th edn, Prentice Hall (2010)
7. Norcross, R.J., Wang, J.C., McInnis B.C., Shieh, L.S.: Pole placement methods for multivariable control of robotic manipulators. J. Dyn. Syst. Meas. Control. Transm., ASME. **108**(4), (1986)
8. Choi, C.H.: Step response improvement by pole placement with observer. In: Proceedings Annual Southeastern Symposium on System Theory, 7–12 2008
9. Mandava, R.K., Manas, K.S., Vundavilli, P.R.: Optimization of PID Controller Parameters for 3-DOF Planar and spatial Manipulator using GA and PSO
10. Kennedy, J., Eberhart, R.: Particle swarm optimization. In: IEEE International Conference on Neural Network, 1942–1948, 1995

FEM-Based Hot Machining of Inconel 718 Alloy

A. Kiran Kumar and P. Venkataramaiah

Abstract Finite element simulation of metal cutting process has acquired much attention by many researchers in the recent past since it is a robust tool to estimate the machining process variables, which are hard to get experimentally. It is well known that machining of hard to cut materials causes large cutting forces, which is responsible for excessive tool wear, rise in power consumption of machines, and also leads to an extreme deflection and accordingly failure of the cutting tool. The objective of this paper is to predict cutting forces under the influence of preheating surface temperature in addition to cutting speed, feed, and depth of cut (doc) in machining of Inconel 718 alloy using Abaqus/CAE. The Johnson–Cook material model is the simplest model in machining simulation which is suitable in relating the material behavior at high strain rate and also suitable for dynamic simulation conditions. An L9 orthogonal array and the signal-to-noise (S/N) ratio are deployed and found the optimum combination of machining parameters at cutting speed of 50 m/min, feed of 0.11 mm/rev, depth of cut of 0.1 mm and preheating temperature of 600 °C in order to minimize the cutting forces and also found depth of cut as the most effective factor. The results were compared with previous experimental results and found satisfactory.

Keywords Hot machining · Abaqus/explicit · Johnson–cook model · Inconel 718 · S/N ratio

List of symbols

A	Yield stress (MPa)
B	Strain hardening parameter (MPa)
n	Strain hardening exponent

A. K. Kumar (✉) · P. Venkataramaiah
Department of Mechanical Engineering, S.V. University, Tirupati 517502, India
e-mail: kirankumarabbili@yahoo.com

P. Venkataramaiah
e-mail: pvramaiah@gmail.com

L. Li et al. (eds.), *Advances in Materials and Manufacturing Engineering*, Lecture Notes in Mechanical Engineering, https://doi.org/10.1007/978-981-15-1307-7_18

C	Strain rate sensitivity parameter
m	Temperature exponent
ε_p	Plastic strain
$\varepsilon^* = (\varepsilon_p{}^*/\varepsilon_0)$	Is dimensionless strain rate
$T^{*m} = (T-T_0)/(T_m-T_0)$; T	is working temp.,
T_0	is room temp.,
T_m	is melting temperature.
$D1$ to $D5$	Are coefficients of Johnson–Cook material shear failure initiation criterion
$\sigma^* = \sigma m/\sigma \mathrm{eq}$	is the stress
σ_{eq}	Equivalent stress
σ_m	Mean stress

1 Introduction

Finite element method is extensively used to analyze the performance of machining, which saves time and reduces the wastage of material compared to experimental investigation and also gives the accurate estimation of machining characteristics. Superalloys have a prominent role in the aerospace industry due to its excellent mechanical, chemical, wear resistance, and thermal properties at elevated temperatures. Because of these exceptional properties, machining of superalloys in conventional method results in high cutting forces. It also influences the surface quality and tool life. Many research studies have been carried out to analyze the machinability of difficult to cut materials using finite element method. The influence of tool nose radius on temperature distribution during machining is investigated and reported that the cutting forces increased with increase in tool nose radius at both room and preheating temperature machining condition [1]. The impact of edge roundness on residual stresses in turning of AISI304 steel has been studied using FE model [2]. Feed force can be taken as a measure to predict surface roughness in FEM since the trend observed in both responses is similar [3]. Temperature measurement during the machining of Ni-based superalloys has been studied as it is crucial factor to control the machining process, avoiding the workpiece damage [4]. J-C model is still recommended as it is the best model for performing the machining simulation process because of its accuracy and easy to apply using FEM [5]. Stresses induced during machining are analyzed and also the temperature distribution during chip formation has been reported using Abaqus software [6]. It is very important to select suitable J-C model parameters which influence the best fit between predicted and experimental results [7, 8, and 9]. Numerical model is selected to study the chip morphology in orthogonal cutting and is compared experimentally to validate the results [10]. The residual stress induced in the machined part using different materials through FEM analysis has been studied [11, 12]. The nose radius has a remarkable influence in chip formation and stress distribution is analyzed through numerical model [13,

14]. In the present work, FEM-based simulation of turning process has been carried out to study the influence of machining parameters and preheating temperature on cutting forces. Simulation runs performed according to L9 orthogonal array and Taguchi (S/N ratio) method has been implemented to find the optimum parameters combination and most influential factor.

2 Finite Element Modeling

Machining simulation is continuously seeking the attention of researchers for better analyzing the chip formation mechanism, predicting the cutting forces, frictional characteristics at the tool–chip interface and surface integrity of the workpiece. Johnson–Cook (J-C) model (Eq. 1) is adopted for workpiece and cutting tool to represent the actual behavior. Damage initiation criterion (Eq. 2) is very important, because its impact on obtaining the suitable parameters behavior of tool–workpiece surface integrity is very high. Hence, building of accurate FEM models is crucial in order to investigate the effect of machining parameters and preheating temperature on the cutting forces. Figure 1 shows the 3D model of workpiece and cutting tool.

$$\lceil \cdot * \rceil$$

$$\sigma_{\text{eq}} = \left[A + B\varepsilon_p^n\right] \| 1 + C \ln(\varepsilon) \| \left[1 - T^{*m}\right] \tag{1}$$

$$\varepsilon_f = \left[D_1 + D_2 \exp(D_3 \sigma^*)\right] \left[1 + D_4 \ln(\varepsilon_p^*)\right] \left[1 + D_5 T^*\right] \tag{2}$$

J-C model parameters for Inconel 718 alloy which is collected from the literature are listed in Table 1. C3D8RT element type is selected which is appropriate to study mechanical and thermal characteristics in machining simulation. The total of 4400

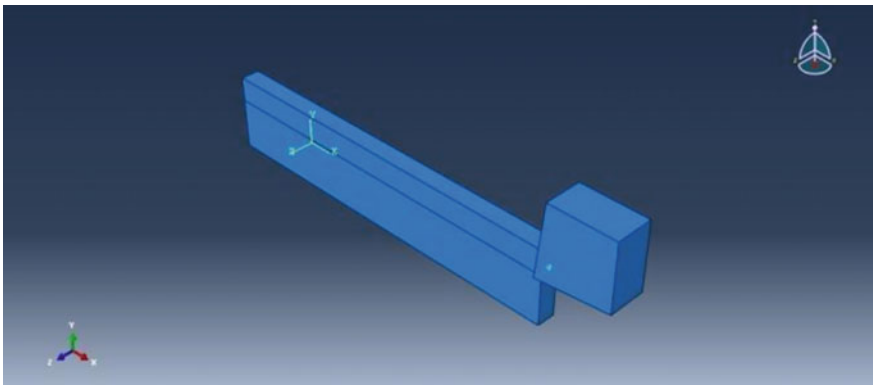

Fig. 1 Assembly of workpiece and cutting tool

Table 1 J-C model parameters

A(MPa)	B(MPa)	n	m	C
980	1370	0.164	1.03	0.020
D1	D2	D3	D4	D5
0.11	0.75	−1.45	0.04	0.89

Table 2 Geometry of cutting tool

Rake angle, α	Clearance angle	Nose radius (mm)
6°	6°	0.8

Table 3 Properties of workpiece and tool

S. No	Parameter	Inconel 718	WC
1	Density (kg/m^3)	8195	15,700
2	Young's modulus (Gpa)	200	705
3	Poisson ratio	0.3	0.23
4	Thermal conductivity (W/m °C)	11.4	24
5	Specific heat (J/Kg/°C)	430	178

elements in the mesh of workpiece and 512 elements in tool were formed. The geometry of the cutting tool and properties of Inconel 718 alloy and tool listed in Table 2 and 3. The workpiece and tool interaction during the machining process has a crucial part in predicting the machining characteristics [15]. The coefficient of friction is selected as 0.6, the tool and workpiece interaction is selected as general contact. The boundary conditions are shown in Fig. 2, the workpiece bottom is considered as fixed, and the cutting tool motion is given along x-direction.

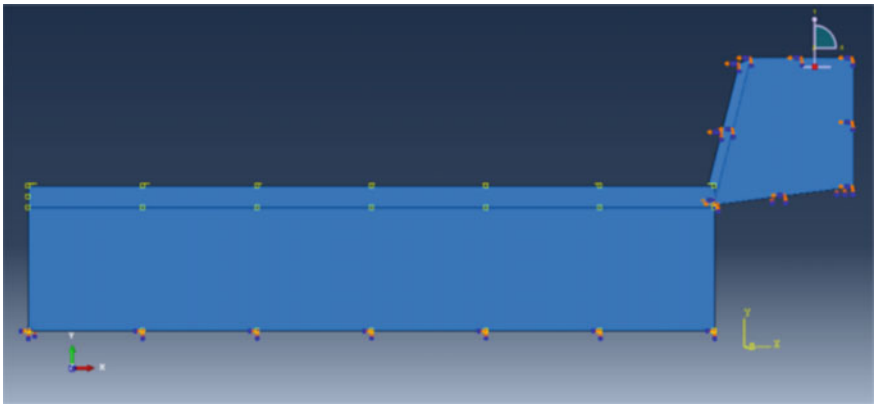

Fig. 2 Boundary conditions of workpiece and cutting tool

Table 4 Levels of input parameters

Cutting speed (m/min)	Feed rate (mm/rev)	Depth of cut (mm)	Preheating Temp. (°C)
50	0.11	0.1	30
100	0.13	0.3	300
150	0.16	0.5	600

The levels of cutting parameters and preheating temperature are listed in Table 4.

3 Results and Discussion

Simulation tests performed according to L9 orthogonal array in Abaqus/Explicit software to assess the influence of machining parameters on cutting forces are listed in Table 5. The cutting force plots obtained from simulation at different conditions are shown in Fig. 3a, b.

Table 5 Simulation results

S NO	Cutting Speed (m/min)	Feed rate (mm/rev)	Depth of cut (mm)	Preheating Temp. (°C)	Cutting Force (N)
1	50	0.11	0.1	30	81.5
2	50	0.13	0.3	300	167.4
3	50	0.16	0.5	600	210.1
4	100	0.11	0.3	600	163.5
5	100	0.13	0.5	30	250.2
6	100	0.16	0.1	300	142.1
7	150	0.11	0.5	300	308.6
8	150	0.13	0.1	600	109.4
9	150	0.16	0.3	30	416.8

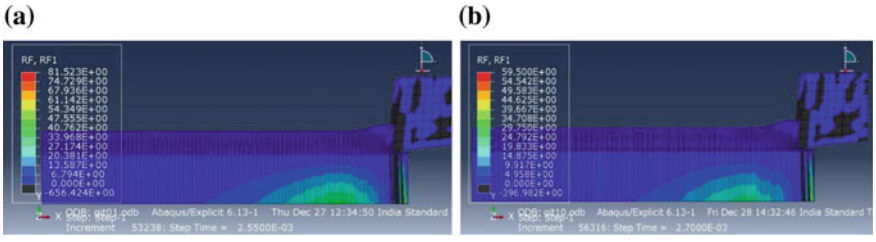

Fig. 3 **a** $v = 50$ m/min, $f = 0.11$ mm/rev, doc $= 0.1$ mm, $T = 30$ °C, **b** ($v = 50$ m/min, $f = 0.11$ mm/rev doc $= 0.1$ mm, $T = 600$ °C

Table 6 S/N ratios of cutting force

S NO	Cutting speed (m/min)	Feed rate (mm/rev)	Depth of cut (mm)	Preheating Temp. (°C)	S/N ratio
1	50	0.11	0.1	30	−38.2232
2	50	0.13	0.3	300	−44.4751
3	50	0.16	0.5	600	−46.4485
4	100	0.11	0.3	600	−44.2704
5	100	0.13	0.5	30	−47.9657
6	100	0.16	0.1	300	−43.0519
7	150	0.11	0.5	300	−49.7879
8	150	0.13	0.1	600	−40.7803
9	150	0.16	0.3	30	−52.3986

Signal-to-ratio (S/N) ratios listed in Table 6 are obtained according to smaller is better approach using Minitab 17. The main effects plot is also obtained for S/N ratios to determine the optimum parameter combination and is shown in Fig. 4. From the main effect plot, it is clear that the optimum combination is at $v = 50$ m/min, $f = 0.11$ mm/rev, doc $= 0.1$ mm, and preheating temperature of 600 °C. Finally, simulation test is performed at optimum combination and the cutting force value obtained is 59.5 N which is reduced compared to all the simulation tests, and therefore, it is clear that the preheating temperature is influencing in reducing the cutting force. It is also compared with experimental results which are obtained in our previous work showing satisfactory at preheating temperature compared to room temperature condition [16].

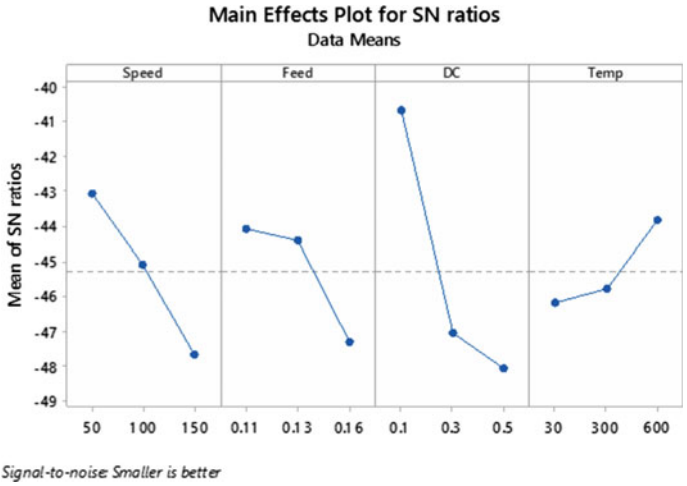

Fig. 4 Main effects plot for S/N ratio

Table 7 Response table for S/N ratio

Level	Cutting speed	Feed rate	DOC	Temp
1	−43.05	−44.09	−40.69	−46.20
2	−45.10	−44.41	−47.05	−45.77
3	−47.66	−47.30	−48.07	−43.83
Delta	4.61	3.21	7.38	2.36
Rank	2	3	1	4

The responses of S/N ratios are presented in Table 7, which shows that the doc has a great influence on cutting forces followed by speed, feed, and temperature. However, the optimum result is obtained at preheating temperature (600 °C) than at room temperature.

4 Conclusions

From the simulation runs of heat-assisted machining of Inconel 718 alloy at different combinations of parameters using Abaqus/Explicit, the following conclusions are drawn:

- The optimum levels of parameters obtained using S/N ratio technique are speed of 50 m/min, feed of 0.11 mm/rev, depth of cut of 0.1 mm, and preheating temperature of 600 °C.
- It is confirmed by performing simulation at the optimum cutting conditions, in which cutting force got reduced and also compared with previous experimental results which are showing satisfactory results in FEM.
- From the S/N ratio response table, it is concluded that depth of cut is more influencing factor on cutting force followed by speed, feed, and preheating temperature.
- It is observed that the cutting force got reduced at preheating condition and also it improves machining performance for materials which are difficult to cut.

References

1. Asit Kumar, P., Maity, K.: Effect of nose radius on forces, and process parameters in hot machining of Inconel 718 using finite element analysis. Eng. Sci. Technol. Int. J. **20**(2017), 687–693 (2016)
2. Ozel, T., Zeren, E.: Finite element modeling the influence of edge roundness on the stress and temperature fields induced by highspeed machining. Int. J. Adv. Manuf. Technol. 255–267 (2006)
3. Ali, Moaz H., Khidhir, Basim A., Ansari, M.N.M., Mohamed, Bashir: FEM to predict the effect of feed rate on surface roughness with cutting force during face milling of titanium alloy. HBRC J. **2013**(9), 263–269 (2013)
4. Diaz-Alvarez, J., Cantero, J.L., Miguelez, H., Soldani, X.: Numerical analysis of thermo mechanical phenomena influencing tool wear in finishing turning of Inconel 718. Int. J. Mech. Sci. **82**, 161–169 (2014)
5. Muthu, E., Senthamarai, K., Jayabal, S.: Finite element simulation in machining of Inconel 718 nickel based super alloy. Int. J. Adv. Eng. Appl. **5**(3), 22–27 (2012)
6. Kumar, B.V.R.M., Reddy, K.H., Kumar, C.R.V.: Finite element model based on abaqus/ explicit to analyze the temperature effects of turning. Int. J. Appl. Eng. Res. ISSN 0973-4562, **11**, 5728–5734, November 8(2016)
7. Abhushawashi, Y., Xiao, X., Astakhov, V.P.: FEM simulation of metal cutting using a new approach to model chip formation. Int. J. Adv. Mach. Form. Oper. **3**, 71–92 (2011)
8. Ng, E.-G., Tahany, I.E.W., Dumitrescu, M., Elbastawi, M.A.: Physics-based simulation of high speed machining. Mach. Sci. Technol. **6**(3), 301–329 (2002)
9. Guo, Y.B., Yen, D.W.: A FEM study on mechanisms of discontinuous chip formation in hard turning. J. Mater. Process. Technol. **155–156**, 1350–1356 (2004)
10. Jeevannavar, A., Hussain, R.: process modeling, simulation and experimental validation for prediction of chip morphology during high speed machining of Al 2024-T3. SAS TECH J. **13**(1), April 2014
11. Miguelez, M.H., Zaera, R., Molinari, A., Cheriguene, R., Rusinek, A.: Residual stresses in orthogonal cutting of metals: the effect of thermo mechanical coupling parameters and of friction. J. Therm. Stresses **32**(3), 269–289 (2009)
12. Nasar, M., Ng, E.G., Elbestawi, M.A.: Modeling the effects of tool-edge radius on residual stresses when orthogonal cutting AISI316L. Int. J. Mach. Tools Manuf. **47**, 401–411 (2007)
13. Woon, K.S., Rahman, M.: The effect of tool edge radius on the chip formation behavior of tool-based micromachining. Int. J. Adv. Manuf. Technol. **50**(9), 961–977 (2010)
14. Parida, A.K.: Analysis of chip geometry in hot machining of Inconel 718 alloy. Ranian J. Sci. Technol. Trans. Mech. Eng. 2228–6187 (2018)
15. Grzesik, W., Nieslony, P., Bartoszuk, M.: Finite element modeling of temperature distribution in the cutting zone in turning processes with differently coated tool. J. Mater. Process. Technol. **164–165**, 1204–1211 (2005)
16. Rehaman, S., Venkataramaih, P., Kiran Kumar, A.: Optimization of process parameters in heat assisted turning of Inconel 718 by WASPAS method and simulation using ABAQUS software. Int. J. Emerg. Technol. Adv. Eng. **7**, 2250–2459 (2017)

Design and Analysis of 3-DOF Spatial Serial Manipulator for Warehouse Applications

Sumit Govind Kanpartiwar, Ravi Kumar Mandava and Pandu R. Vundavilli

Abstract This paper presents a robotic solution for the labor-intensive and time-consuming task of order picking operation carried out in the warehouse of e-commerce industries. The novel design of manipulator which will be mounted on a mobile robotic platform is proposed. A 3-DOF spatial serial manipulator is designed for the said task. Furthermore, the structural analysis and optimization of all the links of the designed manipulator are done by using finite element analysis. Finally, the payload carrying capacity of the proposed manipulator is determined.

Keywords 3-DOF spatial manipulator · Structural analysis · Finite element method

1 Introduction

Robots are being used for various industrial applications like welding, painting, and pick and place operations since 1961. The typical pick and place robots are the devices used to perform repetitive tasks in the industrial and other scenarios. Development in the sensor technology and implementation of artificial intelligence marked the beginning of the third generation of robots. Applications of such robots can be seen in different sectors like health care, household works, and service industries [1]. With the ever-increasing growth of sales volume of e-commerce businesses in the past decade [2] (that is, Amazon, Flipkart, etc.), the expectations of the customer in modern logistic have changed significantly [3]. Warehouse plays an important role in the supply chain of these businesses. Out of various activities carried out in a warehouse, order picking, i.e., retrieving the products from storage in response to

S. G. Kanpartiwar (✉) · P. R. Vundavilli
School of Mechanical Sciences, Indian Institute of Technology, Bhubaneswar, Odisha 752050, India
e-mail: sgk11@iitbbs.ac.in

R. K. Mandava
Department of Mech. Engineering, Vignan's Foundation for Science, Technology & Research, Guntur 522213, India

L. Li et al. (eds.), *Advances in Materials and Manufacturing Engineering*, Lecture Notes in Mechanical Engineering, https://doi.org/10.1007/978-981-15-1307-7_19

customer's requirement is the most critical one [4]. The labor-intensive and time-consuming task of order picking could be automated by using mobile robots to improve the efficiency and save operation costs for e-commerce businesses. Amazon robotics formerly known as Kiva systems had deployed robots for order picking solution in the warehouse. The robot moves the shelving unit from a storage location to pick station, and then the ordered items present in the shelves will be picked by human labor and the shelving unit will return to its storage location. These robots can work continuously and more efficiently than human labors [5]. Liang et al. [6] developed an automatic pick and place system which pick the items at pick station thereby eliminating the human intervention to make the process fully automatic. However, instead of moving shelving unit and then retrieving the items at picking station by a robotic manipulator, robotic manipulator could also be moved to the stationary shelves by mounting it on a mobile robotic platform which will have a box connected to it for collecting the items from shelves.

This paper presents the mechanical design, structural analysis, and optimization of novel 3-DOF spatial serial manipulator which is designed to mount on the robotic research platform [7]. Section 2 explains the robot configuration, material selection, CAD (that is, Solidworks) design, analysis, and optimization using CAE (that is, Ansys) carried out for each link of the manipulator. In Sect. 3, results of the proposed design are discussed, and in Sect. 4, conclusions are drawn.

2 Mechanical Design of Manipulator

2.1 Robot Configuration

In the absence of manipulators, the job of picking and placing items in the shelf is done efficiently by the human operators. To perform the said task by the manipulator, the sizes of the links of the manipulator are decided by taking the ratio of lengths of upper limb parts of human hand [8] (ref. Table 1). The joint axes are designed such that the manipulator will be able to pick the object from rack shelf (ref. Fig. 1) and place it in the box connected to the robotic research platform (ref. Fig. 2). The link lengths of the serial manipulator are decided such that its end effector reaches the object placed on the rack shelf in at least one possible configuration (ref. Fig. 3).

Table 1 Parameters of links of the robot

	$L1$ (upper arm)	$L2$ (forearm)	$L3$ (hand)
Ratio	1.2	1.25	0.75
Link lengths	192	200	123

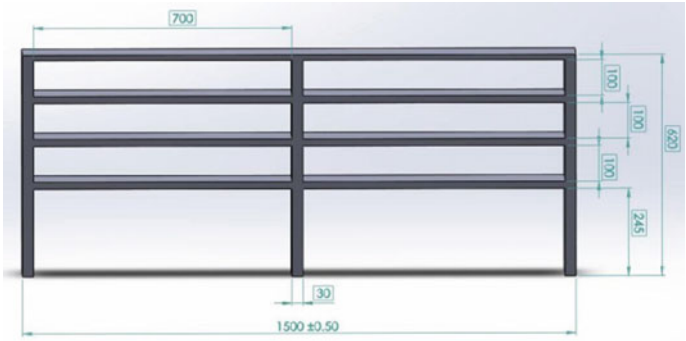

Fig. 1 Schematic diagram showing the rack structure

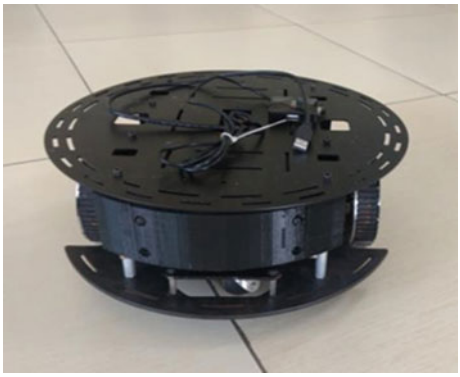

Fig. 2 Mobile robotic platform [7]

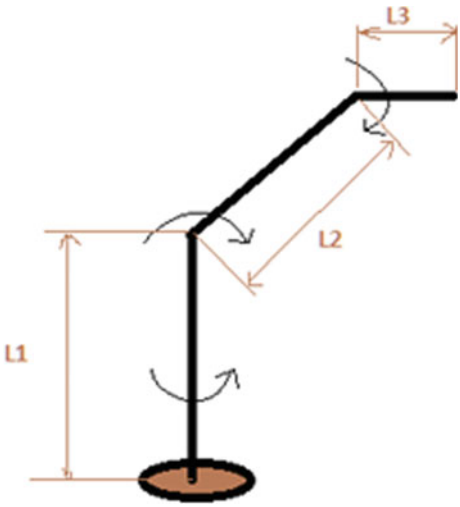

Fig. 3 Diagram showing the robot configuration

Table 2 Mechanical properties of PLA

Sr. no	Property	Value	Units
1	Density	1.25	g/cm^3
2	Elastic modulus	3500	MPa
3	Shear modulus	1287	MPa
4	Poisson's ratio	0.36	–
5	Yield strength	70	MPa
6	Elongation	7	%
7	Ultimate tensile strength	73	MPa

2.2 Material Selection

The links of the manipulator are to be stiff and light in weight to achieve better performance for the manipulator's arm and mobile robotic platform that carry the whole assembly during navigation in the warehouse. So, the material of links must have a high strength to weight ratio and low density. High-strength polymer materials are best suited for such application as it also gives ease in manufacturing of links by using rapid prototyping (RPT) methodology. By comparing mechanical properties of different polymer materials, polylactic acid (PLA) is selected as link material. Polylactic acid is the most extensively researched and utilized biodegradable aliphatic polyester [9]. The mechanical properties of PLA are shown in Table 2.

2.3 Design of the Manipulator Structure

The links of the manipulator are designed in such a way that it should accommodate actuator and controller within it by considering the configuration of the robot. Therefore, the diameter of each link is kept large enough, which also give stiffness and strength to the structure of the manipulator due to increase in the area and polar moment of inertia of each link [10]. The links with proper dimensions are designed in SOLIDWORKS 16 to have an appearance like a human arm. After several iterations concerning the dimensions of the actuator, controller and electronics wiring each link is designed. Forearm link is made out of two parts due to the constraint of space in the 3D-printing machine ($20 \times 20 \times 20$ cm). The final assembly, configuration, and dimensions of the links are given in Figs. 4, 5, and Table 3, respectively.

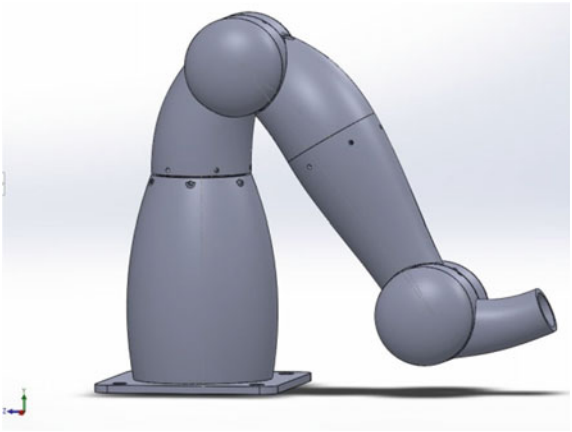

Fig. 4 Schematic diagram showing the final assembly of the spatial serial manipulator

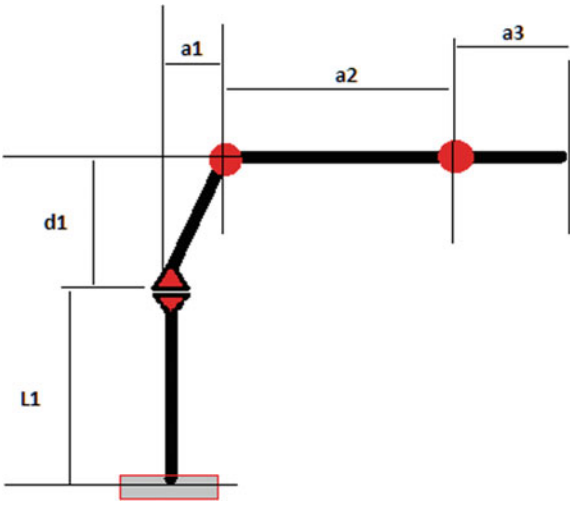

Fig. 5 Line diagram showing the final robot configuration

Table 3 Dimensions of links of the robot

Dimension	Length (mm)
L1	138
d1	70
a1	27
a2	201
a3	103

2.4 Analysis and Optimization of Links

To check whether the designed links can withstand the maximum loads and moments acting on it, structural analysis of each link is carried out in ANSYS 16. The loads and moments applied on the links are calculated by considering the configuration of the robot. The payload capacity of 3 kg along with gravity terms are considered here. Optimization of the link weight is done by varying wall thickness of links for maximum loads and moment acting on it. The screenshots of stress analysis for first, second, third part 1, third part 2, and fourth link are shown in Fig. 6a–e, respectively.

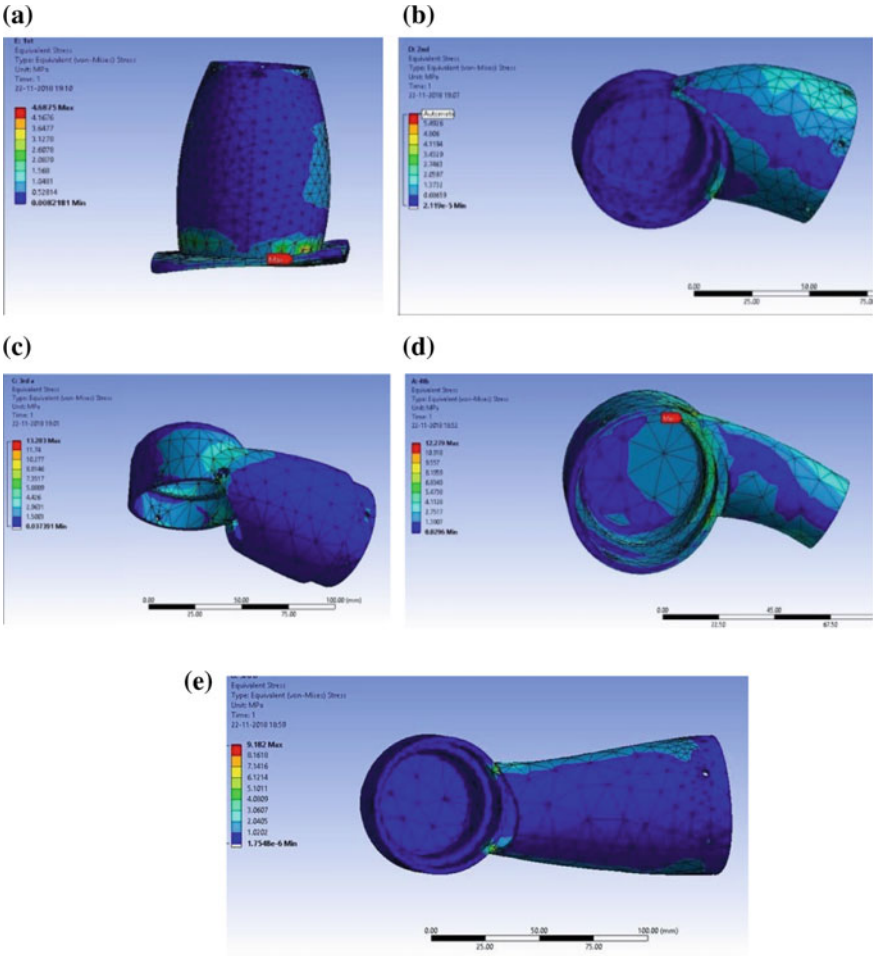

Fig. 6 Schematic diagram showing the screenshots of stress analysis of various links of the manipulator **a** link 1, **b** link 2, **c** link 3 part1, **e** link 3 part 2, and **d** link 4

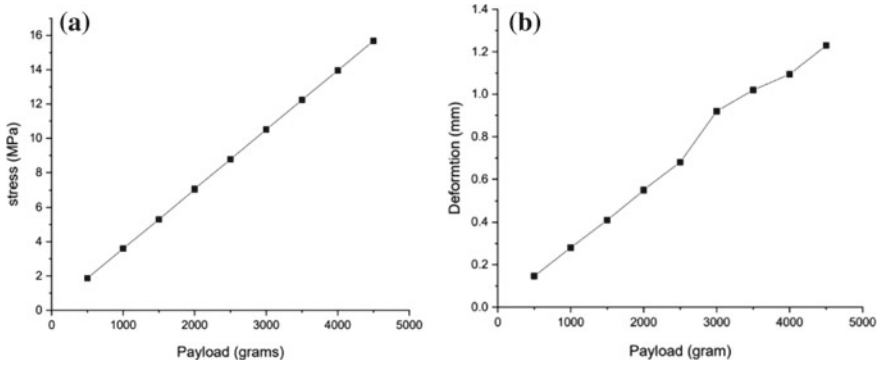

Fig. 7 Analysis of link 4 for various payloads, **a** stress vs payload and **b** deformation vs payload

Table 4 Loads, moments, stresses, and deformation of various links of the manipulator

Link	M (Nmm)	P (N)	Max. stress (σmax)	Deformation (mm)
1	11,048	46.17	4.68	0.353
2	11,048	40.08	6.18	0.082
3 part 1	9983.7	35.48	13.20	0.414
3 part 2	8664	34.46	9.18	0.128
4	3068.2	30.02	12.28	0.952

3 Result and Discussion

A MATLAB code is generated to get the maximum load and moments acting on each link that corresponds to various payloads. The analysis is carried out by applying this load and moment to the links in ANSYS 16. The graphs showing the variation of stresses and deformation with the increase in the payload are shown in Fig. 7a and b, respectively. When the payload is increased beyond 3 kg, the deformation in link 4 is seen to be exceeding 1 mm (ref. to Fig. 7b), which is not allowed to retain the position accuracy of the end effector of the manipulator. Similarly, Table 4 shows the loads and moments acting on various links and the maximum stresses and deformation generated due to it when the payload of 3 kg is applied at the end effector.

4 Conclusions

After thorough research on the warehouse of e-commerce companies, the critical activity of order picking is identified. Various solutions present for improving the performance of this activity have been reviewed, and it is found that the efficiency and time taken can be improved by automating the task of order picking. A robotic

system for this problem is proposed. A novel design of manipulator which will be mounted on the mobile robotic platform is introduced. Modeling of the manipulator is done in SOLIDWORKS 16.0, and analysis and optimization are done by using ANSYS 16.0. It is observed that the designed manipulator is capable of handling 3 kg payload after maintaining its positional accuracy.

References

1. Kore, Y.: Robotics for Engineers. Technon Israel Institute of technology, McGraw-Hill. 168 (1985)
2. Statista (2017). Annual retail e-commerce sales growth worldwide from 2014 to 2020. https://www.statista.com/statistics/288487/forecast-of-global-b2c-e-commerce-growt, last accessed 2018/12/28
3. Manzini, R., Bozer, Y., Heragu, S.: Decision models for the design, optimization and management of warehousing and material handling systems. Int. J. Production Economics **170**, 711–716 (2015)
4. Koster, D., Rene, Le-Duc. T., Roodbergen, K.J.: Design and control of warehouse order picking: A literature review. Eur. J. Oper. Res. **182**(2), 481–501 (2007)
5. Guizzo, E.: Three engineers, hundreds of robots, one warehouse. IEEE Spectr. **45**(7), 26–34 (2008)
6. Liang, C., Chee, K.J., Zou, Y., Zhu, H., Causo, A., Vidas, S., Teng, T., Chen, I.M., Low, K.H., Cheah, C.C.: Automated robot picking system for e-commerce fulfilment warehouse application. In: 14th World Congress in Mechanism and Machine Science, International Federation for the Promotion of Mechanism And Machine Science, Taipei, Taiwan 2015
7. Nugenix, RABBIT differential wheeled mobile robotic platform, http://www.nugenix.co.in/Indoor-Mobile-Robotlast, Accessed 2018/12/29
8. Wang, N., Ma, J., Jin, D., Yu1, B.: A special golden curve in human upper limb's length proportion: a functional partition which is different from anatomy. BioMed Res. Int. 2017, (2017)
9. Farah, S., Anderson, D.G., Langer, R.: Physical and mechanical properties of PLA, and their functions in widespread applications—a comprehensive review. Adv. Drug Deliv. Rev. **107**, 367–392 (2016)
10. Abdel-Malek, K., Paul, B.: Criteria for the design of manipulator's arms for a high stiffness-to-weight ratio. J. Manuf. Syst. **17**(3), 209–220 (1998)

Experimental Investigation on Mechanical Properties of Carbon/Bamboo/Epoxy Hybrid Laminated Composites

Y. S. Rao, B. Manikantesh, P. Sudheer Kumar and A. Yugandhar

Abstract The Composite materials have become a high versatile material due to its excellent physical and mechanical properties. Synthetic fibres are made from organic synthetic high molecular compounds and are made synthetically from raw materials such as petroleum oil. Through synthetic fibres are having remarkable properties over a last few years, natural fibres are gaining attention as viable alternative to synthetic fibres as they are biodegradable. The present work deals with the investigation of mechanical properties of carbon/bamboo/epoxy hybrid laminated composites. The laminates were prepared by hand lay-up method and compressed using compression molding machine at 70 °C and 80 bar pressure. The laminates were prepared in four different orientations from using carbon and bamboo fibres. An experimental study was carried out to determine the mechanical properties. The mechanical properties such as Ultimate Tensile Strength, Flexural Strength and Impact Strength and Hardness were determined. These mechanical properties were determined by conducting tensile test, flexural test, impact test and Rockwell hardness test. The test results obtained through experimentation has been compared with the results of simulation which is done in ABAQUS 6.14 software.

Keywords Carbon fibre · Bamboo fibre · Tensile · Flexural · Impact · And hardness

1 Introduction

Composite materials are combination of two or more materials in such a way we can distinguish separate material phase after manufacturing. They are extremely versatile materials and have found its use starting from aerospace industry to common everyday applications. Fibre reinforced composite materials are widely used because of their high strength to weight ratio and stiffness to weight ratios as compared with many traditional materials. To tell further, the cost of the fibre reinforced composites materials has decreased over the years. This is due to the increased manufacturing

Y. S. Rao (✉) · B. Manikantesh · P. Sudheer Kumar · A. Yugandhar
QIS College of Engineering and Technology, Ongole, AP, India
e-mail: raoseshuy2@gmail.com

L. Li et al. (eds.), *Advances in Materials and Manufacturing Engineering*, Lecture Notes in Mechanical Engineering, https://doi.org/10.1007/978-981-15-1307-7_20

experience accumulated over the years and more effective manufacturing technologies for mass production. Symmetric laminates have a stacking sequence of piles in a composite lay-up which above the laminates midplane is a mirror image of the stacking sequence below the midplane. Advantages of these laminates are that stay flat when in plane loads and also during hot curing are applied.

A hybrid composite is a Fibre Reinforced Polymer (FRP) composite which has more than one fibre as a reinforcement phase embedded into a single matrix phase. Hybridization provides the designers with added degree of freedom in manufacturing composites to achieve high specific stiffness, high specific strength, enhanced dimensional stability, energy absorption, increased failure strain, corrosive resistance as well as reduced cost during fabrication. Composites made of a single reinforcing material system not be suitable if it undergoes different loading conditions during the service life. Hybrid composites may be the best solution for such application.

2 Literature Survey and Review

T D Jagannatha et al. [1] studied the mechanical properties of carbon and glass fibre reinforced epoxy hybrid composite materials. The vacuum bag method is use to fabricate the hybrid composite materials. The mechanical properties such as tensile strength, impact strength, hardness and flexural strength of the hybrid composite materials were evaluate as per ASTM standard. The mechanical properties were improved such as the fibre reinforcement content improved in the matrix laminates. The composition of reinforcement weight percentage of 15, 30, 45, 60% of glass fibre and carbon fibre in 40% epoxy matrix.

Subhankar Biswas et al. [2] studied on investigation of physical, thermal and mechanical properties of jute and bamboo fibre reinforced with epoxy resin. The fabrication are carried out by vacuum bag method. To evaluate the surface morphology, scanning electron microscope analysis, tensile strength, flexural and thermal behaviour as per ASTM standard. Unidirectional orientation are used in a bamboo composite fabrication. The composition of reinforcement weight ratio is 57% of bamboo fibre and 43% of epoxy resin for one specimen and 52% of jute fibre and 42% of epoxy resin for other specimen.

P Tostra et al. [3, 4], has studied the mechanical and electrical properties of carbon fibres reinforced in epoxy resin. The centrifugal casting is used to uniform distribution carbon fibre in epoxy resin matrix. The sample are made of three different sizes pitch based carbon fibre, short carbon fibre and long carbon fibre. To evaluation of flexural strength, flexural modulus and electrical conductivity of carbon fibre reinforced epoxycomposite. Comparing to carbon fibre composite mechanical and electrical properties better than the short and long carbon composite. Meenambika, G.B et al. [5], Zhang, et al. [6], Ramachandran M et al. [7], Anigol et al. [8] studied on mechanical and chemical properties of bamboo/glass fibers reinforced polyester

hybrid composites, structural applications in automotive vehicles, analysis of bamboo fibre composite with polyester and epoxy resin and effect of various fillers on mechanical properties of carbon-epoxy composites respectively.

3 Problem Formulation

Over the last thirty years composite materials, plastics and ceramics have been the dominant emerging materials. The volume and number of applications of composite materials have grown steadily, penetrating and conquering new markets relentlessly. Modern composite materials constitute a significant proportion of the engineered materials market ranging from everyday products to sophisticated niche applications. While composites have already proven their worth as weight-saving materials, the current challenge is to make them cost effective. The efforts to produce economically attractive composite components have resulted in several innovative manufacturing techniques currently being used in the composites industry. It is obvious, especially for composites, that the improvement in manufacturing technology alone is not enough to overcome the cost hurdle. It is essential that there be an integrated effort in design, material, process, tooling, quality assurance, manufacturing, and even program management for composites to become competitive with metals.

3.1 Problem Statement and Objectives

The main focus of the work is to provide a feasible alternative to use traditional material in the automotive application by selecting a suitable proportionality of natural reinforced fibres along with synthetic fibres. The research on bamboo fibre composites are increasing day by day since it has good tensile strength and ductility compared to other natural fibres. This project work is aiming to make a new set of hybrid composites with carbon and bamboo fibres as the reinforcing material using hand lay-up technique and different orientation of the bamboo and carbon fibres. To find the changes in tensile, flexural, impact and hardness properties of the hybrid composites with different orientation of the fibres are need to be compared so as to use in automobile body building and steering wheel.

The main objectives of the research are as follows

To prepare the laminates for tensile, flexural, hardness and impact test as per ASTM standards. To conduct the above mentioned tests on the prepared laminates.
To study the effects of various failure modes with respect to its mechanical properties
To evaluate the mechanical properties using ABAQUS 6.14 software.
To compare the experimental values with that of the simulated values.

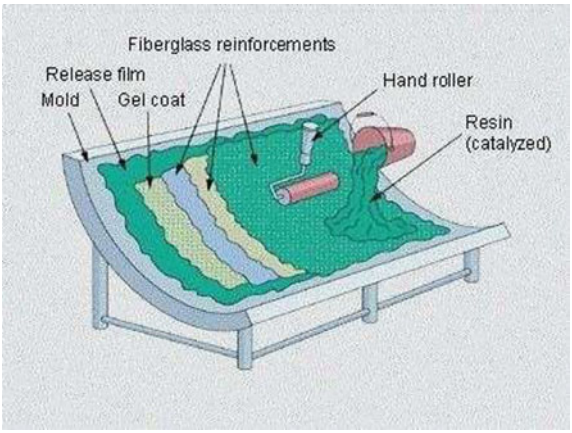

Fig. 1 A hand lay-up method

4 Fabrication of Composite

4.1 Fabrication of Test Specimen Hand Lay-Up Technique

Hand lay-up Technique is one of the most easiest and economic fabrication technique. After cleaning the mould surface thoroughly a releasing layer should be applied on the top and bottom die surface for easy removal of the composite from the die. Wait for some time so that the removing layer get dried. Prepare the reinforcement fibres in short length or long length according to the application. The reinforcement is laid on the mould as a layer using hands and above that the matrix material is being applied. The matrix material should be prepared with proper mixing of hardener in it with the given proportion (Fig. 1).

For thin laminates, Electron beam Curing has incorporated, Here the electron beams are allowed to pass through the composites, once it strikes the matrix, it speedup up the polymerization of the matrix and the cross linking. The matrix materials should be sensitive to the E-beam for this to happen.

4.2 Basic Raw Materials Matrix Material

Epoxy(Lapox L-12) Lapox L-12 (Diglycidyl Ether Bisphenol) is a commonly used polymer resin for the research purposes. The resin has a medium viscosity and various types of resin can be added with it to make different types of polymers according to the need. The choice of hardener depends upon the application to which the final product is meant for, the processing method, and the final properties required for the composites. It has a density of 1120 gm/cm^3.

Fig. 2 Carbon fibre

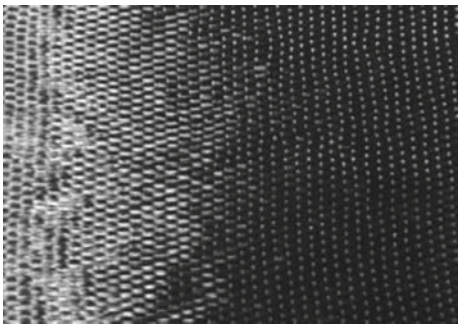

Hardener K-6 Hardener K-6 (Tryethylel Tetramine) is a common type of hardener which is to be used with Lapox L-12. It is of low viscosity and curing will takes place at the room temperature. These products are commonly used in the production of composites as well as the civil engineering applications where fast curing is needed. It has a density of 954 gm/cm^3.

4.3 Reinforcing Material Carbon Fibre

It is material involving of fibres round 5–10 m in thickness then collected generally of carbon molecules. The carbon molecules remain fused composed now crystals that additional or less ranged similar toward elongated axis of the fibre (Fig. 2).

The crystal arrangement provides fibre high strength to volume ratio. Some thousand carbon fibres are twisted composed toward practise yarn, which might remain recycled through itself or woven into a fabric. The properties of carbon fibres, such as high flexibility, high tensile strength, low weight, high resistance, high temperature tolerance and low thermal expansion, make them very popular in aerospace, civil engineering, military and motor sports, along with other competition sports.

4.4 Preparation of Laminates

The procedures of preparing laminate using hand lay-up method are as following:

Initially place a mould box as an opening mould, the mould surface is covered with Teflon sheet over it (used to prevent sticking of laminate to the mould). Apply a thin layer of wax polish over the Teflon sheet, which will act as releasing agent. Then a layer of matrix material (resin) is applied using brush, which is a combination of epoxy (L-12) and hardener (K-6) mixed with in the weight ratio 10:1. Place a layer of fibre at required ply angle and dimension, and then roll over it with suitable roller to uniformly distribute and sweep out the excess resin, also to remove air bubbles

Fig. 3 Laminate preparation

and voids. Wet the fibre by coating sufficient resin and repeat above procedure as required to finish the laminate. Allow the laminate to cure in atmospheric condition for four hours (Fig. 3).

Finally the laminate is compressed, using compression moulding machine at a pressure of 70 kg/cm^2 and temperature of 100 °C for 30 min. This procedure is called post curing, where the heat is applied to consolidate and densify separate plies into a solid laminate while the pressure is required to consolidate individual layers into a laminate. The laminate preparation method is shown in Fig. 4. The hydraulic compression moulding machine, which is used in this work could be controlled automatically or manually. Figure 5 shows the compression moulding machine along with its setting.

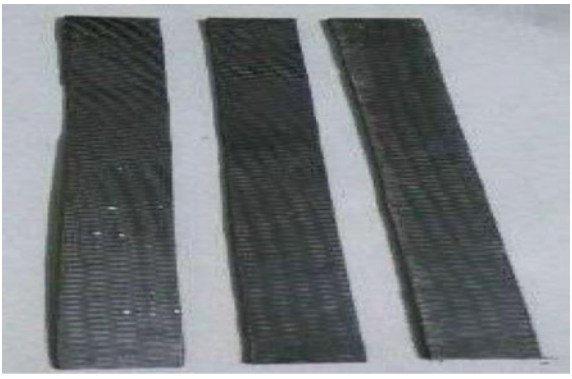

Fig. 4 Tensile specimens before testing

Fig. 5 Tensile specimens after testing

5 Experimental Test

5.1 Tensile Test

Tensile test is a fundamental test in the field of mechanical engineering. The test is mainly carried out to obtain the tensile properties and characteristics of the material. The test is carrying out in such a manner that the prepared piece is allowed to pull in between the jaws of a Universal Testing Machine so that the complete tensile prole of the material will obtain. The test is relatively very simple, low cost and fully standardized. When the specimen is getting pulled it get deformed and there will be a considerable reduction in the cross-sectional area of the specimen. When the material is failed by continuing the pulling, final complete tensile prole will be obtained with ultimate tensile strength which is calculated with the gross cross sectional area. The obtained graph will show how the deformation and finally the breakage will happen according to the applied load on the specimen.

5.2 Tensile Test Specimens

The laminates were prepared from the fibres as per ASTM standards. For tensile test ASTM D3039 standard is used. The tensile test is conducted to determine the Ultimate Tensile Strength, Young's Modulus, Strain and Toughness increase with increase in strain rate. The laminates were prepared from single fibre and hybrid fibres. Five specimens were cut from laminate. The laminates were prepared in 0° and random orientation. The tensile test is performed in computerized Universal Testing Machine (Fig 6).

The laminates were prepared as per the above orientation and stacking order and prepared by hand lay-up method as shown above. The proportion of resin and

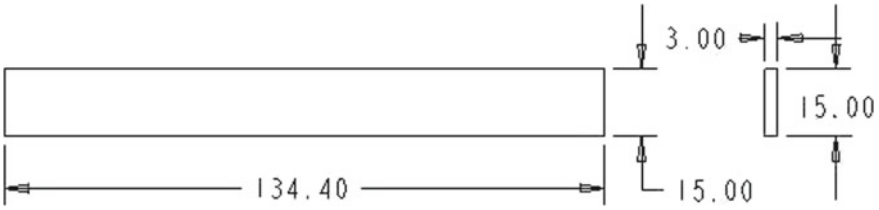

Fig. 6 Flexural test specimen dimensions

Table 1 Properties of Lapox L-12

Glass transition temperature (*Tg*)	120–130 °C
Tensile strength	85 MPa
Tensile modulus	10500 MPa
Elongation at break	0.80%
Flexural strength	112 Mpa
Flexural modulus	10,000 MPa
Compressive strength	190 Mpa
Coefficient of linear thermal expansion	43 e6
Water absorption-24 h at 23 °C	5–10 mg

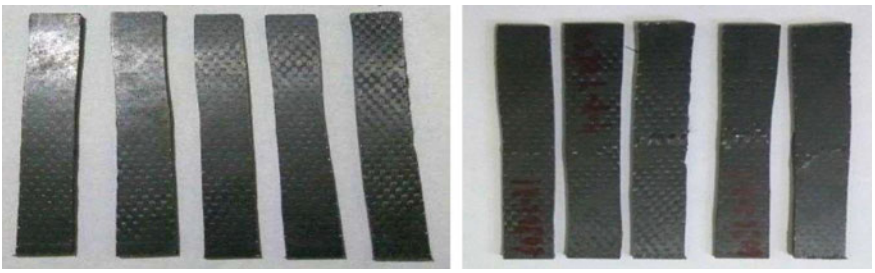

Fig. 7 Bending specimens before and after testing

hardener are taken with respect to fibre weight. The details of the weight proportion are given in Table 1. The tensile test specimens are shown in Fig. 7 (Figs. 8, 9).

5.3 Tensile Test Calculation

The formula for Ultimate Tensile Strength is given by

$$T = \frac{p}{b \times d} \tag{1}$$

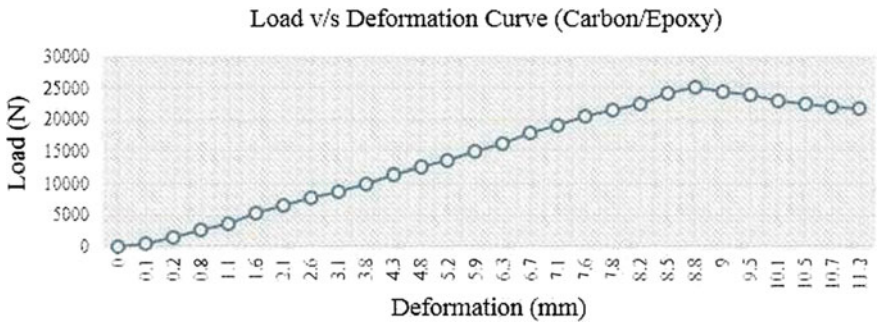

Fig. 8 Load versus deformation plot for carbon/epoxy specimen

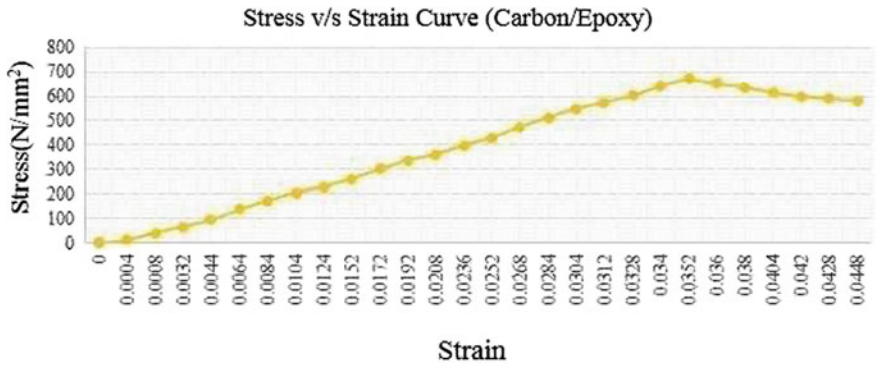

Fig. 9 Stress versus Strain plot for carbon/epoxy specimen 1

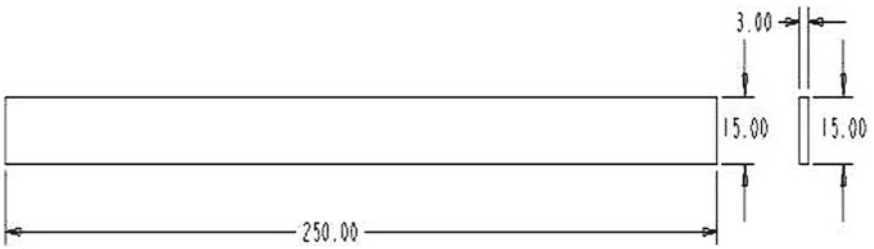

where

$T =$ Ultimate tensile strength in N/mm 2 $P =$ Maximum load in N
$b =$ Width of the specimen in mm
$d =$ Thickness of the specimen in mm

The formula for modulus of elasticity (E) is given by

$$E = \frac{p}{L} \times \frac{1}{b \times d}$$

where

E Young's modulus
P/L Slope of the load as a function deformation
L Length of measuring instrument in mm

5.4 Tensile Test Parameters

- Pre load: Not applicable
- Feed rate: 0.5 mm/min
- Gauge length: 172 mm
- Width of the specimen: 25 mm
- Thickness of the specimen: 3 mm.

5.5 Flexural Test Specimens

The laminates were prepared from the fibres as per ASTM standards. For the flexural test ASTM 790-7 is adopted. A flexural test produces tensile stress in the convex side of the specimen and compression stress in the concave side. This creates an area of shear stress along the midline. To ensure the primary failure comes from tensile or compression stress the shear stress must be minimized. This done by controlling the span to thickness (t) of the specimen. For most material $L/t = 16$ is acceptable. Some materials require $L/t = 32$–64 to keep the shear stress low enough. Here L/t ratio is taken as 32:1. The dimensions of the flexural test specimens are shown in Fig. 6. The span length (L) is 134.4 mm, the width (w) and the thickness (t) are 15 and 3 mm respectively. There are two types of flexural tests. They are

1. 3-point Flexural Test
2. 4-point Flexural Test

The laminate were prepared in the following orientation from carbon and bamboo fibres.

1. Laminate-1 = [C0/B/C0/B/C90/B]s
2. Laminate-2 = [C0/C0/B/C45/C90/B]

The laminates were prepared as per the above orientation and stacking order and prepared by hand lay-up method as shown above. The proportion of resin and hardener are taken with respect to fibre weight. The details of the weight proportion are given in Table 2. The flexural test specimens are shown in Fig. 7.

Table 2 Properties of carbon fibre

Tensile strength	3870 Mpa
Tensile modulus	210 GPa
Elongation of break	1.5%
Thick ness	0.35 mm
Area density	270 g/m^2
Direction of fibre	Unidirectional

5.6 Flexural Test Calculations

The minimum deformation of the fibres occur at the top end portion of the specimen and a large deformation and strain occur in the outer fibre at the midspan which is calculated by the below equation,

Equation for stress is given by the formula

$$\varepsilon = \frac{6\delta h}{L^2}$$

$$\sigma = \frac{3pL}{2bh^2}$$

where

ε Strain
δ Deflection
h Thickness
b Breadth
P Maximumload
L Gaugelength

6 Results and Analysis

Tensile stress versus strain and load versus deformation data's of the specimens of different fibre length are given below. The strength of the fibres and the bonding strength between the fibre and the matrix are account for the tensile properties of the specimen. The ultimate point in figure represent the complete fracture of the specimen after which the graph line is happened to be decreased which shows the progressive failure of the specimen with increase in the load and finally complete failure will takes place with fracture of the specimen and fibre pull out. Stress versus Strain and Load versus Deformation for each fibre length are given below with plot and modulus of elasticity also mentioned separately.

Table 3 Tensile properties of carbon fibre/epoxy specimen specimen No: Tensile

Stress (MPa)	Young's modulus (GPa)	
Specimen 1	672	190.0
Specimen 2	671.33	190.07
Specimen 3	672.26	190.09

6.1 Tensile Properties of Carbon Fibre/Epoxy Specimen

Table shows the tensile properties of Carbon fibre/epoxy specimen in which average stress obtained is 671.86 MPa with a Young's Modulus of 19.08 GPa for specimens (Table 3).

7 Conclusion

In this study, the mechanical properties such as Ultimate Tensile Strength, Flexural Strength, Impact Strength and hardness of the carbon/bamboo epoxy hybrid laminates were investigated. The main aspect examined here is the effect of mechanical properties after addition of bamboo fibre to the layer of carbon fibres.

The conclusion based on the experimental and software evaluation of the work are listed below:

Tensile strength was determined on the specimens prepared as per the standard ASTM D 3039 and the obtained tensile strength and young's modulus value of the Carbon/Epoxy laminate respectively is 96.03 and 89.58% higher than that of the Bamboo/Epoxy laminate.

1. Flexural strength was determined by conducting three point bending test on the prepared specimens which was prepared as per the standard ASTM D790-07. The flexural strength of Laminate-2 specimen has 12 layered laminate which has two layers of carbon fibre in the outer region and another one layer of bamboo fibre in the inner region (remaining layers are respectively) is 90.22% higher than that of the Laminate-4 specimen which has first and fifth layer bamboo fibre and remaining layers are carbon fibre.
2. Impact strength was measured according to the standard ASTM E23-07a. The impact strength of Laminate-1 specimen has 12 layered laminate which has one layer carbon fibre in the outer region and another one layer bamboo fibre in the inner region (remaining layers are respectively) is 64.47% higher than that of the Laminate-4 specimen which has first and fifth layer bamboo fibre and remaining layers are carbon fibre.
3. Hardness was measured according to the standard ASTM D 785. The Rockwell hardness of Laminate-2 specimen has 12 layered laminate which two layers of carbon fiber at its outer layers was higher when compared with that of the other three laminates.

8 Scope for Future Work

- Specimens can be prepared as mat type instead of random orientation of the bamboo fibres reinforced with carbon fibre and epoxy resin, so as to check whether there is any increase in the strength of the composite.
- Specimens can be tested in order to study the micro structure by SEM, EDS, TEM, XRD etc.

References

1. Jagannatha, T.D., Harish, G.: Mechanical properties of carbon/glass fibre reinforced epoxy hybrid polymer composites. Intern. J. Mech. Eng. Robot. Res. **4**(2), 131–137 (2015)
2. Biswasa, S., Shahinura, S., Hasana, M., Ahsan, Q.: Physical, mechanical and thermal properties of jute and bamboo fibre reinforced unidirectional epoxy composites. Procedia Eng. **105**, 933–939 (2015)
3. Saravanan, K.S., Vetrivel, R.: Experimental analysis of carbon/glass fiber reinforced epoxy hybrid composites with different carbon/glass fiber ratios. *Int. J. Innov. Res. Sci.* **5**(5), 6769–6780 (2016)
4. Tsotra, P., Friedrich, K.: Electrical and mechanical properties of functionally graded epoxy-resin/carbon fibre composites. Compos. Part A: Appl. Sci. Manuf. **34**(1), 75–82 (2003)
5. Meenambika, G.B., Raghavendra, H.R.: Mechanical and chemical properties of bamboo/glass fibers reinforced polyester hybrid composites. Ind. Eng. Lett. **4**(4), 39–42 (2014)
6. Zhang, J.: Glass/carbon fibre hybrid composite laminates for structural applications in automotive vehicles. Sustainable Automotive Technologies 2012, pp. 69–74, Springer Berlin Heidelberg (2012)
7. Ramachandran, M., Bansal, S., Fegade, V., Raichurkar, P.: Analysis of bamboo fibre composite with polyester and epoxy resin. Int. J. Text. Eng. Process. **1**(4), 18–21 (2015)
8. Anigol, M.N.B., Anil, S.P.: Study of effect of various fillers on mechanical properties of carbon-epoxy composites. *Int. Res. J. Eng. Technol*. **02**(03), 798–802 June (2015)

Process Parameter Optimization in EDM: A Multi-objective Approach Using Metaheuristic

Surya Narayan Panda, Ajit Kumar Pattanaik, Pradip Kumar Sahu, Prakash Kumar and Bijay Kumar Khamari

Abstract In recent days due to the development of newer types of materials, the non-traditional machining as EDM has gained much popularity due to its efficient output as of machining capability and quality of product. The stated work investigates on optimization of the process along with a parametric study in EDM process efficiency while machining Mild Steel IS1018. For the study, output responses have been chosen as material removal rate and surface roughness and are affected by the input variables, viz. current, pulse ON time and dielectric fluid pressure. The stated two output responses were simultaneously optimized to achieve optimum values by using conventional Taguchi-based grey relational analysis using L_{18} orthogonal array and a metaheuristics method as multi-objective genetic algorithm. The multi-objective function for this mixed integer optimization problem has been developed using goal attainment method considering maximization and minimization of one and other objective. The empirical results were compared and validated with an experimentation, so to analyse the efficiency of the methods. The efficiency of metaheuristic approach as MOGA is found to be noticeable and can be applied to other engineering problems.

Keywords Optimization · Grey relational analysis · Metaheuristics · Multi-objective GA · Goal attainment

S. N. Panda (✉) · P. Kumar
Birsa Institute of Technology Sindri, Dhanbad, Jharkhand, India
e-mail: suryanarayan.uce@gmail.com

P. Kumar
e-mail: kprakash_71@yahoo.co.in

A. K. Pattanaik
GCE, Kalahandi, Odisha, India
e-mail: ajitpuce@gmail.com

P. K. Sahu
Oriental University, Indore 453555, Madhya Pradesh, India
e-mail: pradipsahu2@gmail.com

B. K. Khamari
National Institute of Technology Rourkela, Rourkela, Odisha, India
e-mail: bijayaa.khamari@gmail.com

L. Li et al. (eds.), *Advances in Materials and Manufacturing Engineering*, Lecture Notes in Mechanical Engineering, https://doi.org/10.1007/978-981-15-1307-7_21

1 Introduction

In the generation of manufacturing 4.0 recently, wider variety advanced materials are coming up and also developing difficulties in machining of such materials give scope for non-traditional machining. Electro discharge machining is a non-traditional machining process involves spark erosion process for material removal with good accuracy and precision. Cost-effectiveness analysis of any process is a tedious task for a production engineer, and thus, there must be clear notes about the bottlenecks in the process to predict the required output with minimal cost and loss. The most important notes to study are the parameters, viz. inputs of a process which influence the output of the process, and thus, by analysing the relation and optimizing the process, the efficiency of output can be improved. Researchers worldwide, nowadays, focused on modelling and process optimization in EDM to improve productivity and finishing capability. Researchers [1–6] have investigated and modelled output characteristics like surface characteristics, material removal, etc., with respect to inputs, viz. taking different process parameters like pulse ON/OFF time, current intensity tool shapes, etc., along with thermal traits and vibration response criteria for the process adopting comprehensive experimentation using factorial model of design of experiments, regression and surface response modelling. Investigation into optimization of EDM process parameter has also been carried out by researchers [7–9] using traditional Taguchi hypothesis-based methods and using grey relational coefficient. Azhiri et al. [10] combined Taguchi-based grey relational analysis and ANFIS for study and optimization of wire EDM process in gaseous dielectric media.

Most of researchers in the scope of modelling and optimization of EDM process include traditional methods which may be less effective while studying the interaction between the inputs parameters within the search space. So, in this proposed work, a comparative investigation has been carried out for optimization of process parameters as current, pulse ON time and dielectric pressure for achieving effective output as MRR and surface roughness using Taguchi-based grey relational coefficient and metaheuristic method as multi-objective genetic algorithm (MOGA).

2 Methodology

Experiments were conducted in a die-sinking type electric discharge machine, model BH40ASEB having a maximum current capacity of 40A with a rectangular pulse generator and cylindrical copper electrode. To study the effect of machining input process parameter, rigorous experiment has been conducted using design of experiment approach adopting an orthogonal array as L_{18}. For machining workpiece specimen as Mild Steel IS1018, different set of parameters in different level has been selected accordance with orthogonal matrix to study the outputs as material removal rate and surface quality. Standardized dimension of the workpiece and electrode has been maintained as 80 mm $\times$ 50 mm $\times$ 6 mm, and diameter of the electrode is 10 mm,

respectively. Current, pulse ON time and dielectric fluid pressure are considered as input parameters at three different levels, whereas the effect of these independent parameters has been studied on the performance response characteristics as MRR and surface roughness.

2.1 Taguchi-Based Grey Relational Analysis

Taguchi hypothesized the enhancement of quality of product can be achieved using inputs to quality at each step of the process so by decreasing the deteriorating aspects of interaction of inputs among each other. This quality enhancement is accomplished by the process of design of experiments using orthogonal array, which is a measure of characterization of process parameter's interaction within the search space with fewer test sets.

The grey relational approach gives an ideal way to deal with the constrained and arbitrarily discrete data sets. In grey relational analysis, grey relational grade has been calculated for each experimental sequence, i.e. the comparability and reference sequence. Higher the grade, higher is the efficacy of comparability sequence among all alternatives. The discrete experimented data sets have been normalized so to make the range in between 1 and 0. The normalized output parameters are obtained using larger is better for MRR and Smaller is better for surface roughness and stated in Eqs. (1) and (2), respectively.

$$Z_{ij} = \frac{y_{ij} - \min\left(y_{ij}, i = 1, 2 \ldots n\right)}{\max\left(y_{ij}, i = 1, 2 \ldots n\right) - \min\left(y_{ij}, i = 1, 2 \ldots n\right)} \tag{1}$$

$$Z_{ij} = \frac{\max\left(y_{ij}, i = 1, 2 \ldots n\right) - y_{ij}}{\max\left(y_{ij}, i = 1, 2 \ldots n\right) - \min\left(y_{ij}, i = 1, 2 \ldots n\right)} \tag{2}$$

2.2 Multi-objective Genetic Algorithm (MOGA)

The genetic algorithm is an evolutionary approach proposed by Holland [11] which is helpful for global optimization of the mixed integer model using discrete functions. The genetic algorithm mimics the process of biological evolution by modifying a population of individual points using survival of fittest hypothesis. Genetic algorithm uses mutation and crossover for rapid updating of population. The random crossover and selection procedure can aid to efficient strategic method in search of a global optimum point in a search space so by not trapping into local optimum points. Thus, it turns out to be exceptionally productive and stable in for searching of global optimum solutions. The multi-objective approach in genetic algorithm has been proposed by Deb et al. [12] also using different selection criterion like Pareto optimal font

this approach can be used for finding global optimum value of a mixed integer multi-objective model.

2.3 Synthesis of Multi-objective Problem

The objective of this proposed work of optimization of process parameters is to maximize the material removing rate and to minimize the surface roughness of output product. Thus, in using goal attainment method, the multi-objective optimization problem can be formulated as Eq. (3).

$$Max\ \mathrm{G}(x) = w_1((F(x))/(F_k)) + w_2((-L(x))/(L_k)) \tag{3}$$

Where F_k and L_k are the optimized value of MRR, $F(x)$ and surface roughness $L(x)$ when they are optimized as a single objective case. w_1 and w_2 are the weighing coefficients, and their values are 0.5 and 0.5, respectively (such that $w_1 + w_2 = 1$). The weighing coefficients are selected depending upon the importance of objective function in the multi-objective optimization problem. $G(x)$ is the multi-objective function involves mixed integer problem set of both maximization and minimization.

2.4 Statistical Analysis

The experiments were conducted for studying the different parametric relation, and thus, by selecting different levels of input parameters, the interaction can be analysed using orthogonal array, and required output performance parameter can be noted down. The different levels of inputs are shown in Table 1.

Highest material removal rate with minimum surface roughness is the main output objectives of this stated investigation. For this, the error due to interaction between inputs and outputs can be studied using signal-to-noise ratio. The procedure for determining the S/N ratio values from the output values has been calculated using two assumptions as larger is better case for highest MRR and smaller the better for

Table 1 Levels of factors

Response characteristics	Material removal rate (mm^3/min.), surface roughness (μm)		
Control parameters	Levels		
	1	2	3
Current (A)	15	25	35
Pulse ON time (μs)	250	350	450
Dielectric pressure (kg/cm2)	0.2	0.4	0.6

achieving lowest surface roughness. Both these criteria have been mathematically represented as Eqs. (4) and (5), respectively. After normalizing the S/N ratio values, the deviation sequence and grey relational coefficient have been determined, and this shows the accordance of normalized test outputs to the best values in comparability sequence, represented in Eq. (6).

$$s/n_{\mathrm{HB}} = -10\log_{10}\left[(1/n)\left(\sum 1/y_{ij}^2\right)\right] \tag{4}$$

$$s/n_{\mathrm{HB}} = -10\log_{10}\left[\left(\sum y_{ij}^2/n\right)\right] \tag{5}$$

$$\xi_i(k) = \frac{\Delta_{\min} + \zeta\Delta\max}{\Delta_{oi}(k) + \zeta\Delta\max} \tag{6}$$

Where $\Delta_{0i}(k)$ is the deviation sequence for the reference sequence and comparability sequence as in Eq. (7).

$$\Delta_{oi}(k) = \|y_0(k) - y_i(k)\| \tag{7}$$

$$\Delta_{\min} = \min_{\forall j \in i} \min_{\forall k} \|y_0(k) - y_i(k)\| \tag{8}$$

$$\Delta_{\min} = \max_{\forall j \in i} \max_{\forall k} \|y_0(k) - y_i(k)\| \tag{9}$$

ζ is a identifier coefficient whose value generally considered as 0.5, and $y_0\,(k)$ and $y_j\,(k)$ represent sequence of originals and sequences of comparability, respectively. At the final step of the grey relational analysis, the grey relational grade has been identified as by relating grey relational grade of each performance objective, Eq. (10).

$$\gamma_i = \frac{1}{n}\sum_{k=1}^{n} \xi_i(k) \tag{10}$$

2.5 Mathematical Modelling Using RSM

Response surface system (RSM) is a efficient method for assessing the inter-relation between inputs and outputs. In the reasonable use of RSM, the approximating model is based on observed input and output information from the factorial designed matrix. The development of empirical model showing relationship of inputs and output has been a tedious task, and apparently, regression modelling has been adopted for the said purpose well effectively. Here, in this work, a nonlinear regression modelling is adopted based upon second-order nonlinear polynomial shown in Eq. (11), where

parameters a_0, a_j, a_{jj}, a_{ij}= *0, 1, …, k* are called the regression coefficients.

$$Y = \sum_{j=1}^{k} a_j x_j + \sum_{j=1}^{k} a_{jj} x_j^2 + \sum_{i<j} \sum_{j=2}^{k} a_{ij} x_i x_j \tag{11}$$

$$\begin{aligned} \text{MRR} = {} & 6.209 * X1 - 0.195 * X2 - 21.829* \\ & X3 - 0.094 * X1 * X1 - 20.694* \\ & X3 * X3 + 0.002 * X1 * X2+ \\ & 0.076 * X2 * X3 + 0.444 * X3 * X1 \end{aligned} \tag{12}$$

$$\begin{aligned} \text{Surface Roughness} = {} & 0.742 * X1 + 0.018 * X2- \\ & 19.749 * X3 + 28.835 * X3* \\ & X3 - 0.002 * X1 * X2 - 0.034* \\ & X2 * X3 + 0.039 * X3 * X1 \end{aligned} \tag{13}$$

Where $X1$, $X2$ and $X3$ are the independent input variables as current, pulse ON time and dielectric fluid pressure, respectively.

The adequacy of developed mathematical model can be checked using ANOVA methods, and generally, the coefficient R^2 is the measure of exactness of fitness of the regression model. The derived regression models in Eqs. (12, 13), agree with the value of 86.4 and 82.1% as determination coefficient values when tested separately. This is sufficient argument for accepting the mathematical model thus developed.

3 Results and Discussion

This stated mixed integer multi-objective optimization problem has been solved using Taguchi method-based grey relation analysis and MOGA for achieving optimum value of the highest material removal rate and lowest surface roughness. The highest grey relational grade shows at parameter set level $A_3B_2C_3$ as the best comparability sequence found from the original experimented set, thus by giving best performance characteristics when studied simultaneously. Using multi-objective genetic algorithm, the results also obtained for optimum performance characteristics (Table 2). The comparison of results has been shown in Table 3, and the convergence of objective function in metaheuristic method as MOGA is shown in Fig. 1. Also, the confirmation test in Table 3 shows the effective results of GA with respect to Taguchi-based method at set input parameters 35, 300 and 0.6, respectively, for current, pulse ON time and dielectric fluid pressure.

Table 2 Results of Taguchi-Based grey relational analysis

Expt. no	Current (A)	Pulse on time (μs)	Dielectric pressure (kg/cm^2)	MRR (mm^3/min)	Surface roughness (μm)	Normalized S/N ratio		Deviation sequenced		Grey relational coefficient		Grey relational grade	Rank
						MRR (mm^3/min)	Surface roughness (μm)	MRR (mm^3/min)	Surface roughness (μm)	MRR (mm^3/min)	Surface roughness (μm)		
1	15	250	0.2	33.758	13.2	0.0992	0.5439	0.9008	0.4561	0.357	0.5235	0.4402	14
2	15	350	0.4	32.994	9.24	0.0751	0.091	0.9242	0.909	0.3511	0.3557	0.3534	17
3	15	450	0.6	31.04	8.6	0.0133	0	0.9867	1	0.3363	0.3333	0.3348	18
4	25	250	0.2	67.388	12	0.8053	0.423	0.1947	0.577	0.7335	0.4642	0.5988	12
5	25	350	0.4	67.728	13.1	0.8103	0.5342	0.1897	0.4658	0.7255	0.527	0.6262	11
6	25	450	0.6	63.864	12.4	0.7503	0.4645	0.2497	0.5355	0.6673	0.4835	0.5754	13
7	35	250	0.4	79.83	13.6	0.9784	0.5819	0.0216	0.4181	0.9586	0.545	0.7518	4
8	35	350	0.6	81.529	16.6	1	0.8349	0	0.1651	1	0.7526	0.8763	1
9	35	450	0.2	78.089	13.6	0.956	0.5819	0.044	0.4181	0.9191	0.545	0.732	5
10	15	250	0.6	33.163	9.47	0.0802	0.1223	0.9198	0.8777	0.3522	0.3632	0.3577	16
11	15	350	0.2	30.66	11.7	0	0.3908	1	0.6092	0.3333	0.4517	0.3925	15
12	15	450	0.4	31.762	18.9	0.0361	1	0.9639	0	0.3415	1	0.6707	9
13	25	250	0.4	69.64	12.8	0.8393	0.5048	0.1607	0.4952	0.7577	0.5024	0.63	10
14	25	350	0.6	64.12	16	0.7544	0.7881	0.2456	0.2119	0.671	0.7023	0.6866	8
15	25	450	0.2	63.779	16.2	0.7489	0.8038	0.2511	0.1962	0.667	0.7182	0.6926	7
16	35	250	0.6	77.664	17.5	0.9503	0.9019	0.0497	0.0981	0.9096	0.8368	0.8732	2
17	35	350	0.2	78.131	14.7	0.9573	0.6815	0.0427	0.3185	0.9213	0.6117	0.7665	3
18	35	450	0.4	77.04	13	0.942	0.5247	0.058	0.4753	0.896	0.5136	0.7048	6

Table 3 Comparison of Results

Response characteristics	Optimal process outputs		Optimal process inputs		Confirmation test	
Level	A3B2C3 (Taguchi-GRA)	MOGA	A3B2C3 (Taguchi-GRA)	MOGA	A3B2C3 (Taguchi-GRA)	MOGA
MRR (mm^3/min)	81.529	79.38	–	–	79.681	80.324
Ra (μm)	16.6	9.135	–	–	17.2	10.3
Current (A)	–	–	35	34.537	–	–
Pulse ON time (μs)	–	–	350	296.384	–	–
Dieletric pressure (kg/cm2)	–	–	0.6	0.597	–	–

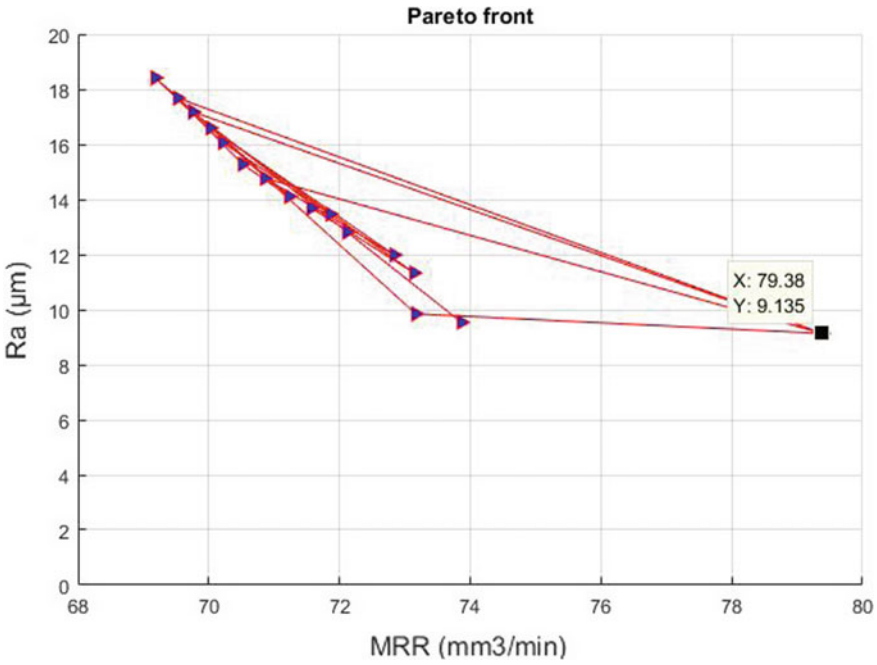

Fig. 1 Convergence traits of MRR and surface roughness in MOGA

4 Conclusions

The optimum process parameters and output performance responses for machining of Mild Steel IS1018 using EDM process have been found using both traditional

Taguchi-based grey relational analysis and metaheuristic-based method as multi-objective genetic algorithm. Both the results were compared for assessment of efficiency of the approaches. From the comparison and confirmation results, it was observed the MOGA approach is more efficient in achieving global optimum values of highest MRR and lowest surface roughness. In recent industrial trends, surface quality precision has been more important for the cause of interchangeability, and thus, MOGA approach is more feasible and efficient, providing better optimized output results in the scope of stated study. Further, it was found that the current and dielectric fluid pressure were the most significant parameter of the EDM process with the highest contribution for the enhancement of process outputs. Thus, input current and dielectric pressure can possibly be assumed as an imperative part for designing of the production process in EDM with less economic loss with high value output. More numbers of levels and process parameters can be introduced for stated process parameter optimization study. The metaheuristic approach can lead to new horizons of scope in the field of optimization in manufacturing processes and other engineering problems.

References

1. Puertas, I., Luis, C.J.: A study on the machining parameters optimisation of electrical discharge machining. J. Mater. Process. Technol. **143**, 521–526 (2003)
2. Chiang, K.T.: Modeling and analysis of the effects of machining parameters on the performance characteristics in the EDM process of Al 2 O 3 + TiC mixed ceramic. Int. J. Adv. Manuf. Technol. **37**(5–6), 523–533 (2008)
3. Shabgard, M.R., Seyedzavvar, M., Oliaei, S.N.B.: Influence of input parameters on characteristics of EDM process. Strojniški Vestn.-J. Mech. Eng. **57**(9), 689–696 (2011)
4. Pour, G.T., Pour, Y.T., Ghoreishi, M.: Thermal model of the electro-spark nanomachining process. Int. J. Mater., Mech. Manuf. **2**(1), 56–59 (2014)
5. Ali, M.Y., Mohamed, A.R., Khan, A.A., Asfana, B., Lutfi, M., Fahmi, M.I.: Empirical modelling of vibration in micro end milling of PMMA. World Appl. Sci. J. (Math. Appl. Eng.) **21**, 73–78 (2013)
6. Hoang, K.T., Yang, S.H.: A study on the effect of different vibration-assisted methods in micro-WEDM. J. Mater. Process. Technol. **213**(9), 1616–1622 (2013)
7. Chen, Y.F., Lin, Y.J., Lin, Y.C., Chen, S.L., Hsu, L.R.: Optimization of electrodischarge machining parameters on ZrO2 ceramic using the Taguchi method. Proc. Inst. Mech. Eng. Part B: J. Eng. Manuf. **224**(2), 195–205 (2010)
8. Pasam, V.K., Battula, S.B., Madar Valli, P., Swapna, M.: Optimizing surface finish in WEDM using the Taguchi parameter design method. J. Braz. Soc. Mech. Sci. Eng. **32**(2), 107–113 (2010)
9. Datta, S., Mahapatra, S.: Modeling, simulation and parametric optimization of wire EDM process using response surface methodology coupled with grey-Taguchi technique. Int. J. Eng., Sci. Technol. **2**(5), 162–183 (2010)
10. Azhiri, R.B., Teimouri, R., Baboly, M.G., Leseman, Z.: Application of Taguchi, ANFIS and grey relational analysis for studying, modeling and optimization of wire EDM process while using gaseous media. Int. J. Adv. Manuf. Technol. **71**(1–4), 279–295 (2014)
11. Holland, J.H.: Genetic algorithms. Sci. Am. **267**(1), 66–73 (1992)
12. Deb, K.: Multi-objective optimization using evolutionary algorithms wiley, Chichester, UK (2001)

Study of Takeoff Constraints for Lifting an Agriculture Pesticide Sprinkling Multi-rotor System

Umamaheswara Rao Mogili and BBVL. Deepak

Abstract The revolution in the mechatronics field made a new era for the monitoring and supervision of agriculture management systems. In precision agriculture, crop protection drones have great potential due to its flexibility in handling to increase crop productivity. However, the multi-rotor aerial system working capability depends on the required thrust to be produced in order to lift the system from the ground position. This work proposes simulation and theoretical static thrust calculations to develop an autonomous multi-rotor system, which is capable of lifting the components, those are helpful for precision farming. This work starts with an analytical approach of the thrust equation and its influences at various parameters explained. The motion equations are derived using the kinetic energy, disk actuator theory and momentum theory. The thrust is calculated using the parameters, motor specifications, propeller dimensions and constant. If the calculated thrust is twice to the total weight of the multi-rotor system, then the system has the ability to fly comfortably toward the crop agriculture field. The calculation is done for different propellers and chosen the best one. The chosen theoretical result validated using a static thrust calculator in a Web site from "gobrushless.com." The relative error between the simulated and theoretical results has shown only 2% of the difference.

Keywords Multi-rotor system · Brushless motors (BLDC) · Propellers · Static thrust equation · Thrust estimation

1 Introduction

The multi-rotor system simple called drone and its applications have grown drastically in the private and public sectors because of its flexibility in operating conditions. In the past, these systems are used for military and security applications [1]. But changes in the environment, the way of its flexibility and cost-effectiveness,

U. R. Mogili (✉) · BBVL. Deepak
National Institute of Technology, Rourkela 769008, Odisha, India
e-mail: umajrfnit@gmail.com

BBVL. Deepak
e-mail: deepak.bbvl@gmail.com

L. Li et al. (eds.), *Advances in Materials and Manufacturing Engineering*, Lecture Notes in Mechanical Engineering, https://doi.org/10.1007/978-981-15-1307-7_22

multi-rotor systems are adapted to the civil applications [2]. Agriculture farming is the main economic thing in most of the developing countries like India.

To build a multi-rotor system for agriculture purpose, a number of components are required such as the inertial measurement unit (IMU), flight controller, BLDC motors, receiver, propellers, LIPO battery and system frame. The total weight of the multi-rotor systems depends upon these components. Whenever designing a multi-rotor system, the selection of motors, propellers, and battery is very important. This support is to give the force of thrust to lift the total weight against gravity. These multi-rotor systems work at lower speeds, and it makes thrust calculation from a propeller system accurately compared to the real thrust produced by the motor [4].

In the multi-rotor system, half pair of the propellers are rotated in counterclockwise, and another half pair of propellers rotate in a clockwise direction to stabilize the gravity effect over the weight of the system. The selection of propellers is important, the E-type propellers are spin faster and draw fewer current and these are efficient in higher revolutions per minute (RPM) on the other side. Slo-Flyer (SF) propellers produce high thrust at lower RPMs. The propellers connected with the BLDC motors, which rotation speeds are used to control the direction of the multi-rotor system accurately by using Euler angles roll, pitch and yaw. The BLDC motor speed influences the generated thrust and if the motor speed is increased, the speed of the multi-rotor system increases to fly high. The propeller thrust is calculated using a theoretical equation which is derived based on momentum theory [5].

From the calculation results, the motors and propellers can be selected, especially for the agriculture applications. These calculations are necessary to find the thrust produced by a BLDC motor. In this study, the static thrust calculation is done using a theoretical equation, and the obtained values are checked with simulation results to observe the efficiency of the propeller before going to be used in the real-time agriculture environment. The paper has three sections as follows: Sect. 2 presents the derivation of propeller's static thrust equation for the multi-rotor system. Section 3 represents the calculation of the thrust generated by the propeller and its validation with online thrust calculator "propeller thrust calculator form." Section 4 presents the theoretical and simulation results and its relative error.

2 Static Thrust Equation for Propellers

The thrust is described as a force to move the multi-rotor system in the air, and it is generated by the propeller unit. Basically, the thrust and its coefficients are calculated using the disk actuator theory, momentum theory and blade element theory. But these theories, which is being used and analyzed for single-rotor helicopters and fixed-wing aircraft, these are the long rotors with high diameter and pitch in size. Coming to the multi-rotors they have a number of propellers, with smaller diameter and pitch. The momentum theory is enough to calculate the static thrust of the propellers, and it is defined by the amount of the thrust produced by the propeller, which is located stationary to the earth. Past works proposed the static thrust equation to estimate a

propeller thrust for lifting the weights. However, the thrust equation is derived based on the momentum theory equation in mathematic terms which is shown in Eq. (1).

$$T = A * \rho * v * \Delta v \tag{1}$$

In Eq. (1), thrust in Newton's (N) represented by T, area of the rotor represented by the A in square meters (m^2), density of the air is represented by ρ in Kg/m^3, v is the velocity of the air at rotor in m/s and Δv is the velocity accelerated by the rotor in m/s. Before going to calculate the static thrust, the calculation of the power is required to determine the relationship between the BLDC motor to propellers in terms of the RPM. It is very difficult to determine the required power to rotate a propeller at a given RPM. Equation (2) gives the power consumption of two-bladed rotors [6].

$$Pw = \text{propeller constant} * D^4 * P * N^3 \tag{2}$$

Where the propeller constant is defined by the type of brand is used. D is the diameter of the rotor, p is the pitch of the rotor both are in meters (m) and N is the RPM value of the motor. The N is calculated using the voltage supplied to the BLDC motor. If the voltage increases, the spinning speed of the motor increases. As per momentum conservation and the law of the gravitational, the thrust produced by the propeller as in Eq. (1) is inflected as below.

$$T = \frac{\pi}{4} * D^2 * \rho * v * \Delta v \tag{3}$$

Where the velocity (v) of the air at the rotor side is always half of the velocity accelerated by the rotor (Δv). As a common rule applied to Eq. (3) and simplified as Eq. (4).

$$T = \frac{\pi}{8} * D^2 * \rho * \Delta v^2 \tag{4}$$

The power absorption of the rotor is related to the velocity of air accelerated at the rotor area. The relation is:

$$\Delta v = 2 * \frac{Pw}{T} \tag{5}$$

Substituting Eq. (5) into Eq. (4):

$$T = \left(\frac{\pi}{2} * D^2 * \rho * Pw^2\right)^{1/3} \tag{6}$$

Applying Newton's second law $F = mg$ for obtaining the mass of the multi-rotor

$$m = \frac{\left(\frac{\pi}{2} * D^2 * \rho * Pw^2\right)^{1/3}}{g} \tag{7}$$

Where m is the mass in (kg) at hovering position, and g is the gravity of the earth is 9.81 m/s^2. Equation (7) is useful to calculate the mass of the multi-rotor system, and the thrust that equals the mass of the multi-rotor system is needed for hovering. The hovering position is very important in agriculture applications while monitoring and sprinkling pesticides over the crop areas. The static thrust equation mentioned in the above given in the flowchart and their sequences can be found in Fig. 1.

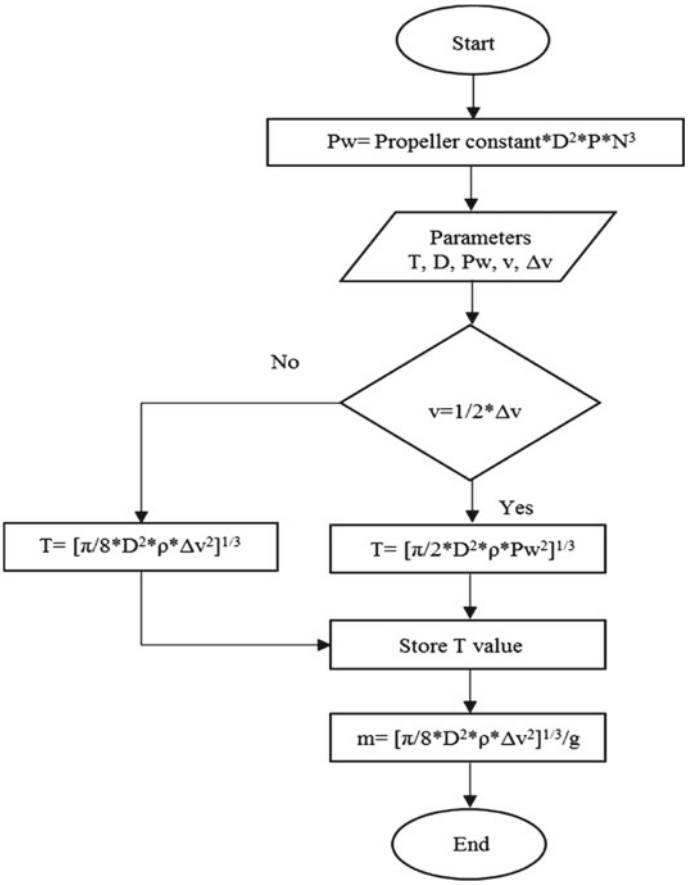

Fig. 1 Flowchart of the thrust equation and its sequences

3 Different Propeller Types and Its Thrust Calculation

The power consumption of various propellers based on calculated, their propeller constants [6] listed in category 1 as Top Flite, Zinger and Master AirScrew propellers with 1.31, category 2 as APC propellers with 1.1 and category 3 as thin carbon fiber folder propellers with 1.18. This is useful for which propeller type could give max thrust as it is required agriculture applications.

According to Eq. (6), the takeoff thrust is calculated and its performance is made a presumption out of its frictional losses. The variables are required to find out the propeller thrust which is propeller diameter (D), pitch (P), the density of the air (ρ), the power consumption of the motor to rotate the propeller (Pw) and propeller constant.

Using online propeller thrust calculator shown in Fig. 2 for simulation and the theory and Eq. (6) for theoretical calculation, the propeller thrust is evaluated for a given set of variables taken from Table 1. For example, take the estimated RPM is 4000 and submitting it into Eq. (6).

$$T = \left(3.141/2 \ * \ 0.254^2 \ * \ 1.225 \ * \ 13.37^2\right)^{1/3} = 2.8 \ N \text{ or } 285.5 \text{ grams.}$$

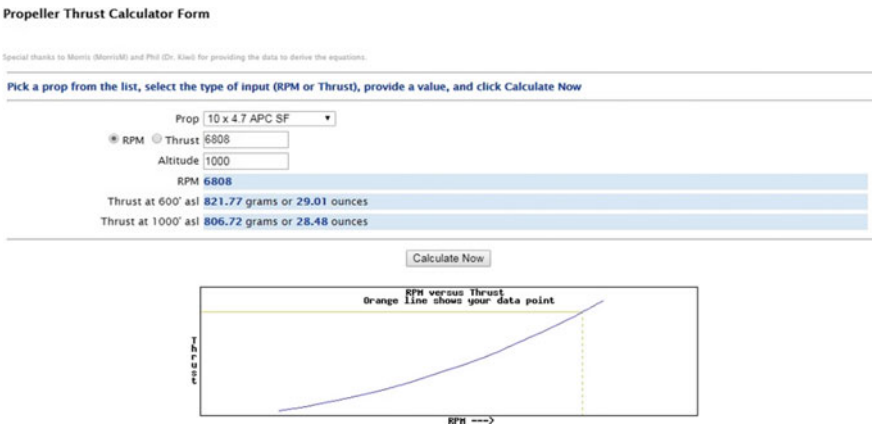

Fig. 2 Propeller thrust calculator form [7]

Table 1 Parameters and coefficient values

Parameter/coefficient	Value
Propeller size	APC SF 10 * 4.7
Motor	920 kV
Air density	1.225 kg/m^3
Rotor constant	1.11
Pi (π)	3.141
Estimated RPM	3000 to 8000

Table 2 Comparison of thrust theoretically and simulation

RPM	Simulation	Propeller type		
		Category 1	Category 2	Category 3
2382	0.79	1.11	1.00	1.04
2723	1.05	1.45	1.30	1.35
3063	1.37	1.83	1.64	1.71
3404	1.73	2.26	2.02	2.11
4084	2.6	3.24	2.90	3.02
4765	3.65	4.39	3.94	4.10
5446	4.91	5.72	5.13	5.34
6127	6.38	7.22	6.48	6.74
6808	8.06	8.90	7.98	8.31

To compare and validate the theoretical results with simulation results calculated by the online calculator "online propeller thrust calculator form" shown in Table 2 of three categories of the propeller types.

4 Results and Discussions

The propeller constant categories are chosen as category 1, 2 and 3 for different types. The RPM values are estimated as 60, 70, 80, 90 and 100% of full throttle for 920 kV BLDC motor with 3.4 and 7.4 voltages. Table 2 shows the simulation and theoretical results of the three categories of the propeller types with different propeller constants. Take a close look at the results of category 2, APC propellers are giving approximately similar results compared to the other 2 types. All results of the thrust are in newton. For better comparison, results calculated the relative error using simulation and theoretical results.

A relative error equation is used to compare both results to find out how much similar they have in percentage. The relative error is designated as

$$R_t = \frac{\text{Theory} - \text{Simulation}}{\text{Theory}} * 100 \tag{8}$$

The relative error is calculated for all three categories and composed all these results shown in Table 3.

Finally, relative errors showing the category 2 propellers have the scenario of nearest to simulation results shown in Table 4. The relative error elaborates APC propeller with constant 1.1, and RPM of 6128 gives the optimum solution to lift the system. Hence, the propellers are useful for the agriculture pesticide spraying

Table 3 Comparison of three categories with relative error

Relative error (in percentage)		
Category 1	Category 2	Category 3
28	20.81	24.03
27.58	19.24	22.22
25.13	16.52	19.88
23.45	14.47	18.01
19.75	10.37	13.90
16.85	7.29	10.97
13.68	4.27	8.05
11.63	1.49	5.34
9.43	−1.01	3.01

Table 4 Category 2 relative results

RPM	Simulation	Category 2	Relative error (%)
2382	0.79	1.00	20.81
2723	1.05	1.30	19.24
3063	1.37	1.64	16.52
3404	1.73	2.02	14.47
4084	2.6	2.90	10.37
4765	3.65	3.94	7.29
5446	4.91	5.13	4.27
6127	6.38	6.48	1.49
6808	8.06	7.98	−1.01

multi-rotor systems. Table 3 shows the constant data percent variation in the 90% efficiency performance.

5 Conclusion

As a conclusion, the results are presented as a comparison of propeller thrust simulation and theoretically. The propellers available in the market are suitable for the different purposes of multi-rotor system applications. But, the research study shows the APC SF rotors are suitable for agriculture applications because of its hovering capacity in the agriculture field. The study of the theoretical calculation proves the category 2 propellers are almost similar to the results of the online thrust calculator. The future scope validates the theoretical results in the agriculture field experimentally.

Acknowledgements This work is supported by SERB, Govt. of India with the Sanction order No. ECR/2017/000140 on Dt. July 5, 2017.

References

1. Jerry, M.: Current and future UAV military users and applications. Air Space Eur. **1**(5/6), 51–58 (1999)
2. Samad, A. M., Kamarulzaman, N., Hamdani, M. A., Mastor, T. A., Hashim, K. A.: The potential of unmanned aerial vehicle (UAV) for a civilian and mapping application. In: 2013 IEEE 3rd International Conference on System Engineering and Technology (ICSET), IEEE, 313–318
3. Mogili, U.R., Deepak, B.B.V.L.: Review on application of drone systems in precision agriculture. Procedia Comput. Sci. **133**, 502–509 (2018)
4. Stepanyan, V., Krishnakumar, K., Bencomo, A.: Identification and reconfigurable control of Impaired Multi-rotor systemDrones. AIAA Science and Technology Forum and Exposition 2016, San Diego, Jan. 2016
5. Douglas, D.F., Phillips, W.F.:. Momentum theory with slipstream rotation applied to wind turbines. In: 31st AIAA Applied Aerodynamics Conference, Fluid Dynamics, and Co-located Conferences, (AIAA 2013–3161), June 24-27, 2013
6. Boucher, R.J.: Electric Motor Handbook, pp. 30–34. AstroFlight Inc., Los Angeles, CA (1994)
7. http://www.gobrushless.com/testing/thrust_calculator.php?prop=15&rb1=1&Value=6808&Altitude=600&submit=Calculate+Now

Condition Monitoring of Turbine Blades with Experimental Validation Using FFT Analyzer

Ravi Prakash Babu Kocharla and Raghu Kumar Bandlamudi

Abstract Turbines in power industry uses pretwisted blades of varying lengths. And these blades are mounted on the rotating shafts with one end fitted in the fir-tree root of the rotor disk. The fatigue of these blades may cause crack to initiate at the stress concentration regions and may propagate for catastrophic failure. This paper addresses the condition monitoring of the turbine blades in the presence of crack using FFT analyzer. The influence of crack on the natural frequencies of turbine blade was investigated by conducting parametric studies using ANSYS software. It was observed that the natural frequencies of the cracked pretwisted blade are varying with angle of twist in all modes of vibration. Also, these natural frequencies were compared for long and short blades whose vibrational behavior was found to be dissimilar under the combined effect of pretwist and the presence of the crack.

Keywords Modal testing · FFT analyzer · Pretwisted blade · Crack · Condition monitoring

1 Introduction

Turbo machineries are more expensive equipment and their failure may cause huge loss. The most critical components in these turbines are its blades. Due to fatigue, cracks may be initiated in these blades and propagate to an unstable stage which may cause an adverse effect on the reliability of the turbines. So, early crack detection and its repair enhance the reliability as well as the durability of these turbines. Vibration monitoring is the promising condition monitoring technique which can be used to study the effect of crack in the blades. The equations of motion for the vibration analysis of pretwisted blades in rotation employing hybrid variables of deformation were derived in the modeling of the problem by Yoo et al. [1]. Chung and Yoo [2] proposed dynamic modeling of rotating cantilever beam to obtain linear differential equations for stretch and flapwise deformations. Yoo and Pierre [3] investigated

R. P. B. Kocharla (✉) · R. K. Bandlamudi
Department of Mechanical Engineering, Prasad V Potluri Siddhartha Institute of Technology, Kanuru, Vijayawada 520007, India
e-mail: rpkocharla@gmail.com

L. Li et al. (eds.), *Advances in Materials and Manufacturing Engineering*, Lecture Notes in Mechanical Engineering, https://doi.org/10.1007/978-981-15-1307-7_23

vibration characteristics of a rectangular plate for its prescribed rotary motion. Huang [4] studied the effect of angle of twist of blades of a pretwisted blade system for their dynamic characteristics. Vadiraja and Sahasrabudhe [5] found the significance of gyroscopic coupling between lagging-extension motions of composite beams. Chen [6] investigated the influence of thickness to width ratio, twist angle, spinning speed and axial load on the natural frequency and buckling load of Timoshenko beams. Sinha and Turner [7] derived the equation of motion for free vibration of typical airfoil blade problems in turbomachinery. The analytical results obtained for the plate were directly validated as the frequency values of airfoil blades in turbomachinery. Cheng et al. [8] studied vibration characteristics of the tapered beam under the influence of location and size of the crack, radius of hub, and rotational speed. Nguyen [9] investigated the coupled mechanism for bending between horizontal and vertical vibration mode shapes of the cracked beam. Akash and Harsha [10] studied the variation of vibration response of the blade with crack at its fir-tree root. Rezaei et al. [11] presented a method for damage detection in nonlinear wind turbine blade model. Segura et al. [12] performed finite element analysis of the blades in group to identify crack initiation process in the blade. Zhao et al. [13] predicted the operating condition of the turbine that leads to the resonance of the blade.

In the literature available, researchers have developed several ways of modeling the problem to identify the vibration behavior of the pretwisted blades. Since, turbines have short blades (HP) in initial stages and long blades (LP) in final stages, vibration monitoring technique can be applied to the blades of different length-to-thickness ratio which helps to understand the fatigue behavior of turbine blades. So, the main scientific challenge to be addressed in this paper is to establish a robust description of crack effects that can be used in more precise fatigue lifetime models and simulations of fatigue behavior. The key elements addressed in this paper are

- Develop the blade models equivalent to LP and HP turbine blades.
- Model a propagating crack in the long and short blade models.
- Analyze the vibration response of long and short blades with crack.

2 Methods and Materials

A 500 MW three-cylinder reheat condensing reaction turbine generator of Bharat Heavy Electrical Limited make is one of the unit in operation at Ramagundam thermal power station in India. The LP turbine last stage blade of this unit was considered to estimate natural frequencies of the blade.

2.1 Geometric and Finite Element Modeling of LP Turbine Last Stage Blade

The geometric modeling of the LP steam turbine last stage blade was developed for the cross-sectional dimensions taken at tip of the blade, middle of the blade, and at the root of the blade. The angle of twist of the mid-span cross section and tip cross section with respect to the root cross section of the blade is 47° and 60°, respectively. Geometric model of the blade is shown in Fig. 1a. Then, the geometric model of the blade was imported into ANSYS software and was discretized using solid brick elements. Eight-noded hexahedral element was used to mesh the blade as shown in Fig. 1b with material properties of chromium steel (X28CrMoNiV49) of the LP turbine last stage blade [14]. To capture the vibration mode shapes accurately, utmost care was taken to model the blade with all important geometric features, and later, it was meshed with fine size elements to obtain results with no errors.

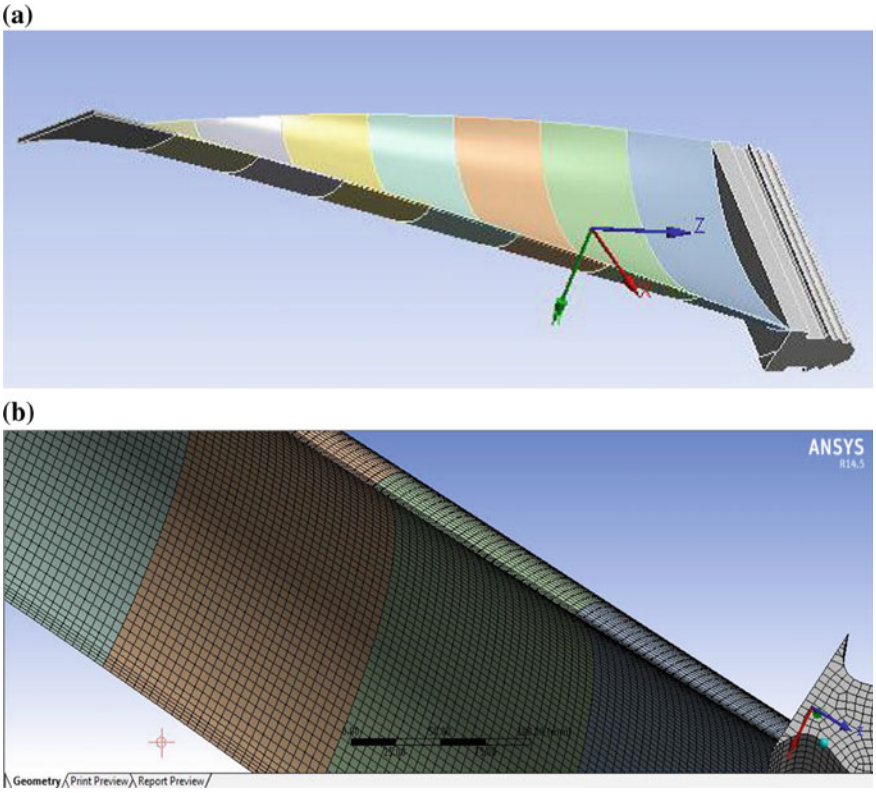

Fig. 1 **a** Geometric model of LP turbine last stage blade. **b** Finite element model of LP turbine last stage blade

2.2 Experimentation

For the pretwisted long blade, specimens were made with length (l)-to-thickness (h) ratio of $l/h = 60$ with angle of twist 15°, 30°, 45°, and 60° each and one straight uniform specimen. Angle of twist of the specimens was considered based on the twists provided for the actual pretwisted blades in power generation. Required angle of pretwist was attained by applying torque on the straight uniform specimens at the equal intervals of its length. Now, these specimens were machined to smooth surface finish for carrying out magnetic particle test to identify the presence of any cracks on the surface of the specimen. Later, ultrasonic test was conducted on the same specimens for identifying internal cracks. Specimens were now confirmed to be free from any internal or surface cracks. Uncracked specimens were converted to cracked specimens by cutting a notch using electronic discharge machining process.

Experiments are conducted on pretwisted long blade specimens to obtain the natural frequencies using laser vibrometer. In the natural frequency test, the test specimen is fixed at one end on a heavy and rigid vice as shown in Fig. 2a to provide boundary conditions of a turbine blade. The inserted length in the vice has been kept in the specimen to resemble the fir-tree root of a blade and free length of the specimen becomes the actual length of the blade.

For pretwisted long blade, length-to-thickness ratio was taken as 60 as it was modeled for low-pressure turbine blades. The natural frequencies were found out by free vibration method. The excitation on the long blade was made by striking with the impact hammer at the free end and its vibration response is recorded in a FFT analyzer. Charge amplifier has been used to generate amplified vibration spectra. FFT dual analyzer was connected to output signals of laser vibrometer (Fig. 2b) and the impact hammer transducer to synchronize the acceleration and force signals for the data acquisition in a computer through a data cable.

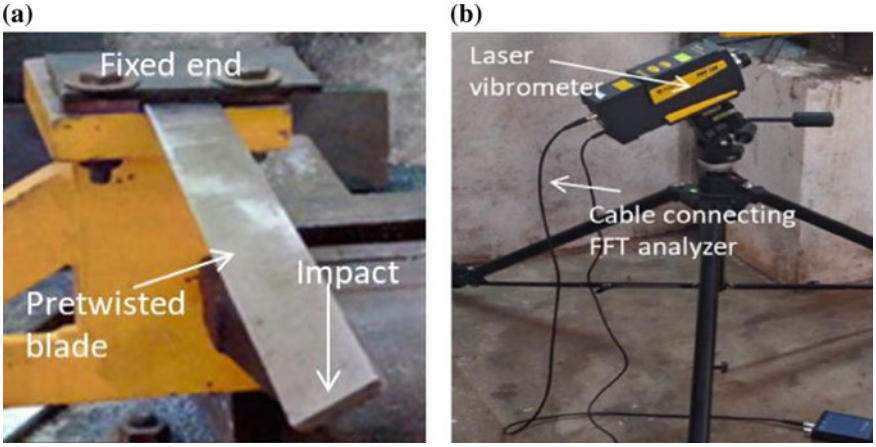

Fig. 2 **a** Test fixture with pretwisted long blade specimen. **b** Laser vibrometer

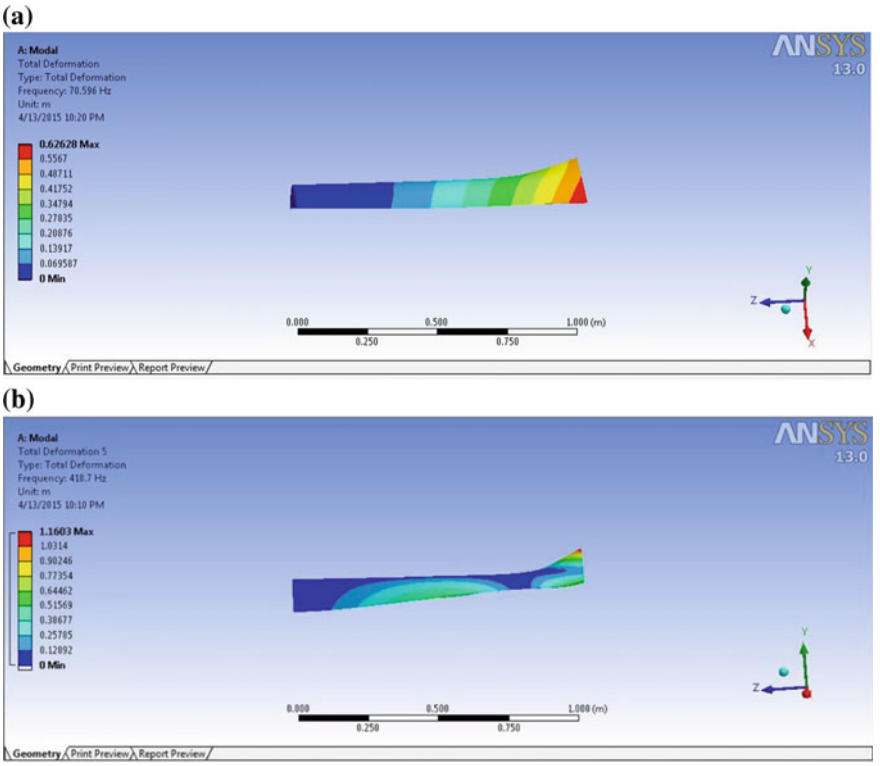

Fig. 3 **a** First mode shape of turbine blade with 60° angle of twist. **b** Second mode shape of turbine blade with 60° angle of twist

3 Results

3.1 Modal Analysis of Turbine Blade

A finite element modal analysis was performed to estimate the natural frequencies of the LP turbine last stage blade. The blade root was constrained for all degrees of freedom as it was attached rigidly to rotor disk. The first and second mode shapes of blade are shown in Fig. 3a, b, respectively.

3.2 Comparison of Natural Frequencies of Turbine Blade and Pretwisted Long Blade Model

A pretwisted long blade model was developed to obtain natural frequencies based on the actual turbine blade frequencies. The first three measured natural frequencies

for corresponding modes of vibration of blade model are compared to validate its vibrational behavior same as the turbine blade. From Fig. 4a, it was found that frequency of first mode is linear with increased angle of twist. Frequency of second mode is increasing with increased angle of twist and frequency of third mode is decreasing with increased angle of twist as shown in Fig. 4b, c, respectively. So, it can be clearly stated that the vibration behavior of the pretwisted long blade model was found to be similar with that of the actual LP turbine last stage blade and further analysis of crack in the blade was carried out using pretwisted long blade model.

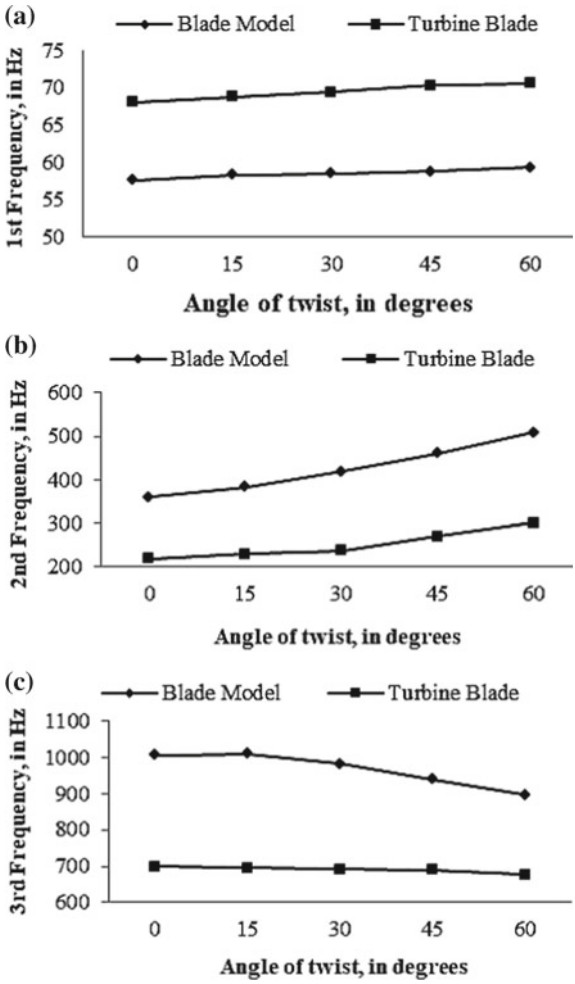

Fig. 4 **a** Comparison of first mode frequencies of turbine blade and blade model. **b** Comparison of second mode frequencies of turbine blade and blade model. **c.** Comparison of third mode frequencies of turbine blade and blade model

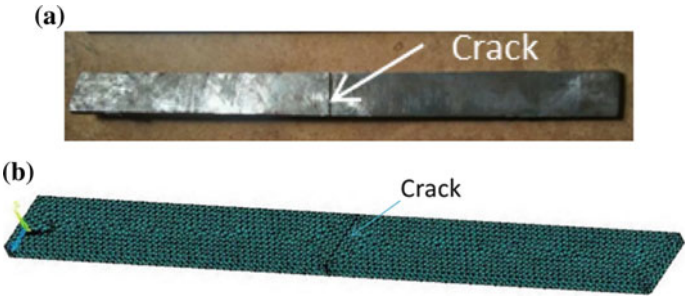

Fig. 5 **a** Cracked pretwisted blade specimen. **b** Finite element model of cracked pretwisted blade

3.3 Experiment Results

Modal testing was conducted on a pretwisted long blade specimen to determine the natural frequencies for resonance condition. Geometry of the crack in the pretwisted blade specimens is shown in Fig. 5a and the finite element model of the cracked pretwisted blade is shown in Fig. 5b.

The experimental results for uncracked specimens and for cracked specimens with crack located at midway of its length were recorded. These results are determined by a curve fitting analytical process that gives the closest possible fit to the measured data. This can be achieved by minimizing the error between the analytical function and the measured data.

It has been observed from the experimental findings that natural frequencies for uncracked pretwisted blades for varying angle of twist were changing with minimal variation as shown in Fig. 6a, whereas for cracked pretwisted blades. The deviation in natural frequencies was more as shown in Fig. 6b. Also, the amplitude of vibration of cracked pretwisted blade model was observed to be more compared to uncracked pretwisted blade model.

4 Discussions

The study has been further extended to HP turbine blades, modeled as pretwisted short blade, whose length-to-thickness ratio was considered as 10. Parametric studies have been carried out for these pretwisted blades to determine the natural frequencies in the presence of crack with varying depths (a) and locations (c).

The natural frequencies of first, second, and third modes for straight uniform and pretwisted long and short blades with crack depth of $a/h = 0.75$ are shown from Figs. 7, 8 and 9. In this analysis, crack depth was considered three-fourth of the thickness because crack propagation remains stable till 75% of its growth. From the results, it was observed that higher values of natural frequencies were recorded for the pretwisted short blades compared with the pretwisted long blades. It may be

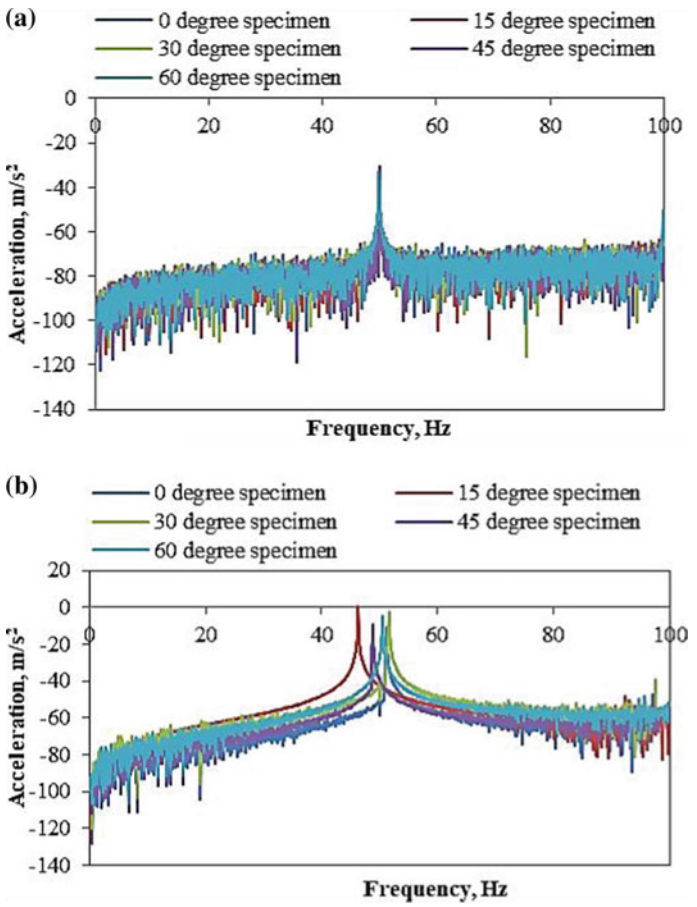

Fig. 6 **a** Frequency response plots for all uncracked pretwisted blade specimens. **b** Frequency response plots for all cracked pretwisted blade specimens

understood that LP turbine blades are more susceptive to resonance condition in a turbine having hundreds of blades with different lengths. It was also observed that lower values of first mode natural frequency are recorded for c/l values 0.1–0.3 in both pretwisted long and short blades as shown in Fig. 7a, b, respectively. Decrease in second mode natural frequency was recorded for c/l values of 0.4–0.7 as shown in Figs. 8a, b, and for third natural frequency, decrease in values were found at *c/l* of 0.8 and 0.9 as shown in Fig. 9a, b. So, it is evident from the results that the crack located near the fixed end of the blade may be detected from the first mode natural frequency analysis and crack located at the middle portion of the blade may be detected from the second mode natural frequency analysis. Third mode natural frequency analysis of the blade helps to detect the crack located at the tip of the blade.

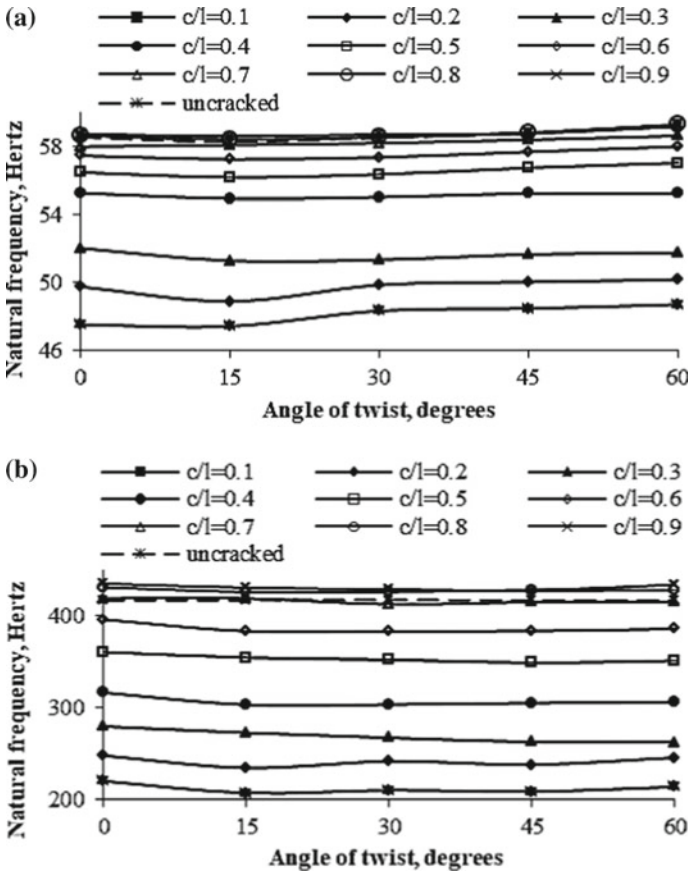

Fig. 7 **a** First mode natural frequencies of long blade model. **b** First mode natural frequencies of short blade model

From the study carried out in this paper, it was emphasized about the necessity of understanding the vibration behavior of the blades of turbine. Vibration analysis of pretwisted long and short blades helps to predict the presence of crack in turbine blades. Pretwisted long blades are having natural frequencies less than that of pretwisted short blades and the decrease of natural frequencies is also much less for long blades compared with short blades for same severity of crack at a given location.

5 Conclusions

The finite element modeling and analysis of the crack and its effect on turbine blades have been attempted in this paper. After modeling and validating turbine blades as

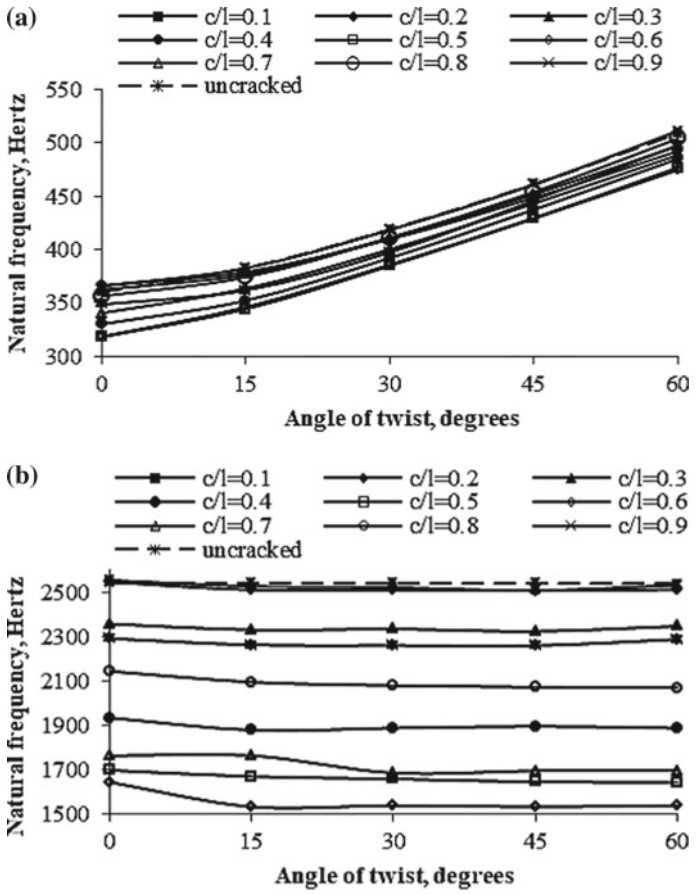

Fig. 8 **a** Second mode natural frequencies of long blade model. **b** Second mode natural frequencies of short blade model

pretwisted blades, natural frequencies were evaluated for varying crack parameters. Experimentation has been conducted for successful validation of theoretical results. From the results, it can be inferred that turbine blades can be modeled as a pretwisted uniform blade to study crack effects using natural frequencies. First mode natural frequency of the blade was decreased for the crack located near the root whereas second and third mode frequencies got decreased for the crack identified at mid position and tip of the blade respectively. The vibration response of turbine blade can be used to predict the condition of the blade based on the reduction in the frequency of a corresponding mode.

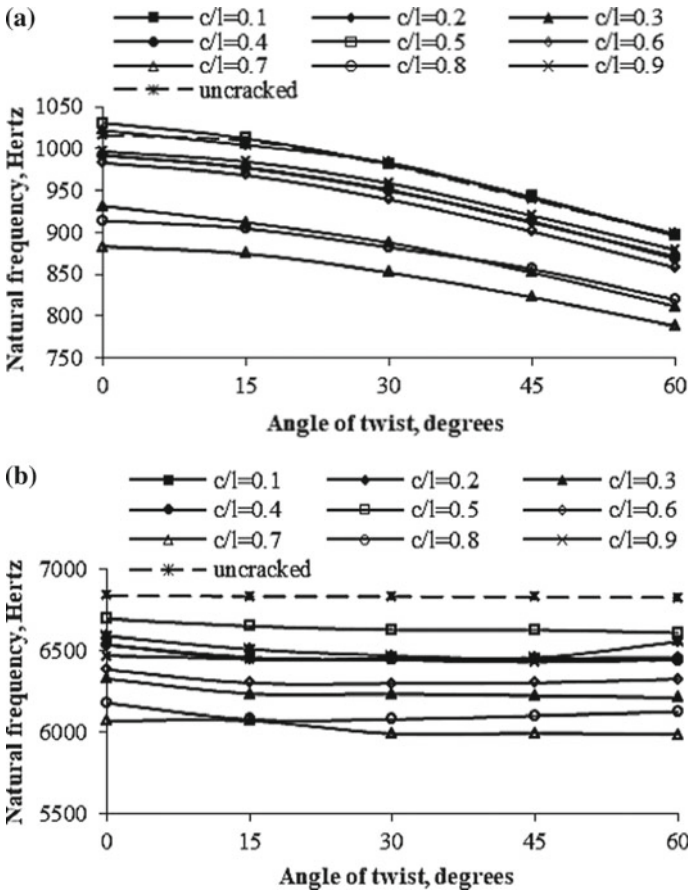

Fig. 9 **a** Third mode natural frequencies of long blade model. **b** Third mode natural frequencies of short blade model

References

1. Yoo, H.H., Park, J.H., Park, J.: Vibration analysis of rotating pre-twisted blades. Comput. Struct. **79**, 1811–1819 (2001)
2. Chung, J., Yoo, H.H.: Dynamic analysis of a rotating cantilever beam by using the finite element method. J. Sound Vib. **249**(1), 147–164 (2002)
3. Yoo, H.H., Pierre, C.: Modal characteristics of a rotating rectangular cantilever plate. J. Sound Vib. **259**(1), 81–96 (2003)
4. Huang, B.W.: Effect of number of blades and distribution of cracks on vibration localization in a cracked pre-twisted blade system. Int. J. Mech. Sci. **48**, 1–10 (2006)
5. Vadiraja, D.N., Sahasrabudhe, A.D.: Vibration analysis and optimal control of rotating pre-twisted thin-walled beams using MFC actuators and sensors. Thin-Walled Structures **47**, 555–567 (2009)
6. Chen, W.R.: On the vibration and stability of spinning axially loaded pre-twisted Timoshenko beams. Finite Elem. Anal. Des. **46**, 1037–1047 (2010)

7. Sinha, S.K., Turner, K.E.: Natural frequencies of a pre-twisted blade in a centrifugal force field. J. Sound Vib. **330**, 2655–2681 (2011)
8. Cheng, Y., Yu, Z., Yuan, Y.: Vibration analysis of a cracked rotating tapered beam using the p-version finite element method. Finite Elem. Anal. Des. **47**, 825–834 (2011)
9. Nguyen, K.V.: Mode shapes analysis of a cracked beam and its application for crack detection. J. Sound Vib. **333**, 848–872 (2014)
10. Akash, S., Harsha, S.P.: Vibration response analysis of last stage LP turbine blades for variable size of crack in root. In: 3rd International Conference on Innovations in Automation and Mechatronics Engineering, ICIAME, Procedia Technology, vol. 23, pp. 232–239 (2016)
11. Rezaei, M.M., Behzad, M., Moradi, H., Haddadpour, H.: Modal-based damage identification for the nonlinear model of modern wind turbine blade. Renew. Energy **94**, 391–409 (2016)
12. Segura, J.A., Castro, L., Rosales, I., Rodriguez, J.A., Urquiza, G., Rodriguez, J.M.: Diagnostic and failure analysis in blades of a 300 MW steam turbine. Eng. Fail. Anal. **82**, 631–641 (2017)
13. Zhao, W., Li, Y., Xue, M., Wang, P., Jiang, J.: Vibration analysis for failure detection in low pressure steam turbine blades in nuclear power plant. Eng. Fail. Anal. **84**, 11–24 (2018)
14. Material of construction, Low pressure turbine moving blades, Bharat Heavy Electrical Limited make, Unit-7 main turbine specifications, Stage-III National Thermal Power Corporation Limited, Ramagundam, BHEL manual (2004)

Outsourcing Strategies in a Two-Stage Supply Chain Model with Insufficient Production Capacity

Debabrata Das and Nirmal Baran Hui

Abstract This paper extends the work carried out by Sinha and Sharmah (Supply-chain coordination model with insufficient production capacity and option for outsourcing. Math. Comput. Model 46: 1442–1452, 2007) on supply chain coordination and outsourcing perspective in a two-stage supply chain. With suitable modification to their model, the conditions are derived in a different way for which outsourcing decision taken by supplier increases the profit of the retailer/supplier/system. Here, we aimed at exploring the impact of different prices, viz. retail price, outsourcing price, penalty cost, selling price of the supplier to the retailer over the system/supplier/retailer's profit, and on supplier's decision of outsourcing. The limiting values of these prices are also obtained with their illustrative problem.

Keywords Outsourcing · Modelling · Supply chain · Insufficient production

1 Introduction

Many companies choose the outsourcing strategy as a tool to rapidly cut cost and to overcome the stock-out condition to maintain goodwill with their customers. With its many benefits, it has some risks also. Many researchers like Gallego and Moon, Thomas and Griffin, Goyal and Gupta have worked in this field with different issues. The recent work in this paper is an extension and based on the work carried out by Sinha and Sharmah [1] on supply chain coordination and outsourcing perspective in a two-stage supply chain [1] where the supplier has lesser capacity to produce than the annual demand faced by the retailer. They analyzed the options of outsourcing as a tool to encounter the lost sale to maximize the profit of supplier, retailer or of the system. Their work was based on earlier work on production lot-sizing model by Goyal and Gopalakrishnan [2] under insufficient production capacity. Later, Handley

D. Das (✉)
Asansol Engineering College, Asansol, India
e-mail: d.das_2007@rediffmail.com

N. B. Hui
National Institute of Technology, Durgapur, India
e-mail: nirmal.hui@me.nitdgp.ac.in

L. Li et al. (eds.), *Advances in Materials and Manufacturing Engineering*, Lecture Notes in Mechanical Engineering, https://doi.org/10.1007/978-981-15-1307-7_24

and Benton [3] identified the critical management practices of the business outsourcing processes. They investigated the influences of strategic evaluation, contractual completeness, and relationship management practices.

Russell and Smith [4] worked on the reversing supply chain outsourcing and framed the sourcing decision in terms of global sourcing, near-sourcing, and in-sourcing. They discussed the conditions influencing outsourcing decision considering the risks and rewards from it. Zhou and Deng [5] modelled a hybrid system for manufacturing and remanufacturing quantities with the capacity constraint for maximizing corporate profit where the remanufacturing process was outsourced. However, they considered the fixed availability of recycled waste products instead of random. Chen and Xiao [6] built supply chain game models to investigate the effect of supply disruption risk and capacity allocation uncertainty on the outsourcing strategies and the retailer's order plans. They studied the impact of channel power on the efficiency of the supply chain.

Giri and Sarker [7] showed the improvement in profit through coordination and third-party logistics (TPL) outsourcing in a supply chain consisting of a monopolistic manufacturer, a TPL service provider (TPLSP), and multiple independent retailers. They considered buyback and revenue-sharing contracts in their model along with uncertain demand but sensitive to retail price and production disruption. Kim et al. [8] examined the operational decisions with tax consideration for structuring a global supply chain in a multinational firm (MNF). They suggested that tax-effect is to be considered with other factors, such as lead time, cost of labour and logistics, in designing a global supply chain. Yunlong and Tiaojun [9] developed two Stackelberg game models in a fresh agro-products supply chain with a supplier, retailer, and TPLSP. They examined the impacts of channel leadership on the pricing and service level decisions and profits with two-game scenarios.

Presently, we have extended the modelling work of [1] to focus on some significant issues on the outsourcing strategies. Our main objective is to explore the inter-relationship of different prices, viz. retail price, outsourcing price, penalty cost, and supplier's offer price to the retailer and how these prices influence the channel/supplier/retailer's profit, and the supplier's decision of outsourcing.

1.1 Notations

D—Annual demand, h_b—Retailer's holding cost, h_v—Supplier's holding cost C_b—Retailer's ordering cost, C_v—Supplier's setup cost, Π_b—Retailer's profit

g—Shortage/penalty cost of a supplier, Q—Lot-size of a retailer, Π_v—Supplier's profit

β—Fraction of annual demand that the supplier can produce, Π_{ch}—System profit

n_1—Integer multiple of retailer's lot-size, P_o—Outsourcing price, P_b—Retail price

P_v—The selling price of a supplier to the retailer, P—Unit production cost of manufacturer, and k_1—Ratio of the annual outsourced quantity to the annual shortage.

2 Without Outsourcing

The profits of retailer, supplier, and system in coordinated policy are derived in [1] using above notations and following integer policy of ordering as mentioned below. Here, the production-deficit from annual demand is not outsourced by the supplier (see [1], Eqs. (1), (4), and (7)). They considered penalty cost for the manufacturer only and penalty cost is incorporated in the manufacturer's profit equation.

$$\Pi_{\mathrm{b}} = \beta D(P_{\mathrm{b}} - P_{\mathrm{V}}) - \frac{\beta D C_{\mathrm{b}}}{Q} - \frac{Q h_{\mathrm{b}}}{2} \tag{1}$$

$$\Pi_{\mathrm{v}} = \beta D(P_{\mathrm{v}} - P) - \frac{\beta D C_{\mathrm{v}}}{n_1 Q} - \frac{h_{\mathrm{v}} Q(n_1 - 1)}{2} - D(1-\beta)g \tag{2}$$

$$\Pi_{\mathrm{ch}} = \beta D(P_{\mathrm{b}} - P) - \frac{\beta D C_{\mathrm{b}}}{Q} - \frac{\beta D C_{\mathrm{v}}}{n_1 Q} - \frac{Q h_{\mathrm{b}}}{2} - \frac{h_v Q(n_1 - 1)}{2} - D(1-\beta)g \tag{3}$$

The optimum value of Q for which only retailer's profit will be optimized, and can be obtained by differentiating Π_{b} with respect to Q. Here, $Q^e = \sqrt{\frac{2\beta D C_{\mathrm{b}}}{h_{\mathrm{b}}}}$ and it is identical with the economic order quantity (EOQ) of retailer. For maximizing the system profit, the optimum value of Q and n_1 can be obtained by taking the first derivative of Π_{ch} with respect to Q and n_1 separately and then equated to zero.

$$\frac{\partial \Pi_{\mathrm{ch}}}{\partial Q} = 0 \rightarrow Q^* = \sqrt{\frac{2\beta D(n_1 C_{\mathrm{b}} + C_{\mathrm{v}})}{n_1\{h_{\mathrm{b}} + h_{\mathrm{v}}(n_1 - 1)\}}} \tag{4}$$

$$\frac{\partial \Pi_{\mathrm{ch}}}{\partial n_1} = 0 \rightarrow n_1 = \sqrt{\frac{2\beta D C_{\mathrm{v}}}{h_{\mathrm{v}} Q^2}} \rightarrow (n_1 Q)^* = \sqrt{\frac{2\beta D C_{\mathrm{v}}}{h_{\mathrm{v}}}} \tag{5}$$

The optimum value of supplier's lot-size $(n_1 Q)^*$ is the same as that of its EOQ but here retailer's lot-size changes from its EOQ obtained by separate optimization of retailer's profit. By substitution of Q from above two expressions of Q and $n_1 Q$ we obtain-$n_1 = \sqrt{\frac{C_{\mathrm{v}}}{C_{\mathrm{b}}}\left(\frac{h_{\mathrm{b}}}{h_{\mathrm{v}}} - 1\right)}$. This expression is analogous to the expression of integer n_1 in integer policy of ordering in a two-echelon system, as $n_1 = \sqrt{\frac{k_1}{k_2} \cdot \frac{e_2}{e_1}}$ where (k_1, k_2) are the ordering costs and (e_1, e_2) are the echelon holding costs of upper and lower echelon, respectively (see [10], p. 937). In the illustrative problem [1], the following data were used from [2]: D = 10,000, β = 0.9, C_{v} = \$200, P_{v} = \$40, P = \$30, g = \$5/unit, and h_{v} = 20% of P = \$6. They also assumed C_{b} = 80, P_{b} = 45, and h_{b} = \$5 for the retailer. In non-coordinated situation, taking Q^* = 536.65 and n_1 = 2, system profit = 124029.7. In coordinated situation, taking Q^* = 774.6 and n_1 = 1, system profit = 125972.0

3 With Outsourcing

The expressions of profits of retailer, supplier, and the system in coordinated policy when supplier decides for outsourcing are given by them as follows.

$$\Pi_{\mathrm{b}}^{'} = [\beta D + k_1(D - \beta D)](P_{\mathrm{b}} - P_{\mathrm{v}}) - [\beta D + k_1(D - \beta D)]\frac{C_{\mathrm{b}}}{Q} - \frac{Qh_{\mathrm{b}}}{2} \tag{6}$$

$$\begin{aligned}\Pi_{\mathrm{v}}^{'} = {} & [\beta D + k_1(D - \beta D)]P_v - [\beta DP + \frac{\beta DC_{\mathrm{v}}}{n_1 Q} + \frac{h_{\mathrm{V}}}{2}(n_1 Q - Q) \\ & + k_1(D - \beta D)]P_{\mathrm{b}} + (1 - k_1)(D - \beta D)g]\end{aligned} \tag{7}$$

The notations for the profit of each member and system in case of without outsourcing are superscripted by a slash to indicate their profit here.

3.1 The Condition for Which Outsourcing Can Give More Profit to the Retailer

The difference of profit of the retailer with an outsourcing strategy to that of without outsourcing must be greater than zero.

$$\begin{aligned}&\Pi_{\mathrm{b}}' - \Pi_{\mathrm{b}} > 0 \\ &=> [\beta D(P_{\mathrm{b}} - P_{\mathrm{V}}) - \frac{\beta DC_{\mathrm{b}}}{Q} - \frac{Qh_{\mathrm{b}}}{2}] - [\beta D + k_1(D - \beta D)](P_{\mathrm{b}} - P_{\mathrm{v}}) \\ &\quad - [\beta D + k_1(D - \beta D)]\frac{C_{\mathrm{b}}}{Q} - \frac{Qhb}{2} > 0 \\ &=> Dk_1(1 - \beta)\left(P_b - P_V - \frac{C_b}{Q}\right) > 0[k_1 > 0, D > 0, (1 - \beta) > 0]\end{aligned} \tag{8}$$

Here, the condition is $P_{\mathrm{b}} - P_{\mathrm{v}} - C_{\mathrm{b}}/Q > 0$. ($C_{\mathrm{b}}/Q < 1$, normally a fractional quantity)

In their illustrative problem [1], they took $P_{\mathrm{v}} = 40$ and from above condition, it is $P_{\mathrm{v}} < 45(P_{\mathrm{b}}) - 1$, i.e. $P_{\mathrm{v}} < 44$. The condition is satisfied and so retailer profit increases in outsourcing compared to the case without outsourcing.

3.2 The Condition for Which Outsourcing Can Be a Better Option for the Supplier

$$\begin{aligned}
&\Pi_{\mathrm{v}}^{'} - \Pi_{\mathrm{v}} > 0 \\
&[\beta D + k_1(D - \beta D)]P_{\mathrm{v}} - \beta DP - \frac{\beta DC_{\mathrm{v}}}{n_1 Q} \\
&\quad - \frac{h_{\mathrm{V}}}{2}(n_1 Q - Q) - \mathrm{k}_1(D - \beta D)]P_{\mathrm{b}} \\
&\quad - (1 - k_1)(D - \beta D)g - \beta D(P_{\mathrm{v}} - P) + \frac{\beta DC_{\mathrm{v}}}{n_1 Q} \\
&\quad + \frac{h_{\mathrm{v}}(n_1 Q - Q)}{2} + D(1 - \beta)g > 0 \\
&\text{Or, } k_1(D - \beta D)P_{\mathrm{v}} - k_1(D - \beta D)P_0 + k_1(D - \beta D)g > 0 \\
&\Rightarrow \quad k_1 D(1 - \beta) \cdot (P_{\mathrm{v}} - P_0 + g) > 0 \\
&[k_1 > 0, D > 0, 0 < \beta < 1] \qquad (9)
\end{aligned}$$

So, here we find the condition as $P_{\mathrm{v}} - P_{\mathrm{o}} + g > 0$.

In their example [1], $P_{\mathrm{o}} = 47$, $g = 5$, and $P_{\mathrm{v}} = 40$. Here, the condition is $P_{\mathrm{v}} > 47 - 5$, i.e. 42, it is not satisfied and so supplier's profit decreases in outsourcing compared to its profit without outsourcing, and the condition remains unfulfilled for $P_{\mathrm{o}} = 52$ also.

3.3 The Condition for Which Outsourcing to Be a Better Option for the System

$$\begin{aligned}
\Pi_{\mathrm{ch}}^{'} - \Pi_{\mathrm{ch}} &= \left(\Pi_{\mathrm{b}}^{'} + \Pi_{\mathrm{v}}^{'}\right) - (\Pi_{\mathrm{b}} + \Pi_{\mathrm{v}}) = \left(\Pi_{\mathrm{b}}^{\prime} - \Pi_{\mathrm{b}}\right) + \left(\Pi_{\mathrm{v}}^{'} - \Pi_{\mathrm{v}}\right) \\
&= \text{Eq. (9)} + \text{Eq. (10)} = k_1(1 - \beta)D\left[P_{\mathrm{b}} - \frac{C_{\mathrm{b}}}{Q} - P_{\mathrm{o}} + g\right] > 0 \\
&\quad [k_1 > 0, D > 0, 0 < \beta < 1] \qquad (10)
\end{aligned}$$

So the condition is $P_{\mathrm{b}} - C_{\mathrm{b}}/Q - P_{\mathrm{o}} + g > 0$. For the illustrative problem in [1], the condition is $P_{\mathrm{o}} < 45 + 5 - 1$, i.e. 49. So, when $P_{\mathrm{o}} = 47$, outsourcing becomes a better option for improving the profit of the system but when $P_{\mathrm{o}} = 52$, the condition is unsatisfied, and so the profit of the system with outsourcing becomes lesser than the system profit earned without outsourcing.

Table 1 Condition and price-limits for outsourcing to be more profitable

Cases	General condition	Price limit	Influence of $k_1 (k_1 > 0)$
For the retailer	$P_b - P_v - (C_b/Q) > 0$	$P_v < 44$	No
For the supplier	$P_v - P_o + g > 0$	$P_v > 42$	No
For the system	$P_b - (C_b/Q) - P_o + g > 0$	$P_o < 49$	No

In above, all three cases, the condition is independent of the fraction of shortage that is outsourced (k_1) as long as the manufacturer chooses outsourcing strategy ($k_1 > 0$).

4 Results and Discussion

The conditions derived above for which outsourcing gives improved profit and the limit of different prices obtained with the example problem are presented in Table 1.

Supplier's decision for outsourcing depends only on retail price, outsourcing price, and penalty cost. Lot-size and other inventory-related cost (ordering/holding cost) have negligible influence over it. When the other prices internal to the system are known, it depends on the outsourcing price. After that whether retailer/supplier/both will gain more profit in outsourcing, compared to their profit without outsourcing, depends on the selling price of the supplier to the retailer (P_v). If P_v is decided between 42 and 44, both members of the supply chain will earn more profit. The improvement in profit is proportional to the fraction outsourced (k_1). It means that under optimized profit condition, either $k_1 = 0$, i.e. outsourcing strategy is not applied, or $k_1 = 1$, i.e. total production-deficit from annual demand is outsourced.

5 Conclusion

In this paper, the limiting values of important prices in outsourcing and impact of these prices along with lot-sizes, quantity outsourced, and other inventory-related prices on the improved profit condition of supplier/retailer/system are found out. These are not deduced explicitly by the previous researchers. The research work presented here has a huge managerial implication as this price analysis straightway directs the top-level managers when they have to take the crucial strategic decision of outsourcing for improving profit. Another managerial aspect is price fixing whose purpose is to coordinate pricing for the mutual benefit of the traders. For example, manufacturers and retailers may set a retail price, a minimum sales price. The research

work further can be extended to a large supply chain with more than two members, with/without demand uncertainty, with/without price-sensitive demand.

References

1. Sinha, S., Sarmah, S.P.: Supply-chain coordination model with insufficient production capacity and option for outsourcing. Math. Comput. Model. **46**, 1442–1452 (2007)
2. Goyal, S.K., Gopalakrishnan, M.: Production lot sizing model with insufficient production capacity. Prod. Plan. Control Manag. Oper. **7**(2), 222–224 (1996)
3. Handley, S.M., Benton Jr., W.C.: Unlocking the business outsourcing process model. J. Oper. Manage. **27**, 344–361 (2009)
4. Russell, R.S., Smith, M.: Reeling in outsourcing: evaluating supply chain risk and reward under economic uncertainty. J. Serv. Sci. **2**(1) (2009)
5. Zhou, Y., Deng, M.: Research on capacity-constrained manufacturing/remanufacturing hybrid system with outsourcing. Appl. Mech. Mater. **423–426**, 2166–2169 (2013)
6. Chen, K., Xiao, T.: Outsourcing strategy and production disruption of a supply chain with demand and capacity allocation uncertainties. Int. J. Prod. Econ. **170**(A), 243–257 (2015)
7. Giri, B.C., Sarker, B.R.: Improving performance by coordinating a supply chain with third-party logistics outsourcing under production disruption. Comput. Ind. Eng. **103**(C), 168–177 (2017)
8. Kim, B., Park, K.S., Jung, S.Y., Park, S.H.: Offshoring and outsourcing in a global supply chain: Impact of the arm's length regulation on transfer pricing. Euro. J. Oper. Res. **266**(1), 88–98 (2018)
9. Xiao, Y.T.: Pricing and cold-chain service level decisions in a fresh agri-products supply chain with logistics outsourcing. Comput. Ind. Eng. **111**, 56–66 (2017)
10. Hillier F., Lieberman G.: Introduction to Operations Research. MGH (McGraw-Hill series in industrial engineering and management science), ISBN: 978-0-07-133346-7 (2001)

Optimization of Machining Parameters to Minimize Surface Roughness During End Milling of AISI D2 Tool Steel Using Genetic Algorithm

Ravikumar D. Patel and Sanket N. Bhavsar

Abstract Today's dies and molds making industries demand for milling of hardened tool steel with less production time and requirement of excellent quality. AISI D2 tool steel has attained high hardness and excellent corrosion resistance at elevated temperature. The experiments were conducted on hardened D2 tool steel using AlCrN coated end mill tool based on response surface methodology (RSM). Central composite design (CCD) method was implemented to design 30 experiments. Analysis of variance (ANOVA) was used to verify adequacy of model. The derived model is utilized to analyze and interaction effect of the input milling parameters with surface roughness. Genetic algorithm was used to optimize of machining parameters to obtain best surface quality on AISI D2 tool steel during milling process. Lowest surface roughness was measured 0.08 after applying genetic algorithm. Optimized value from genetic algorithm was also validated experimentally.

Keywords AISI D2 tool steel · AlCrN coated tool · RSM · ANOVA · GA

1 Introduction

Hard tool steel materials are used to making of forming and cutting dies and molds due to its extremely high strength and hardness [1]. Milling of hardened tool steel is very difficult task due to high wear on tool and demand of superior surface finish [2] . Complexity of end milling operation because of uneven behavior of cutting forces [3].

Coating of AlCrN in end mill tool perform excellent during milling of hardened steel due to its excellent wear resistance and low adhesion strength [4]. Kovalev et al. [5] investigated machining of hard to cut material using TiN-based coated tool. In Al and Cr bond coating, the Cr atom is donor and Al atom is acceptor. Comparison of AlCrN coated and uncoated tool performance was done [6]. AlCrN-based coating has been analyzed with respect to residual stress, structure and hardness by Bourhis

R. D. Patel (✉)
K.D.Polytechnic, Gujarat Technological University, Patan, Gujarat, India
e-mail: raviengineer2007@gmail.com

S. N. Bhavsar
Mechatronics Engineering Department, GCET, V.V. Nagar, Anand, Gujarat, India

L. Li et al. (eds.), *Advances in Materials and Manufacturing Engineering*, Lecture Notes in Mechanical Engineering, https://doi.org/10.1007/978-981-15-1307-7_25

et al. [7]. Fox-Rabinovich et al. [8] found AlCrN coated end mill has more tool life as well as it exhibited better performance compare than AlTiN coated tool due to high cracking resistance with respect to temperature. W. Kalss et al. [9] reported that AlCrN coating tool has excellent oxidation resistance at 1100 °C temperature compare than cemented carbide tool which has high oxidation problem at elevated temperature.

D-grade tool steels with high carbon and high chromium are used in various application [10]. Nowadays, the use of hardened D2 tool steel is highly demand due to its superior mechanical properties. Machining of hardened D2 tool steel is most difficult machining due to its excellent hardness at elevated temperature [11]. Saedon et al. [12] investigated tool life models of AlTiN coated micro-mill tool during milling of hardened D2 tool steel (62 HRC) under dry condition by using response surface methodology CCD method. They observed that cutting speed was main influence parameters for tool life. An experimental and theoretical analysis was done on heat flow during milling of various hardened tool steels by using coated tool in cold air, compressed air and dry air condition by Lincoln [13]. Vinayak et al. [14] analyzed that experimental investigation of D2 tool steel by using of TiAlN coated end mill tool using response surface methodology. Palanisamy et al. [15] explained optimization methods in milling process using genetic algorithm. Sidda reddy et al. [16] optimized surface roughness during end milling of P20 hard steel using genetic algorithm with response surface methodology. Alrashdan et al. [17] optimized two different objective functions like surface roughness as well as energy consumption during end milling of AISI D2 tool steel by ceramic end mill tool using genetic algorithm.

From the review of previous research work, no work was done on machining of hardened D2 steel using AlCrN coated end mill tool. In this research work, hardened D2 steel was machined by AlCrN coated end mill tool using response surface methodology CCD method. ANOVA was used to evaluate the relationship between output response (surface roughness) and input machining parameters. Genetic algorithm was used to optimize the input machining parameters with respect to output response.

2 Experimental Details

A number of experiments were carried out on Jyoti Make P10 CNC vertical milling machine with maximum 10,000 rpm spindle speed. AISI D2 tool steel was machined using Walter made (Ø10 mm AlCrN coated 4 flute) flat end mill tool under dry cutting condition. Cutting speed 50–200 m/min, feed 50–800 mm/min, depth of cut 0.1–1 mm and width of cut 2–10 mm were taken as input parameters for experimental work.

RSM is an superior tool for the development of statistical model in terms of various input milling parameters and their interaction affecting on responses [18]. Response

surface methodology CCD method was used for design of experiments. 30 numbers of experiments were done as shown in Table 1.

Table 1 Design of experiment by response surface methodology

Run	C S (m/min)	FEED (mm/min)	DOC (mm)	WOC (mm)	SR (μm)
1	125	425	1	6	0.51
2	87.5	612.5	0.775	4	0.72
3	162.5	612.5	0.325	8	0.32
4	162.5	612.5	0.325	4	0.25
5	87.5	612.5	0.325	4	0.49
6	87.5	237.5	0.775	8	0.39
7	125	425	0.55	6	0.26
8	87.5	612.5	0.775	8	0.77
9	125	50	0.55	6	0.19
10	125	425	0.55	6	0.26
11	50	425	0.55	6	0.68
12	125	425	0.55	6	0.25
13	162.5	237.5	0.775	4	0.29
14	125	425	0.55	6	0.26
15	87.5	612.5	0.325	8	0.57
16	125	425	0.55	10	0.63
17	87.5	237.5	0.775	4	0.38
18	162.5	237.5	0.325	4	0.18
19	162.5	237.5	0.325	8	0.2
20	125	425	0.55	6	0.26
21	125	425	0.55	2	0.63
22	162.5	612.5	0.775	8	0.61
23	87.5	237.5	0.325	8	0.31
24	162.5	237.5	0.775	8	0.37
25	125	425	0.1	6	0.20
26	200	425	0.55	6	0.51
27	125	425	0.55	6	0.26
28	87.5	237.5	0.325	4	0.25
29	125	800	0.55	6	0.62
30	162.5	612.5	0.775	4	0.59

3 Result and Discussion

Figure 1a shows that surface roughness is reduced with increasing of cutting speed due to reduce the cutting force and surface roughness is increased after 125 m/min due to formation of built-up edge [19]. From Fig. 1b, surface finish is reduced with increasing of feed due to higher thrust force and vibration [15]. Surface finish is reduced with increasing of depth of cut due to high thrust force as shown in Fig. 1c [14].

It has been observed by increasing the width of cut from 4 to 6 mm, surface roughness is improved but after 6 mm surface roughness is increased. Higher surface finish was observed near 6 mm as shown in Fig. 1d.

Reading of surface roughness was recorded by Mitutoyo Surftest SJ 410 as shown in Table 1. ANOVA was implemented to analyze data using design expert software.

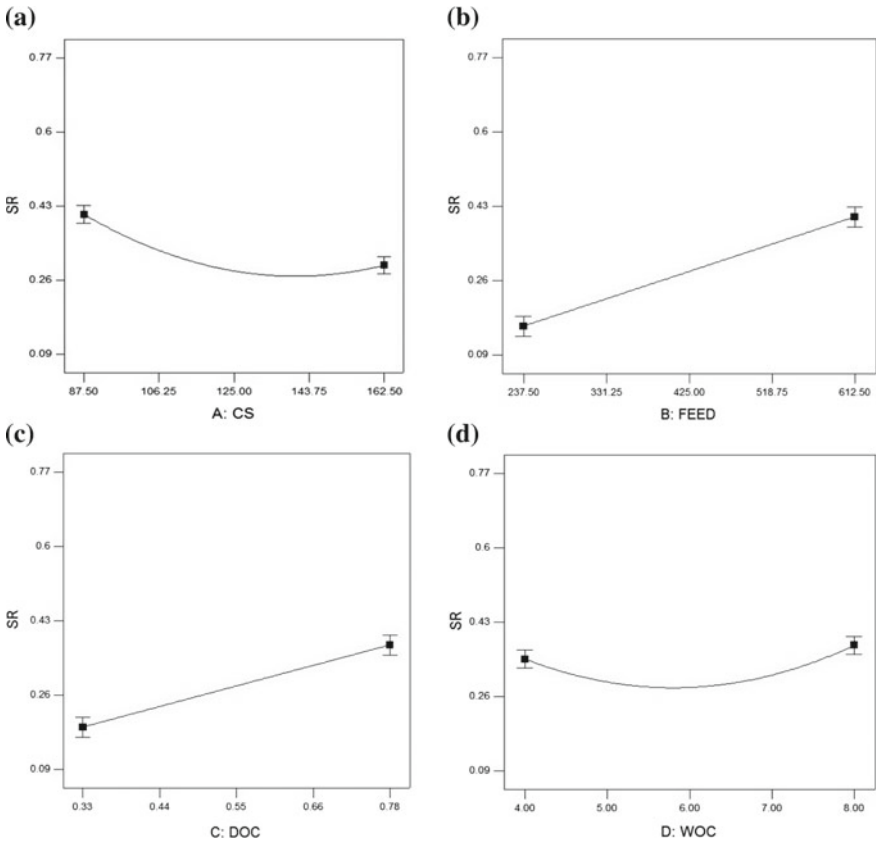

Fig. 1 Relationship between **a** surface roughness (SR) versus cutting speed(CS) **b** SR versus feed **c** SR versus DOC **d** S.R. versus WOC

By removing insignificant terms, regression equation of quadratic model was derived for surface roughness as shown in following Eq. (1);

$$\begin{aligned}\textbf{Surface Roughness} = {} & 1.70308 - 0.013414 * \mathrm{CS} \\ & + 0.0000827407 * \mathrm{FEED} - 0.39088 * \mathrm{DOC} \\ & - 0.22872 * \mathrm{WOC} - 0.00000435556 * \mathrm{CS} * \mathrm{FEED} \\ & + 0.002000 * \mathrm{CS} * \mathrm{DOC} - 0.00000833333 * \mathrm{CS} * \mathrm{WOC} \\ & + 0.000844444 * \mathrm{FEED} * \mathrm{DOC} + 0.00000833333 * \mathrm{FEED} * \mathrm{WOC} \\ & - 0.00972222 * \mathrm{DOC} * \mathrm{WOC} + 0.0000505926 * \mathrm{CS}^2 \\ & + 0.000000672593 * \mathrm{FEED}^2 \\ & + 0.22016 * \mathrm{DOC}^2 + 0.019974 * \mathrm{WOC}^2 \end{aligned} \quad (1)$$

The objective in this research work is to minimize surface roughness. Above mathematical model is developed to obtain minimum surface roughness, optimum combination of various machining parameters like CS, f, DOC and WOC can be found out using genetic algorithm. Feed rate is significant parameters for surface roughness followed by the depth of cut, cutting speed and width of cut.

4 Genetic Algorithm

Genetic algorithm is a mechanized pursuit and dependent on the mechanics of common hereditary qualities. For enhancing successive generations, survival tries to upcoming generation [20].

Each string with infinite length is formed by each bit called a gene. Selection of strings for further study is called population. Population size: 20, generation: 500, selection operator: Rank order, cross over operator: Single point, crossover probability: 0.85, Mutation probability: 0.15, fitness parameters: Surface roughness.

After applying genetic algorithm on derived equation using MATLAB, surface roughness value was obtained 0.08022 μm (as shown in Fig. 2) with C.S. 145.86 m/min, feed 268 mm/min, DOC 0.1 mm and WOC 5.705 mm.

Table 2 shows the comparison of measured value and value after applying genetic algorithm. Lowest surface roughness was measured as 0.18 μm during end milling of hardened D2 tool steel using AlCrN coated tool. Result was validated with experimentally and found the following readings; surface roughness was obtained using C.S. 145 m/min, feed 268 mm/min, DOC 0.1 mm and WOC 6 mm.

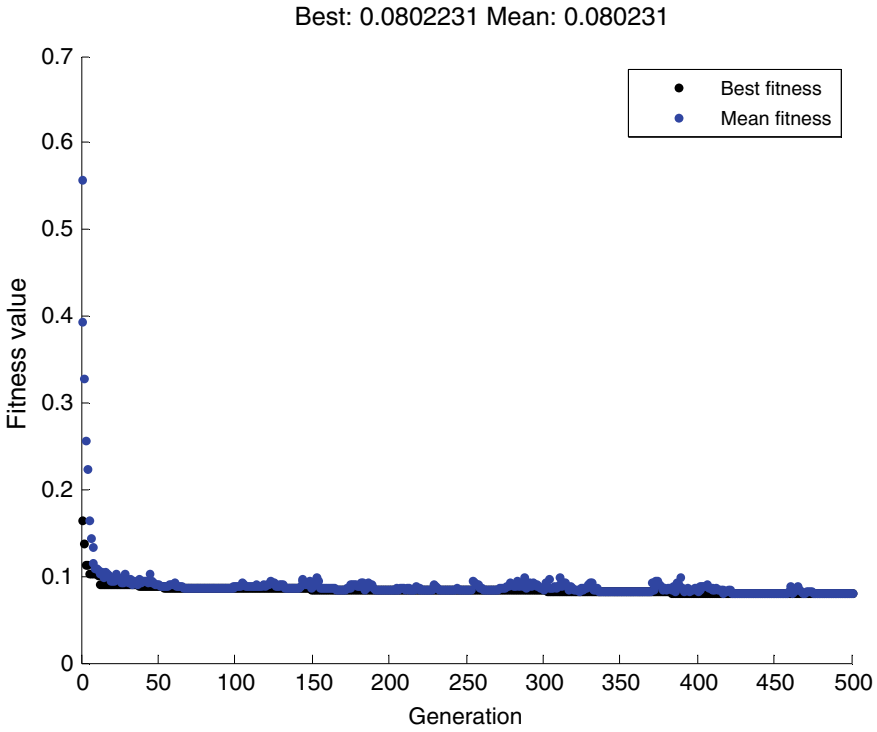

Fig. 2 Fitness value versus generation graph for optimization of surface roughness

Table 2 Comparision of measured value and optimized value of surface roughness

	CS	FEED	DOC	WOC	S.R.
Lowest value from exp table	162.5	237.5	0.325	4	0.18
After GA	145.86	268	0.1	5.705	0.08022
Measured value	145	268	0.1	6	0.12

5 Conclusion

Hard milling of hardened D2 tool steel by AlCrN coated tool was investigated by experimental investigation using response surface methodology. The effect of various input milling machine parameters has been analyzed during machining of AISI D2 tool steel with AlCrN coated tool using response surface methodology CCD method.

The following conclusions can be drawn from this investigation:

- Feed rate is significant parameters for surface roughness followed by the depth of cut, cutting speed and width of cut.
- The quadratic model is fitted for surface roughness.

- After applying of genetic algorithm, 0.08 μm surface roughness value is found using MATLAB software which is also validated by experimentally and found 0.12 μm surface roughness by using cutting speed 145 m/min, feed 268 mm/min, depth of cut 0.1 mm and width of cut 6 mm.

References

1. Durakbasa, M.N., Akdogan, A., Vanli, A.S., Bulutsuz, A.G.: Optimization of end milling parameters and determination of the effects of edge profile for high surface quality of AISI H13 steel by using precise and fast measurements. Measurement **68**, 92–99 (2015)
2. Bergmann, B., Denkena, B., Kohler, J.: Development of cutting edge geometries for hard milling operations. CIRP J. Manuf. Sci. Technol. **8**, 43–52 (2015)
3. Abrão, A.M., José, L.S.R.: Milling of annealed and hardened tool steel with coated carbide and cermet inserts. Int. Congr. Mech. Eng. (2007)
4. Liew, W.Y.H.: Low-speed milling of stainless steel with TiAlN single-layer and TiAlN/AlCrN nano-multilayer coated carbide tools under different lubrication conditions. Wear **269**(7–8), 617–631 (2010)
5. Veldhuis, S., Kovalev, A.I., Wainstein, D.L., Rashkovskiy, A.Y., Fox-rabinovich, G.S., Yamamoto, K.: Impact of Al and Cr alloying in TiN-based PVD coatings on cutting performance during machining of hard to cut materials. Vaccum **84**(1), 184–187 (2010)
6. Yueh-jaw Lin, A.A., Fang, Y.: Wear progressions and tool life enhancement with AlCrN coated inserts in high-speed dry and wet steel lathing. Wear **264**, 226–234 (2008)
7. Le Bourhis, E., Goudeau, P., Staia, M.H., Carrasquero, E., Puchi-cabrera, E.S.: Mechanical properties of hard AlCrN-based coated substrates. Surf. Coat. Technol. **203**(19), 2961–2968 (2009)
8. Parkinson, R., Fox-rabinovich, G.S., Beake, B.D., Endrino, J.L., Veldhuis, S.C.: Effect of mechanical properties measured at room and elevated temperatures on the wear resistance of cutting tools with TiAlN and AlCrN coatings. Surf. Coat. Technol. **200**, 5738–5742 (2006)
9. Kalss, J.L.E.W., Reiter, A., Derflinger, V., Gey, C.: Modern coatings in high performance cutting applications. Int. J. Refract. Metals Hard Mater. **24**, 399–404 (2006)
10. Aslan, E., Camuscu, N.: A comparative study on cutting tool performance in end milling of AISI D3 tool steel. J. Mater. Process. Technol. **170**, 121–126 (2005)
11. Rao, M.S., Venkaiah, N.: Parametric optimization in machining of Nimonic-263 alloy using RSM and particle swarm optimization. Procedia Mater. Sci. **10**, 70–79 (2015)
12. Saad, N.H., Saedon, J.B., Soo, S.L., Aspinwall, D.K., Barnacle, A.: Prediction and optimization of tool life in micromilling AISI D2 (~62 HRC) hardened steel. Procedia Eng. **41**, 1674–1683 (2012)
13. Rodrigues, A.R., Brandao, L.C., Coelho, R.T.: Experimental and theoretical study of workpiece temperature when end milling hardened steels using (TiAl) N-coated and PcBN-tipped tools. J. Mater. Process. Technol. **199**, 234–244 (2008)
14. Gaitonde, V.N., Karnik, S.R., Maciel, C.H.A., Rubio, J.C.C., Abrão, A.M.: Machinability evaluation in hard milling of AISI D2 steel. Mater. Res. **19**(2), 360–369 (2016)
15. Palanisamy, P., Rajendran, I., Shanmugasundaram, S.: Optimization of machining parameters using genetic algorithm and experimental validation for end-milling operations. Int. J. Adv. Manuf. Technol. **32**, 644–655 (2007)
16. Kumar, J.S., Reddy, B.S., Reddy, K.V.K.: Optimization of surface roughness in CNC end milling using response surface methodology and genetic algorithm. Int. J. Eng. Sci. Technol. **3**(8), 102–109 (2011)
17. Alrashdan, A., Bataineh, O., Shbool, M.: Multi-criteria end milling parameters optimization of AISI D2 steel using genetic algorithm. Int. J. Adv. Manuf. Technol. (2014)

18. Sharma, S.: Optimization of machining process parameters for surface roughness of Al-composites. J. Inst. Eng. India Ser. C **94**, 327–333 (2013)
19. Loftus, M., Fan, X.: The influence of cutting force on surface machining quality. Int. J. Prod. Res. **45**(4), 899–911 (2007)
20. Goldberg, D.E.: Genetic Algorithms in Search, Optimization And Machine Learning. Addison-Wesley Publisher, New York (1989)

Robotic Assembly Sequence Generation Using Improved Fruit Fly Algorithm

Gunji Bala Murali, B. B. V. L. Deepak, Bibhuti Bhusan Biswal and Y. Karun Kumar

Abstract Assembly plays a key role in manufacturing, which requires effective assembly sequence to upsurge product quality. In early 90s investigators started research on assembly sequence planning (ASP) problem to obtain the best sequences for the industrial assemblies. At the starting stages, mathematical models are applied to generate feasible sequences. Further, researchers applied artificial intelligence (AI) techniques to achieve the optimal assembly sequences because of its less search space consumption during execution. Meanwhile, few of the researchers developed computer-aided design (CAD)-based and knowledge-based approaches to generate the best sequences, which consume more search space during execution of the algorithm. Keeping the above considerations in mind and the advantages with artificial intelligence techniques, in this paper, fruit fly algorithm with improvement is proposed to generate optimal robotic assembly sequences. This algorithm is developed mainly based on how fruit fly can identify the fruits based on smell. The developed algorithm is applied to the different industrial products to check the enactment of the algorithm.

Keywords Fruit fly algorithm · Assembly sequence generation · Artificial intelligence techniques · Computer-aided design (CAD)

G. B. Murali (✉)
Vellore Institute of Technology, Vellore 632014, Tamilnadu, India
e-mail: bmgunji@gmail.com

B. B. V. L. Deepak · B. B. Biswal
National Institute of Technology, Rourkela 769008, India
e-mail: deepak.bbvl@gmail.com

B. B. Biswal
e-mail: Bibhutibiswal@gmail.com

Y. Karun Kumar
Raghu Engineering College, Visakhapatnam 531162, India
e-mail: karun.kumar.y2k@gmail.com

L. Li et al. (eds.), *Advances in Materials and Manufacturing Engineering*, Lecture Notes in Mechanical Engineering, https://doi.org/10.1007/978-981-15-1307-7_26

1 Introduction

In manufacturing, assembly holds solely 25–30% of overall cost of the final product. To have an operative assembly, the best assembly sequence is required. Continues efforts have kept by the investigators to attain best assembly sequences to reduce the overall cost process time of the manufacturing.

Assembly is not simply connection of the parts one-by-one, it requires many aspects like assembly setup time, fixture arrangement, work cell arrangement and assembly sequence [1]. Achieving an optimal sequence is a difficult task as ASP is a nondeterministic probability (NP) hard combinatorial problem.

In the initial stages of the ASP problem, researchers like Wilson and Latombe [2] have applied mathematical models to attain the feasible sequences. As these methods use the CAD data for generating the optimal sequences, it consumes more space for storing the information related to the assembly especially for more part assemblies. Moreover, these models are failed to attain the cost-effective assembly sequences.

Later researchers shifted the interest towards soft computing techniques like genetic algorithm (GA), ant colony optimization (ACO) algorithm, particle swarm optimization (PSO) and so on because of easiness in implementation for ASP problem. In soft computing techniques, most of the researchers are used GA to obtain the optimal assembly sequences due to the convergence of the solution during execution [3, 4].

Apart from GA, the other algorithms like ACO and PSO are given equal importance in solving the ASP problem.

Falli and Dini [5] proposed ACO algorithm by considering directional changes as the fitness function to generate optimal assembly sequences. This algorithm will work mainly on the shortest path traveled by the ants in search of food based on the pheromone deposition of the ants. Wang et al. [6] considers the assembly is the reverse of disassembly concept to generate the best assembly sequences.

By overcoming the demerits of the individual algorithms to solve the ASP problem, hybrid algorithms (HA) have been developed [7]. These HA algorithms are well suited for intricate products, but these algorithms require more search time as compared to the individual algorithms for smaller part products.

Apart from these regular algorithms, Gunji et al. [8] introduces the assembly subset concept to generate the best assembly sequences using teaching-learning-based optimization (TLBO) algorithm. As this algorithm achieves the optimal assembly sequences in less time, but it requires a skilled person to execute.

Keeping the advantages of soft computing techniques in view, in this paper, fruit fly algorithm with improvement has been proposed to obtain the optimal robotic assembly sequences. This algorithm is developed mainly based on how fruit fly can identify the fruits based on smell. The developed algorithm is applied to ‘19’ parts industrial product to check the enactment of the algorithm.

2 Improved Fruit Fly (IFF) Algorithm

In this section, the improved fruit fly algorithm is proposed to achieve optimal robotic assembly sequences by using robot hand directional changes as the fitness equation for the pulley block assembly. The algorithm works based on the concept, identification of ripened or fermenting of fruits during summer by fruit flies through their sensing and perception characteristics. The visual senses and perceptions of the fruit flies are better than the other species. The individual fruit fly uses its sensitive vision to fly in the direction of the target by sampling the different scents that are present in the surroundings. As the individual fly identifies the best position that is nearer to the target, it directs the flocking location of the flies closer to the food.

Through the iterative evolution, the fly swarm comes closer and closer to the target until it reaches to the fruits. In general fruit fly algorithm, initialization of the fruit fly is considered by assigning the random position in plane consisting of food.

In the existing algorithm, the algorithm uses some random positions based on population size to find the local best position by calculating the smell concentration, which may lead sometimes to a redundant solution.

So, in the improved fruit fly algorithm instead of generating random positions to find local best, a range has been considered to generate positions of the fruit fly to find local best. The range is defined by a fly angle of fruit fly from initialization position of fruit fly. The range is decided by considering the food position region as the 2D plane with the coordinate system.

The detailed proposed methodology is explained in Fig. 1 with the flow chart. In the proposed methodology we are considering the minimization of robot hand direction changes (RHDC) as a suitability equation to assess the eminence of the sequence. The fitness equation in terms of robot hand direction changes is considered in Eq. (1).

$$\sum_{i=1}^{p} \mathrm{RHDC}_i \tag{1}$$

where 'p' represents the part number of the assembly

'RHDC' represents robotic hand directional changes during assembly.

Improved fruit fly algorithm is applied to the block assembly to generate optimal assembly sequences. A detailed proposed methodology is shown in Fig. 1.

In the proposed algorithm, assembly predicates are to be checked with randomly generat400000ed population size (assembly sequences) to check the viability of the sequence. Estimate the directional changes using the fitness equation stated in Eq. (1) to generate optimal assembly sequences. Run the algorithm for the anticipated number of iterations to acquire the best assembly sequences.

The main benefit of this algorithm is, it is very simple to implement the algorithm as the main algorithm is based on two equations: one equation is for the initialization of direction (x_i, y_i) and other equation is for the calculation of the distance (D_i) between the initial random positions to the next updated position for searching the fruit by individual fruit fly. The equations are as follows:

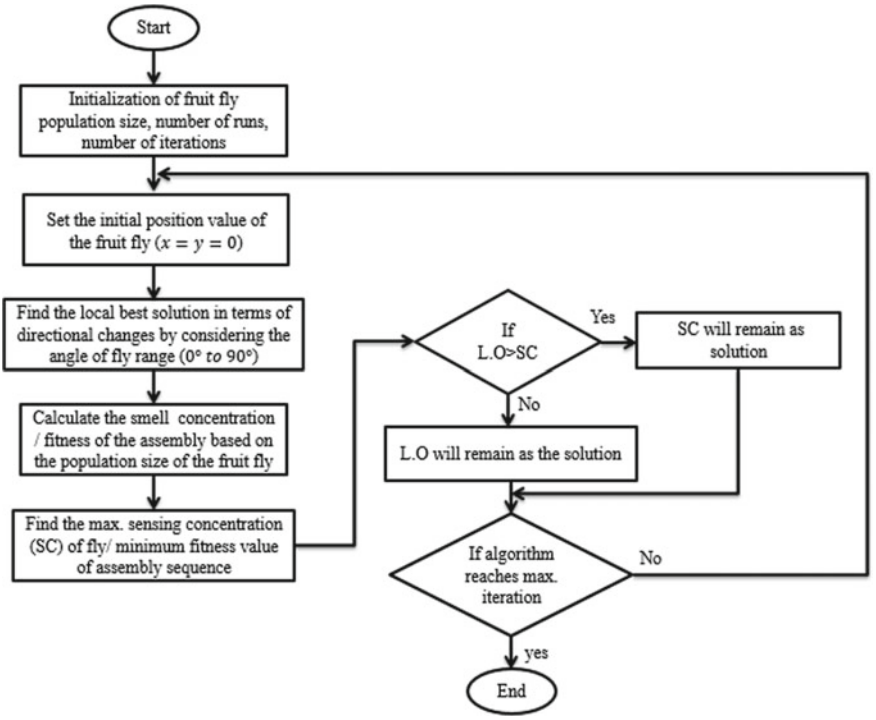

Fig. 1 Represents the improved fruit fly algorithm

$$x_i = x_{\text{position}} + \text{random value} \tag{2}$$

$$y_i = y_{\text{position}} + \text{random value} \tag{3}$$

$$D_i = \sqrt{x_i^2 + y_i^2} \tag{4}$$

Smell concentration (SC_i) is used to substitute in the fitness equation is as follows:

$$\text{SC}_i = \frac{1}{D_i} \tag{5}$$

3 Results and Discussion

In this section, a nineteen-part block assembly considered in Fig. 2 with part names shown in Table 1 to test the performance of the algorithm to generate optimal assembly sequences.

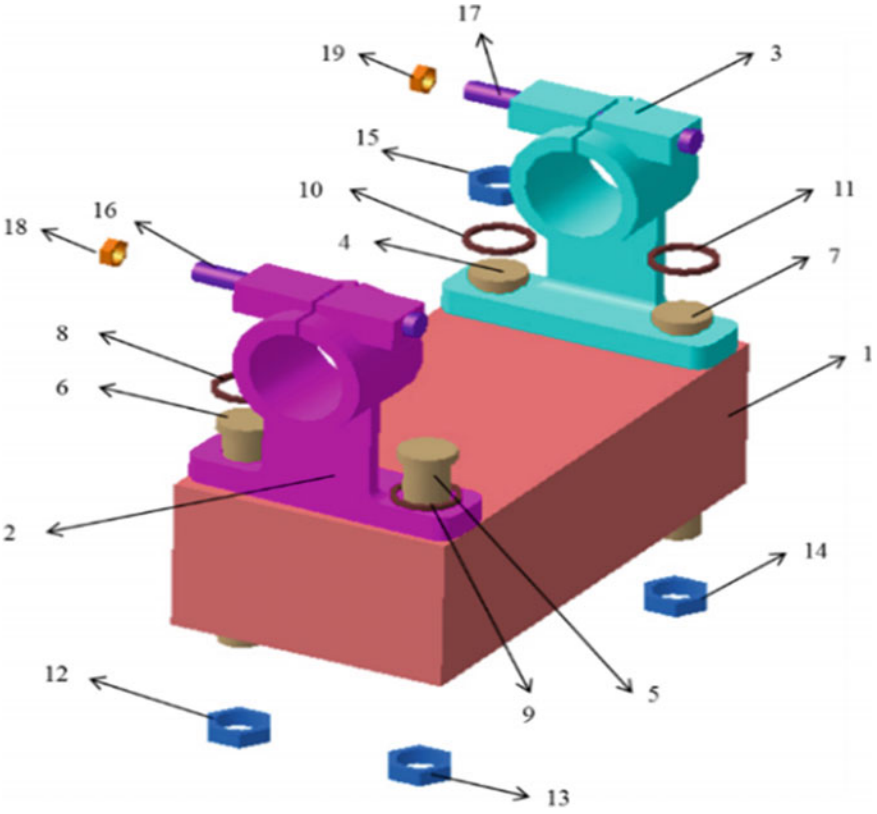

Fig. 2 Detailed block assembly

Table 1 List of part names

S. no	Name of the part
1	Cover
2	Base
3	Motor
4	Motor screws
5	Cover screws
6	Bushings (2 nos.)
7	Grommet (2 nos.)
8	Set screw
9	Standoffs (2 nos.)
10	Sensor
11	End plate
12	End plate screws

Liaison data

	1	2	3	4	5	6	7	8	9	10	11	12	13	14	15	16	17	18	19
1	0	1	1	1	1	1	1	0	0	0	0	1	1	1	1	0	0	0	0
2	1	0	0	0	1	1	0	1	1	0	0	0	0	0	0	1	0	1	0
3	1	0	0	1	0	0	1	0	0	1	1	0	0	0	0	0	1	0	1
4	1	0	1	0	0	0	0	0	0	1	0	0	0	0	1	0	0	0	0
5	1	1	0	0	0	0	0	0	1	0	0	0	1	0	0	0	0	0	0
6	1	1	0	0	0	0	0	1	0	0	0	1	0	0	0	0	0	0	0
7	1	0	1	0	0	0	0	0	0	0	1	0	0	1	0	0	0	0	0
8	0	1	0	0	0	1	0	0	0	0	0	0	0	0	0	0	0	0	0
9	0	1	0	0	1	0	0	0	0	0	0	0	0	0	0	0	0	0	0
10	0	0	1	1	0	0	0	0	0	0	0	0	0	0	0	0	0	0	0
11	0	0	1	0	0	0	1	0	0	0	0	0	0	0	0	0	0	0	0
12	1	0	0	0	0	1	0	0	0	0	0	0	0	0	0	0	0	0	0
13	1	0	0	0	1	0	0	0	0	0	0	0	0	0	0	0	0	0	0
14	1	0	0	0	0	0	1	0	0	0	0	0	0	0	0	0	0	0	0
15	1	0	0	1	0	0	0	0	0	0	0	0	0	0	0	0	0	0	0
16	0	1	0	0	0	0	0	0	0	0	0	0	0	0	0	0	0	1	0
17	0	0	1	0	0	0	0	0	0	0	0	0	0	0	0	0	0	0	1
18	0	1	0	0	0	0	0	0	0	0	0	0	0	0	0	0	1	0	0
19	0	0	1	0	0	0	0	0	0	0	0	0	0	0	0	0	0	1	0

Stability data

	1	2	3	4	5	6	7	8	9	10	11	12	13	14	15	16	17	18	19
1	0	1	2	1	1	2	1	0	0	0	0	1	1	1	1	0	0	0	0
2	1	0	0	0	1	1	0	1	1	0	0	0	0	0	0	1	0	1	0
3	2	0	0	1	0	0	1	0	0	1	1	0	0	0	0	0	1	0	1
4	1	0	1	0	0	0	0	0	0	1	0	0	0	0	1	0	0	0	0
5	1	1	0	0	0	0	0	0	1	0	0	0	1	0	0	0	0	0	0
6	2	1	0	0	0	0	0	1	0	0	0	1	0	0	0	0	0	0	0
7	1	0	1	0	0	0	0	0	0	0	1	0	0	3	0	0	0	0	0
8	0	1	0	0	0	2	0	0	0	0	0	0	0	0	0	0	0	0	0
9	0	1	0	0	1	0	0	0	0	0	0	0	0	0	0	0	0	0	0
10	0	0	1	1	0	0	0	0	0	0	0	0	0	0	0	0	0	0	0
11	0	0	1	0	0	0	1	0	0	0	0	0	0	0	0	0	0	0	0
12	1	0	0	0	0	1	0	0	0	0	0	0	0	0	0	0	0	0	0
13	1	0	0	0	1	0	0	0	0	0	0	0	0	0	0	0	0	0	0
14	1	0	0	0	0	0	3	0	0	0	0	0	0	0	0	0	0	0	0
15	1	0	0	1	0	0	0	0	0	0	0	0	0	0	0	0	0	0	0
16	0	1	0	0	0	0	0	0	0	0	0	0	0	0	0	0	0	1	0
17	0	0	1	0	0	0	0	0	0	0	0	0	0	0	0	0	0	0	1
18	0	1	0	0	0	0	0	0	0	0	0	0	0	0	0	0	1	0	0
19	0	0	1	0	0	0	0	0	0	0	0	0	0	0	0	0	0	1	0

Robotic Hand Directional Changes matrices

$+x$ *direction*

	1	2	3	4	5	6	7	8	9	10	11	12	13	14	15	16	17	18	19
1	0	1	1	0	0	0	0	1	1	1	1	1	1	1	1	1	1	1	1
2	1	0	1	1	0	0	1	1	1	1	1	1	1	1	1	0	1	1	1
3	1	0	0	0	0	0	0	1	0	1	0	1	1	1	1	0	0	1	1
4	0	0	0	0	1	0	1	0	1	0	1	0	1	1	0	1	1	1	1
5	0	0	1	1	0	1	1	1	0	1	1	1	0	1	1	1	1	1	1
6	0	0	1	1	1	0	1	0	1	1	1	0	1	1	1	1	1	1	1
7	0	0	0	1	0	1	0	1	0	1	0	1	0	0	1	1	1	1	1
8	1	0	1	1	1	0	1	0	1	1	1	1	1	1	1	1	1	1	1
9	1	1	1	1	0	1	1	1	0	1	1	1	1	1	1	1	1	1	1
10	1	0	1	0	1	0	1	0	1	0	1	1	1	1	1	1	1	1	1
11	1	1	1	1	0	1	0	1	0	1	0	1	1	1	1	1	1	1	1
12	1	1	1	1	1	0	1	1	1	1	1	0	1	1	1	1	1	1	1
13	1	1	1	1	0	1	1	1	1	1	1	1	0	1	1	1	1	1	1
14	1	1	1	1	1	0	1	1	1	1	1	1	1	0	1	1	1	1	1
15	1	1	1	0	1	0	1	1	1	1	1	1	0	1	1	0	1	1	1
16	1	0	1	1	1	1	1	1	1	1	1	1	1	1	1	1	0	1	0
17	1	0	0	1	1	1	1	1	1	1	1	1	1	1	1	1	0	0	0
18	1	1	1	1	1	1	1	1	1	1	1	1	1	1	1	1	1	0	1
19	1	1	1	1	1	1	1	1	1	1	1	1	1	1	1	1	0	0	0

$-x$ *direction*

	1	2	3	4	5	6	7	8	9	10	11	12	13	14	15	16	17	18	19
1	0	1	1	0	0	0	0	1	1	1	1	1	1	1	1	1	1	1	1
2	1	0	0	0	0	0	0	0	0	1	0	1	1	1	1	1	0	0	1
3	1	1	0	0	1	1	0	1	1	1	1	1	1	1	1	1	0	1	1
4	0	1	0	0	1	1	1	1	1	0	1	1	1	1	1	0	1	1	1
5	0	0	0	1	0	1	0	1	0	1	0	1	0	1	0	1	1	1	1
6	0	0	0	0	1	0	1	0	1	0	1	0	1	1	0	1	1	1	1
7	0	1	0	1	1	1	0	1	1	1	0	1	1	0	1	1	1	1	1
8	1	1	1	0	1	0	1	0	1	0	1	1	1	1	1	1	1	1	1
9	1	1	0	1	0	1	0	1	0	1	0	1	1	1	1	1	1	1	1
10	1	1	1	0	1	1	1	1	1	0	1	1	1	1	1	1	1	1	1
11	1	1	0	1	1	1	0	1	1	1	0	1	1	1	1	1	1	1	1
12	1	1	1	0	1	0	1	1	1	1	1	0	1	1	0	1	1	1	1
13	1	1	1	1	0	1	0	1	1	1	1	1	0	0	1	1	1	1	1
14	1	1	1	1	1	1	1	1	1	1	1	1	1	0	1	1	1	1	1
15	1	1	1	0	1	1	1	1	1	1	1	1	1	1	0	1	1	1	1
16	1	0	0	1	1	1	1	1	1	1	1	1	1	1	1	1	0	0	0
17	1	1	0	1	1	1	1	1	1	1	1	1	1	1	1	1	1	0	1
18	1	1	1	1	1	1	1	1	1	1	1	1	1	1	1	1	1	0	0
19	1	1	1	1	1	1	1	1	1	1	1	1	1	1	1	1	0	1	0

$+y$ *direction*

	1	2	3	4	5	6	7	8	9	10	11	12	13	14	15	16	17	18	19
1	0	1	1	0	0	0	0	1	1	1	1	1	1	1	1	1	1	1	1
2	1	0	1	1	0	0	1	1	0	1	1	1	1	1	1	1	0	1	1
3	1	1	0	0	1	1	0	1	1	1	0	1	1	1	1	1	0	1	1
4	0	1	0	0	1	1	0	1	1	0	0	1	1	0	0	1	1	1	1
5	0	0	1	0	1	1	0	1	1	0	1	1	0	1	1	1	1	1	1
6	0	0	1	1	0	0	1	0	0	1	1	0	0	1	1	1	1	1	1
7	0	1	0	1	1	1	0	1	1	1	0	1	1	1	0	1	1	1	1
8	1	0	1	1	0	0	1	0	0	1	1	1	1	1	1	1	1	1	1
9	1	1	1	1	0	1	1	1	0	1	1	1	1	1	1	1	1	1	1
10	1	1	0	0	1	1	1	0	1	1	0	0	1	1	1	1	1	1	1
11	1	1	1	1	1	1	0	1	1	1	0	1	1	1	1	1	1	1	1
12	1	1	1	1	0	0	1	1	1	1	1	0	0	1	1	1	1	1	1
13	1	1	1	1	0	1	1	1	1	1	1	1	0	1	1	1	1	1	1
14	1	1	1	1	1	0	1	1	1	1	1	1	1	0	1	1	1	1	1
15	1	1	1	0	1	1	1	1	1	1	1	1	0	0	1	1	1	1	1
16	1	1	1	1	0	1	1	1	1	1	1	1	1	1	0	1	1	1	1
17	1	1	0	1	1	1	1	1	1	1	1	1	1	1	1	0	1	1	1
18	1	0	1	1	1	1	1	1	1	1	1	1	1	1	1	1	0	1	1
19	1	1	0	1	1	1	1	1	1	1	1	1	1	1	1	1	1	0	1

$-y$ *direction*

	1	2	3	4	5	6	7	8	9	10	11	12	13	14	15	16	17	18	19
1	0	1	1	0	0	0	0	1	1	1	1	1	1	1	1	1	1	1	1
2	1	0	1	1	0	0	1	0	1	1	1	1	1	1	1	1	1	0	1
3	1	1	0	0	1	1	0	1	1	1	0	1	1	1	1	1	1	0	1
4	0	1	0	0	1	1	1	1	1	0	1	1	1	1	0	1	1	1	1
5	0	0	1	1	0	0	1	0	0	1	1	0	0	1	1	1	1	1	1
6	0	0	1	1	1	0	1	0	1	1	1	0	1	1	1	1	1	1	1
7	0	1	0	0	1	1	0	1	1	0	0	1	1	0	0	1	1	1	1
8	1	1	1	1	1	0	1	0	1	1	1	1	1	1	1	1	1	1	1
9	1	0	1	1	0	0	1	0	0	1	1	1	1	1	1	1	1	1	1
10	1	1	1	0	1	1	1	1	1	0	1	1	1	1	1	1	1	1	1
11	1	1	0	0	1	1	0	1	1	0	0	1	1	1	1	1	1	1	1
12	1	1	1	1	1	0	1	1	1	1	1	0	1	1	1	1	1	1	1
13	1	1	1	1	0	0	1	1	1	1	1	0	0	1	1	1	1	1	1
14	1	1	1	0	1	1	0	1	1	1	1	1	1	0	1	1	1	1	1
15	1	1	1	0	1	1	1	1	1	1	1	1	1	1	0	1	1	1	1
16	1	0	1	1	1	1	1	1	1	1	1	1	0	0	1	1	1	0	1
17	1	1	0	1	1	1	1	1	1	1	1	1	1	1	1	1	0	1	0
18	1	1	1	1	1	1	1	1	1	1	1	1	1	1	1	1	1	0	1
19	1	1	1	1	1	1	1	1	1	1	1	1	1	1	1	1	1	1	0

$+z$ *direction*

	1	2	3	4	5	6	7	8	9	10	11	12	13	14	15	16	17	18	19
1	0	0	0	0	0	0	0	0	0	0	0	1	1	1	1	0	0	0	0
2	1	0	1	1	0	0	1	0	0	1	1	1	1	1	1	0	1	0	1
3	1	1	0	0	1	1	0	1	1	0	0	1	1	1	1	1	0	1	0
4	1	1	0	0	1	1	1	1	1	1	1	1	1	1	1	1	0	1	0
5	1	0	1	1	0	1	1	1	1	1	1	1	1	1	1	0	1	1	1
6	1	0	1	1	1	0	1	1	1	1	1	1	1	1	1	0	1	0	1
7	1	1	0	1	1	1	0	1	1	1	1	1	1	1	1	0	1	1	1
8	1	0	1	1	1	1	1	0	1	1	1	1	1	1	1	0	1	0	1
9	1	0	1	1	1	1	1	1	0	1	1	1	1	1	1	0	1	1	1
10	1	1	0	1	1	1	1	1	1	0	1	1	1	1	1	1	0	1	1
11	1	1	0	1	1	1	1	1	1	1	0	1	1	1	1	1	0	1	1
12	0	0	1	1	1	0	1	0	1	1	0	1	1	1	1	0	1	1	1
13	0	0	1	1	0	1	1	1	0	1	1	1	0	1	1	0	1	1	1
14	0	1	0	1	1	1	0	1	1	1	0	1	1	0	1	1	0	1	1
15	0	1	0	0	1	1	1	1	1	1	0	1	1	1	1	0	1	0	1
16	1	0	1	1	1	1	1	1	1	1	1	1	1	1	1	1	0	1	0
17	1	1	0	1	1	1	1	1	1	1	1	1	1	1	1	1	0	1	0
18	1	1	1	1	1	1	1	1	1	1	1	1	1	1	1	1	0	1	0
19	1	1	1	1	1	1	1	1	1	1	1	1	1	1	1	1	0	1	0

$-z$ *direction*

	1	2	3	4	5	6	7	8	9	10	11	12	13	14	15	16	17	18	19
1	0	1	1	1	1	1	1	1	1	1	0	0	0	0	1	1	1	1	1
2	0	0	1	1	0	0	1	0	0	1	1	0	0	1	1	0	1	1	1
3	0	1	0	0	1	1	0	1	1	0	0	1	1	0	0	1	0	1	1
4	0	1	0	0	1	1	1	1	1	1	1	1	1	1	0	1	1	1	1
5	0	0	1	1	0	1	1	1	1	1	1	1	1	0	1	1	1	1	1
6	0	0	1	1	1	0	1	1	1	1	0	1	1	1	1	1	1	1	1
7	0	1	0	1	1	1	0	1	1	1	1	1	1	1	0	1	1	1	1
8	0	0	1	1	1	1	1	0	1	1	0	1	1	1	1	1	1	1	1
9	0	0	1	1	1	1	1	1	0	1	1	1	0	1	1	1	1	1	1
10	0	1	0	1	1	1	1	1	1	0	1	1	1	1	0	1	1	1	1
11	0	1	0	1	1	1	1	1	1	1	0	1	1	0	1	1	1	1	1
12	1	1	1	1	1	1	1	1	1	1	1	0	1	1	1	1	1	1	1
13	1	1	1	1	1	1	1	1	1	1	1	1	0	1	1	1	1	1	1
14	1	1	1	1	1	1	1	1	1	1	1	1	1	0	1	1	1	1	1
15	1	1	1	1	1	1	1	1	1	1	1	1	1	1	0	1	1	1	1
16	0	0	1	1	0	0	1	0	0	1	1	0	0	1	1	0	1	0	1
17	0	1	0	0	1	1	0	1	1	0	0	1	1	0	0	1	0	1	0
18	0	0	1	1	1	0	1	0	1	1	0	1	1	1	0	1	0	1	0
19	0	1	0	0	1	1	1	1	1	1	1	1	1	1	0	1	0	1	0

The liaison matrix is represented with binary numbers '1' and '0', in which '1' provides the connection among the parts and '0' provides no connection among the parts. In stability matrix '1' indicates partial stability between the parts, '0' indicates no stability between the parts, '2' indicates permanent stability between the parts due to self-arrangement and '3' indicates permanent stability between the parts due

Table 2 List of generated optimal sequences

S.no	Assembly sequences	Number of RHDC	Fitness value
1	1-2-3-10-11-9-8-4-7-5-6-15-14-12-13-16-17-18-19	04	04
2	1-2-3-11-10-8-9-7-4-6-5-15-14-13-12-17-16-19-18	04	04
3	1-3-2-10-11-9-8-4-7-6-5-14-15-12-13-16-17-18-19	04	04
4	1-3-2-11-10-8-9-4-7-5-6-14-15-12-13-16-17-19-18	04	04
5	1-3-2-10-11-9-8-7-4-6-5-15-14-12-13-16-17-18-19	04	04
6	1-2-3-7-4-6-5-11-10-8-9-13-12-15-14-19-18-17-16	04	04

to physical connectors. In RHDC matrices, '1' indicates not possible to assemble the part and '0' indicates possible to assemble the part in that direction.

IFF algorithm is executed for 500 iterations by considering robot hand directional changes as the suitability equation to obtain the best sequences. The algorithm generates '6' best assembly sequences with the fitness value as '04' as shown in Table 2.

4 Conclusion

In this research improved fruit fly algorithm is developed to generate the best assembly sequences. To test the performance of the developed algorithm, a nineteen-part block assembly is considered to generate optimal assembly sequences.

In the further research, the developed algorithm can be implemented to more intricate shape products to test the efficiency of the algorithm.

References

1. Deepak, B.B., Bala Murali, G., Bahubalendruni, M.R., Biswal, B.B.: Assembly sequence planning using soft computing methods: a review. Proc. Inst. Mech. Eng. Part E J. Process. Mech. Eng. **29**, 0954408918764459 (2018)
2. Wilson, R.H., Latombe, J.C.: Geometric reasoning about mechanical assembly. Artif. Intell. **71**(2), 371–396 (1994)
3. Wong, H., Leu, M.C.: Adaptive genetic algorithm for optimal printed circuit board assembly planning. CIRP Ann. Manuf. Technol. **42**(1), 17–20 (1993)
4. Bonneville, F., Perrard, C.. Henrioud, J.M.: A genetic algorithm to generate and evaluate assembly plans. in emerging technologies and factory automation, vol. 2. In: ETFA'95, Proceedings.,. INRIA/IEEE Symposium (1995) pp. 231–239
5. Failli, F., Dini, G.: Ant colony systems in assembly planning: a new approach to sequence detection and optimization. In: 2nd CIRP International Seminar on Intelligent Computation in Manufacturing Engineering-ICME vol. 1. Capri, Italy (2000) pp. 227–232
6. Wang, J.F., Liu, J.H., Li, S.Q., Zhong, Y.F.: Intelligent selective disassembly using the ant colony algorithm. AI EDAM **17**(4), 325–333 (2003)
7. Gunji, B., Deepak, B.B., Bahubalendruni, M., Biswal, B.: Hybridized genetic-immune based strategy to obtain optimal feasible assembly sequences. Int. J. Ind. Eng. Comput. **8**(3), 333–346 (2017)
8. Gunji, A.B., Deepak, B.B.B.V.L., Bahubalendruni, C.R., Biswal, D.B.B.: An optimal robotic assembly sequence planning by assembly subsets detection method using teaching learning-based optimization algorithm. IEEE Trans. Autom. Sci. Eng. **15**(3), 1369–1385 (2018)

Design, Analyze and Manufacture of Hydraulic Spring and Damper for an All-Electric Vehicle

Gulati Komal, Bhattacharjee Dyutiman and Panigrahi Isham

Abstract Electric vehicles are preferred in every country as eco-friendly mode of transport. Weight of the vehicle is a major consideration in EV. Its components are selected and designed considering the weight factor. At the same time, the need for comfort of passengers during ride is also very essential and so, design of customized suspension is very important. Therefore, this paper aims to design, manufacture and analyze spring and damper for an all-electric car. Mathematical modeling and simulations of a two degree of freedom quarter car model have been carried out to find the maximum load transfer on front wheel in various conditions like static, lower speed acceleration and due to braking followed by designing of damper on maximum load. Since hydraulic suspension is cost-effective and thus more affordable than air suspension, so our aim is to optimize the stiffness of hydraulic suspension in such a manner that we get output similar to air suspension in less cost.

Keywords Suspension design · Electric vehicle · Quarter car model · ADAMS

1 Introduction

Sathnish Kumar et al. [1] discussed simulation and mathematical modeling of a quarter car having two degree of freedom. Hsin-Tsun Hsu et al. [2] investigated the dynamic behavior of an electric vehicle (EV). They used multi-body dynamics (MBD) software to design vehicle suspension system. Lin Lin et al. [3] designed and created full floating structure model of cab air suspension system and was further simulated and analyzed to find natural frequency in ADAMS.

G. Komal · B. Dyutiman · P. Isham (✉)
School of Mechanical Engineering, Kalinga Institute of Industrial Technology (Deemed to Be University), Bhubaneswar, Odisha 751024, India
e-mail: ipanigrahifme@kiit.ac.in

G. Komal
e-mail: gulatikml1@gmail.com

L. Li et al. (eds.), *Advances in Materials and Manufacturing Engineering*, Lecture Notes in Mechanical Engineering, https://doi.org/10.1007/978-981-15-1307-7_27

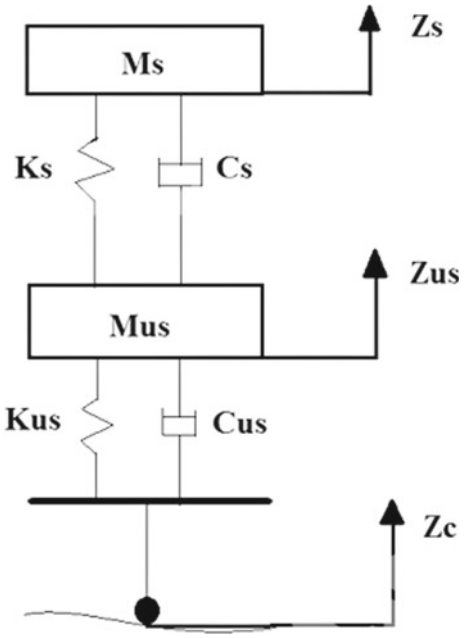

Fig. 1 Quarter car model

2 Theory

Two degree of freedom quarter car model has been used for numerical simulations to evaluate load transfer on front wheel of an all-electric vehicle [1] in various conditions like static, lower speed acceleration and braking. Further taking into consideration three cases: (1) Only driver in vehicle, (2) Half-loaded vehicle, (3) Fully loaded vehicle.

Finding the maximum load and thereby designing damper considering the maximum load in reference to Fig. 1.

3 Methodology

3.1 Experimentation

Firstly, a commercial hydraulic suspension was taken for experimentation. Depending on the requirements and space available by the target vehicle (refer Table 1), the desired stiffness was found; so accordingly, the spring was customized with final active number of turns = 8. The inner and outer diameter of spring was measured using vernier caliper and length was measured by using a measuring tape. It was further taken for testing in universal testing machine in which the spring was made

Table 1 Specifications and parameters required for designing and analyzing the hydraulic suspension for an all-electric vehicle

Sr. no.	Specifications/Parameters	Value
1	Suspension used	MacPherson strut
2	Drive train	Rear wheel drive
3	Weight distribution ration	40:60
4	Maximum number of passengers	8
5	Maximum weight of the car	(575 + (8*75)) kg
6	Empty weight of the car	575 kg
7	Wheel base (L)	2.165 m
8	Height of C.G (h)	0.7 m
9	Total weight of passengers	600 kg
10	Weight of air suspension	1.61 kg
11	Length of air spring	0.54 m
12	Length of hydraulic spring	0.24 m
13	Outer diameter of spring	0.08 m
14	Inner diameter of spring	0.06 m
15	Nuts and bolts weight	0.125 kg
16	Weight of tyre and rim	9.68 kg
17	Weight of hub	7.29 kg
18	Weight of brake caliper	2.88 kg
19	Weight of spring and damper	(1.61 + 1.725) kg = 3.335 kg
20	Weight of double wishbone arms	1.5 kg
21	Total weight of one-wheel assembly	21.35 kg
22	Sprung mass (m_1)	Total weight of car (W)-Unsprung mass (m_2) (wheel and suspension)
23	Type of battery used	Lead acid battery

to solidify at its maximum that is before it starts to fail at static condition keeping temperature at 28 °C and load rate 0.1 kN/sec.

From experiment, displacement versus load graph was found out as shown in Fig. 4 from which it could be found out that at maximum displacement how much static load was transferred to the spring.

3.2 Mathematical Modeling

Now, considering the customized hydraulic steel coil spring, further analyzes were carried out to find the maximum load transfer on front wheel [4] broadly considering three cases:

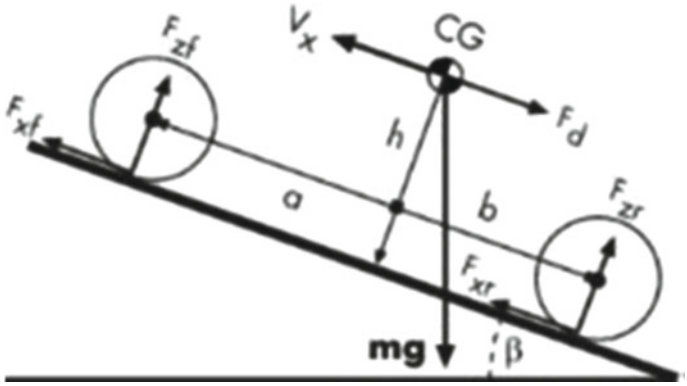

Fig. 2 Dynamic axle load

(1) In static condition (2) Lower speed acceleration (3) Due to braking

Using Fig. 2, maximum load transfer was found out and further design of damper was done in which following parameters were calculated: Stiffness (k), wire diameter (d), solid length of spring (L_s), total number of turns (N), maximum deformation, free length of spring (L_f), spring index (C), Pitch, Wahl's shear stress factor (K) and maximum shear stress induced in spring. Further, taking damping coefficient (C) = 2000 Ns/m, other parameters were calculated: Critical damping coefficient (C_c), damping factor (ζ), natural angular frequency (W_n) and damped angular frequency (W_d).

3.3 Simulation in ADAMS

Simulation in Adams software was done to find characteristics curves of displacement and relative velocity of sprung and unsprung mass of hydraulic suspension [3]. Considering, y_{pk} (amplitude at static state response) for bump/hump = 0.01 m (since the vehicle has to travel on not much rough road surface).

4 Results and Discussions

4.1 Experimental Analysis

It was found from Fig. 3 that at maximum travel, the amount of load transfer in the spring in static condition was $4.1*10^3$ N.

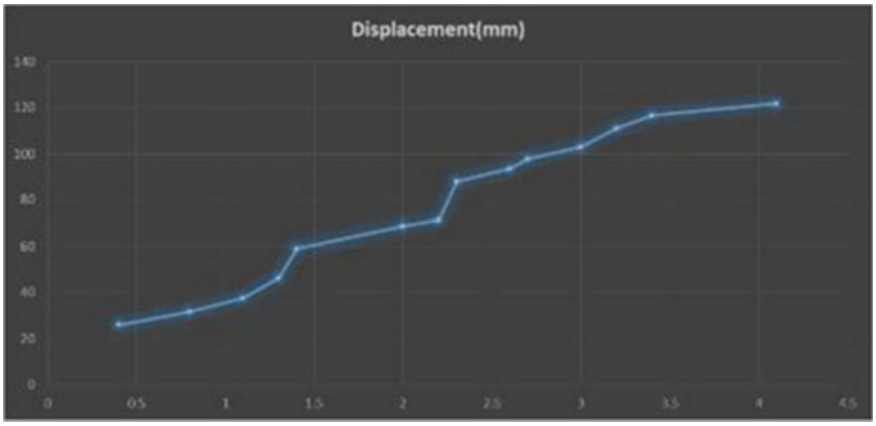

Fig. 3 Graph between displacement versus load

4.2 Mathematical Modeling

Due to braking action:

In case of Fully Loaded Vehicle:

Using, $W_{\text{fs}} = 115$ kg; $L = 2.165$ m; $h = 0.7$ m; deceleration produced $(a) = 1.5$ g

$$\text{Longitudinal load transfer on front wheels } (W_{\text{L}}) = (W_{\text{C}}1_{\text{W}} \times a \times h)/L = 5590.34\,\text{N} \quad (1)$$

$$\text{Net reaction at individual wheel} = W_{\text{fs}} + (W_{\text{L}}/2) = 4400\,\text{N} \quad (2)$$

Spring stiffness calculation:

It was examined that the load transfer on front wheel due to braking when the car is fully loaded experiences maximum load (refer Eq. 2) which came out to be 4400 N.

So, the damper was designed taking maximum load.

$D_1 = 22$ inches, $D_2 = 16$ inches; $D_1 =$ distance from mounting point on chassis to center of the wheel, $D_2 =$ distance from lower arm mounting point to center of the wheel

Applying the moment equation,

$$4400 \times D_1 = \text{FD} \times D_2;\ \text{FD} = 6050\ \text{N}$$
$$P = \text{FDamper} = 6050/\cos 19 = 6400\ \text{N} \quad (3)$$

Taking allowable travel of suspension to be 3 inches

$$k = 6400/(3 \times 25.4) = 83.98\,\text{N/mm} = 84\,\text{N/mm} \quad (4)$$

$$k = \left(Gd\text{^}4\right)/\left(8\ n\ D\text{^}3\right);\ \text{so,}\quad d = 12.35\,\text{mm} \tag{5}$$

$$Ls = nxd = 98.8\,\text{mm};\ N = n + 2(\text{grounded at both the ends}) = 10 \tag{6}$$

$$\text{Maximum deformation} = \left(8PD\text{^}3n\right)/\left(Gd\text{^}4\right) = 76.21\,\text{mm} \tag{7}$$

$$\begin{aligned} &\mathrm{L_f} = Nd + (1.15 \times 76.21) = 211.141\,\text{mm} \\ &\mathrm{C} = D/d = 5.66; \\ &\text{Pitch } = Lf/(N-1) = 23.46\,\text{mm} \\ &\mathrm{K} = ((4C-1)/(4C-4) + (0.615/C)) = 1.269 \end{aligned} \tag{8}$$

$$\text{Maximum shear stress induced in spring} = 8\,\mathrm{K} * P * D/\pi * d_3 = 768.561\,\text{MPa} \tag{9}$$

Damper Calculations:
$C = 2000$ Ns/m [1].

$$C_c = 2 * (m{*}k)1/2 = 12158.94, \tag{10}$$

where m is static load on damper (10) and k is stiffness

$$\zeta = C/Cc = 0.2(\text{approx}) \tag{11}$$

$$W_\mathrm{n} = \text{square root}\ (k/m) = 13.81\,\text{rad/sec} \tag{12}$$

$$W_\mathrm{d} = Wn * (1 - \zeta 2)1/2 = 13.53\,\text{rad/sec} \tag{13}$$

4.3 Simulation in ADAMS

It was found as shown in Fig. 4 that while riding in case of unsprung mass vibrations get damped before that of sprung mass. These results obtained for this customized hydraulic suspension are as per the requirements for a comfortable ride on an all-electric vehicle.

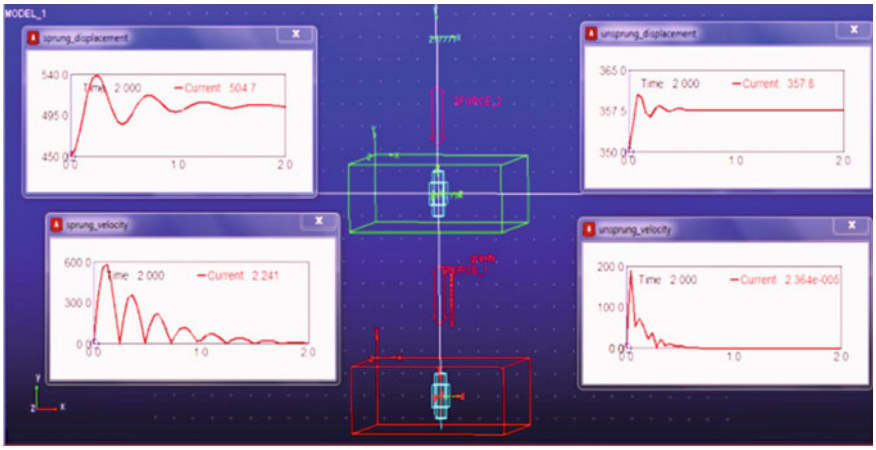

Fig. 4 (center) Model and simulation in ADAMS; (top left) displacement versus time graph due to sprung mass; (bottom left) velocity versus time graph due to sprung mass; (top right) displacement versus time graph due to unsprung mass; (bottom right) velocity versus time graph due to unsprung mass

5 Conclusion

The main aim of this paper is to design, analyze and manufacture a hydraulic spring and damper for an all-electric vehicle which has been successfully accomplished. Various procedures are followed to achieve the target like experimentation, mathematical modeling and simulation in ADAMS software. Through experimentation the stiffness of the commercial hydraulic spring was optimized. This customized hydraulic suspension is cost-effective and gives similar effect while driving as received while riding an air suspension vehicle. The customized spring and damper that was finally designed and manufactured is shown below:

The final specifications that were found as shown in Fig. 5 are: $k = 84$ N/mm, $L_f = 211.141$ mm, $C = 5.66$, Pitch $= 23.46$ mm, $K = 1.269$, $C_s = 2000$ Ns/m, $C_c = 12158.94$, $W_n = 13.81$ rad/sec, $W_d = 13.53$ rad/sec.

Fig. 5 Customized spring and damper

References

1. Sathish Kumar, P., Jancirani, J., John, D., Manikandan, S.: Mathematical modelling and simulation quarter car vehicle suspension. Int. J. Innov. Res. Sci., Eng. Technol. **3**(1), 1280–1283 (2014)
2. Hsu, H.T., Coker, C., Huang, H.: Optimization of an Electric vehicle suspension system using CAE. World Electr. Veh. J. **4**(2032–6653), 179–183 (2010)
3. Lin, L., Wang, T., Huang, Y., Wang, L., Zhang, H., Zheng, Y.: The design and simulation experiment of full floating cab suspensions system for conventional heavy trucks. In: IEEE International Conference on Mechatronics and Automation, Chengdu, pp. 854–858 (2012)
4. Jazar, R.N.: Vehicle Dynamics Theory and Application. Springer International Edition (2017)

Mechanical Performance Optimization of 3D Printing Materials

Shaheidula Batai and M. H. Ali

Abstract 3D printing technique has been developed rapidly and applied to manufacture components of diverse and complicated shapes and structures based on the computer-aided designs. To make 3D printing more promising and useful for more application purposes, mechanical properties of the materials used for printing should be studied and improved by developing new optimization methods. In this paper, a new optimization technique is developed for boosting mechanical properties of the materials by comparing tensile stress and extension of the specimens under different amount of loads in ANSYS. The specimens are made of two types of materials of various geometries and the same weight ratio according to the ISO mechanical test standards. Specimens are made of ABS and PLA. Case C shows the best tensile performances while Case B also shows good performs. Moreover, it is justified that the printing materials built of multi-materials have better properties, as well as the geometrical structures of the materials, influence the tensile performances of the materials significantly.

Keywords 3D printing materials · Mechanical properties · Optimization

1 Introduction

3D printing is becoming more and more popular with the industry and research groups due to its high efficiency in material usage and economic preferences. Since Acrylonitrile Butadiene Styrene (ABS) and Polylactic Acid (PLA) are always chosen for low-cost printers as printing materials, mechanical properties of the parts built of them appeal to the researchers substantially [1]. 3D printing, also known as additive manufacturing (AM), builds the prototype layer by layer based on a number of 2D slices of the 3D model designed by CAD software [2], instead of milling or cutting a part out of a block of material [3]. It is reasonable to make full use of the existing printing materials and conduct some optimization by using a few of

S. Batai · M. H. Ali (✉)
Department of Mechanical Engineering, School of Engineering, Nazarbayev University, Astana, Kazakhstan
e-mail: md.ali@nu.edu.kz

L. Li et al. (eds.), *Advances in Materials and Manufacturing Engineering*, Lecture Notes in Mechanical Engineering, https://doi.org/10.1007/978-981-15-1307-7_28

them simultaneously. Hence, fused deposition mdeling (FDM) and selective laser sintering (SLS) methods can be implemented to form parts from several materials [4]. FDM is an additive manufacturing technique which melts and extrudes a material through a nozzle to produce components layer upon layer. Furthermore, while 3D printers with several nozzles spring up to fulfill the need of achieving complex parts from multi-material, 3D printers with a single nozzle are also being developed [5]. The geometry of each material affects the mechanical properties of the components while the amount of each material used is kept the same. Therefore, in this paper, ABS and PLA are selected, and some simulations on the mechanical properties of the specimens made from them are implemented. Firstly, specimens with various internal geometrical structures, such as drills, honeycombs, pentagonal holes, and square-shaped holes, respectively, are prepared according to ISO standards. The total volume of the drills, honeycombs, pentagonal holes, and the square-shaped holes are the same for the sake of analysis. Secondly, ABS is defined to these specimens as the material in ANSYS. After that, the holes in the specimens are filled with the corresponding structures made of PLA, and mechanical properties of them are analyzed and compared.

2 Literature Review

Unlike conventional mono-material 3D printing methods including fused deposition modeling (FDM), stereolithography (SLA), selective laser sintering (SLS), or PolyJet, multi-material AM can print complicated structures by combining multiple deposition heads within a single integrated system [6–8]. Tomsilav Galeta et al. researched to determine the impact of sample's structure on the tensile strength of the printed materials, where the samples were prepared with a range of internal geometrical structures and results of the tensile tests showed that the honeycomb structure samples are of the highest strength [9]. The conclusion from this paper proved that the internal geometry is of important influence on the mechanical properties of the printing materials. Nevertheless, the tests were only conducted on the specimens with internal structures without fill-ins. L.R. Lopes et al. designed a single material but multi-section sample printed in a zebra-crossing structure and a multi-material sample with two materials in zebra-crossing pattern, respectively, and analyzed the mechanical performance of the samples as well as compared the results [10]. While this paper tested three types of specimens, the influence of the size and orientation of the zebra-crossing structures were not specified. And one more specimen which is in the same pattern as the existing one in Type C but with material 1 as the zebra-crossing structure and material 2 for the other part of the specimen should be added to the specimen Type C.

3 Experimental Procedures

While it is obvious that the application of multiple materials in additive manufacturing can improve the desirable properties of the printed components, it remains to be proved that the geometrical structures of each material influence the mechanical performance of the integrated structures. Thus, it is necessary to predict and optimize the mechanical properties of the components built of multiple materials by varying the internal structures of the material and filling the internal structures with other appropriate materials of the corresponding shapes.

3.1 Specimens Development and Description

Specific specimens listed below are designed according to the ISO tensile test standards, and the corresponding numerical tensile tests are conducted in ANSYS, respectively, on these specimens. Moreover, the results are analyzed and compared separately.

Apart from the first two cases, the same specimens as in Fig. 1 filled with the corresponding shapes made of PLA are listed. As indicated in Fig. 2, there are six cases in this group, where Case A: specimen which is made of ABS; Case B: specimen is made of ABS and a bar-shaped PLA sandwiched in it; Case C: specimen (ABS) with drills which are filled with the fitting cylindrical PLA; Case D: specimen (ABS) with honeycombs which are filled with the fitting hexagonal PLA; Case E: specimen (ABS) with pentagonal holes which are filled with the fitting pentagonal PLA; Case F: specimen (ABS) with square-shaped holes which are filled with the fitting square-shaped PLA. Aside from Case A, in which the specimen is made of a single material (ABS), in other cases, the internal structures are of the same volume of external one. It means ABS accounts for the same percentage in all specimens except the specimen in Case A, so does the PLA.

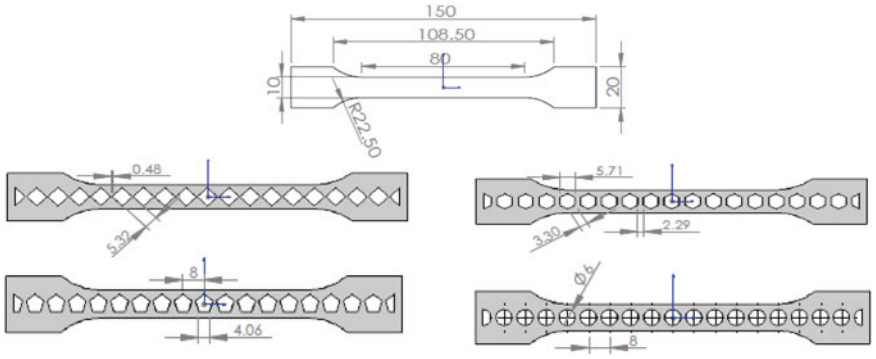

Fig. 1 3D printing specimens' dimensions

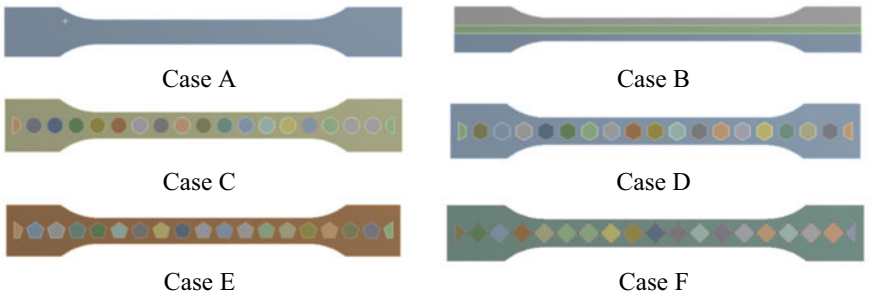

Fig. 2 3D printing specimens built of ABS and PLA

All specimens are prepared in Solidworks. After the intact specimens made of ABS are prepared according to the ISO standards, corresponding holes with different shapes, such as circular, rectangular, pentagonal, and hexagonal, are drilled. Then internal structures of corresponding shaps made of PLA are prepared separately. In the end, the external and internal parts are assembled together to form a specimen.

3.2 Numerical Simulation Conditions

The specimens developed in Solidworks in two groups are tested for the tensile strengths under the loads from 0.2 to 2 KN in ANSYS. Corresponding engineering data is listed in Table 1. Since the mesh size has a significant impact on the test results, the specimens are meshed in 1 mm. And all specimens are loaded by the tensile forces from one end and fixed on the other end.

Table 1 Material parameters for ABS and PLA

Constants	Unit	ABS	PLA
Density	Kg/m^3	1210	1250
Young's modulus	MPa	2900	3500
Poisson's ratio	–	0.422	0.36
Bulk modulus	Pa	6.1966E + 09	4.1667E + 09
Shear modulus	Pa	1.0197E + 09	1.2868E + 09
Tensile strength	MPa	34	46.8
Compressive strength	MPa	7.6	17.9

4 Results and Discussion

Figure 3 shows the simulation results (deformation) of the specimens under the load of 0.2 KN, where Case A shows the highest elongation value (0.215 mm) while the others are around 0.203 mm. Which means, regarding the deformation, specimens made of multi-materials have the advantage over the specimens of mono-material.

Figure 4 illustrates the stress values of the specimens under the loads form 0.2 to 2 KN. According to the line graphs, it is noticeable that Case C shows the lowest stress values while Case B presents the stress values somewhat larger than it. Case A experiences the largest stress as other cases undergo more or less the same stress amount.

As shown in Fig. 5, the specimens apart from Case A experience the lower elongation. According to Figs. 4 and 5, it is obvious that multi-material has better mechanical performances including stress and elongation than the mono-material. As for the

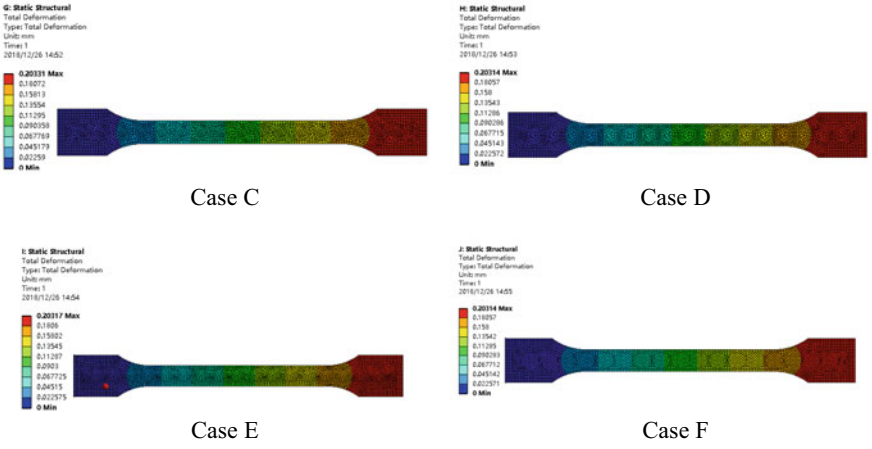

Fig. 3 Deformation results of a few specimens under the load of 0.2 KN

Fig. 4 Stress values of the specimens

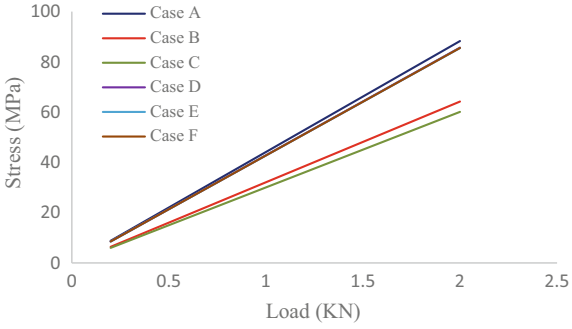

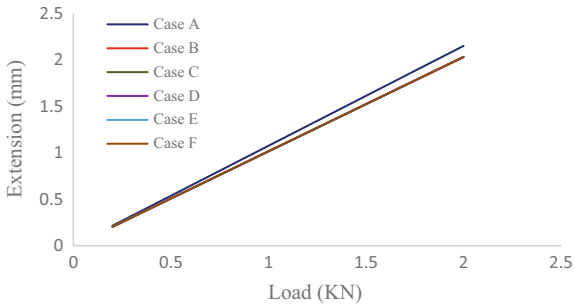

Fig. 5 Elongation values of the specimens

different geometrical structure's impact of the materials on the mechanical performances, Case C and Case B have the best mechanical properties. Particularly, Case C is preferable with its desirable mechanical performances.

5 Conclusion

In summary, a number of specific specimens are designed and developed, and they are tested for the tensile performances under the tensile loads from 0.2 to 2 KN. Specimens are made of ABS and PLA, where Case C shows the best tensile performances while Case B also performs well. Moreover, printing materials built of multi-material have better properties, and the geometrical structures of the materials influence the tensile performances of the materials significantly.

References

1. Ksawery, S.: Mechanical properties of FDM and SLA low-cost 3-D prints. Procedia Eng. **136**, 257–262 (2016)
2. Michael, D.: Mechanical behaviour of ABS: an experimental study using FDM and injection moulding techniques. J. Manuf. Process. **21**, 39–45 (2016)
3. Dizon, J.R.C., Espera, A.H.: Mechanical characterization of 3D-printed polymers. Addit. Manuf. **20**, 44–67 (2018)
4. Gaziz, Y., Amangeldi, S.H., Ali, M.H., Nazym, B., Asset, A., Islam, G.: Composite materials property determination by rule of mixture and monte carlo simulation (2018)
5. Khondoker, M.A.H., Sameoto, D.: Enhanced bonding of immiscible polymers via intermixed co-extrusion in fused deposition modelling. In: 41st Annual Meeting of the Adhesion Society, pp. 1–3 (2018)
6. Sanz-Izquierdo, B., Parker, E.A.: 3-D printing of elements in frequency selective arrays. IEEE Trans. Antennas Propag. **62**, 6060–6066 (2014)
7. Mirotznik, M.S., Larimore, Z.: Multi-material additive manufacturing of antennas. In: International Workshop on Antenna Technology (iWAT), pp. 123–126, IEEE (2016)
8. Nassar, I.T., Weller, T.M.: An Electrically-Small, 3-D Cube Antenna Fabricated with Additive Manufacturing, pp. 58–60. BioWireleSS, Austin (2013)

9. Tomislav, G., Pero, R.: Influence of structure on mechanical properties of 3D printed objects. In: Sergej, H., Grzegorz, K. International Conference on Manufacturing Engineering and Materials, ICMEM 2016, pp. 6–10, Nový Smokovec, Slovakia (2016)
10. Lopesa, L.R.: Multi-material 3D printing: the relevance of materials affinity on the boundary interface performance. Addit. Manuf. **23**, 45–52 (2018)

Studies on Tribological and Metal Forming Performance of Vegetable Oil-Based Lubricants

T. P. Jeevan and S. R. Jayaram

Abstract Oils derived from vegetable source are being investigated to serve as a possible alternative to conventional oils, currently being used as base oil in metal forming and metalworking processes. In the present investigation, friction and wear studies on AISI 304L with chemically modified neem and mahua oil-based lubricants are made with the aid of pin-on-disc tribometer. Feasibility of chemically modified neem and mahua oils as lubricant for drawing AISI 304L is also investigated. Neem and mahua oils are chemically modified by esterification and epoxidation process. Raw and chemically modified oils are compared with mineral oil-based lubricants. Chemically modified version of oil showed better resistance in the prevention of material wear and friction under frictional slide over base plate of the pin on the disc. The thickness profile, punch load and draw-in-length are observed for the deep-drawn cups under raw and formulated vegetable oils and are compared with mineral oil. The results obtained indicate that vegetable oils are good alternative to mineral oils for metal forming applications.

Keywords Neem · Mahua · Tribometer · Deep drawing

1 Introduction

Lubricants have a significant function in modern manufacturing and financial development of world, primarily by decreasing friction and wear between surfaces in contacts [1, 2]. Thus, annually, 38 million metric tons of lubricants have been utilised worldwide in the last decade, with petroleum-based oils sharing the larger part [3, 4]. Investigation into eco-friendly cutting fluids appears as top priority in lubrication in the early 1990s, resulting in an increasing number of environmentally friendly fluids and lubricants in the marketplace. The vegetable oils triacylglycerol structure create it an excellent applicant for latent use as a base stock for lubricants and cutting fluids due to its environmentally friendliness, renewability and less toxicity, and also,

T. P. Jeevan (✉) · S. R. Jayaram
Faculty of Mechanical Engineering, Malnad College of Engineering, Hassan, Karnataka, India
e-mail: jeevantpmce@gmail.com

L. Li et al. (eds.), *Advances in Materials and Manufacturing Engineering*, Lecture Notes in Mechanical Engineering, https://doi.org/10.1007/978-981-15-1307-7_29

they have outstanding lubricating properties such as higher viscosity index, higher lubricity and lower volatility [5, 6].

Neem and mahua oils fall under the category of non-edible vegetable that is plentifully available in various regions of India. These oils are also used for many medicinal applications and in production of biodiesel. The base structure of these non-edible vegetable oils offers attractive character because of long and polar fatty acid chains [7, 8]. In addition to this, they generate lubricant films with high potency that act together strongly with surfaces in contact, dropping both friction and wear. High oleic acid composition in their structure form potential sources for industrial usage. Tribological studies are necessary to understand the behaviour of the material under various operating lubrication conditions. They throw light on the usefulness of the combination of the material and lubricant under different operating conditions. Lubrication plays an important role in drawing process as it reduces friction at the tool–workpiece interface, thus enhancing the ability to produce a good quality part.

2 Methodology

2.1 Chemical Modification of Raw Vegetable Oils

The raw vegetable oils have certain limitations like low thermo-oxidative stability. In the present work, raw vegetable oils were modified by esterification and epoxidation process to increase their oxidation stability. The extent of modification of oils is observed through the changes in properties of the oils. Physico-chemical properties of raw and modified vegetable oils are tabulated in Table 1.

Table 1 Physico-chemical properties of raw and modified vegetable oils

Properties	MO	MME	NRO	NME	MME
Kinematic viscosity @ 40 °C (cSt)	32.20	48.55	68.04	04.0	03.7
Kinematic viscosity @ 100 °C (cSt)	11.70	9.18	10.15	02.26	3.20
Viscosity index	180.6	174	134	145	174
Saponofication value (mg KOH g^{-1})	140	191	166	130	141
Total acid value (mg KOH g^{-1})	01.86	39	23	0.5	0.8
Flash point (°C)	190.0	226	172	204	76
Pour point (°C)	8.00	13	9	1	2
Iodine value (mg l g^{-1})	07.52	62	66	60	72

2.2 Pin-on-Disc Tribometer Experiments

Investigations are performed on AISI 304L pins for the mineral oil, raw and modified versions of the vegetable oils using a pin-on-disc tribometer (ASTM G 99). Tribological tests are conducted with the wear track diameter of 100 mm at sliding speed of 800 rpm for 100, 150 and 200 N load. The total run time for each trial is 30 min. The volumetric wear and frictional coefficient for various sliding distances are recorded. The frictional coefficient variation and wear as a function of sliding distance for varying loads and oils are drawn.

2.3 Deep Drawing Experiment Details

Drawing operation is performed using hydraulic press of capacity 250 tons (Fig. 1). A straight draw dies of upper diameters 80, 100 and 150 mm is fixed to the upper ram which slides downwards to form a cup sample over a stationary straight punch of upper diameters 80, 100 and 150 mm. AISI304L sheet of 1.2 mm thickness is sheared into blanks of diameter 80, 100 and 150 mm. Lubricant is uniformly applied manually on both sides of the blank. The blank is placed on the die and held by blank holder with appropriate load. Then the punch is moved into the die with a speed of 2 mm/sec to draw cups. The load exerted by the punch on the blank and the punch travel are recorded using load cell and dial indicator, respectively. The process of drawing is repeated under mineral oil and raw and modified versions of

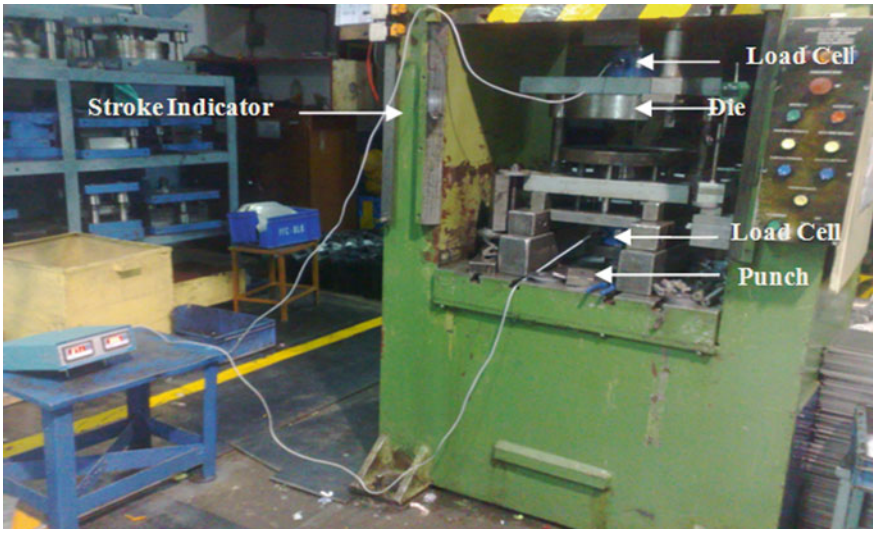

Fig. 1 Deep drawing setup. *Courtsey* Peenya Fine Comps. Ltd, Bengaluru, India

two vegetable oils for different cup diameters. The process parameters like punch load, punch pressure and blank holding force are measured for each experiment and recorded.

2.4 *Tribological Behaviour of AISI 304L*

The frictional coefficient variation against sliding distance for 100 N loads is shown in Fig. 2. The raw and modified form of neem and mahua oils exhibited slightly lower friction for selected operating conditions. The lower friction values are accredited to polar nature of fatty acid structure and viscosity properties. Modified versions of neem and mahua exhibited more resistance to wear for the investigated sliding distances and loads compared to mineral oil due to stronger adsorption capability because of high oleic acid composition in the oils as shown in Fig. 3. The lesser wear

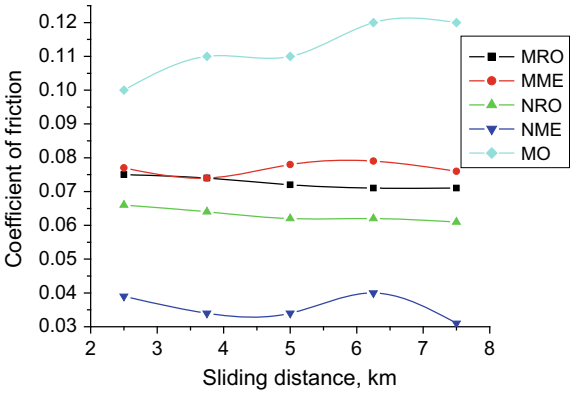

Fig. 2 Frictional coefficient variation with sliding distance at 100 N

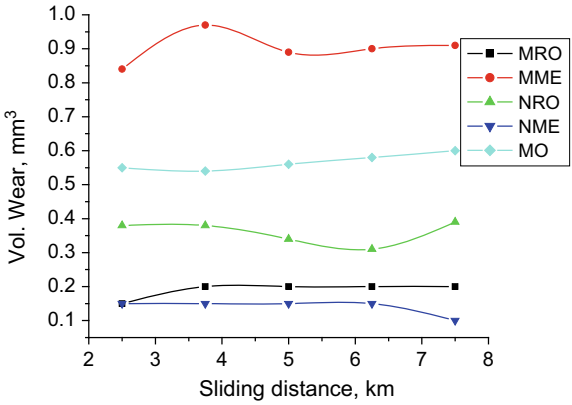

Fig. 3 Wear rate for different sliding distance at 100 N

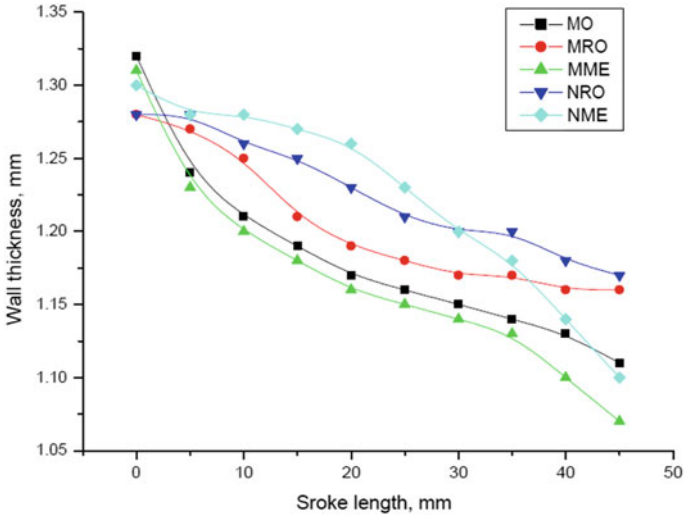

Fig. 4 Variation of wall thickness profile with stroke

trends can be accredited to presence of high composition of oleic and linoliec fatty acids in the structure of the neem and mahua oils.

2.5 Metal Forming Performance

2.5.1 Thickness Profile

The thickness profile of the drawn component decides the quality of the product. At the same time, thickness profile monitoring is one of the challenges faced very often by the manufacturers. A uniform wall thickness is noticed (Fig. 4) under raw versions of neem and mahua oil indicating better lubrication between surfaces of drawing. This may be due to its monounsaturated fatty acid structure of oil.

2.5.2 Draw-in-Length

The draw-in-lengths indicate the effect of friction between blank and die. The increase in length indicates lower friction during the operation. Variation of draw-in-length for different oils is shown in Fig. 5. Higher values of draw-in-lengths are seen for neem methyl ester compared to other vegetable oils and mineral oil.

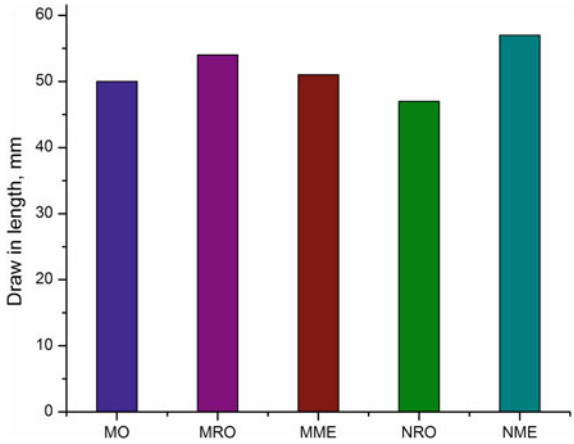

Fig. 5 Variation of draw-in-length for different oils

2.5.3 Punch Load

Punch load is a combination of work required for plastic deformation, redundant work, friction work and work required for ironing. It is one of the important parameters to decide the effectiveness of lubricants used in deep drawing. This force is measured from initial pure radial drawing of blank to the end of its stretch. Better lubrication performance between the drawing surfaces can be obtained by reducing the punch load. The punch forces measured under different modes of lubrication are shown in Fig. 6. MME showed 11.5% reduction in punch load compared to mineral oil. Vegetable oils in their modified form showed similar trends like mineral oil. Among the two tested vegetable oils, modified neem oil offers better lubrication for drawing AISI 304L cups with more than 30 mm depth. This may be attributed

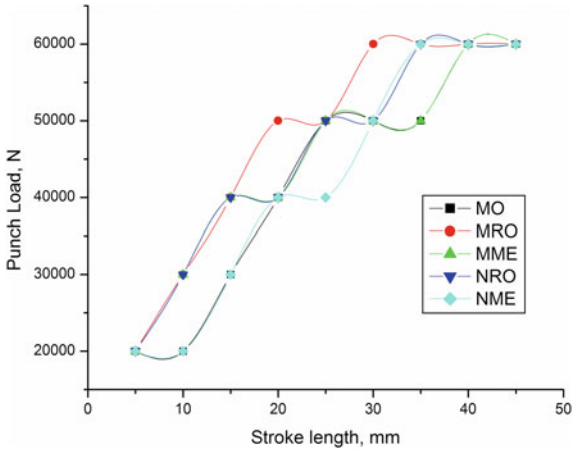

Fig. 6 Variation of punch load with stroke

because of saturated fatty acids such as stearic and palmitic acids along with higher value of oleic and linoleic acid composition.

3 Conclusions

A considerable cutback in coefficient of friction of AISI 304L for modified versions of neem and mahua oils is recorded compared to mineral oil. However, they exhibit slightly higher wear at high load operation. Both vegetable oil-based lubricants in their raw form emerge as a suitable forming lubricant especially for deep drawing, yielding lower punch forces, uniform wall thickness and better draw-in-lengths compared to conventional oil.

References

1. Rakić, R.: The influence of tribological properties of lubricating oils on the reliability of gears. Ind. Lubr. Tribol. **51**(4), 170–179 (1999)
2. Maleque, M.A., Masjuki, H.H., Sapuan, S.M.: Vegetable-based biodegradable lubricating oil additives. Ind. Lubr. Tribol. **55**(3), 137–143 (2003)
3. Siniawski, M.T., Saniei, N., Adhikari, B., Doezema, L.A.: Influence of fatty acid composition on the tribological performance of two vegetable-based lubricants. Lubr. Sci. **24**(2), 101–110 (2007)
4. Shashidhara, Y.M., Jayaram, S.R.: Vegetable oils as a potential cutting fluid—an evolution. Tribol. Int. **43**(5), 1073–1081 (2010)
5. Singh, Yashvir: Tribological behavior as lubricant additive and physiochemical characterization of Jatropha oil blends. Friction **3**(4), 320–332 (2015). https://doi.org/10.1007/s40544-015-0095
6. SathwikChatra, K.R., Jayadas, N.H., Satish, V.K. (2012). Natural oil based lubricants. In: Nosonovsky, M., Bhushan, B. (eds.) Green Tribology-biomimetics, Energy Conservation and Sustainability, p. 287. Springer, Heidelberg
7. Xinhu, Wu, Zhao, Gaiqing, Wang, Xiaobo, Liu, Weimin: Green tribology-biomimetics, energy conservation and sustainability. Tribol. Lett. **65**, 51 (2017). https://doi.org/10.1007/s11249-017-0833-9
8. Jeevan, T.P., Jayaram, S.R.: Tribological properties and machining performance of vegetable oil-based metalworking fluids—a review. Mod. Mech. Eng. **8**, 42–65 (2018). https://doi.org/10.4236/mme.2018.81004

Analysis of Fiber Laser Micro-drilling on Quartz

A. Sen, Biswanath Doloi and B. Bhattacharyya

Abstract In the present research work, an analysis of fiber laser percussion micro-drilling of quartz is conducted in order to find out the effect of the process parameters on the entry diameter of micro-hole. A response surface methodology-based experimental design planned and experiments have been conducted for the analysis. The considered process parameters are laser power, pulse frequency, duty cycle, and air pressure. The experimental results reveal that a target value of the micro-hole diameter of 100 μm is generated with the combinations of pulse frequency of 52.05 kHz, duty cycle of 69.47%, laser power of 34.25 W, and air pressure of 1.50 kgf/cm^2.

Keywords Fiber laser · Micro-drilling · Quartz · Entry hole diameter

1 Introduction

Quartz is considered one of the best choices material in the applications of frequency and timing references due to its piezoelectric properties, high mechanical, and frequency stability. Quartz even has improved corrosive resistance and hardness properties compared to various metals. Thus, fabrication of micro-machining features on quartz has observed rapid growth in the domain of micro-electric mechanical systems (MEMS), lab-on-chip devices especially. Past research works have shown that the various non-traditional micro-machining approaches such as ultrasonic machining (USM) [1], electro-discharge machining (EDM) [2], and abrasive water jet machining (AWJM) [3] are rapidly utilized to generate precise micro-machining features on quartz. However, the aforesaid machining approaches suffer from high machining time along with its non-flexibility in compared with the highly flexible and fast machining approach such as laser beam micro-machining process.

In the present research work, an infrared fiber laser system with the nanosecond pulsed regime is utilized to generate micro-holes on quartz. Past research works have

A. Sen (✉)
Department of Mechanical Engineering, Calcutta Institute of Technology, Howrah 711316, India
e-mail: abhishek.sen1986@gmail.com

B. Doloi · B. Bhattacharyya
Department of Production Engineering, Jadavpur University, Kolkata 700032, India

L. Li et al. (eds.), *Advances in Materials and Manufacturing Engineering*, Lecture Notes in Mechanical Engineering, https://doi.org/10.1007/978-981-15-1307-7_30

shown that nanosecond pulsed lasers are advantageous than ultra-violet and ultra-short lasers [4]. Laser percussion micro-drilling operation is conducted to achieve smaller dimensions of micro-holes in comparison with laser trepanning operation. The main aim of the research work is to carry out fiber laser percussion micro-drilling operation on a transparent quartz material and subsequently analyze the effectiveness of process variables on the entry hole diameter. Besides, to achieve the desired target value of the entry hole diameter within the considered domain of process variables by single-objective optimization.

2 Materials and Methods

In the present research study, multi-diodes pumped infrared fiber laser system of 50 W is utilized to carry out a total of 31 micro-holes on quartz having dimensions of 25X25X1 mm^3. The diameter of present laser beam at focused condition is 21 μm. The considered process parameters are laser power (X_1), pulse frequency (X_2), duty cycle (X_3), and air pressure (X_4). The ranges of the process parameters are selected from the previous research study of Sen et al. [5].

Response surface methodology (RSM)-based modeling by central composite design (CCD) with an alpha (α) value of 2.000 and subsequent analyses of fiber laser micro-drilling process parameters on entry hole diameter have been made. In this experimentation, four factors along with their five levels have been considered. Minitab-statistical software has been used for designing the experimental plan. Leica optical microscope of 50X lens is utilized to measure the entry micro-hole dimensions.

3 Results and Discussions

Considering four variables and utilizing the experimental results from the 31 experiments, an empirical model has been established based on RSM for correlating entry hole diameter (Y_1) with fiber laser micro-drilling process parameters. Table 1 represents the ANOVA results for the entry hole diameter. Step-wise regression method is employed during the analysis of variance (ANOVA) to determine the adequacy of the model. From Table 1, it is observed that the associated p-terms for the model, linear and square terms of entry hole diameters are below 0.05. The lack-of-fit value of the model indicates non-significant, i.e., 0.395 for entry hole diameter. Further, all the adequacy measured R^2, adjusted R^2 and predicted R^2 are found out to be in reasonable agreement which is close to 1. Hence, the adequacy of the model is validated. The corresponding empirical equations for the response, i.e., the entry hole diameter, are obtained as follows:

$$Y_1 = -24 - 1.55X_1 + 1.17X_2 + 3.93X_3 + 48.5X_4$$

Table 1 ANOVA table for entry hole diameter

Source	DF	Adjusted SS	Adjusted MS	*F*-value	*P*-value
Model	14	2109.50	150.678	60.96	0.000
Linear	4	931.38	232.845	94.20	0.000
Pulse frequency	1	177.29	177.290	71.73	0.000
Duty cycle	1	14.31	14.307	5.79	0.029
Laser power	1	207.27	207.270	83.86	0.000
Air pressure	1	532.51	532.513	215.44	0.000
Square	4	425.31	106.328	43.02	0.000
Two-way interaction	6	752.81	125.468	50.76	0.000
Error	16	39.55	2.472		
Lack-of-fit	10	26.95	2.695	1.28	0.395
Pure error	6	12.60	2.100		
Total	30	2149.04			
		S	R^2	R^2 Adjusted	R^2 Predicted
Model summary		1.57217	98.16	96.55	91.98

$$
\begin{aligned}
&- 0.0932X_1 \times X_1 + 0.1098X_2 \times X_2 + 0.0104X_3 \\
&\times X_3 - 2.28X_4 \times X_4 + 0.0049X_1 \times X_2 \\
&+ 0.3194X_1 \times X_3 + 0.608X_1 \times X_4 \\
&- 0.3747X_2 \times X_3 - 1.046X_2 \times X_4 - 0.043X_3 \times X_4
\end{aligned} \tag{1}
$$

3.1 Effect of Process Parameters on the Entry Hole Diameter

The different response surfaces have been executed with respect to two process variables on the considered response, while the other two remaining process parameters at their constant values. The results of parametric analysis of entry hole diameter with respect to process variables such as laser power, pulse frequency, duty cycle, and air pressure have been discussed with the aid of surface plot.

Figure 1 shows the effect of pulse frequency and laser power on the entry hole diameter. The constant parameters are duty cycle of 60% and air pressure of 2.5 kgf/cm^2. From Fig. 1, it is observed that the entry hole diameter tends to fall at high the values of pulse frequency. The reverse phenomenon is observed when the laser power increases, i.e., a simultaneous increment in the values of entry hole diameter is also observed.

Laser power is associated with laser pulse energy; however, change in the values of pulse frequency is not associated with the change in laser pulse energy. The increment

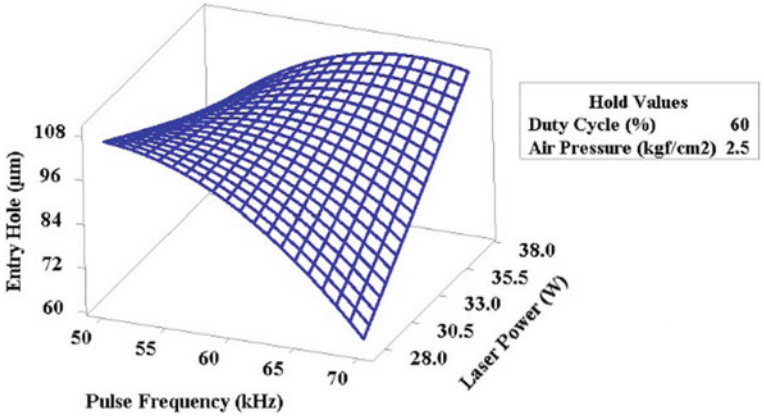

Fig. 1 Effect of pulse frequency and laser power on entry diameter of micro-hole

in pulse frequency also follows gradual decrement in laser peak power. In addition, laser peak power follows a gradual decrease in the values when pulse frequency increases. Thus, a gradual decrement in the values of the entry hole diameter is observed at high pulse frequency. Higher pulse energy is irradiated on the surface of quartz during high laser power. As a result, more amount of molten material is removed from the top surface of the quartz at higher laser power under high pulse energy, and thus, the entry hole diameter tends to increase rapidly.

Figure 2 represents the surface plot of the duty cycle and air pressure on the entry hole diameter. The constant parameters are pulse frequency of 60 kHz and laser power of 32.5 W. From Fig. 2, it is observed that with the increment in the air pressure with the moderate values of the duty cycle, entry hole diameter tends to increase simultaneously.

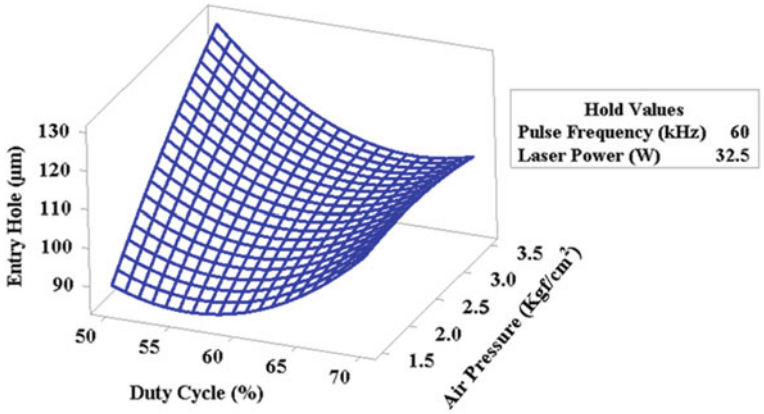

Fig. 2 Effect of duty cycle and air pressure on entry diameter of micro-hole

Duty cycle is associated with both laser peak power and average laser power. Higher duty cycle leads to high laser average power; however, a simultaneous decrement of laser peak power is evitable. In micro-drilling operation of a transparent material like quartz, laser beam penetration rate plays a significant role in achieving desired dimensions of the micro-holes. At each laser shot on the quartz, some amount of molten material is melted and evaporated. As the operation regime is in nanosecond pulse, some amount of molten material will adhere to the periphery of micro-hole dimensions along with surrounding of the micro-holes. High laser pulse energy aids in the opening of the entry hole diameter. Besides, this, sputtering and HAZ are inevitable during irradiation high laser energy on the quartz surface. High pressurized air pressure helps to remove the molten material from the surrounding of micro-holes. Thus, the removal of molten material is achieved both via high laser peak power and air pressure.

3.2 *Optimization of Fiber Laser Micro-hole Drilling on Quartz*

To achieve the desired target value of the entry hole diameter based on mathematical Eq. (1), a single-objective optimization has been carried out. A target value of 100 μm of micro-hole entry diameter of quartz is obtained to utilize various micro-machining applications. Figure 3 represents the optimization results of entry hole diameter of quartz. The current optimal settings for the achieving target value of 100 μm of micro-hole entry diameter are pulse frequency of 52.05 kHz, duty cycle of 69.47%, laser power of 34.25 W, and air pressure of 1.50 kgf/cm^2.

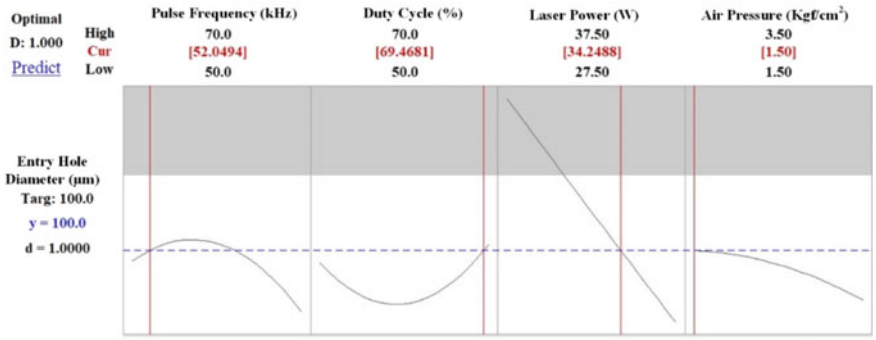

Fig. 3 Single objective result for entry diameter of micro-hole

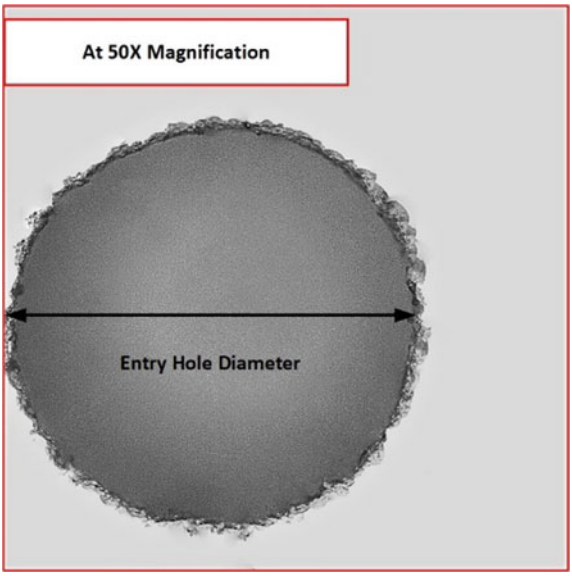

Fig. 4 Microscopic view of micro-hole on quartz at optimal condition

3.3 Confirmation Experiment

Confirmation experiments are conducted to validate the predicted results at the optimum experimental parameter settings which are obtained through the RSM and to evaluate the errors in the developed model. A total of three experiments are carried out, and the errors are 4.23%, 4.56%, 4.78%, respectively. A microscopic view of fiber laser-generated micro-hole diameter of quartz at the entry side is shown in Fig. 4 at optimal conditions.

4 Conclusions

In the present research work, a pulsed fiber laser system working in nanosecond pulse regime is employed to generate micro-holes on transparent quartz. An RSM-based experimental design is utilized to carry out a total of 31 experiments to analyze the effect of various process parameters on the entry diameter of micro-hole drilled on quartz. From the ANOVA table, the experimental model is validated through associated p-terms and a lack-of-fit test. Response surface plots reveal that the combination of high laser power and low pulse frequency increases the entry diameter of micro-hole. At high air pressure in combination with low duty cycle, produce higher values of entry micro-hole diameter. Single-objective optimization results show that the micro-hole diameter of 100 μm on quartz is achieved at the combination of pulse

frequency of 52.05 kHz, duty cycle of 69.47%, laser power of 34.25 W, and air pressure of 1.50 kgf/cm^2. The confirmatory test also shows the experimental results are within the considered ranges of the predicted results.

Further, the fiber laser percussion drilling process can be optimized to minimize the circularity and the taper angle of micro-hole drilled on quartz materials.

Acknowledgements The authors would like to express their gratitude toward the assistance aided by CAS Ph-IV program of the Production Engineering Department of Jadavpur University under the University Grants Commission, New Delhi, India, and Calcutta Institute of Technology, Howrah, India.

References

1. Egashira, K., Masuzawa, T., Fujino, M., Sun, X.Q.: Application of USM to micromachining by on-the-machine tool fabrication. Int. J. Electr. Mach. **2**, 31–36 (1997)
2. Sarkar, B.R., Doloi, B., Bhattacharyya, B.: Electrochemical discharge micro-machining of engineering materials. In: Non-traditional Micromachining Processes, 1st edn. Springer, Cham (2017)
3. Qi, H., Fan, J., Wang, J.: A study of the micro-machining process on quartz crystals using an abrasive slurry jet. Proc. Inst. Mech. Eng. Part B J. Eng. Manuf. **229**(3), 421–434 (2015)
4. Zhang, J., Sugioka, K., Midorikawa, K.: High-quality and high-efficiency machining of glass materials by laser-induced plasma-assisted ablation using conventional nanosecond UV, visible, and infrared lasers. Appl. Phys. A. **69**(1), S879–S882 (1999)
5. Sen, A., Doloi, B., Bhattacharyya, B.: An experimental investigation into fibre laser micro-drilling of quartz. Int. J. Mechatron. S Manuf. Syst. **11**(2–3), 182–202 (2018)

Bending Behavior of Sandwich Composite Structures of 3D-Printed Materials

M. H. Ali and Shaheidula Batai

Abstract Recently, many researches in 3D printing has focused on designing and printing sandwich honeycomb structures by using additive manufacturing. Their desirable mechanical properties, such as being of high strength/stiffness to weight ratio, appeal to use in the aerospace and automotive industries. Especially, cellular materials and structures are widely used in most of the energy-absorbing mechanisms due to the high strength as well as excellent energy-absorbing properties. In this research, deformation and mechanical strength of the sandwich structures with a honeycomb core, solid cores of the same weight, and the same thickness are compared, respectively. Where the honeycomb core is made of polylactic acid (PLA),and the face sheets are built of ABS. The thickness of the face sheets is kept the same for all the specimens. Therefore, only the differences of the core structures can influence the results of the experiments. According to the experimental results based on Von-Mises stress distribution and deformation rule under the bending loads, a sandwich structure with honeycomb core indicates better mechanical performances in terms of deformation and stress than the bending loads for the same weight.

Keywords Sandwich structures · Honeycomb composites · Bending behavior

1 Introduction

Since 3D-printed polymeric parts have been demanded tremendously in applications such as robotics and aerospace, designing, and 3D printing of the honeycomb structures made of polymeric materials have been attractive [1]. Especially, cellular materials and structures are widely used in most energy-absorbing mechanisms due to the high strength as well as amazing energy-absorbing properties [2]. In modern manufacturing, additive manufacturing is the desired method to build them, since additive manufacturing processes have provided efficient and low-cost methods to researchers and customers by building research prototypes without costing much

M. H. Ali (✉) · S. Batai
Department of Mechanical Engineering, School of Engineering, Nazarbayev University, Astana, Kazakhstan
e-mail: md.ali@nu.edu.kz

L. Li et al. (eds.), *Advances in Materials and Manufacturing Engineering*, Lecture Notes in Mechanical Engineering, https://doi.org/10.1007/978-981-15-1307-7_31

or manufacturing components which are extremely challenging to make with traditional manufacturing methods [3]. Sandwich structures with different types of honeycomb cores have lots of advantages including being light-weighted and being of high strength-to-weight ratio properties [4]. Usually, sandwich structures consist of two strong face sheets with a light-weighted cellular core which is made of polymeric materials [5]. As lightweight sandwich structures with cellular core are broadly applied in aerospace, automobile, medical instruments, and building industrial area due to their excellent flexural stiffness and high energy-absorption capabilities [6], relevant studies draw the attention of many researchers. Among them, Shaoyu HOU et al. studied the mechanical properties of the sandwich composites with three different honeycomb cores such as re-entrant honeycomb, diamond honeycomb, and conventional honeycomb. Moreover, in their study, they tried to analyze the specimens which consist of two face sheets of unidirectional carbon fiber reinforced composite and a 3D-printed honeycomb core of polymeric material by conducting low-velocity impact test on them [7]. Also, David J. McGregor et al. studied the mechanical properties of the hexagonal lattice structure fabricated with additive manufacturing by analyzing the effect of geometric deviations on the mechanical performances of the structures [8]. Pawel Baranowski et al. conducted another interesting study. They tried to analyze the deformation of honeycomb cellular structures built with Laser engineering net shaping technology under specific loading experimentally and with numerical simulation. As for the specimens, two honeycomb topologies with different elementary cells were designed and developed, and comparison on their deformation, fatigue, and energy-absorption capabilities were made under the dynamic loading [9]. Apart from the researches made on the mechanical properties and behaviors of 3D-printed honeycomb sandwich structures, research was made by Garam Kim et al. to determine the effect of fluid, such as water and oil, on the mechanical performances of the cellular structures as they to be prone to fluid ingression [10]. In our study, deformation and mechanical strength of the sandwich structures with honeycomb core or solid cores of the same weight or the same thickness are compared, respectively. Also, the honeycomb core is made of PLA, while the face sheets are built of ABS. The thickness of the face sheets is kept the same for all specimens. Therefore, only the differences of the core structures can influence the results of the experiments.

2 Numerical Simulation

Since additive manufacturing is a commonly used method to produce the honeycomb sandwich structures, in our study as a part of 3D-printing research honeycomb, sandwich structures are compared with the ordinary sandwich structure with solid sheet core of the same thickness and weight as the honeycomb core under 3-point bending loads. As ABS and PLA are common 3D printing materials, their bending behavior is of importance while they are provided as the materials for the sandwich structures.

2.1 Design and Development of Sandwich Structures

The specimens of sandwich structures were designed using SOLIDWORKS software. Honeycomb core thickness is 3 mm, and the solid plate core of the same weight is 1.08 mm in thickness. Another solid plate core was prepared for comparison, which is the same in thickness as the honeycomb core, 3 mm. All cores used in this study are made of PLA, while the face sheets are made of ABS with a thickness of 1 mm.

Sandwich composite with honeycomb core is shown in Fig. 1. To be more convenient, the structure name is abbreviated as SH (3 mm) subsequently in this paper.

Mechanical parameters used for ABS and PLA are listed in Table 1. Dimensions of the cores and face sheets are listed in Table 2. Figure 2 shows the composite plate with solid plate core with a thickness of 1.08 mm. During the experiment, it is called SSP (1.08 mm). In this composite plate, the core is made of the same amount of material as the honeycomb core of the specimen in Fig. 1. Another specimen has the same structure as the structure in Fig. 2, except for the thickness of the core, whose

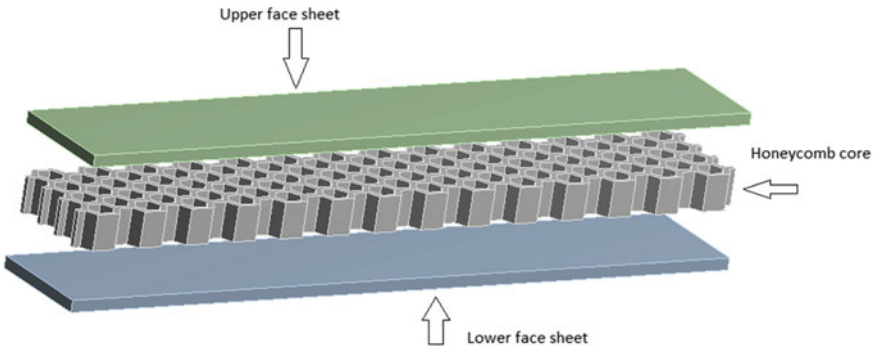

Fig. 1 Sandwich composite with honeycomb core

Table 1 Material parameters for ABS and PLA [11]

Constants	Unit	PLA	ABS
Density	Kg/m^3	1250	1210
Young's modulus	MPa	3500	2900
Poisson's ratio	–	0.36	0.422
Bulk modulus	Pa	4.1667×10^9	6.1966×10^9
Shear modulus	Pa	1.2868×10^9	1.0197×10^9
Tensile strength	MPa	46.8	34
Compressive strength	MPa	17.9	7.6

Table 2 Dimensions of sandwich structures

Components	Length (mm)	Width (mm)	Thickness (mm)
SH (3 mm) core	60.62	10	3
SSP (1.08 mm) core	60.62	10	1.08
SSP (3 mm) core	60.62	10	3
Face sheet	60.62	10	1

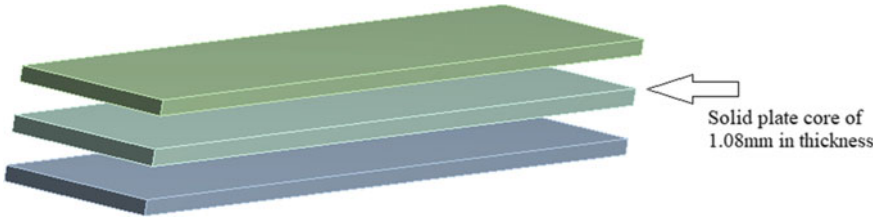

Fig. 2 Sandwich composite with solid plate core with a thickness of 1.08 mm

thickness is the same as that of the honeycomb core in Fig. 1, and this specimen is named SSP (3 mm).

2.2 Finite Element Modeling on Sandwich Structures Under 3-Point Bending

ANSYS is used to study the mechanical properties of the sandwich structures with various cores under the bending load ranging from 200 to 2000 N. To be more specific, the load is line load. The boundary conditions and meshing are shown in Fig. 3. The load is applied to the indenter, while the bottom of the support is fixed. Moreover, the mesh size is 1 mm. In this study, stress distribution on the sandwich structures is characterized using Von-Mises stress, while total deformation is taken as another indication of the mechanical behavior, while subject to the bending loads (Fig. 4).

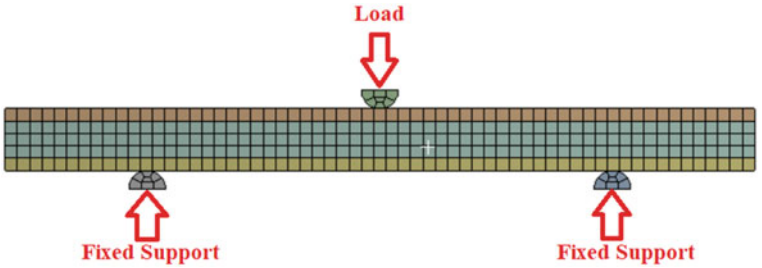

Fig. 3 -point bending (boundary conditions and meshing) and each fixed support is located 10 mm away from the nearest free end

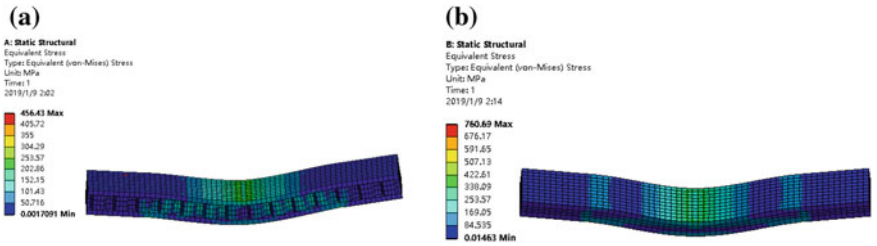

Fig. 4 Von-Mises stress distribution under the load of 1000 N: **a** Sandwich structure with honeycomb core stress distribution, **b** Sandwich structure with solid plate core with a thickness of 1.08 mm stress distribution

3 Results and Discussion

According to the stress distribution on the sandwich structures with various cores, the sandwich composite with honeycomb core presents rather lower maximum stress than the one with the solid plate core of the same weight as its, while the composite structure with the core of the same thickness as its shows a bit higher maxim stress value than it. Figure 5 shows the sandwich structure with a honeycomb core (SH) deforms more than the SSP (3 mm) having the same weight. SH's deformation pattern

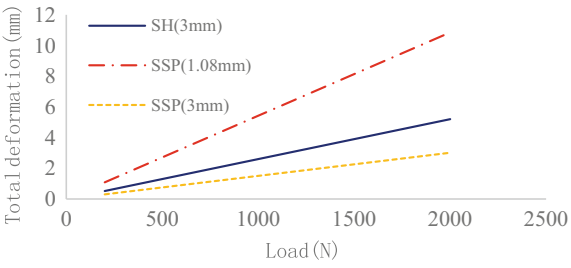

Fig. 5 Maximum total deformation of the sandwich composites under the bending loads from 200 to 2000 N

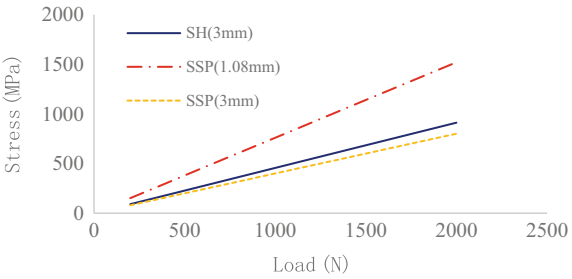

Fig. 6 Maximum Von-Mises stress on the sandwich structure of different cores under the loads from 200 to 2000 N

is even closer to the deformation pattern of the structure with the solid core of the same thickness.

As shown in Fig. 6, SH undergoes significantly less stress than SFP (1.08 mm) under the loading from 200 to 2000 N. While they differ in thickness, they are the same in weight. It can be inferred that honeycomb core undergoes less stress than the solid plate core of the same weight as it. As for SSP (3 mm) and SH (3 mm), these two specimens are of the same thickness while the SSP (3 mm) is three times heavier than the SH (3 mm). Despite this, they demonstrate more or less the same stress resistance performance. Therefore, while keeping the same mechanical performance, the honeycomb structure can substitute heavier solid structures than it.

4 Conclusion

According to the Von-Mises stress distribution and deformation on the sandwich structures under the loads, a sandwich structure with honeycomb core indicates better mechanical performances in deformation, and the stress against three times bending loads concerning the same weight. Therefore, it is preferable to utilize honeycomb structures in 3D printing to make parts with strong mechanical properties as well as low weight.

References

1. Biranchi, P.: Experimental and numerical modelling of mechanical properties of 3D printed honeycomb structures. Measurement. 495–506 (2018)
2. Simon, R.G., Bates.: Compressive behaviour of 3D printed thermoplastic polyurethane honeycombs with graded densities. Mater. Des. 130–142 (2019)
3. Robert, S.: A Comparative Finite Element Stress Analysis of Isotropic and Fusion Deposited 3D Printed Polymer (2014)
4. Chun, L.: Mechanical Performance of 3D-Printing Plastic Honeycomb Sandwich Structure. Int. J. Precis. Eng. Manuf.-Green Technol. **5**, 47–54 (2018)
5. Tiantian, L.: Bending behavior of sandwich composite structures with tunable 3D-printed core materials. Compos. Struct. **175**, 46–57 (2017)

6. Sarvestani, H.Y.: 3D printed meta-sandwich structures: failure mechanism, energy absorption, and multi-hit capability. Compos. Struct. Mater. Des. **160**, 179–193 (2018)
7. Shaoyu, H.: Mechanicalproperties of sandwich composites with 3d-printed auxetic and non-auxetic lattice cores under low-velocity impact. Mater. Des. **160**, 1305–1321 (2018)
8. McGregor, D.J.: Mechanical properties of hexagonal lattice structures fabricated using continuous liquid interface production additive manufacturing. Addit. Manuf. **25**, 10–18 (2019)
9. Paweł, B.: Deformation of honeycomb cellular structures manufactured with Laser Engineered Net Shaping (LENS) technology under quasi-static loading: Experimental testing and simulation. Addit. Manuf. **25**, 307–316 (2019)
10. Garam, K.: Investigating the effects of fluid intrusion on Nomex honeycomb sandwich structures with carbon fiber facesheets. Compos. Struct. **206**, 535–549 (2018)
11. The Difference between ABS and PLA for 3D Printing. http://www.protoparadigm.com/news-updates/the-difference-between-abs-and-pla-for-3d-printing. Last Accessed July 2015

Development and Fabrication of Automated Paper Recycling Machine

Rupesh G. Telrandhe, Dhananjay R. Ikhar and Anil C. Gawande

Abstract The present project work deals with the recycling of automated paper manufacturing machine. The paper manufacturing machine consists of some major components like paper crusher, sedimentation tank, rollers, conveyor belts, power system, etc. Paper recycling is important from the environmental perspective, as systematic collection and recycling of waste paper can significantly reduce the generation of environmental losses. A survey from the National Environmental Engineering Research Institute (NEERI), Nagpur, shows that 17 trees are required for the production of 1 ton. Also, the Indian Government statistics say that paper consumption in India is 9 million tons [1]. But as per our census, it is minimum 15 kg per capita. Thus, it is demanding to reuse the used paper. Thus, the paper manufacturing machine is too fabricated and automates to reduce labour cost and time. This will be done to enable waste paper conversion into a useful product. The chemicals used in this work are pollutant-free [2], and now, there is no harm to the environment.

Keywords Waste paper · Paper recycling · Automated machine

1 Introduction

The production and use of paper have a number of adverse effects on the environment which are known collectively as paper pollution [3]. Paper industry contributed to air, water and land pollution [4]. Paper recycling is the process of recovering and reusing waste papers. Manual recycling of paper recycling mechanism consumes more time. If we observe automation wise, many automated machines are available. But these machines are beyond the reach of the common people and can only be affordable by large-scale industries sector. So, at the initial level, automated machines can be fabricated, which can fulfil the need for such product which will be able to afford and utilized for recycling of the paper.

R. G. Telrandhe (✉) · D. R. Ikhar · A. C. Gawande
Datta Meghe Institute of Engineering Technology and Research, Wardha, Maharashtra, India
e-mail: rupeshtelrandhe1988@gmail.com

L. Li et al. (eds.), *Advances in Materials and Manufacturing Engineering*, Lecture Notes in Mechanical Engineering, https://doi.org/10.1007/978-981-15-1307-7_32

2 Experimental Set-up

This section describes the development and fabrication of the experimental set-up used to generate useful papers from waste paper recycling machine. Extensive data was generated by varying different parameters over wide ranges. This chapter deals with the experimental set-up, procedure and data collection. The set-up of the paper recycling machine is as shown in figure below. Experimental set-up shows the simplicity of the machine. The components are automatically operated. Line diagram for the whole waste paper recycling machine is shown in Fig. 1.

Waste paper recycling process contains mainly four steps which contain four important compartments and they are the grinder, settling section, pressing rollers and drying. A grinder is having a capacity of 1.5 litres per minute is used with the blades operating on 1 HP motor for crushing the paper and water mixture to form the pulp. Then the pulp is poured into the settling tank where it mixed with the chemicals. This pulp is transferred to the feeding tank from where it allowed flowing on the conveyor belt. Now, the uniformly distributed pulp is allowed to flow into the pressing section where the water gets separated out from it. It undergoes from the series of 4 rollers for proper uniformity. Then, it passes through the drying section where the blower is arranged with a heating coil to pass hot air in the drying zone, in this zone the water gets evaporated and the paper gets collected. Figure 2 shows the 3D model of the Project.

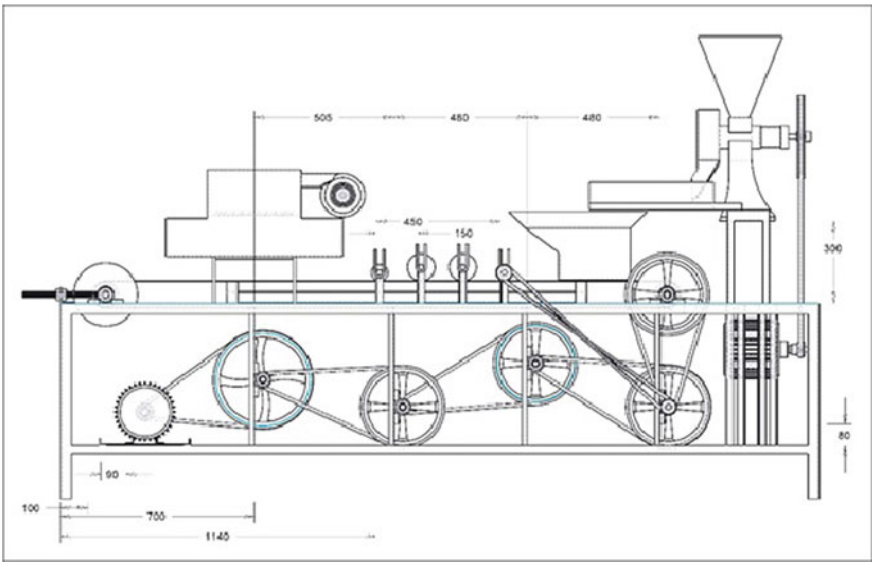

Fig. 1 Experimental set-up

Fig. 2 3-D Model of experimental set-up

2.1 Details of Chemical Used

In the paper recycling machine, to manufacture the good quality paper few chemicals [5] are used. The following chemicals are used according to their properties which react with paper pulp. Paper chemicals are a group of chemicals that are used to influence paper properties.

1. Hydrogen peroxide: In paper making, the alum reacts with rosin sizes of various types, helping to attach the newly form rosin aluminates to fibres sizing next the paper water resistant along which cationic charge is also used to flocculate anionic trash including paper fines and other anionic ally charged material by neutralization.
2. Rosin: It is added in the pulp to increase the strength of the paper and also increases the water resistance capacity,
3. Caustic soda: It also sometimes called lye is a corrosive substance and because of this property it is widely paper pulping and to remove ink. Table 1 indicates the proportion of the chemical for 1 kg of paper.
4. The chemicals used for this work is pollution free so there is no effect on environment.

Table 1 Chemicals and its quantity

Chemicals	Quantity for 1 kg of paper pulp (g)
Hydrogen peroxide	20
Rosin	20
Caustic soda	10

2.2 Operating Procedure

In the paper recycling machine, the operating procedure is carried out by using the following basic stages like

- Formation of pulp
- Stirring and settling section
- Pressing
- Drying.

1. First, the waste paper is allowed to soak in water with chemicals for 5–6 min.
2. Then, this mixture is poured into the hopper where it will crush to form the slurry (slurry is a mixture of crushed paper, water and chemicals).
3. Then, that slurry is allowed to flow into the sedimentation tank from which it will continue flowing uniformly on the conveyor belt.
4. Then, it passes through the first roller which is having the initial pressing and that gives a first uniform pressing.
5. Now, the pulp is allowed to flow from the high-pressure roller it will make the pulp as thin as possible.
6. It transfers under the dryer section where the water content in the pulp gets evaporated out.
7. And the paper gets collected from the end section by using the cloth.

3 Results and Discussions

When the paper recycling machine is used to manufacture the paper, it is found that the machine is effectively producing the paper using waste paper. The total set-up can be used as the paper manufacturing machine. The machine is producing fine craft paper sheet. The machine is capable of giving entrepreneurship to someone without using any external machines. Table 2 shows the experimental results.

The paper obtained by using the machine is shown in Fig. 3.

Figure 4 shows the outputs of the paper recycling machine.

Comparison of Recycled paper and Virgin paper.

While comparing recycled paper with virgin paper, it is observed that recycled paper is very economical than virgin paper. The following parameters compare how to recycle paper is boon for the environment. The statistics in the table comparing both the papers are given by NEERI, Nagpur, which is the biggest research centre in Vidharbha region contributes to various environmental projects of the government. One of their recent surveys is as shown in Table 3.

Table 2 Experimental results

Amount of crushed paper(g)	Water required(ml.)	Chemical added(g)	Length of paper(m)	Thickness (mm)
1000	3500	Rosin—25 g Caustic soda—30 g Hydrogen peroxide—10 g	7	0.5
150	1000	Rosin—15 g Caustic soda—10 g Hydrogen peroxide—5 g	1	0.5

Fig. 3 Outputs of the paper recycling machine

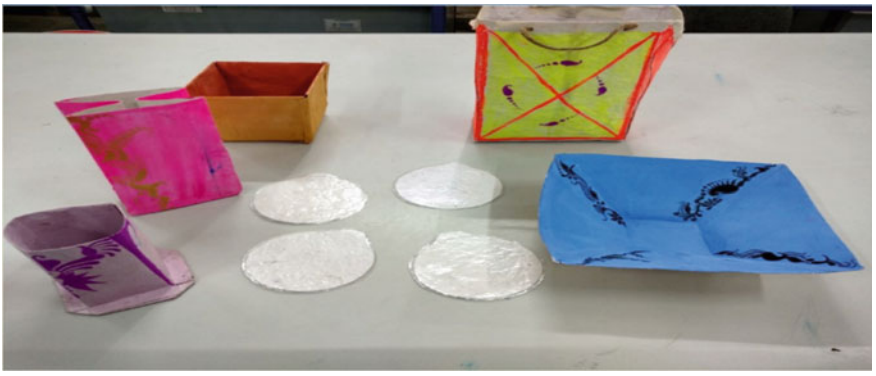

Fig. 4 Outputs of the paper recycling machine

Table 3 Comparison of recycled paper and virgin paper

Parameters	1 ton virgin fibre paper	1 ton 100% recycled paper	Environmental savings from recycled paper (%)
Trees	24 trees	0 trees	100
Energy	33 million BTUs	22 million BTUs	33
Greenhouse gases released-CO2 equivalent	2540 kg	1602 kg	37
Waste water	86,508 L	44,043 L	49
Solid waste	871 kg	531 kg	39

4 Conclusions

1. It has been concluded that the paper recycling machine produces 20 cm paper in one minute
2. The simplicity of operation of this machine ensures that no too much technical skill is needed to operate it. When the machine is well maintained, its durability is guaranteed.
3. It is the one practice from institute level against the unusual deforestation.
4. The use of this project in the small-scale producers of waste papers can contribute more than the large-scale producers so that they will be able to make nature go green and lessen the deforestation done for the production of the paper.
5. The development of automatic operated used paper recycling machine is much cheaper than the manually recycling industries. The fabricated machine can serve dual purposes, and it can be manned permanently at a stationary position or it could be shifted from one place to another as the case may be.

References

1. Raghuchandra, R.: Discussion paper on collection and recycling of waste paper in India. Ministry of environment and forests notification, 12th may 2011 on e-waste (management and handling) rules, 2011
2. Shrivastav, P.F.: Report on ecological and environmental factors in a paper industry, (volume III), central pulp and paper research institute: technological overview in Indian paper industry with suggestive measures for improved environment management. Prepared for Indian Paper Manufacturer Association, April, Saharanpur, Uttar Pradesh. India (2000)
3. Čabalová, I., Kačík, F., Geffert, A., Kačíková, D.: The effects of paper recycling and its environmental impact. Technical University in Zvolen, Faculty of Wood Sciences and Technology Slovakia
4. Yamashita, M., Suzuki, K.: Human society viewed from the perspective of 3R-Eco activities and environmental measures: part II—relationships between the use of waste paper, recycling of used

paper, and environmental Burden. Department of Environmental Systems Science, Doshisha University, 1–3 Miyakodani, Tatara, Kyo-tanabe, Kyoto, 610-0394, Japan (2014)
5. Kujur, S.K.: Globalisation, Energy efficiency and Material Consumption in a Resource based Industry: A Case of India's Pulp and Paper Industry 1980–81 to 2009–10

Stability Study of a Tapered Rotating Sandwich Beam with Asymmetric Configuration and Variable Temperature Gradient Under Dynamic Condition

M. Pradhan and P. R. Dash

Abstract The stability study of a tapered rotating sandwich beam with a variable temperature gradient under dynamic condition is investigated. The sequential steps used to reach the goal are (i) applying the extended Hamilton's principle, (ii) non-dimensionalizing the equations of motion, (iii) selecting shape functions from previous work to model the system mathematically depending on the boundary conditions, and (iv) using the Galerkin methodology. The influences of different system parameters on the regions of instability are considered and presented graphically. The results obtained with uniform and variable thermal gradients are compared.

Keywords Rotation parameter · Rotating sandwich beam · Non-uniformity parameter · Variable temperature gradient

Nomenclature

g	Shear parameter
B	Beam width
$(h_1)_x$	$(h_1)_l\left(1+\frac{x}{l}\alpha_1\right)$
$(h_3)_x$	$(h_3)_l\left(1+\frac{x}{l}\alpha_3\right)$
$(h_2)_x$	$(h_2)_0\left(2+\frac{x}{l}\left(\frac{(h_1)_0}{(h_2)_0}\right)\alpha_1+\frac{x}{l}\left(\frac{(h_3)_0}{(h_2)_0}\right)\alpha_3\right)$
t	Time
$w(x,t)$	Deflection of beam in transverse direction
ρ_i	Density of ith layer
ω	Excitation function frequency
g^*	$G\,(1+j\eta)$, complex shear parameter
h_{21}	$(h_2)_x \big/ (h_1)_x$

M. Pradhan (✉) · P. R. Dash
Department of Mechanical Engineering, VSSUT, Burla 768018, India
e-mail: osme.madhusmita@gmail.com

P. R. Dash
e-mail: prdash_india@yahoo.co.in

L. Li et al. (eds.), *Advances in Materials and Manufacturing Engineering*, Lecture Notes in Mechanical Engineering, https://doi.org/10.1007/978-981-15-1307-7_33

h_{31} $(h_3)_x / (h_1)_x$
lh_{10} $l / (h_1)_0$
$\overline{m}$ Mass/unit length of beam
$\overline{\omega}$ Excitation frequency non-dimensionalized
E_{31} E_3 / E_1
λ_0, λ_1 Rotation parameter
Ω_0 Uniform angular velocity of the beam around z'-axis

1 Introduction

With the aims of achieving superior properties like higher stiffness-to-weight ratio, high module sandwich beams (SBs) have been used extensively in recent years in comparison with ordinary beams in applications to engineering structures range from helicopter rotor blades to aircraft panels. SBs are also affected by temperature gradients, and so, those must be considered when designing the blades of gas and steam turbines. However, varying the cross-sectional configuration of a SB proves to be economical.

In previous work, Bhat [1] used the Rayleigh–Ritz approach to investigate the mode shapes and natural frequencies of a cantilever beam rotating at various speeds. Carnegie [2] established a theoretical expression for the work done by a cantilever blade, while rotating. Kar and Sujata [3] illustrated the effect of temperature on the Young's modulus of a non-uniform beam vibrating parametrically. Sujata and Kar [4] studied the dynamic behavior of a rotating SB by changing its boundary conditions. Ko [5] reviewed the flexural behavior of a tapered SB by considering linearly or uniformly distributed masses. Parida and Dash [6] analyzed a revolving beam of varying depth of linear nature with a temperature gradient and concluded that the temperature gradient influenced the stability. Pradhan and Dash [7] analyzed the consequence of temperature gradient on a non-uniform SB asymmetric configuration again and found that the stability was affected by taper parameter and temperature gradient. Pradhan et al. [8] studied the consequence of a temperature gradient on an asymmetric SB placed on a Pasternak foundation and concluded that, the stability depended on the foundation stiffness and the thermal gradient. Kar and Ray [9] even analyzed the performances SBs with different boundary conditions to investigate the instability of the system. The above brief literature survey shows that the effects of a uniform temperature gradient on the system have been considered previously. However, the temperature gradient for a non-uniform beam should be variable rather than constant. Till date, no distinguished work has been done with variable temperature gradients. In the present work, constant and variable temperature gradients are considered for analysis.

Table 1 Various mechanical properties of material

Mechanical properties/materials	Density (kg m^{-3})	Tensile Ultimate strength (Pa)	Modulus of elasticity (Pa)
ASTM A36 steel, plate	7.80 g/cc	550 MPa	200 GPa
Cu-Al alloy CuAl8Fe3	7.85 g/cc	470 MPa	170 GPa
Mechanical properties/materials	Density (kg m^{-3})	Tensile ultimate strength (Pa)	Modulus of rigidity (Pa)
Plywood	0.65 g/cc	13.8 MPa	620 MPa

1.1 Materials for the System

In this analysis, for the construction of three-layer sandwich beam, the structural steel and copper–aluminum alloy are considered for upper and lower layers, respectively, and plywood is used as viscoelastic middle layer. A suitable adhesive is used to join the layers. The materials considered in the construction of the beam with their different mechanical properties are given in Table 1.

1.2 System Modeling

Figure 1 shows the schematic diagram of a tapered SB of length l rotating with constant angular speed about the vertical axis. The system is acted upon by an axial force $P(t) = P_0 + P_1 \cos(\omega t)$, where P_0 is the maximum value static load and P_1 is the maximum magnitude of the dynamic load. At the extreme left-hand end, the thicknesses of the top, middle, and bottom layers are $2h_{1_0}$, $2h_{2_0}$, and $2h_{3_0}$, respectively. The corresponding thicknesses at the extreme right-hand end are $2h_{1_l}$, $2h_{2_l}$, and $2h_{3_l}$, respectively. Without considering temperature gradient, the Young's modulus of elasticity for the upper and lower layers are E_1 and E_3, respectively. The radial distance of the beam from the axis about which it rotates is b, which is referred to as the set-off

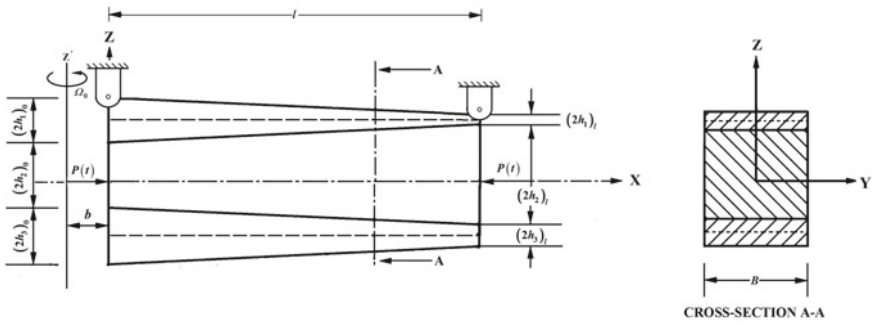

Fig. 1 System modeling

distance. The modulus of rigidity of the core layer is given by $G_2^* = G_2(1 + j\eta)$, which is a complex quantity.

The assumptions underlying the governing equations of motion and the boundary conditions of the physical system are those made by Pradhan and Dash [8]. However, the following two additional assumptions are made herein.

1. The temperature gradient is assumed to obey Fourier's law of heat conduction, with heat transfer along the longitudinal axis of the beam only.
2. Every point in a given cross section is at the same distance from the heat source. It is therefore assumed that the thermal gradient in the transverse direction for the aforementioned cross section is zero.
3. The respective expressions for potential energy, kinetic energy, and work done are as follows:

$$V = \frac{1}{2}\int_0^l E_{1,x}A_{1,x}U_{1,x}^2\mathrm{d}x + \frac{1}{2}\int_0^l E_{3,x}A_{3,x}U_{3,x}^2\mathrm{d}x + \frac{1}{2}\int_0^l \left(E_{1,x}I_{1,x} + E_{3,x}I_{3,x}\right)w_{,xx}^2\mathrm{d}x + \frac{1}{2}G_2^*\int_0^l A_{2,x}\gamma_2^2\mathrm{d}x$$

$$T = \frac{1}{2}\int_0^l \overline{m}w_{,t}^2\mathrm{d}x + \frac{1}{2}\Omega_0^2\int_0^l \left[\overline{m}(b+x)\int_0^x w_{,x}^2\,\mathrm{d}x\right]\mathrm{d}x + \frac{1}{2}\int_0^l \overline{m}\Omega_0^2 w^2\mathrm{d}x$$

and

$$w_p = \frac{1}{2}\int_0^l p(t)w_{,x}^2\,\mathrm{d}x$$

where U_3 and U_1 are the displacements along longitudinal direction in the lower and upper layers, respectively, $w_{,x} = \frac{\partial w}{\partial x}$, $w_{,t} = \frac{\partial w}{\partial t}$, and γ_2 is the strain due to shear in the core and is given by $\gamma_2 = \frac{U_1 - U_3}{2h_2} - \frac{Cw_{,x}}{2h_2}$.

U_3 is eliminated by using Kerwin's assumption [10].

Applying Hamilton's principle, the subsequent non-dimensional equations of motion are acquired

$$\overline{mw}_{,\overline{tt}} + \left[1 + \frac{\lambda_0^2\left(1 + E_{31}h_{31}^3\right)}{(lh_{10})^2(1 + E_{31}h_{31})}\left\{\frac{f}{l^2} - \left(\overline{x} + \overline{b}\right)^2\right\}\right]\overline{w}_{,\overline{xxxx}} - \frac{2\lambda_0^2\left(1 + E_{31}h_{31}^3\right)}{(lh_{10})^2(1 + E_{31}h_{31})}\left(\overline{x} + \overline{b}\right)\overline{w}_{,\overline{xxx}}$$

$$+\left[-\frac{\lambda_0^2\left(1+E_{31}h_{31}^3\right)}{(lh_{10})^2(1+E_{31}h_{31})}-\lambda_0^2\left\{\frac{f}{l^2}-\left(\overline{x}+\overline{b}\right)^2\right\}\right.$$
$$\left.-3g^*\left(1+\frac{h_{12}+h_{32}}{2}\right)^2+\overline{p}(\overline{t})\right]\overline{w}_{,\overline{xx}}+\lambda_0^2\left(\overline{x}+\overline{b}\right)\overline{w}_{,\overline{x}}$$
$$+\frac{3}{2}g^*lh_{10}h_{12}\left(1+\frac{h_{12}+h_{32}}{2}\right)(1+\alpha)\frac{2(h_2)_0}{C}\gamma_{2,\overline{x}}=0 \tag{1}$$

$$\frac{2(h_2)_0}{C}\gamma_{2,\overline{xx}}-\frac{g^*}{4}h_{12}^2\left(\frac{1+E_{31}h_{31}^3}{1+\alpha^2E_{31}h_{31}}\right)(1+\alpha)\left[(1+\alpha)\frac{2(h_2)_0}{C}\gamma_2\right.$$
$$\left.-\left(\frac{2\left(1+\left((h_{12}+h_{32})/2\right)\right)}{(lh_{10}h_{12})}\right)\overline{w}_{,\overline{x}}\right]=0 \tag{2}$$

In the above,

$$\overline{w}_{,\overline{xxxx}}=\frac{\partial^4\overline{w}}{\partial\overline{x}^4},\ \overline{w}_{,\overline{xx}}=\frac{\partial^2\overline{w}}{\partial\overline{x}^2},\ \gamma_{2,\overline{xxx}}=\frac{\partial^3\gamma_2}{\partial\overline{x}^3},\ \gamma_{2,\overline{xx}}$$
$$=\frac{\partial^2\gamma_2}{\partial\overline{x}^2},\ \overline{x}=\frac{x}{l},\ \overline{U}=\frac{U}{l},\ \overline{w}=\frac{w}{l},\ \overline{t}=\frac{t}{t_0},$$
$$C=(h_1)_l+(2h_2)_l+(h_3)_lt_0=\left[\frac{\rho_1A_{1_0}l^4}{E_1(I_1)_0}\right]^{1/2},$$
$$\overline{P}_0=\frac{P_0l^2}{E_1(I_1)_0},\ \overline{P}_1=\frac{P_1l^2}{E_1(I_1)_0},$$
$$\overline{P}=\overline{P}_0+\overline{P}_1\cos\left(\overline{\omega}\overline{t}\right),\ \overline{\omega}=\omega t_0,\ \lambda_0$$
$$=\sqrt{\left(\frac{\overline{m}\Omega_0^2l^4}{2(E_1(I_1)_0+E_3(I_3)_0)}\right)}$$
$$\lambda_1=\sqrt{\left(\frac{3\overline{m}\Omega_0^2l^2}{2(E_1(A_1)_0+E_3(A_3)_0)}\right)}$$

The parameters those are cross-sectional dependent are,

$$\overline{m}=(1-\overline{x})+\overline{x}\left(\frac{(h_1)_l}{(h_1)_0}\right)\left(\frac{\rho_2}{\rho_1}\right)\left(\frac{(h_2)_0}{(h_1)_0}(1-\overline{x})\left(\frac{\rho_3}{\rho_1}\right)\frac{(h_3)_0}{(h_1)_0}\right)(1-\overline{x})$$
$$+\overline{x}\left(\frac{(h_2)_l}{(h_1)_0}\right)\left(\frac{\rho_2}{\rho_1}\right)+\left(\frac{(h_3)_l}{(h_1)_0}\right)\left(\frac{\rho_3}{\rho_1}\right)\overline{x}$$
$$g*=\frac{G_2^*h_{21}(lh_{10})^2}{E_{1,x}\left(1+E_{31}h_{31}^3\right)}$$

The end conditions to be satisfied at the extremes are

$$\left[1+\frac{\lambda_0^2\left(1+E_{31}h_{31}^3\right)}{(lh_{10})^2(1+E_{31}h_{31})}\left\{\frac{f}{l^2}-\left(\overline{x}+\overline{b}\right)^2\right\}\right]\overline{w}_{,\overline{xxx}}$$
$$-\frac{2\lambda_0^2\left(1+E_{31}h_{31}^3\right)}{(lh_{10})^2(1+E_{31}h_{31})}\left(\overline{x}+\overline{b}\right)\overline{w}_{,\overline{xx}}=0 \tag{3}$$

Or

$$\overline{w}_{,\overline{x}}=0 \tag{4}$$

$$\left[\frac{\lambda_0^2\left(1+E_{31}h_{31}^3\right)}{(lh_{10})^2(1+E_{31}h_{31})}-\lambda_0^2\left\{\frac{f}{l^2}-\left(\overline{x}+\overline{b}\right)^2\right\}\right.$$
$$\left.-3g^*\left(1+\frac{h_{12}+h_{32}}{2}\right)^2+\overline{p}\left(\overline{t}\right)\right]\overline{w}_{,\overline{x}}=0 \tag{5}$$

Or

$$\overline{w}=0 \tag{6}$$

$$\frac{3}{2}g^*lh_{10}h_{12}\left(1+\frac{h_{12}+h_{32}}{2}\right)(1+\alpha)\frac{2(h_2)_0}{C}\gamma_{2,\overline{x}}=0 \tag{7}$$

Or

$$\gamma_2=0 \tag{8}$$

1.3 Approximate Series Solution

The above mentioned Eqs. (1) and (2) are simplified and mentioned as in the

$$\overline{w}\left(\overline{x},\overline{t}\right)=\sum_{i=1}^{i=p}w_i(\overline{x})\,f_i\left(\overline{t}\right) \tag{9}$$

$$\overline{\gamma}_2\left(\overline{x},\overline{t}\right)=\sum_{k=p+1}^{k=2p}\gamma_k(\overline{x})\,f_k\left(\overline{t}\right) \tag{10}$$

where w_i and γ_k are the shape functions, f_i and f_k are the generalized coordinates, and w_i and γ_k are chosen to satisfy as many boundary conditions as possible [11]. Here, as per Ray and Kar [9], the shape functions are chosen accordingly for the

different boundary conditions. Putting the above equations into Eqs. (1) and (2) and using the general Galerkin method yield the following matrix equations of motion in the generalized coordinates.

$$[m]\left\{\ddot{Q}_1\right\} + [k_{11}]\{Q_1\} + [k_{12}]\{Q_2\} = \{0\} \tag{11}$$

$$[k_{21}]\{Q_1\} + [k_{22}]\{Q_2\} = \{0\} \tag{12}$$

where

$$\{Q_1\} = \left\{f_1, \ldots, f_p\right\}^{\mathrm{T}} \tag{13}$$

$$\{Q_2\} = \left\{f_{p+1}, \ldots, f_{2p}\right\}^{\mathrm{T}} \tag{14}$$

$$M_{ij} = \int_0^1 \overline{m} w_i w_j \mathrm{d}\overline{x} \tag{15}$$

$$\begin{aligned} k_{11ij} = & \int_0^1 \left[1 + \lambda_1 \left\{\frac{f}{l^2} - \left(\overline{x} + \overline{b}\right)^2\right\}\right] w_i'' w_j'' \mathrm{d}\overline{x} \\ & + \lambda_0^2 \int_0^1 \left\{\frac{f}{l^2} - \left(\overline{x} + \overline{b}\right)^2\right\} w_i' w_j' \mathrm{d}\overline{x} \\ & + \int_0^1 \left\{3g^*\left(1 + \frac{h_{12} + h_{32}}{2}\right)^2 - \overline{p}(\overline{t})\right\} w_i' w_j' \mathrm{d}\overline{x} \end{aligned} \tag{16}$$

$$\begin{aligned} k_{12jl} = & -\left(\frac{3}{2}\right) \int_0^1 g^* l h_{10} h_{12} (1 + \alpha) \\ & \times \left(1 + \frac{h_{12} + h_{32}}{2}\right) \left(u_l w_i' \mathrm{d}\overline{x}\right) [k_{21}] = [k_{12}]^{\mathrm{T}} \end{aligned} \tag{17}$$

$$\begin{aligned} k_{22kl} = & 3 \int_0^1 (l h_{10})^2 \left\{\frac{\left(1 + \alpha^2 E_{31} h_{31}\right)}{\left(1 + E_{31} h_{31}^3\right)}\right\} \left(u_k' u_l' \mathrm{d}\overline{x}\right) \\ & + \frac{3}{4} \int_0^1 g^* (l h_{10})^2 h_{12}^2 (1 + \alpha)^2 (u_k u_l \mathrm{d}\overline{x}) \end{aligned} \tag{18}$$

In the above, $u_k = \frac{2h_2}{C}\gamma_k$, $u_l = \frac{2h_2}{C}\gamma_l$, and $w_i' = \frac{\partial w_i}{\partial x}$

$f = (l+b)^2$ for, $x = l = b^2$, for $x = 0 = \frac{l^2}{3} + b^2 + bl$, for other cases.
Equations (11) and (12) are simplified further to

$$[m]\{\ddot{Q}_1\} + \left[[k] - \overline{P}_0[H]\right]\{Q_1\} - \overline{P}_1 cos\left(\overline{\omega t}\right)[H]\{Q_1\} = \{0\} \tag{19}$$

where

$$[k] = \left[\overline{k}\right] - [k_{12}][k_{22}]^{-1}[k_{12}]^{\mathrm{T}} \tag{20}$$

$$H_{ij} = \int_0^1 w_i^{'} w_j^{'} \mathrm{d}\overline{x} \tag{21}$$

$$\begin{aligned}\left[\overline{k}\right]_{ij} = &\int_0^1 \left[1 + \lambda_1\left\{\frac{f}{l^2} - \left(\overline{x} + \overline{b}\right)^2\right\}\right] w_i'' w_j'' \mathrm{d}\overline{x} \\ &+ \lambda_0^2 \int_0^1 \left\{\frac{f}{l^2} - \left(\overline{x} + \overline{b}\right)^2\right\} w_i^{'} w_j^{'} \mathrm{d}\overline{x} \\ &+ \left\{3g^*\left(1 + \frac{h_{12} + h_{32}}{2}\right)^2\right\} \int_0^1 w_i^{'} w_j^{'} \mathrm{d}\overline{x}\end{aligned} \tag{22}$$

2 Instability Regions

Let for $[m]^{-1}\{k\}$, $[L]$ be a modal matrix. Introducing the linear transformation $\{Q_1\} = [m]^{-1}\{k\}$, where a set of new generalized coordinates is $\{u\}$ and a set of Hill's equation with complex coefficient is obtained from (19).

$$\ddot{u}_N + \omega_N^{*2} u_N + 2\varepsilon \cos\overline{\omega t}[B]u_N = 0 \tag{23}$$

where the distinct eigenvalues for $[m]^{-1}\{k\}$ are ω_N^{*2} and are given by $\varepsilon = \frac{\overline{P}_1}{2} < 1$, $[B] = -[m]^{-1}[L]^{-1}[H][L]$

As per Saito-Otomi [12], the modified Hsu's method is used to found the simple and combination resonance zones.

3 Numerical Results and Discussion

Here, number of graphs drawn considering uniform and variable temperature gradients with the hub radius, rotation parameter, and taper parameters for their various values. To keep minimum number of figures, some of the results are elaborated without figures. For certain parameter values, when considering a uniform rotating beam without thermal gradient, the equations of motion reduced to those of Kar and Sujata [4] and the results obtained are found to be similar.

Here, $\psi = \psi_0(1-\xi)$ is assumed as the temperature at any point ξ which is above the reference temperature. As per Kar and Sujata [3], the variation of modulus of elasticity of the beam can be written by choosing $\psi = \psi_0$, the temperature at the end $\xi = 1$ as the reference temperature as,

$$E(\xi) = E_1[1 - \lambda\psi_1(1-\xi)], 0 \le \lambda\psi_1 < 1 = E_1 T(\xi)$$

where λ is the coefficient of thermal expansion for the beam material, $\delta = \lambda\psi_1$ is the temperature gradient parameter, and $T(\xi) = \left[1 - \delta_\xi(1-\xi)\right]$, where $\delta_\xi = \left(A \big/ A_\xi\right)\delta$ is the variable temperature gradient parameter. Here, the following is considered:$\alpha = \frac{E_{1\xi}A_{1\xi}}{E_{3\xi}A_{3\xi}} = \frac{E_1 T(\xi)A_1}{E_3 T(\xi)A_3} = \frac{E_1 A_1\left[1-\delta_{1\xi}(1-\xi)\right]}{E_3 A_3\left[1-\delta_{2\xi}(1-\xi)\right]}$

Where δ_1 and δ_2 are the temperature gradients in the upper and lower layers, respectively. The values used for the different parameters are as follows:

$\eta = 0.01, b = 0.05, g = 0.1, \lambda_0 = 0.05, \lambda_1 = 0.1, \delta_1 = 0.1, \delta_2 = 0.2$ and $P_0 = 0.05$.

3.1 Regions of Instability

Figures 2 and 3 show the effects of δ_1. The dynamic stability decreases as δ_1 is increased from 0.5 to 1 because the zones are shifted toward lower excitation frequencies, thereby making the system unstable.

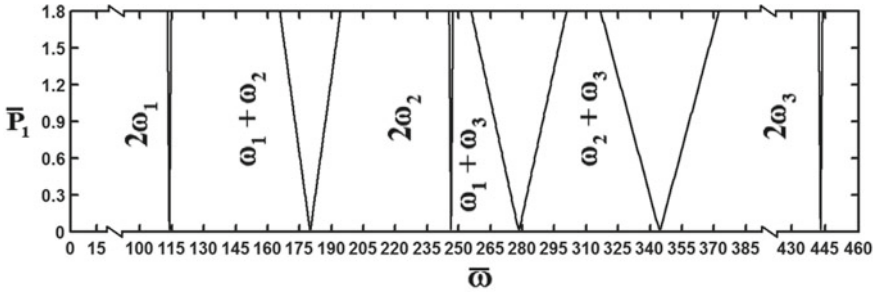

Fig. 2 Stability plot for $\delta_1 = 0.5$

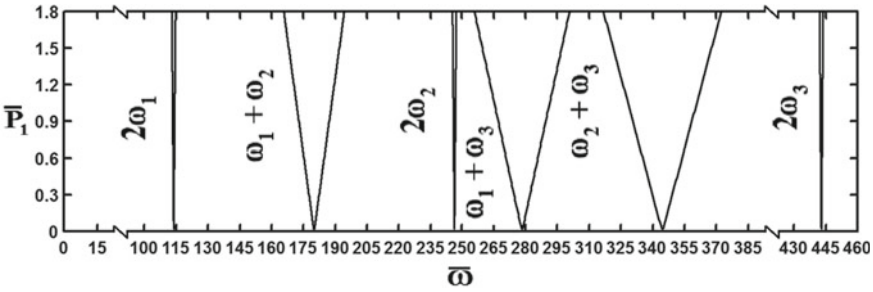

Fig. 3 Stability plot for $\delta_1 = 1$

Figures 4 and 5 show the effects of δ_{ξ_1}. The dynamic stability decreases as δ_{ξ_1} is varying from 0.5 to 1 because the zones shifted toward lower excitation frequencies, thereby making the system vulnerable. Comparing Figs. 4 and 5 with Figs. 2 and 3 shows that the system stability worsens, when a variable thermal gradient is considered instead of uniform one. As shown in Figs. 6 and 7, increasing Ω_0 from 10 to 20 shifted the resonance zones toward higher excitation frequencies, thereby stabilizing the system.

Again in Figs. 8 and 9, the resonance zones shifted toward lower excitation frequencies as b is increased, thereby making the system unstable.

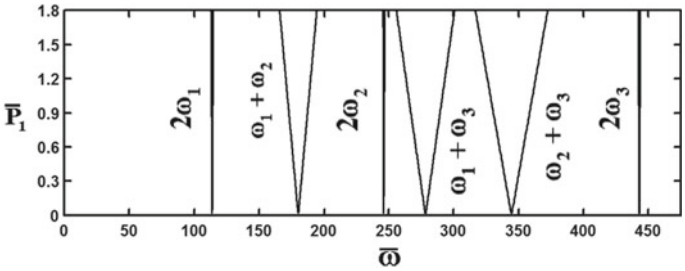

Fig. 4 Stability plot for $\delta_{\xi_1} = 0.5$

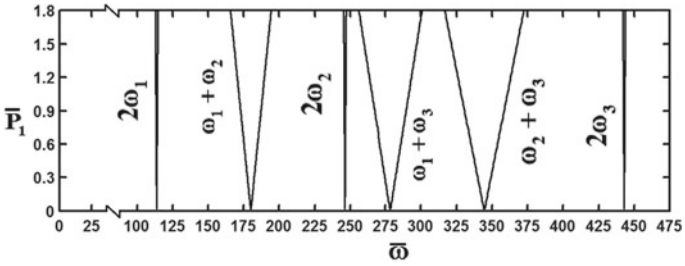

Fig. 5 Stability plot for $\delta_{\xi_1} = 1$

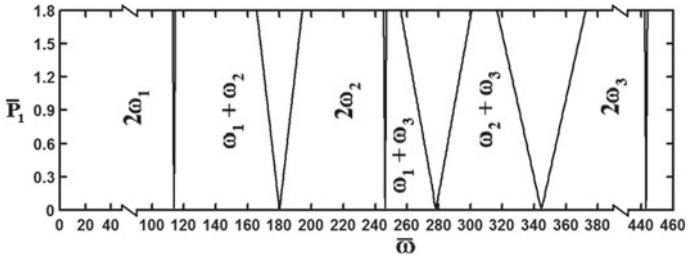

Fig. 6 Stability plot for $\Omega_0 = 10$

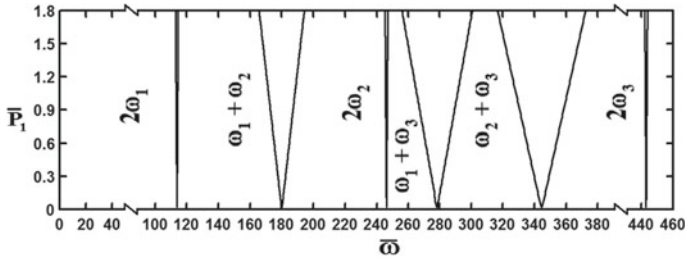

Fig. 7 Stability plot for $\Omega_0 = 20$

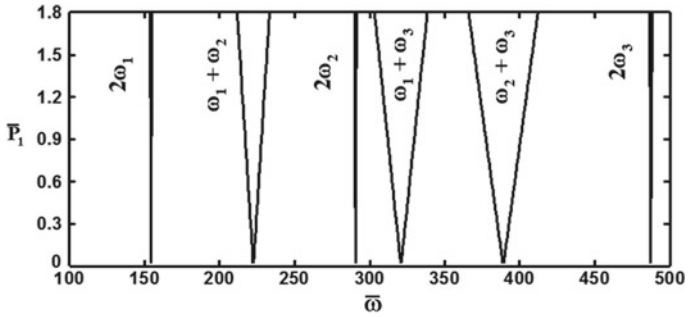

Fig. 8 Stability plot for $b = 0.05$

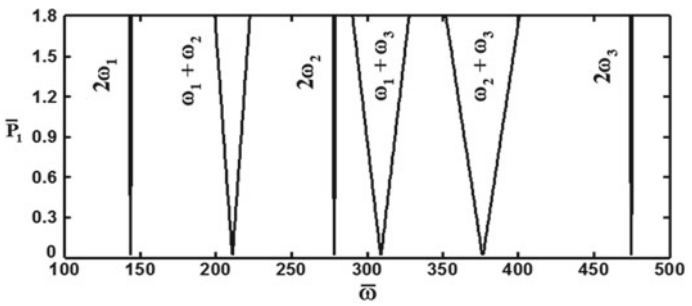

Fig. 9 Stability plot for $b = 0.1$

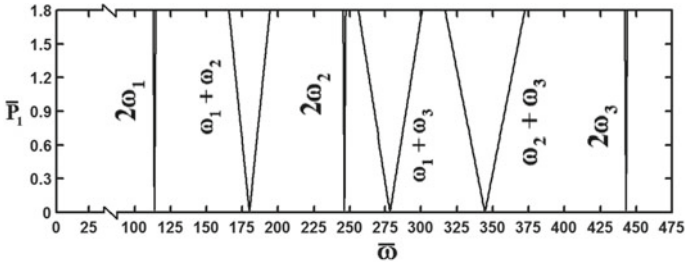

Fig. 10 Stability plot for $\delta_{\xi_2} = 0.5$

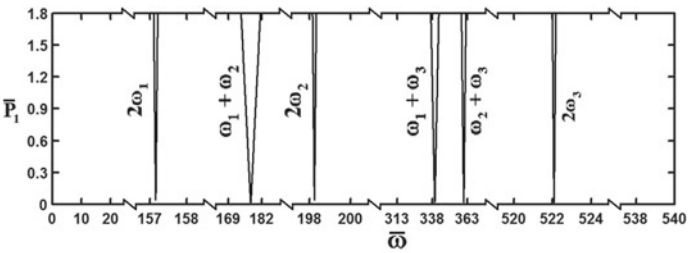

Fig. 11 Stability plot for $\delta_{\xi_2} = 1$

The dynamic stability improves as δ_2 is increased from 0.5 to 1 because the zones shifted toward higher excitation frequencies, thereby making the system more stable. Figures similar to those of Figs. 10 and 11, so not presented here. Figures 10 and 11 show the effects of δ_{ξ_2}. The dynamic stability increases as δ_{ξ_2} is increased from 0.5 to 1 because the zones shifted toward higher excitation frequencies, thereby making the system less susceptible to periodic forces. The system with a variable thermal gradient for the bottom layer is more stable than one with a uniform thermal gradient.

4 Conclusion

Investigations were made of the dynamic stabilities of a linearly tapered asymmetric rotating SB explored to a harmonic axial load with a variable temperature gradient under clamped–pinned end condition. From the results, it is concluded that the system stability worsens with increase of the hub radius, the taper parameters, and the temperature gradient in the top layer. By contrast, faster rotation and larger temperature gradient in the bottom layer improve the system stability. It is also found that the results vary depending on whether the temperature gradient varies or is uniform. The system stability improves with a larger variable temperature gradient in the bottom layer but degrades with a larger variable temperature gradient in the top layer.

References

1. Bhat, R.B.: Transverse vibrations of a rotating uniform cantilever beam with tip mass as predicted by using beam characteristic orthogonal polynomials in the Rayleigh-Ritz method. J. Sound Vib. **105**(2), 199–210 (1986)
2. Carnegie, W.: Vibrations of rotating cantilever blading: theoretical approaches to the frequency problem based on energy methods. J. Mech. Eng. Sci. **1**(3), 235–240 (1959)
3. Kar, R.C., Sujata, T.: Parametric instability of a non-uniform beam with thermal gradient resting on a Pasternak foundation. Comput. Struct. **29**(4), 591–599 (1988)
4. Kar, R.C., Sujata, T.: Dynamic stability of a rotating beam with various boundary conditions. Comput. Struct. **40**(3), 753–773 (1991)
5. Ko, C.L.: Flexural behavior of a rotating sandwich tapered beam. AIAA J. **27**(3), 359–369 (1989)
6. Parida, R., Dash, P.: Dynamic stability analysis of a circularly tapered rotating beam subjected to axial pulsating load and thermal gradient under various boundary conditions. Int. J. Acoust. Vib. **21**(2), 139–144 (2016)
7. Pradhan, M., Dash, P.R.: Stability of an asymmetric tapered sandwich beam resting on a variable Pasternak foundation subjected to a pulsating axial load with thermal gradient". Compos. Struct. **140**, 816–834 (2016)
8. Pradhan, M., Dash, P.R., Pradhan, P.K.: Static and dynamic stability analysis of an asymmetric sandwich beam resting on a variable Pasternak foundation subjected to thermal gradient. Meccanica **51**(3), 725–739 (2016)
9. Ray, K., Kar, R.C.: Parametric instability of a sandwich beam under various boundary conditions. Comput. Struct. **55**(5), 857–870 (1995)
10. Kerwin Jr., E.M.: Damping of flexural waves by a constrained viscoelastic layer. J. Acoust. Soc. Am. **31**(7), 952–962 (1959)
11. Leipholz, H.: Stability Theory, 2nd edn. John Wiley and Sons, Chichestar (1987)
12. Saito, H., Otomi, K.: Parametric response of viscoelastically supported beams. J. Sound Vib. **63**(2), 169–178 (1979)

Experimental Investigations on Activated-TIG Welding of Inconel 625 and AISI 304 Alloys

Santhiyagu Joseph Vijay, S. Mohanasundaram, P. Ramkumar, Hong Gun Kim, Alexandre Tugirumubano and Sun Ho Go

Abstract Activated-TIG (A-TIG) welding is an offshoot of gas tungsten arc welding process (GTAW), which uses a flux, applied over the faying surface before carrying out welding. It results in increased joint penetration and depth-to-width ratio. In this present investigation, Inconel 625 and AISI 304 are welded individually and together using A-TIG process. Owing to their high resistance to corrosion and wear, those materials are commonly used in marine and ship building applications. The process parameters are fixed based on a number of experimental trials and the welding is carried out using the optimized parameters. Investigations on the weldments such as tensile strength and microstructure are carried out and presented. When compared to GTAW process, results show that the weldments exhibit better mechanical and metallurgical properties while welded using A-TIG process. It is also imperative from the results that A-TIG process is a good contender for dissimilar joints as well.

Keywords Inconel 625 · AISI 304 · A-TIG process · Tensile strength · Microstructure

1 Introduction

Activated tungsten Inert gas welding (A-TIG) is an offshoot of GTAW process with similar process characteristics but enhanced performance. The enhanced performance include improved weld quality by producing weld pool with better geometrical characteristics having higher depth of penetration [1]. The variation in A-TIG process is that it uses a coating of flux on the faying surface before the welding is carried out. The materials, which are subjected to similar as well as dissimilar material welding, are Inconel 625 and AISI 304. Inconel 625 is classified as a superalloy

S. J. Vijay (✉) · S. Mohanasundaram · P. Ramkumar
Department of Mechanical Engineering, Karunya Institute of Technology and Sciences, Coimbatore 641114, Tamil Nadu, India
e-mail: vijayjoseph.2001@gmail.com

H. G. Kim · A. Tugirumubano · S. H. Go
Carbon Technology Laboratory, Department of Mechanical and Automotive Engineering, Jeonju University, Jeonju 55069, South Korea

L. Li et al. (eds.), *Advances in Materials and Manufacturing Engineering*, Lecture Notes in Mechanical Engineering, https://doi.org/10.1007/978-981-15-1307-7_34

with Ni as the base material. The other alloying elements, such as chromium, molybdenum carbon and niobium in nickel–chromium matrix, strengthen the compound [2]. The alloy can retain its high strength at very high temperature. The alloy with a non-magnetic characteristics and better corrosion resistance also does not precipitate at room temperature or at elevated temperature [3]. The alloy is commonly used in marine, aeronautical, petrochemical and aerospace industries. Some of the other applications include reactor cores, pressurized water reactors, heat exchange tubes, etc. [4]. On the other hand, AISI 304 exhibits property combinations which encompasses better mechanical and metallurgical properties. It has characteristics such as good formability, better weldability and high resistance to stress corrosion cracking [5]. Owing to its resistance to corrosion and better heat dissipation properties, austenitic stainless steel is extensively used in fabrication industry [6]. Most common applications of AISI 304 include structural material for nuclear reactors, petrochemical pipe value bodies, ship vessel internal structures, containers in chemical and processing industries, etc. [7]. However, the hardness of the material is low and does not have very good tribological properties as well limiting its applications. Dissimilar materials are being welded so that the property that is deficient in one metal can be compensated by another metal by appropriately choosing right combinations [8]. There are various welding methods for the joining of different metals of different composition. A-TIG is one such process which produces weldments with good bead appearance and better weld bead quality for dissimilar welding [9]. Many researchers have studied various process parameters, effect of those parameters on the evolution of microstructure and weldability of dissimilar materials. They have reported the optimum conditions to obtain better weld quality. But for the material combination studied in this paper and A-TIG has been hitherto reported [10, 11].

2 Experimental Set-Up

2.1 Materials and Methods

The combination of materials used for the study is Inconel 625 and AISI 304. The base material plate having thickness of about 5 mm is cut into a strip of 100 mm × 50 mm × 5 mm by shearing machine and then machined with a milling machine for a good surface finish.

A-TIG is chosen to weld those materials. In this welding, the depth of penetration of welding could be increased by the activated flux, and on the other hand, the heat-affected zone on the parent metal could be minimized. The variables that affect weld bead geometry, weld penetration and overall weld quality include welding current, arc voltage (arc length), travelling speed, shielding gas and its flow rate, heat input at each joint and total heat input, electrode diameter, polarity and torch angle. The selected value of parameters for welding is mentioned in Table 1.

Table 1 Process parameters for A-TIG welding

Process parameters	Units	GTAW welding	A-TIG welding
Current	A	200 (first pass) 140 (second pass)	180, single-pass complete penetration
Voltage	V	15.1–33.57	15.1–33.57
Travelling speed	mm/min	90 (approx.)	90 (approx.)
Shielding gas	–	Argon	Argon
Shielding gas flow rate	cm^3/min	18	18
Heat input (at each pass)	kJ/min	0.735–0.816 (first pass) 0.570–0.603 (second pass)	0.789–0.949
Total heat input	kJ/min	1.362	0.869

The sheets of Inconel 625 and AISI 304 are immersed in sodium hydride baths to remove contaminants. After the sodium hydride treatment, the specimens were immersed in an H_2SO_4 bath 165 °F (74 °C) for just 3 min. The specimen were then immersed for 25 min in HNO and HFl acids and then rinsed to remove contaminants. The materials to be welded are made ready by making the necessary edge preparation. To obtain a good surface finish, milling operation is carried on and is machined to a dimension of about 50 mm length, 30 mm width and 5 mm thickness. The specimens that are to be welded are cleaned with acetone even before the application of ceramic powders as flux. Since the flux is found in powdered form, it is mixed with acetone to form a paste. The paste is applied over the specimen with the help of brush using forward and reverse stroke over the desired area. The fluxes used are chromium oxide, titanium oxide and calcium oxide. The specimen is clamped to the vice to reduce distortion during welding. Polarity is set to Direct Current Electrode Negative.

3 Results and Discussions

3.1 Tensile Strength

The specimens from the weld are machined as per ASTM E08 standard to get a flat dog bone shape tensile specimens as shown Fig. 1. The tensile test as per the specified standard was performed with the position rate of 1 mm/min at an atmospheric temperature (27 °C) in a 50 kN UTM machine. During the test, the uniform incremental axial load was applied in order to get the load–displacement values which were used to determine the tensile strength and elongation at failure. The tensile tested samples were visually evaluated and noted that fracture occurred in the welded location of the manufactured samples. The result obtained from the tensile test as load vs displacement graph is furnished in Table 2.

Fig. 1 Typical tensile test specimen as per ASTM E08 standard

Table 2 Tensile strength of weldments for various fluxes and material combinations

Flux used	Tensile strength (N/mm^2)		
	Inconel 625-Inconel 625	AISI 304-AISI 304	Inconel 625-AISI 304
Without flux	488.92	618.67	228.33
Titanium oxide	422.84	628.83	515.59
Calcium oxide	425.4	460.3	492.3
Chromium oxide	501.35	533.76	540.05

The result shows that calcium oxide and chromium oxide flux had enriched the tensile strength when compared with the specimen welded in the absence of flux. Titanium oxide flux produces an intermediate tensile strength when compared to parent similar welding. The reason for the increase in the tensile strength may be the increase in the current density and the arc force acting at the weld nugget, enabling a better material flow and penetration. The materials also consolidate well during the application of those fluxes.

The specimens were then cut from the welding plates for metallographic examinations. Specimens were polished using emery sheets. The specimens were then polished with 0.5 μm diamond paste. After etching using marble's reagent, microstructures of base parent metal, heat-affected zone, fusion zone (weld zone) and weld metal pool in the weldment were assessed by a scanning electron microscope (SEM).

Figures 2, 3, 4, 5 and 6 show the SEM micrographs of the welded sample. Figures 2 and 3 show the SEM images of the parent metal in as received condition. Figure 4 shows the SEM image of the welded portion of Inconel. Figures 5 and 6 show the interface between the dissimilar materials at the fusion zone. From the SEM

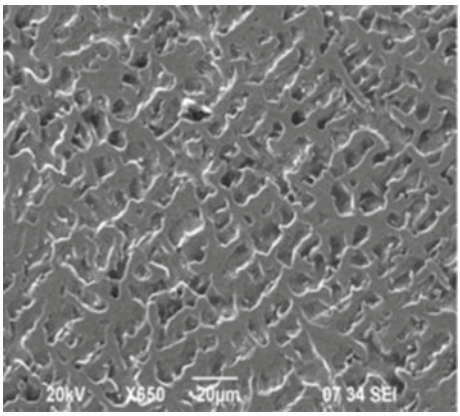

Fig. 2 SEM image of Inconel 625

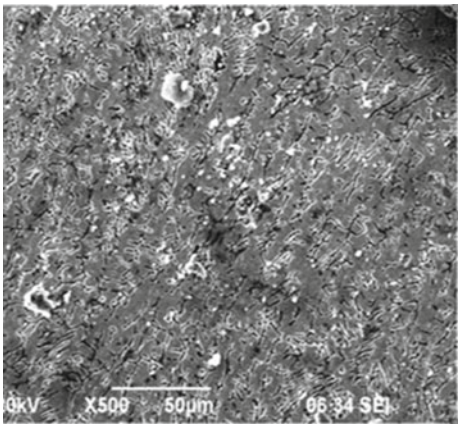

Fig. 3 SEM image of AISI 304

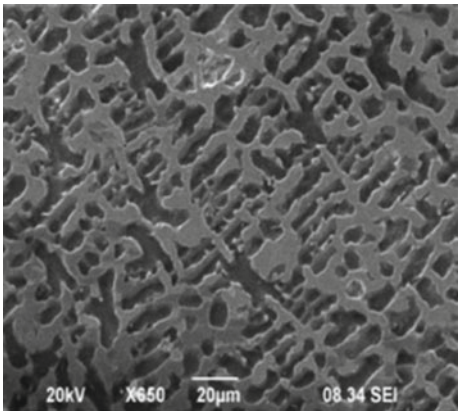

Fig. 4 SEM image of weld material microstructure

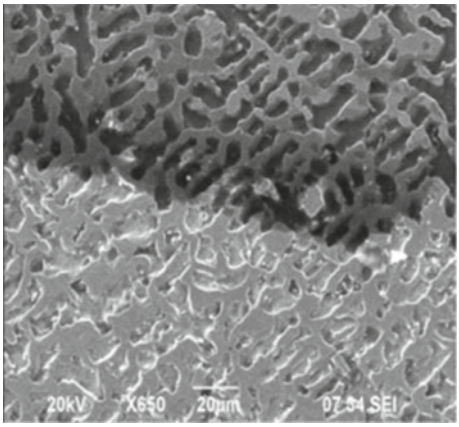

Fig. 5 SEM image of fusion boundary microstructure

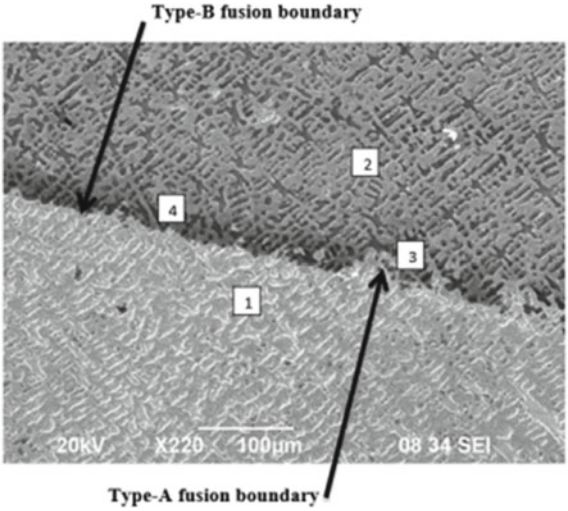

Fig. 6 Magnified SEM image of fusion boundary microstructure. 1. HAZ; 2. Weld Zone; 3. Type-A fusion boundary; 4. Type-B fusion boundary

images (Figs. 5 and 6), it was found that there were two different categories of fusion boundaries. They are interchangeably distributed along the boundary interface. The first category of fusion boundary is mainly located at the corner. The second category of fusion boundaries is located amidst the primary weld bead. The length measured in the first category fusion boundary was roughly around 15% of the overall length of it. The composition variation of heat-affected zone (HAZ) and the diffusion of various elements of the alloys are observed on either sides of that fusion boundary, but on the side, where Inconel 625 was present, the second type fusion boundary is predominant and looks different when compared to the first type. It takes different hindering effect by changing from cellular microstructure to dendritic microstructure at the place of element diffusion.

4 Conclusion

From conducting trials on similar welding of AISI 304, Inconel 625 and dissimilar welding of AISI 304 and Inconel 625, it is found that

- The UTS of similar welding of Inconel 625 coated with chromium oxide is the maximum of 859 MPa while the ultimate tensile strength of similar welding of AISI 304 coated with chromium oxide is 506 MPa
- The ultimate tensile strength of dissimilar welding of AISI 304 and Inconel 625 coated with chromium oxide is 679 MPa
- The study demonstrated that A-TIG process has the ability to make dissimilar joints of plate thickness of 5 mm. This can be achieved in single pass having a complete penetration of weld metal throughout the depth.
- Titanium oxide and chromium oxide fluxes had given the complete penetration.
- Microstructures revealed two different categories of fusion boundaries. It also showed that the fusion boundaries are distributed along the weld interface.

References

1. Marya, M.: Theoretical and experimental assessment of chloride effects in the A-TIG welding of magnesium. Weld. World **46**(7–8), 7–21 (2002)
2. Shakil, M., Ahmad, M., Tariq, N.H., Hasan, B.A., Akhter, J.I., Ahmed, E., Mehmood, M., Choudhry, M.A., Iqbal, M.: Microstructure and hardness studies of electron beam welded Inconel 625 and stainless steel 304L. Vacuum **110**, 121–126 (2014)
3. Song, K.H., Nakata, K.: Effect of precipitation on post-heat-treated Inconel 625 alloy after friction stir welding. Mater. Des. **31**(6), 2942–2947 (2010)
4. Shankar, V., Rao, K.B.S., Mannan, S.L.: Microstructure and mechanical properties of Inconel 625 superalloy. J. Nucl. Mater. **288**(2–3), 222–232 (2001)
5. Arivazhagan, N., Singh, S., Prakash, S., Reddy, G.M.: Investigation on AISI 304 austenitic stainless steel to AISI 4140 low alloy steel dissimilar joints by gas tungsten arc, electron beam and friction welding. Mater. Des. **32**(5), 3036–3050 (2011)
6. Buytoz, S., Ulutan, M.: In situ synthesis of SiC reinforced MMC surface on AISI 304 stainless steel by TIG surface alloying. Surf. Coat. Technol. **200**(12–13), 3698–3704 (2006)
7. Kumar, S., Shahi, A.S.: Effect of heat input on the microstructure and mechanical properties of gas tungsten arc welded AISI 304 stainless steel joints. Mater. Des. **32**(6), 3617–3623 (2011)
8. Meshram, S.D., Mohandas, T., Reddy, G.M.: Friction welding of dissimilar pure metals. J. Mater. Process. Technol. **184**(1–3), 330–337 (2007)
9. Modenesi, P.J., Apolinario, E.R., Pereira, I.: TIG welding with single-component fluxes. J. Mater. Process. Technol. **99**(1–3), 260–265 (2000)
10. Dupont, J.N., Banovic, S.W., Marder, A.R.: Microstructural evolution and weldability of dissimilar welds between a super austenitic stainless steel and nickel-based alloys. Weld. J. **82**(6), 125 (2003)
11. Naffakh, H., Shamanian, M., Ashrafizadeh, F.: Dissimilar welding of AISI 310 austenitic stainless steel to nickel-based alloy Inconel 657. J. Mater. Process. Technol. **209**(7), 3628–3639 (2009)

Experimental Investigation on Low-Pressure Receiver Incorporated Domestic Refrigerator with Al_2O_3 Nanoparticles

Vemuloori Vasu, Donthu Rakesh, K. Bintu Sumanth and V. Uma Sai Vara Prasad

Abstract Decades onwards research has been going on for enhancing COP of refrigerators used for domestic needs. Here, in this work, an attempt was made to enhance COP by applying both subcooling and superheating simultaneously using LPR to VCR system. This paper studies experimentally about the performance analysis of a 165 L low-pressure receiver (LPR) incorporated domestic refrigerator with Al_2O_3 nanoparticles dispersed in the lubricant oil. According to the (American society of heating, refrigerating and air-conditioning engineers. Atlanta, Georgia, from the 1994 ASHRAE Handbook—Refrigeration [1]) recommendations, a suitable low-pressure receiver was designed, fabricated, and installed to 165 L capacity refrigerator in between evaporator and compressor with the Al_2O_3 nanoparticles dispersed in lubricant oil. The system was subjected to various loads such as 100, 150, 200, and 250 W. The performance parameters such as the compressor power, refrigeration effect, and COP are evaluated and a comparison is made between with and without LPR and nanoparticles. The investigation outcomes revealed that there is an appreciable change in the COP, i.e., 14.2% increment with addition of the Al_2O_3 nanoparticles to the refrigeration system with LPR. It is also found that out of four loads, the COP of LPR refrigerator with Al_2O_3 nanoparticles is the higher at 200 W.

Keywords Refrigerator · Al_2O_3 nanoparticles · Low-pressure receiver

V. Vasu (✉) · K. Bintu Sumanth
Department of Mechanical Engineering, V R Siddhartha Engineering College, Vijayawada, Andhra Pradesh, India
e-mail: vemuloori.vasu@gmail.com

D. Rakesh
Department of Mechanical Engineering, Sree Vidyanikethan Engineering College, Sree Sainath Nagar, Tirupati, Andhra Pradesh, India

V. Uma Sai Vara Prasad
Department of Mechanical Engineering, VFSTR (Deemed to be University), Vadlamudi, Guntur, Andhra Pradesh, India

L. Li et al. (eds.), *Advances in Materials and Manufacturing Engineering*, Lecture Notes in Mechanical Engineering, https://doi.org/10.1007/978-981-15-1307-7_35

1 Introduction

Nowadays, refrigerators are widely used for storage of foods which may deteriorate at ambient temperatures; decay due to growth of bacteria and other processes is slower in refrigerators work at low temperatures. In the present scenario, most of the domestic refrigerators are working based on the vapor compression refrigeration system. It is slightly similar to a reversed Rankin cycle. The vapor compression refrigeration system contains four main parts namely compressor, condenser, expansion device, and evaporator. Refrigeration and air conditioning are two major power consumptions throughout the world, by increasing the COP of systems power consumption was reduced, from the decades onwards research going on to enhance COP of refrigeration systems.

Sendil Kumar et al. [2] conducted experimental investigation on nano-Al_2O_3-PAG oil. In this research, R134a refrigeration system using nano-Al_2O_3-PAG oil as nano-refrigerant is employed. The attained outcomes show that there is no problem of using Al_2O_3 nano-refrigerant in R134a system. Performance of refrigeration system was better than pure lubricant with R134a refrigerant. By using nano-lubricant of 0.2%v, concentration of Al_2O_3 energy consumption is reduced about 10.32%. Lung-yuejeng et al. [3] conducted studies on replacement of R134a refrigerant and polyester (POE) lubricant oil with hydrocarbon refrigerant and mineral oil.

Experimental results show that 60% R134a and 0.1 wt% Al_2O_3 nanoparticles is the best and optimum conditions. At these conditions, power consumption of the compressor reduced about 2.4% and COP was increased by 4.4%. A nano-fluid is an advanced heat transfer fluid which may be used to overcome the limitations of poor thermo-physical properties like lower thermal conductivity and higher friction factor of base fluids. Many researchers have come to a conclusion that the application of nano-fluids improved the fluid thermal conduction and consequently increased the heat transfer characteristics. The idea of nano-fluid is first proposed by Choi [4] in 1995.

Nano-fluids are found to have advantages like (a) higher thermal conductivity, (b) high stability, (c) lower dynamic viscosity, (d) negligible pressure drop, and (e) negligible pipe wall corrosion. In the last twenty years, different analysis teams showed and confirmed nano-fluids as a promising future for heat transfer applications with their higher stability and improvement in thermal conduction, voluminous compositions [4–6].

The low-pressure receiver then acted as an accumulator and liquid subcooler to ensure no liquid returned to the compressor [7]. A (LPR) vessel is placed in the low-pressure side of refrigeration system. Its motive was to permit refrigerant from the evaporator to LPR for separating liquid and gas and store the liquid. The high-pressure liquid line from the condenser passes through the bottom of the receiver where the low-pressure liquid is collected. The heat from the high-pressure line causes the liquid in the bottom of the receiver to boil while subcooling the liquid line. The vapor existing at the top side of the LPR is drawn back to the compressor

over the high-pressure liquid line, superheating it and ensuring no liquid returns to the compressor [1].

Another substitute for existing refrigeration systems was therefore investigated. The research study was shown that the incorporation of LPR enhances the effectiveness and reliability of large chlorofluorocarbon (CFC) and ammonia refrigeration systems [1]. In lot of small capillary-based systems, designers need to ensure that the entire liquid refrigerant was evaporated at the exit of the evaporator and there are a few degrees of superheat to prevent liquid returning to the compressor. In a low-pressure receiver system, the aim is to overfeed the evaporator and therefore control of superheat by the expansion device is not required. Therefore, the consolidation of LPR and capillary tube will provide an economic and fuel efficient system that could operate reliably over a wide range of duties [1, 8, 9].

Literature review showed that both the methods, i.e., incorporating low-pressure receiver and dispersing nanoparticles into lubricant oil of refrigerator increases the COP of refrigerator. This work describes some of the technical developments of a novel refrigerator. Here, in this research work, the above two were added to refrigeration system simultaneously.

2 Fabrication and Erection of Low-Pressure Receiver and Setup

Steps followed to fabricate low-pressure receiver:

1. Fabrication of LPR bottom and top parts as per design specifications.
2. Erection of all necessary ports to top and bottom parts as per design specifications.
3. LPR volume control dummy fabrication and pressure testing.
4. Condenser coil bending along dummy surface Fig. 1.
5. Insertion of condenser coil with dummy in LPR and sealing by brazing and full welding Fig. 1.
6. Conducting pressure test to inspect leaks by using CO_2.
7. Cleaning of receiver inner surface by using pump.
8. Painting work to LPR.
9. Set up erection and erection of receiver to set up Fig. 3 (Table 1).

3 Experimental Testing Procedure

First, the refrigerator test rig is checked properly for any refrigerant leakage, all component line connections, electrical connections, etc. The main power switch is switched on. The hand shut valve V_2 and V_3 should be opened and hand shut valve V_1 should be closed before starting the unit for run the unit with low-pressure receiver Fig. 2. The readings of pressure gauges (suction, discharge) and energy meter were

Fig. 1 Fabrication of low-pressure receiver

Table 1 Specifications of test rig

S. No.	Setup	Material	Specification
1	*Refrigerator* a. Compressor b. Condenser c. Evaporator	Hermetically sealed Copper, forced Draught air cooled Plate type	165 L 1/2HP No of tubes-22, surface area- 2798 cm^2
2	*Refrigerant*	R134a	240 g
3	Nanoparticles for investigation	Al_2O_3	Average diameter 30–50 nm size and density 5606 kg/m^3 were used
4	*Low-pressure receiver*	Steel like SA516/517 Grade 60/70 material.	Vessel diameter—7 cm Total length of receiver—18 cm Net effective volume of receiver—316.4 cm^3

noted. Temperature readings should be noted at respective locations by using infrared thermometer. The readings of various pressure gauges are noted and absence of any reading indicates the leakage of pipe line or leakage of gas. The unit is run for half an hour and the following readings are taken once in 20 min.

- Discharge pressure gauge (P_1)
- Suction pressure gauge (P_2)
- Discharge pressure gauge at compressor exit point (T_2)
- Discharge temperature at condenser exit point (T_3)
- Suction temperature at compressor inlet (T_1)
- Ambient temperature (T_a)
- LPR liquid out temperature (T_3l)

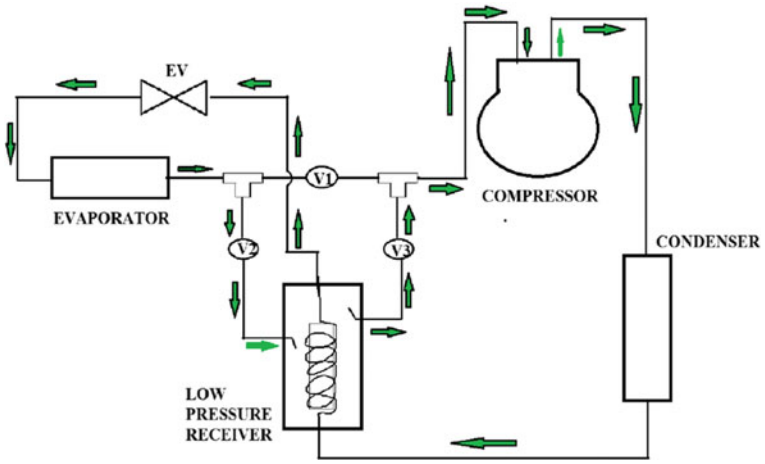

Fig. 2 Line diagram with and without LPR

- LPR liquid in temperature (T_3)
- LPR suction out temperature (T_1)
- LPR suction in temperature (T_1l)
- Refrigerant inlet temperature
- into evaporator (T_4) (Fig. 3).

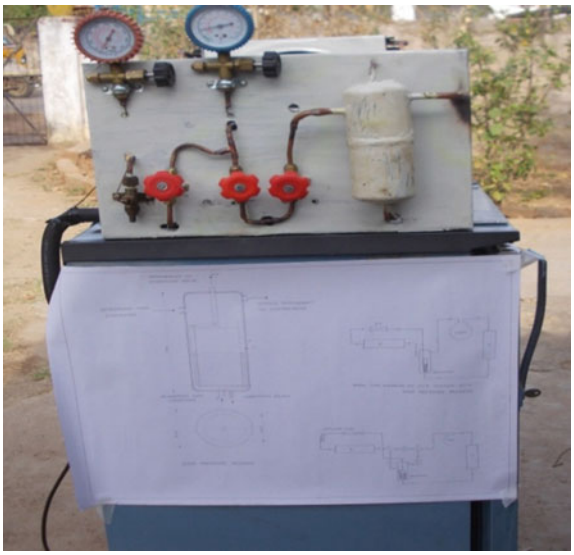

Fig. 3 Experimental setup

The *P–h* chart is drawn accordingly and the COP and cooling capacity are found with the help of formulae. Also, the readings of current and final energy meter are noted down.

$$\begin{aligned}\text{Coefficient of performance (COP)} &= (\text{Refrigerating effect})/(\text{work done})\\ &= (h_1 - h_4)/(h_2 - h_1) \qquad (1)\end{aligned}$$

$$\text{Cooling capacity} = m(h_1 - h_4) \qquad (2)$$

where m = mass flow rate in kg/mini
h_1 = enthalpy of refrigerant in
h_4 = enthalpy of refrigerant at end of expansion.
h_3 = enthalpy of refrigerant at the end of cooling of refrigerant or condenser outlet
h_2 = enthalpy of superheated vapor refrigerant at the end of compression in where, enthalpy units in kJ/kg.

3.1 Vessel Design Analysis

The design low-pressure receiver corresponds to approximately to a 1 ton refrigeration load in evaporator. The vapor volume flow rate is the summation of the evaporated refrigerant from the load and the vapor from the low-pressure receiver for maintaining a constant liquid level in vessel.

3.2 Vertical Vessel

The following vertical vessel model recommendations are considered.

1. According to [1] recommendations

(a) Vessel diameter: $D_{\text{vessel}} = 6.8$ cm (=7 cm)

(b) length of the liquid section corresponds to surge and ballast;

$$L \text{ liquid} = (v_{\text{surge}} + v_{\text{ballast})}/\left((\pi/4) \times D^2_{\text{vessel}}\right) = 13.7\,\text{cm}(= 14\,\text{cm})$$

(c) Height of nozzle above maximum liquid level

$$H = D_{\text{vessel}}/5 = 1.37\,\text{cm}(=2\,\text{cm})$$

(d) sum the length to determine the total length

$$\begin{aligned}L_{\text{vessel}} &= L_{\text{liquid}} + H + \text{allowance(i.e., vertical separation distance)}\\ L_{\text{vessel}} &= 18\,\text{cm}.\end{aligned}$$

Fig. 4 Trans-o-sonic sonicator and prepared Al_2O_3 in POE nano-lubricant having weight concentration of 0.9 wt%

4 Preparation of Nano-lubricant

In present work, Al_2O_3 nanoparticles are introduced into refrigeration system by adding Al_2O_3 nanoparticles to the lubricant oil in the compressor. The Al_2O_3 nanoparticles having mean diameter 20–40 nm size and density 5606 kg/m^3 were used for this investigation. For the preparation of nano-lubricant standard and effective method, i.e., two-step methods are used.

While preparation of lubricant, stability of lubricant and Al_2O_3 nanoparticle concentration are to be considered as very important. Required quantity of nanoparticles is weighed on mass balance and mixed with POE oil. This prepared mixture was kept in hot plate magnetic stirrer for 6 h. After stirring, the prepared mixture is subjected to ultrasonic sounds on sonicator for 10 h as shown in Fig. 4. Nanoparticles fully separated by ultrasonic sounds are generated by sonicator with 30 kHz frequency. No surfactant was added to prepare nano-lubricant, because it may affect thermophysical properties of refrigerant and also system performance. The following images are the prepared nano-lubricant after ultrasonifications.

5 Results and Discussion

The experimental investigation is done on the LPR incorporated refrigerator to find Al_2O_3 nanoparticles, and experiments are conducted with and without Al_2O_3 nanoparticles (Fig. 5).

6 Conclusion

The liquid overfeed system (low-pressure receiver system) has been successfully implemented in industries, and so, the implementation of this LPR system to domestic

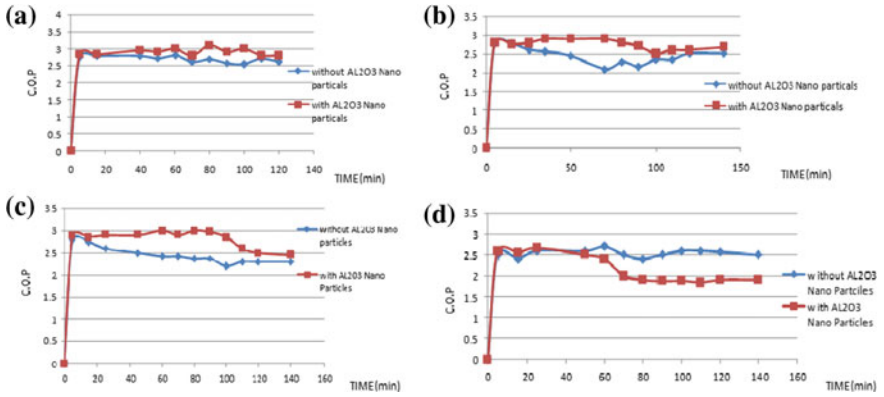

Fig. 5 **a** Graph between COP verses time at 100 W load. **b**. Graph between COP verses time at 150 W load. **c** Graph between COP verses time at 200 W load. **d** Graph between COP versus time at 250 W load

refrigeration with Al_2O_3 nanoparticles is encouraged in this work to achieve better performance.

The performance of low-pressure receiver and Al_2O_3 nanoparticles on domestic refrigerator is evaluated at different loads such as 100, 150, 200, and 250 W in freezer. It is found that the performance parameters, i.e., compressor work, refrigeration effect, and respective COP are going to be increased. The comparison of performance parameters with and without Al_2O_3 nanoparticles is made at the following loads in the evaporator (Table 2).

There is an appreciable change in COP (14.2% increase in COP) with the addition of AL_20_3 nanoparticles to LPR incorporated domestic refrigerator. It is found that in the above four loads, the COP of refrigerator with LPR has been the highest at 200 W and at high heat loads, i.e., above 200 W, the COP of refrigerator with LPR is decreased. The reason may be at high heat loads, the LPR may be not having liquid refrigerant up to designed level.

The use of a LPR and Al_2O_3 nanoparticles was shown as an efficient and effective method to enhance COP of refrigerator further.

Table 2 Comparison of performance parameters at various loads

Load (W)	Compressor work (W)		Refrigeration effect (W)		COP	
	With Al_2O_3	Without Al_2O_3	With Al_2O_3	Without Al_2O_3	With Al_2O_3	Without Al_2O_3
100	135.8	105	372.1	273.8	2.7	2.6
150	195.5	177.8	535.6	416.3	2.75	2.34
200	235	216.7	662.2	524.4	2.81	2.41
250	325	255.6	705	661.6	2.1	2.58

References

1. American society of heating, refrigerating and air-conditioning engineers. Atlanta, Georgia, from the 1994 ASHRAE Handbook—Refrigeration
2. Sendil Kumar, D., Elansezhian, R.: Experimental study on Al_2O_3-R134a nano refrigerant in refrigeration system. Int. J. Mod. Eng. Res. **2**, 3927–3929 (2012)
3. Jeng, L.-Y., Jwo, C.-S., Teng, T.-P., Ho, C.: Effects of Nano lubricant on performance of hydrocarbon refrigerant system. J. Vac. Sci. Technol. **B 27**, 1473–1477 (2009)
4. Murshed, S.M.S., Leong, K.C., Yang, C.: Enhanced thermal conductivity of TiO_2- water based nanofluids. Int. J. Therm. Sci. **44**(4), 367–373 (2005)
5. Yu, W., Choi, S.S.U.S.: The role of interfacial layers in the enhanced thermal conductivity of nanofluids: a renovated Maxwell model. J. Nanoparticle Res. **5**(1/2), 167–171 (2003)
6. Vasconcelos, A.A., Cárdenas Gómez, A.O., Bandarra Filho, E.P., Parise, J.A.R.: Experimental evaluation of SWCNT-water nanofluid as a secondary fluid in a refrigeration system. Appl. Therm. Eng. **111**, 1487–1492 (2017)
7. Evans, J., Hammond, E., Gigiel, A.: Development of a noval multi-capillary, multi-temperature commercial refrigerator cabinet with common low pressure receiver. Int. J. Refrig. **31**(3), 464–471 (2008)
8. Cengel, Y.: Heat and Mass Transfer, 4e. McGraw Hill Publication (2012)
9. Arora, C.P.: Refrigeration and Air conditioning PHI Publications (2010)

Numerical Examination of Sharp V-Notches Using Notch-Flank Displacement Collocation Method

Mirzaul Karim Hussain and K. S. R. K. Murthy

Abstract In this paper, a recently developed notch-flank displacement collocation technique (NDCT) is utilized to determine the notch stress intensity factors (NSIFs) of sharp V-notches. The mode I and mode II NSIFs are determined using the notch flanks opening and sliding finite element (FE) displacements, respectively. The rigid body displacements, which play an important role in the displacement components, are not neglected to calculate the NSIFs. The NSIFs of various benchmark configurations under pure mode I and mixed-mode (I/II) loading conditions have been calculated.

Keywords Stress intensity factor · Finite element · NDCT · NSIF

1 Introduction

Notch stress intensity factor (NSIF) plays an important role in the assessment of static and fatigue strength of brittle materials for the components having sharp V-notches. For the sharp V-notches, Williams [1] suggested that the singular stress field exists in the vicinity of the sharp V-notches, and the singularity stress field can be described in terms of NSIFs. Therefore, many techniques have been developed by researchers to compute the NSIFs accurately in the past decades. A boundary collocation method and a body force method were proposed by Gross and Mendelson [2] and Chen [3], respectively, to evaluate the NSIFs. Using finite element (FE) stresses, Ju and Chung [4] and Liu et al. [5] determined the NSIFs utilizing least-squares methods. Ayatollahi and Nejati [6] developed a method using FE displacements to calculate the NSIFs. It has been known that the notch-flank displacements are most accurate, and taking these advantage authors developed a notch-flank displacement collocation technique (NDCT) [7] and a point substitution displacement technique [8] to obtain the mixed-mode (I/II) NSIFs. The presence of rigid body components in the displacement field plays a major role in the accuracy in NSIFs calculated from the FE displacements. In the method proposed by authors [7], the rigid body components in the displacement

M. K. Hussain (✉) · K. S. R. K. Murthy
Department of Mechanical Engineering, Indian Institute of Technology Guwahati, Guwahati 781039, India
e-mail: mirzaul@iitg.ac.in

L. Li et al. (eds.), *Advances in Materials and Manufacturing Engineering*, Lecture Notes in Mechanical Engineering, https://doi.org/10.1007/978-981-15-1307-7_36

field are not neglected, rather, nicely negotiated using simple formulae. Thus, the main thrust of the present work is to demonstrate efficacy the NDCT proposed by authors [7] in terms of accurate estimation of the NSIFs of various notched specimens with straight and curved boundaries under mode I and mixed-mode (I/II) loading conditions.

2 Theoretical Background

The displacement field near a sharp V-notch (Fig. 1) in terms of the Williams constants can be given as [4]

$$\begin{aligned} u &= \frac{\kappa+1}{2G}A_0 + \frac{A_1}{2G}r^{\lambda_1^{\mathrm{I}}}\left\{\left(\kappa+\lambda_1^{\mathrm{I}}\cos 2\alpha+\cos 2\alpha\lambda_1^{\mathrm{I}}\right)\cos\lambda_1^{\mathrm{I}}\theta-\lambda_1^{\mathrm{I}}\cos\left(\lambda_1^{\mathrm{I}}-2\right)\theta\right\} \\ &\quad + \frac{B_1}{2G}r^{\lambda_1^{\mathrm{II}}}\left\{\left(-\kappa-\lambda_1^{\mathrm{II}}\cos 2\alpha+\cos 2\alpha\lambda_1^{\mathrm{II}}\right)\sin\lambda_1^{\mathrm{II}}\theta+\lambda_1^{\mathrm{II}}\sin\left(\lambda_1^{\mathrm{II}}-2\right)\theta\right\} - \frac{\kappa+1}{2G}B_2 r\sin\theta \\ v &= \frac{A_1}{2G}r^{\lambda_1^{\mathrm{I}}}\left\{\left(\kappa-\lambda_1^{\mathrm{I}}\cos 2\alpha-\cos 2\alpha\lambda_1^{\mathrm{I}}\right)\sin\lambda_1^{\mathrm{I}}\theta+\lambda_n^{\mathrm{I}}\sin\left(\lambda_1^{\mathrm{I}}-2\right)\theta\right\} + \frac{\kappa+1}{2G}B_0 \\ &\quad + \frac{B_1}{2G}r^{\lambda_1^{\mathrm{II}}}\left\{\left(\kappa-\lambda_1^{\mathrm{II}}\cos 2\alpha+\cos 2\alpha\lambda_1^{\mathrm{II}}\right)\cos\lambda_1^{\mathrm{II}}\theta+\lambda_1^{\mathrm{II}}\cos\left(\lambda_1^{\mathrm{II}}-2\right)\theta\right\} + \frac{\kappa+1}{2G}B_2 r\cos\theta \end{aligned} \quad (1)$$

where κ equals to $(3-\nu)/(1+\nu)$ for plane stress, $G = E/2(1+\nu)$ is the shear modulus, ν and E are the Poisson's ratio and Young's modulus, respectively, and λ_1^{I} and λ_1^{II} are the modes I and II eigenvalues, respectively. Mode I and mode II NSIFs can be obtained as [2]

$$\begin{aligned} K_{\mathrm{I}} &= \sqrt{2\pi}\lambda_1^{\mathrm{I}}\left(1+\lambda_1^{\mathrm{I}}-\lambda_1^{\mathrm{I}}\cos 2\alpha-\cos 2\alpha\lambda_1^{\mathrm{I}}\right)A_1 \\ K_{\mathrm{II}} &= \sqrt{2\pi}\lambda_1^{\mathrm{II}}\left(-1+\lambda_1^{\mathrm{II}}-\lambda_1^{\mathrm{II}}\cos 2\alpha+\cos 2\alpha\lambda_1^{\mathrm{II}}\right)B_1 \end{aligned} \quad (2)$$

It can be shown that [7], the notch opening displacement (NOD) and notch sliding displacement (NSD) can be written as

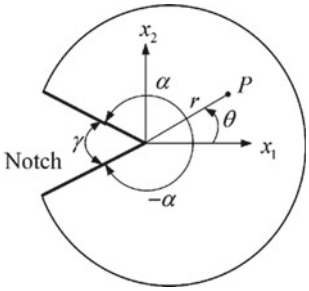

Fig. 1 Notch geometry

$$\Delta v = v^{\mathrm{I}}_{\theta=+\alpha} - v^{\mathrm{I}}_{\theta=-\alpha} = 2\frac{A_1}{2G} r^{\lambda^{\mathrm{I}}_1} \left[\begin{array}{r} \left(\kappa - \lambda^{\mathrm{I}}_1 \cos 2\alpha - \cos 2\alpha \lambda^{\mathrm{I}}_1\right) \sin \lambda^{\mathrm{I}}_1 \alpha \\ +\lambda^{\mathrm{I}}_1 \sin\left(\lambda^{\mathrm{I}}_1 - 2\right)\alpha \end{array} \right] = 2A_1 C_1 r^{\lambda^{\mathrm{I}}_1}$$

$$\Delta u_\alpha = u^{\mathrm{II}}_{\theta=+\alpha} - u^{\mathrm{II}}_{\theta=-\alpha} = 2\frac{B_1}{2G} r^{\lambda^{\mathrm{II}}_1} \left[\begin{array}{r} \left(-\kappa - \lambda^{\mathrm{II}}_1 \cos 2\alpha + \cos 2\alpha \lambda^{\mathrm{II}}_1\right) \sin \lambda^{\mathrm{II}}_1 \alpha \\ +\lambda^{\mathrm{II}}_1 \sin\left(\lambda^{\mathrm{II}}_1 - 2\right)\alpha \end{array} \right]$$

$$- 2\frac{\kappa + 1}{2G} B_2 r \sin\alpha = 2B_1 C_2 r^{\lambda^{\mathrm{II}}_1} + 2B_2 C_3 r \tag{3}$$

where C_1, C_2 and C_3 are constants of material property and geometry. Now, the NOD can be rewritten in logarithm form as

$$\ln(\Delta v) = \ln(2A_1 C_1) + \lambda^{\mathrm{I}}_1 \ln(r) \tag{4}$$

Considering N number of nodes along the notch flanks (as shown in Fig. 2a) and the residual R_{I} between the FE and analytical NOD can be written as

$$R_{\mathrm{I}} = \sum_{j=1}^{N} \left[\ln\left(\Delta v_j^{FE}\right) - \ln(A_1) - \ln(2C_1) - \lambda^{\mathrm{I}}_1 \ln\left(r_j\right)\right]^2 \tag{5}$$

For the minimum value of R_{I}, the partial differentiation of R_{I} with respect to $\ln(A_1)$ should be equals to zero, and after some algebraic calculations A_1 can be obtained as [7]

$$A_1 = \exp\left[\frac{1}{N}\sum_{j=1}^{N} \ln\left(\Delta v_j^{FE} r_j^{-\lambda^{\mathrm{I}}_1}\right)\right] \Big/ 2C_1 \tag{6}$$

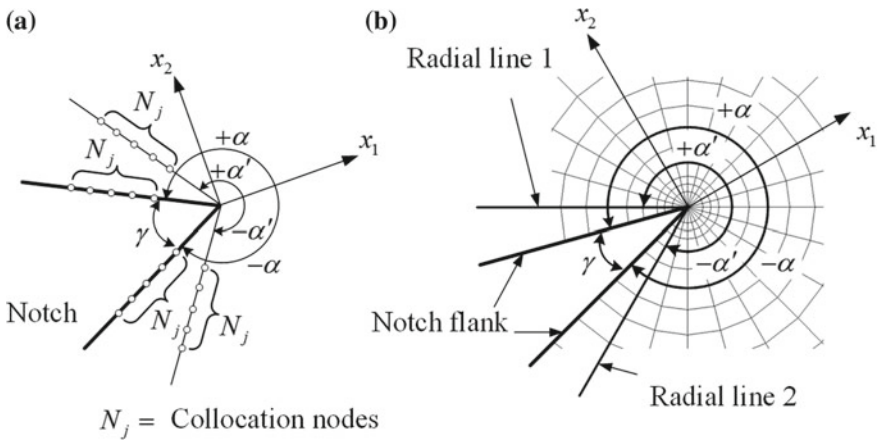

Fig. 2 **a** Selection of the collocation nodes and **b** notch tip elements

The notch sliding displacement ($\Delta u_{\alpha'}$) along the two radial lines (Fig. 2b) can be written as [7]

$$\Delta u_{\alpha'} = u_{\theta=+\alpha'} - u_{\theta=-\alpha'} = 2B_1 C_2' r^{\lambda_1^{II}} + 2B_2 C_3' r \tag{7}$$

where C_2' and C_3' are constants. The effective notch sliding displacement (ENSD) Δu can be obtained as [7]

$$\Delta u = \Delta u_\alpha C_3' - \Delta u_{\alpha'} C_3 = 2B_1 \left(C_2 C_3' - C_2' C_3\right) r^{\lambda_1^{II}} = 2B_1 C_4 r^{\lambda_1^{II}} \tag{8}$$

Similar to mode I, by minimizing the residual between the analytical ENSD and FE ENSD, B_1 can be obtained as [7] (more details can be read from [7])

$$B_1 = \exp\left[\frac{1}{N}\sum_{j=1}^{N} \ln\left(\Delta u_j^{FE} r_j^{-\lambda_1^{II}}\right)\right] \Big/ 2C_4 \tag{9}$$

3 Results and Discussions

3.1 Example 1: Mode I Specimen

A pure mode I example of a single edge notched plate under uniform tension (SENT), as shown in Fig. 3a is considered as the first example. The geometry and loading parameters are $w = 10$, $h = 12$ and $\sigma = 1.0$ (Fig. 3a). The NSIFs are determined for $a/w = 0.5$ and $\gamma = 0°$, 30°, 60°, and 90°. Young's modulus $E = 1$ and Poisson's

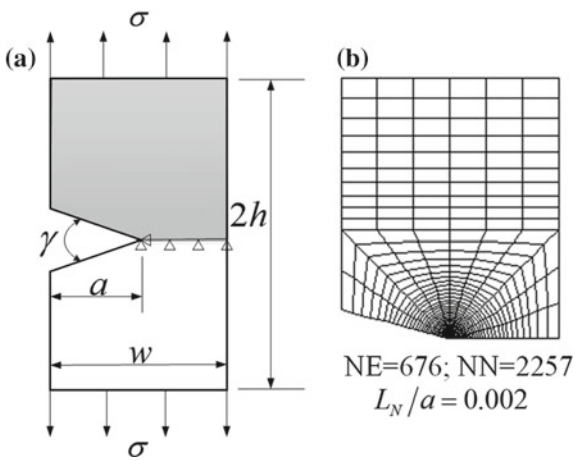

Fig. 3 **a** SENT specimen and **b** typical FE mesh

Table 1 Normalized NSIFs $F_{\mathrm{I}} = K_{\mathrm{I}} \Big/ \sigma(\tau)\sqrt{\pi}a^{(1-\lambda_1^I)}$ for the SENT specimen

$\gamma(^\circ)$	F_{I}		
	Present	Gross and Mendelson [2]	Chen [3]
0	2.8083	2.8237	–
30	2.8327	2.8448	2.8440
60	2.9584	2.9716	2.9700
90	3.3174	3.3244	3.3220

ratio $\nu = 0.25$ are considered. All units are consistent. One-half of the SENT is modeled in ANSYS 14.5 (due to symmetry). A typical FE mesh is shown in Fig. 3b. For calculating A_1, using Eq. (6), 20 consecutive nodes starting from the 7th node from the notch tip are considered. After mesh convergence study, 20 consecutive nodes are found to be a reliable set within the singularity dominating zone (SDZ) for the present meshes. The values of normalized NSIF F_{I} for the SENT are listed in Table 1. The present results are in excellent agreement with the available results.

3.2 Example 2: Mixed-Mode (I/II) Specimens

The second set of examples considered are an angled single edge notched plate under uniform tension (ASENT) and a sharp V-notched Brazilian disc (SV-BD) under compressive loading. The geometry and loading parameters for the ASENT are $w = 10$, $h = 35$ and $\sigma = 1$ as shown in Fig. 4a. The geometry and loading parameters for the SV-BD are $w = 60$ and $F = 1$ as shown in Fig. 4d. The NSIFs are determined for $\beta = 15^\circ$ and 30°, and notch angles $\gamma = 30^\circ$, 60°, and 90°. Young's modulus $E = 1$ and Poisson's ratio $\nu = 0.25$ are considered. All units are consistent. Typical FE meshes used for the ASENT and the SV-BD are shown in Fig. 4b, e with the magnified portion of the notch tips in Fig. 4c, f respectively.

For mixed-mode problems, 20 consecutive nodes starting from the 7th node along the notch flanks and radial directions (radial lines 1 and 2 as shown in Fig. 2b) are found to be within the SDZ for the present meshes after convergence study. Therefore, these 20 nodes are used to calculate the Williams coefficients using Eqs. (6) and (9). The normalized NSIFs $F_{I\,(II)} = K_{I\,(II)} \Big/ \sigma\sqrt{\pi}a^{\left(1-\lambda_1^{I\,(II)}\right)}$ and $F_{I\,(II)} = K_{I\,(II)} w^{\lambda_1^{I\,(II)}} \Big/ F$ for the ASENT ($a/w = 0.5$) and SV-BD ($a/w = 0.4$) specimens, respectively, are listed in Table 2. Again, an excellent agreement can be noticed with the available results. Some new results for the SV-BD specimens are also reported in Table 2.

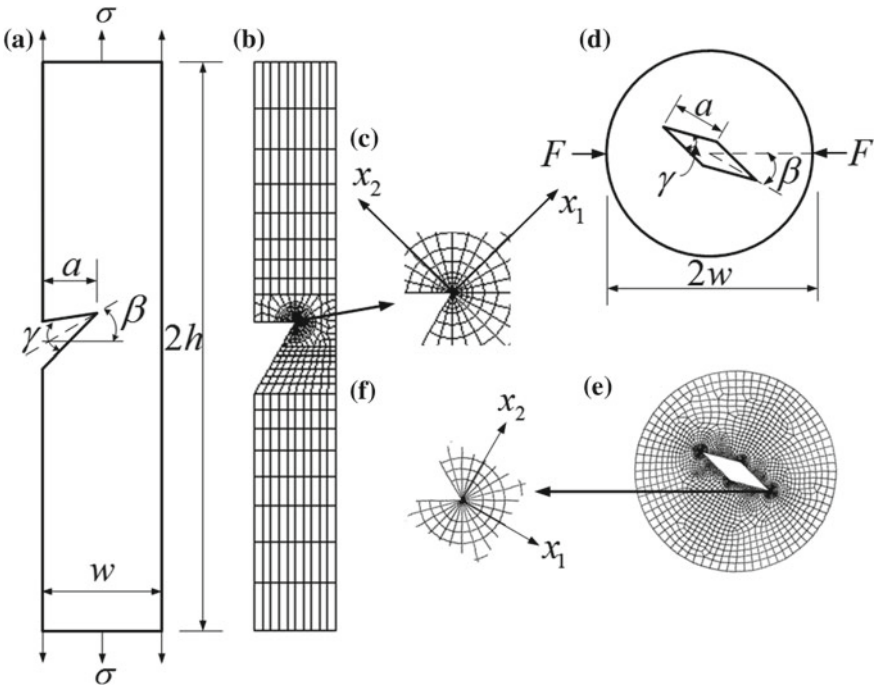

Fig. 4 **a** ASENT, **b** FE mesh used for the ASENT, **c** magnified view at the notch tip, **d** SV-BD, **e** FE mesh used for the SV-BD and **f** magnified view at the notch tip

Table 2 Normalized NSIFs for the ASENT and SV-BD specimens

$\beta(^\circ)$	$\gamma(^\circ)$	ASENT ($(a/w = 0.5)$)				SV-BD ($(a/w = 0.4)$)	
		F_{I}		F_{II}		F_{I}	F_{II}
		Present	Chen [3]	Present	Chen [3]	Present	Present
15	30	2.7716	2.7670	0.5377	0.5410	0.3583	0.7424
	60	2.8917	2.8870	0.7656	0.7660	0.5826	1.1715
	90	3.2352	3.2300	1.1154	1.1160	1.1528	2.6159
30	30	2.5507	2.5460	1.0043	1.0100	0.0934	1.0964
	60	2.6562	2.6530	1.4274	1.4280	0.0106	1.7057
	90	2.9672	2.9640	2.0922	2.0950	0.3145	2.7195

4 Conclusions

In this paper, the NSIFs of various configurations using the notch-flank displacement collocation technique (NDCT) are calculated. The rigid body displacements are nicely bypassed to evaluate the NSIFs. The NSIFs obtained are found to be in good agreement with the available solutions.

References

1. Williams, M.L.: Stress singularities resulting from various boundary conditions in angular corners of plates in extension. J. Appl. Mech. **19**(4), 526–528 (1952)
2. Gross, B., Mendelson, A.: Plane elastostatic analysis of V-notched plates. Int. J. Fract. Mech. **8**(3), 267–276 (1972)
3. Chen, D.H.: Stress intensity factors for V-notched strip under tension or in-plane bending. Int. J. Fract. **70**, 81–97 (1995)
4. Ju, S.H., Chung, H.Y.: Accuracy and limit of a least-squares method to calculate 3D notch SIFs. Int. J. Fract. **148**(2), 169–183 (2007)
5. Liu, Y., Wu, Z., Liang, Y., Liu, X.: Numerical methods for determination of stress intensity factors of singular stress field. Eng. Fract. Mech. **75**(16), 4793–4803 (2008)
6. Ayatollahi, M.R., Nejati, M.: Determination of NSIFs and coefficients of higher order terms for sharp notches using finite element method. Int. J. Mech. Sci. **53**(3), 164–177 (2011)
7. Hussain, M.K., Murthy, K.S.R.K.: Calculation of mixed mode (I/II) stress intensities at sharp V-notches using finite element notch opening and sliding displacements. Fatigue Fract. Eng. Mater. Struct. **42**(5), 1130–1147 (2019)
8. Hussain, M.K., Murthy, K.S.R.K.: A point substitution displacement technique for estimation of elastic notch stress intensities of sharp V-notched bodies. Theoret. Appl. Fract. Mech. **97**, 87–97 (2018)

Assessing the Material-Dependent Stress Distribution in Fractured Bone and Orthopedic Fixing Plate by Finite Element Analysis

Y. Naidubabu, V. V. Kondaiah, Ravikumar Dumpala and B. Ratna Sunil

Abstract In the present study, three different metals 316L stainless steel, titanium, and magnesium were considered as load-bearing implant materials, and computer-aided design (CAD) and finite element analysis (FEA) were used to investigate the stress distribution in the bone and fixing plates under static load conditions. From the results, it was clearly demonstrated that the reduced von Mises stress in the implant plate and increased stress distribution in the bone reduced the stress shielding when magnesium was used as the implant material compared with 316L steel and titanium. The maximum stress was noticed in the implants, and the minimum stress was observed in the bone in all three cases. Reduced stresses in the implant and increased stresses in the bone implanted with magnesium indicate decreased stress shielding. From the present study, it is demonstrated that the stress shielding effect can be reduced with magnesium implant and suggested as promising candidate for load-bearing implant applications.

Keywords Magnesium · Stress shielding · Degradation · 316L steel · Titanium

1 Introduction

Metallic implants are the best candidates for load-bearing implant applications [1]. However, the available metallic implants possess higher mechanical properties compared with the natural bone. In such conditions, stress shielding is a phenomenon that arises due to the difference in the modulus of elasticity of the implant metal and the bone [2]. Lower normal stresses which develop in the fractured bone compared

Y. Naidubabu
Department of Mechanical Engineering, Rajiv Gandhi University of Knowledge Technologies (AP-IIIT), Nuzvid 521201, India

V. V. Kondaiah · B. Ratna Sunil (✉)
Department of Mechanical Engineering, Bapatla Engineering College, Bapatla 522101, India
e-mail: bratnasunil@gmail.com

R. Dumpala
Department of Mechanical Engineering, Visvesvaraya National Institute of Technology, Nagpur 440010, India

L. Li et al. (eds.), *Advances in Materials and Manufacturing Engineering*, Lecture Notes in Mechanical Engineering, https://doi.org/10.1007/978-981-15-1307-7_37

with implant metal influence the bone remodeling rate which promotes low-density bones [3–5]. The most common metals such as 316L steel, Co–Cr alloys, Ti–6Al–4V alloy, and commercially pure titanium show stress shielding phenomenon [1]. It is true that the stress shielding can be observed in the bones with hip joints where a stem is inserted into the femur bone. However, there are a few reports which clearly explained the occurrence of stress shielding also in the case of bone fixing plates [6–8]. Due to their biodegradable behavior, recently magnesium (Mg) and its alloys have grabbed the attention in the biomedical field as promising candidates for temporary implant applications targeted for coronary stents and bone fixing plates [9]. For the past decade, different investigations were done on several Mg alloys which mainly focused on the degradation behavior of Mg, toxicity and local tissue response, corrosion mechanisms, etc. Mg has mechanical properties almost similar to the human bone, and hence, it is believed that Mg can minimize the stress shielding problem compared with the other metallic systems [10]. However, the validation of this belief was not completely investigated. Therefore, in the present study, computer-aided design (CAD) and simulation was used to study the stress distribution in the fractured bone implanted with Mg fixing plate by using finite element analysis (FEA) and compared with the existing implants made of 316L steel and titanium with an aim to understand the material-dependent stress shielding phenomena in orthopedic fixing plates.

2 Finite Element Analysis

The three-dimensional geometric model of human femur bone, the selected region to study in the present work (as indicated with black arrow), the fixing plate, screw and the bone region implanted with fixing plate modeled CATIA® (computer-aided design (CAD) software) are shown in Fig. 1. The circumference of the bone along the bone axis was slightly removed to fix the implant plate as shown in Fig. 1d.

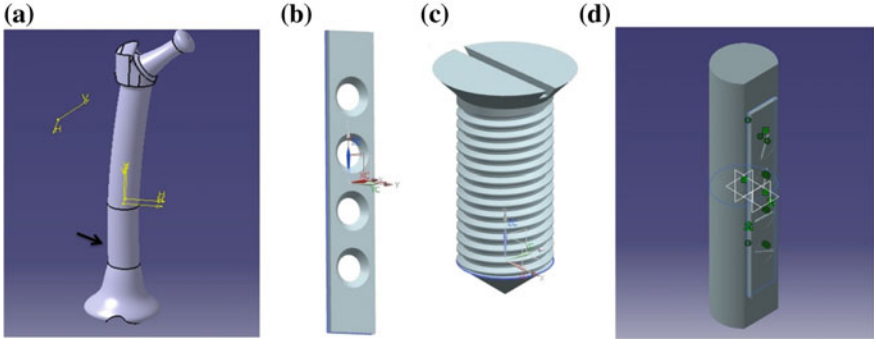

Fig. 1 Geometric modeling of bone and implants: **a** femur bone, **b** fixing plate, **c** screw, and **d** fractured bone implant assembly

In the present work, four screws were considered and the plate was fixed on the bone by considering a crack in the center of the femur bone across the bone axis. The individual geometrically designed bodies have been assembled and to get a complete model. The geometric model of bone was designed by considering 120 mm length and 28.6 mm diameter. Further, fixing plate dimensions were selected as 2 mm thickness, 15 mm width, and 60 mm length while designing the geometric model. Four holes of each having 8 mm diameter of the profile that matches with the head of the screws were designed on the bone fixing plate. Four screws having V-shaped bottom for better support were placed in their respective holes. The screws contain a tapered head of 10 mm diameter for up to 2 mm length, a threaded portion of 11 mm, and an extended V-shaped end having 3 mm length.

The stress distribution studies within the bone and the implant were carried out by finite element analysis (FEA) by using ANSYS Workbench® (ANSYS Inc., USA) software. The three-dimensional model of the assembled bone and fixing plate that was generated using CATIA® has been imported into ANSYS Workbench® for finite element analysis. Automesh option was selected to divide the CAD model into number of fine elements as shown in Fig. 2. The bottom nodes were constrained in all degrees of freedom, and a load of 50 kg (490 N, compressive type) was applied on the other end of the bone by assuming the self-weight of a typical patient. Material properties of bone, magnesium, 316L stainless steel, and titanium have been provided as the required input data before applying the boundary conditions to the model. The screw material was considered as respective metals of the fixing plates. Table 1 shows the material properties for bone, 316L stainless steel, titanium, and magnesium used as inputs for ANSYS Workbench®.

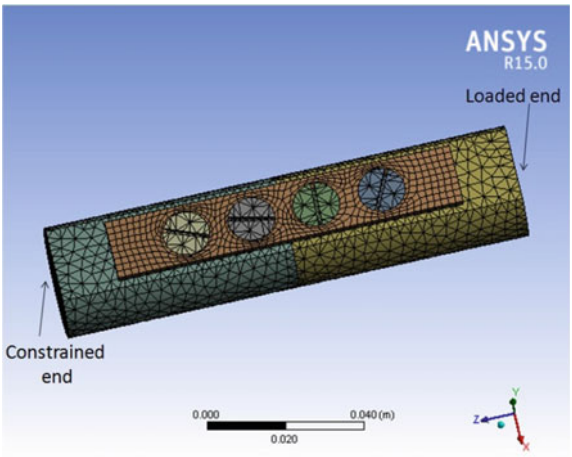

Fig. 2 The 3D model of the bone and implant after meshing

Table 1 Mechanical properties of different implant materials and bone [1, 10, 11]

Material	Density (g/cc)	Yield strength (Pa)	Poisson's ratio	Young's modulus (Pa)	Bulk modulus	Shear modulus
Bone	2.08	1.35E+08	0.3	1.35E+10	–	3.28E+09
316L stainless steel	8	1.40E+08	0.3	1.93E+11	1.93E+11	1.93E+11
Titanium	4.5	1.40E+08	0.34	1.16E+11	1.16E+11	1.16E+11
Magnesium	1.74	1.35E+08	0.29	4.50E+10	4.50E+10	4.50E+10

3 Results and Discussion

Figure 3 shows the von Mises stress distribution resulted within the fractured bone and the implant subjected to static load condition. The maximum and minimum stress values are listed in Table 2.

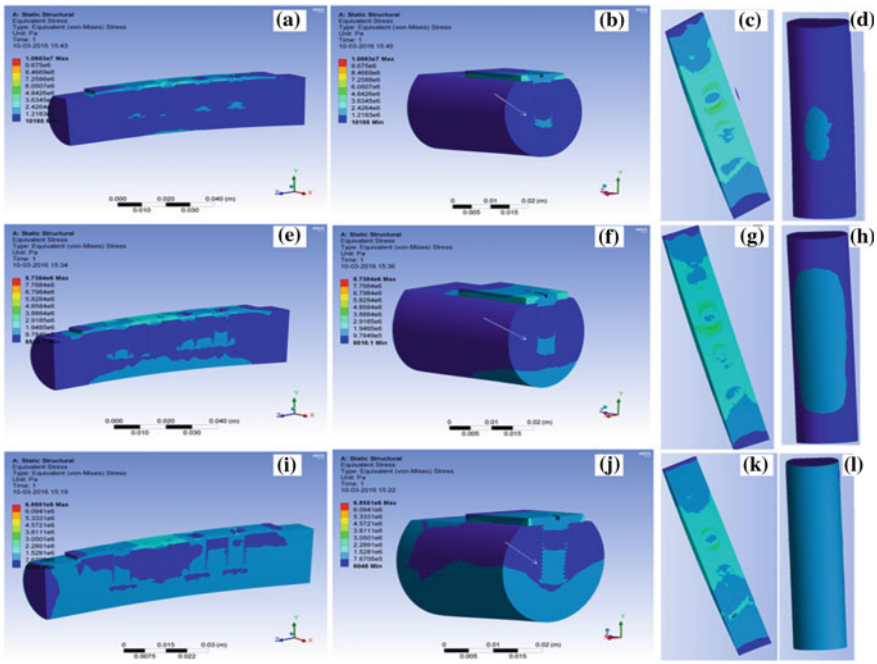

Fig. 3 von Mises stress distribution: **a** bone with 316L steel implant sectioned in longitudinal direction, **b** traverse direction, **c** implant–bone interface, **d** bone region opposite to the implant, **e** bone with titanium implant sectioned in longitudinal direction, **f** traverse direction, **g** implant–bone interface, **h** bone region opposite to the implant, **i** bone with Mg implant sectioned in longitudinal direction, **j** traverse direction, **k** implant–bone interface, **l** bone region opposite to the implant

Table 2 Maximum and minimum von Mises stress in the bone implant assembly with different implant materials

Implant material	von Mises stress (Pa)	
	Maximum	Minimum
316L steel	10.8×10^{6}	10,185
Titanium	8.73×10^{6}	8510
Magnesium	6.85×10^{6}	6048

From the obtained results, it can be clearly understood that the 316L steel implant exhibited higher stress values (both maximum and minimum) compared with the titanium and magnesium implants.

In the case of Mg, the maximum and minimum stresses were observed as lower compared with the other implants. The longitudinal and traverse sections of the bone and 316L steel implant as shown in Fig. 3a, b confirm the maximum stress distribution in the implant and a minimum stress in the bone. Similarly, the longitudinal and traverse cross sections of the bone and implant in the case of titanium and magnesium demonstrate the increased stress distribution in the bone compared with that of bone supported with 316L steel (Fig. 3e, f, i, j). Among the three bones, Mg-implanted bone has shown higher stresses close to the stress developed in the Mg implant material. In all the cases, implant–bone and screw–bone interfaces have experienced load transfer and that was clearly reflected in the higher stress distribution. It was also a common observation for all the materials that the maximum stress was recorded in the implant metal and minimum stress was recorded in the fractured bone. Interestingly, the stresses in the screw edges were observed as higher for Mg compared with titanium and 316L steel as indicated with white arrow in Fig. 3b, f, j.

Figure 3c, g, k shows the stress distribution in 316L steel, titanium, and Mg implants at the implant–bone interface region, respectively. The magnitude and distribution of von Mises stress were noticed as lower for Mg implant compared with the other. Similarly, the von Mises stress distribution in the bone region on the opposite side of the implant as shown in Fig. 3d, h, l was higher and wider for the bone implanted with Mg compared with the other metals. These two observations clearly suggest that the stress that is developed in the fractured bone is a dependent on the implant material. The stresses developed in the bone certainly influence the rate of bone remodeling [6–8]. Therefore, it can be demonstrated that the bone with a metallic fixing plate of higher Young's modulus will experience lower stresses which directly influence the bone resorption and may cause stress shielding effect. In this context, using metals with lower Young's modulus for bone fixing plates reduces the stress shielding effect. Therefore, Mg which has Young's modulus (40 GPa) close to that of natural human bone is the best suitable metal compared with other metallic systems as a load-bearing implant material. Hence, the present study clearly demonstrates that the use of Mg and its alloys as biodegradable metals can address the stress shielding effect and also offers additional advantages such as biodegradability and non-toxicity in the biomedical field particularly for temporary implant applications.

4 Conclusions

The present study clearly demonstrates that the bone with Mg implant has higher stresses compared with 316L and titanium implant under static load conditions. Maximum stress was noticed in the implant material, and minimum stress was noticed in the bone in all the three cases. The difference between the maximum stress and minimum stress was recorded as reduced in the case of Mg compared with the other metals. This clearly suggests that the stress shielding can be reduced in the bone implanted with Mg metal and validates the use of Mg as a viable implant metal for temporary implant applications which offer lower stress shielding effect along with biodegradability and non-toxicity properties.

References

1. Park, J., Lakes, R.S.: Biomaterials An Introduction, 6th edn, pp. 1–16. Springer Science and Business Media, New York (2007)
2. Ridzvan, M.I.Z., Shuib, S., Hassan, A.Y., Shokri, A.A., Mohamad Ibrahim, M.N.: Problems of stress shielding and improvement to the hip implant design: a review. J. Med. Sci. **7**(3), 460–467 (2007)
3. Wolff, J.: The Law of Bone Remodeling. Springer, Berlin (1986)
4. Frost, H.M.: Wolff's Law and bone's structural adaptations to mechanical usage: an overview for clinicians. Angle Orthod. **64**(3), 175–188 (1994)
5. Chen, J.H., Liu, C., You, L., Simmons, C.A.: Boning up on Wolff's Law: mechanical regulation of the cells that make and maintain bone. J. Biomech. **43**, 108–118 (2010)
6. Woo, S.L.-Y., Simon, B.R., Akeson, W.H., McCarty, M.P.: An interdisciplinary approach to evaluate the effect of internal fixation plate on long bone remodelling. J. Biomech. **10**(2), 87–95 (1977)
7. McCartney, W., MacDonald, B.J., Hashmi, M.S.J.: Comparative performance of a flexible fixation implant to a rigid implant in static and repetitive incremental loading. J. Mater. Process. Technol. **169**(3), 476–484 (2005)
8. Haase, K., Rouhi, G.: A discussion on plating factors that affect stress shielding using finite element analysis. J. Biomech. Sci. Eng. **5**(2), 129–141 (2010)
9. Staiger, M.P., Pietak, A.M., Huadmai, J., Dias, G.: Magnesium alloys as degradable biomaterials. Biomaterials **27**(9), 1728–1734 (2006)
10. Travis, K.N., Nick, B.: Magnesium Biomaterials Design, Testing, and Best Practice. Springer, UK (2014)
11. Breitbart, A.S., Ablaza, V.J.: Implant materials. In: Thorne, C.H., Bartlett, S.P., Beasley, R.W., Aston, S.J., Gurtner, G.C., Spear, S.L. (eds.) Grabb and Smith's Plastic Surgery, 6th edn, pp. 58–67. Lippincott Williams & Wilkins (LWW), USA (2007)

Production Planning in Flexible Manufacturing System by Considering the Multi-Objective Functions

B. Satish Kumar, G. Janardhana Raju and G. Ranga Janardhana

Abstract In modern-day manufacturing process, flexible manufacturing system (FMS) is used for efficient production of parts. For manufacturing of specific parts, parts should be processed in a specified sequence of operations. It will be better to identify different possible sequence of operations on different machines and their cost implications in case of any machine failures. In this paper, a case study is considered in which three machines produce three different parts by doing different operations. Each machine can perform all the different operations to produce all the three parts. All the operations can be done in all the three machines, and the production timings and corresponding costs are varying from machine to machine. The sequence of operations for different parts is different. The combined objective function (COF) is formulated by considering the two objectives minimizing the total flow time and minimization of total tool cost with equal weightages. MATLAB Code is written for identifying all the possible sequences of operations, computed their total flow time and tool costs. Best sequences are identified when all machines are working; first machine fails, second machine fails and third machine fails based on COF values.

Keywords Production planning · Combined objective function · Manufacturing costs · Flexible manufacturing system · Multi objective optimization · Idle time · Failure of machines · Total flow time · Total tool cost

B. Satish Kumar (✉)
Department of Mechanical Engineering, Vignana Bharathi Institute of Technology, Hyderabad, India
e-mail: satishbk91@gmail.com

G. Janardhana Raju
Nalla Narasimha Reddy Education Society's Group of Institutions, Hyderabad, India

G. Ranga Janardhana
Department of Mechanical Engineering, University College of Engineering, JNTU Anantapur, Ananthapuramu, Anantapur, India

L. Li et al. (eds.), *Advances in Materials and Manufacturing Engineering*, Lecture Notes in Mechanical Engineering, https://doi.org/10.1007/978-981-15-1307-7_38

1 Introduction

Flexible manufacturing systems (FMS) is a group of machines most preferably CNC which are coordinated by a common control center which has the ability and flexibility to deal with the variety of products. Though the flexibility in the manufacturing systems is an advantage, it proves to be a very complicated task when it comes to scheduling of parts in a changing environment. Flexible manufacturing is a concept that allows manufacturing systems to be built under highly customized production requirements. FMS is called flexible because of its capability to process a variety of part styles and quick responses to changing demand patterns. There are various types of flexibility, namely product mix flexibility, volume flexibility, manufacturing flexibility, and delivery flexibility. FMS is highly suitable for mid-variety and mid-volume part type production. Proper sequencing and scheduling are required for high productivity. FMS is an arrangement of machines interconnected by a transport system. The transporter carries work to the machines on pallets or other interface units so that work–machine registration is accurate, rapid, automatic and a central computer controls both machines and transport system which are shown in Fig. 1.

The FMS may need the high initial investment but it can be operated with low maintenance and minimum use of energy in the manufacturing activity. The FMS can be used in any production activity; some examples can be as automotive industry aerospace industry, metal forming, automobile spare parts, plastics and plastic accessories, manufacturing of healthcare equipment medicine manufacturing units, electrical instruments, electronic goods, and many more.

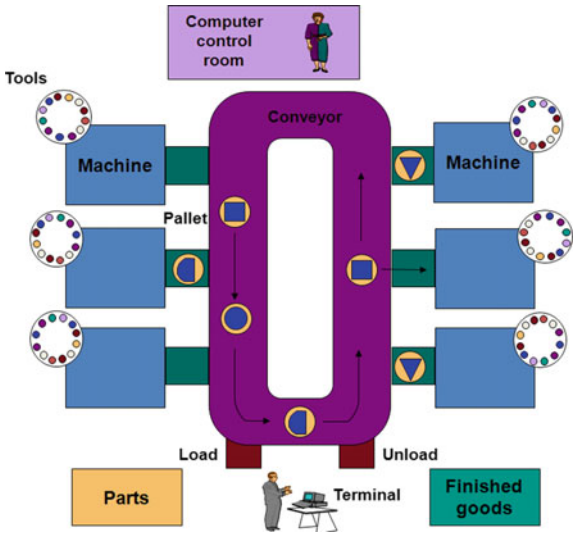

Fig. 1 Typical view of FMS

1.1 Literature Review

J. Jerald et al. used different Algorithms like GA, SA, MA & PSOA for solving the multi objective scheduling problem with the objectives of minimizing the idle time of the machine and minimizing the total penalty cost for not meeting the due dates. The results obtained by different algorithms are compared [1]. Jian-Hung Chen and Shinn-Ying Ho proposed an efficient multi-objective genetic algorithm (EMOGA) for planning FMS. Minimizing total flow time, machine workload unbalance, greatest machine workload, and total tool cost are the four objectives they considered while problem formulation. This problem solved by Using EMOGA [2, 3]. Zengqiang Jiang, Le Zuo, and Mingcheng E had studied that the FMS took four objective functions—quality, time, cost, and energy consumption. Given more importance to the energy consumption of production activity and tried to minimize the energy consumed. Applied GA for solving problem and observed that the machines are operated in different stages like stop, start up, no load, processing consume energy differently in different stages [4]. Rao et al. used the time deviation method to solve job sequence problem to minimize the total elapsed time. The processing of N jobs with M machines are considered [5]. Reza Kia prepared a FMS model to take decisions of dynamic environment. This model can accommodate various things like use of alternative processing units, alternative operation sequence, minimizing the time, change in production volumes, etc. Additional feature of this model is that it can balance the work load by using variable number of cells. They reduced the production time by considerable amount [6]. Satish et al. proposed a suitable material handling system for different layouts at different speeds of material handling system [7]. Srinivas et al. concluded that in order to overcome the limitations of existing protocols, proposed protocol An Efficient Backbone Based Quick Link Failure Recovery Multi-cast Routing Protocol [8]. Srinivas et al. proposed L2R protocol to generate an alternate path for link failures in backbone networks. For ensuring the link failure recovery, L2R is implemented [9]. Mahesh proposed a method for integration of scheduling with material requirement planning (MRP) and capacity requirements planning (CRP), to generate a near to optimal production schedule at low cost considering the practical difficulties in a real time job shop environment [3]. From the literature considered a problem of processing 3 parts on three machines. This problem is solved by Jian et al. by applying EMOGA, they have not considered the machine failures, an attempt is made to solve same problem by considering the machine failures.

1.2 Problem Statement

Sample problem considered from the literature of Jian-Hung Chen and Shinn-Ying Ho paper for minimizing total flow time and total tool cost [10] (Tables 1 and 2).

Nomenclature

f_1—Total processing time of three parts in required production quantity.

Table 1 Details of Processing time and operation indexes for producing three parts on three machines

Operation index		Part 1				Part 2			Part 3		
		1	2	3	4	1	2	3	1	2	3
Processing time	Machine-1	1	3	3	5	9	2	9	7	8	7
	Machine-2	7	5	4	6	4	1	4	1	6	2
	Machine-3	6	9	5	1	2	5	1	3	3	5
Tool cost	Machine-1	1	2	1	6	1	8	4	8	3	6
	Machine-2	2	3	7	5	9	2	5	9	8	5
	Machine-3	4	5	4	2	8	7	8	9	6	2
Production volume		51				39			23		

Table 2 Details of traveling times between the machines

	Machine 1	Machine 2	Machine 3
Machine 1	4	11	17
Machine 2	11	3	9
Machine 3	7	18	5

Table 3 Details of part index, operation index, and machine index for sample calculations

Part index	1	2	3
Operation index	1 2 3 4	1 2 3	1 2 3
Machine index	3 3 3 1	2 1 2	3 1 2

f_2—Total transportation time in between machines.
$F_1 = f_1 + f_2$—Total machining and transportation time for each operation index.
F_2—Tool cost for each operation index.
MPFT—Maximum possible flow time.
MPTC—Maximum possible tool cost.
COF—Combined objective function.

$$\text{COF} = W_1 \times (F_1 \div \text{MPFT}) + W_2(F_2 \div \text{MPTC}) \tag{1}$$

Equal weightages are considered, i.e., $W_1 = 0.5$ and $W_2 = 0.5$ (Table 3)

Step 1 :

To find

$$f_1 = 51 \times (6 + 9 + 5 + 5) + 39 \times (4 + 2 + 4) + 23(3 + 8 + 5)$$
$$= 51 \times 25 + 39 \times 10 + 23 \times 16 = 1275 + 390 + 368 = 2033.$$

To find

$$f_2 = 51(5 + 5 + 7) + 39(11 + 11) + 23(7 + 11) = 867 + 858 + 414 = 2139$$

$$F_1 = f_1 + f_2 = 2033 + 2139 = 4172$$

Step 2 :

To find F_2

$$F_2 = [(4 + 5 + 4 + 6) + (9 + 8 + 5) + (9 + 3 + 2)] \times 100 = 5500$$

2 Programming

Combined objective function (COF) is formulated by considering the equal weightages to both the objectives i.e minimization of total flow time and tool cost minimization. For calculating the objective function values for all the possible operation index sequences, code was written in MATLAB by using Eq. (1). Considered the machine failures and best operations Indexes and their COF values are tabulated shown in Table 4 .

3 Results and Discussion

In this present paper, considered formulated COF by considering two objectives, i.e., minimization of flow time and tool cost made an attempt by considering some additional constraints like all machines are working, first machine not working, second machine not working, and third machine not working. These working conditions are considered by writing the program in MATLAB shown in Figs. 2 and 3. By considering all these constraints, corresponding objective function values, i.e., F_1, F_2, and COF, are calculated. Studied the effect of failure of machines on objective functions while production is going on and products are manufactured with the use of available working machines.

4 Conclusions

Results show that operation index 1111,122,333 gives the minimum COF value when all machines are working. Operation index 2233,222,233 gives minimum COF value when Machine 1 fails, operation index 1113,111,333 gives minimum COF value when Machine 2 fails, and operation index 1111,122,111 gives minimum COF value. When all machines are working, better results were observed. Machines 1 and 2 failures have more negative impact than Machine 1 failures.

In future, planning to develop an algorithm for identifying the better operation index for objective function which is having three or more objectives, and when all machines are working, any one machine fails and any two machines fail.

Table 4 Details of best COF values for different machine indexes

Sl. No.	Part 1				Part 2			Part 3			F_1	F_2	CoF
	OP-1	OP-2	OP-3	OP-4	OP-1	OP-2	OP-3	OP-1	OP-2	OP-3			
When all machines are working													
1	1	1	1	1	1	2	2	3	3	3	2799	3500	0.463
2	1	1	1	1	1	2	2	2	3	3	2845	3500	0.467
3	1	1	1	3	1	2	2	3	3	3	3258	3100	0.470
4	1	1	1	1	1	2	2	1	1	3	3259	3100	0.470
5	1	1	1	3	1	2	2	2	3	3	3304	3100	0.473
When machine 1 fails													
6	2	2	3	3	2	2	2	2	3	3	2899	4400	0.573
7	2	2	2	3	2	2	2	3	3	3	2700	4700	0.579
8	2	2	2	3	2	2	2	2	3	3	2746	4700	0.583
9	2	2	3	3	2	2	2	2	2	3	2922	4600	0.590
10	2	2	3	3	2	2	2	2	2	2	2715	4900	0.595
When machine 2 fails													
11	1	1	1	3	1	1	1	3	3	3	3258	3600	0.573
12	1	1	1	1	1	1	1	1	1	3	3259	3600	0.573
13	1	1	1	1	1	1	1	3	1	3	3236	3700	0.579
14	1	1	1	1	1	1	1	1	1	1	3006	4000	0.582
15	1	1	1	3	1	1	1	1	1	3	3718	3200	0.583
When machine 3 fails													
16	1	1	1	1	1	2	2	1	1	1	3006	3500	0.566

(continued)

Table 4 (continued)

Sl. No.	Part 1				Part 2			Part 3			F_1	F_2	CoF
	OP-1	OP-2	OP-3	OP-4	OP-1	OP-2	OP-3	OP-1	OP-2	OP-3			
17	1	1	1	1	1	2	2	2	1	2	3075	3500	0.572
18	1	1	1	1	1	2	2	2	2	2	2661	4000	0.572
19	1	1	1	1	1	2	2	2	1	1	3029	3600	0.576
20	1	1	1	1	2	2	2	1	1	2	2545	4200	0.577

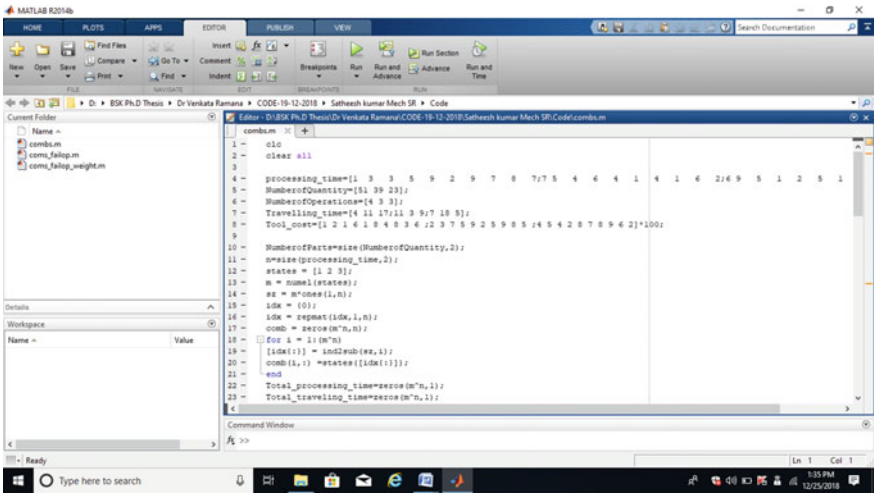

Fig. 2 Screenshot of program in MATLAB

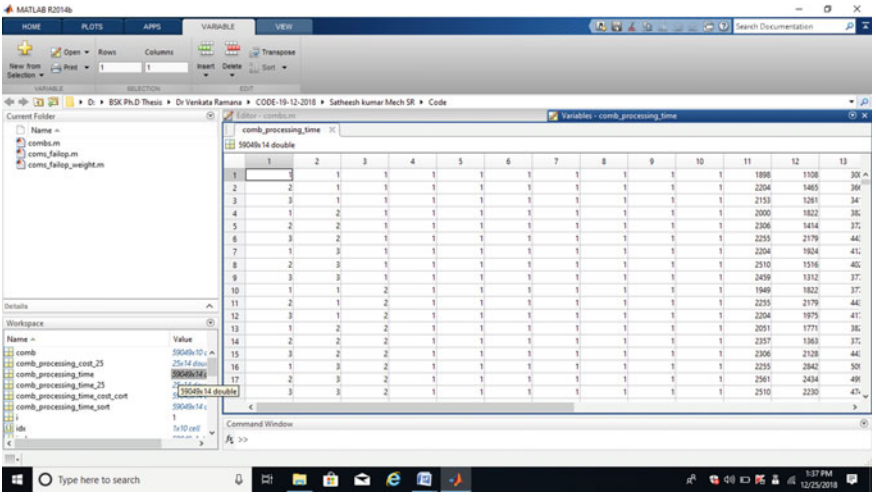

Fig. 3 Screenshot of results

References

1. Jerald, J., Asokan, P., Prabaharan, G., Saravanan, R.: Scheduling optimisation of flexible manufacturing systems using particle swarm optimization algorithm. Int. J. Adv. Manuf. Technol. **25**(9), 964–971 (2005)
2. Chen, J.-H., Ho, S.-Y.: A novel approach to production planning of flexible manufacturing systems using an efficient multi-objective genetic algorithm International. J. Mach. Tools Manuf. **45**(7), 949–957 (2005)

3. Jiang, Z., Le, Z, Mingcheng, E.: Study on multi-objective flexible job-shop scheduling problem considering energy consumption. J. Ind. Eng. Manag. **7**(3), 589–604 (2013)
4. Rao, N.N., Raju, O.N., Ramesh Babu, I.: Modified heuristic time deviation technique for job sequencing and Computation of minimum total elapsed time. Int. J. Comput. Sci. Inf. Technol. **5**(3), 67–77 (2013)
5. Mekni, S., Chaâr, B.C.: Multi objective flexible job shop scheduling using a modified invasive weed optimization. Int. J. Soft Comput. **6**(1), 25–36 (2015)
6. Kia, R., Shirazi, H., Javadian, N., Tavakkoli-Moghaddam, R.: A multi-objective model for designing a group layout of a dynamic cellular manufacturing system. J. Ind. Eng. Int. **9**(8), 35–46 (2013)
7. Kumar, M.S., Kumar, B.S.: Performance analysis of material handling systems for a layout with different speeds. Int. J. Mech. Prod. Eng. Res. Dev. **8**(5), 1–16 (2018)
8. Deepika, Kumar, S.P., Srinivas, A.: An efficient backbone based quick link failure recovery multicast routing protocol. Perspect. Sci. **8**(1), 135–137 (2016)
9. Deepika, Phani Kumar, S., Srinivas, A.: L2R: Multicast routing protocol for effective localized route recovery in backbone networks. Int. J. Control Theor. Appl. **33**(9), 79–87 (2016)
10. Mahesh, V.: Integrated model for machine scheduling and inventory management under finite capacity settings. Int. J. Mech. Eng. Technol. **9**(10), 1021–1032 (2018)
11. Shahrestani, F.K., Mahbobi, H., Mohebi, E., Mosaffa, H.B.: Optimization of scheduling flexible manufacturing systems by using multi-objective Genetic algorithm interdisciplinary. J. Contemp. Res. Bus. **5**(1), 1015–1023 (2013)

Acoustic Emission-Based Grinding Wheel Condition Monitoring Using Decision Tree Machine Learning Classifiers

D. S. B. Mouli and K. Rameshkumar

Abstract Condition monitoring has emerged as an important technique in manufacturing industries for predictive maintenance and on-line monitoring of the processes and equipments. Due to the availability of sensors and signal processing technology, implementing condition monitoring systems in a manufacturing environment has become easy. In this paper, grinding wheel conditions in a surface grinding process are predicted with a simple decision tree-based machine learning classifier using time-domain acoustic emission signature. A grinding wheel attachment is designed and fabricated for capturing acoustic emission (AE) signal from the grinding wheel. Grinding wheel conditions are established using grinding wheel life cycle plot by monitoring surface roughness produced by the silicon carbide grinding wheel for the entire grinding cycle. AE signals were captured using the experimental set-up established for this study and statistical features are extracted from transients of AE. Classification and regression trees (CART) are used for establishing a correlation between AE features and grinding wheel conditions. The performance of the CART algorithms is evaluated using Gini index, towing and maximum deviation split criterions. Results indicate CART algorithms are efficiently predicting the grinding wheel condition with good accuracy.

Keywords Grinding · Condition monitoring · Acoustic emission · Decision tree

1 Introduction

Grinding is one of the important manufacturing processes used to produce components with close dimensional accuracy and high surface finish. For precision machining applications, AE sensors have a better level of precision in capturing the condition of the grinding tool such as subsurface damage and anisotropy of the material. Dornfeld and Cai [1] studied the application AE for grinding wheel condition monitoring.

D. S. B. Mouli · K. Rameshkumar (✉)
Department of Mechanical Engineering, Amrita School of Engineering, Amrita Vishwa Vidyapeetham, Coimbatore 641112, India
e-mail: k_rameshkumar@cb.amrita.edu

L. Li et al. (eds.), *Advances in Materials and Manufacturing Engineering*, Lecture Notes in Mechanical Engineering, https://doi.org/10.1007/978-981-15-1307-7_39

Inasaki and Okamura [2] investigated suitability of AE sensors for monitoring of dressing and grinding processes.

Suitability of AE sensors for monitoring and control of precision manufacturing processes were investigated by Lee et al. [3]. Liao et al. [4] conducted experiments in a surface grinding process, and AE signals were captured and analyzed using wavelet features. Grinding wheel conditions are distinguished by Liao et al. [5] using classifiers such as decision trees, naïve Bayes and neural nets. A detailed survey has been made by Roth et al. [6] focusing on tool condition monitoring of the various metal cutting process. Arun et al. [7] monitored the cylindrical grinding using AE signature using machine learning classifiers. Dressing condition of the Al_2O_3 grinding wheel in a surface grinding process was investigated by Alexandre et al. [8] using AE and fuzzy methods.

Off late, Krishnakumar et al. [9] predicted tool conditions by extracting AE features in time, frequency, time-frequency domains using machine learning classifiers. Krishnakumar et al. [10] done feature level fusion using acoustic and vibration signals for tool condition monitoring. Krishnakumar et al. [11] monitored tool condition using acoustic and vibration signals using wavelet domain using machine learning classifiers.

In this study, the condition of grinding wheel mounted in a surface grinding machine is monitored using the acoustic emission sensors. The AE signal is captured using a data acquisition system and features of the AE signal are extracted in time domain. Extracted features are trained using classification and regression decision tree (CART) algorithm. The trained CART model is used for predicting the grinding wheel condition. Experimental set-up and grinding wheel conditions

AE sensor (micro-30D) with 150–400 kHz operating frequency supplied by Physical Acoustic Corporation, USA is used in this study for AE signal acquisition. Investigations were carried out to locate the AE sensor for capturing the AE during the grinding process. For capturing the AE signal from the grinding wheel, an AE sensor attachment is designed and fabricated. The attachment with the experimental set-up is shown in Fig. 1. A spring-loaded SiC ceramic bit is made to contact with the rotating SiC grinding wheel. AE sensor is fixed firmly over the ceramic bit. AE originating from the grinding wheel is transmitted to the ceramic material and is captured by the AE sensor. Grinding was carried out by fixing depth of cut as 0.05 mm, grinding wheel speed as 2900 rpm and feed rate of 0.5 mm/rev., for the entire grinding cycle starting from the new grinding wheel until the grinding wheel becomes dull.

Grinding wheel life plot and grinding wheel conditions are shown in Fig. 2. Grinding wheel conditions are identified using the grinding wheel life plot. At the end of each grinding pass, surface roughness produced by the grinding wheel in workpiece is recorded. Number of passes carried out in this study is 44. This means that at the end of 4th pass the grinding wheel has become dull and produced a surface roughness value ‘Ra’ of more than 0.273. Using the grinding wheel life plot, based on the change in slope of the plot, grinding wheel conditions are established and shown in Fig. 2.

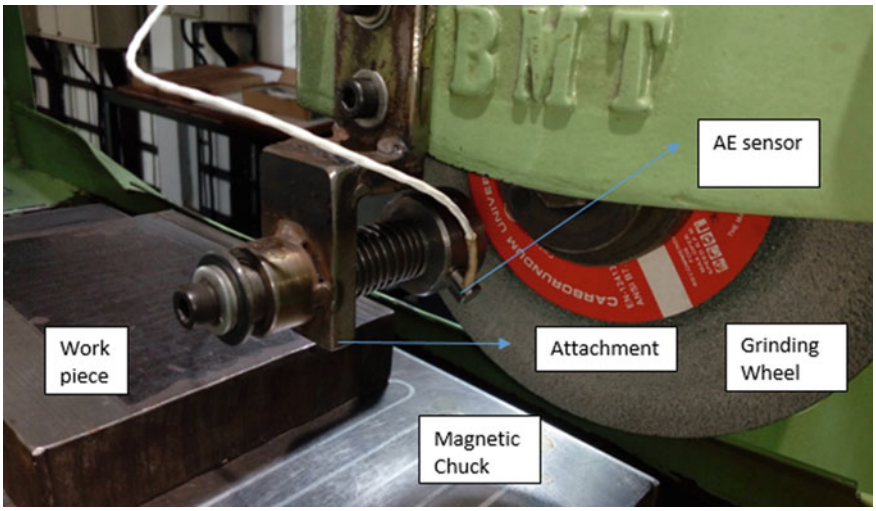

Fig. 1 AE sensor attachment

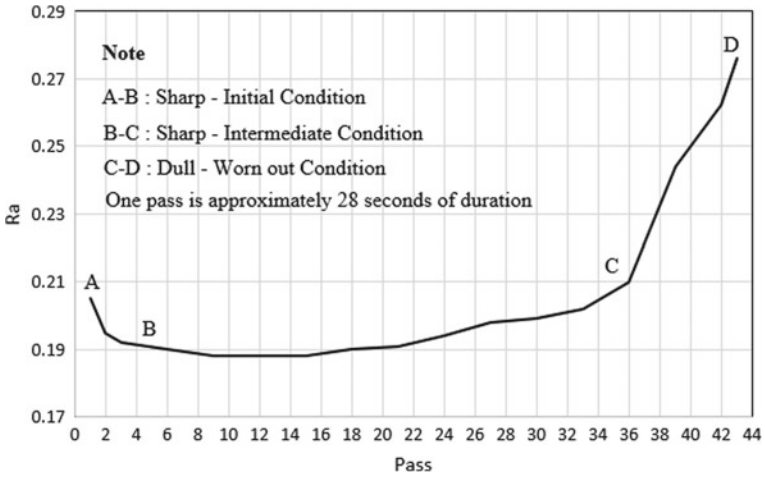

Fig. 2 Grinding wheel life plot

1.1 AE Feature Extraction

AE features are extracted, and signal processing is carried out to predict the condition of the grinding wheel. AE signals were captured with a sampling rate of 1MSPS. AE signals are amplified using a pre-amplifier with a gain of 60 dB. The threshold of 25 dB is used for capturing the AE data in all three conditions of the tool using the AEWin software supplied by M/s Mistras Corporation, USA. AE features such

as Rise-time, Count, Duration, RMS and ASL features were extracted. Among the features, it is observed that 'Count' and 'RMS' feature of AE has a strong correlation with the grinding wheel tool condition. The 'RMS' and 'Count' feature data are used in machine learning classifiers for testing and training. Number of data points used for building the statistical classifiers are 320, 636 and 407 for the tool conditions A, B and C, respectively.

2 Grinding Wheel Condition Classification Using Decision Trees

2.1 CART Model for Classification

Decision trees are a simple supervisory learning classifier and are used for classification or regression of continuous or discrete data [12]. Breiman [13] first introduced the CART model for classification and regression applications. The CART decision tree is a recursive partitioning approach is built by using a binary split. Binary split implies and divides an attribute into ranges like greater than or equal to and less than or equal to. Each step in prediction involves checking the value of predictor in order to proceed to the next stage for prediction. The CART procedure implemented in this study is shown in Fig. 3. Various split criterions used in this study for the best split include the Gini index, maximum deviance and towing rule [13].

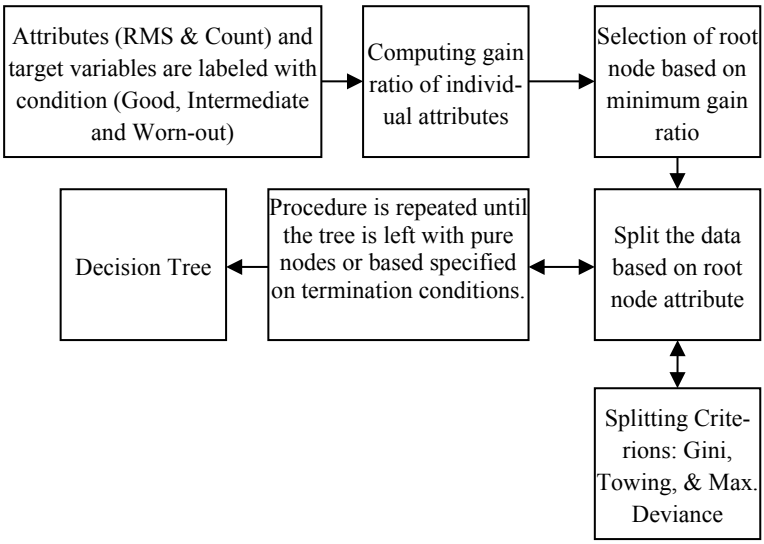

Fig. 3 CART procedure [13]

3 Results and Discussions

3.1 Performance of CART Algorithms

The accuracy of classification, mis-classification rate and kappa statists is used for evaluating the performance of CART classifiers using confusion matrix. Tenfold cross-validation is performed to compute the performance of classifiers. The accuracy of classifiers and kappa statistics is shown in Table 1. The results indicate simple classifiers such as CART is able to capture the conditions of the grinding wheel with good accuracy. Medium tree classifier is predicting the grinding wheel conditions with higher classification accuracy compared to simple and complex trees using Gini, towing and maximum deviance criterions considered in this study.

Kappa statistics proposed by Landis and Koch [14] is also used for evaluating the performance of the classifier. A 'Kappa' value of 0.81–1 is termed as a perfectly good classifier. A 'Kappa' value of 0.61–0.80 is a substantial classifier, 0.41–0.60 is a moderate one, 0.21–0.40 is termed as fair and 0–0.20 is called as slight. It is noted that all the CART trees for Gini, towing and maximum deviation criterion are giving kappa value in the range 0.81–1. Hence, all CART classifiers proposed in this study are perfect good classifiers for predicting the grinding wheel condition. Average percent of mis-classification of instances in different grinding wheel conditions are shown in Table 2. Mis-classification percent are averaged for simple, medium and complex trees.

It is observed that higher percent of condition 'A' (sharp-initial) instances are mis-classified as Condition 'B' (sharp–intermediate). Mis-classification rate of 10.62%,

Table 1 Classification accuracy and kappa statistics of CART Classifiers

Classifier	Classification accuracy (%)/Kappa statistics		
	Gini index	Towing	Max. deviance
CART—simple trees	92.01/0.876	91.93/0.874	91.34/0.866
CART—medium tree	93.10/0.892	93.40/0.897	93.06/0.891
CART—complex tree	92.08/0.876	92.15/0.877	92.01/0.874

Table 2 Average Mis-classification of CART algorithm

Mis-classification (%)									
Criterion	Gini index			Towing rule			Max. deviance		
Conditions	A	B	C	A	B	C	A	B	C
A	–	10.62	2.70	–	10.20	1.41	–	10.80	3.4
B	6.13	–	2.30	5.81	–	2.41	6.70	–	2.30
C	1.40	0.40	–	1.47	0.20	–	0.50	0.57	–

10.20% and 10.80% is reported for Gini, towing and maximum deviance split criterions, respectively. The reasons for mis-classification may be due to both conditions have sharp grinding edges. The classifier was unable to classify approximately 10% of instances, which are close to the transition range. The condition change from 'sharp-initial' to 'sharp-intermediate' has to be studied in detail for improving the classification accuracy of the classifier.

4 Conclusions

In this work, grinding wheel conditions are predicted using classification and regression trees using dominant AE features, Count and RMS. For capturing AE signature, a grinding wheel attachment has been designed and fabricated. Grinding wheel conditions, namely 'sharp-initial,' 'sharp-intermediate' and 'dull-worn-out,' are identified using the grinding wheel life plot. Three CART models, namely simple, medium and complex trees, are used for grinding wheel condition prediction using split criterions Gini index, maximum deviance and towing rule.

It is observed that CART classifiers are producing good classification accuracy of more than 90% for all trees considered in this study. Mis-classification percent are around 10% for the AE data collected during the transition from 'sharp-initial' to 'sharp-intermediate' condition. Mis-classification of 'sharp-intermediate' condition as 'dull-worn out' condition of the grinding wheel is 2.3%, 2.41% and 2.3% for Gini, towing, maximum deviance criterions, respectively. This shows the effectiveness of the CART algorithm and the ability of the AE sensor capturing the grinding wheel condition. Kappa also indicates that the proposed CART model is a perfect classifier for predicting the grinding wheel condition.

Acknowledgements This research is supported by Directorate of Extramural Research and Intellectual Property Rights (ER & IPR), Defence Research and Development Organization (DRDO), ERIP/ER/0803740/M/01/1194, 13 January 2010.

References

1. Dornfeld, D., Cai, H.G.: An investigation of grinding and wheel loading using acoustic emission. J. Eng. Ind. **106**(1), 28–33 (1984)
2. Inasaki, I., Okamura, K.: Monitoring of dressing and grinding processes with acoustic emission signals. CIRP Ann. Manuf. Technol. **34**(1), 277–280 (1985)
3. Lee, D.E., Hwang, I., Valente, C.M., Oliveira, J.F.G., Dornfeld, D.A.: Precision manufacturing process monitoring with acoustic emission. Int. J. Mach. Tools Manuf. **46**(2), 176–188 (2006)
4. Liao, T.W., Ting, C.F., Qu, J., Blau, P.J.: A wavelet-based methodology for grinding wheel condition monitoring. Int. J. Mach. Tools Manuf. **47**(3), 580–592 (2007)
5. Liao, T.W.: Feature extraction and selection from acoustic emission signals with an application in grinding wheel condition monitoring. Eng. Appl. Artif. Intell. **23**(1), 74–84 (2010)

6. Roth, J.T., Djurdjanovic, D., Yang, X., Mears, L., Kurfess, T.: Quality and inspection of machining operations: tool condition monitoring. J. Manuf. Sci. Eng. **132**(4), 041015 (2010)
7. Arun, A., Rameshkumar, K., Unnikrishnan, D., Sumesh, A.: Tool condition monitoring of cylindrical grinding process using acoustic emission sensor. Mater. Today: Proc. **5**(5), 11888–11899 (2018)
8. Alexandre, F.A., Lopes, W.N., Dotto, F.R.L., Ferreira, F.I., Aguiar, P.R., Bianchi, E.C., Lopes, J.C.: Tool condition monitoring of aluminum oxide grinding wheel using AE and fuzzy model. Int. J. Adv. Manuf. Technol. **96**(1–4), 67–79 (2018)
9. Krishnakumar, P., Rameshkumar, K., Ramachandran, K.I.: Acoustic emission-based tool condition classification in a precision high-speed machining of titanium alloy: a machine learning approach. Int. J. Comput. Intell. Appl. **17**(03), 1850017 (2018)
10. Krishnakumar, P., Rameshkumar, K., Ramachandran, K.I.: Feature level fusion of vibration and acoustic emission signals in tool condition monitoring using machine learning classifiers. Int. J. Prog. Health Manag. **9**, 1–15 (2018)
11. Krishnakumar, P., Rameshkumar, K., Ramachandran, K.I.: Machine learning based tool condition monitoring using acoustic and vibration data in high speed milling. Int. J. Intell. Decis. Technol. **1**, 1–18 (2018)
12. Quinlan, J.R.: C4. 5: Programming for Machine Learning, vol. 38, p. 48. Morgan Kauffmann (1993)
13. Breiman, L.: Classification and Regression Trees. Routledge (2017)
14. Landis, J. R., Koch, G.G.: The measurement of observer agreement for categorical data. Biometrics, 159–174 (1977)

Impact of Collaborative Drivers of NPD on Quality Cost and Customer Satisfaction

Sudeshna Roy, Nipu Modak and Pranab K. Dan

Abstract 'MAKE IN INDIA' necessitates the collaborative approach in new product development (NPD) activities in Indian manufacturing industries for attaining global success. Collaboration nature is one of the phenomena requires to be developed within the organization for industrial sustainability. This requires communication infrastructure (CI), conflict management (CM), concurrent engineering team (CET), and collaborative product design (CPD) for NPD success to produce cost-effective quality products for customer satisfaction. Structural equation modeling (SEM) is employed to develop a framework depicting the interrelationship among the constructs based on the empirical data collected from 263 experts of Indian manufacturing companies. The analysis interprets that sound CI can improve NPD success along with better CET and CPD. It also able to smoothly handle the conflicts occurred within the firm. CM, CET, and CPD have positive impact on NPD success among which CET motivates CPD for successful NPD.

Keywords New product development · Concurrent engineering team · Cost · Quality · Customer satisfaction

1 Introduction

New product development (NPD) is the inevitable part of manufacturing firms to sustain in the global competitive market environment [1]. Collaborative approach in NPD has identified as one of the promising areas as open innovation among the internal and external teams can offer various competitive advantages [2]. Incorporation

S. Roy (✉) · N. Modak
Department of Mechanical Engineering, Jadavpur University, Kolkata 700032, India
e-mail: sudeshnaroy689@gmail.com

N. Modak
e-mail: nmechju@gmail.com

P. K. Dan
Rajendra Mishra School of Engineering Entrepreneurship, Indian Institute of Technology, Kharagpur, West Bengal 721302, India
e-mail: pkdan@see.iitkgp.ac.in

L. Li et al. (eds.), *Advances in Materials and Manufacturing Engineering*, Lecture Notes in Mechanical Engineering, https://doi.org/10.1007/978-981-15-1307-7_40

of cross-functional team activities develops the concurrent engineering team (CET) ensuring a suitable environment of collaborative NPD [1].

The collaborative approach requires a strong communication infrastructure (CI) for better NPD performance. Conflict management (CM) activities of the firm eliminate the differences among the team members [3]. This collaborative culture of the firm introduces collaborative product design (CPD) approaches supported by CET for reducing development time and cost [4]. The development of high-quality products at minimal cost is the key objective of any firm to attain high degree of customer satisfaction [5]. Unavailability of comprehensive framework addressing the drivers of collaborative approach in NPD has been identified. The key objective of the empirical research is to develop a framework depicting the combined impact of CET, CI, CM, and CPD for NPD success and their interrelationships as well to develop high-quality product in minimum cost for customer satisfaction.

2 Theoretical Background for Hypotheses Development

Collaborative product development requires synchronization among the various functional groups for continuation of simultaneously concurrent and interdependent activities for developing concurrent engineering culture. CET is the concept of cross-functional team culture of working together as a team which develops the sharing nature within the firm for achieving success. CET motivates the team to adopt CPD culture for NPD success [6]. CPD associates industrial designers as well as engineering designers to develop functional and reliable new products as per requirements in which customers are also involved [7]. CI motivates the bi-directional flow of information for encouraging NPD success. Communication among the different functional team members generates internal collaboration through sharing of information, knowledge, and idea which helps in decision-making and problem-solving in a challenging environment which motivates the CET as well [1]. CI also minimizes the differences occurred during the development activities and offers a better CM [3]. CM is a collective effort to minimize the conflicts within the team for NPD success [8]. The above discussions evince to draw the interpretations that:

H1a: CET positively influences NPD success of the firm.
H1b: CET develops the culture of CPD within the firm.
H2a: A better CI provides an enriched NPD success in the firm.
H2b: CI motivates CET culture within the firm.
H2c: Strong CI efficiently handles conflicts within the firm and provides better CM.
H3: CM within the firm encourages NPD success of the firm.
H4: A sound CPD helps in motivating NPD success.

The discussed theoretical background helps in framing the comprehensive path model as illustrated in Fig. 1 based on the estimated hypotheses.

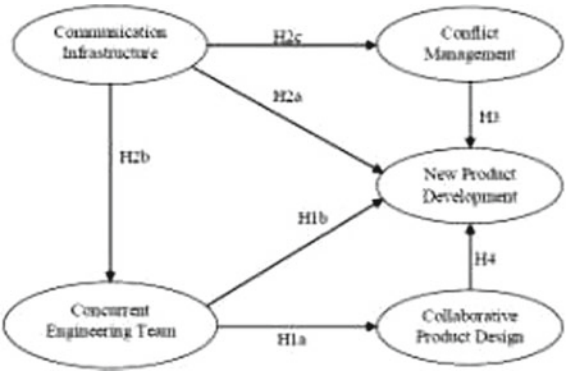

Fig. 1 Path model of constructs representing hypotheses

3 Research Methodology

Structural equation modeling (SEM) approach is employed for hypotheses testing among the latent constructs quantified by their indicators as identified from literature as well as experts' opinion [9]. IBM SPSS AMOS 21.0 is used for structural model formation by using the maximum-likelihood (ML) estimation method for hypotheses testing. A semi-structured questionnaire containing both closed-end and open-end sections for accumulating degree of implementation of the indicators has been developed. This study accumulates data from 263 manufacturing experts from various types of organizations. The demographic details of the respondents are listed in Table 1.

Table 1 Demographic profiles of respondents

Classifications	Total	%	Classifications	Total	%
Geographical Location: Indian Manufacturing Industries	263	100	Organization Type	-	-
			Fabrication	46	17.49
			Electrical Equipment	33	12.55
Respondent's Profile	-	-	Industrial valves	32	12.17
Executive	69	26.23	Textile Machineries	27	10.27
			Fire-fighting Equipment	26	9.89
Manager	83	31.56	Hydraulics & Pneumatics	25	9.50
			Burner and Heater	22	8.37
Senior Manager	48	18.25	Material handling Equipment	21	7.98
			Cell and battery	14	5.32
Vice President	36	13.69	R&D sectors	9	3.42
			Air ventilators	8	3.04
President	27	10.27			

4 Empirical Results and Discussions

4.1 Analysis of Measurement Validity

After data accumulation through seven-point Likert scale, the construct validity and the reliability of the data have been calculated using average variance extracted (AVE), composite reliability (CR), and Cronbach's alpha (α), respectively, using IBM SPSS 21.0. Values of AVE and CR greater than 0.5 are considered as consistent and reliable, whereas for α, the value is greater than or equals to 0.8. After that, principal component-based EFA is employed to recognize the manifest variables having higher loading values (>0.60) to use those indicators for measurement model development. Standardized regression weights (SRWs) of those identified indicators are calculated as enlisted in Table 2 including the values of validity and reliability indices.

4.2 Measurement Model

Confirmatory factor analysis incorporates estimation of model fitness through calculation of various fitness parameters and their values enlisted as $\chi 2 = 57.293$, degrees of freedom = 343, χ^2/degrees of freedom = 1.668, RMSEA = 0.047, GFI = 0.883, AGFI = 0.862. These values are within a permissible range to consider the measurement model as valid one. Values of AVE, CR and, α are range between 0.49 to 0.60, 0.59 to 0.71 and 0.762 to 0.890, respectively, as enlisted in Table 2.

4.3 Structural Model

Structural model development infers the interrelationships among the latent constructs including their manifest variables. This also incorporates model-to-data fitness tests and the values of fitness parameters are obtained as $\chi^2 = 594.007$, degrees of freedom = 394, χ^2/degrees of freedom = 1.506, RMSEA = 0.039, GFI = 0.913, AGFI = 0.882. The structural model showing the hypothesized relationships among latent constructs including their indicators are represented in Fig. 2. The positive impact of CET on NPD success (H1a) and CPD (H1b) is depicted by the path estimate 0.50 ($p < 0.01$) and 0.63 ($p < 0.01$). Similarly, the influential role of CI on NPD success (H2a), CET (H2b), and CM (H2c) is justified by the path estimates as 0.96, 0.90, and 0.93, respectively, all significant for $p < 0.01$. The role of CM and CPD on NPD success is also obtained by the positive path values 0.38 and 0.51, respectively, significant for $p < 0.01$. These path values are enlisted in Table 3.

The structural model in Fig. 2 depicts the combined impact of drivers of collaborative approaches on NPD success as well as their linkages to develop high-quality

Table 2 Latent constructs and manifest variables with path estimates and reliability indices

Latent constructs along with their manifests	FL	SRW
Concurrent engineering team (CET) [AVE = 0.51; CR = 0.62; α = 0.863]	–	–
1. Concurrency of process and product design in same group (m1)	0.911	0.49
2. Early stage manufacturing activities (m2)	0.895	0.54
3. Concurrency of process/product design in various groups (m3)	0.836	0.91
4. Early stage involvement of functional groups (m4)	0.784	0.61
5. Idea generation and sharing of information (m5)	0.767	0.75
6. Managerial support and motivation (m6)	0.736	0.99
7. Inter department opinion sharing (m7)	0.693	0.76
8. Coordination to achieve the target (m8)	0.652	0.89
9. Knowledge integration	0.583	
10. Strategic consideration	0.540	
Communication infrastructure (CI) [AVE = 0.55; CR = 0.68; α = 0.885]	–	–
1. Regular meeting for problem-solving (m9)	0.864	0.94
2. Virtual communication (m10)	0.782	0.94
3. Internet-based telecommunication tools (m11)	0.743	0.57
4. NPD database system (m12)	0.675	0.83
5. Face-to-face meetings in between virtual teams (m13)	0.613	0.87
6. Video conference	0.587	
Conflict management (CM) [AVE = 0.49; CR = 0.59; α = 0.762]	–	–
1. Commitment to collaboration (m14)	0.836	0.69
2. Effectiveness of conflict handling teams (m15)	0.771	0.88
3. Application of improved conflict handling process (m16)	0.647	0.93
4. Effectiveness of communication management	0.592	
Collaborative product design (CPD) [AVE = 0.54; CR = 0.67; α = 0.876]	–	–
1. Connection and cooperation with other companies (m17)	0.894	0.59
2. Cooperative relationship between companies (m18)	0.818	0.48
3. Application of team-collaboration practices (m19)	0.762	0.54
4. Cross-organizational linkage (m20)	0.733	0.95
5. Continued and parallel responsibility of different design disciplines for product and process specifications (m21)	0.647	0.58
NDP success [AVE = 0.60; CR = 0.71; α = 0.890]	–	–
1. Percentage of sales by NPD (m22)	0.928	0.67
2. Attain return on investment (m23)	0.896	0.80
3. Attain profitability goal (m24)	0.851	0.71
4. Customer satisfaction (m25)	0.810	0.77
5. Achievement of design goals (m26)	0.792	0.94
6. Meet quality guidelines (m27)	0.765	0.95

(continued)

Table 2 (continued)

Latent constructs along with their manifests	FL	SRW
7. Profitability relative to spending (m28)	0.699	0.66
8. Revenue growth	0.587	
9. International market share	0.554	
10. Attain margin goal	0.510	

Notes All *t*-values are significant to $p < 0.001$

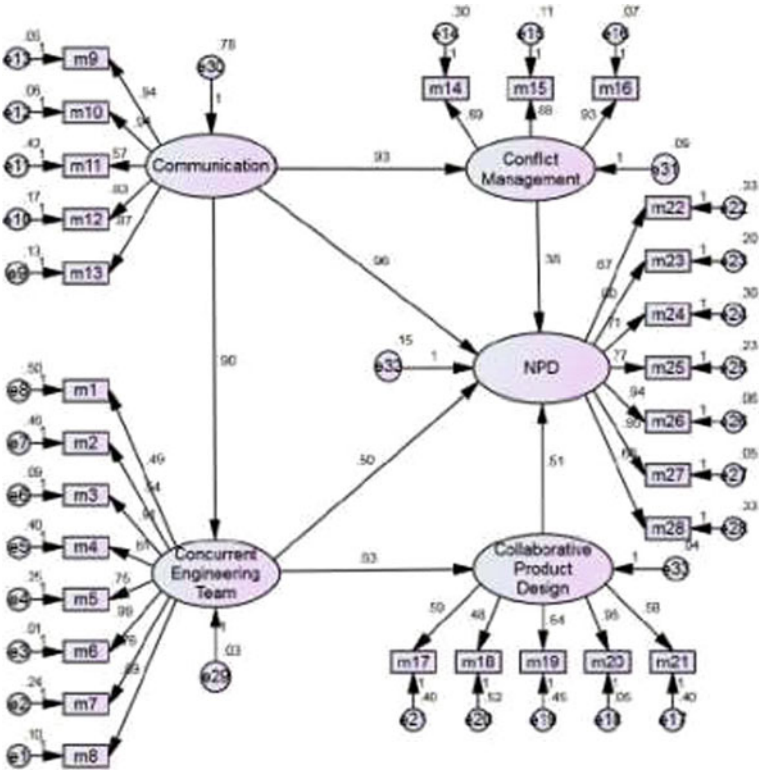

Fig. 2 SEM model after execution depicting the interrelationships of latent constructs

products in reduced cost for customer satisfaction. This model clearly infers the contribution of each indicator to measure their respective latent construct as mentioned in Table 2 along with it represents the path estimates among the latent constructs as listed in Table 3.

Table 3 Statistics of path estimates

Path descriptions	Hypotheses	Standardized estimates	*t*-values
CET → NDP	H1a	0.50(***)	12.005
CET → CPD	H1b	0.63(***)	11.252
CI → PDP	H2a	0.96(***)	7.136
CI → CET	H2b	0.90(***)	10.118
CI → CM	H2c	0.93(***)	11.125
CM → NPD	H3	0.38(***)	9.007
CPD → NPD	H4	0.51(***)	8.858

Notes ***indicate the significance at p-value < 0.01

5 Conclusions

This study realizes the impact of a collaborative culture in Indian manufacturing industries to frame 'MAKE IN INDIA' realistic. It requires implementation of CET, CI, CM, and CPD in practical field. The positive impact of the aforementioned factors for NPD success is identified among which CI provides better CET and CM culture. CET, in turn, influences CPD for development of new products with high quality and reduced cost to achieve customer satisfaction. This study is also an effort to identify the indicators of latent constructs and their contribution to implementing the respective factors in practical scenario. Managerial support and motivation have been recognized as the most vital parameter to establish an effective CET. For smooth communication within the same team and various functional groups, meetings on regular basis for problem-solving and virtual communication are equally essential. Application of improved conflict handling process helps in overcoming the differences occurred within the organization for smooth operation of NPD activities. In the case of CPD, cross-organizational linkage is identified as the most impactful parameter. Among various indicators of NPD success, this study recognizes meeting quality guidelines as the vital one followed by achievement of design goals, attain return on investment, customer satisfaction, attain profitability goal, percentage of sale by NPD and profitability relative to spending. This interprets that customers are always looking for quality products at low cost. This tends to the customer satisfaction in turn the NPD success of the firm. The present work enables us to arrive at the following important conclusion.

Acknowledgements The research work was supported by a grant from the DST INSPIRE of India.

References

1. Roy, S., Dan, P.K., Modak, N.: Effect of teamwork culture on NPD team's capability in Indian engineering manufacturing sector. Manag. Sci. Lett. **8**(7), 767–784 (2018)
2. Lv, B., Qi, X.: Research on partner combination selection of the supply chain collaborative product innovation based on product innovative resources. Comput. Ind. Eng. **128**, 245–253 (2019)
3. Green, S.G., McComb, S.A., Compton, W.D.: Promoting effective linkages between cross-functional project teams and the organization. Adv. Manag. Organ. Qual. **5**(1), 29–70 (2000)
4. Mcharek, M., Hammadi, M., Azib, T., Larouci, C., Choley, J.Y.: Collaborative design process and product knowledge methodology for mechatronic systems. Comput. Ind. **105**, 213–228 (2019)
5. Cooper, R.G., Kleinschmidt, E.J.: Winning business in product development: the critical success factors. Res. Technol. Manag. **50**(3), 52–66 (2007)
6. Roy, S., Dan, P.K., Modak, N.: Cascading effects of management actions on NPD in the manufacturing sector: the Indian context. J. Manuf. Technol. Manag. **29**(7), 1115–1137 (2018)
7. Kim, K., Lee, K.P.: Collaborative product design processes of industrial design and engineering design in consumer product companies. Des. Stud. **46**, 226–260 (2016)
8. Hubka, V., Eder, W.E.: Design Science: Introduction to the Needs, Scope and Organization of Engineering Design Knowledge, 1st edn. Springer, London (1996)
9. Fabrigar, L.R., Porter, R.D., Norris, M.E.: Some things you should know about structural equation modeling but never thought to ask. J. Consum. Psychol. **20**(2), 221–225 (2010)

Flow Forming of Tubes: Modeling and Optimization Using RSM, Composite Desirability Function, and TLBO

Prabas Banerjee, Nirmal Baran Hui, Mithilesh Dikshit and Saikat Som

Abstract Modeling of backward flow forming process is attempted in this study using response surface method. Three inputs such as infeed, feed speed ratio, and axial stagger and three responses, such as spring-back, inside diameter of flow-formed tube and ovality of the inside diameter, are considered in this study. Multi-objective optimization technique was done using composite desirability function and TLBO to attain an optimum combination of input parameters. TLBO was found to be more accurate as compared to composite desirability function.

Keywords Flow forming · Spring-back · Ovality · Response surface methodology · Composite desirability function · TLBO

1 Introduction

Metal flow forming is used for manufacturing dimensionally accurate products and mostly used in defense, aerospace, and automobile sectors [1]. It is a chipless [2] manufacturing process resulting in low material waste [3]. A large number of materials can be formed such as aluminum alloys, steel, copper, brass, and titanium [4]. Quality of the flow-formed product depends on its process parameters, and modeling of this process is very complex. Important process parameters are an axial feed of rollers, the rotational speed of the preform, the thickness of the preform, type of material used [5] and various responses such as surface roughness, ovality, and diametral growth are measured [6]. Numerous studies were carried by the researchers [7], still there exists an enormous gap and no such concrete study in this perspective.

P. Banerjee (✉) · N. B. Hui
National Institute of Technology Durgapur, Durgapur, West Bengal, India
e-mail: pb.15me1101@phd.nitdgp.ac.in

M. Dikshit
Manipal University of Technology, Manipal, Rajasthan, India

S. Som
Kannad Institute of Engineering and Management, Mankar, WB, India

L. Li et al. (eds.), *Advances in Materials and Manufacturing Engineering*, Lecture Notes in Mechanical Engineering, https://doi.org/10.1007/978-981-15-1307-7_41

Table 1 Input factors and levels used in the experiments

No.	Factors	Levels		
1	Infeed (IF)	3	3.5	4
2	Feed speed ratio (FS)	0.5	0.6	0.7
3	Axial stagger (AS)	9.5	11	12.5

2 Process Models Using RSM, Composite Desirability, and TLBO

The preform (material: AA6082) was a tube with an internal diameter 118.5 mm, the thickness of 7 mm, and an initial length of 180 mm. Three rollers were placed with an axial stagger of 9.5 mm and rotation stagger of 120° around the circumference of the preform. Response surface method has been used by researchers [8] to investigate the impact of different process parameters on multiple process responses. Three inputs of three labels each have been considered during the study (refer to Table 1).

The response of the model can be expressed as

$$Y = C(\mathrm{IF})^{a_1}(\mathrm{FS})^{a_2}(\mathrm{AS})^{a_3} \in' \tag{1}$$

where C is a constant, a_1, a_2, a_3 are the exponents and $\in'$ is the experimental error.

Since there exists more than one response (ovality, spring-back and inside diameter), RSM-based model prediction might not be suitable. Therefore, composite desirability and TLBO approaches were used for this purpose, and their performances were compared.

3 Results and Discussion

Three responses such as internal diameter, spring-back, and ovality are measured in this study. A total of twenty experiments with one repetition each were performed. In the flow forming process, it is necessary to reduce the thickness keeping the internal diameter intact. Spring-back is a measure of the difference between programmed thickness and the final thickness of a flow-formed material. In other words, spring-back can be stated as a material property in which a material experiences elastic recovery before getting permanently deformed. However, due to the changes in stress, some amount of ovality is observed. Ovality is the difference between the maximum and minimum diameter of a flow-formed product. Initially, a coded form of ANOVA is used to find out the empirical relationship of the responses. During this process, backward elimination was followed, and final expressions for the three responses are given in Eq. (2). It is important to note that the interaction effects of different factors were neglected, and linear and square effects of the inputs were only considered.

$$\begin{aligned} \text{ID} &= 120.513 + 0.01553\text{AS} - 5.32\text{FS} - 0.247\text{IF} + 4.16\text{FS}^2 \\ \text{SB} &= -1.474 + 0.279\text{AS} + 0.638\text{FS} + 0.054\text{IF} - 0.01293\text{AS}^2 \\ \text{OV} &= 0.491 - 0.00421\text{AS} - 1.043\text{FS} - 0.00841\text{IF} + 0.686\text{FS}^2 \end{aligned} \quad (2)$$

Table 2 shows the different statistical parameters for the responses. It has been observed that the model accuracy for the response ID is very high, whereas the same for the other two responses are also satisfactory. For all the responses, low difference between the R^2 and R^2-adj also indicates that the developed models are good and accurate for predictions and insignificant parameters are not present in the model. It is also noted that the lack-of-fit is very low and linear factors are contributing the maximum. In the case of ID, IF contributes more, whereas, in the other two responses, the contribution of FS is the maximum. Thamasett [9] also explained that ID is directly proportional to the IF, an increase in IF leads to more changes in ID. It is because the higher infeed demands higher forming forces leading to more deformation of the mandrel and changes in ID, whereas the contribution of FS on SB and OV is found to be more. Forming forces increase with higher infeed, but the roller needs to be in contact for permanent deformation to take place. Higher feed speed ratio does not ensure longer roller workpiece contact that enhances the elastic distortion of material. Also, AA6082 is a well-known material for higher spring-back under compressive forces. Also, the feed speed ratio is the ratio between the axial feed of the roller and the rotational speed of mandrel. Keeping the rotational speed of mandrel same, when the axial feed of roller is increased, the ovality of the flow-formed tube is improved. Faster axial transverse of the roller may lead to insufficient roller workpiece contact which may also cause inadequate plastic deformation. Also, it has been observed that axial plastic flow for metal will be proper with appropriate circumferential to axial contact length ratio and it only happens due to the feed speed ratio.

Histograms of residuals of three responses are seen to be normally distributed, and normal probability plots are well correlated showing the models are accurate and significant parameters exist in the model. Response surface plots for the three responses are presented in Fig. 1. For each response, there are three plots. In each plot, one input parameter is unchanged, and the other two are varied simultaneously. It has been observed that ovality and spring-back are more nonlinear with the inputs than the internal diameter. Following observations are also noted from Fig. 1.

Table 2 Statistical parameters observed through ANOVA

Response	ID	SB	OV
R^2 in %	90.69	70.8	79.33
R^2-(adj) in %	89.62	67.46	76.97
F-table (Lack of fit)	1.46	1.57	1.28
Contributions % by the linear terms	86.27	65.13	76.01
Highest contributing factor	IF (77.87%)	FS (54.51%)	FS (67.91%)

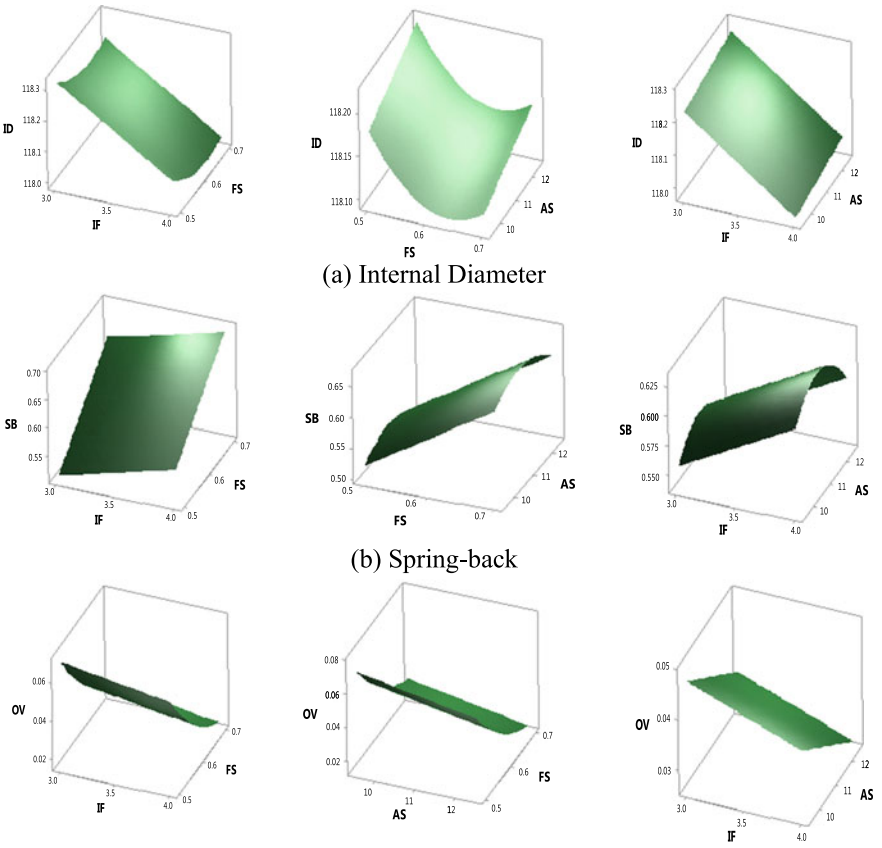

Fig. 1 Response surface plots for internal diameter (ID), spring-back (SB) and ovality (OV)

(a) Higher changes in ID are observed for a lower level of IF, FS and a higher level of AS.
(b) Spring-back is nonlinearly varying with AS. Highest change is observed for middle level of AS and higher levels of IF and FS. Therefore, it is necessary to decrease the values of IF and FS for low spring-back.
(c) Ovality is also nonlinear with all the parameters. Lowest ovality is noted for higher levels of all three inputs.

3.1 *Multi-response Optimization Using Composite Desirability Function and Teaching Learning-Based Optimization (TLBO)*

Initially, the composite desirability function was evaluated of the flow forming process model created using RSM, and the best combination of inputs leading to a minimum value of all the three responses are determined. Here, the objective was

Minimize Eq. (2) **subject to** $3 \leq \text{IF} \leq 4$; $0.5 \leq \text{FS} \leq 0.7$; $9.5 \leq \text{AS} \leq 12.5$

The result is shown in Fig. 2. The best result is obtained with IF = 3.9, FS = 0.55, and AS = 12.46 and optimal responses are ID = 118.083 mm, SB = 0.546 mm, and OV = 0.0339 mm corresponding to the composited desirability of 0.7865.

The TLBO was implemented by Mohanty et al. [10], Rao et al. [11] and found to be a good optimization tool for multi-objective optimization. TLBO is preferred over the other metastatic approaches because controlling only one parameter namely teaching factor is required. It has been used in this study to minimize the responses mentioned in Eq. (2) in the ranges of the inputs mentioned above. During this study, ten population sizes, 30 numbers of generations are selected. Table 3 depicts the comparison between the results obtained through composite desirability function

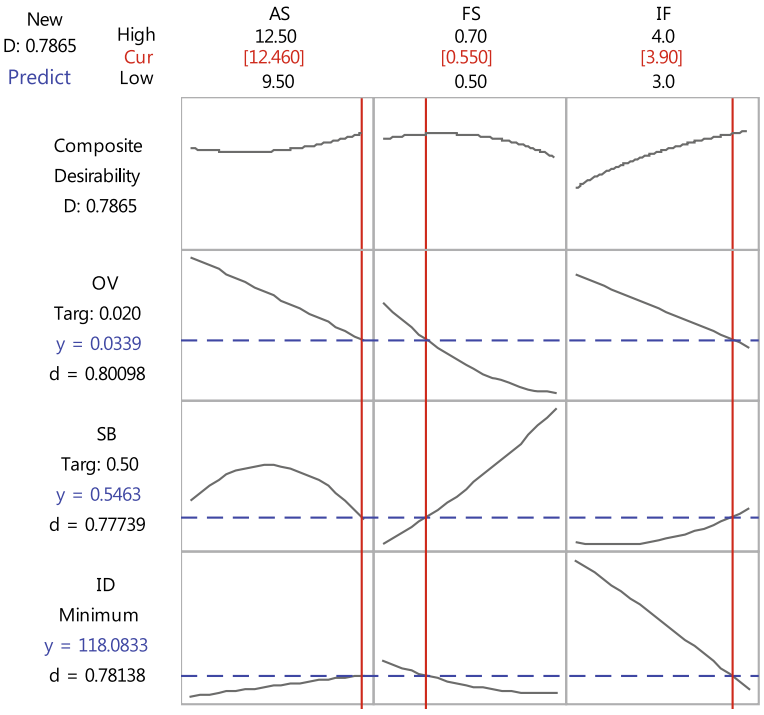

Fig. 2 Optimization results of the model using composite desirability function

Table 3 Confirmation test

	Inputs			Responses (in millimeter)					
	AS	FS	IF	Expt. ID	Pred. ID	Expt. SB	Pred. SB	Expt. OV	Pred. OV
CDF	12.46	0.55	3.9	118.19	118.04	0.572	0.546	0.036	0.034
TLBO	10.1	0.6	3.96	117.99	118.01	0.613	0.618	0.035	0.036

(CDF) and TLBO. Predicted results obtained through TLBO method were found to be closer to the experimental values. Also, TLBO method is more effective and efficient to achieve the optimal set of input parameters.

4 Conclusion

With the help of RSM design, the effects of essential input parameters were investigated, and their influences were determined on output parameters such as inside diameter, spring-back, and ovality. The relationships between outputs with inputs were derived, and the most influential parameter was identified.

(i) For the inside diameter, the infeed was the most significant parameter (77.87%).
(ii) For the spring-back, the feed speed ratio had more percentage significance (54.51%) than the other input parameters.
(iii) For the ovality, the highest significant (67.91%) input is feed speed ratio.

The optimal forming parameters were obtained using both composite desirability function as well as TLBO method. From the composite desirability, the optimal values of axial stagger, feed speed ratio, and infeed are obtained as 12.46 mm, 0.55 mm/rev and 3.9 mm, respectively. Likewise, TLBO method was employed to achieve the optimal values of input parameters which were 10.1 mm, 0.6 mm/rev, 3.96 mm for axial stagger, feed speed ratio, and infeed, respectively. Confirmation test was done to evaluate the deviation of predicted values from the experimental values. The optimization using TLBO methodology took minimum effort and provided more accurate results.

Appendix: Experimental Data

Run No.	Inputs			Responses					
	AS (mm)	FS	IF (mm)	Original			Duplicates		
				ID (mm)	SB (mm)	OV (mm)	ID (mm)	SB (mm)	OV (mm)
1	9.5	0.5	3	118.31	0.535	0.09	118.278	0.488	0.08
2	12.5	0.5	3	118.335	0.543	0.07	118.363	0.47	0.05
3	9.5	0.7	3	118.253	0.635	0.03	118.193	0.615	0.03
4	12.5	0.7	3	118.28	0.645	0.05	118.32	0.585	0.02
5	9.5	0.5	4	118.033	0.558	0.09	118.02	0.493	0.04
6	12.5	0.5	4	118.085	0.548	0.05	118.083	0.488	0.02
7	9.5	0.7	4	118.028	0.708	0.02	118.008	0.703	0.03
8	12.5	0.7	4	118.008	0.66	0.02	118.025	0.638	0.01
9	9.5	0.6	3.5	118.148	0.578	0.03	118.083	0.512	0.04
10	12.5	0.6	3.5	118.123	0.568	0.02	118.198	0.52	0.06
11	11	0.5	3.5	118.23	0.565	0.06	118.258	0.523	0.08
12	11	0.7	3.5	118.088	0.673	0.01	118.128	0.625	0.02
13	11	0.6	3	118.238	0.563	0.03	118.243	0.508	0.031
14	11	0.6	4	118.03	0.691	0.06	118.023	0.64	0.0315
15	11	0.6	3.5	118.1	0.629	0.05	118.131	0.58	0.0301
16	11	0.6	3.5	118.11	0.635	0.05	118.133	0.583	0.0299
17	11	0.6	3.5	118.07	0.632	0.05	118.132	0.577	0.0298
18	11	0.6	3.5	118.118	0.63	0.05	118.135	0.581	0.0306
19	11	0.6	3.5	118.04	0.643	0.05	118.134	0.579	0.0302

(continued)

(continued)

Run No.	Inputs			Responses					
	AS (mm)	FS	IF (mm)	Original			Duplicates		
				ID (mm)	SB (mm)	OV (mm)	ID (mm)	SB (mm)	OV (mm)
20	11	0.6	3.5	118.17	0.633	0.05	118.136	0.582	0.03012

References

1. Kalpakjian, S., Rajagopal, S.: Spinning of tubes. J. Appl. Metal Working **2**(3), 211–223 (1982)
2. Wong, C.C., Dean, T.A., Lin, J.: A review of spinning, shear forming and flow forming. Int. J. Mach. Tools Manuf. **43**, 1419–1435 (2003)
3. Music, O., Allwood, J.M., Kawai, K.: A review of mechanics of metal spinning. J. Mater. Process. Technol. **210**, 3–23 (2010)
4. Marini, D., Corney, J.: A methodology for assessing the feasibility of producing components by flow forming. Prod. Manuf. Res. **5**(1), 210–234 (2017)
5. Poddar, B., Banerjee, P., Kumar, K.R., Hui, N.B.: Flow forming of thin walled precision shells. Sadhana **43**, 208 (2018)
6. Ranjan, K.M., Narasimhan, K.: An investigation of the development of defects during flow forming of high strength thin wall steel tubes. J. Fail. Anal. Prev. **1**(5), 69–76 (2001)
7. Aghchai, A.J., Razani, N.A., Mollaei, B.: Flow forming optimization based on diametral growth using finite element method and response surface methodology. J. Eng. Manuf. **226**(12), 2002–2012 (2012)
8. Srinivasulu, M., Komaraiah, M., Rao, C.S.K.P.: Experimental investigations to predict mean diameter of AA6082 tube in flow forming process—a DOE approach. IOSR J. Eng. **2**, 52–60 (2012)
9. Thamasett, E.: Forces and deformations during ironing of cylindrical, rotationally symmetrical hollow bodies made of Aluminium, TH Stuttgart (1961)
10. Mohanty, C.P., Satpathy, M.P., Mahapatra, S.S., Singh, M.R.: Optimization of cryo-treated EDM variables using TOPSIS-based TLBO algorithm. Sādhanā **43**(4), 51 (2018)
11. Rao, R.V., Savsani, V.J., Vakharia, D.P.: Teaching–learning-based optimization: a novel method for constrained mechanical design optimization problems. Comput. Aided Des. **43**(3), 303–315 (2011)

Investigation on Weld Bead Geometry of AISI 201LN in GMAW-Cold Metal Transfer (CMT) Process

Vivek Singh, M. Chandrasekaran and Sutanu Samanta

Abstract The welding of thin sheet of austenitic stainless steel (SS201LN) is a challenging task due to distortion and high heat input associated during tungsten inert gas (TIG) process. A robotic cold metal transfer (CMT) process is the modified version of gas metal arc welding (GMAW) process in which the heat input is reduced due to controlled wire feeding and higher welding speed. In this work, GMAW (with CMT) process of AISI 201LN stainless steel plate is performed using Box–Behnken design (BBD). Wire feed rate (*WFR*), welding speed (*S*), and nozzle to work distance (*NTD*) are considered weld parameters to investigate process characteristics of weld bead viz., penetration (*P*), width (*W*), and reinforcement (*R*). Predictive models are developed using response surface methodology (RSM) and model validation shows an average error % of 2.61 for penetration. ANOVA analysis shows that *WFR* and welding speed are the most influencing factors, whereas *NTD* having the least influence in determining penetration. The parametric optimization of all responses simultaneously is carried out using desirability analysis (DA) obtaining composite desirability of 0.7216 mm/min.

Keywords AISI 201LN · CMT · Weld bead · RSM · Desirability analysis

1 Introduction

Austenitic stainless steels are gaining popularity in industries due to their enhanced mechanical properties and excellent corrosion resistance. Nickel (Ni) is an expensive alloying element which constitutes a major part of the total cost of stainless steel. Usually, by adding Ni, the austenitic phase in stainless steel is stabilized [1, 2]. Recent advancements have proved that yield strength of austenitic stainless steel

V. Singh
Research scholar (NERIST)/Department of Mechanical Engineering, AKGEC, Ghaziabad, Uttar Pradesh, India

M. Chandrasekaran (✉) · S. Samanta
Department of Mechanical Engineering, North Eastern Regional Institute of Science and Technology (NERIST) (DU), Nirjuli, Itanagar, Arunachal Pradesh 791109, India
e-mail: mchse1@yahoo.com

L. Li et al. (eds.), *Advances in Materials and Manufacturing Engineering*, Lecture Notes in Mechanical Engineering, https://doi.org/10.1007/978-981-15-1307-7_42

can be doubled by increasing the nitrogen content in it. Nitrogen addition acts as solid solution strengthening element in stainless steel, increasing the yield strength at room temperature and at subzero temperatures [3].

AISI 304L and AISI 316L are commonly used austenitic stainless steels for the fabrication of cryogenic tanks. These steels operate at very low temperatures and hence require higher toughness and lateral expansion at –196 °C. AISI 201LN is gaining popularity as a substitute for AISI 304L/316L in cryogenic industry due to its economy, higher strength, and excellent toughness property. In conventional GMAW process, metal transfer occurs with the aid of electromagnetic force, whereas in CMT, no such forces are required, and it leads to lesser spatter. CMT is especially suited for thin sheets where less heat input is required during welding [4].

TIG welding process is generally used for welding of austenitic grades to obtain high-quality weld. However, due to high production rate and ease of automation, GMAW process is often preferred over GTAW process [5]. CMT process is widely used for thin sheets due to higher weld quality, low heat input, and higher productivity than conventional GMAW process. Many researchers have investigated weld parameters with conventional GMAW process. Limited investigation is carried out on robotic CMT process. The mode of metal transfer plays a vital role in reducing heat input and spatter-free high-quality weld [6]. In CMT process, an oscillating wire is fed in forward and reverse direction with an oscillating frequency up to 70 Hz. The wire is fed in the forward direction to weld pool during arcing period. As the wire dips in the weld pool, the current is lowered and arc is extinguished. The reversed motion of the wire assists droplet detachment during short circuit. The wire motion is reversed to initiate the formation of another droplet [7]. In this work, an experimental investigation was carried out to study the effect of different weld parameters on weld bead characteristics viz., penetration (P), bead width (W), and reinforcement (R) in GMAW (CMT) process of AISI 201LN stainless steel plate.

2 Plan of Investigation

2.1 Welding Experiments

The current work is based on robotic CMT welding to investigate AISI 201LN. In preliminary welding investigation, wire feed rate (*WFR*), welding speed (S), and nozzle to tip distance (*NTD*) have found as most influencing factors for investigating the weld bead geometry. The parameters levels are 6, 7, 8 m/min; 500, 600, 700 mm/min and 10, 15, 20 mm, respectively, for *WFR*, *S,* and *NTD*. For carrying out full factorial design of experiments, it requires $3^3 = 27$ experiments. In this work, Box–Behnken design (BBD) of experiments with 15 experimental runs has been employed. This minimizes number of experimental runs required to carry out experimental investigation which leads to saving time and cost. These independent factors were varied in order to study the effect on the responses such as penetration (P), bead width

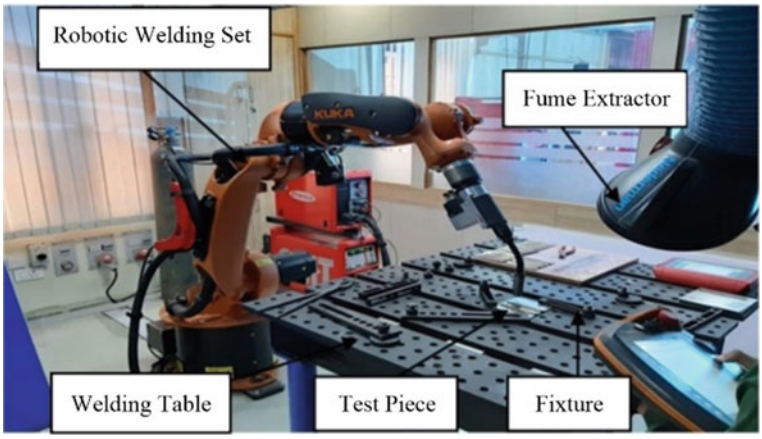

Fig. 1 A robotic controlled CMT experimental set up (Make: KUKA)

(W), and reinforcement (R). Welding experiments are carried out in robotic CMT process with bead on plate experiments on stainless steel (AISI 201LN) plates of size 150 mm × 150 mm × 3 mm. Figure 1 shows Fronius TPS 4000 CMT welding power source integrated with robotic set up (Make: KUKA) used in this work. The filler wire (ER316L) of diameter 1.0 mm and Argon + 2.5% Co_2 shielding gas was used with a gas flow rate of 15 l/min. After welding, transverse sections of the weld sample were cut from middle of each plate to examine weld bead profile. These samples were then polished to get a mirror-like finish and etched. The cross sections of weld bead profile were then analyzed at 20X magnification using vision measurement machine. The responses obtained in the analysis are shown in Table 1.

2.2 Development of Predictive Models

The predictive models of welding responses are developed with various influencing factors. The relationship between responses (Y), i.e., penetration, bead width, and reinforcement are the function of various factors such as *WFR*, *S*, *NTD* can be represented as

$$Y = f(WFR, S, NTD) \tag{1}$$

In this work, response surface methodology (RSM) is used to relate between welding factors and responses. The experimental results are analyzed in Minitab 17® statistical software at 95% confidence level and the model relationship was obtained. The following are different RSM model equations obtained; model equations are validated.

Table 1 Experimental results (Box-Behnken design)

Bead No.	*WFR*	*S*	*NTD*	*P* (mm)	*R* (mm)	*W* (mm)
1	8	500	15	1.816	2.492	7.245
2	6	700	15	0.738	1.954	5.426
3	6	600	20	0.614	2.098	5.364
4	8	700	15	1.389	2.087	5.832
5	7	600	15	1.501	2.176	5.839
6	7	700	10	0.758	2.078	3.812
7	7	600	15	1.515	2.224	5.839
8	8	600	20	1.6	2.395	6.13
9	7	500	20	1.612	2.425	5.345
10	7	500	10	1.631	2.354	5.482
11	8	600	10	0.948	2.186	6.275
12	7	600	15	1.529	2.241	5.714
13	6	500	15	1.606	2.195	5.799
14	7	700	20	0.785	2.264	3.956
15	6	600	10	1.282	1.961	4.956

$$P = 5.55 + 0.030WFR - 0.00927\,S - 0.1192\,NTD - 0.1066WFR \times WFR - 0.000002\,S \times S - 0.01190NTD \times NTD + 0.001103WFR \times S + 0.06600WFR \times NTD + 0.000023\,S \times NTD$$

$$(R^2 = 98.84\%,\ R^2(\text{Adj}) = 96.74\%) \tag{2}$$

$$R = -0.79 + 1.374WFR - 0.00466\,S - 0.0714NTD - 0.0760WFR \times WFR + 0.000004\,S \times S + 0.000892NTD \times NTD - 0.000410WFR \times S + 0.00360WFR \times NTD + 0.000058\,S \times NTD$$

$$\left(R^2 = 97.28\%,\ R^2(\text{Adj}) = 92.38\%\right) \tag{3}$$

$$W = 4.92 - 6.71WFR + 0.0553S + 1.042NTD + 0.655WFR \times WFR - 0.000038S \times S - 0.03086NTD \times NTD - 0.00260WFR \times S - 0.0277WFR \times NTD + 0.000141S \times NTD$$

$$\left(R^2 = 97.74\%,\ R^2(\text{Adj}) = 93.67\%\right) \tag{4}$$

2.3 ANOVA Analysis

The adequacy of the models was checked using analysis of variance (ANOVA). Models with *P*-values less than 0.05 are considered adequate. Factors having *P*-values less than 0.05 are considered significant in determining the response.

The ANOVA result for responses shows that for predicting *P*, *S* have significant contribution of 49.36% followed by *WFR* 12.60% and *NTD* are found less significant. Also have significant contribution in predicting *R* contributing 40.80% while contribution of *WFR* and *NTD* were 31.53% and 12.65%, respectively. Percentage contribution of *S* and *WFR* on bead width is obtained as 29.12 and 19.23%, respectively. *NTD* is the least significant factor.

2.4 Validation of Models

The conformity tests were conducted to validate the developed model by considering different welding parameters design matrix. The selected welding parameters for model validation are: wire feed rate, *WFR* (6.5, 7.5, 6, 7 and 7.5 m/min), welding speed, *S* (550, 650, 550, 550 and 700 mm/min), nozzle to work distance, *NTD* (15, 10, 15, 15 and 15 mm). The average predicted percentage error found for *W*, *R,* and *P* are 3.01%, 3.41%, and 2.61%, respectively.

3 Optimization Using Desirability Analysis

After building the predictive model, a numerical optimization technique using desirability function analysis is used to optimize the welding responses. The objective of optimization is to find the best settings that maximize penetration and minimize reinforcement and bead width. The desirability value ranges from 0 to 1. The factors setting with maximum desirability are the optimal welding parameter. Figure 2 shows the desirability optimization plot for various responses and it obtains combined desirability values of 0.7216 providing 6.0 m/min wire feed rate, 512.12 mm/min welding speed, and 10 mm *NTD*. The optimum welding parameter obtained in this work provides guideline for cryogenic vessel fabrication industries.

3.1 Model Analysis

Surface plots were drawn to study the variation of response surface with different factor combinations. Obtained surface plots are shown in Fig. 3a–d.

The following are the effect of welding parameters in GMAW (CMT) process:

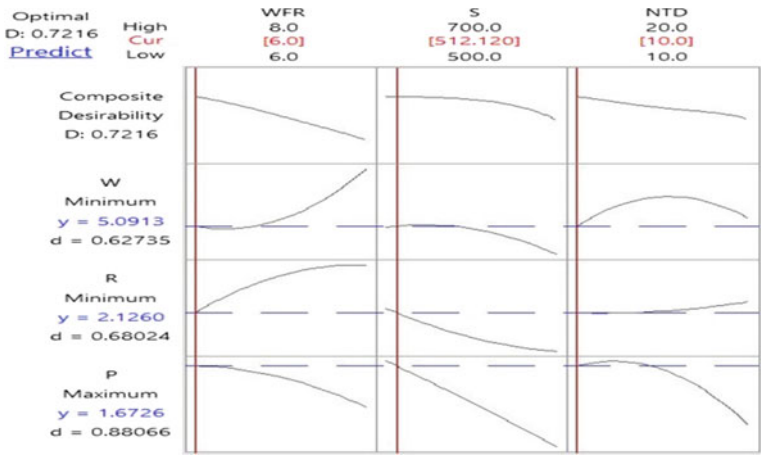

Fig. 2 Desirability optimization plot

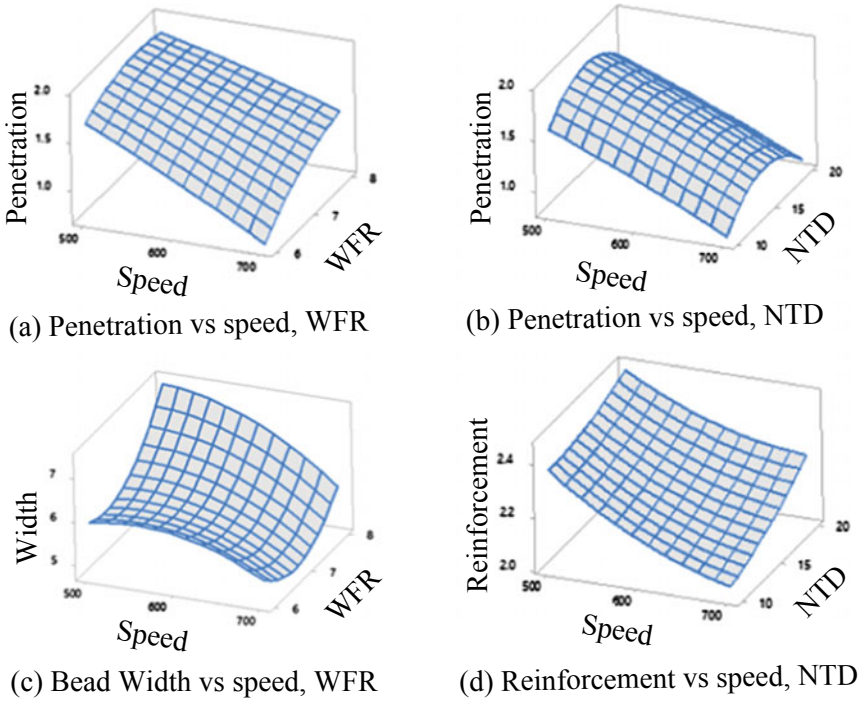

(a) Penetration vs speed, WFR

(b) Penetration vs speed, NTD

(c) Bead Width vs speed, WFR

(d) Reinforcement vs speed, NTD

Fig. 3 **a–d** Surface plots

Wire feed rate: The effect on wire feed rate on different weld bead characteristics (P, W, R) shows that increase in *WFR* increases *P* and *W*. *WFR* is directly proportional to welding current.

Nozzle to work distance: In CMT process, an oscillating wire is fed in forward and reverse direction, *NTD* having least influence on the penetration and bead width. As in conventional GMAW, *NTD* is a major influencing parameter and penetration increases with decrease in *NTD*. Reinforcement increases with increase in *NTD*.

Weld speed: The weld speed is inversely proportion with penetration, bead width, and reinforcement. As the weld speed decreases, the heat input per unit length increases resulting increase in penetration and wider bead width, while increase in welding speed reduces heat input which leads to lesser penetration and narrow bead width.

4 Conclusion

In the present work, during robotic CMT process of GMAW investigation of AISI 201LN stainless steel, the following conclusions are drawn.

- The penetration (*P*) and bead width (*W)* are increasing with increase in *WFR* and decrease with welding speed. *NTD* is least influence parameter on penetration.
- The weld reinforcement (*R*) increases as *NTD* increases, while it decreases with the increases in welding speed. The increase in welding speed reduces the volume of deposited molten metal per unit length resulting decrease in weld reinforcement.
- ANOVA analysis shows that *WFR* and welding speed are the most influencing factors in determining penetration. The predictive performance of the model shows good co-relationship with experimental prediction; the maximum average percentage of error of 2.61 is obtained for penetration.
- The simultaneous optimization for all responses is performed and obtained composite desirability of 0.7216 providing 6.0 m/min *WFR*, 512.12 mm/min *S* and 10 mm *NTD*. The obtained optimum welding parameters provide guide line for fabrication of thin sheet cryogenic tank using GMAW (CMT) process.

References

1. Vashishtha, H., Taiwade, R.V., Sharma, S., Patil, A.P.: Effect of welding processes on microstructural and mechanical properties of dissimilar weldments between conventional austenitic and high nitrogen austenitic stainless steels. J. Manuf. Process. **25**, 49–59 (2017)
2. Chuaiphan, W., Srijaroenpramong, L.: Effect of welding speed on microstructures, mechanical properties and corrosion behavior of GTA-welded AISI 201 stainless steel sheets. J. Mater. Process. Technol. **214**(2), 402–408 (2014)
3. Toit, M.D., Pistorious, P.C.: Nitrogen control during autogenous arc welding of stainless steel—part 1 : experimental observations. Weld. J., pp. 219–224 (2003)

4. Selvi, S., Vishvaksenan, A., Rajasekar, E.: Cold metal transfer (CMT) technology—an overview. Def. Technol. **14**(1), 28–44 (2018)
5. Ghosh, P.K., Kulkarni, S.G., Kumar, M., Dhiman, H.K.: Pulsed current GMAW for superior weld quality of austenitic stainless steel sheet. ISIJ Int. **47**(1), 138–145 (2007)
6. Talalaev, R., Veinthal, R., Laansoo, A., Sarkans, M.: Cold metal transfer (CMT) welding of thin sheet metal products. Est. J. Eng. **18**(3), 243 (2012)
7. Gungor, B., Kaluc, E., Taban, E., Sik, A.: Mechanical and microstructural properties of robotic cold metal transfer (CMT) welded 5083-H111 and 6082-T651 aluminum alloys. Mater. Des. **54**, 207–211 (2014)

Creating Productive Conditions for Electric Discharge Machining of Non-conductive Ceramics

Sanjeev Verma, P. S. Satsangi and K. D. Chattopadhyay

Abstract Fabricating structures from non-conductive ceramic materials like silicon nitride (Si_3N_4) is difficult through traditional machining, but their applications are increasing in engineering field due to their high hardness, low thermal conductivity and resistance to oxidation. High electrical resistivity of such ceramics restricts the use of electric discharge machining (EDM) on them. An assistive electrode together with graphite powder-mixed dielectric mixture of hydrocarbon fluids was used to create favourable conditions for deposition of conductive layer on the non-conductive SiAlON having 10^5 Ω cm resistivity. The experiments were conducted according to Taguchi design. Analysis of variance using signal-to-noise ratios showcased significant parameters and their optimal values for material removal, electrode wear and size overcut. The elemental composition of the sample confirmed the deposition of carbon particles on ceramic surface which has helped in propagation of sparking beyond exhaustion of assistive layer. The SEM images confirmed the presence of deposited carbon layer and material removal by spalling and evaporation.

Keywords Assistive layer · Powder-mixed EDM · Non-conductive ceramics · Taguchi method · SEM images

1 Introduction

Ceramics exhibiting good wear resistance, light weight, low thermal expansion coefficient and high specific strength have the perfect amalgamation of properties required

S. Verma (✉)
CSIR-CSIO, Central Scientific Instruments Organization, Chandigarh 160030, India
e-mail: sanjeevverma@csio.res.in

P. S. Satsangi
PEC, Punjab Engineering College, Chandigarh 160012, India

K. D. Chattopadhyay
Chitkara University, Rajpura, Punjab 140401, India

L. Li et al. (eds.), *Advances in Materials and Manufacturing Engineering*, Lecture Notes in Mechanical Engineering, https://doi.org/10.1007/978-981-15-1307-7_43

for diverse applications. The industrial demand of these advanced ceramics is continuously on the rise, but still the applications are limited because of their poor machinability by conventional techniques. If these were electrically conductive (resistivity < 100–333 Ω cm), electrical discharge machining (EDM) and electro-chemical machining (ECM) could be applied to reshape them. Electro-chemical discharge machining (ECDM) can only be used to machine micro-grooves, micro-slots and poses a risk of corrosion. Various techniques like assistive electrodes, powder-mixed dielectric, decomposed carbon from working oil, etc., were tried to machine shapes through EDM.

Mohri et al. [1] machined a non-conductive ceramic using an assistive electrode and found that cracked carbon from dielectric fluid provides electrical conductivity to the ceramic. Fukuzawa et al. [2] machined Si_3N_4 and ZrO_2 using assistive electrode and the discharges were produced incessantly due to formation of the electrically conductive layer. Sabur et al. [3] concluded that the stability of pyrolytic carbon layer depends on the input power, material of workpiece and tool, dielectric liquid, polarity and discharge duration while EDM of non-conductive ZrO_2 ceramic using assistive electrode. Hanaoka et al. [4] found that the machinable limit of electrical conductivity to machine Si_3N_4 composites is below 4×10^{-2} S m^{-1}. Liu et al. [5] used copper sheet as an assistive electrode to EDM a large surface area on cubic boron nitride and polycrystalline diamond. Ji et al. [6] found that ZnO/Al_2O_3, having electrical resistivity of 3410 Ω cm, can be machined using copper electrode. Gotoh et al. [7] found that a pulse discharge longer than the set pulse duration resulted in the generation of electrically conductive layer on the insulating ceramic surface. Chakraborty et al. [8] established that the right working fluid plays an important role. Pachaury and Tandon [9] reviewed the challenges during EDM of ZrO_2, Al_2O_3, Si_3N_4, SiC and their composites. Farooqui and Patil [10] presented a perspective on shaping of advanced ceramics by EDM and unfolded the challenges involved. Hosel et al. [11] used lacquer-based assistive electrode to start and sustain machining of precise channels on Zirconia. Kucukturk and Cogun [12] found that Al_2O_3 ceramic is most difficult to EDM as compared to ZrO_2, SiC, B_4C, glass, etc., using graphite powder-mixed dielectric liquid and assistive layer. Kolli and Kumar [13] found that the addition of 15 g/l boron carbide powder in dielectric provides maximum MRR during EDM of titanium alloys. Kliuev et al. [14] carried out EDM drilling in non-conducting ZrO_2 ceramic of holes of 1 mm diameter up to 1.5 mm depth in deionised water using assistive layer.

From the above prior art, it can be seen that the extension of machinable limit of electrical resistivity for EDM, bigger machining cuts, improvement in formation of carbon layer creation on the surface of electrically resistive ceramics require further investigations.

2 Methodology

A copper foil of thickness 0.06 mm was affixed on the surface of non-conductive SiAlON with conductive adhesive to initiate the discharge, as shown in Fig. 1. Initial electrical sparks occurs in the machining gap between the assistive layer and tool electrode. As the machining progresses, pyrolytic carbon produced from disassociation of dielectric medium at high instantaneous energy and the copper electrode particles gets adhered to the surface, thus providing the essential electrical conductivity for machining to progress even after the assistive electrode material layer is machined.

The typical properties of SiAlON and elemental composition measured using energy dispersive X-ray spectroscopy on Hitachi SU8010 Scanning Electron Microscope, are given Table 1. Electrical Resistivity was measured using Keithley Electrometer 6517B. Electrolytic copper of 99.98% purity and diameter 3 mm was used as an electrode. To achieve the favourable conditions for producing larger pyrolytic carbon in the sparking gap, a special dielectric fluid was made using carbon-rich Indian Oil Company Limited (IOCL) hydrocarbon oil having 8–21 carbon atoms per molecule and 'Electronica' make 'Elektra' dielectric in various proportions. The graphite powder of 30–40 μm size and 99% purity from Nanoshel LLC, USA, was added to the dielectric mixture @ 30 g/l along with a stirring system and pump for circulation.

Comprehensive pilot experimentation decided the levels of control factors for quality machining, as given in Table 2. The quality machining is implied as initia-

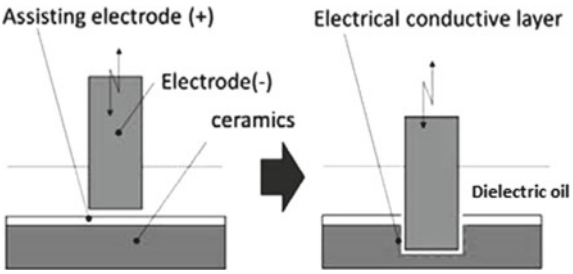

Fig. 1 Schematic view of assistive electrode method

Table 1 Typical physical and mechanical properties of SiAlON

Composition (wt%)	Si-19.4, Al-35.9, C-9.8, N-1, O-34
Density	3.8 g/cm^3
Young's modulus	340 GPa
Hardness (Gpa/HVN)	13.24/1350
Fracture toughness (K_{1c})	5.7 MPa m$^{1/2}$
Thermal exp. coefficient	5.6×10^{-6}/°C
Electrical resistivity	100,000 Ω cm
Workpiece size (mm)	12.7 × 12.7 × 4.7

Table 2 Control factors and their levels used in Taguchi and RSM

Current (A)	1, 3, 5
Sparking gap voltage (V)	40, 50, 70
Additive percentage (%)	20, 35, 50
Duty factor (%)	48, 54, 60
On time (μs)	2, 20, 50
Rotation speed (RPM)	20, 30, 40
Tool polarity	Negative
Graphite powder (g/l)	30
Open gap voltage	135 V

tion of machining cut beyond the assistive layer, controlled EDM and no electrode bending. The machining was done on 'Electronica' die-sinking ELEKTRA PULS SE35 machine for 60 min for each trial and average values of three trials for Material removal rate (MRR) as depth of hole machined in mm/hour and Electrode wear rate (EWR) in gm/hour are shown in Table 3. Weight of material was measured using Wensar HPB 1000H scale. The diameter of machined hole measured using Vaiseshika microscope was used to calculate the size overcut (OVC) in mm.

3 Design of Experiments

The Taguchi methodology (TM) uses orthogonal array (OA) and signal-to-noise ratios (S/N ratio) for robust design and analysis of variance (ANOVA). For six control factors having three levels each, Taguchi L_{27} orthogonal array was selected for the experimentation. TM, ANOVA and main effect plots for S/N ratios determined the significant parameters and optimum parameters values for each of the output characteristics.

4 Results and Discussion

ANOVA Table 4 depicts the most significant controlling parameters for MRR and main effects plots, shown in Fig. 2, illustrates the optimum values for achieving highest MRR. Similarly, main effect plots and ANOVA for lowest OVC and EWR were calculated and tabulated in Table 5.

Table 3 Taguchi L27 OA and the observed value of MRR, EWR and OVC

Expt. No.	Current (A)	Gap voltage (V)	On time (μs)	Duty factor (%)	Additive percentage (%)	Rotation (RPM)	MRR-depth (mm/hour)	EWR (gm/hour)	OVC (mm)
1	1	40	2	48	20	20	0.34	0.011	0.12
2	1	40	20	54	35	30	0.54	0.023	0.05
3	1	40	50	60	50	40	0.45	0.008	0.08
4	1	50	2	54	35	40	0.25	0.018	0.01
5	1	50	20	60	50	20	0.26	0.010	0.02
6	1	50	50	48	20	30	0.93	0.010	0.05
7	1	70	2	60	50	30	0.31	0.010	0.04
8	1	70	20	48	20	40	1.01	0.013	0.03
9	1	70	50	54	35	20	0.48	0.014	0.02
10	3	40	2	54	50	30	0.21	0.010	0.03
11	3	40	20	60	20	40	0.26	0.004	0.01
12	3	40	50	48	35	20	0.29	0.008	0.01
13	3	50	2	60	20	20	0.37	0.009	0.04
14	3	50	20	48	35	30	0.56	0.013	0.01
15	3	50	50	54	50	40	0.37	0.005	0.09
16	3	70	2	48	35	40	0.46	0.010	0.06
17	3	70	20	54	50	20	0.34	0.010	0.07
18	3	70	50	60	20	30	0.36	0.006	0.01
19	5	40	2	60	35	40	0.32	0.004	0.01
20	5	40	20	48	50	20	0.18	0.004	0.06

(continued)

Table 3 (continued)

Expt. No.	Current (A)	Gap voltage (V)	On time (μs)	Duty factor (%)	Additive percentage (%)	Rotation (RPM)	MRR-depth (mm/hour)	EWR (gm/hour)	OVC (mm)
21	5	40	50	54	20	30	0.31	0.005	0.12
22	5	50	2	48	50	30	0.34	0.007	0.04
23	5	50	20	54	20	40	0.39	0.005	0.22
24	5	50	50	60	35	20	0.36	0.007	0.01
25	5	70	2	54	20	20	0.49	0.008	0.20
26	5	70	20	60	35	30	0.77	0.010	0.02
27	5	70	50	48	50	40	0.20	0.006	0.08

Table 4 ANOVA table for SN ratios for MRR in terms of depth of hole

Source	DF	Seq SS	Adj SS	Adj MS	*F*-value	*P*-value
Current	2	34.09	34.09	17.05	954.37	0.001
Voltage	2	48.22	48.22	24.11	1349.67	0.001
On time	2	17.28	17.28	8.64	483.64	0.002
Duty factor	2	5.41	5.41	2.71	151.51	0.007
Additive %	2	85.15	85.15	42.58	2383.54	0.000
Rotation	2	24.23	24.23	12.11	678.15	0.001
Current * voltage	4	25.84	25.84	6.46	361.74	0.003
Current * on time	4	56.05	56.05	14.01	784.45	0.001
Voltage * on time	4	65.73	65.73	16.43	919.89	0.001
Residual error	2	0.04	0.04	0.02		
Total	26	362.05				

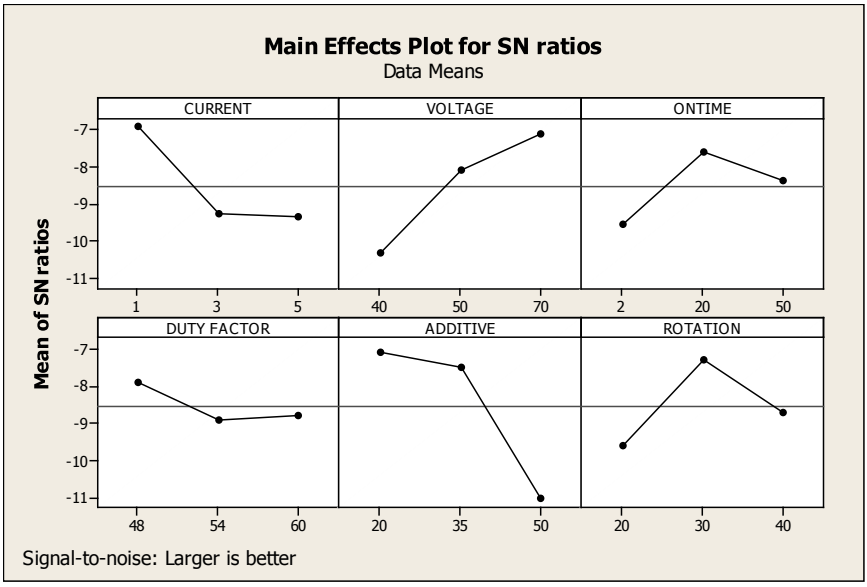

Fig. 2 Main effects plot of MRR

4.1 Composition Analysis of the Machined Surface

The elemental composition of the workpiece given in Table 6, established that the carbon percentage on the machined surface has increased almost threefolds after the EDM. It is due to the deposition of cracked carbon on the workpiece. The elemental percentage of oxygen, aluminium and silicon gets reduced because the electrical

Table 5 Significant parameters and optimized values

Output and significant factors	Current (A)	Voltage (V)	On time (μs)	Duty factor (%)	Percentage additive	Rotation (RPM)
MRR	1 significant	70 significant	20	48	20 significant	30
OVC	3 significant	50	20	60 significant	35 significant	30
EWR	5 significant	40	50	60	20 significant	40 significant

Table 6 Elemental composition of workpiece

Element	(Elemental weight %)	
	Before EDM	After EDM
Carbon	9.76	24.58
Nitrogen	0.96	0.00
Oxygen	34.01	27.60
Aluminium	35.90	31.18
Silicon	19.38	16.64
Copper	0.00	0.00

discharge machining has taken place on the workpiece and they have got mixed with dielectric medium as a part of eroded particles.

4.2 Microstructure Topography of the Machined Surface

The machined workpiece surface was qualitatively studied using field emission scanning electron microscope, JEOL JSM-6510LV, as shown in Fig. 3 micrographs. The various phases of melting and resolidification, residual cavities of removed grains, resolidified balls and droplets seen on the machined surface indicated that the ceramic was made molten or evaporated by the spark thermal energy. As the electrical resistivity of ceramics is high, the discharge channel is not formed relatively easily. But due to creation of suitable conditions for spark to occur, thermal stresses were reduced and no significant microcracks were found on the machined surface.

The temperature within the ionization channel rises around 8000–12,000 °C rapidly and causes instantaneous local melting of material at the surface of tool electrode and work piece. The melted eroded particles get solidified as small spheres within dielectric fluid and on the workpiece surface. A crater is formed by erosion due to the removal of material from the sparking zone. When working with ceramics, the formation of ionization channel does not take place easily as they are electrically non-conductive material. When the cracked carbon from the dielectric gets deposited

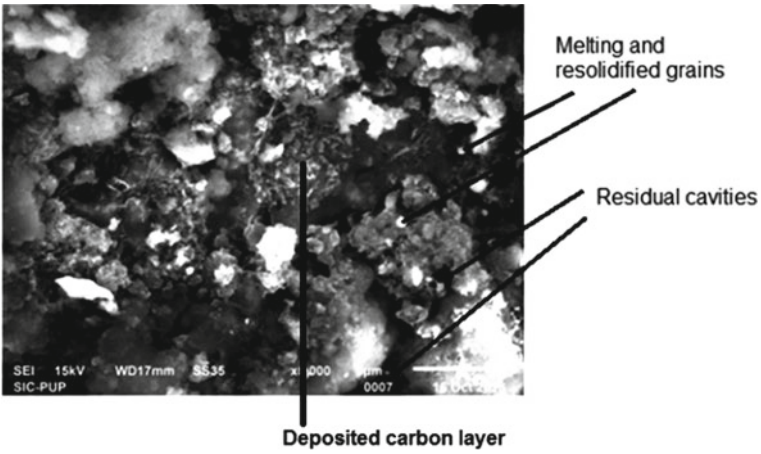

Fig. 3 SEM image of EDM surface showing residual cavities and deposited carbon layer

on the workpiece, the possibility of formation of ionization channel increases and material is removed due to melting and vaporization. The irregular shape of craters indicates that the erosion also takes place because of spalling. Also due to addition of electrically conductive powders to the dielectric, the chances of ionization get increased. The additive powder gets energized and arranges itself in the form of chains under the sparking area. This decreases the insulating strength of the dielectric fluid and causes early explosion in the gap and more rapid material erosion from the workpiece. The decreased insulating strength of the sparking zone results in increased sparking gap distance, thus resulting in formation of fewer cracks.

5 Conclusions

The following conclusions can be drawn from the results:

1. The process has been developed to create conditions to EDM the non-conductive ceramics having resistivity of about 10^5 Ω cm (Table 3 and Fig. 3).
2. The process can now be used to drill holes in non-conductive ceramics, which otherwise could not have been possible.
3. The process can also be used to reshape and machine non-conductive ceramic components.
4. Using adhesive copper sheet as an assistive electrode and powder and additive mixed dielectric medium, non-conductive SiAlON can be machined effectively.
5. The different combination of parameters which resulted in maximum MRR, minimum OVC and minimum EWR are shown in Table 5.
6. The composition of the EDM surface got changed owing to the carbon element deposition from the graphite powder and the working fluid (Table 6).

References

1. Mohri, N., Fukuzawa, Y., Tani, T., et al.: Assisting electrode method for machining insulating ceramics. CIRP Ann. **45**(1), 201–204 (1996)
2. Fukuzawa, Y., Mohri, N., Gotoh, H., et al.: Three dimensional machining of insulating ceramics materials with EDM. Trans. Nonferr. Metal Soc. **19**(1), 150–156 (2009)
3. Sabur, A., Ali, M.Y., Maleque, M.A., et al.: Investigation of material removal characteristics in EDM of nonconductive ZrO_2 ceramic. Procedia Eng. **56**, 696–701 (2013)
4. Hanaoka, D., Fukuzawa, Y., Ramirez, C., et al.: Electrical discharge machining of ceramic/carbon nanostructure composites. Procedia CIRP **6**, 95–100 (2013)
5. Liu, Y.H., Ji, R.J., Li, X.P., et al.: Electric discharge milling of insulating ceramics. Proc. Inst. Mech. Eng. BJ Eng. Manuf. **222**(2), 361–366 (2008)
6. Ji, R., Liu, Y., Diao, R., et al.: Influence of electrical resistivity and machining parameters on electrical discharge machining performance of engineering ceramics. PLoS One **9**(11), 1–9 (2014)
7. Gotoh, H., Tani, T., Mohri, N.: EDM of insulating ceramics by electrical conductive surface layer control. Procedia CIRP **42**, 201–205 (2016)
8. Chakraborty, S., Dey, V., Ghosh, S.K.: A review on the use of dielectric fluids and their effects in electrical discharge machining characteristics. Precis. Eng. **40**, 1–6 (2015)
9. Pachaury, Y., Tandon, P.: An overview of electric discharge machining of ceramics and ceramic based composites. J. Manuf. Process **25**, 369–390 (2017)
10. Farooqui, M.N., Patil, N.G.: A perspective on shaping of advanced ceramics by electro discharge machining. Procedia Manuf. **20**, 65–72 (2018)
11. Hosel, T., Muller, C., Reinecke, H.: Spark erosive structuring of electrically nonconductive zirconia with an assisting electrode. CIRP J. Manuf. Sci. Technol. **4**(4), 357–361 (2011)
12. Kucukturk, G., Cogun, C.: A new method for machining of electrically nonconductive work-pieces using Electric Discharge Machining technique. Mach. Sci. Technol. **14**(2), 189–207 (2010)
13. Kolli, M., Kumar, A.: Effect of boron carbide powder mixed into dielectric fluid on electrical discharge machining of titanium alloy. Procedia Mater. Sci. **5**, 1957–1965 (2014)
14. Kliuev, M., Maradia, U., Wegener, K.: EDM drilling of non-conducting materials in deionised water. Procedia CIRP **68**, 11–16 (2018)

A Critical Study of Bead-on-Plate Laser Welding of Niobium Alloy PWC-11

Santosh Kumar Gupta, Susmita Datta, Sanjib Jaypuria, Dilip Kumar Pratihar and Partha Saha

Abstract In the present work, laser welding of PWC-11 alloy has been tried in bead-on-plate (BOP) configuration. Experiments have been carried out to determine the range of input parameters for full penetration welding. Laser power (P) and scanning velocity (V) are selected as the input parameters for BOP experiments. Weld width, penetration depth and micro-hardness are the outputs for BOP experiments. The weld profile is analyzed using optical microscope to calculate the aspect ratio and relate its dependence on laser power and scanning velocity. The fusion zone is characterized by scanning electron microscope (SEM) and X-ray diffraction (XRD). Laser power and scanning velocity are to be maintained on the higher level to obtain full penetration weld and to avoid the formation of laser plume. The micro-hardness test has showed that the fusion zone has high hardness value in comparison to the base metal. The increment in the micro-hardness of the fusion zone is due to the formation of phases of oxides and nitride, which is confirmed by the XRD phase analysis. The SEM micrographs reveal the increase in grain size of the fusion zone and EDAX analysis of fusion zone indicates the presence of nitrogen and oxygen. From the present study, it is obvious that the key challenge is to re-establish the present methods of fabrication by laser to avoid the contamination of the future joint by oxygen, nitrogen, carbon dioxide at the time of welding along with weld geometry optimization with a focus on minimization of weld width.

Keywords Bead-on-plate welding · Thermal gradient · PWC-11 alloy · Laser welding · Niobium alloy

1 Introduction

Laser welding is an autogenic welding technique and has emerged as a substitute of conventional fabrication techniques. In laser welding, the high energy density of the laser is used for carrying out manufacturing with sectarian heating and very narrow heat-affected zone. Niobium and its alloys possess some of the significant properties

S. K. Gupta · S. Datta · S. Jaypuria (✉) · D. K. Pratihar · P. Saha
Indian Institute of Technology Kharagpur, Kharagpur 721302, India
e-mail: sanjibjaypuria@iitkgp.ac.in

L. Li et al. (eds.), *Advances in Materials and Manufacturing Engineering*, Lecture Notes in Mechanical Engineering, https://doi.org/10.1007/978-981-15-1307-7_44

to find their applications as high-temperature structural materials. These properties are strength at elevated temperature, chemical stability with liquid alkali metals, high rupture duration limit and lower mass-to-volume ratio as compared to other refractory materials [1]. Niobium proves its adequacy in the nuclear environment as absorption efficiency of neutron is low and its fabrication is easy as compared to other potential materials to be used as a structural material in the high-temperature reactor (HTR), engines of aerospace and space nuclear reactors [2]. Niobium has high affinity with hydrogen and gets brittle at a normal temperature as observed in titanium and zirconium. Niobium bonds with carbon, nitrogen, oxygen and boron at high temperatures and thus results in hard and brittle compounds. This increases the hardness of the fusion zone, which is highly desired as a property in high-temperature structural materials [3]. The alloy attains high-temperature strength due to the formation of niobium-based carbides in the matrix. Electron beam welded PWC-11 sheets were tested at the temperature of 1350 K to assess the creep rupture property and it was found out that fusion zone is more creep resistant as compared to base metal for the two conditions of annealing and aging [4]. Welding of niobium-based alloy is a tedious task due to its reactive nature that results into the contamination of fusion zone, high melting temperature and high thermal conductivity.

As a result, limited work is accessible for the study of laser welding of Nb–1Zr–0.1C in the available literature. A detailed study of laser welding of PWC-11 alloy is to be investigated by taking into account its relevance as structural material in HTR. Therefore, a systematic study of bead-on-plate welding of Nb–1Zr–0.1C is carried out using Nd: YAG laser. The response of input parameters on the weld-bead profile and hardness induced in the fusion zone is studied. The process parameters for bead-on-plate welding are laser power (P), scanning speed (V) and laser spot radius (R). The experiments are carried out in continuous wave (CW) mode. The responses are penetration depth (PD), weld width (WW) and hardness. The present work is directed to establish a domain of process parameters to obtain full penetration weld and other desired mechanical characteristics, which ensures its application as high-temperature structural material. In addition to this, a preliminary metallurgical characterization has been investigated about micro-hardness, phase and precipitates.

2 Experimentation

The sheets of PWC-11 alloy are prepared using niobium, zirconium and carbide powder. The composition of the niobium alloy is detailed in Table 1. Figure 1a depicts schematic of laser bead-on-plate welding of dimension 50 mm × 20 mm ×

Table 1 Composition of PWC-11 alloy

Zr (wt%)	C (wt%)	Impurities (ppm)	Nb (wt%)
0.9–1.2	0.1–0.13	H-4, N-41, O-132	Reminder

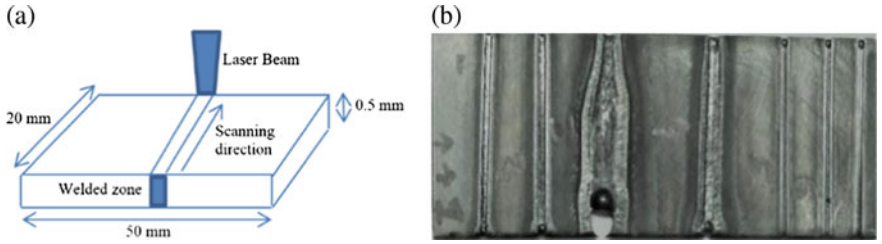

Fig. 1 **a** Schematic diagram for BOP laser welding for experimental specimen, **b** photograph of BOP laser welding on niobium alloy sheet

0.5 mm, which is polished, etched and ultrasonically cleaned prior to the welding. Figure 1b represents the actual PWC-11 bead-on-plate welding.

Laser welding is carried out using a 1750 W solid-state fiber-coupled diode-pumped laser of wavelength 1064 μm. Scanning of laser beam is done in longitudinal direction for bead-on-plate experiments. Argon is used as shielding gas to avoid contamination of the melt pool. The laser spot diameter is kept constant at 400 μm for the experiments. The laser power (W) has been varied in the range of 800–1200 W and scanning speed (V) is varied in the window of 400–1400 mm/min. Clamping is given on the both sides of sheet to minimize distortion. The samples are welded using different combinations of input parameters. Transverse surfaces of the welded samples are examined using optical microscope to examine and measure the weld-bead profile. Scanning electron microscope is used to conduct the detailed analysis of microstructure. Phase analysis is done for different zones formed in the weld using X-ray diffraction. Micro-hardness of weld cross-section is measured for holding time of 10 s at a load of 50 g.

3 Results and Discussion

The optimal range of input parameters is estimated for full penetration welding by analyzing the weld-bead profile. The weld penetration along the thickness and weld-bead width are measured for each combination of input parameters. Aspect ratio is the ratio of weld depth of penetration to weld width and higher aspect ratio is desirable. The higher the aspect ratio, the better is the weld quality. From Fig. 2, it is evitable that with the combinations of input parameters (that is, laser power = 800 W and scanning velocity = 400 mm/min and laser power = 1200 W and scanning velocity = 1000 mm/min) we are able to obtain full penetration with the expense of wider weld width and heat-affected zone (HAZ). For the combination of input parameters: 800 W and 400 mm/min, we are able to obtain weld of penetration of 756 μm and bead width of 1796 μm. Aspect ratio for the input combination of 800 W and 400 mm/min is 0.420 and for the combination of 1200 W, 1000 mm/min there is a slight increase of 0.073 in aspect ratio. Laser welding has been tried in the

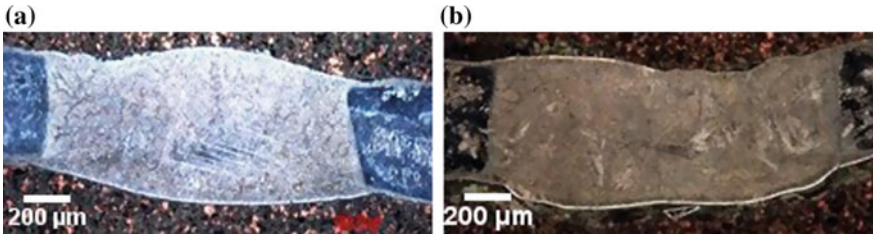

Fig. 2 Optical images of **a** bead profile for the combination of 800 W and 400 mm/min, **b** bead profile for the combination of 1200 W and 1000 mm/min

present study to minimize the weld-bead area and heat-affected zone (HAZ). Laser being the mode of welding, the weld width in both the cases is very large, which is highly undesirable. To overcome this problem of increased weld width, an optimal range for scanning velocity needs to be selected to avoid the formation of plume. Plume absorbs the incident laser beam and thus resulting in larger weld width at the top surface. This plume formation further results in the decrease of penetration depth.

3.1 XRD Phase Analysis and Examination of Micro-hardness of Weld Zone and Base Plate

The phase analysis of PWC-11 alloy reveals the formation of phases like Nb_2N, Nb_2C, NbO_2, ZrC, Nb_2O_5, Nb_4O_5, ZrO_2 and Zr_3O [5, 6]. Figure 3 illustrates the XRD phase pattern of welded PWC-11 alloy. Nb_2O_5 and ZrC phases are found to have high-intensity peaks. Carbide is added in small weight percentage of 0.1% to the alloy specifically to form phases like Nb_2C that enhances the creep and micro-hardness property of the alloy [7, 8].

Micro-hardness of the base metal, HAZ and weld-bead are analyzed as depicted in Fig. 4. It shows the variation of micro-hardness starting from the weld centerline toward the base plate. The micro-hardness of the fusion zone has considerably high value in comparison with that of base metal. The value of micro-hardness ranges from 270.9303 VHN in molten zone to 96.632 VHN in the base metal, when the laser power is 800 W and scanning velocity is 400 mm/min. Micro-hardness value of the fusion zone increases to 661.66 VHN with an increase of laser power and scanning velocity by 400 W and 600 mm/min, respectively, as compared to the previous combination. The micro-hardness is considerably high owing to the formation of Nb_2O_5 and Nb_2N [9] phases in the molten pool. The formation of these two phases results into a loss of ductility and causes embrittlement in the fusion zone.

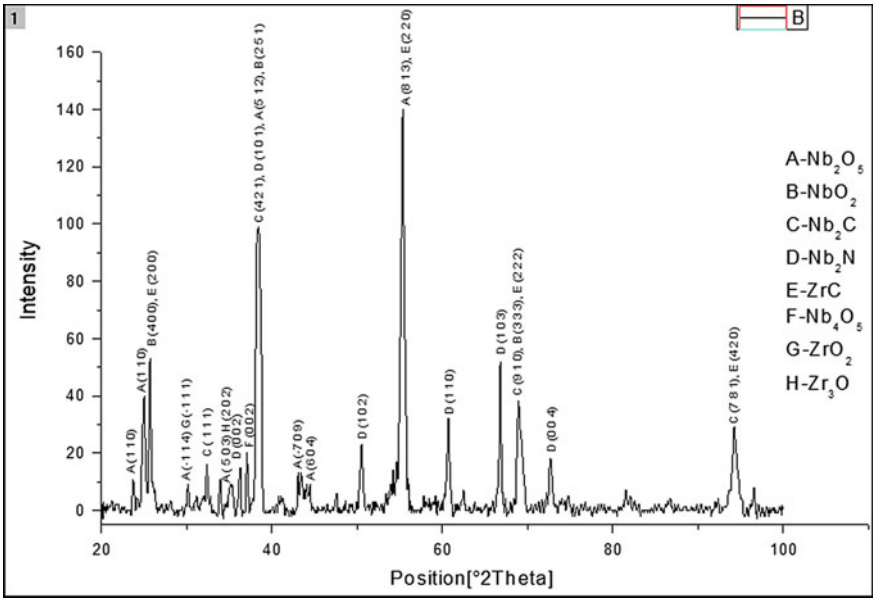

Fig. 3 XRD pattern of welded zone in PWC-11 alloy

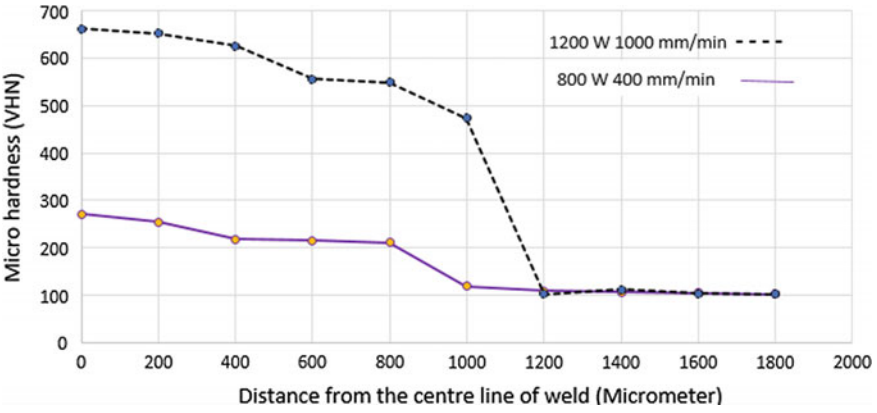

Fig. 4 Variation of micro-hardness across the width of the laser beam welds

3.2 Examination of Microstructure and EDS Analysis of Weld Zone and Heat-Affected Zone

Figure 5 illustrates the grain structure of the fusion zone and base metal of the laser-welded PWC-11 alloy. Precipitates of carbides can be found at the top and bottom surface of the fusion but in the middle portion, there is no precipitate as it has been

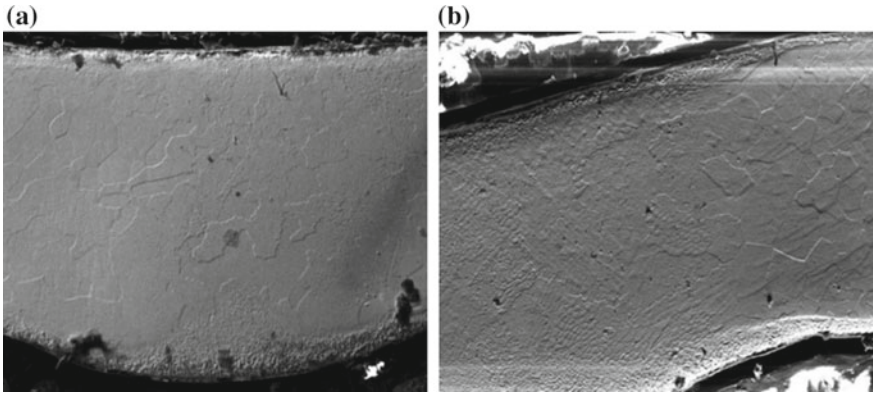

Fig. 5 Scanning electron micrograph, **a** fusion zone of laser beam weld, **b** fusion zone and base metal interface of laser beam weld

dissolved during the welding. Grain size formed in the welded region is considerably large and elongated as compared to that in the base metal which is shown in Fig. 5b. The carbide dissolution due to heating helped in the formation of the large-sized grains in the welded zone. Figure 5b demonstrates the growth of equi-axed grains, which is smaller in the middle region of the fusion zone, as compared to that found in the HAZ. Thermal gradient is the main reason behind the difference in the sizes of the grain in these two areas. Due to the high cooling rate subjected to a large thermal gradient in the center of the fusion region, the grain size is found to be smaller. As we move away from the center of the fusion zone, the cooling rate which is proportional to thermal gradient decreases and thus results in increase in the size of the grain. Increase in the micro-hardness of the fusion is a result of the contamination due to the formation of oxides and nitrides [10, 11]. The oxide and nitride phases are confirmed from the phase analysis. However, the region with the larger grain structure has a low value of micro-hardness. In addition to SEM micrograph analysis, EDAX analysis is carried out to find the possible elements present in the fusion and interface zone. It also seems that the larger and elongated grain frequency is found to be more in fusion zone compared to base metal [12]. These larger grains may be due to the dynamic recrystallization of deformed grains by the heat of laser welding. The EDS result indicates an increase of carbon and oxygen content in the fusion zone, which implies that the possibility of carbide and oxide formation is more as compared to the base and HAZ.

4 Conclusion

Bead-on-plate laser welding of PWC-11 alloy is carried out to determine the range of input parameters, i.e., laser power and scanning velocity for full penetration welding. The following conclusion could be inferred from the study.

- The laser power and scanning velocity should be kept high due to high thermal conductivity and it melts at the temperature of 2470 °C. Bead width obtained in the preliminary study is large, which is unsatisfactory, as laser being the mode of welding.
- The micro-hardness in the fusion zone is considerably higher in magnitude in comparison to that of the base plate. The phases formed in the molten zone mainly consist of oxides and nitrides, which increase the micro-hardness of the welded region. Thus, making this zone prone to brittle failure and development of cracks take place.
- Degradation in the mechanical properties of the fusion zone is caused due to improper welding process like an insufficient flow of shielding gas to avoid contamination.

Acknowledgements We would like to thank MHRD, Govt. of India and Laser Laboratory, IIT Kharagpur for their financial and technical help during this study.

References

1. Delgrosso, E.J., Carlson, C.E., Kaminsky, J.J.: Development of niobium-zirconium-carbon alloys. J. Less-Common Metals **12**, 173–201 (1967)
2. Vishwanadh, B., Vaibhav, K., Jha, S.K., Mirji, K.V., Samajdar. I., Srivastava, D., Tewari, R., Saibaba, N., Dey, G.K.: Development of Nb–1%Zr–0.1%C alloy as structural components for high temperature reactors. J. Nucl. Mater. **427**, 350–358 (2012)
3. Torkamany, M.J., Ghaini, F.M., Poursalehi, R.: Dissimilar pulsed Nd: YAG laser welding of pure niobium to Ti–6Al–4V. Mater. Des. **53**, 915–920 (2014)
4. Badgujar, B.P., Kumar, S., Jha, M.N., Samajdar, I., Mascarenhas, M.R., Tewari, R., Dey. G.K.: An investigation of electron beam welding of Nb-1Zr-0.1C alloy: process parameters and microstructural analysis. J. Manufact. Process. **28**, 326–335 (2017)
5. Vishwanadh. B., Arya, A., Tewari, R., Dey, G.K.: Formation mechanism of stable NbC carbide phase in Nb-1Zr-0.1C (wt.%) alloy. Acta Mater. **144**, 470–483 (2018)
6. Franchini, F., Pierantozzi, P.: Electron beam welding of dissimilar materials Niobium-base alloy C-103 with titanium-base alloy Ti–6AI–4V ELI. Weld. Int. **6**(10), 792–797 (2009)
7. Wojcik, C.C.: Processing properties and application of high-temperature Niobium alloys. Mater. Res. Soc. Symp. Proc. **322**, 519–530 (1994)
8. Chaudhuri, A., Sarkar, A., Kapoor, R., Singh, R.N., Chakravartty, J.K., Suwas S.: Microstructural features of hot deformed Nb-1Zr-0.1C Alloy. J. Min. Metals Mater. Soc. **66**, 1923–1929 (2014)
9. Sanjines, R., Benkahoul, M., Sandu, C.S., Schmid, P.E., Levy, F.: Electronic states and physical properties of hexagonal β-Nb2N and δ'-NbN nitrides. Thin Solid Films **494**, 190–195 (2006)

10. El-Genk, M.S., Tournier, J.M.: A review of refractory metal alloys and mechanically alloyed-oxide dispersion strengthened steels for space nuclear power systems. J. Nucl. Mater. **340**, 93–112 (2004)
11. Aimone, P., Yang, M.: Niobium alloys for the chemical process industry. Int. J. Refract Metal Hard Mater. **71**, 335–339 (2018)
12. Vishwanadh, B., Naina, R.H., Majumdar, S., Tewari, R., Dey, G.K.: A study on the oxidation behaviour of Nb Alloy (Nb-1pctZr-0.1 pct C) and Silicide-Coated Nb Alloys. Metall. Mater. Trans. A **44**, 2258–2269 (2013)

Effect of Amplitude Oscillation on Spiking in Electron Beam Welding of Copper Plate

Sanjib Jaypuria, Santosh Kumar Gupta, Dilip Kumar Pratihar, Debalay Chakrabarti and M. N. Jha

Abstract Both electron and laser beam welding are gaining importance and popularity due to their inherent advantages like high heat density, low heat affected area and fewer defects compared to traditional fusion welding. However, spiking defect is the most common in these high-power densities welding, where both melting and evaporation participate in the fusion process. Spiking is an instantaneous non-uniform rise in bead penetration throughout the joint, which can seriously affect the properties and strength of the joint. These defects can lead to premature failure of the welded components. Oscillation of electron beam could be an effective method to improve the welding fusion and solidification, so to eliminate defects in the weld. Here, the electron beam welding of highly conductive ETP-Cu alloy plate was conducted by varying the amplitude of oscillation. Spiking phenomenon was represented as the standard deviation of penetration in the study. Electron beam used without oscillation yielded the minimum spiking and the same was seen to increase with increase of amplitude of oscillation. It was found that spiking is mostly dependent on keyhole stability. It could also be concluded that an optimum combination of oscillation parameters is necessary to minimize the spiking phenomena in copper weld.

Keywords Beam oscillation · Amplitude · Electron beam welding · Weld bead · Spiking

1 Introduction

Electron beam welding is an advanced fusion welding process, which is used in aerospace, automotive, nuclear and power industries. The widespread use of electron beam welding is due to the high-energy density, low heat input and high aspect ratio of the joint. The ability to weld thick plates, reflective metals and refectory materials make the process as the preferred one for most of the industries [1]. Copper is one

S. Jaypuria (✉) · S. K. Gupta · D. K. Pratihar · D. Chakrabarti
Indian Institute of Technology Kharagpur, Kharagpur 721302, India
e-mail: sanjibjaypuria@iitkgp.ac.in

M. N. Jha
Bhabha Atomic Research Centre, Mumbai 400085, India

L. Li et al. (eds.), *Advances in Materials and Manufacturing Engineering*, Lecture Notes in Mechanical Engineering, https://doi.org/10.1007/978-981-15-1307-7_45

of the frequently used industrial metals because of its excellent heat and electrical conductivity. In contrast, it is very problematic to achieve a sound quality copper joint due to their higher thermal conductivity and reflectivity. Electron beam welding is one such fabrication technique, which enables a sound quality copper joint with much ease [1, 2]. In electron beam welding, the electron beam acts as a source, where the high-speed electrons strike with the metal plate and getting converted to heat energy. The electromagnetic arrangement in electron beam welding also facilitates variation scanning profiles with different frequencies and amplitudes [3]. However, in the case of partial penetration welding using electron beam, the penetration depth is not uniform in the welding direction, and this penetration depth is a typical irregular defect observed in high-energy-density welding. This unexpected change in the local penetration in periodic sequences increases the stress concentration in the localized tip and leads to the crack in the root of the keyhole [3].

The problem of root spiking and associated spike root porosity in partial penetration electron beam welding was established, and several studies had been conducted to investigate the behavior of spiking during the welding. Reported studies [4, 5] found out using an X-ray pinhole camera that the dynamic beam–metal interaction was the cause of the most of root defects in the high-energy-density welding. Spiking phenomena were characterized by the beam stability, which was a breakdown of the natural oscillation of the electron beam. The relatively fixed position of the beam in keyhole dissipates the larger amount of energy to the keyhole cavity base producing additional penetration. It was reported [6] that the instability of keyhole is caused mainly by the collision of upward and downward flows in the keyhole due to the pressure difference in the molten liquid. The probability of forming root pores and spikes was found to be more in high-power welding schedules, where keyhole instability is more frequent as compared to that of low-power welding. Few researchers [7, 8] studied various kinds of defects in bead-on-plate EBW on copper plates. They showed that the porosity had been increased with the increase in beam power, depth of focus and with the decrease of travel speed. However, there is no reported work on the behavior of spiking generation with beam oscillation parameters.

It was observed from the literature that spiking is an associated defect in electron beam welding and there was no solid correlation found between the input process parameters and occurrence of spiking. It was also seen in some literature that defects formation in electron beam welded joints could be minimized through beam oscillation parameters. Therefore, in the present work, electron beam welding of copper plate was conducted by varying the amplitude of beam oscillation. The transverse weld section was used to measure the standard deviation of penetration in a specific length, which is a direct measure of spiking phenomena. Then a detailed study was conducted for finding the influence of oscillation amplitude on spiking formation during electron beam welding of copper plate.

2 Experimentation and Data Collection

Electrolytic tough pitched copper (ETP-Cu) of 20 mm thickness was considered for experimentation. The said specimen consists of 99.28 wt% copper and a few impurities. Before the experimentation, the copper plates were cleaned through wire brush and acetone to remove dirt and possible oxide layers. Bead-on-plate welding was conducted by keeping the heat input constant and varying the amplitude of oscillation in electron beam welding setup located at IIT Kharagpur, India. The experimental setup of EBW along with one welded specimen is shown in Fig. 1a, b, respectively. Circular scanning path was maintained in all the experiments except one experiment, where no beam oscillation parameters were used. The experimental combinations used in the study are given in Table 1 along with the responses of the study. The welded specimens were subjected to post-weld treatment to remove the surface defects and further, metallurgical characterization. A transverse specimen was cut from each combination to measure the bead width and penetration. In addition to this, a longitudinal section was cut from the middle plane of the fusion area to measure the variation in penetration for a specific length. Both transverse and longitudinal weld section was passed through polishing and etching to reveal the

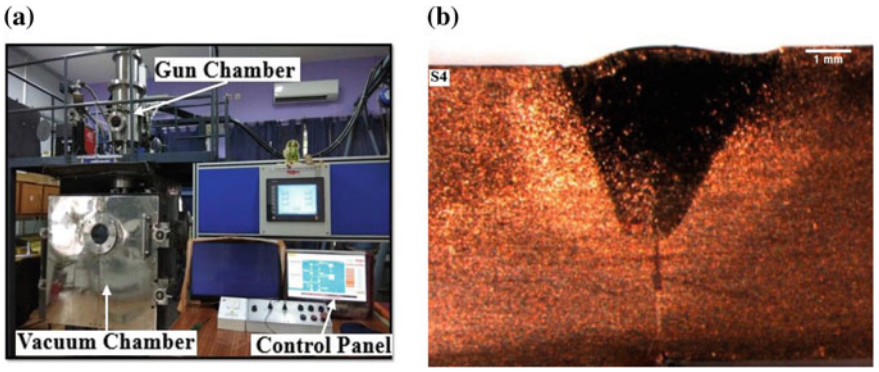

Fig. 1 **a** Electron beam welding setup, **b** partial penetrated copper weld

Table 1 Experimental Combinations along with bead and spiking responses

Sample no.	Power (kW)	Speed (mm/min)	Frequency (Hz)	Amplitude (mm)	Bead width (mm)	Bead penetration (mm)	Standard deviation of penetration
S1	6.3	700	0	0	2.486	5.801	0.2253
S2	6.3	700	600	0.2	2.759	6.117	0.2731
S3	6.3	700	600	0.3	3.190	6.275	0.3927
S4	6.3	700	600	0.4	3.080	6.422	0.2882

fusion zone properly. The longitudinal sections were observed under the macroscope, and the macroscopic images with spikes were manually measured with open-source plot digitizer software. The standard deviation of each peak point of the specific figure was considered as the standard deviation of penetration, which is a measure of non-uniformity of penetration and indicates the spiking phenomena in a given sample. Here, the weld-bead parameters, namely bead width and penetration along with standard deviation of penetration were considered as the responses.

3 Result and Discussion

Electron beam welding of copper plates in bead-on-plate configuration was conducted by varying amplitude oscillation. The weld-bead parameters and standard deviation of penetration were measured for each combination. The details of experimental combination along with responses are given in Table 1. It is seen from Fig. 2a that the bead width had an increasing trend with an increase of amplitude. When an electron beam was used in welding without any oscillation parameters, then the beam scan path was just like a straight line. So, heat energy of the beam was mostly used in drilling action of the beam, and normal high aspect ratio weld can be obtained. However, when an electron beam with some defined scanning path (here, circular path) along with amplitude and frequency was provided to the metal parts, then the beam had to maintain a circular path with the provided oscillation diameter. Therefore, the heat energy of the beam was also utilized for heating the circular path and ultimately the bead width increases. Although there is reduction of heat input with the increase of oscillation amplitude, the bead penetration was increasing with the increase of oscillation amplitude. Figure 2b indicates the trend of bead penetration with amplitude of oscillation. It might be due to the high thermal conductivity and low melting temperature of copper, which enabled drilling action of the beam more easily than low conductive metals.

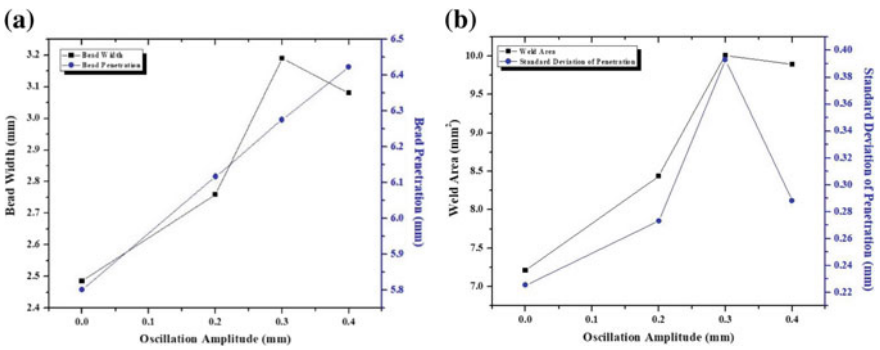

Fig. 2 Variations of **a** bead geometry and **b** spiking with beam oscillation amplitude

Spiking is the defect, where the instability in the electron beam results in a non-uniform increase in bead penetration. Thus, a molten spike forms at the root of the weld instantaneously, which indicates the high rate of solidification at the spike area than elsewhere of the weld. Keyhole instability is considered as the prime reason for spiking in many literatures. Therefore, the keyhole formation and spiking in weld are discussed in brief to get the established reason behind the spike formation. In the keyhole mode of electron beam welding, the beam is focused on producing an incident power density at the metal surface that is sufficient to initiate vaporization. The keyhole is formed by displacing the liquid melt induced by the evaporation recoil pressure based on the local equilibrium temperature, while surface tension and hydrostatic pressure resist the keyhole opening. The instability of the keyhole is mainly caused by the collision of upward and downward flows due to the pressure components in the liquid melt.

Uniform weld penetration in electron beam welding is characterized by continually oscillated beam interaction with metal, which is able to maintain the periodic scanning path from top to bottom of the keyhole. The oscillatory motion of the beam during welding is due to the continuous attainment of unwelded metal, which is because of the welding speed and the forces associated with the keyhole equilibrium. Spiking is formed, when there is a breakdown for a short while in the oscillation of the beam, and the beam–metal interaction becomes fixed on a particular point in the keyhole. This allows to transfer significant beam energy to the bottom of the keyhole and penetration increases.

It was observed that in most of the cases, the spiking phenomena were increasing with the beam oscillation. It could be because of the larger cavity opening with the larger amplitude, which gave the larger entering path to the beam for further drilling action. In addition to this, the larger amplitude helped to achieve the larger weld bead, which was supposed to be detrimental in maintaining keyhole stability and an increase of spiking tendency in the weld. It can be evident from Fig. 3, where S3 has the maximum spiking tendency because of largest weld-bead area among all combinations. S1 sample without any oscillation parameters is found to have the minimum weld area and minimum spiking tendency. The higher value of spiking,

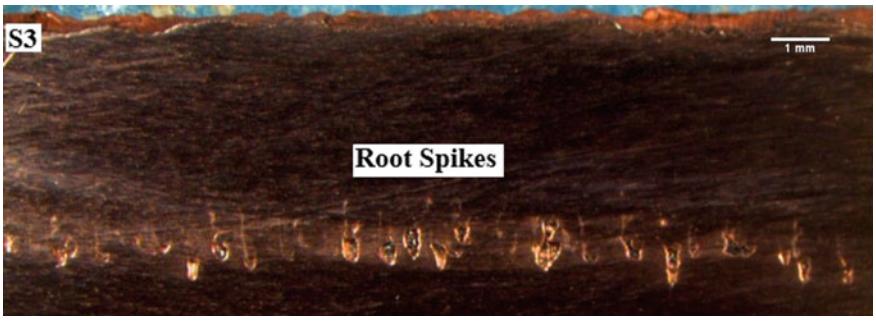

Fig. 3 Root spikes in electron beam welded copper plate (S3)

as represented by the standard deviation of penetration, indicated unstable keyhole, because the spiking phenomena are generated by keyhole-drilling mechanism. This unstable keyhole-drilling mechanism is due to the loss of equilibrium between inside pressure of keyhole and weld-bead load. Although there is the same heat input to all experimental combinations, the varying amplitude is changing the weld area, and more area is available for evaporation of metal. This excessive evaporation creates instability in the keyhole and helps to form spikes and other root defects. In addition to this, the weld schedule with the higher spiking means there is a little excess of penetration, which increased the susceptibility of root pore formation and causes a detrimental effect on the weld joint.

4 Conclusion

Here, the electron beam welding of copper plates was carried out with varying amplitude oscillation to study the spiking formation in the welds. Spiking was measured in terms of the standard deviation of penetration in the study. The following conclusions could be made based on this study.

1. The spiking phenomena were observed in all samples irrespective of beam oscillation parameters. Therefore, it could be said that a proper combination of power, speed and beam oscillation is required to minimize the spiking phenomena in copper weld.
2. An optimized amplitude oscillation is necessary to minimize the spiking. The amplitude of 0.3 mm was seen to produce the highest value of standard deviation, and weld without oscillation had the least value of standard deviation. The smaller value of oscillation amplitude was found to be more suitable for the suppression of spiking in the welding of copper.
3. Keyhole instability was found to be the prime cause of spiking phenomena, which was caused by the increment of weld area with an increase of amplitude. The excessive weld-bead load increased the evaporation pressure and broke the equilibrium of keyhole, which subsequently, broke the natural oscillation of the beam and spikes were generated.

References

1. Jaypuria, S., Meher, J., Kanigalpula, P.K.C., Pratihar, D.K.: Electron beam butt welding of Cu-Cr-Zr alloy plates: experimental investigations, studies on metallurgical and mechanical properties. Fusion Eng. Des. **137**, 209–220 (2018)
2. Wei, P.S., Chuang, K.C., Ku, J.S., DebRoy, T.: Mechanisms of spiking and humping in keyhole welding. In: IEEE transactions on Components, Packaging and Manufacturing Technology, pp. 383–394 (2012)

3. Kanigalpula, P.K.C., Jaypuria, S., Pratihar, D.K., Jha, M.N.: Experimental investigations, input-output modeling, and optimization of spiking phenomenon in electron beam welding of ETP copper plates. Measurement **129**, 302–318 (2018)
4. Tong, H., Geidt, W.H.: A dynamic interpretation of electron beam welding. Weld. J. **49**, 259–266 (1970)
5. Armstrong, R.E.: Control of spiking in partial penetration electron beam welds. Weld. J. **49**(8), 382–388 (1970)
6. Pastor, M., Zhao, H., DebRoy, T.: Pore formation during continuous wave Nd: YAG laser welding of aluminium for automotive applications. Weld. J. Int. **15**(4), 275–281 (2001)
7. Johnson, L.D.: Some observations on the electron beam welding of copper. Weld. J. **49**, 55–60 (1970)
8. O'Brien, T.P., Pence, P.E., Funk, E.R., McMaster, R.C.: Suppression of spiking in partial penetration EB welding with feedback control. Weld. J. **53**(8), 332–338 (1974)

Gas Tungsten Arc Welding of Inconel 825 Sheet: Study on Weld Bead Geometry and GA Optimization

Bishub Choudhury and M. Chandrasekaran

Abstract In this work, gas tungsten arc welding (GTAW) on Inconel 825 is carried out which is a solid solution-based nickel-based alloy known for its excellent corrosion resistance properties and high strength. A Box–Behnken design (BBD) of 27 experimental runs was adopted for this study. Welding current (I), welding speed (V), gas flow rate (GFR) and arc length (N) are selected as process parameters to investigate different weld bead characteristics such as penetration (P), front width (FW) and front height (FH). Statistical models were developed using the RSM approach and model graph analysis is carried out for determining the influence of process parameters on the weld bead geometry. Finally, Genetic Algorithm(GA) is implemented to optimize the weld bead geometry of the welds. Results indicate, with an increase in welding current penetration and front width increases and decreases with an increase in welding speed. Results of GA provides an optimal perimeter combination of $I =$ 120 A, $V = 181$ mm/min, $GFR = 9.2$ l/min and $N = 2.4$ mm, while considering the required penetration as 2.5 mm. Also, the results obtained using the GA approach is found beneficial for the fabrication industry.

Keywords Inconel 825 · GTAW · Weld bead geometry · RSM · GA

1 Introduction

Inconel 825 is a popular nickel-based alloy known for its wide range of applicability, especially in marine and aerospace industries, due to its high strength and high corrosion resistance properties in various environments. Fabrication of this material is difficult due to their higher dynamic shear strength and higher strain hardening tendency [1, 2]; GTAW is a very popular and versatile welding approach which can be used for any kind of material of thickness as high as 15 mm. This process exhibits advantages like high quality and low distortion weld, reduced spatter, minimal finish, etc., which makes it suitable for welding the nickel-based alloys [1, 3].

B. Choudhury · M. Chandrasekaran (✉)
North Eastern Regional Institute of Science and Technology (NERIST) (DU), Nirjuli, Itanagar, Arunachal Pradesh 791109, India
e-mail: mchse1@yahoo.com

L. Li et al. (eds.), *Advances in Materials and Manufacturing Engineering*, Lecture Notes in Mechanical Engineering, https://doi.org/10.1007/978-981-15-1307-7_46

Weld quality is mainly evaluated by weld bead geometry and mechanical properties of a weld. The weld bead geometry is further associated with various quality characteristics such as penetration, front width, front height, back width and back height. Welding optimization is a multi-factor and multi-response technique, which optimizes different responses considering optimum parameters within the factors limit; simultaneous optimization requires appropriate optimization tools [3]. In recent past, many researchers have used various conventional or soft computing-based optimization methods to optimize various welding characteristics. Gunaraj and Murugan [4] have highlighted the use of RSM by designing a four-factor five-level central composite design (CCD) for predicting various weld responses. Datta et al. [5] applied Taguchi-grey approach for optimization of the weld bead. Further, the significant process factors were identified by the analysis of variance method (ANOVA).

Kim et al. [6], used response surface methodology (RSM) and genetic algorithm (GA) for determining GMA welding conditions. First, in a relatively broad region, near-optimal conditions were determined through GA, and then the optimal conditions were determined using RSM approach in a relatively small region. Correia et al. [7] compare these two techniques, i.e. RSM and GA in the optimization of a GMAW welding process. GA can locate optimal condition without generating a specific model unlike RSM approach. Dey et al. [8] adopted regression analysis and GA optimization technique to minimize the weldment area, while satisfying maximum bead penetration. In this proposed work, RSM-GA approach is used to optimize the GTAW process parameters in order to optimize the weld bead geometry of the weld.

2 Experimental Investigations

In this present investigation, 2.5 mm thick Inconel 825 strip of dimension 60 × 25 mm is selected; a square butt joint is selected for investigation of GTAW of Inconel 825. Four welding parameters such as welding current (I), welding speed (V), gas flow rate (GFR) and arc length (N) are selected, as per their significance in weld quality. The working ranges of each parameter were defined by conducting a series of preliminary experiments. The ranges obtained are—welding current: 80–120 A, welding speed: 180–230 mm/min, gas flow rate: 6–12 l/min and arc length: 2–3 mm. Box–Behnken (BBD) experimental design having 27 experimental trials was adopted to carry out the GTAW welding experiments. Figure 1 shows the welding setup used and the welding experiments were conducted as explained by Choudhury and Chandrasekaran [3]. According to the results obtained (refer Table 1), the maximum and minimum values of penetration are observed as 2.69 mm (max) and 1.20 mm (min), respectively. Figure 2 represents the best and the worst specimens in terms of weld bead geometry (WBG).

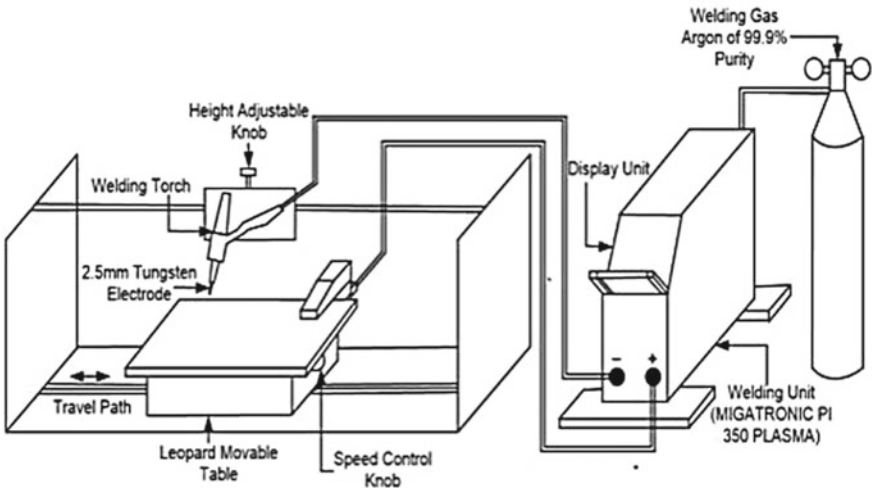

Fig. 1 Welding setup

3 RSM Modelling

Response surface methodology (RSM) is a combination of mathematical and statistical techniques, in which the mathematical models were developed by regression method using the experimental data. Here, the relationship between the dependent variable, i.e. bead geometry and the independent variables, i.e. welding current, welding speed, gas flow rate and arc length is expressed as.

$$Y = f(I, V, \text{GFR}, N) \tag{1}$$

In order to optimize the response Y, a second-order polynomial equation is need to be develop which can be expressed as

$$Y = b_0 + \sum b_i x_i + \sum \cdot \sum b_{ij} x_i x_j + \sum b_{ii} x_{ii}^2 + \xi \tag{2}$$

where b_0 is the constant terms of regression equation, the coefficient b_i is linear terms, b_{ij} is interaction term and b_{ii} is quadratic terms. In this work three RSM models, viz. penetration (P), front height (FH) and front width (FW) were developed using MINITAB 17 software at a confidence level of 95% and are expressed as follows.

$$\begin{aligned} \boldsymbol{P} = {} & -3.8 + 0.1398\, I + 0.0387\, V - 0.358\, \text{GFR} - 2.74\, N - 0.000494\, I * I \\ & - 0.000092\, V^2 + 0.00419\, \text{GFR}^2 + 0.656\, N^2 - 0.000017\, I^2 - 0.00147\, I * \text{GFR} \\ & - 0.00128\, I * N + 0.00096\, V * \text{GFR} - 0.00610\, V * N + 0.0823\, \text{GFR} * N \end{aligned} \tag{3}$$

Table 1 Experimental results

Sl. no.	Process parameters				Experimental results		
	I	*V*	*GFR*	*N*	*P* (mm)	*FW* (mm)	*FH* (mm)
1	100	205	9	2.5	2.25	4.92	0.19
2	80	205	9	3.0	1.97	4.09	0.49
3	100	180	9	2.0	2.48	4.92	0.11
4	100	205	9	2.5	2.25	4.93	0.19
5	100	230	9	3	2.02	4.48	0.26
6	80	205	9	2	2.10	3.53	0.49
7	100	180	9	3	2.54	5.10	0.20
8	120	180	9	2.5	2.52	6.80	0.09
9	100	230	9	2	2.27	5.13	0.30
10	120	230	9	2.5	2.24	5.85	0.50
11	80	205	6	2.5	1.44	4.26	0.59
12	100	205	12	2	2.10	4.77	0.51
13	120	205	6	2.5	2.69	6.37	0.40
14	100	180	6	2.5	2.68	5.91	0.17
15	80	205	12	2.5	1.61	4.39	0.69
16	80	180	9	2.5	1.45	4.51	0.77
17	100	205	9	2.5	2.11	4.10	0.10
18	100	230	6	2.5	2.05	5.17	0.19
19	100	205	6	2	2.59	4.61	0.12
20	100	230	12	2.5	1.96	4.44	0.23
21	100	205	6	3	2.29	5.06	0.22
22	120	205	9	3	2.35	5.97	0.26
23	100	205	12	3	2.28	4.41	0.15
24	120	205	12	2.5	2.51	6.24	0.14
25	120	205	9	2	2.53	6.28	0.23
26	80	230	9	2.5	1.20	3.68	0.41
27	100	180	12	2.5	2.31	5.13	0.18

$$R^2 = 87.65\%, \quad R^2(\text{adj}) = 73.23\%$$

$$\begin{aligned} \boldsymbol{FW} = {} & 11.2 - 0.059\, I - 0.144\, V - 0.103\ \text{GFR} + 8.33\, N + 0.000943\, I^2 \\ & + 0.000435\, V^2 + 0.0251\ \text{GFR}^2 - 0.302\, N^2 - 0.000056\, I * V - 0.00107\, I * \text{GFR} \\ & - 0.0218\, I * N + 0.00018\, V * \text{GFR} - 0.0168\, V * N - 0.134\ \text{GFR} * N \end{aligned} \tag{4}$$

$$R^2 = 93.35\%, \quad R^2(\text{adj}) = 85.59\%$$

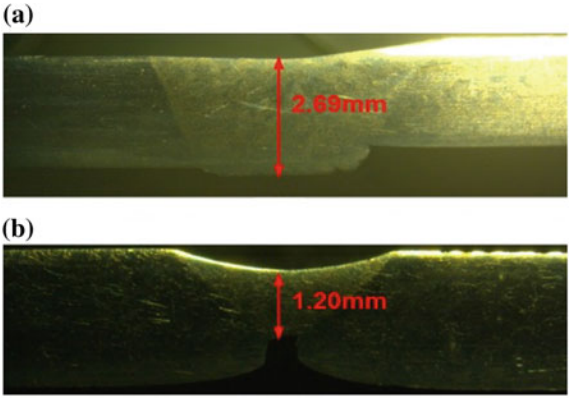

Fig. 2 **a** Best WBG, **b** worst WBG

$$\begin{aligned} FH = {} & 13.10 - 0.2089\, I - 0.0561\, V + 0.379\,\text{GFR} + 1.51\, N + 0.000575\, I^2 \\ & + 0.000039\, V^2 + 0.00350\,\text{GFR}^2 + 0.008\, N * N^2 + 0.000477\, I * V - 0.001521\, I * \text{GFR} \\ & + 0.00060\, I * N + 0.000110\, V * \text{GFR} - 0.00270\, V * N - 0.1262\,\text{GFR} * N \end{aligned} \quad (5)$$

$$R^2 = 91.76\%, \quad R^2(\text{adj}) = 82.14\%$$

4 Results and Discussion

4.1 Model Analysis

Model analysis is carried out by using surface plot representation. These 3D plots are often used to provide a better understanding between process parameters and the responses. Figures 3a–c represent the graphical demonstration between the penetrations (*P*), front width (*FW*) and front height (*FH*) with respect to *I* and *V,* respectively. In first case, it is observed that with an increase in welding current penetration increases and it decreases with an increase in welding speed. This is due to more molten metal with higher welding current which consequently increases the penetration value, while an increase in welding speed reduces the deposition rate.

In second case, front width increases with an increase in welding current and decreases with increase in welding speed. This may due to the more amount of molten metal that leads to larger bead size. In third case, front height decreases with an increase in welding current which may due to the solidification of more molten metal. Again in terms of welding speed, only a minute change is observed for front height.

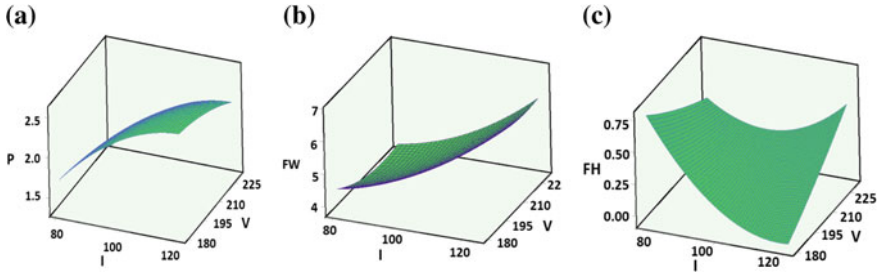

Fig. 3 **a** *P* versus *I* and *V*, **b** *FW* versus *I* and *V*, **c** *FH* versus *I* and *V*

4.2 Optimization Using Genetic Algorithm (GA)

Genetic algorithm (GA) is a popular computerized search and optimization algorithm that resolves many complex nonlinear problems and shows a wide range of its applicability in various fields of application [9]. The objective function of multiple response factors is obtained using weighted combination of all responses. Equation 6 shows the formulated combined objective function to be maximized.

$$\text{Maximize } Y = W_1 P + W_2 \text{FW} + W_3 \text{FH} \tag{6}$$

where P is the penetration which needs to maximize while minimizing the front width (FW) and front height (FH) of the weld bead geometry. The lower bound and upper bound of the current process is as follows, $80 \leq I \leq 120$, $180 \leq V \leq 230$, $6 \leq GFR \leq 12$, $2 \leq N \leq 3$. The optimization was achieved using built-in GA toolbox MATLAB® 9.0. The simultaneous optimization of process performance produces 21 Pareto-optimal fronts as shown in Table 2. The minimum values of FW and FH were found to be equal to 3.84 mm and 0.01 mm, respectively, whereas the maximum value of P is found to be 2.84 mm. If we consider our target penetration value be 2.5 mm, the optimal parametric combination obtained is $I = 120$ A, $V = 181$ mm/min, $GFR = 9.2$ l/min and $N = 2.4$ mm. The predicted response values for *P, FW* and *FH* for the optimal setting is obtained as 2.52 mm, 6.66 mm and 0.03 mm, respectively.

4.3 Industry Needs Based Optimization

The simultaneous optimization of *P*, *FW* and *FH* using genetic algorithm provide 21 optimal solutions known as the Pareto-optimal fronts. In arranging increasing order of *P*, the result will provide optimum combination of process parameters for specific value of *P*. The present work provides optimum parameters the any value of *P* between 1.34 and 2.84 mm. This is an important requirement of fabrication industry rather than obtaining single optimum parameters that optimize either single of more than one response.

Table 2 GA optimization results

Sl. no.	Welding current (I)	Welding speed (V)	Gas flow rate (GFR)	Arc length (N)	Penetration (P)	Front width (FW)	Front height (FH)
1	112	180	6.1	2.8	2.81	7.26	0.23
2	120	180	12	2.4	2.33	6.68	0.08
3	80	187	12	2.0	1.69	4.15	0.99
4	120	181	6	2.9	2.84	7.26	0.27
5	83	185	6.5	2.9	1.92	5.10	0.71
6	120	181	6	2.6	2.79	7.20	0.14
7	118	224	7	2.6	2.28	6.11	0.50
8	80	222	6.6	2.7	1.34	4.24	0.42
9	119	186	8	2.4	2.61	6.58	0.04
10	85	184	6.4	2.9	2.01	5.16	0.65
11	119	223	10.6	2.6	2.18	5.81	0.35
12	119	187	11	2.6	2.40	6.33	0.05
13	80	219	8.3	2.5	1.44	3.96	0.43
14	120	180	7.3	2.4	2.72	6.87	0.01
15	80	218	9	2.2	1.55	3.84	0.49
16	120	186	7	2.6	2.69	6.82	0.12
17	120	181	9.2	2.4	2.52	6.66	0.03
18	80	202	9.2	2.7	1.62	4.10	0.55
19	118	225	10.5	2.6	2.16	5.71	0.34
20	117	230	10.4	2.6	2.11	5.66	0.39
21	84	181	11.5	2.0	1.79	4.35	0.85

5 Conclusion

In this work, the gas tungsten arc welding (GTAW) investigation of Inconel 825 is carried out using Box–Behnken (BBD) experimental design. The influence of weld parameters on weld bead geometry such as penetration (P), front width (FW) and front height (FH) are studied. The developed statistical model using RSM analysis is found accurate enough to predict the weld bead geometry of Inconel 825 weldments. Model graph analysis indicates that an increase in I, P and FW increases and decreases with increase in V. This may due to more amount of molten metal with higher welding current and less deposition rate with higher welding speed.

The parametric optimization using genetic algorithm is carried out for obtaining a penetration of 2.5 mm (full penetration) while minimizing the FH and FW of the weld bead simultaneously. Optimal parametric combination for the same is obtained as $I = 120$ A, $V = 181$ mm/min, $GFR = 9.2$ l/min and $N = 2.4$ mm. Also, the results

obtained during GA is found quite beneficial for the manufacturing industry within the define parameters limits while welding Inconel 825.

Acknowledgements The authors would like to thank the authorities of IIT Guwahati and MSME Tool Room Guwahati for providing the facilities to carry out this work.

References

1. John, N., Dupont, J.C., Lippold, S.D., Kiser.: Welding Metallurgy and Weldability of Nickel Based Alloys. Wiley, Hoboken, NJ (2009)
2. Caron, J.L., Sowards, J.W.: Weldabillity of Nickel Based Alloys, vol. 6. Elsevier Ltd. (2014)
3. Choudhury, B., Chandrasekaran, M.: Study on gas tungsten arc welding characteristics of nickel based aerospace alloys. Mater. Today Proc. **5**, 7337–7345 (2018)
4. Gunaraj, V., Murugan, N.: Application of response surface methodology for predicting weld bead quality in submerged arc welding of pipes. J. Mater. Process. Technol. **1**(88), 266–275 (1999)
5. Datta, S., Bandyopadhya, A., Pal, P.K.: Grey-based Taguchi method for optimization of bead geometry in submerged arc bead-on-plate welding. Int. J. Adv. Manuf. Technol. **39**, 1136–1143 (2008)
6. Kim, D., Rhee, S., Park, H.: Modelling and optimization of a GMA welding process by genetic algorithm and response surface methodology. Int. J. Prod. Res. **40**(7), 1699–1711 (2002)
7. Correia, D.S., Gonçalves, C.V., da Cunha S.S. Jr., Ferraresi, V.A.: Comparison between genetic algorithms and response surface methodology in GMAW welding optimization. J. Mater. Process. Technol. **160**, 70–76 (2005)
8. Dey, V., Pratihar, D.K., Datta, G.L., Jha, M.N., Saha, T.K., Bapat, A.V.: Optimization of bead geometry in electron beam welding using a genetic algorithm. J. Mater. Process. Technol. **209**, 1151–1157 (2009)
9. Whitley, Darrell: A genetic algorithm tutorial. Stat. Comput. **4**, 65–85 (1994)

Stability Study of a Tapered Rotating Sandwich Beam with Asymmetric Configuration and Variable Gradient Under Static Condition

M. Pradhan, P. R. Dash and S. Mohanty

Abstract The stability study of a rotating non-uniform sandwich beam with a variable temperature gradient under static condition is carried out. The sequential steps used to reach the goal are applying extended Hamilton's principle, non-dimensionalizing the equations, selecting shape functions from previous work to model the system mathematically depending on the boundary conditions, and using the Galerkin methodology. The consequence of different parameters on the buckling loads for static condition is studied and presented graphically.

Keywords Rotating sandwich beam · Non-uniformity parameter · Variable temperature gradient · Buckling loads for static condition

Nomenclature

g	Shear parameter
B	Beam width
t	Time
γ_2	Shear strain in the core
$(h_2)_x$	$(h_2)_0\left(2+\frac{x}{l}\left(\frac{(h_1)_0}{(h_2)_0}\right)\alpha_1+\frac{x}{l}\left(\frac{(h_3)_0}{(h_2)_0}\right)\alpha_3\right)$
$E(\xi)$	Variation of modulus of beam elasticity
$\overline{m}$	Mass/unit length of beam
$w(x,t)$	Beam deflection in transverse direction
$\overline{\omega}$	Excitation frequency non-dimensionalized
E_{31}	E_3 / E_1
$T(\xi)$	Distribution of elasticity modulus
δ	Temperature gradient parameter
g^*	$g\,(1+j\eta)$, complex shear parameter
h_{21}	$(h_2)_x/(h_1)_x$

M. Pradhan (✉) · P. R. Dash · S. Mohanty
Department of Mechanical Engineering, VSSUT, Burla 768018, India
e-mail: osme.madhusmita@gmail.com

L. Li et al. (eds.), *Advances in Materials and Manufacturing Engineering*, Lecture Notes in Mechanical Engineering, https://doi.org/10.1007/978-981-15-1307-7_47

$(h_1)_x$	$(h_1)_l\left(1+\frac{x}{l}\alpha_1\right)$
h_{31}	$(h_3)_x \big/ (h_1)_x$
lh_{10}	$l \big/ (h_1)_0$
ρ_i	Density of ith layer
ω	Excitation function frequency
λ_0, λ_1	Rotation parameter
Ω_0	Uniform angular velocity of the beam around z'-axis

1 Introduction

With the aims of achieving superior properties like higher stiffness-to-weight ratio and high-module, sandwich beams (SBs) have been used extensively in recent years in comparison to ordinary beams in applications to engineering structures range from helicopter rotor blades to aircraft panels. SBs are also affected by temperature gradients, so those must be considered when designing the blades of gas and steam turbines. However, varying the cross-sectional configuration of a SB proves to be economical.

In previous work, Carnegie [1] established a theoretical expression for the work done by a cantilever rotating blade. Tomar and Jain [2] evaluated a rotating beam to find the effect of a uniform temperature gradient on it. The effect of temperature on a non-uniform beam vibrating parametrically was studied by Kar and Sujata [3]. Ko [4] reviewed the flexural behavior of a tapered SB by considering uniformly distributed masses. Kar and Sujata [5] studied the dynamic behavior of a rotating SB by changing its boundary conditions. Kar and Ray [6] even analyzed the performances of SBs with different boundary conditions to investigate the instability of the system. Using finite elements, Lin and Chen [7] presented the dynamic stability of a rotating SB. Dash et al. [8] showed that reducing the weight of an asymmetric SB makes the system economical. The analysis of a revolving beam of linearly varying depth with a temperature gradient is studied by Parida and Dash [9]. Pradhan and Dash [10] analyzed the consequence of temperature gradient on a non-uniform SB asymmetric in configuration and revealed that the stability was affected by taper parameter and temperature gradient. Pradhan et al. [11] studied the consequence of a temperature gradient on an asymmetric SB placed on a Pasternak foundation and found that the stability depended on the foundation stiffness and the temperature gradient. The response of viscoelastically supported beams are investigated by Saito and Otomi [12].

The above brief literature survey shows that the effects of a uniform temperature gradient on the system have been considered previously. However, the temperature gradient for a non-uniform beam should be variable rather than constant. Till date, no distinguished work has been done with variable temperature gradients. In the present work, constant and variable temperature gradients are considered for analysis of the system.

Table 1 Different mechanical properties of materials considered

Mechanical properties/materials	Density (kg/m^3)	Ultimate tensile strength (Pa)	Modulus of elasticity (Pa)
ASTM A36 Steel, plate	7.80 g/cc	550 MPa	200 GPa
Cu–Al Alloy CuAl8Fe3	7.85 g/cc	470 MPa	170 GPa
Mechanical properties/materials	Density (kg/m^3)	Ultimate tensile strength (Pa)	Modulus of rigidity (Pa)
Plywood	0.65 g/cc	13.8 MPa	620 GPa

1.1 Materials

In this analysis for the construction of three-layer sandwich beam, the structural steel and copper–aluminum alloy are considered for upper and lower layers, respectively, and plywood is used as viscoelastic middle layer. A suitable adhesive is used to join the layers. The materials considered in the construction of the beam with their different mechanical properties are given in Table 1.

1.2 System Modeling

Figure 1 shows the schematic of a tapered SB of length l rotating with constant angular speed about the vertical axis. The system is acted upon by an axial force $P(t) = P_0 + P_1 \cos(\omega t)$, where P_0 is the maximum static load and P_1 is the maximum magnitude of the dynamic load. At the extreme left-hand end, the thicknesses of the top, middle, and bottom layers are $2h_{1_0}$, $2h_{2_0}$, and $2h_{3_0}$, respectively. The corresponding thicknesses at the extreme right-hand end are $2h_{1_l}$, $2h_{2_l}$, and $2h_{3_l}$ respectively. Neglecting temperature, Young's module of elasticity for the top and bottom layers is E_1 and E_3, respectively. The radial distance of the beam from the

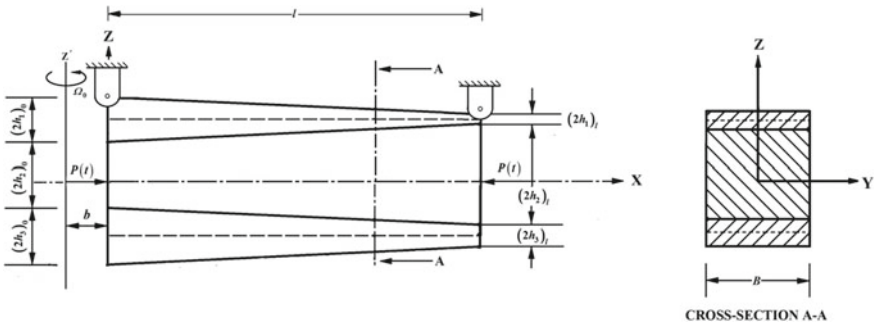

Fig. 1 System modeling

axis about which it rotates is b, which is referred to as the set-off distance. The modulus of rigidity of the core layer is given by $G_2^* = G_2(1 + j\eta)$, which is a complex quantity.

The assumptions underlying the governing equations of motion and the boundary conditions of the physical system are those made by Pradhan and Dash [10]. However, the following two additional assumptions are made herein.

1. The temperature gradient is assumed to obey Fourier's law of heat conduction, with heat transfer along the longitudinal axis of the beam only.
2. Every point in a given cross section is at the same distance from the heat source. It is therefore assumed that the thermal gradient in the transverse direction for the above mentioned cross section is zero.

The respective expressions for strain energy (V) and kinetic energy (T) and work done are as follows:

$$V = \frac{1}{2}\int_0^l E_{1,x}A_{1,x}U_{1,x}^2\mathrm{d}x + \frac{1}{2}\int_0^l E_{3,x}A_{3,x}U_{3,x}^2\mathrm{d}x + \frac{1}{2}\int_0^l \left(E_{1,x}I_{1,x} + E_{3,x}I_{3,x}\right)w_{,xx}^2\mathrm{d}x + \frac{1}{2}G_2^*\int_0^l A_{2,x}\gamma_2^2\mathrm{d}x$$

$$T = \frac{1}{2}\int_0^l \overline{m}w_{,t}^2\mathrm{d}x + \frac{1}{2}\Omega_0^2\int_0^l \left[\overline{m}(b+x)\int_0^x w_{,x}^2\,\mathrm{d}x\right]\mathrm{d}x + \frac{1}{2}\int_0^l \overline{m}\Omega_0^2 w^2\mathrm{d}x$$

and

$$w_p = \frac{1}{2}\int_0^l p(t)w_{,x}^2\,\mathrm{d}x$$

where U_3 and U_1 are the displacements along longitudinal direction in the lower and upper layers, respectively; $w_{,x} = \frac{\partial w}{\partial x}$, $w_{,t} = \frac{\partial w}{\partial t}$, and γ_2 are the strains due to shear in the core and are given by $\gamma_2 = \frac{U_1 - U_3}{2h_2} - \frac{Cw_{,x}}{2h_2}$.

Kerwin's assumption [13] is considered to eliminate U_3.

Applying Hamilton's principle, namely that $\delta\int_{t_1}^{t_2}\left(T - V + w_p\right)\mathrm{d}t = 0$, the subsequent non-dimensional equations of motion are acquired.

$$\overline{mw}_{,\overline{tt}} + \left[1 + \frac{\lambda_0^2\left(1 + E_{31}h_{31}^3\right)}{(lh_{10})^2(1 + E_{31}h_{31})}\left\{\frac{f}{l^2} - \left(\overline{x} + \overline{b}\right)^2\right\}\right]\overline{w}_{,\overline{xxxx}} - \frac{2\lambda_0^2\left(1 + E_{31}h_{31}^3\right)}{(lh_{10})^2(1 + E_{31}h_{31})}\left(\overline{x} + \overline{b}\right)\overline{w}_{,\overline{xxx}} + \left[-\frac{\lambda_0^2\left(1 + E_{31}h_{31}^3\right)}{(lh_{10})^2(1 + E_{31}h_{31})} - \lambda_0^2\left\{\frac{f}{l^2} - \left(\overline{x} + \overline{b}\right)^2\right\} - 3g^*\left(1 + \frac{h_{12} + h_{32}}{2}\right)^2 + \overline{p}(\overline{t})\right]\overline{w}_{,\overline{xx}}$$

$$+\lambda_0^2(\overline{x}+\overline{b})\overline{w}_{,\overline{x}}+\frac{3}{2}g^* l h_{10}h_{12}\left(1+\frac{h_{12}+h_{32}}{2}\right)(1+\alpha)\frac{2(h_2)_0}{C}\gamma_{2,\overline{x}}=0 \tag{1}$$

$$\frac{2(h_2)_0}{C}\gamma_{2,\overline{xx}}-\frac{g^*}{4}h_{12}^2\left(\frac{1+E_{31}h_{31}^3}{1+\alpha^2E_{31}h_{31}}\right)(1+\alpha)$$
$$\times\left[(1+\alpha)\frac{2(h_2)_0}{C}\gamma_2-\left(\frac{2(1+((h_{12}+h_{32})/2))}{(lh_{10}h_{12})}\right)\overline{w}_{,\overline{x}}\right]=0 \tag{2}$$

In the above

$$\overline{w}_{,\overline{xxxx}}=\frac{\partial^4\overline{w}}{\partial\overline{x}^4},\ \overline{w}_{,\overline{xx}}=\frac{\partial^2\overline{w}}{\partial\overline{x}^2},\ \gamma_{2,\overline{xxx}}=\frac{\partial^3\gamma_2}{\partial\overline{x}^3},\ \gamma_{2,\overline{xx}}=\frac{\partial^2\gamma_2}{\partial\overline{x}^2},$$

$$\overline{x}=\frac{x}{l},\overline{U}=\frac{U}{l},\overline{w}=\frac{w}{l},\overline{t}=\frac{t}{t_0},\ C=(h_1)_l+(2h_2)_l+(h_3)_l$$

$$t_0=\left[\frac{\rho_1A_{1_0}l^4}{E_1(I_1)_0}\right]^{\frac{1}{2}},\ \overline{P}_0=\frac{P_0l^2}{E_1(I_1)_0},\ \overline{P}_1=\frac{P_1l^2}{E_1(I_1)_0},\ \overline{P}=\overline{P}_0+\overline{P}_1\cos\left(\overline{w}\overline{t}\right),\overline{\omega}=\omega t_0,$$

$$\lambda_0=\sqrt{\left(\frac{\overline{m}\Omega_0^2l^4}{2(E_1(I_1)_0+E_3(I_3)_0)}\right)}$$

$$\lambda_1=\sqrt{\left(\frac{3\overline{m}\Omega_0^2l^2}{2(E_1(A_1)_0+E_3(A_3)_0)}\right)}$$

The parameters those are cross-sectional dependent are

$$\overline{m}=(1-\overline{x})+\overline{x}\left(\frac{(h_1)_l}{(h_1)_0}\right)\left(\frac{\rho_2}{\rho_1}\right)\left(\frac{(h_2)_0}{(h_1)_0}(1-\overline{x})\left(\frac{\rho_3}{\rho_1}\right)\frac{(h_3)_0}{(h_1)_0}\right)(1-\overline{x})$$
$$+\overline{x}\left(\frac{(h_2)_l}{(h_1)_0}\right)\left(\frac{\rho_2}{\rho_1}\right)+\left(\frac{(h_3)_l}{(h_1)_0}\right)\left(\frac{\rho_3}{\rho_1}\right)\overline{x}$$

$$g*=\frac{G_2^*h_{21}(lh_{10})^2}{E_{1,x}\left(1+E_{31}h_{31}^3\right)}$$

The end conditions those are to be satisfied at the extremes

$$\begin{matrix}\left[1+\frac{\lambda_0^2\left(1+E_{31}h_{31}^3\right)}{(lh_{10})^2(1+E_{31}h_{31})}\left\{\frac{f}{l^2}-\left(\overline{x}+\overline{b}\right)^2\right\}\right]\overline{w}_{,\overline{xxx}}\\ -\frac{2\lambda_0^2\left(1+E_{31}h_{31}^3\right)}{(lh_{10})^2(1+E_{31}h_{31})}\left(\overline{x}+\overline{b}\right)\overline{w}_{,\overline{xx}}=0\end{matrix} \tag{3}$$

Or,

$$\overline{w}_{,\overline{x}}=0 \tag{4}$$

$$\left[\frac{\lambda_0^2\left(1+E_{31}h_{31}^3\right)}{(lh_{10})^2(1+E_{31}h_{31})}-\lambda_0^2\left\{\frac{f}{l^2}-(\overline{x}+\overline{b})^2\right\}-3g^*\left(1+\frac{h_{12}+h_{32}}{2}\right)^2+\overline{p}(\overline{t})\right]\overline{w}_{,\overline{x}}=0 \tag{5}$$

Or,

$$\overline{w}=0 \tag{6}$$

$$\frac{3}{2}g^*lh_{10}h_{12}\left(1+\frac{h_{12}+h_{32}}{2}\right)(1+\alpha)\frac{2(h_2)_0}{C}\gamma_{2,\overline{x}}=0 \tag{7}$$

Or,

$$\gamma_2=0 \tag{8}$$

1.3 Approximate Series of Solution

The above-mentioned Eqs. (1) and (2) are simplified and mentioned as in the

$$\overline{w}(\overline{x},\overline{t})=\sum_{i=1}^{i=p}w_i(\overline{x})f_i(\overline{t}) \tag{9}$$

$$\overline{\gamma}_2(\overline{x},\overline{t})=\sum_{k=p+1}^{k=2p}\gamma_k(\overline{x})f_k(\overline{t}) \tag{10}$$

where w_i and γ_k are the shape functions f_i and f_k are the generalized coordinates, and w_i and γ_k are chosen to satisfy as many boundary conditions as possible [14]. Here as per Ray and Kar [6], the shape functions are chosen accordingly to the different boundary conditions.

For the clamped–pinned case, we have

$w_i(\overline{x})=2(i+2)\overline{x}^{(i+1)}-(4i+6)\overline{x}^{(i+2)}+2(i+1)\overline{x}^{(i+3)}$, $\gamma_{\overline{k}}(\overline{x})=\left(\overline{k}+1\right)\overline{x}^{\overline{k}}-\overline{k}\overline{x}^{(\overline{k}+1)}$, where $\overline{k}=k-p$. Putting the above equations into (1) and (2) and applying the general Galerkin methodology yield the following equations of motion in matrix form in the generalized coordinates.

$$[m]\left\{\ddot{Q}_1\right\}+[k_{11}]\{Q_1\}+[k_{12}]\{Q_2\}=\{0\} \tag{11}$$

$$[k_{21}]\{Q_1\}+[k_{22}]\{Q_2\}=\{0\} \tag{12}$$

where

$$\{Q_1\} = \left\{f_1, \ldots, f_p\right\}^{\mathrm{T}} \tag{13}$$

$$\{Q_2\} = \left\{f_{p+1}, \ldots, f_{2p}\right\}^{\mathrm{T}} \tag{14}$$

$$M_{ij} = \int_0^1 \overline{m} w_i w_j \mathrm{d}\overline{x} \tag{15}$$

$$k_{11ij} = \int_0^1 \left[1 + \lambda_1 \left\{\frac{f}{l^2} - \left(\overline{x} + \overline{b}\right)^2\right\}\right] w_i'' w_j'' \mathrm{d}\overline{x} + \lambda_0^2 \int_0^1 \left\{\frac{f}{l^2} - \left(\overline{x} + \overline{b}\right)^2\right\} w_i' w_j' \mathrm{d}\overline{x}$$
$$+ \int_0^1 \left\{3g^*\left(1 + \frac{h_{12} + h_{32}}{2}\right)^2 - \overline{p}(\overline{t})\right\} w_i' w_j' \mathrm{d}\overline{x} \tag{16}$$

$$k_{12jl} = -\left(\frac{3}{2}\right) \int_0^1 g^* l h_{10} h_{12} (1 + \alpha)\left(1 + \frac{h_{12} + h_{32}}{2}\right)\left(u_l w_i' \mathrm{d}\overline{x}\right) \tag{17}$$

$$k_{22kl} = 3 \int_0^1 (l h_{10})^2 \left\{\frac{\left(1 + \alpha^2 E_{31} h_{31}\right)}{\left(1 + E_{31} h_{31}^3\right)}\right\}\left(u_k' u_l' \mathrm{d}\overline{x}\right) + \frac{3}{4} \int_0^1 g^* (l h_{10})^2 h_{12}^2 (1 + \alpha)^2 (u_k u_l \mathrm{d}\overline{x}) \tag{18}$$

$$[k_{21}] = [k_{12}]^{\mathrm{T}}$$

In the above, $u_k = \frac{2h_2}{C}\gamma_k$, $u_l = \frac{2h_2}{C}\gamma_l$, and $w_i' = \frac{\partial w_i}{\partial x}$.

$f = (l + b)^2$ for, $x = l$, $= b^2$, for $x = 0$, $= \frac{l^2}{3} + b^2 + bl$, for other cases.

Equations (11) and (12) are simplified further to

$$[m]\left\{\ddot{Q}_1\right\} + \left[[k] - \overline{P}_0[H]\right]\{Q_1\} - \overline{P}_1 \cos\left(\overline{\omega t}\right)[H]\{Q_1\} = \{0\} \tag{19}$$

where

$$[k] = \left[\overline{k}\right] - [k_{12}][k_{22}]^{-1}[k_{12}]^{\mathrm{T}} \tag{20}$$

$$H_{ij} = \int_0^1 w_i{}' w_j' \mathrm{d}\overline{x} \tag{21}$$

$$[\overline{k}]_{ij} = \int_0^1 \left[1 + \lambda_1 \left\{\frac{f}{l^2} - \left(\overline{x} + \overline{b}\right)^2\right\}\right] w_i'' w_j'' \mathrm{d}\overline{x} + \lambda_0^2 \int_0^1 \left\{\frac{f}{l^2} - \left(\overline{x} + \overline{b}\right)^2\right\} w_i' w_j' \mathrm{d}\overline{x}$$
$$+ \left\{3g^* \left(1 + \frac{h_{12} + h_{32}}{2}\right)^2\right\} \int_0^1 w_i' w_j' \mathrm{d}\overline{x} \tag{22}$$

1.4 Buckling Loads for Static Condition

Consideration of $\overline{P}_1 = 0$ and $\left\{\ddot{Q}_1\right\} = 0$ in Eq. (19) leads to eigenvalue problem $[k]^{-1}[H]\{Q_1\} = (1/P_0)\{Q_1\}$. The reciprocal of the eigenvalues of $[k]^{-1}[H]$ is considered as the buckling loads for static condition $(P_0)_{\text{crit}}$ for the first few modes.

2 Numerical Results and Discussion

Here a number of graphs are drawn considering uniform and variable temperature gradients with the hub radius, rotation parameter, and taper parameters for their various values. To keep minimum number of figures, some of the results are elaborated without figures. For certain parameter values, when considering a uniform rotating beam without thermal gradient, the equations of motion reduced to those of Kar and Sujata [5] and the results obtained are found to be similar.

Here $\psi = \psi_0(1 - \xi)$ is assumed as the temperature at any point ξ which is above the reference temperature. As per Kar and Sujata [3], the variation of modulus of elasticity of the beam can be written by choosing $\psi = \psi_0$, the temperature at the end $\xi = 1$ as the reference temperature as,

$$\begin{aligned} E(\xi) &= E_1[1 - \lambda\psi_1(1 - \xi)], \quad 0 \le \lambda\psi_1 < 1 \\ &= E_1 T(\xi) \end{aligned}$$

where λ is the coefficient of thermal expansion for the beam material, $\delta = \lambda\psi_1$ is the temperature gradient parameter and $T(\xi) = \left[1 - \delta_\xi(1 - \xi)\right]$, where $\delta_\xi = \left(\frac{A}{A_\xi}\right)\delta$ is the variable temperature gradient parameter. Here, the following is considered:

$$\alpha = \frac{E_{1\xi} A_{1\xi}}{E_{3\xi} A_{3\xi}} = \frac{E_1 T(\xi) A_1}{E_3 T(\xi) A_3} = \frac{E_1 A_1 \left[1 - \delta_{1\xi}(1 - \xi)\right]}{E_3 A_3 \left[1 - \delta_{2\xi}(1 - \xi)\right]},$$

where δ_1 and δ_2 are the temperature gradients in the upper and lower layers, respectively. Unless stated otherwise, the parameter values used are as follows:

$$\eta = 0.01, b = 0.05, g = 0.1, \lambda_0 = 0.05, \lambda_1 = 0.1, \delta_1 = 0.1, \delta_2 = 0.2, \text{ and } P_0 = 0.05.$$

Figure 2 shows the effects of α_1 on the buckling loads for static condition. The buckling loads for static condition decrease with α_1 for all the three modes, thus making the system unstable. As shown in Fig. 3, the buckling load decreases with b in a nonlinear manner. So, this parameter destabilizes the system.

The nature of the graph in Fig. 3 is shown also in Fig. 4, where the destabilization of the system increases with δ_1 because the static buckling load decreases. However, the stability of the system is increasing with increase in δ_2 as the static buckling loads are increasing which is shown in Fig. 5.

But when we analyze considering variable temperature gradient, the consequences are similar as that of constant temperature gradient; however, the static buckling loads further decrease considering variable temperature gradient for top layer, and static buckling loads further increase considering variable temperature gradient for bottom layer as shown in Figs. 6 and 7 respectively.

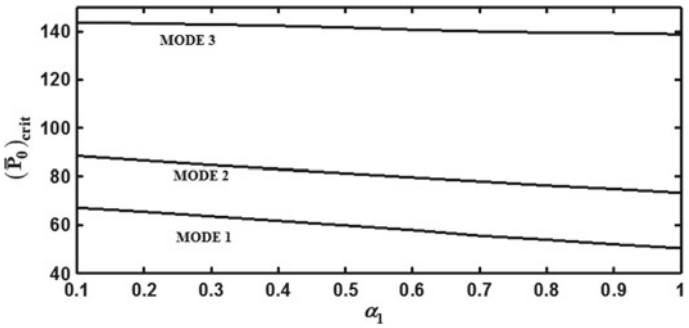

Fig. 2 Dependence of $(\overline{P}_0)_{\text{crit}}$ on α_1

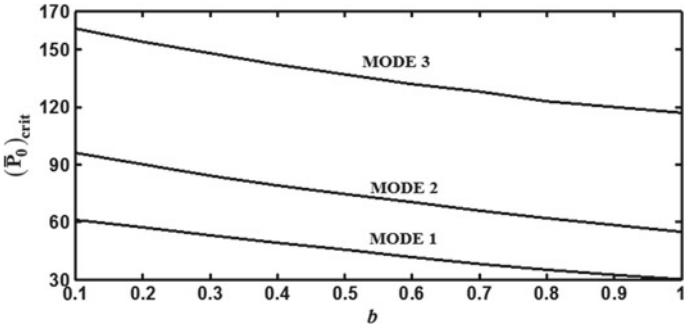

Fig. 3 Dependence of $(\overline{P}_0)_{\text{crit}}$ on b

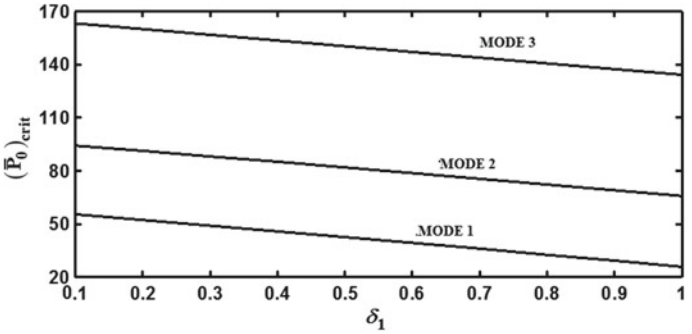

Fig. 4 Dependence of $\left(\overline{P}_0\right)_{\text{crit}}$ on δ_1

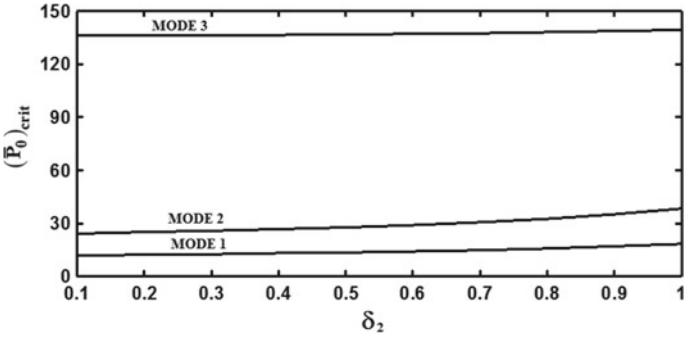

Fig. 5 Dependence of $\left(\overline{P}_0\right)_{\text{crit}}$ on δ_2

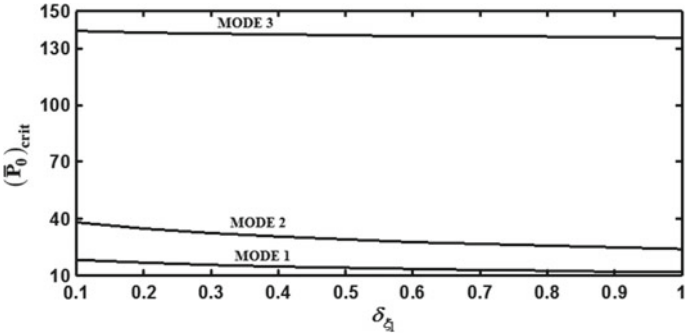

Fig. 6 Dependence of $\left(\overline{P}_0\right)_{\text{crit}}$ on δ_{ξ_1}

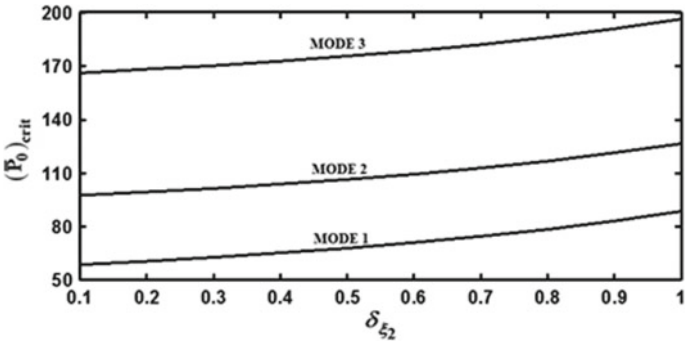

Fig. 7 Dependence of $\left(\overline{P}_0\right)_{\text{crit}}$ on δ_{ξ_2}

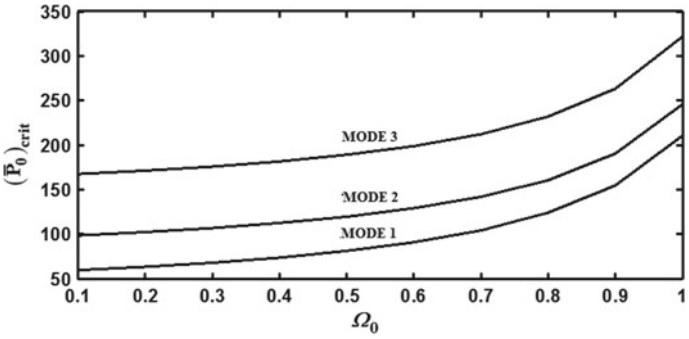

Fig. 8 Dependence of $\left(\overline{P}_0\right)_{\text{crit}}$ on Ω_0

The buckling loads for static condition increase in a nonlinear manner, with increase in the values of Ω_0, which is depicted in Fig. 8, thus increasing the stability of the system.

Stability of the system is found to be dependent upon the magnitudes of δ_1 and δ_2. The stability of the system is dependent upon the magnitudes of δ_{ξ_1} and δ_{ξ_2} and also upon the types of tapering of the top and bottom elastic layers, when variable temperature gradient is taken into consideration.

To minimize the number of graphs, the effects related to α_3 are not shown because they are similar to those of α_1. Furthermore, the buckling loads for static condition are independent of η.

3 Conclusion

Investigations were made for the static stabilities of a linearly tapered asymmetric rotating SB subjected to a pulsating axial load with a variable temperature gradient under clamped–pinned end condition. From the results, it is concluded that the system stability worsens with increase of the hub radius, the taper parameters, and the temperature gradient in the top layer. By contrast, faster rotation and larger temperature gradient in the bottom layer improve the system stability. It is also found that the results vary depending on whether the temperature gradient varies or is uniform. The system stability improves with a larger variable temperature gradient in the bottom layer but degrades with a larger variable temperature gradient in the top layer.

References

1. Carnegie, W.: Vibrations of rotating cantilever blading: theoretical approaches to the frequency problem based on energy methods. J. Mech. Eng. Sci. **1**(3), 235–240 (1959)
2. Tomar, J.S., Jain, R.: Effect of thermal gradient on frequencies of a wedge-shaped rotating beam. AIAA J. **22**(6), 848–850 (1984)
3. Kar, R.C., Sujata, T.: Parametric instability of a non-uniform beam with thermal gradient resting on a Pasternak foundation. Comput. Struct. **29**(4), 591–599 (1988)
4. Ko, C.L.: Flexural behavior of a rotating sandwich tapered beam. AIAA J. **27**(3), 359–369 (1989)
5. Kar, R.C., Sujata, T.: Dynamic stability of a rotating beam with various boundary conditions. Comput. Struct. **40**(3), 753–773 (1991)
6. Ray, K., Kar, R.C.: Parametric instability of a sandwich beam under various boundary conditions. Comput. Struct. **55**(5), 857–870 (1995)
7. Lin, C.Y., Chen, L.W.: Dynamic stability of a rotating beam with a constrained damping layer. J. Sound Vib. **267**(2), 209–225 (2003)
8. Dash, P.R., Maharathi, B.B., Ray, K.: Dynamic stability of an asymmetric sandwich beam resting on a Paternak foundation. J. Aerosp. Sci. Technol. **62**(1), 66 (2010)
9. Parida, R., Dash, P.: Dynamic stability analysis of a circularly tapered rotating beam subjected to axial pulsating load and thermal gradient under various boundary conditions. Int. J. Acoust. Vib. **21**(2), 139–144 (2016)
10. Pradhan, M., Dash, P.R.: Stability of an asymmetric tapered sandwich beam resting on a variable Pasternak foundation subjected to a pulsating axial load with thermal gradient. Compos. Struct. **140**, 816–834 (2016)
11. Pradhan, M., Dash, P.R., Pradhan, P.K.: Static and dynamic stability analysis of an asymmetric sandwich beam resting on a variable Pasternak foundation subjected to thermal gradient. Meccanica **51**(3), 725–739 (2016)
12. Saito, H., Otomi, K.: Parametric response of viscoelastically supported beams. J. Sound Vib. **63**(2), 169–178 (1979)
13. Kerwin, E.M., Jr.: Damping of flexural waves by a constrained viscoelastic layer. J. Acoust. Soc. Am. **31**(7), 952–962 (1959)
14. Leipholz, H.: Stability Theory, 2nd edn. Wiley, Chichestar (1987)

Weld Quality Prediction of PAW by Using PSO Trained RBFNN

Kadivendi Srinivas, Pandu R. Vundavilli and M. Manzoor Hussain

Abstract Selection of process parameters in welding environment is more complex while determining the weld bead quality. For the selection of best parameters, artificial intelligence tools like neural networks blended with stochastic optimization technique like particle swarm optimization (PSO) proved to be very effective. In this paper, an attempt has been made to predict the weld bead quality using neural network trained PSO. Bead on plate experiments was conducted using plasma arc welding on superalloy Inconel material. Multiple regression mathematical equations developed by response surface methodology (RSM) were used for the analysis. The developed methodology will be very useful for automation.

Keywords Particle swarm optimization · Bead on plate trails · Plasma arc welding · Radial basis function neural networks

1 Introduction

Plasma arc welding (PAW) is said to be well-accepted arc welding process due to its high productivity. The welding strength depends on the geometry of the weld bead, material properties, and microstructure. The current study deals with weld bead geometry analysis of plasma arc welded Inconel 617 superalloy plates, which is reliant on several input process parameters such as welding current, voltage, speed of weld, plasma and shielding gas flow rates, torch standoff distance, torch angles, and others. At the same time, costly materials like superalloy Inconel 617 found

K. Srinivas (✉)
Department of Mechanical Engineering, DVR and Dr. HS MIC College of Technology, Kanchikacherla, AP 521180, India
e-mail: kadivendi@gmail.com

P. R. Vundavilli
School of Mechanical Sciences, Indian Institute of Technology Bhubaneswar, Odisha 751013, India

M. Manzoor Hussain
Department of Mechanical Engineering, Jawaharlal Nehru Technological University, Hyderabad, Telangana 500085, India

L. Li et al. (eds.), *Advances in Materials and Manufacturing Engineering*, Lecture Notes in Mechanical Engineering, https://doi.org/10.1007/978-981-15-1307-7_48

more number of applications in high-temperature gas reactors and nuclear fuel power plants and aerospace. Bead on plate experimentation found to be cost-effective to provide information about the weld bead dimensions with less material wastage before proceeding to the butt joints. So, automation of the process is very essential to study the effect of process parameters on weld bead geometry, which reflects the weld quality. Therefore, modeling of input–output relations, optimization of process parameters, becomes important aspect in welding automation.

Garg et al. [1] used PSO technique to train artificial neural network (ANN) for prediction of flank wear in drilling in response to four input parameters namely drill diameter, feed rate, spindle speed, and spindle motor current. Later, they concluded that this technique gives better prediction results compared to the backpropagation neural networks (BPNN). Dhas et al. [2] developed models to predict the submerged arc weld (SMAW) quality applying genetic algorithm based on neural network (NNGA) and neural network-based particle swarm optimization (NNPSO) techniques. Finally, they reported that NNPSO has advantage when compared with other developed models in terms of computational time and accuracy. Ahmed et al. [3] employed two different artificial intelligence technique (AIT)-based models namely multilayer perceptron NN and RBFNN and recommended that RBFNN is powerful tool for analysis and modeling of prediction of weld bead geometry in shielded metal arc welding. Anand et al. [4] performed experimentation on Incoloy 800H using friction stir welding. Later, they developed BBPNN, IBPNN, GANN, QPNN, LMNN models and found that GANN is performing better than other. Cheruku et al. [5] used PSO-based clustering approach along with DBI index as fitness function for medical datasets. Later, they found from the results that PSO-RBFNN is more accurate when compared to conventional neural network classifiers. Srinivas et al. [6] developed regression models from conducting experiments on experimentation on PAW. Further, they developed BPNN and RBFNN models and concluded that results of RBFNN model prediction are closer to experimental values with more accuracy. Hu et al. [7] applied PSO-RBFNN algorithm for prediction of regional logistics demand. In their work, they concluded that PSO-RBFNN overcomes its own drawbacks and achieves much better prediction and optimization results. Malviya et al. [8] investigated the weld bead quality of MIG welding by collecting data from the design of experiments. Further, they used PSO to tune various neural networks in both forward and reverse directions. Later, they compared percentage deviation in prediction of different parameters by PSO-tuned MLFFNN and RBFNN, respectively. Praga-Alejo et al. [9] developed GA-based RBFNN for laser penetrated welding process. In that work, they stated that this model performs better for predicting the responses in welding. Shanmukhi et al. [10] performed modeling of multi-input–multi-output electro-discharge machining processes using RBFNN. They implemented batch mode of training for developed RBFNN using GA and PSO. In that work, they depicted that PSO-RBFNN performs better compared to GA-RBFNN. Datta et al. [11] developed MLFNN, RBFNN, counter propagation neural networks to carry forward and reverse mapping of MIG welding process. They found in their work that optimization tool GA performs better compared to BPA. Ai et al. [12] have done laser welding of dissimilar metals and used GA-RBFNN for process modeling and parametric optimization.

Finally, they concluded that the experimental results of weld seam geometry are in good agreement with the optimal weld seam. Zhou et al. [13] performed experimentation on multiaxis ball-end milling on Inconel 718 material and for optimization gray relation analysis coupled with RBFNN and GA. They found that a considerable increment in the gray relation grades after using PSO optimization.

From the extensive literature survey, it is observed that many of the researchers are using neural network techniques extensively in the modeling and GA-PSO as optimization tools for process optimization. Researchers are also coupling GA and PSO technique with neural networks and obtaining reasonably good results. In this work, an attempt is made to determine the optimal weld bead parameters for plasma arc welding of Inconel 617 using PSO-RBFNN approach.

2 Methodology

2.1 Experimental Procedure

In the current work, Inconel 617 superalloy sheets of 2 mm thick are used for the base material and melt in mode plasma arc welding is performed on it. In order to find the range of process parameters for full-depth penetration, pilot experiments are carried out initially. The weld speed (N), weld current (I), and plasma gas flow rate (G) are taken as the process parameters. A weld speed range of 250–300 mm/min, weld current range of 80–105 A, and gas flow rate range of 2–2.5 L/min are considered for the experimentation.

In the design of experiments, central composite design (CCD) method is considered for the conduction of experiments. The welded plates are cut along the cross section by using wire cut EDM. The cut sections of weld bead are mounted on specimen mounting machine and etching is performed. These specimens are used to find the bead dimensions namely front width (FW), back width (BW), front depth (FD), and back depth, (BD) respectively. The measured data is feed into Minitab to investigate and to find the multiple regression equations.

2.2 Problem Statement

Radial basis function neural network has excellent ability to estimate any nonlinear mapping. RBFNN has better fitting capability and higher prediction accuracy and gives noise-free data. The convergence rate of RBFNN is faster than other neural networks compared to BPNN. On the other hand, stochastic optimization technique like particle swarm optimization technique (PSO) falls into the local optimum values instead of global optimum and its convergent rate is also low. To overcome the drawbacks of PSO and RBFNN combining, these two approaches may yield better

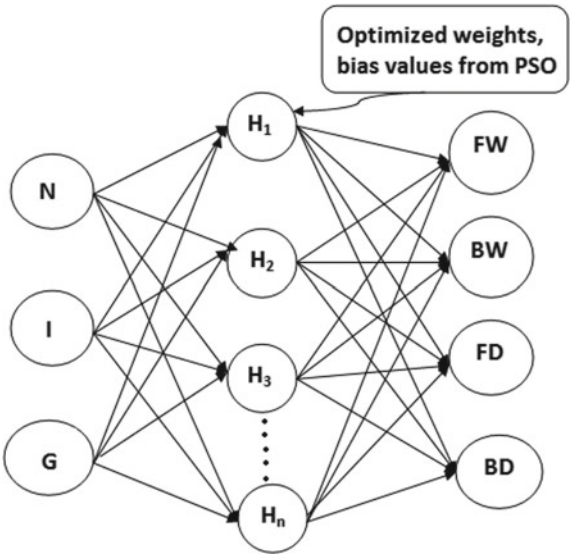

Fig. 1 Physical model of PSO-RBFNN network

results [7]. In this paper, PSO algorithm is used to optimize the weights and threshold values of RBFNN. The architecture of the PSO-RBFNN model shown in Fig. 1.

2.3 Modeling and Optimization Methods

Radial Basis Function Neural Network

The three layers of the RBNNN are input, hidden, and output layers. The input of three neurons considered as weld speed (N), weld current (I), and plasma gas flow rate (G). The output layers of the network consist of four neurons namely FW, BW, FD, and BD. A systematic study was performed to determine the number of hidden neurons. In the training period, normalized input data feeds into the network by generating 1000 cases along with 20 experimental test cases. Transfer functions of the neural network always play key role in the prediction of the network performance. The following are the transfer functions considered for the input, hidden, and output layers.

$$\begin{array}{lll} \text{Input layer:} & \text{Linear} & y{=}x \\ \text{Hidden layer:} & \text{Gaussian} & y = e\left(-||x-\mu||^2/2\sigma^2\right) \\ \text{Output layer:} & \text{Log}-\text{sigmoid} & y{=}\ 1/1{+}e^{-\mathrm{a}}1^x \end{array}$$

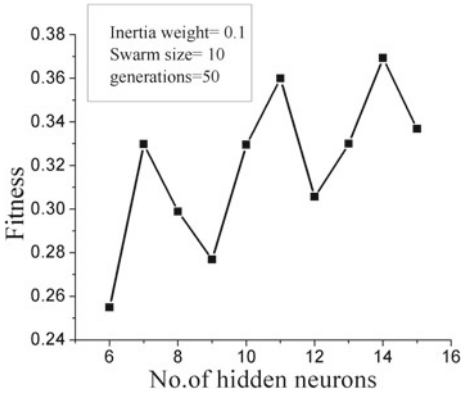

Fig. 2 PSO parametric study for number of neurons versus best fitness

Particle Swarm Optimization

To determine the number of hidden neurons in the neural network, study has been conducted. Number of hidden layers varied systematically to determine the best fitness value and the graph obtained shown in Fig. 2. For this study, the swarm size, inertia weight and number of generations are kept equal to 0.1, 10, and 50, respectively. Further, parametric study is carried out to evaluate the optimal parameters of the PSO.

3 Results and Discussion

The multiple regression equations representing the front width, back width, front depth, and back depth of weld bead are given in Eqs. (1), (2), (3), and (4), respectively.

$$\begin{aligned} \text{FW} &= 12.4 + 0.443\,I - 0.0304\,N - 20.73\,G \\ &\quad - 0.001516\,I*I + 0.000157\,N*N + 5.73\,G*G \\ &\quad - 0.000320\,I*N - 0.0112\,I*G - 0.01520\,N*G \end{aligned} \tag{1}$$

$$\begin{aligned} \text{BW} &= -16.8 - 0.651\,I + 0.051\,N + 35.1\,G + 0.005873\,I*I \\ &\quad + 0.000260\,N*N - 5.88\,G*G - 0.001360\,I*N \\ &\quad + 0.0280\,I*G - 0.0384\,N*G \end{aligned} \tag{2}$$

$$\begin{aligned} \text{FD} &= 7.12 - 0.114\,I - 0.0899\,N + 9.18\,G + 0.001847\,I*I \\ &\quad + 0.000206\,N*N - 2.34\,G*G - 0.000556\,I*N \\ &\quad - 0.0148\,I*G + 0.00900\,N*G \end{aligned} \tag{3}$$

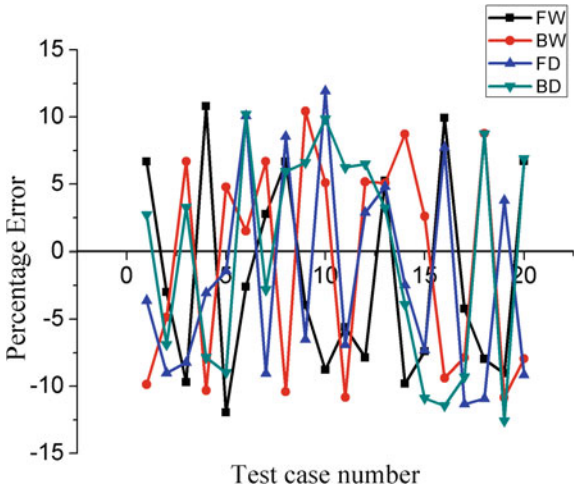

Fig. 3 Percentage error of responses in PSP-RBFNN approach

$$\begin{aligned} \text{BD} = {} & 15.0 - 0.076\, I - 0.1355\, N + 5.27\, G + 0.001137\, I * I \\ & + 0.000348\, N * N - 1.08\, G * G - 0.000472\, I * N \\ & + 0.0208\, I * G - 0.00760\, N * G \end{aligned} \tag{4}$$

The above multiple equations are used to train the neural network by generating more data. After training the neural network with the PSO-RBFNN model, the model predicted values are recorded for the 20 experimental cases to know the accuracy of prediction. This is done by writing a test program in MATLAB environment. The percentage error deviation obtained for responses are {−9.708, 10.79}, {−10.84, 10.42}, {−11.34, 11.92} and {−11.44, 10.19} for FW, BW, FD, and BD, respectively. The percentage error graphs of all the responses shown in Fig. 3.

4 Conclusions

Neural network-based approach PSO-RBFNN is developed to model the input–output relations and weld bead quality prediction for plasma arc welded Inconel 617 superalloy bead on plate experimentation. Huge data generated with multiple regression equations is used to train the established neural network model. From the study, it is observed that PSO-RBFNN has accessible to RBFNN for better level of adaptableness. Therefore, it is right choice for searching the optimal solutions in welding and its bead quality prediction. And also, PSO execution is simple and flexible. The average error prediction of the responses is also reasonably in accepted level.

References

1. Garg, S., Patra, K., Pal, S.K.: Particle swarm optimization of a neural network model in a machining process. Sadhana **39**(3), 533–548 (2014)
2. Dhas, J.E., Kumanan, S., Jesuthanam, C.P.: Prediction of weld quality using intelligent decision making tools. Artif. Intell. Res. **1**(2), 131–148 (2012)
3. Ahmed, A.N., Noor, C.M., Allawi, M.F., El-Shafie, A.: RBF-NN-based model for prediction of weld bead geometry in Shielded Metal Arc Welding (SMAW). Neural Comput. Appl. **29**(3), 889–899 (2018)
4. Anand, K., Barik, B.K., Tamilmannan, K., Sathiya, P.: Artificial neural network modeling studies to predict the friction welding process parameters of Incoloy 800H joints. Eng. Sci. Technol. Int. J. **18**(3), 394–407 (2015)
5. Cheruku, R., Edla, D.R., Kuppili, V., Dharavath, R.: PSO-RBFNN: a PSO-based clustering approach for RBFNN design to classify disease data. In: International Conference on Artificial Neural Networks, pp. 411–419. Springer, Cham (2017)
6. Srinivas, K., Vundavilli, P.R., Hussain, M.M., Saiteja, M.: Prediction of welded joint strength in plasma arc welding: a comparative study using back-propagation and radial basis neural networks. IOP Conf. Ser. Mater. Sci. Eng. IOP Publ. **149**(1), 012033 (2016)
7. Hu, Z., Zhang, Y., Yao, L.: Radial basis function neural network with particle swarm optimization algorithms for regional logistics demand prediction. In: Discrete Dynamics in Nature and Society (2014)
8. Malviya, R., Pratihar, D.K.: Tuning of neural networks using particle swarm optimization to model MIG welding process. Swarm Evol. Comput. **1**(4), 223–235 (2011)
9. Praga-Alejo, R.J., Torres-Treviño, L.M., González, D.S., Acevedo-Dávila, J., Cepeda, F.: A radial basis function redesigned for predicting a welding process. In: Mexican International Conference on Artificial Intelligence, pp. 257–268. Springer, Berlin, Heidelberg(2010)
10. Shanmukhi, K., Vundavilli, P.R., Surekha, B.: Modeling of ECDM micro-drilling process using GA-and PSO-trained radial basis function neural network. Soft. Comput. **19**(8), 2193–2202 (2015)
11. Datta, S., Deepanshu, Pratihar D.K.: Modelling of input-output relationships of metal inert gas welding process using soft computing-based approaches. Int. J. Comput. Intell. Stud. **6**(1), 1–28 (2017)
12. Ai, Y., Shao, X., Jiang, P., Li, P., Liu, Y., Yue, C.: Process modeling and parameter optimization using radial basis function neural network and genetic algorithm for laser welding of dissimilar materials. Appl. Phys. A **121**(2), 555–569 (2015)
13. Zhou, J., Ren, J., Yao, C.: Multi-objective optimization of multi-axis ball-end milling Inconel 718 via grey relational analysis coupled with RBF neural network and PSO algorithm. Measurement **102**, 271–285 (2017)

Static Loading Analysis of Connecting Rod Used in Four-Wheeler (SUV) by FEA

Atul Singh Rajput and Mohammad Hamza

Abstract Connecting rod is a significant element in internal combustion engine. The main tenacity of a connecting rod is transmission of the reciprocating motion of the piston to the rotary motion of the crankshaft. There are dissimilar materials and production methods are used to manufacture a connecting rod. Connecting rods are commonly composed of steel alloy or aluminum alloy or titanium alloy and it is usually manufactured by drop forging process. This article explains the finite element analysis of connecting rod. In the present work, connecting rod is made of materials forged 4340 AISI Steel, TiAl4V Titanium alloy and 7075 Aluminum alloy for sport utility vehicles (SUV) were compared on the basis of total deformation, Von Mises stress, and Von Mises strain. A two-dimensional drawing is prepared from the calculations. A parametric model of connecting rod is modeled using SOLID WORKS 16.0 software. Analysis is carried out by using ANSYS workbench 16.0 software. The best combinations of parameters like Von Mises stress and strain, deformation, etc. for four-wheeler connecting rod were done in ANSYS workbench16.0 and finally, results are compared with different material.

Keywords ANSYS · Connecting rod · Finite element · SUV · Static loading

1 Introduction

The internal combustion engine is a crank-slider mechanism, where the piston is the slider in this case. The piston is stimulated up and down by the rotary motion of crankshaft in its four strokes specifically suction, compression, expansion or power, and exhaust stroke. The piston is placed within a combustion compartment. This force changes the connecting rod, crankshaft over a distance, which transforms chemical energy into required mechanical energy [1].

A. S. Rajput · M. Hamza (✉)
National Institute of Technical Teachers Training and Research, Kolkata 700106, India
e-mail: md.hamza@hotmail.com

A. S. Rajput
e-mail: singhatul55@gmail.com

L. Li et al. (eds.), *Advances in Materials and Manufacturing Engineering*, Lecture Notes in Mechanical Engineering, https://doi.org/10.1007/978-981-15-1307-7_49

The piston and the crankshaft are intermediately connected with the connecting rod. Minor part of the connecting rod is linked to the piston and big end to the crankshaft. It joins the piston with the gudgeon pin [2]. The purpose of the connecting rod is to transform piston's linear motion into crankshaft's rotary motion. Force is applied to connecting rod generated by gas pressure and the interior force of the interchanging body [3].

Finite element analysis transacts with structural analysis with many parameters which modifies its working and explains the better result to eliminate the difficulties connected with it. The calculation of stresses and strains is done in FEA through structural analysis, by applying the structural model in ANSYS16.0. The structural analysis is implemented to form a higher and a lower stress zone from the given data of the material, boundary condition, forces.

2 Theoretical Calculations of Connecting Rod

A connecting rod is an internal combustion engine supporter which is engaged to exchange the compressive forces and force of tensile. The connecting rod is supposed to be same at both ends hinged for buckling around x-axis and as so on both ends are set for buckling around y-axis. Through x-axis and y-axis, the connecting rod should be evenly tough for buckling [4].

A = cross-sectional area.
l = length.
σ_c = compressive yield stress.
F = crippling load.
I_{xx} and I_{yy} = moment of inertia (MI) around x-axis and y-axis, respectively.
K_{xx} and K_{yy} = gyration radius around x-axis and y-axis, respectively.

Rankine's–Gordon formula,

$$F \text{ about } x\text{-axis} = \frac{\sigma_c A}{1 + a\left[\frac{l}{K_{xx}}\right]^2}$$

2.1 Pressure Calculation for 2000 cc Engine

Medium size SUV specifications of engine type air-cooled four-stroke
Stroke × Bore (mm) = 84.0 × 89.9 = 7551.6 mm^2 Displacement = 1,993 CC
Maximum power = 280 hp (209 kW)@5,200 rpm maximum torque = 415 Nm@rpm
Ratio of compression = 9.6:1 Petrol C8H18's density = 737.21 kg/m^3
Mass = Density × Volume = 737.22E−9 × 1993E−3 = 1.469 kg

Temperature = 550 K Petrol's molecular weight = 114.228 g/mole Now, from the gas equations,

$$P = \frac{(1.469 \times 72.86 \times 550)}{1993} == 29.54 \text{ MPa}$$

2.2 Design Calculation of 7075 Al Alloy

Flange thickness and section web = t, section width = $4t$

Section height, $H = 4 \times t$, section area, $A = 2(4 \times t \times t) + (3 \times t \times t) = 11t^2$ (Fig. 1)

$$\frac{I_{XX}}{I_{YY}} = 3.2 \quad \text{Now, } K_{XX} = \sqrt{\frac{I_{XX}}{A}} = \sqrt{\frac{34.91t^4}{11t^2}} = 1.78t$$

Connecting rod length (L) = 2 × stroke = 2 × 89.9 = 179.8 mm

The maximum gas force,

$$P_{\text{gas}} = 163{,}703.86 \text{ N}$$

Now, Rankine's–Gordon formula [5],

$$F = P_{\text{sa}} \times \text{Factor of Safety} = 163{,}703.86 \times 1.5 = 245.555.80 \text{ N}, \ \sigma_{\text{c}} = 503 \text{ MPa}$$

$$\text{Rankine Constant, } a = \frac{\sigma_{\text{c}}}{\Pi^2 E} = \frac{503}{\Pi^2 \times 0.7170 \times 10^5} = 0.00071, \ t = 8.9 \approx 9 \text{ mm}$$

Now, Flange thickness and section web = t = 9 mm

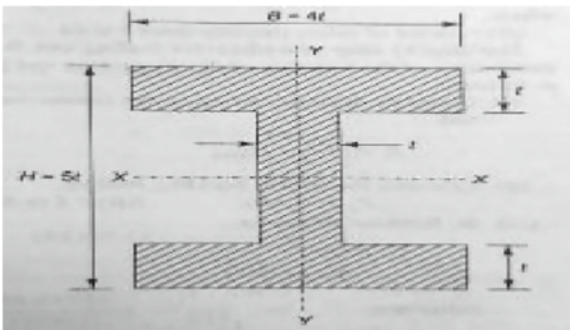

Fig. 1 In section standard dimension

Section width, $B = 4 \times t = 4 \times 9 = 36$ mm, section height $H = 5 \times t = 5 \times 9 = 40$ mm,
Section area, $A = 2(4 \times t \times t) + 3 \times t \times t = 11t^2 = 891$ mm^2
Crank end height $= H \times 2 = 1.1 \times H = 44$ mm, piston end height $= 0.8 \times H = 32$ mm.

2.3 Design Calculation of Forged 4340AISI Steel

Now, similarly, Flange thickness and section web $= t = 9.5$ mm
Section width, $B = 4 \times t = 4 \times 9.5 = 38$ mm, height, $H = 5 \times t = 5 \times 9.5 = 47.5$ mm
Sectional area, $A = 2 \times (4 \times t \times t) + 3 \times t \times t = 11 \times t^2 = 992.75$ mm^2
Crank end height $= H \times 2 = 1.1 \times H = 52.25$ mm, piston end height $= 0.8 \times H = 38$ mm.

2.4 Design Calculation of TiAl 4V

Now, Flange thickness and section web $(t) = 4.8$ mm, $B = 4 \times t = 4 \times 9.5 = 19.2$ mm
$H = 5 \times t = 5 \times 9.5 = 24$ mm, $A = 2(4 \times t \times t) + 3 \times t \times t = 253.44$ mm^2
Crank end height $= H \times 2 = 1.1 \times H = 26.4$ mm, piston end height $= 0.8 \times H = 19.2$ mm.

3 Material Properties

The different materials used for the connecting rod are Forged 4340AISI Steel, 7075 Al Alloy, and TiAl 4V. The required mechanical properties for analysis of all the materials used for connecting rod are shown in Table 1.

4 Results and Discussions

For the analysis of connecting rod 24,556 N, force is applied as per the numerical results obtained in the design calculations at small end keeping big end of connecting rod fixed.

Table 1 Material properties

Parameters material	Elastic modulus (GPa)	Ultimate tensile strength (MPa)	Yield compressive strength (MPa)	Poisson's ratio	Density (kg/m^3)
Forged 4340AISI steel	205	710	698	0.29	7850
7075Al alloy	71.7	503	501	0.33	2810
TiAl 4V	113.8	890	880	0.34	4430

4.1 Analysis for Material Forged 4340AISI Steel

The total deformation of connecting rod after applied force of 24,556 N is shown in Fig. 2. Small end of connecting rod will show the maximum deformation, and there will be no deformation at the bigger end of connecting rod as it is fixed. The maximum deformation of 0.102 mm will occur at small end.

From Fig. 3, the numerical estimated values of maximum and minimum Von Mises strain occurring at small and big end of connecting rod during static analysis

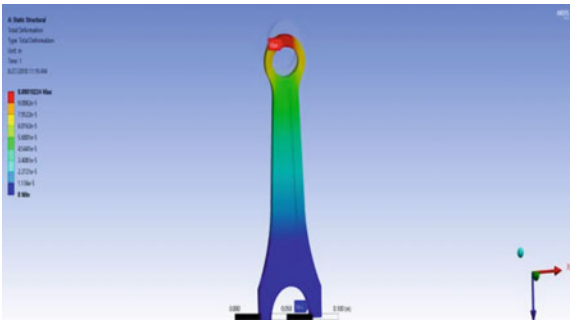

Fig. 2 Total deformation of forged 4340AISI steel connecting rod

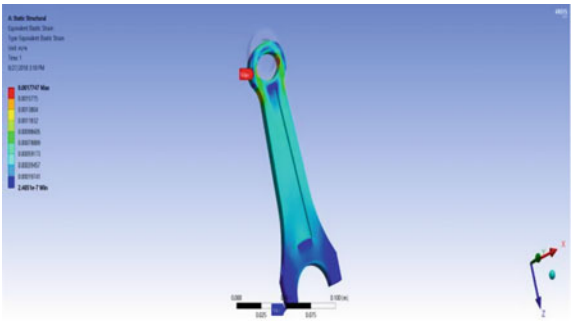

Fig. 3 Von Mises strain of forged 4340AISI steel connecting rod

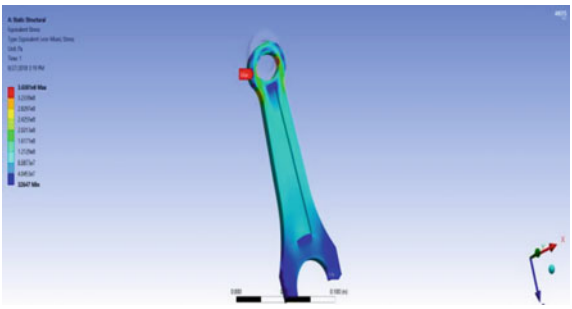

Fig. 4 Von mises stress of forged 4340AISI steel connecting rod

Table 2 Comparison of results

Sr. no.	Type forged	7075 Al alloy	TiAl 4V	4340AISI steel
1	Total deformation (mm)	0.102	0.292	0.184
2	Equivalent strain	1.777e−3	5.079e−3	3.201e−3
3	Equivalent stress (Pa)	3.638e8	3.642e8	3.643e8
4	Weight (kg)	0.365	0.130	0.206
5	Stiffness (MN/m)	240.745	84.095	133.456

for force of 24,556 N is 0.00177 and 2.485e−7, respectively. Von Mises strain regions are very correctly distinguished in the figure of the present connecting rod model.

From Fig. 4, it is observed that maximum stress occurs at small end of the connecting rod after applying force of 24,556 N and minimum amount of stress is developed at big end of connecting rod which is fixed.

5 Comparison of Results

For current study, force of 24,556 N is used for analysis of three different materials of connecting rod. The parameters found out by ANSYS workbench 16.0 are tabulated in Table 2.

6 Graphs

Finite element analysis of connecting rod under static loading condition has been done by ANSYS workbench 16.0 for the force of 24,556 N. The results obtained for different materials of connecting rod are plotted in the below graphs in Fig. 5.

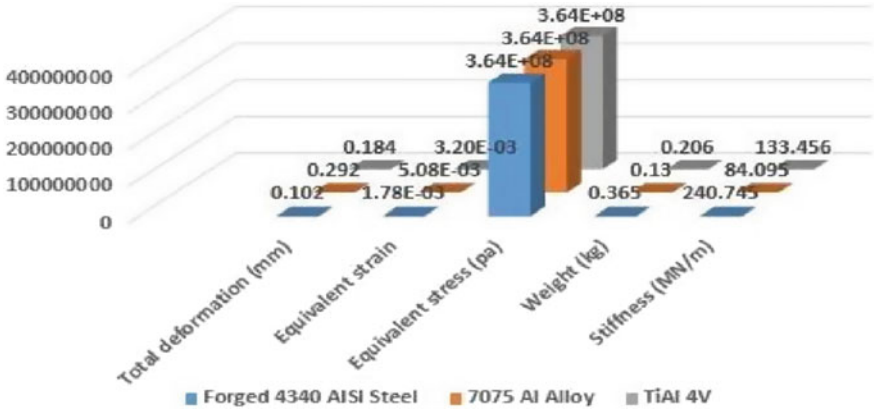

Fig. 5 Graph of total deformation for different specimens

7 Conclusions

- By evaluating the outcomes of FORGED 4340AISI STEEL, 7075 AL ALLOY, and TIAL 4V used for connecting rod analysis, it is found that equivalent Von Mises stress for all the materials is approximately the same.
- From the static analysis of the connecting rod, the stress is found maximum at the small end.
- Relating the atypical consequences found from the investigation of connecting rod, it is concluded that the deformation of FORGED 4340AISI STEEL is less than the 7075 AL ALLOY, so FORGED 4340AISI STEEL can be exercised for manufacturing of connecting rod for extended permanency.

References

1. Om, P., et al.: Optimizing the design of connecting rod under static and fatigue loading. Int. J. Res. Manage., Sci. Technol. (IJRMST) **1**, 3456–3459 (2013)
2. VG, V., LK, V.: Analysis of connecting rod using forged steel. Int. J. Sci. Eng. Res. Des. (IJSERD) **4**, 678–683 (2013)
3. Serag, S., Sevien, L.: Optimal Design of the Connecting Rod in Modelling, Simulation and Control, vol. 24, pp. 49–63. AMSE Press (1989)
4. Yoo, Y.M., Haug, E.J., Choi, K.K.: Shape optimal design of an engine connecting rod. J. Mech. Trans. Autom. Des. Trans. ASME **106**, 415–419 (1984)
5. Sarihan, V., Song, J.: Optimization of the wrist pin end of an automobile engine connecting rod with an interference fit. J. Mech. Des. Trans. ASME Press **112**, 406–412 (1990)

Design and Implementation of Product Embodied Riser for Energy Conservation in an Aluminum Casting Process

K. Prabhuram, V. Subrammaniyan and M. Thenarasu

Abstract Traditionally in the foundry industrial practices, after the casting process is done, the runner and the riser are removed and reused to manufacture new components by re-melting them. This paper suggests an idea to design the riser in order to form a by-product of a desired shape on solidification so that the energy spent on re-melting these riser components is cut down. In this method, the solid riser obtained after solidification of the casting is used as a raw material or a semi-finished product and subjected to other processes without forming further cast products by re-melting it. The casting method adopted to experimentally verify the claim is green sand mold casting method to cast a cuboid pattern of cast aluminum grade LM4. A simple geometry of a cylinder of diameter 35 mm was chosen as the riser geometry and the mold was designed to house the actual product of a cuboid and the by-product as the cylinder. The results of this experiment confirm that 23.54% of energy conservation is achieved by the implementation of this method. The last section of this paper provides insights on the environmental impact of this method when adopted and applied to the foundry industries on a global scale. Since this method brings down the energy requirements of the casting industries, it highly benefits the industry in both economic and environmental aspects. This validates the need for innovation in the designing of newer manufacturing concepts to end up beneficial to the world.

Keywords Optimal riser design · Energy conservation · Metal casting · Product embodied risers · Carbon footprint

1 Introduction

Metal casting is the basic manufacturing process for about 90% of the manufactured metal products in the world [1]. Risers are one of the basic components of a sand casting process. Risers are used to reduce defects due to shrinkage and other factors. Once the casting is solidified, the risers are removed to be subjected to re-melting

K. Prabhuram · V. Subrammaniyan · M. Thenarasu (✉)
Department of Mechanical Engineering, Amrita School of Engineering, Amrita Vishwa Vidyapeetham, Coimbatore, India
e-mail: m_thenarasu@cb.amrita.edu

L. Li et al. (eds.), *Advances in Materials and Manufacturing Engineering*, Lecture Notes in Mechanical Engineering, https://doi.org/10.1007/978-981-15-1307-7_50

leading to an increase in energy consumption. In order to cut down the gratuitous wastage of energy, the riser can be designed in a way such that a near-product is embodied in the dimensions of it. Such progressive ideas to conserve energy are indispensable for making foundries to be environmentally and economically beneficial.

Generally, the riser volume is optimized to conserve energy in the process of casting, thereby improving the yield therefore decreasing the energy wasted. Morthland et al. [2] improved the energy conservation in the process of casting by minimizing the gate size and the volume of the riser, while ensuring that the product is without defect. Tavakoli et al. have done topology optimization on the riser by using finite element analysis and other numerical computing methods such as SIMP method to incorporate nonlinear unsteady heat transfer during casting [3]. The application of certain concepts to result in optimal design is essential. One such technique was proposed to make use of parabolic metal flow concept in the design of top risers to reduce microporocities [4]. Mathew et al. (2016) have worked on a method to recover the dissipating heat from the solidifying casting by using shots of three different metals, namely aluminum, copper, and steel. On comparison, copper shots have given better results when used to preheat the raw materials [5]. Energy audits are an effective way to monitor the energy consumption in a foundry. The importance of periodic energy audits is highlighted by Prashanth et al. [6]. A case study conducted in the foundry industries of Scandinavian countries by Patrik et al. shows that more than half of the foundries lack energy strategy and others' energy strategies are primarily financially motivated [7].

2 Methodology

The method chosen for this experiment is green sand casting method.

2.1 Riser Design

Some of the possibilities for the shape of the riser for sand casting processes are shown in Fig. 1. Factors to be considered while designing the risers are [8],

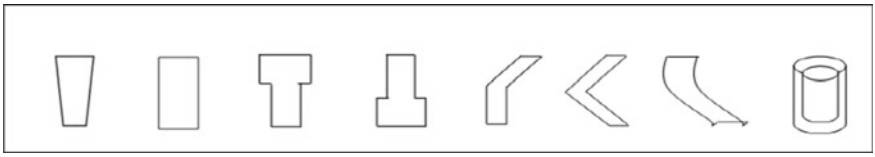

Fig. 1 Various shapes of risers

- Risers serve as the reserve for the molten metal as the molten metal solidifies. The molten metal from the riser fills the cavity during shrinkage of the product.
- Machining allowances.
- Risers prevent porosity due to non-uniform solidification as it has high head.

Thus, the actual dimension of the risers should be greater than the dimension required. A 35 mm cylindrical pattern is chosen as the riser geometry.

2.2 Mold Making and Metal Pouring

A cubical block of length 75 mm, width 75 mm, and height 50 mm was chosen as the pattern. Molding green sand was prepared by an appropriate sequence of mixing quartz, clay, charcoal powder, water, and other additives [9]. The molding sand was placed around the pattern and compacted to form the mold. The top gate riser system was made in the cope. The sectional view of the mold and cylindrical riser is shown in Fig. 2. The material chosen for this study is cast aluminum LM4 because the riser is to be obtained as a by-product of this process. This by-product will be subjected to other processes such as machining along with the main product. Thus, the selection of a metal with better machinability is essential. Aluminum LM4 being intermediately machinable is a fairly better choice [10]. The raw material was melted in an electrical furnace to about 1000 K and poured into the mold prepared. K-type thermocouples were placed near the riser and the mold cavity to observe the temperature change [11] of the molten metal during solidification [12].

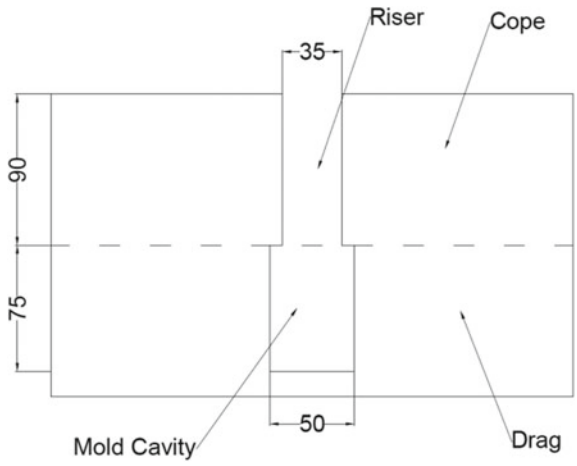

Fig. 2 Cut section of mold cavity

3 Results and Discussion

The obtained product after the solidification of the molten metal is shown in Fig. 3. The temperature change was recorded from the thermocouple, and a temperature–time graph (Fig. 4) is plotted for both the products in the mold cavity and the cylindrical riser component. This cooling is governed by the transient diffusion heat Eq. (1).

$$K\left(\frac{\partial^2 T}{\partial x^2}+\frac{\partial^2 T}{\partial y^2}+\frac{\partial^2 T}{\partial z^2}\right)=\frac{\partial q}{\partial t} \tag{1}$$

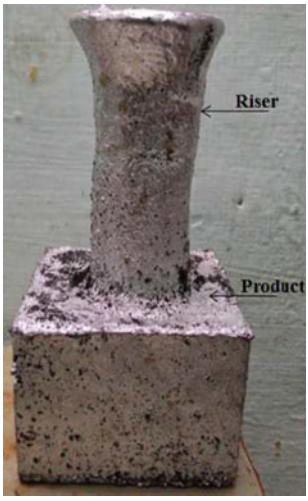

Fig. 3 Cast product

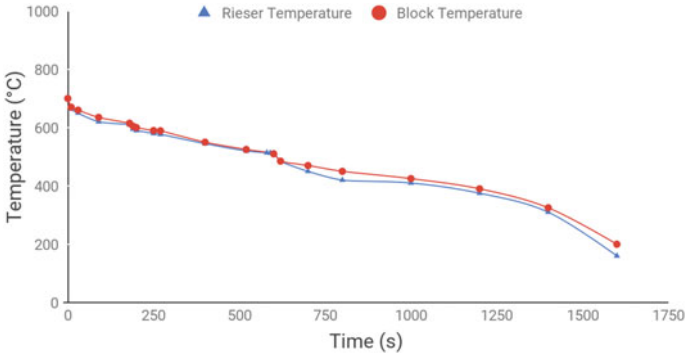

Fig. 4 Rate of cooling of the riser and the block

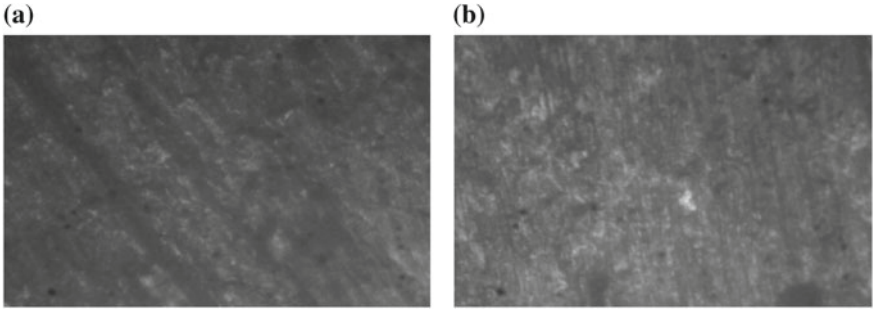

Fig. 5 **a** Riser micro-structure, **b** block micro-structure

where heat flux (2),

$$q = \int \rho c \, \mathrm{d}T \tag{2}$$

T is the temperature, and K is the thermal conductivity of LM4. Using chvorinov's rule, the calculation of the estimated time taken for the thorough solidification of the product is done. After the product is thoroughly solidified, the riser is detached from the product. From Fig. 4, it is observed that there is no significant deviation between cooling paths of the riser and the product. That implies that their cooling rates differ very insignificantly. Since there is very less difference between the cooling rates, the mechanical properties of the actual product and the by-product do not differ to a considerable extent. This proves that this method can be used to obtain by-product with similar mechanical properties of the actual product.

The values of the Brinell hardness test of the block are 87, 102, and 94, and the values of riser are 95, 89, and 105. From the values, it is inferred that the mechanical properties do not vary to a considerable extent. The micro-structures of the riser and the block are compared (Fig. 5). This proves that there is only a lesser possibility of change in the metallurgical properties of the obtained products.

3.1 Estimated Energy Savings and Impact on the Environment

The required energy to melt the metal is 1809 kJ. It is calculated from the power input to the furnace. The properties of aluminum LM4 are given in Table 1.

The specific energy consumption of the metal is calculated to be 1775.4 kJ.

In order to calculate the energy that will be consumed by the top gate riser when it is subjected to re-melting, the ratio of their volumes is used (3).

Volume of cylindrical riser obtained $= 8.659 \times 10^{-5}$ m^3.
Ratio of the cylinder to the total volume, $R = 23.54\%$.

Table 1 Properties of chosen aluminum LM4

Density ρ	Specific heat capacity c	Volume V	Molten mass $\rho \times V$
2770 kg/m^3	0.91 kJ/kg K	3.6784×10^{-4} m^3	1.019 kg

$$\begin{aligned} \text{Energy that can be saved} &= \text{specific energy consumption} \times R \\ &= 417.93 \text{ kJ} \end{aligned} \tag{3}$$

$$\text{Energy savings} = \frac{417.93}{1775.4} \times 100 = 23.54\% \tag{4}$$

Data shows that the melting of metal during a casting process consumes a major part of the input energy (Fig. 6). Thus, by modeling the riser in order to obtain a by-product, about 23.54% of the energy that is spent on re-melting can be saved during the casting process.

This method is very beneficial when applied on a global scale. This exact method cannot be generalized to all the sand castings produced in the world as the size and dimensions of the components vary. However, the impact of this method on the environmental and the economic benefits is validated. Figure 7 gives the consumption by source of energy. It can be clearly seen that most of the energy sources of foundries are high emitters of carbon dioxide. By application of the method, not only carbon dioxide emissions are brought down, but also the overhead costs encountered by the company due to electricity and fuel consumption are also reduced. This drop in the expenses of an industry is very compelling for the foundries that have financially motivated energy strategies.

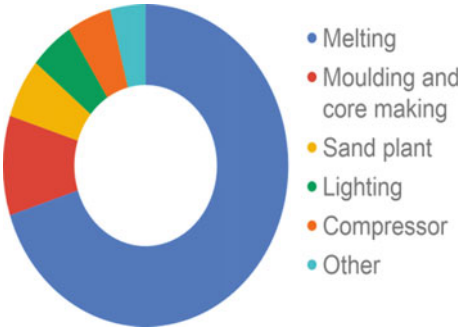

Fig. 6 Consumption of energy by various processes in casting [13]

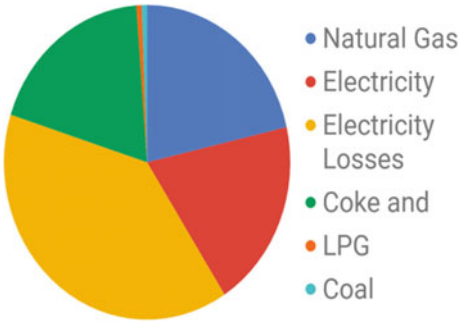

Fig. 7 Energy sources for melting [1]

4 Conclusion

From the experiment, the possibility of the design of product embodied risers and the importance of their implementation for energy conservation and economic benefits for the foundry industry have been validated. In the above-chosen example, the cylindrical portion attached to the cube is obtained only by casting. The cylindrical component can be further rolled or extruded and joined by welding which is less energy-consuming. The cooling rate of the riser is comparatively higher because of the higher area-to-volume ratio. For the material properties of aluminum to change considerably, the cooling rate of the casting should be about 375 K/min [14]. But the present cooling rates fluctuate only between 10 and 20 K. Hence, material properties and the micro-structure remain unchanged. This method can be applied to few other processes such as manufacturing tapered components. Most of the available energy conservation and efficiency strategies are financially not attractive and require more investment to have the industry running at higher energy efficiency. However, this method will turn out to be very attractive for most of the foundry industries because the by-product of the actual process is also valuable equally in the market with a reduced expense of energy costs due to manufacturing.

References

1. U.S. Department of Energy Office of Industrial Technologies: Energy and Environmental Profile of the U.S. Metalcasting Industry https://www.energy.gov/sites/prod/files/2013/11/f4/profile_0.pdf (1999). last accessed 11 Jan 2019
2. Morthland, T.E., Byrne, P.E., Tortorelli, D.A., Dantzig, J.A.: Optimal riser design for metal castings. Metall. Mater. Trans. **26**(4), 871–885 (1995)
3. Tavakoli, R., Davami, P.: Optimal riser design in sand casting process by topology optimization with SIMP method I: poisson approximation of nonlinear heat transfer equation. Struct. Multi. Optim. **36**(2), 193–202 (2008)
4. Laxminarayana, P., Chennakesava Reddy, A.: Design of top risers using parabolic metal flow concept during solidification. In: National Conference on Advanced Materials and Manufacturing Techniques (2004)

5. Mathew, M.M., Thenarasu, M., Aravind, G., Selvaraj, J.: Performance comparison for aluminium, copper and steel shots in waste heat recovery and scrap preheating from solidifying molten metal (2006)
6. Prashanth, M.S., Eshwar, R., Patel, V.K., Selvaraj, J., Rohit, R., Rahul, R., Menon, G.K.: A multi faceted approach to energy conservation in foundries. Procedia Eng. **97**, 1815–1824 (2014)
7. Thollander, P., Backlund, S., Trianni, A., Cagno, E.: Beyond barriers–a case study on driving forces for improved energy efficiency in the foundry industries in Finland, France, Germany, Italy, Poland, Spain, and Sweden. Appl. Energy **111**, 636–643 (2013)
8. Kalpakjian, S., Vijai Sekar, K.S., Schmid, S.R.: Manufacturing Engineering and Technology, 7th edn. Pearson (2014)
9. Srinivasan, K., Siddharth, C.S.K., Arun Kaarthic, L.V., Thenarasu, M.: Evaluation of mechanical properties, economic and environmental benefits of partially replacing silica sand with biomass ash for aluminium casting. Mater. Today Proc. **5**(5), 12984–12992 (2018)
10. Aluminium Gutters & Rainwater Pipe Fittings, Hall and Botterill. https://www.gutter.co.uk/ (2014)
11. Sun, H.-C., Chao, L.-S.: An investigation into the effective heat transfer coefficient in the casting of aluminum in a green-sand mold. Mater. Trans. **50**(6), 1396–1403 (2009)
12. Sui, D.-S., Cui, Z.-S..: Regularized determination of interfacial heat transfer coefficient during ZL102 solidification process. Trans. Nonferrous Met. Soc. China **18**(2), 399–404 (2008)
13. Arasu, M., Rogers Jeffrey, L.: Energy consumption studies in cast iron foundries. In: Transactions of 57th Indian Foundry Congress, Kolkata, India (2009)
14. Milkereit, B., Kessler, O., Schick, C.: Determination of critical cooling rate for hardening aluminum alloys using HyperDSC. In: Application Note-Differential Scanning Calorimetry application (2010)

Reliability, Availability and Maintainability Analysis for Transportation Vehicles—A Case Study in APSRTC

E. Govindarajulu and S. Sai Rakesh

Abstract Performance of a system depends on the reliability of its subsystems if any, the maintenance efficiency, and the operating conditions. Failures are more frequent if the size and complexity of the systems increase and the effect of these failures on system performance is critical. Therefore, reliability and maintainability analysis is required to identify the bottlenecks in system for designed reliability and maintainability. In this paper, a methodology has been presented and is applied on road transportation vehicles in Andhra Pradesh State Road Transport Corporation (APSRTC) as a case study. The best fit for time between failures (TBF) of subsystems is identified with Anderson–Darling (A–D) values and the respective parameters are calculated. Also, availabilities are estimated for all types of vehicles and bottlenecks are identified. This method will help to identify the optimal maintenance intervals for each subsystem as well as the system.

Keywords Reliability · Availability · Maintainability · Time between failures · Time to repair · Road transport passenger vehicles

1 Introduction

Since the failure of any system cannot be prevented completely, it is important to minimize its probability of occurrence and its impact if they do occur [1]. Most of the complex mechanical systems consist of many subsystems. The performance of this system is mostly affected by reliability, availability, and maintainability of its subsystems/components.

Reliability analysis is used as a tool for the planning and operation of these systems. Reliability analysis will help to identify the critical and sensitive subsystems that have a major effect on system failure. Therefore, a focus on reliability is necessary

E. Govindarajulu (✉) · S. Sai Rakesh
Vignan Foundation for Science, Technology and Research, Guntur, India
e-mail: govind305@gmail.com

S. Sai Rakesh
e-mail: sairakesh102@gmail.com

L. Li et al. (eds.), *Advances in Materials and Manufacturing Engineering*, Lecture Notes in Mechanical Engineering, https://doi.org/10.1007/978-981-15-1307-7_51

for the improvement of equipment performance and to ensure the equipment's availability for the operation. Reliability and pattern of failures of a system/component may be affected by external factors like operating conditions, environmental stress, and the experience of the operator. Reliability analysis of such system is required to get realistic information from the operating environment. To maintain the designed reliability and availability characteristics and to achieve the expected performance, an effective maintenance plan is required.

Maintainability analysis is to determine the conditions under which the maintenance or repairs are to be accomplished. There are two basic categories of maintenance are there, one is scheduled (or preventative) maintenance and the other is forced (or corrective) maintenance. Scheduled maintenance is performed at constant time intervals even if the system is working satisfactorily. Such maintenance will prolong the life of components, decrease the number of failures, and increase the MTTF of the system. Corrective maintenance follows in-service failures. As soon as the failure occurs, replacement, adjustment, or repair of a component is done to bring back the system to normal operating state [2]. These maintenance actions are called maintenance plan for a system. The first guideline for maintenance plane will be given by the manufacturer. This will then be optimized depending upon the failure rates, working conditions, desired performance levels, etc. To this end and to develop an optimal maintenance/inspection plan, learning about the existing maintenance procedures of equipment and the statistical analysis of field data is essential.

In this paper, we described a problem that has not addressed well in the literature is that the reliability and maintainability analysis of road transport passenger vehicles with operational data from maintenance sheds.

The next is data collection, sorting, and classification as per standards. Then the assumption validation i.e., the independent and identically distributed (i.i.d) nature of TBF and TTR. For this common methods used are trend test to detect the pattern of failure and serial correlation test for the dependency of multiple repairable systems are explained [3]. The Anderson–Darling test is used for the identification of the best-fit distribution for both TBF and TTR if the assumption is valid. If the assumption is not valid, then it may not be appropriate to do reliability analysis with statistical techniques; therefore, a non-stationary model such as non-homogeneous Poisson process (NHPP) must be fitted. The approach for fitting an NHPP to non-stationary data is different from the techniques involved in fitting a distribution function to i.i.d. A functional form that has been most commonly applied to repairable systems is the NHPP model based on the power-law process [4].

2 Data Collection, Analysis, and Results

Case study: Road transport passenger vehicles used to haul's passenger was considered as the case study. Any vehicle, either gas or diesel, can be described as a highly complex machine with different main and subsystems that have to interact in such a way that it has to perform in accordance with its design parameters. It can then fulfill

its primary function of hauling predetermined calculated maximum loads at certain calculated running times [5].

For a vehicle to be in the state of availability means that it is not out of operation due to preventive maintenance or inoperable due to a failure. Availability depends not only on maintenance downtimes but also on the probability of the vehicle's failure to perform its functions (unreliability effect). The stochastic nature of road transport passenger vehicle breakdowns and the corrective maintenance is to fix them are problems to keep track of the availability of the road transport passenger vehicle. If more road transport passenger vehicles are withdrawn from a fleet due to failure, the fleet operator cannot provide the required transportation capacity to cover the scheduled services. From the analysis of the operation data obtained from APSRTC., a sample of TVG (ordinary passenger vehicle/bus), collected in the year 2017–18, it follows that about 25% of all the failures found in TVG are related to transmission problems and brake problems (27%). To enhance the availability of the fleet, there is a need to identify the bottlenecks in transportation vehicles.

2.1 Data Collection and Sorting

Reliability and maintainability analysis of road transport passenger vehicles is based on the realistic data of operation and maintenance collected on sixty passenger vehicles. The data are collected from actual maintenance shed of APSRTC. The operation and maintenance of buses in various conditions were observed, which provides the reliable and extensive information necessary for availability analysis.

To analysis the data for availability characteristics of a system, the basic steps must be performed are data collection from maintenance records of maintenance shed, sorting, and classification (i.e., TBF, TTR, TTF, frequency of failure, total uptime, total downtime, total maintenance hours, etc.) of data, which is shown in Table 1.

After sorting and classification of the data, the next is to identify the most frequent occurrences using Pareto chart for the failures system as shown in Fig. 1.

Similarly, for all types of vehicles, data have been collected and sorted as per standard format and (i.e., TBF, TTR, TTF, frequency of failure, total uptime, total downtime, total maintenance hours, etc.) are shown in Fig. 2.

2.2 Analysis of TBF and TTR Data

If the data are independent identically distributed (i.i.d), then the data are analyzed to determine the characteristics of failure time and repair time distributions of each subsystem of vehicles to estimate the availability. For this, the best-fit probability distributions are used. To identify the best-fit distribution for the given failure and repair data of each subsystem, the maximum likelihood estimation method with

Table 1 Failure, repair, and logistic delay time of TVG vehicles

Vehicle number	Repair time (h) TTR	Logistic delay (h)	TBF (h)	Total time (h)
2742 TVG BS3	5.10	1.00	570.30	576.40
5937 TVG BS2	3.00	0.15	975.15	978.30
712 TVG	0.30	0.30	2340.30	2340.90
35 TVG	3.00	0.30	3426.00	3429.30
T21 TVG	1.00	0.30	3573.00	3574.30
191 TVG	19.00	2.00	5372.00	5393.00
79 TVG	3.00	2.00	6439.00	6444.00
805 TVG	1.00	1.00	6831.00	6833.00
35 TVG	6.00	2.30	7321.30	7329.60
712 TVG	2.00	2.00	516.00	520.00
4908 TVG	19.00	5.00	2859.00	2883.00
5937 TVG	6.00	1.00	5506.00	5513.00
5939 TVG	8.00	3.00	5820.00	5831.00
6005 TVG	2.00	1.00	5815.00	5818.00
0072 TVG	7.30	0.30	7085.30	7092.90
5942 TVG	1.00	2.00	5084.00	5087.00
344 MTVG	1.50	0.40	4986.00	4987.90
Total	88.20	24.05	74,519.35	74,631.60

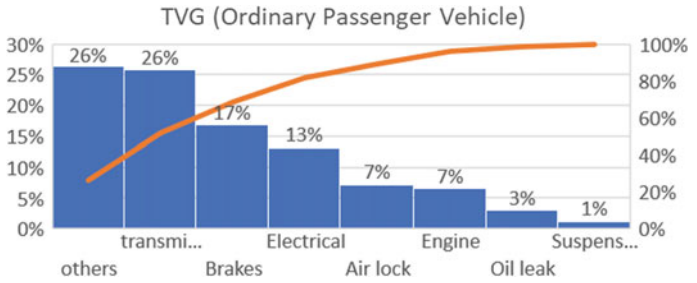

Fig. 1 Pareto chart for TVG vehicle

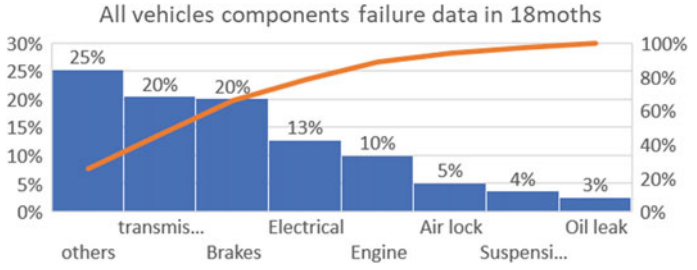

Fig. 2 Pareto chart for all vehicles

Anderson–Darling (A–D) goodness-of-fit test is used. A lower value indicates that the distribution fits the data better.

2.3 Availability Analysis

Availability is an important metric used to assess the performance of repairable systems and includes both the aspects of reliability and maintainability of a component or system. Classification of availability based on the types of downtimes used for computation can be found in many regular textbooks such as in [5]. Inherent availability (A_{Inh}) is defined as the steady state availability when only CM time of the system is considered and achieved availability (A_{ach}) considers only active maintenance time. On the other hand, operational availability $\left(A_{\text{op}}\right)$ considers the total down time. This can also be termed as posterior availability based on actual events that happened to the system when it had been in operation.

$$A_{\text{ach}} = \frac{\text{MTBF}}{\text{CM time} + \text{PM time} + \text{MTBF}} \tag{1}$$

$$A_{\text{Inh}} = \frac{\text{MTBF}}{\text{CM time} + \text{MTBF}} \tag{2}$$

Based on the above definitions, availabilities of each vehicle/fleet are estimated. Reference source not found. and (1). In these definitions, CM time reflects the efficiency and speed of the maintenance personnel, as well as their expertise and training level. PM is to prolong or to mitigate failures of a component or system. But the total downtime includes CM, PM, and logistic delay times.

Inherent and achieved availabilities are calculated for different types of buses and are shown in Table 2.

From the data available in Table 1, the MTBF of the system is 4570.98 h, and the MTTR is 4.92303 h.

Therefore, inherent availability (A_{Inh}) of TVG vehicle is 4570.98/(4570.98 + 4.92303) = 99.88%.

Table 2 Vehicle class and its availability

Type of bus	Achieved availability (%)	Inherent availability (%)
TVG	97.40	99.88
SML	99.20	99.86
UD	95.00	99.91
SL	96.30	99.77
EXP	81.60	99.97

For getting achieved availability, PM's downtime is required and are calculated by using major repair time and minor repair time of the components, i.e., 82 major repairs occurred and each repair will be completed in 2 h, and similarly, 85 minor repairs occurred and each repair will complete in 1 h. To complete these major and minor repairs, the total downtime required is 290 h per 15 vehicles. Preventive maintenance (PM) time for a vehicle is 102.352 h. Similarly, corrective maintenance downtime = 4.923 h. Therefore,

$$\begin{aligned}\text{achieved availability } (A_{\text{ach}}) &= 4570.98/(4570.98 + 4.92303 + 102.352)\\ &= 97.40\%\end{aligned}$$

Similarly, the achieved availabilities of all other types of buses are calculated and shown in Table 2.

3 Conclusion

This paper presents a methodology for the identification of appropriate model for system having multiple repairable units. This paper discusses different scenarios for analyzing multiple repairable units, based on trend, intensity. The framework presented in the paper enables to identify the critical subsystems that are failure frequent and having the weaknesses in maintenance activities. The presented methodology was verified for the on-road transport passenger heavy vehicles as case study. It is found that the transmission and braking systems are the bottlenecks in transportation vehicles. Availabilities are estimated for each subsystem with the i.i.d failure and maintenance data. The results of the analysis can be used to develop an optimal inspection/maintenance schedule for subsystems and for the entire system.

References

1. Blischke, W.R., Murthy, D.N.P.: Case studies in reliability and maintenance. In: Blischke, W.R., Prabhakar Murthy, D.N. (eds.) Wiley Series in Probability and Statistics. Wiley, Hoboken, NJ (2003)
2. Ramakumar, R.: Engineering Reliability: Fundamentals and Applications. Prentice Hall (1993)
3. Louit, D.M., Pascual, R., Jardine, A.K.S.: A practical procedure for the selection of time-to-failure models based on the assessment of trends in maintenance data. Reliab. Eng. Syst. Saf. **94**, 1618–1628 (2009)
4. Dibakoane, K.C.: Challenges Affecting the Reliability of Diesel Locomotives within the South African Railway Industry. University of Johannesburg (2013)
5. Elsayed, E.A.: Reliability Engineering. Wiley (2012)

A Novel Approach for Utilization of Walnut Shell Ash as Reinforcement in Aluminum Matrix Composites

Parasa Yugandhar Babu, Phani Kumar Jogi, K. Ramakanth and P. Ravindra Babu

Abstract This paper aims to propose a solid waste management technique through a novel utilization of the agro solid waste in production of the industrially required materials. In this paper, Walnut Shell Ash (WSA) in two different percentages of 2 and 4% has been used as reinforcement in Aluminum-6061 matrix to fabricate composites through stir casting technique. The composites casted are tested for density, hardness, microhardness, and sliding wear properties. Captivatingly casted composites have shown a great improvement in all aspects, reduction in density with an increase in reinforcement, and increase in hardness and resistance to wear with an increase in % of reinforcement; this is because of the formation of an efficient bonding between reinforcement and the matrix material. This paper also presents the effect of aging on the composite's hardness and found that aging has increased the hardness of the materials.

Keywords Walnut shell ash · Stir casting · Microhardness · Sliding wear

1 Introduction

Aluminum matrix composites have been extensively studied as an attractive choice for more industries because of their interesting properties like high strength to weight ratio, stiffness, and wear resistance than that of the alloy. Though this composite has many loftier properties compared to the alloys, their usage in the industry was limited because of their expensiveness incurred in reinforcements and processing techniques. So, in the present scenario, search for alternative reinforcement materials has become the need of hour in the material industry. Though nations spend a lot of money on solid waste management still grappling with the challenge of preventing environmental

P. Yugandhar Babu (✉)
Department of Mechanical Engineering, Gudlavalleru Engineering College, Seshadari Rao Knowledge Village, Gudlavalleru, A.P. 521356, India
e-mail: yugandharbabuparasa@gmail.com

P. Kumar Jogi · K. Ramakanth · P. Ravindra Babu
Faculty of Mechanical Engineering, Gudlavalleru Engineering College, Seshadari Rao Knowledge Village, Gudlavalleru, A.P. 521356, India

L. Li et al. (eds.), *Advances in Materials and Manufacturing Engineering*, Lecture Notes in Mechanical Engineering, https://doi.org/10.1007/978-981-15-1307-7_52

degradation due to non-systematic waste management. A proper utilization of this waste would reduce the degradation of the natural resources. For this, a concept called "waste hierarchy" was formed. This hierarchy consists of 3 Rs as Reduce, Reuse, and Recycle. Current researches are concentrating to convert the waste materials into green materials that would be used in industrial applications. The recycling of solid waste may be taken as an alternative for reinforcing material in the production of AMC's. A very few researchers have shown interest on this problem and exhibited their works and a few of them including, Hima Gireesh et al. [1], have reinforced pure aluminum with Aloe Vera powder and fly ash and derived that the composites thus produced have an apparently low density and increased in the ultimate tensile yield strengths of the composites. Ravi Kumar et al. [2] have fabricated composites with ZrO_2 and coconut shell ash (CSA) with different % starting from 0 to 10%. And, they found that the density was decreased to an extent and has increased further increase in the reinforcement %. Flexural strength of CSA composites has pull rank the ZrO_2 composites. Alnema et al. [3] have fabricated aluminum matrix hybrid composites with a fixed weight % of reinforcement of 10% with various ratios of 1:10, 2:8, 3:7, and 4:6 of bamboo leaf ash (BLA) and SiC and observed that with an increase in the BLA content, hardness and ultimate tensile strength has increased with decrease in the % elongation. Usman et al. [4] studied the properties of the composites fabricated with bagasse ash (BA) with a % variation from 0% to 30 vol% and found that composites with 10 vol% reinforcement are good in ultimate tensile strength and impact strength. Alaneme and Adewale [5] implemented hybrid composite technique with rice husk ash (RHA) and SiC reinforcements mixed in different weight ratios to prepare 5, 7.5, and 10 wt% reinforced composites and studied their corrosive resistance in NaCl solution and found that the results of the hybrid composites are comparable with that of the composites reinforced with SiC alone. Prasad and Krishna [6] have prepared composites of aluminum reinforced with RHA with stir casting technique and observed that the porosity, tensile strength, hardness, and toughness have increased compared with the pure alloy.

In this present study, we are interested to follow the footprints of the earlier researchers in using the organic reinforcements to fabricate AMC's and would like to investigate their density, porosity, macrohardness, microhardness, and sliding wear characteristics. The primary aim is to fabricate an organically reinforced composite which is economically superior in the desired properties.

2 Materials and Methods

2.1 Materials

For present research, Aluminum-6061 of ϕ80 mm was selected as matrix material with Walnut Shell Ash (WSA) as reinforcement. The chemical composition of Al6061 was tabulated in Table 1.

Table 1 Chemical composition of Al-6061

Constituent	Si	Fe	Cu	Mn	Mg	Cr	Zn	Ti	Al
%	0.65	0.7	0.25	0.15	0.9	0.07	0.25	0.15	Reminder

2.2 Methods

Preparation of Walnut Shell Ash (WSA). The dry walnut shell is collected from waste at dry fruit market in Vijayawada. These walnut shells are burned in a metallic drum at a temperature of 3500 °C for 1 h and then that burnt shells are made into coarse powder by using a hammer; this coarse ash powder was milled in planetary ball mill. The ash then obtained was further heated in muffle furnace to decarbonize the ash by removing the carbonaceous material present in the burnt ash and then that WSA was sieved in a sieve shaker at various mesh sizes of to a grit size of 150 μm.

Fabrication of Composites: A bottom pouring stir casting machine is employed for fabrication of composite materials. A die of size 200 × 200 × 7 mm is used for casting purpose. A weighted quantity Al6061 alloy bar was charged into the furnace crucible and heated above the liquidus temperature of the alloy and was maintained there, and a calculated amount of reinforcement was added to the molten metal and was stirred for 5 min at 600 rpm using mechanical stirrer. The molten metal was then poured into the die which was preheated to a temperature of 400 °C.

Density and porosity Measurement: The porosity levels of a material can be evaluated by comparing the densities of the produced composite's theoretical (ρ_{th}) and experimental (ρ_{ex}). The experimental density was evaluated by the density testing apparatus. The fundamental rule of mixture is employed for calculating theoretical density [6].

$$m_{th} = \rho_m V_m + \rho_r V_r \tag{1}$$

where ρ_m theoretical density of matrix, v_m is the volume fraction of matrix, ρ_r is theoretical density of reinforcement, and v_r is the volume fraction of reinforcement [6]. Porosity $= (\rho - \rho_{ex}/\rho_{th}) * 100$.

Hardness Test: To measure micro and macrohardness of the fabricated composites, specimens of 10 × 10 × 7 mm are prepared and their surface was polished. Vickers microhardness testing is employed for measuring microhardness and Brinell hardness testing machine was employed for measuring macrohardness. An average of three samples was taken to determine the hardness of the specimens.

Sliding Wear: The pin-on-disk apparatus was employed to conduct dry sliding wear tests at room temperature with varying sliding distance, sliding speed, applied load against EN18 stainless steel disk with ϕ100 mm and 8 mm thickness. The surface of disk was cleaned with abrasive paper of grit size 120 for every experimental trial.

3 Results and Discussion

Walnut Shell Ash reinforced composites are successfully fabricated in two different compositions and are tested for mechanical properties. The results are discussed in detail in the subsequent sections.

3.1 Density and Porosity

Table 2 clears the density of the composites decreased with increase in the content of WSA; this is because of the presence of low-density WSA in a fraction of composition. The theoretical and experimental densities variation is shown in Fig. 1a.

There is a difference observed between the theoretical and experimental densities; this is because of the presence of porosity in the casted composites. The porosity of the WSA composites increased with an increase in the content of reinforcement. The maximum value obtained is at 4% reinforcement recorded as 4.18%. The maximum porosity level that might be accepted for AMC's is limited to 4% [6]. Figure 1b shows the variation of porosity for various composites.

Table 2 Density and porosity of composites

Sample code	Experimental density (g cm^{-3})	Theoretical density (g cm^{-3})	Porosity (%)
Al1	2.63	2.7	2.59
Al2	2.58	2.68	3.73
Al3	2.52	2.63	4.18

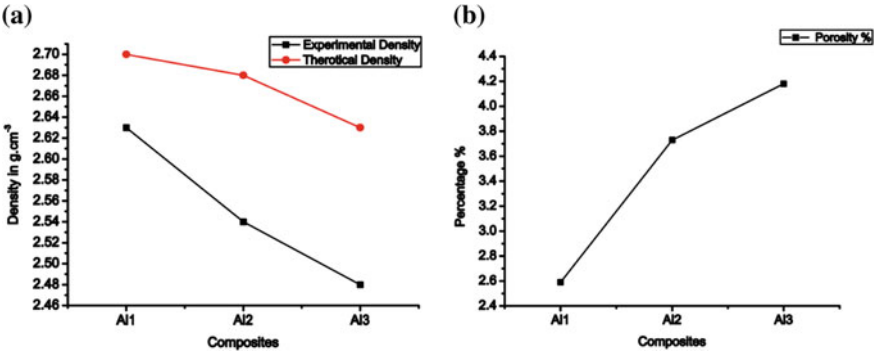

Fig. 1 **a** Comparison of variation of densities of WSA composites, **b** variation of porosity %

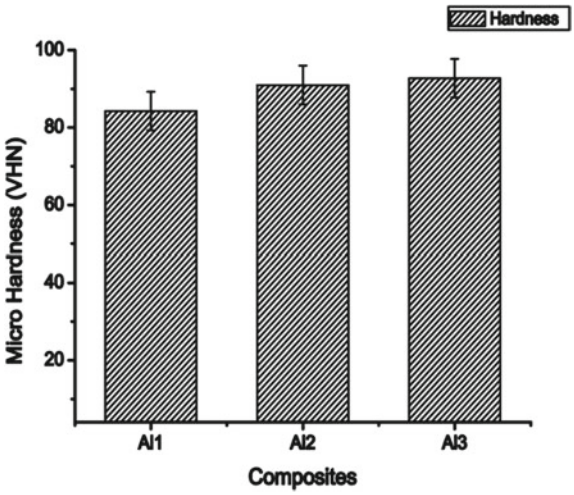

Fig. 2 Variation of hardness and *Y* error plot was plotted to show the range of the hardness values as the hardness values are taken as an average of three samples

3.2 Hardness Measurement

The hardness values of the pure alloy and the composites with 2 and 4% WSA composites increased with increasing content of WSA. This shows that the presence of the WSA particle has improved the overall hardness as the matrix material is so soft and the reinforcing particles are hard enough to provide the required hardness to the composite. Figure 2 shows the variation of hardness with the change in reinforcement %.

3.3 Wear Test Results

The wear test was conducted and the average wear rates of various composites at different sliding distance and loads are measured and these are plotted on the graph below illustrative.

Figure 3a shows the variations of average wear rate of pure alloy with varying sliding distance and load. It is observed that at 35 N load the average wear rate is 14.8×10^{-3} mm^3 m^{-1}. With decreasing in the load, the wear rate is also decreased and it is recorded that at 15 N load the average wear rate is 6.818×10^{-3} mm^3 m^{-1}.

Figure 3b shows the variation of average wear rates with increase in load and travel distance for 2% WSA composites. It is observed that there is a very high average wear rate when the specimen is loaded with 25 N and made to slide for a distance of 1 km and is recorded as 9.8×10^{-3} mm^3 m^{-1}. Figure 3c shows the variation of average wear rates with increase in load and travel distance for 4% WSA composites. It is observed that there is a very high average wear rate when the specimen is loaded with 25 N and made to slide for a distance of 750 m and is recorded as 7.7×10^{-3} mm^3 m^{-1}. Figure 3d shows the variation of wear rates of composites varying with

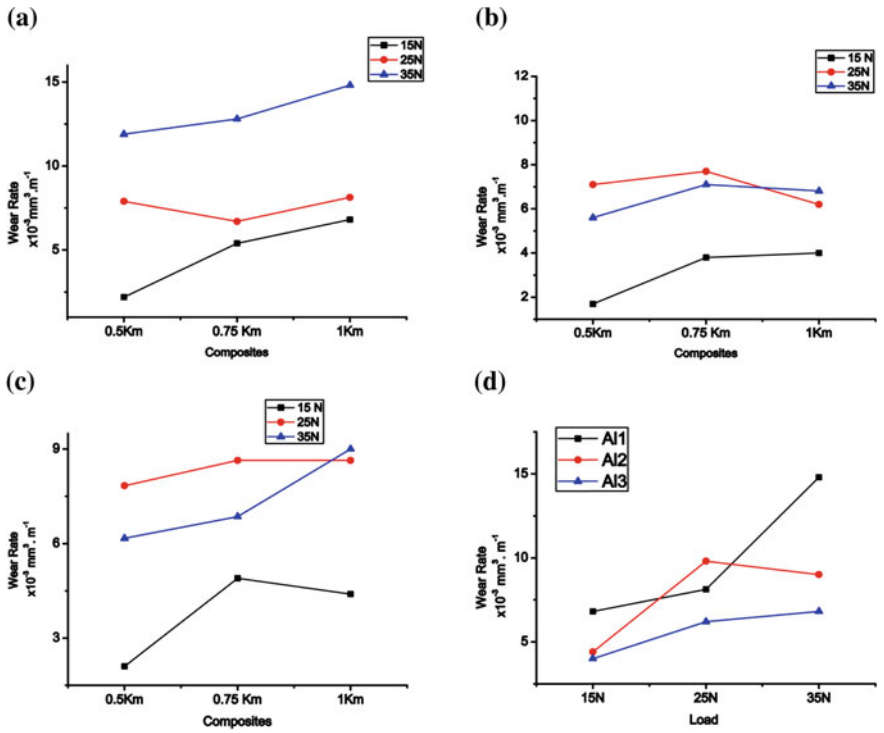

Fig. 3 Average wear rate graphs for various combinations. **a** Al1—wear rate versus travel distance at various loads, **b** Al2—average wear rate versus travel distance at various loads, **c** Al3—wear rate versus travel distance at various loads, **d** 13—comparison of various wear rate versus loads for various composites

the % of WSA. It is found that the composites with 4% of WSA have outperformed all the remaining materials providing a low average wear rate.

4 Conclusions

- It is observed that the composites have outperformed the pure material in terms of density and it is recorded 2% WSA composites resulted 3.72% decrement in density and 4% WSA composite has also shown a similar tend with 5.70% as top.
- The microhardness of the samples is measured and recorded that the composites have shown an increment of 7.9% and 10.09% for 2% and 4% WSA composites, respectively, compared with the pure alloy.
- In dry sliding wear test, it is recorded that the composite with 4% WSA has outperformed all the samples recording a lower average wear rate of 6.81×10^{-3} mm^3 m^{-1}. Compared with the pure alloy, it is nearly 30% decrement in average wear rate.

References

1. Hima Gireesh, Ch., Durga Prasad, K.G., Ramji, K., Vinay, P.V.: Mechanical characterization of aluminium metal matrix composite reinforced with aloe vera powder. Mater. Today Proc. **5**(2), 3289–3297 (2018)
2. Ravi Kumar, K., Pridhar, T., Sree Balaji, V.S.: Mechanical properties and characterization of zirconium oxide (ZrO_2) and coconut shell ash (CSA) reinforced aluminium (Al 6082) matrix hybrid composite. J. Alloys Compd. **765**, 171–179 (2018)
3. Alaneme, K.K., Olubambi, P.A., Afolabi, A.S., Bodurin, M.O.: Corrosion and tribological studies of bamboo leaf ash and alumina reinforced Al-Mg-Si alloy matrix hybrid Composites in chloride medium. Int. J. Electrochem. Sci. **9**, 5663–5674 (2014)
4. Usman, A.M., Raji, A., Waziri, N.H., Hassan, M.A.: Production and characterisation of aluminium alloy—bagasse ash composites. IOSR J. Mech. Civ. Eng. **11**(4), 38–44 (2014)
5. Alaneme, K.K., Adewale, T.M.: Influence of rice husk ash-silicon carbide weight ratios on the mechanical behavior of Al-Mg-Si alloy matrix hybrid composites. Int. Conf. Tribol. Serbia Trib. **13**, 160–168 (2013)
6. Prasad, D., Krishna, A.: Fabrication and characterization of A356.2-rice husk ash composite using stir casting technique. Int. J. Eng. Sci. Technol. **2**, 7603–7608 (2010)

Analysis of Different Types of Micro Grains in Stick Welded Mild Steel Plates

Bijaya Kumar Khamari, Swapan Kumar Karak, Pradip Kumar Sahu, Surya Narayan Panda and Bibhuti Bhusan Biswal

Abstract Nowadays, arc welding is the most essential thing in every field. Therefore, researchers are focusing on the improvement of the quality of the arc welding. For that microstructure plays a major role in this work, mild steel plates were taken as workpiece material to do welding operation in stick welding. V-edge was prepared to conduct butt welding between the plates which has to be joined by application of 120 A current. After cooling, the microstructure of the welded specimen was observed. Importantly, two main constituents' ferrite and pearlite were found mostly. Eight varieties of ferrite were analyzed in fusion zone and heat-affected zone. The primary ferrites were distinguished in the heat-affected zone and the Widmanstatten ferrites in fusion zone in between the dendritic structures. The primary ferrites have been more circular in nature and the Widmanstatten ferrites were columnar. The mechanical properties also vary due to the variation of ferrite structures. Pearlites were observed in between the ferrites with more percentage of carbon content which is the most distinguished feature of pearlite grains.

Keywords Mild steel · Microstructure · Ferrite · Pearlite · Widmanstatten ferrites · V-groove · Butt joint · Stick welding

B. K. Khamari (✉) · S. K. Karak
National Institute of Technology Rourkela, Rourkela, Odisha, India
e-mail: bijayaa.khamari@gmail.com

S. K. Karak
e-mail: karaksk@gmail.com

P. K. Sahu
Oriental University, Indore, Madhya Pradesh 453555, India
e-mail: pradipsahu2@gmail.com

S. N. Panda
Birsa Institute of Technology Sindri, Dhanbad, India
e-mail: suryanarayan.uce@gmail.com

B. B. Biswal
National Institute of Technology Meghalaya, Shillong, Meghalaya, India
e-mail: bibhuti.biswal@gmail.com

L. Li et al. (eds.), *Advances in Materials and Manufacturing Engineering*, Lecture Notes in Mechanical Engineering, https://doi.org/10.1007/978-981-15-1307-7_53

1 Introduction

Electricity is the major requirement for arc welding to join metal with the same or different metal with the help of an arc that is created between base metal and electrode to melt the workpiece. To the same or different metals are joined by the help of arc that is formed between workpiece and electrode. The heat of the arc melts the workpieces and after solidification, a prefect's joint is constructed. After welding operation, the microstructure of the sample can be examined. Lakshminarayanan et al. [1] varied different welding processes like SMAW, GMAW, and GTAW by taking stainless steel as workpiece material to investigate the microstructure and different mechanical properties. Ebrahimnia et al. [2] have been taken four different shielding gases to find out the influence on the microstructure of the welded sample. Buchely et al. [3] used hardfacing alloys as filler material to weld ASTM A36 carbon steel in SMAW welding process. Three hardfacing alloys were used. First was CR rich alloy, second was W rich alloy, and third was complex carbide alloy has been used and the effect was studied in the microstructure of welded specimen. Kacar and Baylan [4] considered X5CrNi18-10 grade austenitic and X20CrMo13 grade martensitic stainless steel as workpiece material in manual metal arc welding to investigate the microstructure and different mechanical properties.

Sadeghian et al. [5] investigated the microstructure and mechanical properties of the welded samples by taking UNS S32750 super duplex stainless steel (SDSS)/API X-65 high strength low alloy steel as workpiece materials. Arivazhagan et al. [6] conducted three different welding processes to find out the microstructure and mechanical properties of the welded specimens. Fujii et al. [7] observed the mechanical properties and microstructure of titanium plates of 2 mm thick. Here, the variable parameter was welding speed which is key factor for change in microstructure and mechanical properties. Ghomashchi et al. [8] investigated the microstructure of shielded metal arc welded steel samples. The grain boundary and different constituents of microstructure like different types of ferrites and pearlites were clearly presented in their work.

This paper identified the different types of ferrites and pearlites that have been found in stick welded mild steel plates and how the constituents affect the microstructure and hardness which are very different from the base metal.

2 Material and Methodology

Mild steel plates were considered as working material for stick welding. For welding operation, V-groove has been prepared on 5-mm-thick material and welding was done by applying 120 A current. The length and width of the workpiece were taken to be 10 cm and 5 cm, respectively. The welding operation has been conducted by taking E6013 as welding electrodes. The model and real welded plates are presented in Figs. 1 and 2, respectively.

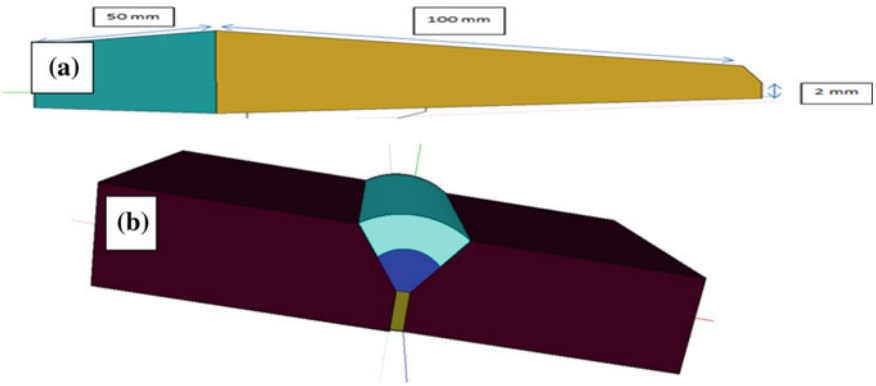

Fig. 1 **a** Workpiece model with dimensions, **b** welded model with dimension

Fig. 2 Real welded sample

2.1 Optical Microscopy

The samples were grinded using belt grinder. After completion of grinding, the samples were polished using emery papers viz. 1/0, 2/0, 3/0, and 4/0 in a progressive manner. Now, the samples were cloth polished using Alumina paste and finally, diamond polished to get a fine mirror appearance on the surface which needs to be observed under the microscope. After polishing, the etchant was prepared. 4% Nital was used as an etchant for mild steel samples. Preparation of 4% Nital involved measuring 96 mL using measuring flask in which 4 mL of concentrated nitric acid was added. The polished samples were taken and dipped in the etchant for a few seconds and the sample was kept in a Petri dish. After etching, the samples were taken for microstructural observation under optical microscope.

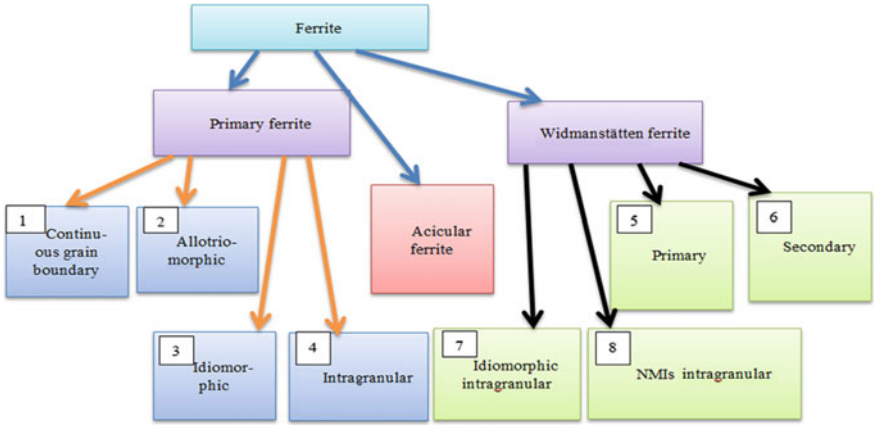

Fig. 3 Different types of ferrite in microstructure

3 Result and Discussion

3.1 Microstructure Analysis

The microstructure of the welded mild steel contains both ferrite and pearlite. The category of different types of ferrite was presented in Fig. 3 and their microstructures were shown in Fig. 4, respectively.

Continuous grain boundary ferrite and allotriomorphic primary ferrites were presented in Fig. 4(1, 2), respectively. These structures were continuously spread like a river. Then the idiomorphic and intergranular primary ferrites were shown in Fig. 4(3, 4) which was situated in a small area in between the pearlite structures. The primary and secondary Widmanstatten ferrites were shown in Fig. 4(5, 6), respectively. Lastly, idiomorphic intergranular and NMIs intergranular Widmanstatten ferrites were columnar and needle-like structures which were presented in Figs. 4(7, 8), respectively.

Mostly, the microstructure of mild steel was done with 50-μm scale and all the mentioned structures are found in fusion zone and heat-affected zone of the welded plate.

4 Conclusion

After welding of the base metal, the original microstructure of the base metal changed and new structures have been formed due to heat input and input parameters. The microstructure of fusion zone is dendritic in nature due to melting of the base metal

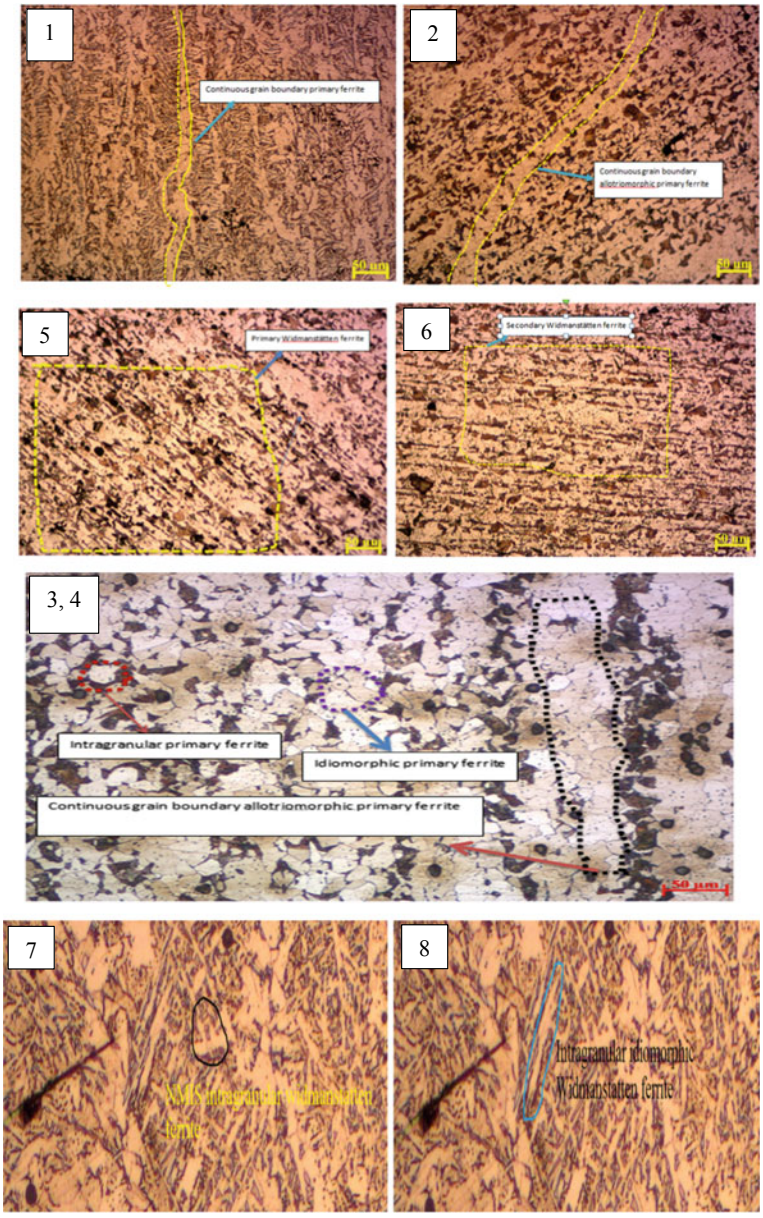

Fig. 4 Microstructure of different ferrites from 1 to 8 as per Fig. 3

and welding rod which was formed a weld pool. Due to recrystallization of the micrograins from the liquid state to solid state, dendritic structures are formed. Mostly, in fusion zone, the Widmanstatten type of ferrites was formed. The primary ferrites were seen in heat-affected zone.

References

1. Lakshminarayanan, A.K., Shanmugam, K., Balasubramanian, V.: Effect of welding processes on tensile and impact properties, hardness and microstructure of AISI 409M ferritic stainless joints fabricated by duplex stainless steel filler metal. J. Iron Steel Res. Int. **16**(5), 66–72 (2009)
2. Ebrahimnia, M., Goodarzi, M., Nouri, M., Sheikhi, M.: Study of the effect of shielding gas composition on the mechanical weld properties of steel ST 37-2 in gas metal arc welding. Mater. Des. **30**(9), 3891–3895 (2009)
3. Buchely, M.F., Gutierrez, J.C., Leon, L.M., Toro, A.: The effect of microstructure on abrasive wear of hardfacing alloys. Wear **259**(1–6), 52–61 (2005)
4. Kacar, R., Baylan, O.: An investigation of microstructure/property relationships in dissimilar welds between martensitic and austenitic stainless steels. Mater. Des. **25**(4), 317–329 (2004)
5. Sadeghian, M., Shamanian, M., Shafyei, A.: Effect of heat input on microstructure and mechanical properties of dissimilar joints between super duplex stainless steel and high strength low alloy steel. Mater. Des. **60**, 678–684 (2014)
6. Arivazhagan, N., Singh, S., Prakash, S., Reddy, G.M.: Investigation on AISI 304 austenitic stainless steel to AISI 4140 low alloy steel dissimilar joints by gas tungsten arc, electron beam and friction welding. Mater. Des. **32**(5), 3036–3050 (2011)
7. Fujii, H., Sun, Y., Kato, H., Nakata, K.: Investigation of welding parameter dependent microstructure and mechanical properties in friction stir welded pure Ti joints. Mater. Sci. Eng., A **527**(15), 3386–3391 (2010)
8. Ghomashchi, R., Costin, W., Kurji, R.: Evolution of weld metal microstructure in shielded metal arc welding of X70 HSLA steel with cellulosic electrodes: a case study. Mater. Charact. **107**, 317–326 (2015)

Optimization of Process Parameters on Abrasive Jet Machining of Ceramic

Indranil Mandal, Thia Paul and Biswanath Doloi

Abstract In this present work, fabrication of abrasive jet machining (AJM) setup and parametric study of various process parameters in AJM setup have been carried out. Main important output response is material removal rate (MRR) during the AJM. The main input variables that affect the output responses are nozzle diameter (ND), gas pressure and stand-off distance (SOD). Silicon carbide abrasive with grit size of 100 μm has been chosen to find out the effect of process parameters during making holes on ceramic plate. Experiments have been done by selecting L_9 orthogonal array, and results have been optimized with response surface methodology. ANOVA is used to identify the significant process parameters. Statistical results (at a 95% confidence level) show that the percentage contribution of nozzle diameter, stand-off distance and gas pressure on metal removal rate is 42%, 46.9% and 9.7%, respectively. The result shows that the maximum MRR value of 0.018 g/s has been obtained by Taguchi's optimization method. From the results obtained by ANOVA, it has been found out that the stand-off distance is the most significant parameter. Contour plot has been used to determine desirable material removal rate and corresponding operating conditions during abrasive jet machining of ceramic.

Keywords AJM · Taguchi method · MRR · ANOVA

1 Introduction of Abrasive Jet Machining (AJM) Process

Abrasive jet machining is a non-conventional machining process which is applied for machining of various super alloys, electronics devices and also for brittle materials such as ceramic and glass. In AJM, fine abrasive grits along with air or gas are mixed in a mixing chamber and impinge on the surface of the workpiece with high velocity through a nozzle. As a result of this, erosive action takes place, and materials

I. Mandal · B. Doloi
Department of Production Engineering, Jadavpur University, Kolkata, West Bengal, India
e-mail: mandal.indranil2@gmail.com

T. Paul (✉)
Department of Mechanical Engineering, JIS College of Engineering, Kalyani, West Bengal, India
e-mail: thiapaul8@gmail.com

L. Li et al. (eds.), *Advances in Materials and Manufacturing Engineering*, Lecture Notes in Mechanical Engineering, https://doi.org/10.1007/978-981-15-1307-7_54

are removed from the surface of the workpiece. Research work on AJM has been performed by various researchers.

Models of erosion are compared with the efficiency of machining of ceramic materials during AJM Process. Deterioration of strength does not take place. Micromachining of ceramic materials without any damage can be done in AJM Process [1]. The effect of input process variables on holes produced and material removal rate during abrasive jet drilling on glass sheet are presented. MRR increases as gas pressure increases [2]. During machining of brittle materials in AJM, abrasive particles impinge on the surface, and cracks are propagated due to which materials are removed. An analytical model has shown that removal of metal depends on various properties of workpiece material such as geometry [3]. AJM process is effectively used for machining of brittle and hard materials by using silicon carbide abrasive. The effect of input variables on MRR and MFR during AJM has been presented. MRR and MFR are increased as stand-off distance increases [4]. During AJM process, the penetration rate and material removal rate are dependent on mixture ratio, size of abrasive grains, gas pressure and stand-off distance. MRR and penetration rate are increased as mixture ratio increases [5]. Taguchi method of optimization and ANOVA are applied for machining of ceramic tiles in AJM for finding the effect of input variables on kerf width and MRR. Ceramics are widely used all over the world for their main characteristics of high module of elasticity and high toughness. Ceramics are used as tiles in space shuttle program, roof tiles as coatings of jet engine turbine blades, pipes, etc. [6].

2 Experimentation

In this present work, AJM setup has been fabricated for finding out the effect of process parameters on output responses during drilling on ceramic plate. Taguchi method of optimization has been performed based on the results of structured experimental plan.

2.1 Experimental Setup Details

AJM setup of size 200.66 cm × 91.44 cm × 60.96 cm has been fabricated as shown in Fig. 1 which consists of mixing chamber, nozzle, compressor, machining chamber, FRL unit and pressure gauge and nozzles of brass material of different sizes (2, 2.5 and 3 mm).

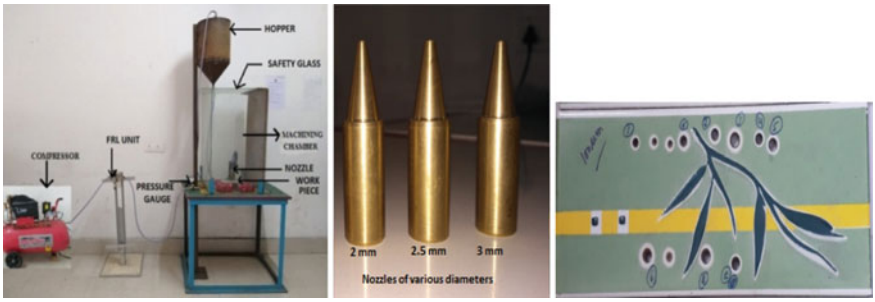

Fig. 1 Abrasive jet machining setup for making holes on ceramic tile at different nozzle diameters, SODs and pressures

2.2 Design of Experiments and Observed Data

The main input parameters for this experiment are gas pressure, SOD and nozzle diameter (ND). In this method, all of the *S*/*N* ratio values of MRR were calculated based on higher the better quality principle. L_9 orthogonal array has been used, i.e., total nine set of experiments were conducted. Three different levels of process parameters were selected to carry out the experiment as shown in Table 1. Table 2 represents the experimental plan and observed MRR.

From Table 2, it has been found out that larger MRR of 0.018 g/s is obtained at parametric combinations such as ND of 3 mm, SOD of 9 mm and pressure of 4.6 kgf/cm^2.

3 Results and Discussion

For optimization, Taguchi method was implemented to observe the effect of input process parameters on output response, i.e., material removal rate. ANOVA test was performed for finding out the most significant parameter in AJM process.

Table 1 Process parameters with various levels

Sl. no.	Parameters	Level 1	Level 2	Level 3
01	Nozzle diameter (mm)	2	2.5	3
02	Stand-off distance (mm)	5	7	9
03	Pressure (kgf/cm^2)	4.2	4.6	4.9

Table 2 Experimental design matrix and observed MRR

Sl. no.	Nozzle diameter (mm)	SOD (mm)	Pressure (kgf/cm^2)	W_1 (g)	W_2 (g)	Machining time (s) (T)	MRR (g/s) ($W_1 - W_2$)/2
1	2.0	5	4.2	141.56	141.50	10	0.006
2	2.0	7	4.6	141.43	141.29	12.72	0.011
3	2.0	9	4.9	141.29	141.06	17.69	0.013
4	2.5	5	4.6	141.06	140.89	14.17	0.012
5	2.5	7	4.9	140.89	140.69	12.5	0.016
6	2.5	9	4.2	140.69	140.57	7.06	0.017
7	3.0	5	4.9	140.57	140.38	15.83	0.012
8	3.0	7	4.2	140.38	140.17	16.15	0.013
9	3.0	9	4.6	140.11	139.95	8.89	0.018

where W_1 and W_2 are weight before machining and weight after machining, respectively

3.1 Optimization of Process Parameters

The experimental results have been transformed into means and signal-to-noise (S/N) ratio, and it is shown in Table 3. The mean and S/N ratios for MRR have been calculated by statistical software "**MINITAB 16**."

From the response table of S/N ratio (Table 4), the rank order of process parameters has been achieved as stand-off distance, nozzle diameter and gas pressure.

Figure 2 depicts the S/N ratio variation for MRR with respect to input process parameters. From the plot, it has been observed that the MRR is increasing and decreasing as the nozzle diameter increases, whereas for SOD, MRR is increasing,

Table 3 Mean value and signal-to-noise ratio for MRR

Sl. no.	Nozzle dia (mm)	SOD (mm)	Pressure (kgf/cm^2)	MRR (g/s)	S/N ratio	Mean value
1	2.0	5	4.2	0.006	−44.4370	0.006
2	2.0	7	4.6	0.011	−39.1721	0.011
3	2.0	9	4.9	0.013	−37.7211	0.013
4	2.5	5	4.6	0.012	−38.4164	0.012
5	2.5	7	4.9	0.016	−35.9176	0.016
6	2.5	9	4.2	0.017	−35.3910	0.017
7	3.0	5	4.9	0.012	−38.4164	0.012
8	3.0	7	4.2	0.013	−37.7211	0.013
9	3.0	9	4.6	0.018	−34.8945	0.018

Table 4 Response table for signal-to-noise ratio for MRR

Level	Nozzle dia (mm)	Stand-off distance (mm)	Pressure (kgf/cm^2)
1	−40.44	−40.42	−39.18
2	−36.57	−37.60	−37.49
3	−37.01	−36.00	−37.35
Delta	3.87	4.42	1.83
Rank	2	1	3

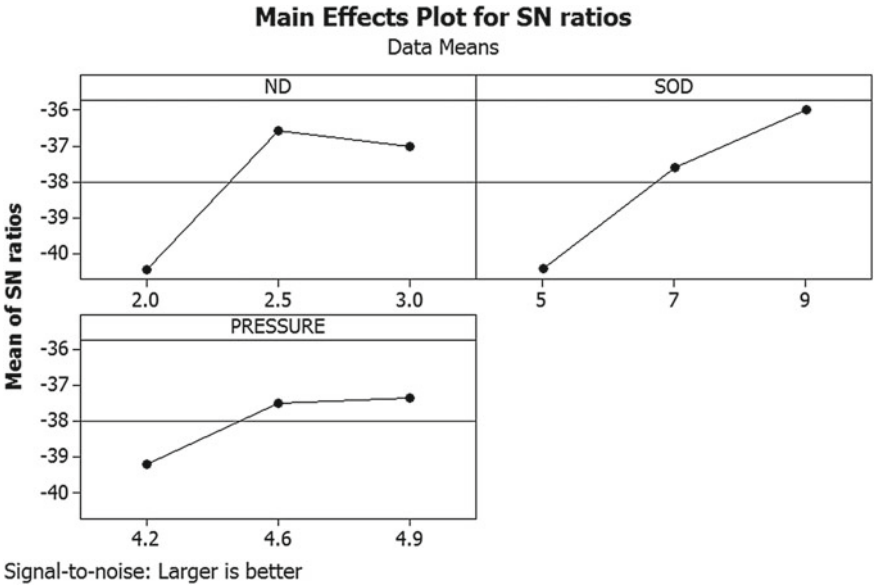

Fig. 2 Main effects plot of *S*/*N* ratio for MRR

and for gas pressure, the MRR is increasing and then remains constant for gas pressure variation from 4.6 to 4.9 kgf/cm^2.

3.2 Analysis of Variance (ANOVA)

For the identification of the main statistically significant process parameters and for determining the percentage contribution of process parameters on MRR, ANOVA test was performed at a significance level of 95% confidence level. Table 5 shows the results of ANOVA test of *S*/*N* ratio data for MRR.

The conclusion made from above Table 5 is that nozzle diameter and stand-off distance are significant factors as corresponding *P* values are less than 0.05, and

Table 5 Results of analysis of variance of *S/N* ratio for MRR

Source	DF	Seq SS	Adj SS	Adj MS	*F*	*P*	% contribution
ND	2	26.9381	26.9381	13.4691	30.86	0.031*	42
SOD	2	30.0600	30.0600	15.0300	34.43	0.028*	46.9
Pressure	2	6.2258	6.2258	3.1129	7.13	0.123	9.7
Residual error	2	0.8730	0.8730	0.4365			1.4
Total	8	64.0970					100
$S = 0.6607$			$R^2 = 98.6\%$			R^2 (adj) = 94.6	

*Significant factor
where *DF* degrees of freedom, *Seq SS* sequential sum of squares, *Adj SS* adjusted sum of square, *Adj MS* adjusted mean square and *F* fisher ratio

the developed model is significant. From the results obtained by ANOVA, it has been established that the most significant parameter is stand-off distance (SOD) for controlling MRR in AJM based on the present analysis as it has highest percentage of contribution of 46.9% compared to that of gas pressure and nozzle diameter.

3.3 Contour Plot Showing MRR Variation

Contour plot represents output response variable (MRR) related to input predictor variables (SOD, gas pressure and ND). Contour plot is preferable for obtaining desirable condition for drilling on ceramic tile. Figure 3 shows the preferable range of gas pressure and ND to obtain maximum MRR. The preferable range of gas pressure lies between 4.3 and 4.6 kgf/cm^2, and the SOD is 9 mm. As gas pressure goes away from its preferable range, the MRR decreases. There is no change in MRR level within the preferable range of gas pressure. The preferable range of SOD lies between 7 and 9 mm, and ND lies between 2.3 and 3 mm. MRR increases with increase in SOD.

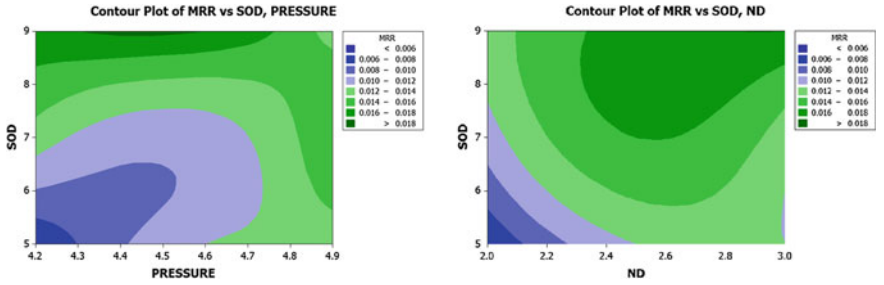

Fig. 3 Contour plot of MRR versus SOD, pressure and contour plot of MRR versus SOD, ND

4 Conclusions

AJM setup has been properly designed and fabricated to carry out drilling operation Based on Taguchi method of optimization and analysis of variance (ANOVA) test, following conclusions can be drawn:

i. Maximum MRR value of 0.018 g/s was obtained at optimum parametric conditions such as gas pressure of 4.6 kgf/cm^2, SOD of 9 mm and nozzle diameter of 3 mm during AJM process.
ii. Statistical results at a 95% confidence level show that the SOD, nozzle diameter and gas pressure have percentage contribution of 46.9, 42 and 9.7% on MRR, respectively, by using abrasive particle of size 100 μm.
iii. From the results obtained by ANOVA, it has been found that the stand-off distance is the most significant parameter during abrasive jet machining of ceramic tile.

References

1. Wakuda, M., Yamauchi, Y., Kanzaki, S.: Effect of work piece properties on machinability in abrasive jet machining of ceramic materials. Precis. Eng., Int. Soc. Precis. Eng. Nanotechnol. **26**(2), 193–198 (2002)
2. Chandra, B., Singh, J.: A study of effect of process parameters of abrasive jet machining. Int. J. Eng. Sci. Technol. **3**(1), 504–513 (2011)
3. Khodke, P.M., Tidke, D.J., Ramarao, A.V.: An analytical model for material removal in abrasive jet machining for brittle materials. Mater. Manuf. Process. **11**(4), 535–554 (1996)
4. Ray, P.K., Paul, A.K.: Some studies on abrasive jet machining. J. Inst. Eng. (India) **68**, 27–30 (1987)
5. Verma, A.P., Lal, G.K.: An experimental study of abrasive jet machining. Int. J. Mach. Tool Des. Res. **24**(1), 19–29 (1984)
6. Srikanth, D.V., Sreenivasa Rao, M.: Application of Taguchi & response surface methodology in optimization for machining of ceramics with abrasive jet machining. In: 4th International Conference on Materials Processing and Characterization, vol. 2, no. 4–5, pp. 3308–3317 (2015)

Multi-objective Optimization of Al–Al_2O_3 MMC During Electro Discharge Machining Using Desirability Function Approach

Manas Ranjan Panda, Sasank Sekhar Panda and H. K. Narang

Abstract The manufacturing industries particularly aerospace and automobile industries are always in the search of advanced materials. Al–Al_2O_3 metal matrix composites (MMC) can be a good choice because of its excellent mechanical properties, so it became very much essential for the researchers to study its mechanical properties. Evidence shows that addition of aluminium oxide as reinforcement helps in improvement of mechanical properties of the composites materials. In the present study, Al–Al_2O_3 MMC is prepared and machined using Electro Discharge Machining (EDM) to know the effect of process parameters. The process parameters chosen for this experiment were voltage (V), discharge current (I_p) and duty cycle (t), while responses were chosen as material removal rate (MMR) and surface roughness (R_a). Taguchi L_9 orthogonal array was selected for conducting experiments. Results of the experiments were analysed using desirability function to get an idea about the optimum parameter setting of the selected process parameters.

Keywords Al–Al_2O_3 composite · EDM · Desirability function · Taguchi method

1 Introduction

Composite materials possess low specific gravity which helps in enhancing properties like strength and elastic modulus, and thus, it has huge demand in the areas of aircrafts, aviation, automobile industries and advance manufacturing. Composite materials were prepared from two or more composing materials which have noticeably different chemical or physical compositions [1]. The constituent elements largely comprise a reinforcing material, fillers and a composite matrix binder which differ in form or composition on a macro-scale. The constituent components hold their very own characters, i.e. they do not merge totally into each other despite the fact that they act combine. Typically, the constituent material shows an interface

M. R. Panda (✉) · S. S. Panda
Department of Mechanical Engineering, GIET University, Gunupur, Odisha 765022, India
e-mail: mrpanda172@gmail.com

H. K. Narang
Department of Mechanical, NIT, Raipur, Chhattisgarh 492010, India

L. Li et al. (eds.), *Advances in Materials and Manufacturing Engineering*, Lecture Notes in Mechanical Engineering, https://doi.org/10.1007/978-981-15-1307-7_55

between each other and can be distinguished physically. Composites having heterogeneous structures suit the significance of explicit capacity and configuration, mixed with properties which limit the extension for characterization. In any case, the new assortments of composites are being prepared, each with their very own particular reason and qualities like the flake, filled, particulate and laminar composites. Particles or fibres reinforced in a matrix of another material are the most appropriate case of everyday composite materials, which are mainly used for structural parts. The major advantages of aluminium-based MMCs are high strength, controlled thermal expansion coefficient, enhanced electrical properties, high temperature properties, etc. [2].

The present investigation deals with machinability of metal matrix composites (MMCs) focused around parametric examination and multi-objective optimization in connection to machining execution highlights. Al is chosen as the matrix material because of its good electrical and mechanical properties which is very much necessary for the composites in various work environments. Al is also less costly, readily available and has excellent corrosion resistance properties. Al_2O_3 is chosen as the reinforcing material because it is found in enhancing hardness, wear resistance and tensile strength of the Al metal matrix composites.

AMMCs have higher specific strength and stiffness than that of traditional engineering materials; besides this, it also has enough thermal fatigue resistance and adequate creep strength even at high temperature. Traditional machining of such materials gives excessive tool wear, poor material removal rate and increased surface roughness, thereby reducing the tool life. Thus, to overcome from these challenges, many researchers have utilized electro discharge machining to successfully machine composite materials. This will minimize noise and dust problem. In addition to this, it reduces extensive plastic deformation and subsequent heat generation associated with conventional machining. Electro Discharge Machining appears to be promising technique including higher machining rate with good precision, for machining of composites.

2 Literature Survey

Rani et al. [3] researched the impacts of EDM on Al606130%Al_2O_3 MMCs. Selected parameters are T_{on}, T_{off} and peak current, while the responses were chosen as MRR and TWR. High machining rate was seen with high current and high pulse on time. Tool wear rate considerably increased with less pulse on time and low peak current. To know the surface phenomena, Kumar et al. [4] highlighted the performance parameters as MRR, TWR, surface roughness (SR) and mentioned that with increase in peak current and pulse on time, surface roughness increased. Chen and Mahdivian [5] investigated that the electric spark is developed from different wave forms current and voltage of several electrical circuits, and it was shown that material removal rate is a function of discharge energy. Hocheng et al. [6] examined the relationship between the process parameters which are Ton time and peak current. Larger peak

current and Ton time are prescribed so as to do the EDM machining effectively. Singh et al. [7] investigated electro discharge machining on Al/10%SiCp composites using Taguchi technique coupled with grey relational analysis. They deliberate the multi-objective optimization of the machining parameters with metal removal rate, tool wear rate, taper produced, radial overcut and surface roughness. Velmurgan et al. [8] studied the effect of pulse on time, current, voltage, flushing pressure by taking MRR and TWR along with surface roughness as responses, and in this study, the material is chosen as Al 6061 MMC reinforced with 10% SiC. Purohit and sahu [9] studied a unique approach of hybrid optimization combined with PCA to identify the effect of process parameters on the responses. The process parameters were chosen as pulse on time, peak current, gap voltage with the responses like MRR and TWR. Further TOPSIS algorithm was implemented to convert multi-response into single response optimization. Jung and Kwon [10] have attempted to find the optimal condition for EDM machining of micro-holes with maximum aspect ratio with the help of Grey-Taguchi analysis and found that electrode wear along with clearance at entrance and exit has significant effect during machining.

Form the above survey, evidence suggests that the Al-based composites are gaining interest, but no research has been carried out on Al–Al_2O_3 metal matrix composite for multi-response optimization during EDM machining. Hence, it became very much interesting to know the behaviour of machining parameters of EDM during multi-objective optimization.

3 Experimentation

3.1 Fabrication of Al–Al_2O_3 Composite

The first challenge to this study is to identify a good and economical method to produce Al–Al_2O_3 composite with suitable proportion of Al_2O_3 in the mixture. From the extensive literature survey, it was found that powder metallurgy is the best method to produce this composite because of advantages like better hardness and good compressive strength. The weight percentage of Al_2O_3 is taken as 10%, as literatures show that the composite gives best mechanical properties when the percentage of Al_2O_3 is 5–15% in the composite. All the experiments are performed in a die-sinking type EDM machine as shown in the Fig. 1.

Mixing and blending of the composite are carried out in a ball planetary mill machine. The mixture further compacted by an universal testing machine with continuous loading. In total, nine numbers of samples were prepared of size 25 mm diameters with 5 mm thickness. A stainless steel die of 25 mm diameter of outer diameter with a compressive force of 20 ton is used while fabrication. The green samples obtained from the above process were further sintered in a tubular furnace (shown in Fig. 2) at a temperature of 605 °C and a holding time of one hour. Samples were brought to room temperature by air cooling for the next 24 h.

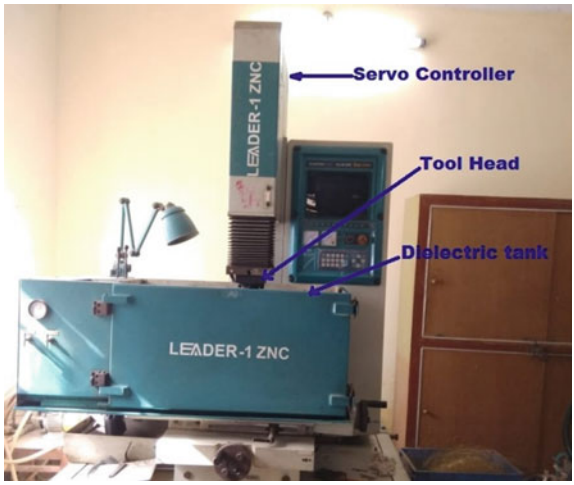

Fig. 1 EDM machine

Fig. 2 Horizontal tubular furnace

3.2 Taguchi Design and Electro Discharge Machining

The current research is mainly intent to identify the effect of major machining parameters on different performance parameters during machining. Transformer oil is used as dielectric fluid with a cylindrical copper tool having diameter of 10 mm is used for the machining. Tool is made as anode, and workpiece is held on the vice connected to the cathode of the D.C. power supply. The time of machining is fixed to ten minutes for all the nine specimens. All the specimens are thoroughly cleaned to remove impurities present over the machining surface. Figure 3 shows the samples after machining.

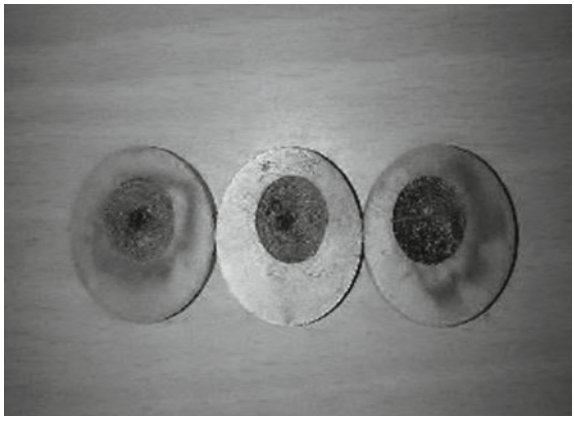

Fig. 3 Test samples after machining

Table 1 Process parameters with its levels

Parameters	Voltage (V) in Volts	Peak current (I_p) in Amp	Duty cycle (t)
Level 1	50	7	75
Level 2	60	8	100
Level 3	70	9	125

Based on the literature review, the process parameters which have significant effect on the machining were chosen, and the parameters with its levels are given in Table 1.

3.3 Measurement of Performance Parameters

MRR: The material removal rate is measured with the help of volume calculation method. In this method, the weight of each specimen before machining and after machining is measured with the help of an electronic balance weight measuring machine. The formula used for MRR calculation is given:

$$\text{Material Removal Rate in mm}^3/\text{min},\ \text{MRR} = \left(\frac{W_i - W_f}{\rho \times T}\right) \tag{1}$$

where ρ = density of the composite material = 2.29×10^{-3} gm/mm^3, T = Time in minutes = 10 min.

Surface Roughness: The surface texture at the machined surface of specimen is measured with the help of a diamond stylus Talysurf machine is shown in Fig. 4. The quantitative evaluation is done to identify the effect of machining parameters of EDM on the surface after machining, and the same surface can be compared with

Fig. 4 Surface roughness measuring device with diamond probe

Table 2 Taguchi experimental design and performance parameters

Sl. no.	Voltage (V)	Current (I_p)	Duty cycle (t)	MRR (mm^3/min)	Surface roughness (R_a)
1	7	50	75	4.464	6.851
2	7	60	100	3.821	5.682
3	7	70	125	1.517	7.685
4	8	50	100	1.4712	6.932
5	8	60	125	5.958	5.882
6	8	70	75	3.347	5.684
7	9	50	125	6.9891	7.736
8	9	60	75	4.6287	6.024
9	9	70	100	8.1652	7.035

other machined surface. The experimental runs as per Taguchi design along with performance parameters are given in Table 2.

4 Result Analysis

4.1 Desirability Function Approach

The method starts with finding the individual desirability index for each performance parameter. The desirability index can be calculated with the help of functions taken from Derringer et al. The desirability index for material removal rate can be calculated for larger-the-better criteria given by

$$D_{\mathrm{MRR}} = \left(\frac{y' - y_{\min}}{y_{\max} - y_{\min}}\right)^r, \quad \text{if } y_{\min} \le y' \le y_{\max} \tag{2}$$

$D_{\mathrm{MRR}} = 0$, if $y' \le y_{\min}$ and $D_{\mathrm{MRR}} = 1$, if $y' \ge y_{\max}$.

The desirability index for surface roughness can be calculated for smaller-the-better criteria given by

$$D_{\mathrm{SR}} = \left(\frac{y' - y_{\max}}{y_{\min} - y_{\max}}\right)^r, \quad \text{if } y_{\min} \le y' \le y_{\max} \tag{3}$$

$D_{\mathrm{SR}} = 1$, if $y' \le y_{\min}$ and $D_{\mathrm{SR}} = 0$, if $y' \ge y_{\max}$, where y' is the response value against each individual run, and $y_{\max}$ and $y_{\min}$ are the maximum and minimum response values among all experimental runs. r represents the weight $= 1$, and the upper limit and lower limit of the performance parameters from the Taguchi design were presented in Table 3.

The overall desirability index, which is nothing but the combination of desirability values of both the response, can be calculated by using following formula [11] where D_i is individual responses and k is the total number of responses.

$$D_0 = (D_1 \times D_2 \times D_3 \cdots D_i)^{(1/k)} \tag{4}$$

Table 4 shows the calculated desirability values of all individual responses along with overall desirability index. The higher the value of D_0 indicates better MRR with lesser roughness. Since the objective of this research is to maximize overall

Table 3 Upper limit ($y_{\max}$) and lower limit ($y_{\min}$) of MRR and SR

Performance parameters	Upper limit	Lower limit
Material removal rate (MRR)	8.166	1.473
Surface roughness (SR)	7.74	5.69

Table 4 Calculated desirability values responses and overall desirability index along with *S/N* ratio

Sl. no.	D_{MRR}	D_{SR}	D_0	*S/N* ratio
1	0.4469	0.433659	0.440222	−7.12657
2	0.3508	1.003902	0.59345	−4.53231
3	0.0066	0.026829	0.013281	−37.5356
4	0.0000	0.394146	0.003432	−49.2893
5	0.6701	0.906341	0.779322	−2.16567
6	0.2800	1.002927	0.529918	−5.51582
7	0.8242	0.001951	0.040101	−27.9368
8	0.4715	0.837073	0.628231	−4.03762
9	0.9999	0.343902	0.586397	−4.63617

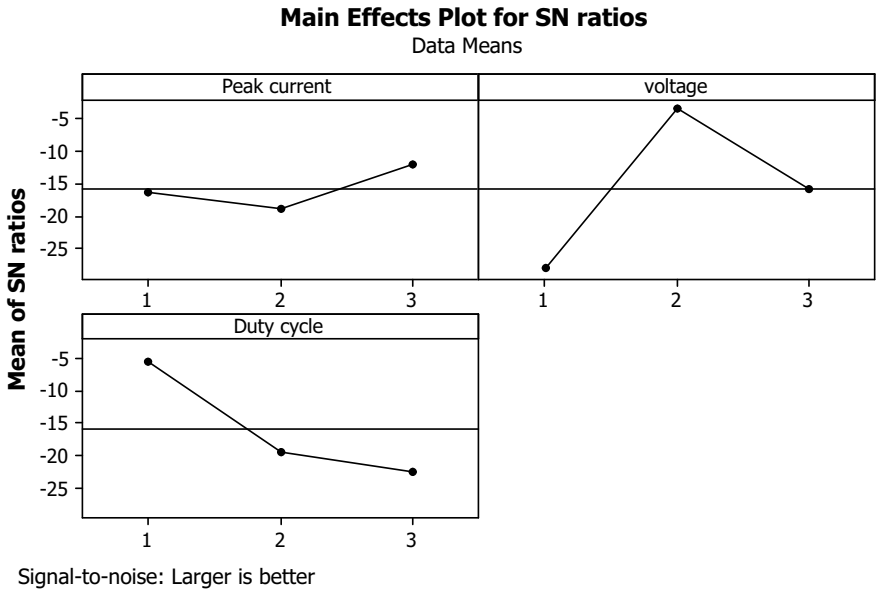

Fig. 5 Main effect plots

desirability index through optimal process setting, the signal-to-noise ratio was found out by using larger-the-better formulae and tabulated below.

Taguchi analysis is made by using MINITAB software with overall desirability index as output response. The main effect plot for *S*/*N* ratios of all the experimental run is given in Fig. 5. As the *S*/*N* ratio is calculated by taking larger-the-better criteria, hence, it is quite evidence that the optimal parameter setting is voltage 60 V, peak current 9 A and duty cycle 75.

5 Conclusion

In this study, an extensive experimental investigation was carried out to observe the behaviour of EDM process parameters and their effect during machining of Al–Al_2O_3 metal matrix composite. The study also aims to show the importance of each process parameter on the responses during machining. The analysed result shows that among all the three process parameters supply voltage plays a vital role for the chosen responses. The optimal parameter setting is found to be voltage at 60 V, peak current at 9 A and duty cycle at 75. The study concludes that Al–Al_2O_3 metal matrix composite with reinforcement weight percent of 10% can be machined effectively in EDM.

References

1. Surappa, M.K.: Aluminium matrix composites: challenges and opportunities. Sadhana **28**(1–2), 319–334 (2003)
2. Rosso, M.: Ceramic and metal matrix composites: routes and properties. J. Mater. Process. Technol. **175**(1), 364–375 (2006)
3. Rani, A., Nanimina, A.M., Ahmed, F.: Non-conventional machining of aluminium metal matrix composites. In: International Conference on Electrical Engineering, pp. 26–31 (2009)
4. Kumar, S., Singh, R., Singh, T.P., Sethi, B.L.: Surface modification by electrical discharge machining: a review. J. Mater. Process. Technol. **209**(8), 3675–3687 (2009)
5. Chen, Y., Mahdivian, S.M.: Analysis of electro-discharge machining process and its comparison with experiments. J. Mater. Process. Technol. **104**(1), 150–157 (2000)
6. Hocheng, H., Lei, W.T., Hsu, H.S.: Preliminary study of material removal in electrical-discharge machining of SiC/Al. J. Mater. Process. Technol. **63**(1), 813–818 (1997)
7. Singh, S., Maheshwari, S., Pandey, P.C.: Some investigations into the electric discharge machining of hardened tool steel using different electrode materials. J. Mater. Process. Technol. **149**(1), 272–277 (2004)
8. Velmurugan, C., Subramanian, R., Thirugnanam, S., Ananadavel, B.: Experimental investigations on machining characteristics of Al 6061 hybrid metal matrix composites processed by electrical discharge machining. Int. J. Eng., Sci. Technol. **3**(8), 87–101 (2011)
9. Purohit, R., Sahu, P.: Electric discharge machining and mathematical modeling of Al-Alloy-20% SiC composites using copper electrode. Int. J. Mech. Prod. Eng. Res. Dev. **2**, 37–46 (2012)
10. Jung, J.H., Kwon, W.T.: Optimization of EDM process for multiple performance characteristics using Taguchi method and Grey relational analysis. J. Mech. Sci. Technol. **24**(5), 1083–1090 (2010)
11. Panda, M.R., Mahapatraand, S.S., Mohanty, C.P.: Parametric investigation of friction stir welding on AA6061 using Taguchi technique. Mater. Today Proc. **2**(4–5), 2399–2406 (2015)

Parametric Optimization of Permeability of Green Sand Mould Using ANN and ANFIS Methods

Prafulla Kumar Sahoo, Sarojrani Pattnaik and Mihir Kumar Sutar

Abstract In foundry industries, various additives are used to increase the sand mould properties such as green strength and permeability number. In the present paper, camphor has been used as additive to enhance the mould's permeability so as to improve the casting quality. The optimum quantity of camphor that can be added to the sand mixture was found to be 1 wt%. Further, prediction of green sand mould permeability number has been done using both artificial neural network (ANN) and adaptive neuro-fuzzy interference system (ANFIS). The models were built using experimental data as per Taguchi's L27 orthogonal array (OA). The predicted permeability numbers by both models were found to be very close to that of experimental values; however, the predictability of ANFIS model was found to be better than ANN model as the error percent was less in former case.

Keywords ANN · ANFIS · OA · Permeability · Camphor

1 Introduction

Green sand moulds have been widely used for casting all types of materials. Sand is the main moulding material as it possesses desired foundry properties such as adequate refractoriness to withstand high temperature of the melt, good modulability to form moulds, good permeability so that gases and hot air can escape easily from the mould, chemical stability to remain unreactive with the hot melt and good collapsibility so that casting can be taken out easily [1]. Binders are used to provide cohesion to the foundry sand moulds so that it would gain enough strength to hold its shape after ramming. Binders in excess quantity when added to the foundry sand cause decrease in mould permeability which would otherwise cause casting defects such as blowholes and pinhole porosity [2]. The moisture content of green sand is nothing but the unbound water and a fraction of fragile physical bonding of water which can be removed on heating the mould at 105–110 °C [3]. If the moisture content rises

P. K. Sahoo · S. Pattnaik · M. K. Sutar (✉)
Mechanical Engineering Department, Veer Surendra Sai University of Technology, Burla, Odisha, India
e-mail: mihirsutar05@gmail.com

L. Li et al. (eds.), *Advances in Materials and Manufacturing Engineering*, Lecture Notes in Mechanical Engineering, https://doi.org/10.1007/978-981-15-1307-7_56

in the mould, the binder absorbs the water which causes its swelling thereby pushes the sand grains apart, and it results in decreased mould density and permeability.

Casting properties are very much affected by sand mould properties which depend on many controllable factors such as sand grain fineness number, clay and moisture content, percent of additives, degree of ramming, type of metal being cast and size of the casting [4]. It is very difficult to control all the factors at a time, and thus, few factors/parameters are kept constant, while others are varied. However, it is very much essential to determine the optimum level of each chosen moulding sand parameter for producing a sound casting. Permeability is one of the important sand mould properties which can be controlled by adequate venting, reduced ramming blows, increasing the sand grain size, etc. [5–7]. Chevan and Nanjundaswamy [8] found that the addition of flyash increased the mould's permeability. Seidu and Kutelu [9] determined that the sawdust containing sand mould showed higher green strength, whereas coal dust containing sand mould exhibited improved sand porosity and permeability.

Shehu and Bhatti [10] used yam flour as binder for making sand moulds which can be used in local foundries in Nigeria. The authors tested mould properties such as permeability, green and dry compressive strengths, collapsibility and shatter index. The results obtained from the aforementioned tests showed that the yam flour can be successfully used as sand binder for casting malleable iron and non-ferrous metals. Ameen and Hassan [11] studied about the effect of additives, namely oat flour, glycerine and sodium carbonate (Na_2CO_3) on the mechanical properties of carbon steel casting. The results revealed that the sand mould containing Na_2CO_3 exhibited improved casting mechanical properties. Solenicki et al. [12] determined the thermal conductivity of moulding sand mixtures using a specially designed instrument in order to control the scabbing defects, a very common problem occurring in green sand mould system.

Presently, many research works on improving the permeability of moulding sand using various additives such as flyash, coal dust and sawdust have been done. However, till now, there is not any literature where camphor powder has been used as additive to enhance the mould permeability. Camphor is a cheaply available crystalline organic compound whose melting temperature is about 179 °C and boiling temperature is about 204 °C. In the present work, camphor in the form of fine powder has been added to the moulding sand mixture containing silica sand, bentonite and water. The percent of camphor was varied from 1 to 3 wt% so as to determine its optimum quantity for increased mould permeability. The experiments were set as per Taguchi's L27 OA, and further, ANFIS and ANN models were developed based upon the experimental data to predict the mould's permeability number. Also, the predicted results were compared with the experimental ones to know the percentage of error by both methods.

2 Experimental Procedure

The three input process parameters at three levels, i.e. low (−1), medium (0) and high (+1) (Table 1) chosen in this study are clay percent, camphor powder and moisture content, and output process parameter is sand permeability number. The selection of the levels of the camphor powder was based on trial and error experiments conducted in the laboratory before going for real experimentation. It was found that below 1 wt% of it did not significantly improved the permeability of the sand mould, and above 3 wt% of it reduced the mould strength though increased the mould's permeability. Thus, the percent of camphor powder was limited to 3 wt%. The standard AFS sand specimens (2-inch height × 2-inch diameter) were prepared for determining the permeability number. The accuracy of the model depends on the number of training data, i.e. the more the data, the more the accuracy of the model. Therefore, Taguchi's L27 OA has been used to conduct the experiments. The chemical properties and grain shape of the silica sand are shown in Table 2 and Fig. 1.

Table 1 Input process parameters with their levels

Parameters (%)	Levels		
	− 1	0	+1
Camphor	1	2	3
Clay	8	9	10
Moisture	4	5	6

Table 2 Chemical properties of silica sand

Key constituents	SiO_2	Al_2O_3	K_2O	NaO	MgO	CaO	Fe_2O_3	TiO_2
wt%	95.61	1.74	0.31	0.01	0.01	0.02	0.62	0.04

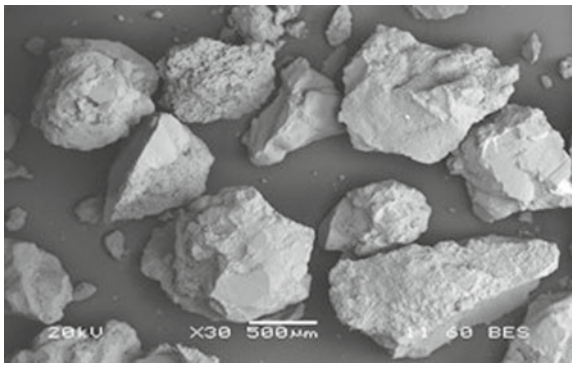

Fig. 1 Grain shape of silica sand used in sand mould preparation

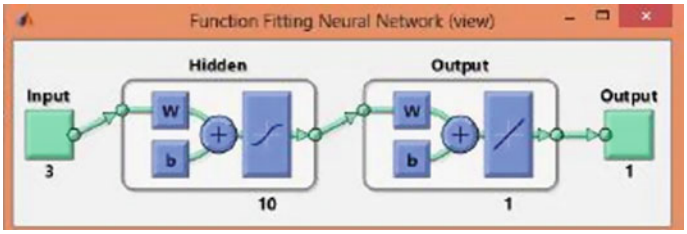

Fig. 2 Structure of neural network model

3 Methodology

3.1 ANN

The ANN structure is usually in three layers, namely input, hidden and output layers. Nowadays, advanced technique like ANN is also implemented in foundry industries to control the input process parameters of green sand mould for obtaining defect-free casting. Designing and training of the ANN model were done using MATLAB neural network toolbox 8.3. The experimental data in the form of input and target values has been stored in the workspace of the MATLAB. Figure 2 shows that the structure of the neural network model. The aforementioned input parameters were the inputs of the model, and the permeability was the output parameter. Using 70% of experimental data, the ANN model was trained, and further, the model was validated using 15% of experimental data.

3.2 Neuro-Fuzzy Model

The input process parameters and output process parameter remained same for ANN and ANFIS models. The training data was loaded to ANFIS using MATLAB Fuzzy Logic Toolbox 2.2.16, and it automatically created a Sugeno-type FIS for learning input and output data using Gaussian-type membership function. The structure of neurons and layers created by ANFIS model is shown in Fig. 3. The actual results by experimentation and the predicted results by both models have been presented in Table 3.

4 Results and Discussions

The analysis of mean (ANOM) was conducted on the experimental data, as shown in Table 4, and it is very clear that the optimum percent of camphor content in the moulding sand mixture is found to be 1 wt%. The camphor powder is the most

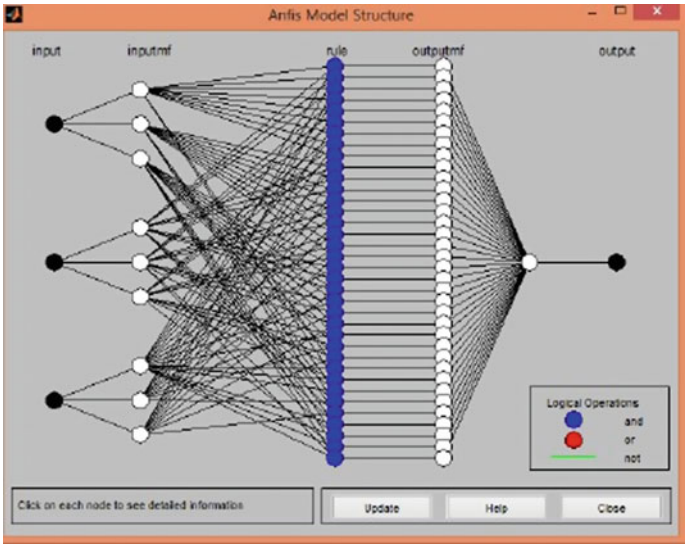

Fig. 3 Structure of neurons and layers of neuro-fuzzy model

significant process parameter influencing the mould permeability as it is ranked 1, which is followed by clay content. It was found that the increase in camphor content beyond 1 wt% led to decrease in mould's permeability. It might have occurred due to agglomeration of camphor particles at few places leading to nonuniform distribution in the sand mixture. The highest mould permeability can be achieved when the sand mixture contains 1 wt% camphor, 10 wt% clay and 6 wt% moisture.

70, 15 and 15% of experimental data were used for training, validation and testing the models. From the regression plot for ANN, it was found that the regression value for training was 0.95541, which is very close to 1 showing linear relationship between input and output. Similarly, the regression values for validation and testing were found to be 0.91127 and 0.88709. The results are predicted by both ANN and neuro-fuzzy models as shown in Table 3, it is observed that the maximum percentage of error in ANFIS model is 3.77%, and in case of ANN, the maximum percentage of error is 4.11%. It shows that the ANFIS model can predict the sand mould properties better than ANN model owing to its better learning and generalization capability at relatively less time. From the analysis it is observed that both the models have predicted as par with the experimental values and are in good agreement with that of the predicted values.

Table 3 Experimental and predicted results of permeability number of sand mould

Sl. No	Camphor powder	Clay	Moisture	Permeability no. (experimental)	ANN (predicted)	ANN (% error)	ANFIS (predicted)	ANFIS (% error)
1	1	8	4	277	266.42	3.82	279	0.72
2	1	8	5	265	271.41	2.42	267	0.75
3	1	8	6	272	277.50	2.02	276	1.47
4	1	9	4	249	235.11	5.58	252	1.20
5	1	9	5	266	244.77	7.98	267	0.37
6	1	9	6	259	258.45	0.21	269	3.86
7	1	10	4	247	212.72	13.88	262	6.07
8	1	10	5	231	210.48	8.88	234	1.29
9	1	10	6	221	219.12	0.85	224	1.36
10	2	8	4	258	242.65	5.95	259	0.39
11	2	8	5	241	249.98	3.73	243	0.83
12	2	8	6	233	251.44	7.91	236	1.29
13	2	9	4	230	224.21	2.52	233	1.30
14	2	9	5	224	222.41	0.71	248	10.71
15	2	9	6	217	220.60	1.66	225	3.69
16	2	10	4	209	195.46	6.48	214	2.39
17	2	10	5	198	195.53	1.25	205	3.53
18	2	10	6	200	198.90	0.55	201	0.5
19	3	8	4	222	225.32	1.50	222	0
20	3	8	5	218	230.11	5.56	221	1.36
21	3	8	6	213	228.95	7.49	217	1.88
22	3	9	4	226	219.45	2.90	229	1.33
23	3	9	5	216	210.39	2.60	246	13.89
24	3	9	6	206	200.86	2.50	240	16.51
25	3	10	4	203	193.51	4.67	207	1.97
26	3	10	5	201	189.61	5.67	238	18.41
27	3	10	6	195	198.08	1.58	204	4.62

Table 4 ANOM of sand mould permeability number

Input parameter	Camphor powder (%)	Clay (%)	Moisture (%)
Level			
1	254.1	244.3	235.7
2	223.3	232.6	228.9
3	211.1	211.7	224.0
Delta	43.0	32.7	11.7
Rank	1	2	3

5 Conclusions

The conclusions drawn from present work are given below:

- Camphor powder can be used as additive for increasing the sand mould's permeability.
- The optimum quantity of camphor powder that can be added to the sand mixture is 1 wt%, and thereafter, permeability decreases.
- The highest mould permeability can be achieved when the sand mixture contains 1 wt% camphor, 10 wt% clay and 6 wt% moisture.
- ANFIS model better predicted the permeability number of sand mould as regards to ANN model.

References

1. Orumwense, F.F.O.: Moulding properties of synthetic sand mixtures. A Comp. Study. Scand. J. Metall. **31**, 100–106 (2002)
2. Surekha, B., Kaushik, L.K., Pandey, A.K., Vundavilli, P.R.: Parappagoudar multi-objective optimization of green sand mould system using evolutionary algorithms. Int. J. Adv. Manuf. Techol. **58**, 9–17 (2012)
3. Baker, S.G.: Building the foundation for green sand. Mod. Cast. **95**, 26–29 (2005)
4. Beeley, P.R.: Foundry man **73**, xix–xvi (1980)
5. Ihom, A.P., Ogbodo, J.N., Allen, A.M., Nwonye, E.I., Iiochionwu, C.: Analysis and prediction of green permeability values in sand moulds using multiple linear regression model. Afr. J. Eng. Res. **2**, 8–13 (2014)
6. Brown, J.R.: Foseco Foundryman's Handbook. 10th Edn. Pergamon Press Plc. pp. 10–68 (1994)
7. Heine, R.W., Loper Jr., C.R., Rosenthal, P.C.: Principles of Metal Casting, 2nd edn, pp. 100–150. Tata Mcgraw-Hill Publishing Company Ltd, New Delhi (1967)
8. Chavan, T.K., Nanjundaswamy, H.M.: Effect of variation of different additives on green sand mold properties for olivine sand. Int. J. Res. Eng. Adv. Technol. **1**(4), 2320–8791 (2013)
9. Seidu, O.S., Kutelu, B.J.: Effects of additives on some selected properties of base sand. J. Minerals Mater Charact. Eng. **2**, 507–512 (2014)
10. Shehu, T., Bhatti, R.S.: The use of yam flour (starch) as binder for sand mould production in nigeria. World Appl. Sci. J. **16**(6), 858–862 (2012)
11. Ameen, H.A., Hassan, K.S.: Effect of the sand mould additives on some mechanical properties of carbon steel ck45 casts. J. Eng. **4**(17), 729–739 (2017)
12. Solenicki, G., Budic, I., Ciglar, D.: Determination of thermal conductivity in foundry mould mixtures. Metalurgija **49**(1), 3–7 (2010)

Accurate Estimation of Mixed-Mode Stress Intensity Factors Using Crack Flank Displacements

S. Sajith, K. S. R. K. Murthy and P. S. Robi

Abstract Accurate estimation of mixed-mode stress intensity factors is essential for the fracture and fatigue studies of structural components. A recently proposed displacement-based method utilizing the nodal values of crack opening and crack sliding displacements for the estimation of stress intensity factors is discussed in this work. Convergence characteristics of the present method are studied using finite element meshes of various mesh densities. The performance analysis of the present method is carried out using various benchmark examples available in literature, and the SIF solutions are compared with the commonly used techniques such as displacement extrapolation, interaction integral and *J*-integral techniques. The present method requires less computational efforts only than its path independent integral counterparts. Furthermore, unlike the other popular displacement method considered in this study, the present method also provides the sign of the mode II stress intensity factor. This enables the present method to be used for the fatigue crack growth simulations.

Keywords Stress intensity factor · Crack · Mixed mode fracture · Displacement technique · Fatigue crack growth

1 Introduction

In linear elastic fracture mechanics, the strength and structural integrity of the cracked structured are evaluated using the stress intensity factor (SIF), proposed by Irwin [1]. SIF also plays a vital role in estimating the fatigue life of structural components [2]. Due to which many analytical, experimental and numerical methods are in use for the SIF determination.

A summary of analytical and semi-analytical solutions for SIF solutions of simple geometries is available in the handbooks [3, 4]. Various numerical methods, especially finite element methods (FEM) and boundary element-based methods, are

S. Sajith (✉) · K. S. R. K. Murthy · P. S. Robi
Department of Mechanical Engineering, Indian Institute of Technology Guwahati, Guwahati 781039, India
e-mail: s.sajith@iitg.ac.in

L. Li et al. (eds.), *Advances in Materials and Manufacturing Engineering*, Lecture Notes in Mechanical Engineering, https://doi.org/10.1007/978-981-15-1307-7_57

widely used for the estimation of SIFs in practical applications. The development of quarter-point singular element (QPE) [5] solved the problem associated with the crack tip singularity. Several FEM-based methods employing QPEs at the crack tip have been developed [6–8]. These SIF determination methods can be broadly classified into stress based, displacement based and energy based. The commonly used SIF estimation methods are displacement extrapolation technique (DET) [9], displacement correlation technique (DCT) [10], interior collocation technique [11], *J*-integral [12] and interaction integral (*I*-integral) [13].

The path independent integral methods and the DET are widely used in commercial finite element packages such as ANSYS and ABAQUS. The independent path methods offer an accurate solution, but the evaluations have to be performed on a number of contours, which in turn requires more computational effort. The interior collocation method offers accurate solutions but requires special mesh pattern around the crack tip. The DET technique is incorporated into the commercial FE package such as ANSYS (KCALC command), but for mixed-mode loading, it fails to provide the sign of the mode II SIF and thus cannot be used for the fatigue crack growth simulations.

In damage tolerance analysis and in fatigue crack growth studies [2, 14, 15] involving numerous steps of analysis, an accurate and simple method for the determination of mixed-mode I/II stress intensity factor is preferred. Recently, Sajith et al. [16] proposed a simple and efficient technique for the determination SIFs under mixed-mode loading. The primary objective of this study is to emphasize the importance of the proposed SIF evaluation method using additional benchmark problems.

2 Theoretical Background

The method proposed is based on the generalized Westergaard's approach proposed by Sanford [19] and using the modified Airy's stress function for mode I (opening mode) and mode II (shear mode). The detailed formulations of the proposed technique are given in [16, 17]. The proposed technique utilizes the crack flank opening displacement (COD) and crack flank sliding displacement (CSD) for the estimation of the mixed-mode (I/II) SIFs.

The crack tip displacements under opening mode (mode I) and sliding mode (mode II) in terms of three parameters can be written as [16]

$$u^{\mathrm{I}} = \frac{A_0}{2G} r^{1/2} \left[(\kappa - 1) \cos\frac{\theta}{2} + \sin\theta \sin\frac{\theta}{2} \right] + \frac{A_1}{2G} r^{3/2} \left[\frac{(\kappa - 1)}{3} \cos\frac{3\theta}{2} - \sin\theta \sin\frac{\theta}{2} \right] + \frac{B_0(\kappa + 1)}{4G} r \cos\theta$$

$$v^{\mathrm{I}} = \frac{A_0}{2G} r^{1/2} \left[(\kappa + 1) \sin\frac{\theta}{2} - \sin\theta \cos\frac{\theta}{2} \right] +$$

$$\frac{A_1}{2G}r^{3/2}\left[\frac{(\kappa+1)}{3}\sin\frac{3\theta}{2} - \sin\theta\cos\frac{\theta}{2}\right] - \frac{B_0\nu(\kappa+1)}{4G}r\sin\theta \tag{1}$$

$$u^{\mathrm{II}} = \frac{C_0}{2G}r^{1/2}\left[(\kappa+1)\sin\frac{\theta}{2} + \sin\theta\cos\frac{\theta}{2}\right] + \frac{C_1}{2G}r^{3/2}\left[\frac{(\kappa+1)}{3}\sin\frac{3\theta}{2} + \sin\theta\cos\frac{\theta}{2}\right] + \frac{D_0(\kappa+1)}{4G}r\sin\theta$$

$$v^{\mathrm{II}} = \frac{C_0}{2G}r^{1/2}\left[(1-\kappa)\cos\frac{\theta}{2} + \sin\theta\sin\frac{\theta}{2}\right] + \frac{C_1}{2G}r^{3/2}\left[\frac{(1-\kappa)}{3}\cos\frac{3\theta}{2} - \sin\theta\sin\frac{\theta}{2}\right] - \frac{D_0(\kappa+1)}{4G}r\cos\theta \tag{2}$$

where u^{I},v^{I} are the opening mode displacements obtained from FE analysis in x and y directions, respectively (Fig. 1), and u^{II}, v^{II} are sliding mode displacements (Fig. 1a). $\kappa = (3-\nu)/(1+\nu)$ for plane stress conditions. G is the modulus of rigidity and ν is Poisson's ratio.A_0, A_1, B_0 and C_0, C_1, D_0 denotes coefficients of Generalized Westergaard [18] in opening and sliding modes, respectively. The COD and CSD can be superimposed to obtain the mixed-mode (I/II) displacements.

$$u = u^{\mathrm{I}} + u^{\mathrm{II}} \text{ and } v = v^{\mathrm{I}} + v^{\mathrm{II}} \tag{3}$$

Figure 1b shows a typical crack tip mesh pattern along with the QPEs. The points 1 and 2 are at the quarter-point nodes at opposite crack flanks (with node 1 being at $\theta = +180°$ and node 2 at $\theta = -180°$, respectively) and nodes 3 and 4 are the corner nodes of the crack flank QPEs. Referring to Eq. (3), for $\theta = \pm 180°$ (i.e., at the crack faces) the u and v components of the displacement in mixed-mode loading conditions can be obtained.

The crack opening displacements Δv and Δu in any loading is given as

$$\Delta v = v_{180°} - v_{-180°} = \frac{A_0(\kappa+1)}{G}r^{1/2} - \frac{A_1(\kappa+1)}{3G}r^{3/2}$$

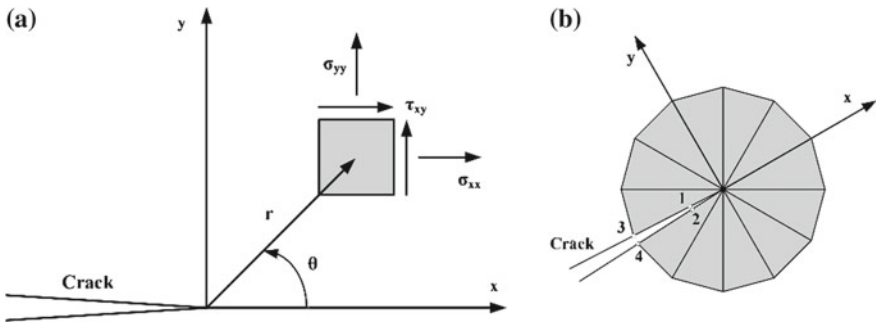

Fig. 1 **a** Coordinate system around the crack tip and **b** QPEs around the crack tip

$$\Delta u = u_{180^\circ} - u_{-180^\circ} = \frac{C_0(\kappa+1)}{G} r^{1/2} - \frac{C_1(\kappa+1)}{3G} r^{3/2} \tag{4}$$

By solving the above Eq. (4) at two radial locations r_1 (or r_2) and r_3 (or r_4) on the crack flank for A_0 and C_0, one can calculate the mixed-mode SIFs K_{I} and K_{II} as

$$K_{\mathrm{I}} = \sqrt{2\pi} A_0 \quad \text{and} \quad K_{\mathrm{II}} = \sqrt{2\pi} C_0 \tag{5}$$

It can be noticed from Eqs. (4) and (5) that actual signs (positive or negative) of the SIFs (which depends on the direction of the crack front and the loading direction) can also be furnished by the proposed technique.

3 Numerical Examples

Numerical evaluation is carried out for the performance validation of the present method, and benchmark problems available in the literature are utilized for this purpose. FE analysis of the benchmark examples considered in this study is carried out using the commercial software ANSYS. Meshing is done using eight-noded isoparametric quadrilateral (Q8) elements, and collapsed Q8 QPEs are used around the crack tip to form a spider web pattern. For modeling the material response, plane stress conditions are assumed. Young's modulus $E = 1.0$, Poisson's ratio $\nu = 0.3$ and the applied stress $\sigma = 1.0$ are assumed in all the example problems. SIFs are also computed using the DET available in ANSYS (KCALC), *J*-integral and *I*-integral techniques. In order to study the efficacy of the crack flank displacement technique, these values along with the published solutions are compared with that obtained using the present technique.

3.1 Slant Edge Cracked Plate Subjected to Bending Loads

The benchmark example assessed here is a slant edge cracked plate (SECP) subjected to bending loads (as shown in Fig. 2a). The geometric parameters for this problem are $h/b = 1.0$, $h_1/h = 1.5$ and $a/b = 0.3,\ 0.4,\ 0.6$. Due to lack of symmetry, the whole domain is modeled using finite elements. Figure 2b–d shows the three different finite element meshes employed to study the convergence characteristics of the proposed method using the SECP configuration with $a/b = 0.4$. The ratio of the length of QPE to the crack length $\left(L_Q/a\right)$ of meshes of different mesh density is 0.4, 0.2 and 0.1 for mesh 1, mesh 2 and mesh 3, respectively. The number of elements (NE) and number of nodes (NN) in each mesh are also shown in Fig. 2. Tables 1 and 2 show the results of the analyses for the normalized K_{I} and K_{II}, respectively.

It is very interesting to notice from the results of Tables 1 and 2 that accurate values of both the SIFs K_{I} and K_{II} have been estimated by the present technique.

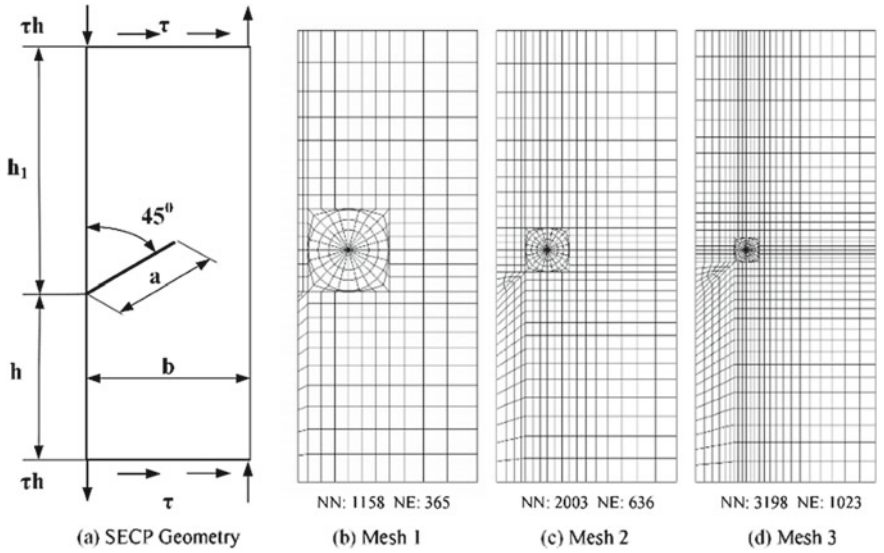

Fig. 2 **a** Geometry of SECP and **b–d** different meshes used for finite element analysis

Table 1 Normalized mode I SIFs

a/b	Mesh	$K_I/\sigma\sqrt{\pi a}$			
		Chen [19]	Present	DET	*I*-integral
0.3	Mesh 1	0.687	0.6859	0.6859	0.6876
	Mesh 2	0.687	0.6873	0.6873	0.6875
	Mesh 3	0.687	0.6878	0.6878	0.6876
0.4	Mesh 1	0.727	0.7252	0.7252	0.7280
	Mesh 2	0.727	0.7268	0.7264	0.7280
	Mesh 3	0.727	0.7278	0.7275	0.7281
0.6	Mesh 1	0.883	0.8824	0.8823	0.8836
	Mesh 2	0.883	0.8833	0.8834	0.8837
	Mesh 3	0.883	0.8836	0.8837	0.8838

Furthermore, the convergence of the extracted SIFs can be noticed from Tables 1 and 2. The results in Tables 1 and 2 clearly show that the proposed technique is capable of providing accurate the mixed-mode (I/II) SIFs even in the relatively coarse meshes similar to that of J and I integrals. It can be noted from the above examples that the maximum percentage relative error in the computed SIFs by the present technique is less than 1%.

Table 2 Normalized mode II SIFs

a/b	Mesh	$K_{II}/\sigma\sqrt{\pi a}$			
		Chen [19]	Present	DET	I-integral
0.3	Mesh 1	0.314	0.3116	0.3119	0.3145
	Mesh 2	0.314	0.3125	0.3128	0.3144
	Mesh 3	0.314	0.3135	0.3133	0.3144
0.4	Mesh 1	0.316	0.3155	0.3153	0.3161
	Mesh 2	0.316	0.3154	0.3151	0.3159
	Mesh 3	0.316	0.3151	0.3151	0.3159
0.6	Mesh 1	0.345	0.3477	0.3478	0.3437
	Mesh 2	0.345	0.3456	0.3455	0.3436
	Mesh 3	0.345	0.3443	0.3445	0.3436

4 Conclusions

A simple and efficient displacement-based method, using the crack flank displacements, is evaluated in this work for the estimation of mode I, mode II and mixed-mode I/II stress intensity factors. The results presented in this paper clearly show that irrespective of the mesh refinement, the present method is capable of estimation of accurate values of SIFs. The proposed method is also providing the sign of the mode II stress intensity factors which makes it convenient to use for the fatigue crack growth simulations. Owing to the simplicity and ease of implementation, the present method can easily be employed in the existing commercial FE packages.

Notes

The present work is an extension of [16] using different benchmark examples to show the efficiency of the crack flank displacement-based method over a wide range of typical cracked configurations. More detailed explanations about the proposed method and the complete theoretical formulations can be found in [16].

References

1. Irwin, G.: Analysis of stresses and strains near the end of a crack transversing a plate. J. Appl. Mech. **24**, 361–370 (1957)
2. Sajith, S., Murthy, K.S.R.K., Robi, P.S.: Prediction of Accurate mixed mode fatigue crack growth curves using the paris' law. J. Inst. Eng. Ser. C **100**, 165–174 (2019)
3. Tada, H., Paris, P.C., Irwin, G.R.: The Stress Analysis of Cracks Handbook, 3rd Edn. Three Park Avenue New York, NY 10016-5990: ASME; (2000). https://doi.org/10.1115/1.801535
4. Murakami, Y.: Stress Intensity Factors Handbook. Pergamon (1987)
5. Henshell, R.D., Shaw, K.G.: Crack tip finite elements are unnecessary. Int. J. Numer. Methods Eng. **9**, 495–507 (1975). https://doi.org/10.1002/nme.1620090302

6. Murthy, K.S.R.K., Mukhopadhyay, M.: Unification of stress intensity factor (SIF) extraction methods with an h-adaptive finite element scheme. **17**, 509–520 (2001)
7. Banks-Sills, L., Sherman, D.: Comparison of methods for calculating stress intensity factors with quarter-point elements. **32**, 127–140 (1986). https://doi.org/10.1007/bf00019788
8. Lim, I.L., Johnston, I.W., Choi, S.K.: On stress intensity factor computation from the quarter-point element displacements. Commun. Appl. Numer. Methods **8**, 291–300 (1992)
9. Barsoum, R.S.: Triangular quarter-point elements as elastic and perfectly-plastic crack tip elements. Int. J. Numer. Methods Eng. **11**, 85–98 (1977). https://doi.org/10.1002/nme.1620110109
10. Tracey, D.M.: Discussion of 'on the use of isoparametric finite elements in linear fracture mechanics' by R.S. Barsoum. Int. J. Numer. Methods Eng. **11**, 401–402 (1977)
11. Jogdand, P.V., Murthy, K.S.R.K.: A finite element based interior collocation method for the computation of stress intensity factors and T-stresses. Eng. Fract. Mech. **77**, 1116–1127 (2010)
12. Rice, J.R.: A path independent integral and the approximate analysis of strain concentration by notches and cracks. J. Appl. Mech. **35**, 379 (1968). https://doi.org/10.1115/1.3601206
13. Shih, C.F., Moran, B., Nakamura, T.: Energy release rate along a three-dimensional crack front in a thermally stressed body. Int. J. Fract. **30**, 79–102 (1986). https://doi.org/10.1007/bf00034019
14. Sajith, S., Murthy, K.S.R.K., Robi, P.S.: Fatigue crack growth and life prediction under mixed-mode loading. AIP Conf. Proc. **1943**, 020068 (2018). https://doi.org/10.1063/1.5029644
15. Sajith, S., Murthy, K.S.R.K., Robi, P.S.: Fatigue life prediction under mixed-mode loading using equivalent stress intensity factor models. In: Jayakumar, V., Ranganathan, S., Devika, D., Sridevi, S. (Eds.) MATEC Web Conference, vol. 172, p. 03005 (2018). https://doi.org/10.1051/matecconf/201817203005
16. Sajith, S., Murthy, K., Robi, P.: A simple technique for estimation of mixed mode (I/II) stress intensity factors. J. Mech. Mater. Struct. **13**, 141–154 (2018). https://doi.org/10.2140/jomms.2018.13.141
17. Sajith, S., Murthy, K.S.R.K., Robi, P.S.: A novel method for computation of mixed mode stress intensity factors of 2D cracked configurations. In: Proceeding 5th International Congress on Computational Mechanics and Simulation, pp. 840–847 (2014). https://doi.org/10.3850/978-981-09-1139-3_202
18. Sanford, R.J.: A critical re-examination of the westergaard method for solving opening-mode crack problems. Mech. Res. Commun. **6**, 289–294 (1979)
19. Chen, C.H., Wang, C.L.: Stress intensity factors and T-stresses for offset double edge-cracked plates under mixed-mode loadings. Int. J. Fract. **152**, 149–162 (2008)

Performance Comparison of Nanofluids in Laminar Convective Flow Region Through a Channel

Md Insiat Islam Rabby, S. A. M. Shafwat Amin, Sazedur Rahman, Farzad Hossain, Mohammad Ahnaf Shahriar and A. K. M. Sadrul Islam

Abstract In this numerical study, the thermal performance of Al_2O_3–H_2O, CuO–H_2O, SiC–H_2O and TiO_2–H_2O nanofluids has been analyzed for laminar flow region of a channel which is fully developed. For this purpose, the figure of merit (FOM), power for pumping, Nusselt number enhancement ratio and heat transfer coefficient ratio of base fluid and nanofluids are calculated for constant Reynolds number and (1–5%) volume concentration of four nanofluids. The computational analysis and results show that the FOM is higher for Al_2O_3–water nanofluid compared to others at constant Reynolds number. On the other hand, the Nusselt number enhancement ratio is higher for CuO–water nanofluid compared to others, and Al_2O_3–water shows higher enhancement ratio of heat transfer coefficient compared to others, and this is happened because of the higher thermal and physical properties like thermal conductivity, density and viscosity of the Al_2O_3–water. And at constant heat transfer coefficient, the pumping power has been reduced for all the nanofluids compared to pure water, and Al_2O_3–water shows more reduction of pumping power compared to other nanofluids.

Keywords Figure of merit · Pumping power · Nusselt number enhancement ratio · Heat transfer enhancement ratio

1 Introduction

From the last few decades, the importance and research on nanotechnology are the most fundamental and effective topics of thermal engineering. At present to improve heat transfer efficiency and heat transfer rate, nanoparticles are used with base fluids. Beside this, the utilization of pumping power to get this enhancement is also less, and this is the most advantage thing to using nanoparticles in working fluids. Basically, by adding small amount of solid particles with the base or working fluid, the thermal conductivity of the fluid can be increased noticeably. And by using this concept,

M. I. I. Rabby (✉) · S. A. M. Shafwat Amin · S. Rahman · F. Hossain · M. A. Shahriar · A. K. M. Sadrul Islam
Military Institute of Science and Technology, Dhaka, Bangladesh
e-mail: insiatislam8@gmail.com

L. Li et al. (eds.), *Advances in Materials and Manufacturing Engineering*, Lecture Notes in Mechanical Engineering, https://doi.org/10.1007/978-981-15-1307-7_58

researchers have been made nanofluid which is the combination of base fluids (water, engine oil or ethylene glycol) and very small amount of solid particles at nanoscale size (1–100 nm). Al_2O_3, CuO, TiO_2, SiC, SiO_2, Fe_2O_3, MgO, etc. particles are used as nanoparticle to mix with base fluids. Different researchers carried out their investigation on nanofluids at heat transfer application. Xuan and Li 2003 [1] worked on Cu–water nanofluid through a 10-mm inward distance across tube for convective transfer of heat. The results from their investigation reveal that at turbulent, the friction factors for volume fraction 1 and 2% of nanofluids are showed similar value compared to pure water. Williams et al. 2008 [2] experimentally carried his study on the convective turbulent heat exchange of alumina–H_2O and zirconium–H_2O water nanofluids in a tube. They investigated that nanofluids provide enhancement of heat exchange and behavior of viscous pressure drop. Rea et al. [3] led an investigation on the convective warmth exchange and weight drop of alumina–H_2O and zirconium–H_2O nanofluids in a tube for laminar flow which width is 4.5 mm (inward). But from their discoveries, there is no deviation in convective heat exchange and weight drop of nanofluid has been found. Heris et al. [4] played out an exploratory investigation to decide the loss of pressure and transfer of heat qualities of Al_2O_3–H_2O and CuO–H_2O nanofluids through a triangular conduit under uniform heat flux at laminar flow area. Their outcomes demonstrated that, at similar/constant volume concentration and Reynolds number, utilizing CuO nanoparticle is less beneficial than Al_2O_3 nanoparticles. Yu et al. [5] worked with SiC–water nanofluid for turbulent flow and a comparison parameter the figure of the merit which is denoted by heat transfer enhancement and pumping power ratio were presented in their study. Their result showed that SiC–water nanofluid provided the value of FOM 0.8 and Al_2O_3–water nanofluid provided the value of FOM 0.6 which indicates that SiC–water nanofluid is more favorable in case of pumping power penalty. Yu and Dong [6] studied on convective thermal performance investigation of nanofluids (Al_2O_3–water and Al_2O_3–polyalphaolefin) for cooling applications, and their result reveals that in case of constant pumping power condition, the nanofluid's and the base fluid's overall effectiveness will not be changed significantly when both the hydrodynamic and thermal performances are considered. Sarkar [7] carried out his research work on performance analyses of the nanofluids Al_2O_3, TiO_2, CuO and Cu as cooling application for cooled gas cooler (shell-and-tube) in CO_2 refrigeration cycle which is transcritical. Their research shows that the effectiveness of nanofluid is preferable to use it as coolant in the gas cooler to develop and improve the performance of the cycle of CO_2 refrigeration. Monjur [8] investigated on energy savings of heat exchanger, and they showed that for constant heat transfer coefficient, Al_2O_3–water, CuO–water and TiO_2–water required less pumping power and volumetric flow rate compared to pure water. Ingole et al. [9] investigated on pumping power of car radiator by using Al_2O_3–water nanofluid, and they find that 2% volume concentration of Al_2O_3–water need 23.81% less pumping power compared to pure water.

The above maximum researches only show higher heat transfer rate by using nanofluids, but very few papers show the justification of required pumping power study to get the higher heat transfer rate and also comparison between nanofluids

on the basis of required pumping power. So in the present work, the thermal performance of four nanofluids Al_2O_3–H_2O, CuO–H_2O, SiC–H_2O and TiO_2–H_2O has been studied, and the results are compared on the basis of pumping power requirement. Moreover, the figure of merit (FOM), Nusselt number enhancement ratio, heat transfer coefficient ratio and pumping power of base fluid along with nanofluids are calculated for constant Reynolds number and (1–5%) volume fraction. Basically, the overall performance of water-based nanofluids in the forced convective laminar regime is discussed in terms of three merits criteria. They are Nusselt number enhancement ratio, heat transfer enhancement ratio and figure of merit (FOM). The first two ones are usually used to compare different fluids of heat transfer, while other can be mainly used to evaluate nanofluid's overall energetic performance for operating condition in a real system. Meanwhile, a higher value of figure of merit represents more gain in the heat exchange enhancement compared to the pumping power increment.

2 Physical Geometry and Boundary Condition

Parallel plates with a steady heat flux on both walls are presented to examine the performance of all the nanofluids through the channel of Fig. 1 by employing numerical method using ANSYS fluent software. The distance between two horizontal plates is 4 mm, and length is 600 mm length. A constant uniform heat flux of 500 W/m^2 is applied on the wall boundary of the parallel plates, and fluid is permitted to flow with constant temperature of 303 K at the opening of the parallel plates with a presumption of no slip condition on the parallel plate's wall which are considered. All the heat exchange and fluid dynamic parameters are extricated after the thermal and hydrodynamic improvement of the fluid stream, and in this case, for taking all the

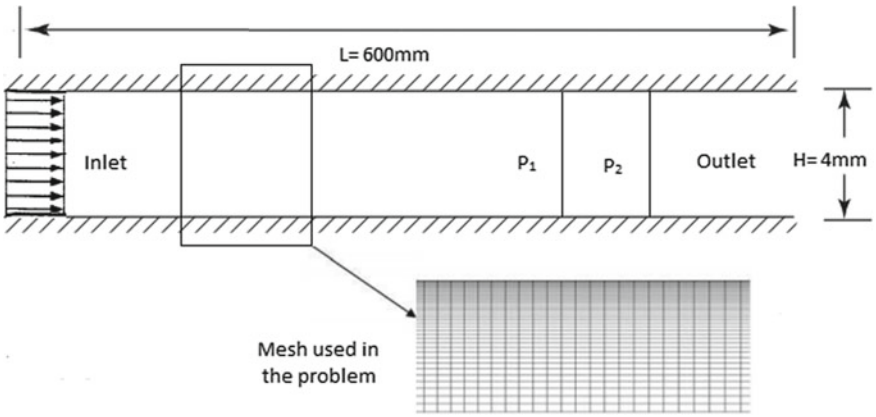

Fig. 1 Corresponding geometry of present work with mesh

measurements the standard entrance length is considered $x/D = 60$. For calculating the heat transfer enhancement and pressure loss, the temperatures are taken at line which is situated 590 mm from inlet, and pressures are taken at lines which are situated from 565 to 555 mm from the inlet.

3 Numerical and Computational Method

We use ANSYS (fluent) which is commercial computational fluid dynamics software for this numerical analysis. All the governing equations for momentum, mass, energy and laminar quantities have been solved by adopting a control volume technique. A simple algorithm has been used for velocity pressure coupling purpose, and a second-order upwind method has been used to solve energy and momentum equation. At inlet laminar inlet velocity and at the outlet boundary pressure, outlet is considered. Under relaxation factors, 0.4 for pressure, 0.76 for momentum, 1 for energy and 0.9 for density equation are considered for parallel plate. All the used nanoparticles with volume fractions (1, 2, 3, 4 and 5%) are mixed with water separately and tested with a wide range of Reynolds number 400–1100 and then results are compared with base fluid water.

4 Methodology

The governing equations for continuity, momentum and energy for forced convection under laminar steady-state flow conditions are represented as follows:

Continuity equation: In steady flow, the conversations of mass eq^{n}:

$$\frac{\partial u}{\partial x} + \frac{\partial v}{\partial y} = 0 \tag{1}$$

Momentum equation: For laminar flow, the momentum equation:

$$\rho\left(u\frac{\partial u}{\partial x} + v\frac{\partial u}{\partial y}\right) = \mu\frac{\partial^2 u}{\partial y^2} \tag{2}$$

Energy equation:

$$(E_{in} - E_{out}) = k\frac{d^2T}{\partial x^2}\mathrm{d}x\mathrm{d}y + k\frac{d^2T}{\partial y^2}\mathrm{d}x\mathrm{d}y = k\left(\frac{d^2T}{\partial x^2} + \frac{d^2T}{\partial y^2}\right)\mathrm{d}x\mathrm{d}y \tag{3}$$

5 Thermal and Fluid Dynamics Properties

The Reynolds number for nanofluids:

$$Re = \frac{\rho_{nf} U_{av} D_h}{\mu_{nf}} \tag{4}$$

Average Nusselt number:

$$Nu = \frac{h_c D_h}{K_{nf}} \tag{5}$$

Rate of heat transfer

$$Q_{nf} = m_{nf} C_{P_{nf}} \Delta T \tag{6}$$

Average heat transfer coefficient h_c:

$$h_c = \frac{Q_{nf}}{A_w(\Delta T)} \tag{7}$$

Temperature difference:

$$\Delta T = \frac{(T_w - T_o) - (T_w - T_i),}{\ln\left(\frac{T_w - T_o}{T_w - T_i}\right)} \tag{8}$$

Pressure difference:

$$\Delta P = \frac{f L \rho U^2}{2 D_h} \tag{9}$$

Nusselt number enhancement ratio

$$= \frac{Nu_{nf}}{Nu_{bf}} \tag{10}$$

Overall heat transfer coefficient enhancement ratio

$$= \frac{h_{nf}}{h_{nf}} \tag{11}$$

The pumping power per unit length:

$$W = \frac{(\pi/4) D^2 U_{av} \Delta P}{L} \tag{12}$$

The figure of merit,

$$\text{FOM} = \left(\frac{h_{nf}}{h_{bf}}\right)\left(\frac{W_{bf}}{W_{nf}}\right) \tag{13}$$

6 Thermophysical Properties of Nanofluids

Dynamic viscosity: There are several equations for dynamic viscosity; among them, we use Pak and Cho [10] equation for TiO_2, Nguyen [11] equation for CuO, Maiga [12] equation for Al_2O_3 and Chein [13] equation for SiC. The equation can be expressed as:

For TiO_2–water nanofluid:

$$\mu_{nf} = \mu_{bf}(1.0683 + 4.70\emptyset + 167.7\emptyset^2) \tag{14}$$

For CuO–water nanofluid:

$$\mu_{nf} = \mu_{bf}(1.475 - 0.319\emptyset + 0.051\emptyset^2 + 0.009\emptyset^3 \tag{15}$$

For Al_2O_3–water nanofluid:

$$\mu_{nf} = \left(1 + 7.3\emptyset + 123\emptyset^2\right)\mu_f \tag{16}$$

For SiC–water nanofluid:

$$\mu_{nf} = \mu_{bf}\left[1 + 10.6\emptyset + (10.6\emptyset)^2\right] \tag{17}$$

Thermal conductivity: There are several thermal conductivity equations; among them, we use Pak and Cho [10] equation for TiO_2, CuO and Al_2O_3. For SiC, we use Maxwell [14] mode equation. The following formulas are:

For TiO_2–water nanofluid:

$$K_{nf} = (1.0084 + 2.1796\emptyset) \tag{18}$$

For Al_2O_3–water nanofluid:

$$K_{nf} = K_{bf}(1.0021 + 7.3349\emptyset) \tag{19}$$

For SiC–water and CuO–water:

$$K_{nf} = \frac{K_p + 2K_{bf} + 2\left(K_p - K_{bf}\right)\emptyset}{K_p + 2K_{bf} - \left(K_p - K_{bf}\right)\emptyset \times K_{bf}} \tag{20}$$

Density: (Xuan and Roetzel, 2000) [15] eq^{n}

$$\rho_{nf} = \rho_p \emptyset + \rho_{bf}(1 - \emptyset) \tag{21}$$

Specific Heat: Pak and Cho, 1998 [10] equation:

$$C_{nf} = (1 - \emptyset)C_w + \emptyset C_p \tag{22}$$

7 Code Validation Test

For channel flow, at uniform velocity and constant heat flux water was passed through it and a range of Reynolds number (400-1100) were considered for calculating Nusselt numbers to validate the present work with validated equation of Nusselt number for channel flow. At fully developed zone, obtaining Nusselt number is compared with the constant value of Nusselt number 8.23 at constant heat flux for parallel plate and with the Pahor and Turtor [16] theoretical equation which is shown in Fig. 2. Pahor and Turton (1959) equation:

$$\boldsymbol{Nu} = 8.24\left(1 + \frac{3.79}{\boldsymbol{Pe}^2} + \ldots\right), \quad \boldsymbol{Pe} \gg 1 \boldsymbol{Pe} = \textbf{Pkclet number}; \tag{23}$$

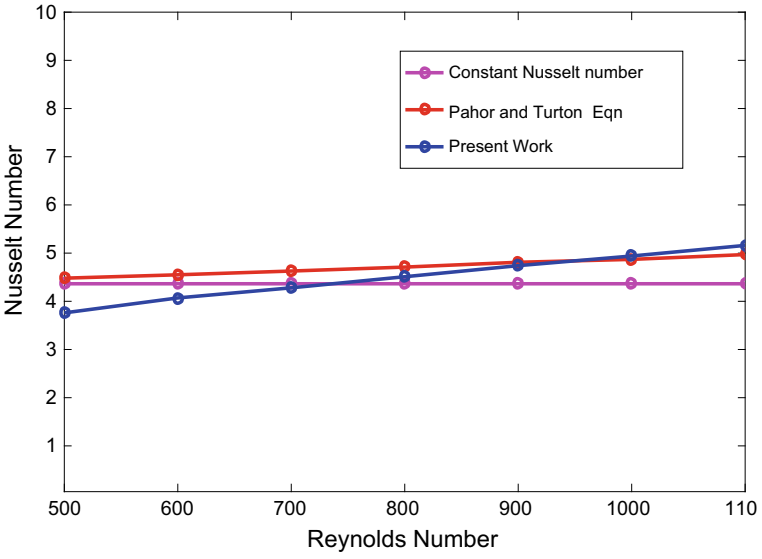

Fig. 2 Comparison of Nusselt number between experimental equation and current study for different Reynolds number of water

$$Nu = 8.118(1 - 0.031Pe), \quad Pe \ll 1 \tag{24}$$

8 Results

Displayed Fig. 3 indicates the effective heat transfer coefficient for Al_2O_3–water, CuO water, SiC–water and TiO_2–water nanofluids at a constant volume fraction of 3%. Other percentages showed similar trends. The result indicates that for all volume fractions of Al_2O_3 nanoparticles, the heat transfer coefficient is higher than other nanofluids. Similar trend has been also described by Mohammed et al. [17] and Koo and Kleinstreuer, [18]. Figure 4 shows the differentiation of pumping power requirement per unit length of Al_2O_3–water nanofluid with different values of heat transfer coefficient and volume concentration. From graphs, it is clear that by the increment of the values of heat transfer coefficient, the pumping power becomes higher in case of same volume concentration. For $\emptyset = 1$–5%, the pumping power for Al_2O_3–water nanofluids is reduced by 20–75% compared to water for same heat transfer rate. Other nanofluids provide similar trends. For CuO–water, the pumping power is reduced by 5% to 55%. For SiC–water and TiO_2–water nanofluids, the pumping

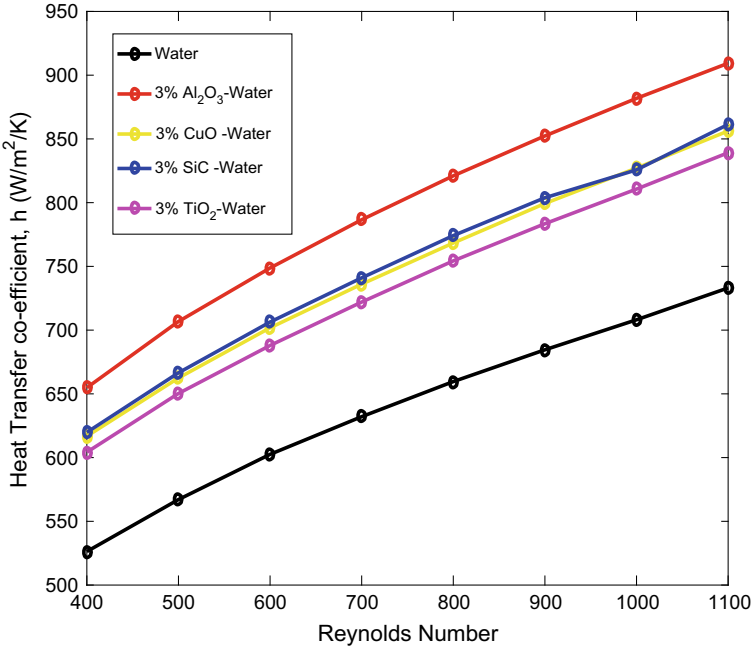

Fig. 3 Variation of heat transfer coefficient with Reynolds number of 3% volume fraction for all nanofluids

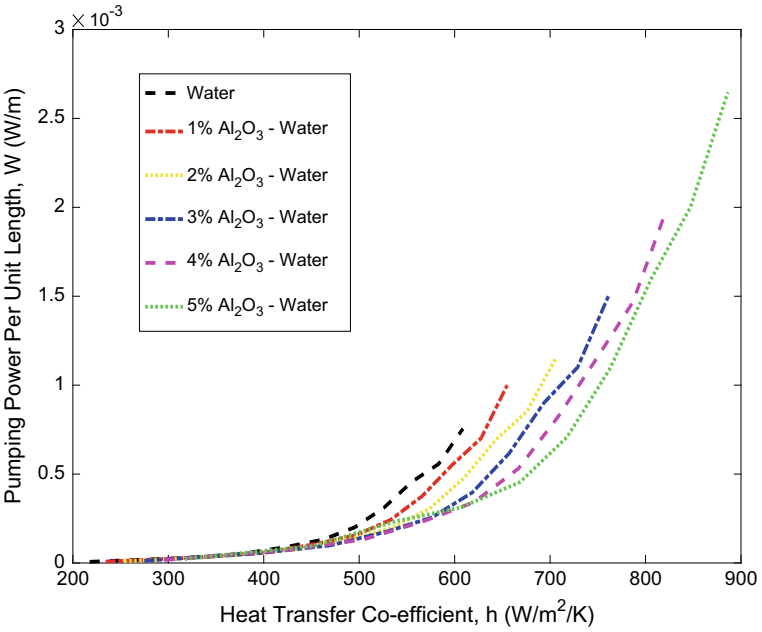

Fig. 4 Variation of pumping power per unit length with heat transfer coefficient for Al_2O_3–water nanofluid

power reduction is almost same 4–45% compared to pure water. Figure 5 shows, the change of pumping power with different heat transfer coefficient at constant volume fraction of 3%. Hence, the results of Fig. 5 indicates that Al_2O_3–water requires lower pumping power in comparison to others for all volume fractions. From Fig. 6, it is analyzed that Nusselt number enhancement ratio is increasing with the increase of volume fraction. Nusselt number enhancement ratio for Al_2O_3 is less than other three nanofluids. From Fig. 7, it is observed that with the increase of volume fractions, heat transfer coefficient enhancement ratio is also increasing. Here, Al_2O_3 shows more enhancement ratio than other three nanofluids, and TiO_2 gives less enhancement ratio comparatively with others. In Fig. 8, the FOM vs. volume fraction graph is shown which indicates that with increasing of volume fraction, FOM is also increasing at constant Reynolds number. For Al_2O_3–water, FOM is higher than other nanofluids; CuO and TiO_2 show almost same result. And more value of FOM indicates more heat transfer enhancement.

To analyze the performance of all used nanofluids, a comparison Table 1 has been introduced below. In this table, for all the nanofluids at a uniform heat transfer coefficient of 700 W/m^2-k for the optimum 3% volume concentration, the pumping power benefit, reduction in volumetric flow rate, pressure difference and mass flow rate have been analyzed for channel. For optimum 3% volume fraction of channel, pumping power benefit of Al_2O_3 is more than other nanofluids, and it is examined that SiC shows less pumping power benefit among them. Similarly, the mass flow

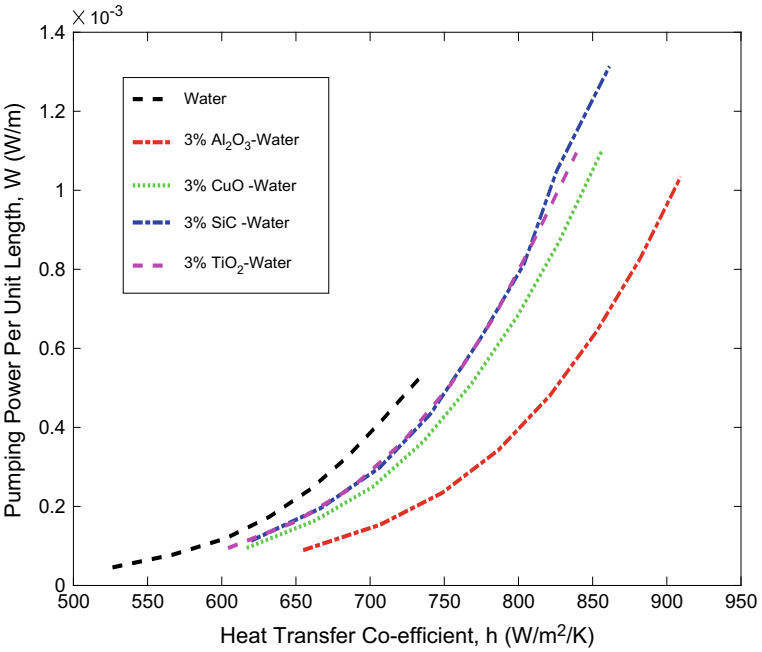

Fig. 5 Differentiation of pumping power per unit length with heat transfer coefficient of nanofluids

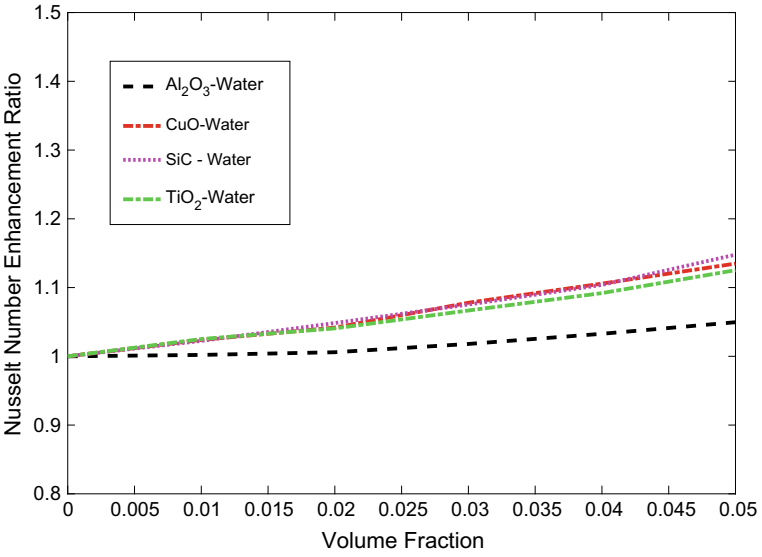

Fig. 6 Variation of Nusselt number enhancement ratio with volume fraction of all nanofluids

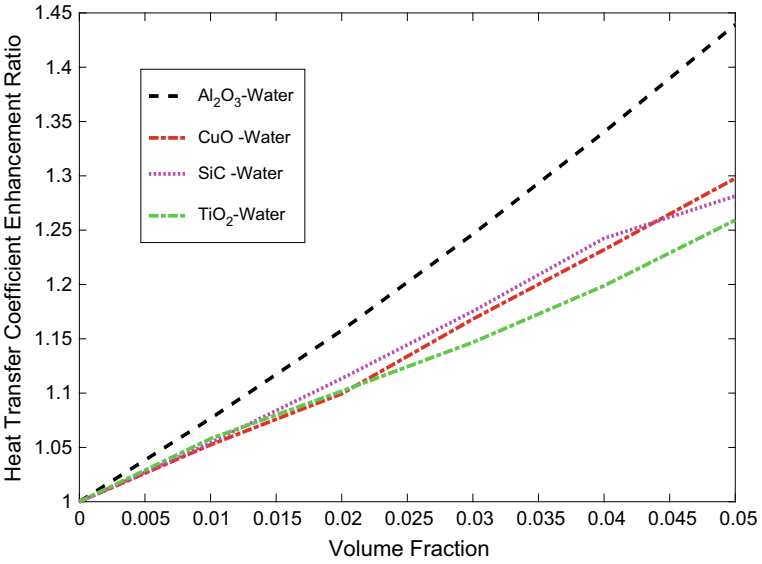

Fig. 7 Variation of heat transfer coefficient enhancement ratio with volume fraction of all nanofluids

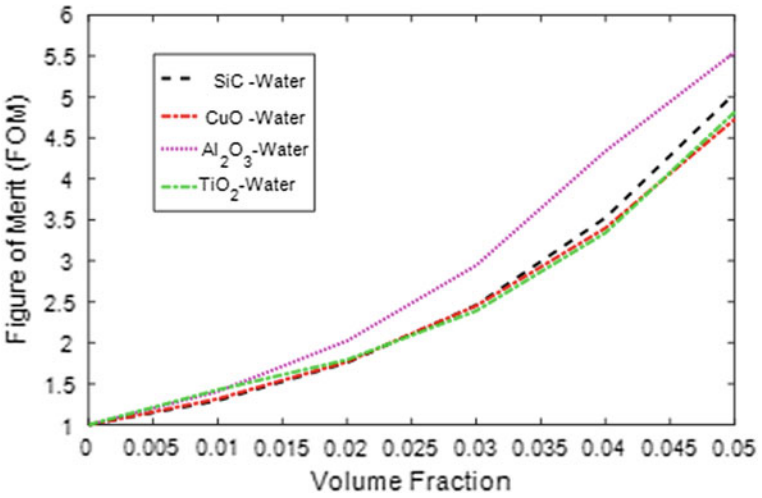

Fig. 8 Variation of FOM with volume fraction of all nanofluids

rate reduction for TiO_2 is less than other nanofluids, and Al_2O_3 gives more reduction in mass flow rate.

Table 1 Differentiation of performance of all the used nanofluids (Ø = 3%) with base fluid water

Type of fluid parameter	Water	3% Al_2O_3	3% CuO	3% SiC	3% TiO_2
Heat transfer coefficient (W/m^2-K)	700	700	700	700	700
Reynolds number	967	488	597	585	630
Nusselt number	9.1	7.50	8.43	8.41	8.4
Pressure loss (Pa/m)	0.7935	0.5032	0.67121	0.71838	0.6856
Pumping power per unit length (W/m)	0.000387	0.000147	0.000249	0.000280	0.000282
Power advantage (W/m)	–	0.000240	0.000138	0.000107	0.000105
Power advantage (%)	–	62%	36%	28%	27.5%
Velocity (m/s)	0.09685	0.05958	0.07275	0.07789	0.07838
Volumetric flow rate (m^3/s)	0.000004868	0.00000299	0.000003657	0.0000003915	0.000003940
Reduction in volumetric flow rate (%)	–	38.47%	24.87%	19.58%	19.06%
Mass flow rate (Kg/s)	0.004849	0.003250	0.004246	0.004160	0.004279
Reduction in mass flow rate (%)	–	33%	12.47%	14.2%	11.77%

9 Conclusion

In the present work, four different nanofluids Al_2O_3–water, CuO–water, SiC–water and TiO_2–water have been studied through typical parallel plates to observe the performance comparison between them on the basis of heat transfer enhancement and the pumping power benefits. Among the four nanofluids, Al_2O_3–water shows more heat transfer enhancement ratio compared to others, and also to get this more heat transfer, Al_2O_3–water required lower pumping power compared to others which is cleared from the graph of FOM. Beside this, Al_2O_3–water also needs lower volumetric/mass flow rate for getting higher heat transfer compared to water and other nanofluids which is also cleared from comparison table. However, TiO_2–water provides lowest performance between all, and CuO–water and SiC–water show almost same performance in heat transfer application on the basis of FOM and pumping power benefit.

References

1. Xuan, Y., Li, Q.: Investigation on convective heat transfer and flow features of nanofluids. ASME J. Heat Transfer **151–155**, 125 (2003). https://doi.org/10.1115/1.1532008
2. Williams, W., Buongiorno, J., Hu, L.-W.: Experimental Investigation of turbulent convective heat transfer and pressure loss of alumina/water and zirconia/ water nanoparticle colloids (nanofluids) in horizontal tubes. ASME J. Heat Transfer **130**(4), 042412 (2008). https://doi.org/10.1115/1.2818775

3. Rea, U., McKrell, T., Hu, L.-W., and Buongiorno, J.: Laminar convective heat transfer and viscous pressure loss of alumina-water and zirconia-water nanofluids. Int. J. Heat Mass Transfer **52**, 2042–2048 (2012). https://doi.org/10.1007/978-3-642-28314-7_65
4. Heris, S.Z., Etemad, S.G., Esfahany, M.N.: Experimental investigation of oxide nanofluids laminar flow convective heat transfer. Int. Commun. Heat Mass Transfer **33**, 529–535 (2006). https://doi.org/10.1016/j.icheatmasstransfer.2006.01.005
5. Yu, W., France, D. M., Smith, D. S., Singh, D., Timofeeva, E. V., Routbort, J. L. Heat transfer to a silicon carbide/water nanofluid. Int. J. Heat Mass Transf. **52**(15–16), 3606–3612. https://doi.org/10.1016/j.ijheatmasstransfer.2009.02
6. Yu, L., Dong, L.: Study of the thermal effectiveness of laminar forced convection of nanofluids for liquid cooling applications. IEEE Appl. Therm. Eng. **3**(10) (2013). https://doi.org/10.1109/tcpmt.2013.2265261
7. Sarkar, J.: Performance of nanofluid-cooled shell and tube gas cooler in transcritical CO_2 refrigeration systems. Appl. Therm. Eng. **31**, 2541–2548 (2011). https://doi.org/10.1016/j.applthermaleng.2011.04.019
8. Ehsan, M.M., Noor, S., Salehin, S., Islam, A.S.: Application of nanofluid in heat exchangers for energy savings. Thermo fluid Modeling for Energy Efficiency Applications, Edn. 1st, Chapter: 4, pp. 73–101 (2015). https://doi.org/10.1016/b978-0-12-802397-6.00004-x
9. Ingole, P.A., Shinde, S.M., Patil, P.A.: Experimental investigation of pumping power and effectiveness of car radiator using Al_2O_3. In: Nanofluid International Conference on Ideas, Impact and Innovation in Mechanical Engineering (ICIIIME 2017) ISSN: 2321–8169, vol. 5(6), pp. 135–141 (2017)
10. Pak, B.C., Cho, Y.: Hydrodynamic and heat transfer study of dispersed fluid with submicron based Al_2O_3 and CuO nanofluids in a triangular duct. J. Disper. Sci. Technol. **34**, 1368–1375 (2013)
11. Nguyen, C., Desgranges, F., Roy, G., Galanis, N., Mare, T., Boucher, S., Anguemintsa, H.: Temperature and particle-size dependent viscosity data for water-based nanofluids—hysteresis phenomenon. Int. J. Heat Fluid Flow **28**(6), 1492–1506 (2007). https://doi.org/10.1016/j.ijheatfluidflow.2007.02.004
12. Maiga, E.B., Nguyen, C.T., Galanis, N., Roy, G.: Heat transfer behaviors of nanofluids in a uniformly heated tube. Super Lattices Microstruct. **35**, 543–557 (2004). https://doi.org/10.1016/j.spmi.2003.09.012
13. Chen, H., Ding, Y., He, Y., Tan, C.: Rheological behaviour of ethylene glycol based titanium nanofluids. Chem. Phys. Lett. **444**(4–6), 333–337 (2007). https://doi.org/10.1016/j.cplett.2007.07.046
14. Maxwell, J.C.: A Treatise on Electricity and Magnetism. Clarendon Press, Oxford (1873)
15. Xuan, Y., Roetzel, W.: Conceptions for heat transfer correlation of nanofluids. Int. J. Heat Mass Transfer **43**, 3701–3707 (2000). https://doi.org/10.1016/S0017-9310(99)00369-5
16. Hatton, A.P., Turton, J.S.: Heat transfer in the thermal entry length with laminar flow between parallel walls at uniform temperature. Int. J. Heat Mass Transfer **5**, 673–679 (1962)
17. Mohammed, H.A., Bhaskaran, G., Shualib, N.H., Abu-Mulaweh, H.I.: Influence of nanofluids on parallel flow square microchannel heat exchanger performance. Int. Commun. Heat Mass Transf. **38**, 1–9 (2011). https://doi.org/10.1016/j.icheatmasstransfer.2010.09.007
18. Koo, J., Kleinstreuer, C.: Impact analysis of nanoparticle motion mechanisms on the thermal conductivity of nanofluids. Int. Commun. Heat Mass Transf. **32**, 1111–1118 (2005). https://doi.org/10.1016/j.icheatmasstransfer.2005.05.014

Microstructural and Mechanical Behaviour of Al6061/Gr/WC Hybrid Metal Matrix Composite

Gangadhara Rao, Pandu R. Vundavilli and K. Meera Saheb

Abstract This paper aims to analyse the microstructural and mechanical behaviour of aluminium hybrid metal matrix composite produced by the stir casting process. Initially, test samples are prepared using Al6061 alloy as matrix and graphite (Gr) as reinforcement by varying its weight concentrations in 3, 6, 9 and 12%. The analysis showed that adding Gr by 9 wt% resulted in better tensile strength, percentage elongation and hardness. Consequently, hybrid composites were produced by reinforcing with two metal powders, Gr at 9 wt% and varying Tungsten carbide (WC) wt. Percentages by 1, 2 and 3 wt%. Samples are again tested for tensile strength, percentage of elongation and hardness as cast and T6 heat treated. The results showed that heat-treated samples showed superior mechanical behaviour than at the as cast conditions.

Keywords Aluminium hybrid metal matrix composites · Stir casting · T6 heat treatment · Mechanical properties

1 Introduction

Tailor-made metal matrix composites due to their enhanced microstructural and mechanical properties are finding application in a variety of engineering fields [1, 2]. Aluminium metal matrix composites (AlMMCs) are engineered a combination of metal as matrix material and other material particles as reinforcement material.

Gangadhara Rao (✉)
Department of Mechanical Engineering, Aditya College of Engineering & Technology, Surampalem 533437, India
e-mail: audibalav@gmail.com

P. R. Vundavilli
School of Mechanical Sciences, IIT Bhubaneswar, Bhubaneswar 752050, India
e-mail: pandu@iitbbs.ac.in

Gangadhara Rao · K. Meera Saheb
Department of Mechanical Engineering, JNTUK, Kakinada 533002, India
e-mail: meera.aec@gmail.com

L. Li et al. (eds.), *Advances in Materials and Manufacturing Engineering*, Lecture Notes in Mechanical Engineering, https://doi.org/10.1007/978-981-15-1307-7_59

Besides being very light in weight, good strength and stiffness, they also exhibit excellent tribological properties which are rather a difficult finding in monolithic and alloy metals. Lightweight MMCs find their applications in automobile, aerospace, structural and other fields. Al6061/Gr/WC are extensively used in applications like ultra-precision instruments, satellite, wireless communications, a heat sink for microchips, heat exchanging devices and thermally stable metrological equipment owing to their low wear and coefficient of friction, low density and high thermal conductivity.

Hamid et al. [3] investigated the mechanical properties and microstructure of Al6061alloy as matrix and nano Al_2O_3 particles as reinforcements. The results showed improvement in reinforcement particle uniform distribution. Also, Ponugoti et al. [4] used stir casting to produce Al6061/ Gr MMCs using pit furnace, and their findings showed a considerable improvement in the tribological properties of composites. Furthermore, Samal et al. [5] used silicon carbide and graphite as reinforcements in the MMCs, and they observed negligible improvement in the hardness but appreciable improvement in compressive, flexural strength and density of the composites. Reddy et al. [6] reported that friction surfacing of titanium alloy would enhance the tribological properties of AlMMCs. Omrani et al. [7] showed that graphite reinforcement would improve the self-lubricating properties of AlMMCs. Kumar et al. [8] work on Al6061-WC-Gr hybrid MMCs reveals good improvement in physical, mechanical and the tribological properties of the composites. However, it suffers one of the important T6 heat treatment. In the present paper, an attempt is made to fabricate and improve the microstructural as well as mechanical properties of Al6061/Gr and Al6061/9%Gr/WC hybrid MMCs. Both composites are tested under two standard testing methods, i.e. (1) as cast and (2) heat-treated condition, respectively. In order to enhance certain mechanical properties, such as hardness, tensile strength and percentage elongation of Al6061/Gr to some extent, another reinforcement, namely tungsten carbide (WC) is introduced into the Al6061/9%Gr MMCs.

2 Fabrication of the Composites

In the present work, Al6061 is used as matrix material with two metal powders, namely graphite and tungsten carbide as reinforcements. The preparation of the metal matrix composite is carried out in a pit furnace. Initially, the matrix metal, Al6061 alloy is heated above its supercritical temperature in a graphite crucible and liquefied. Once the melt reaches a stabilized temperature, the stirring process is started using a mechanical stirrer. During this stirring process, the preheated (200 °C) predetermined (3, 6, 9 and 12) wt% Gr is added to the melt. Proper care is taken while mixing the graphite powder since it is light in weight compared to Al6061. The stirring process is continued for some time (for about 10 min) until a uniform distribution of graphite particulate in the matrix melt is observed. To avoid oxidation, the entire melting process is carried under a controlled environment. Then, the liquid composite melt is poured into preheated (325 °C) die of size 120 × 120 × 8 mm

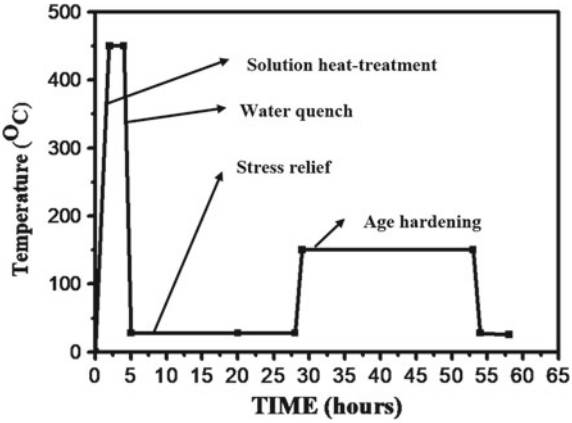

Fig. 1 Schematic diagram showing the steps involved in heat treatment process

and allowed to solidify properly. During the casting process, hexachloroethane is used in order to avoid oxidation. These samples are tested for mechanical properties, and, that weight percentage of the sample which shows better properties is further analysed in hybrid composites. A similar procedure is adopted to produce hybrid composites with WC reinforcements with varying wt. percentages.

2.1 Solutionized Heat Treatment

The fabricated Al6061/Gr specimens are heat treated and aged at T6 condition. During this process, the composites are exposed to solutionizing at 535 °C for one hour then quenched in water. Further, these quenched specimens are aged at 172 °C for ten hours and quenched in air. From these specimens, the optimal percentage of graphite is decided. Similar treatment is applied for Al6061/9%Gr/WC composites. The processes of T6 treatment are shown in Fig. 1, respectively.

2.2 Microstructural Analysis

The microstructural analysis of Al6061/9%Gr and Al6061/9%Gr/3%WC is shown in Fig. 2. The images indicate the percentage of Graphite and WC in Fig. 2a, b.

Graphite is not visible due to pitting action of the polishing and etching process because Gr is a very soft material and better known for its self-lubricating qualities. So, we can observe only debris in the image. In contrast to graphite, WC particles are observed vividly because they are hard in nature.

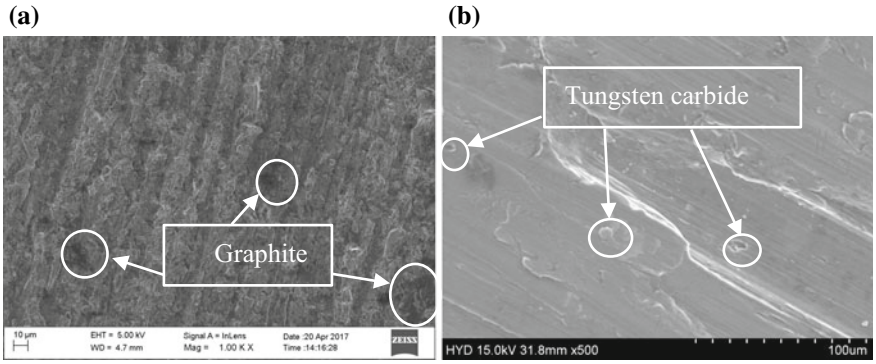

Fig. 2 Schematic diagrams showing the SEM images for **a** as cast Al6061/9%Gr **b** heat-treated Al6061/9%Gr/WC

3 Mechanical Properties

The mechanical properties of Al6061/Gr and Al6061/Gr/WC specimens are tested both at the cast and heat-treated conditions, respectively. Figure 3 shows the specimens used to conduct tensile and hardness test and are cut from the prepared AlMMCs castings as per the ASTM B557: 2006 and ASTM IS 1501:2002 standards, respectively. The universal testing machine (model: TUV-C-200) and Brinell's hardness testing machine (model: Excetek-EX40) are used in this study. For Brinell's hardness measurement, a steel ball with a diameter of 5 mm is used as indenter and applied a load of 250 kgf for 25 s. To avoid the measurement uncertainties, the hardness of the sample is measured at three distinct locations, and the average value of the three readings is considered as the hardness of the sample.

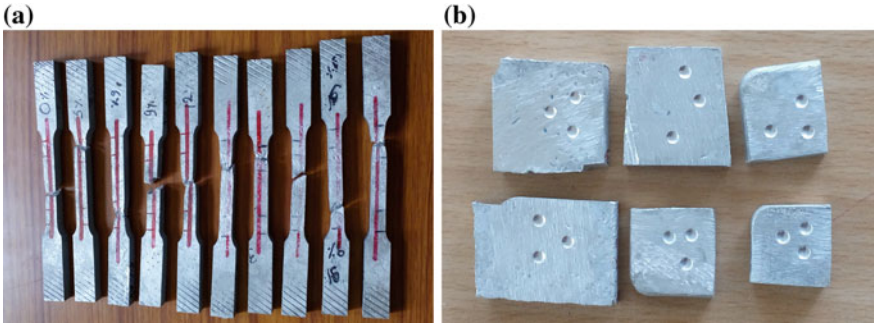

Fig. 3 Schematic diagram showing: **a** tensile test specimen and **b** hardness

4 Results and Discussions

Initially, metal matrix composites of Al6061/Gr with the designated percentage of 0, 3, 6, 9 and 12 wt% are prepared and tested for their mechanical properties such as tensile strength, percentage of elongation and hardness shown in Fig. 4a, c and e, respectively. It can be observed from the plots that heat-treated specimens have shown superior mechanical properties compared to the cast conditions. Figure 4a

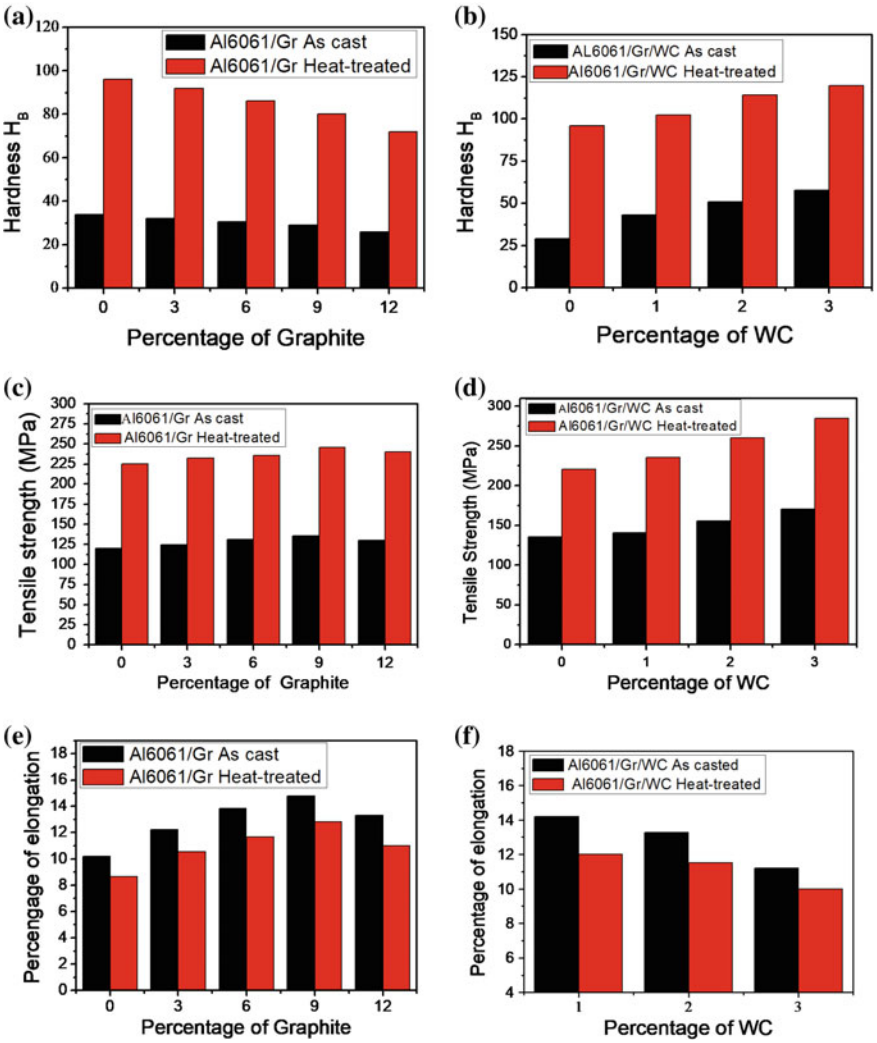

Fig. 4 Schematic diagrams showing **a** and **b** hardness, **c** and **d** tensile strength, **e** and **f** percentage of elongation—as cast and heat-treated condition

compares the hardness with varying Gr wt. percentage at both cast as well as heat treatment conditions. The hardness is found to be showing a declining trend with an increase in Gr wt. percentage at both conditions; however, it is more pronounced with the heat-treated condition. This may be due to the formation of precipitates in the matrix alloy during the process of solutionizing and age hardening in T6 heat treatment. Similarly, Fig. 4c shows the comparison of tensile strength with increasing Gr wt. percentage. It can be observed that the tensile strength shows an increasing trend with increasing Gr wt. percentage at both testing conditions. Figure 4e shows the performance of percentage elongation with Gr wt. percentage. The percentage of elongation showed an increasing trend until 9% Gr, but after that, it showed a decreasing trend in both cast and heat treatment conditions. This may be due to an increase in graphite percentage lead to poor interfacial bonding strength. So, the composite would fail before much elongation. The maximum tensile strength of 250 MPa and a maximum of 12 percentage of elongation are observed at 9% Gr, respectively. Therefore, based on the above parameters, 9% Gr as reinforcement will be the best composition.

In order to improve the hardness, WC of weight percentage 1, 2 and 3% is added to the metal matrix of Al6061/9%Gr MMC, respectively. The mechanical properties of Al6061/9%Gr/ WC as cast and heat-treated condition are plotted in Fig. 4b, d and f, respectively. Figure 4b clearly shows the addition of WC results in an increasing trend in the hardness at both as cast and heat-treated conditions. A similar trend is observed with tensile strength which can be observed in Fig. 4d.

However, the percentage of elongation shows a decreasing trend with an increase in the WC percentage. The reduced percentage of elongation can be attributed to the hard nature of WC particulates which opposes the grain boundary sliding. However, the maximum variation in percentage elongation at 3% WC wt. compared to 0% WC wt. is around 14% which is minimal.

Therefore, it can be concluded that the addition of WC for Al6061/9%Gr/ increased the hardness and tensile strength appreciably and reduced the percentage of elongation by a small margin forT6 heat treatment as well as cast conditions.

5 Conclusions

The present paper deals with the investigation microstructural and mechanical behaviour of Al6061/Gr and Al6061/Gr/WC MMCs in both cast and heat-treated conditions. The mechanical properties, such as tensile strength and percentage elongation, have shown an improvement in their values when the percentage of graphite is increased from 3 to 9%, and the hardness values have shown a decreasing trend during the above period. Further, the hybrid AlMMCs (Al6061/9%Gr/ WC) also tested for their mechanical properties and identified that the heat-treated hybrid MMCs are found to exhibit superior performance when compared with the as cast specimens.

References

1. Kaushik, N., Singhaal, S.: Mechanical and metallurgical examinations of stir cast aluminium matrix composites: a review study. Int. J. Eng. Technol. **9**(4), 3201–3217 (2017)
2. Robert, M.J.: Mechanics of Composite Materials, 2nd Edn. Tailor and Francis, Inc. (1999)
3. Ezatpour, H.R., Sajjadi, S.A., Sabzevar, M.H., Huang, Y.: Investigation of microstructure and mechanical properties of Al6061-nanocomposite fabricated by stir casting. Mater. Des. **55**, 921–928 (2014)
4. Ponugoti, G., Alluru, G.K., Vundavilli, P.R.: Trans. Indian Inst. Met. 71, 2465 (2018). https://doi.org/10.1007/s12666-018-1377-x
5. Slobodan, M., et al.: Tribological potential of hybrid composites based on zinc and aluminium alloys reinforced with SiC and graphite particles. Tribol. Ind. 34(4) 177–185 (2012)
6. Reddy, G.M., Prasad, K.S., Rao, K.S., Mohandas, T.: Friction surfacing of titanium alloy with aluminium metal matrix composite. Surf. Eng. **27**(2), 92–98 (2011)
7. Omrani, E., Moghadam, A.D., Menezes, P.L., Rohatgi, P.K.: Influences of graphite reinforcement on the tribological properties of self-lubricating aluminum matrix composites for green tribology, sustainability, and energy efficiency—a review. Int. J. Adv. Manuf. Technol. **83**(1–4), 325–346 (2016)
8. Kumar, G.B.V., Swamy, A.R.K., Ramesha, A.: Studies on properties of as-cast Al6061-WC-Gr hybrid MMCs. J. Compos. Mater. 46(17) 2111–2122 (2012)

Experimental Investigation on Friction Stir Welding of Dissimilar Alloys AA7075 and Pure Copper: Effect of Tool Material and Process Parameters on Mechanical Properties

B. Supraja Reddy and B. Ram Gopal Reddy

Abstract In this study was analyzed the effect of tool material, tool geometry and process parameters on mechanical properties and microstructure of friction stir dissimilar welded AA7075 and pure copper joints. Different welded samples were produced by varying tool material H13 and HSS, tool geometry like cone pin length 4.8 and 5 mm, the rotational speeds 750 and 900 RPM, and in all experiments, the feed and tilting angle are constant at 16 mm/min and 2°. These parameters were used for better understanding the effect of dissimilar AA7075 and pure copper welded joints on tensile strength, microstructure and hardness. Results showed that the good strengthen AA7075 and pure copper friction stir welded joints could be obtained when a tool is H13 material and cone-shaped tool. H13 tool gives quality AA7075 and pure copper friction stir welded joints compare to HSS tool at speed of 750 Rpm, feed of 16 mm/min and tilting angle 2°.

Keywords Friction stir welding · Tool material · Tool shape · Process parameters · Mechanical properties

1 Introduction

As one of the joining of dissimilar materials is increasingly used in various industries like automotives, aerospace, ship buildings and electronics industries, joining of two metals using fusion welding is very difficult because of poor welds result from formation of brittle and hard intermetallic compounds in a large scale at welded joints. Al–Cu alloys are used in various applications especially used in engineering structures because of their unparalleled efficiency, but it was very difficult to perform high-quality welds and difficult to avoid formation of intermetallic compounds by fusion methods. Friction stir welding (FSW) is especially used for solid-state joining

B. Supraja Reddy (✉)
VR Siddhartha Engineering College, Vijayawada, India
e-mail: suprajakolli9@gmail.com

B. Ram Gopal Reddy
RVR and JC College of Engineering, Guntur, India

L. Li et al. (eds.), *Advances in Materials and Manufacturing Engineering*, Lecture Notes in Mechanical Engineering, https://doi.org/10.1007/978-981-15-1307-7_60

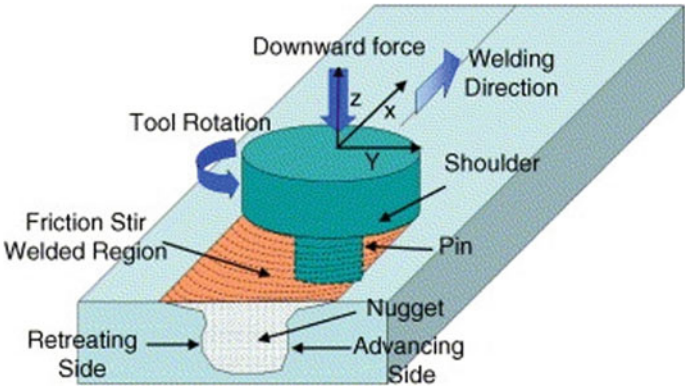

Fig. 1 FSW process

process because of heat generated by the process does not reach the melting temperature of the material to be joined [1, 2]. Friction stir welding (FSW) is capable of joining dissimilar metals without melting, the formation of brittle intermetallic compounds can be reduced, and the grain boundaries due to liquation can be eliminated and also avoid many metallurgical reactions between dissimilar metals at the elevated temperatures [3]. The defect-free welded joints are obtained mainly based on the tool material, shape of the tool pin and material flow behaviors [4] (Fig. 1).

Khaliq et al. focused on effect of tool materials and design of tool on mechanical properties of welds and also observed that Hchcr tool gives better performance than HSS tool for AA6061-O friction stir welded joints [5]. Mohammed et al. were showed the relation between design of tool pin and material flow of AA7075-AA6061 dissimilar friction stir welded joints. They were observed that well-known formation of onion rings and introducing a flat on the cone of the tool pin changes the flow of material at stirred zone and affect the tensile strength and hardness of the welded joint [6]. UgenderSingarapu et al. study the effect of friction stir welding process parameters on mechanical properties of AZ31B magnesium alloys. They were reported that the successful AZ31B magnesium friction welded joints found at tool material of SS, HSS and H13, rotational speed of 900–1400 rpm and welding speed of 25–75 mm/min, and the results are validated through ANOVA [7]. Richmire et al. showed tool rotation and traverse speed influence the stir zone for AM60 Mg alloy friction stir welded joints. They were determined that both toll rotation and traverse speed posses significant effects on the stirred zone hardness and also the interaction between the two factors were statistically assessed using Taguchi method [8]. Ilangovan et al. were investigated the effect of tool pin on microstructure and tensile strength of AA6061-AA5086 friction stir welded joints. They were observed that threaded and tapered cylindrical tools yielded defect-free joints compared to straight cylindrical tool and also observed formation of finer and uniformly precipitates and fine grains joints were fabricated by threaded pin compared to tapered pin [9]. Bozkurt et al. focused on the effect of tool material on AA2124-T4 alloy metal

MMC friction stir welded joints and used uncoated tool, coated tools with CrN and AlTiN. They were observed macrostructures, microstructures, tensile strength, wear resistance and chemical analysis for different tool materials, and results showed that the good welds are obtained for AlTiN-coated tool [10]. Karimi et al. were applied friction stir welding successfully on 1100Al alloy and AISI 1045 steel and studied the effect of tool material and pin offset on tensile and microstructure of joints. They were reported the best tool for welding of 1100 Al alloy, and AISI 1045 steel was WC tool with 1 mm offset at Al matrix [11]. In this investigation shows performance of tool material on dissimilar friction stir welded joints.

2 Experimental Work

The experiment was done on AA7075 and pure copper dissimilar friction stir welded joints with the thickness of 5 mm plates as shown in Fig. 2. The welding plate's dimensions are 150 mm x 100 mm x 5 mm. The specimens were cut as per ASTM E8 M Standards by wire cut method as shown in Fig. 3. The welded joints were produced by single-pass method on vertical milling machine. The copper placed in advancing side and AA7075 in retreating side as shown in Fig. 2.

The H13 and HSS tools are used in this investigation with cone-shaped probe. The shoulder diameter is 20 mm, pin length is 4.8 mm, and tool tilting angle is 2° with respect to *Z*-axis. The chemical composition of dissimilar metals AA7075 and pure copper is shown in Table 1.

The AA7075 and pure copper friction stir welded butt joints welded by vertical milling machine and used single-pass method. The production of quality weld needs a selection of tool material for specific metals and also tool shape. Different tool materials, process parameters and mechanical properties for AA7075 and pure copper friction stir welded joints are shown in Table 2. The tensile tests were carried at room temperature, according ASTM Standards using FIE/UTN-40 machine and microstructures done in ASTM E112. The hardness test done on Brinell hardness testing machine. The tensile specimens are shown in Fig. 3. The welded butt joints

Fig. 2 FSW experimental setup

Fig. 3 Specimens

Table 1 Chemical composition of AA7075 and pure copper

AA7075	Al 89.56%	Cu 1.302%	Mg 2.378%	Zn 6.096%
Pure copper	Cu 99.66%			

Table 2 Tool materials, process parameters and mechanical properties

S. no.	Tool material	Tool shape	Speed (RPM)	Feed (mm/min)	Tensile strength (Mpa)	Hardness (HBN)	Elongation (%)
1	H13	Cone	750	16	105.91	103.2	2.3
2	HSS	Cone	750	16	50.99	98.87	2.64
3	H13	Cone	900	16	67.08	102.33	1.13
4	HSS	Cone	900	16	66.43	109.33	1.62

produced by different tool materials, process parameters and investigated its effect on tensile properties and microstructures. The tool shape was shown in Fig. 4. AA7075 plate placed in advancing side, pure copper placed in retreating side, and these plates are welded by cone-shaped tools of material H13 and HSS.

Figure 5 shows the formation of AA7075, and pure copper friction stir welded joints are welded by H13 tool using speed 750 Rpm, feed 16 mm/min and tilting angle is 2°. Figure 6 shows the formation of welded joints are welded by HSS tool and using speed 750 Rpm, feed 16 mm/min and tilting angle is 2°. H13 tool gives quality welds compared to HSS tool for AA7075 and pure copper friction stir welded joints.

Fig. 4 FSW tool

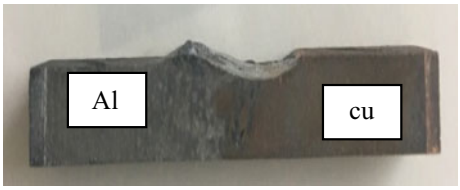

Fig. 5 Formation joint for H13

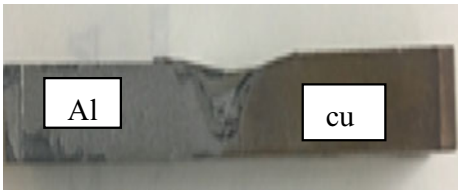

Fig. 6 Formation of joint for HSS

3 Results and Discussions

3.1 Tensile Strength

In this investigation discussed about effect of tool materials on tensile strength of dissimilar AA7075 and pure copper welded joints. Two different materials were used in this work, and Fig. 7 shows the tensile strength for welded joints. The maximum strength joints occurred at H13 tool, speed of 750 rpm and feed of 16 mm/min compared to other tool and parameters because of excessive heat and lack of heat. The elongation varies the tensile strength.

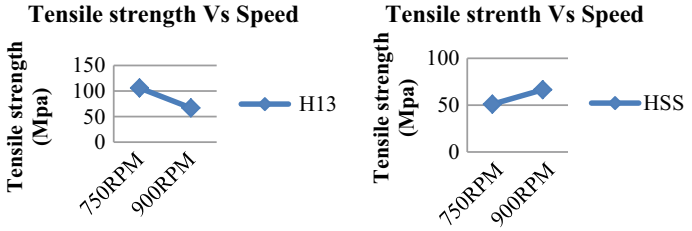

Fig. 7 Tensile strength for H13 and HSS Tools

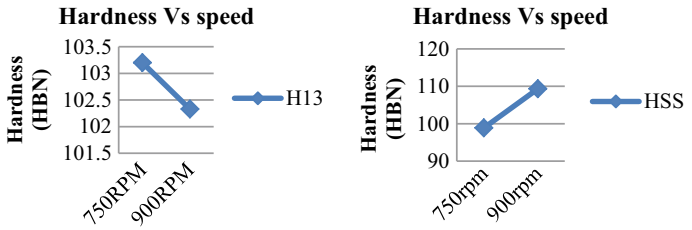

Fig. 8 Hardness for H13 and HSS tools

3.2 Hardness

The speed increases as the hardness decreases for Al/Cu dissimilar joints using H13 tool as shown in Fig. 8. The speed increases as the hardness also increases for HSS tool shown in Fig. 8. Dynamic recrystallization eliminated the strain hardening because of fine grains. The hardness was more in stirred zone compared to heat-affected zone. The maximum hardness occurred at 750 rpm for H13 tool.

3.3 Microstructure

In this investigation observed that the flow of material at joint interface as shown in Fig. 9. The figure shows copper deposited on aluminum side, and the interface shows the coarse grains effect of Tool HSS at the joint. Figure 9 had shown the interface shows the fine grain effect of Tool H13 at the joint. The fine grain structure occurred at H13 compared to HSS.

Figure 10 shows the SEM analysis of magnification (15 kV $\times$ 500 SE 100 um) for H13 and HSS Tools. It shows the better joint formation for joints using H13 tool.

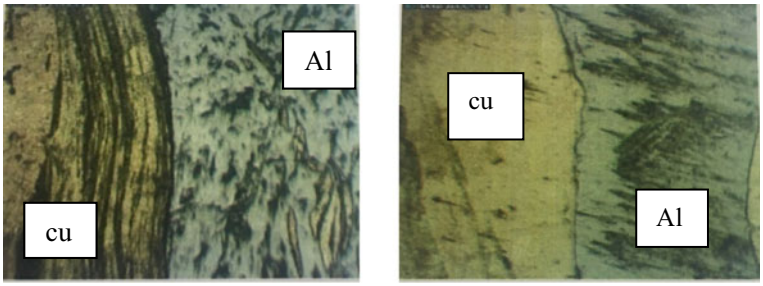

Fig. 9 Microstructure for HSS and H13 tools

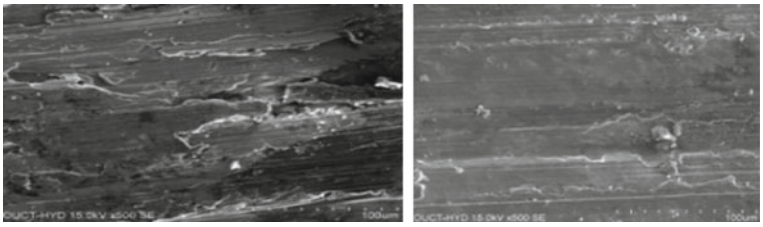

Fig. 10 SEM images for HSS and H13

4 Conclusions

This investigation focused on effect of tool material on AA7075 and pure copper friction stir welded joints. In this present work, the effects of tool materials on mechanical and microstructure of joints were investigated. In this study observed that when the rotational speed increases the tensile strength decreases for dissimilar metal joints. The quality welds obtained, when the tool material H13, rotational speed of 750 rpm, feed of 16 mm/min and tilting angle of 2°. These parameters give better mechanical properties for tensile strength as well as hardness. H13 tool gives quality welds for AA7075 and pure copper dissimilar joints because of excellent combination of high toughness and fatigue resistance compared to HSS tool. The H13 tool changes the material flow of the stirred zone is effect on tensile strength and hardness of the dissimilar joints. Finally, this study shows H13 tool was better for AA7075 and pure copper friction stir dissimilar welded joints compared to HSS tool.

References

1. Thomas, W.M., Nicholas, E.D., Smith, S.D., Das, S.K., Kaufman, J.G., Lienert, T.J: Aluminum 2001 e proceedings of the TMS 2001 aluminum autom and join ses. TMS 213 (2001)

2. Thomas, W.M., Johnson, K.I., Wiesner, C.S.,: Friction stir welding e recent developments in tool and process technologies. Adv. Eng. Mater **5**, 485–490 (2003)
3. LiYMurr, L.E., McClure, J.C.,: Flow visualization residual microstructures associated with the friction-stir welding of 2024 aluminum to 6061 aluminum. Mater Sci. Eng. A **271**, 213–223 (1999)
4. Somasekharan, A.C., Murr, E.: Fundamental studies of the friction-stir welding of magnesium alloys to 6061-T6 aluminum. Magnes. Tech. 31–36 (2004)
5. Khaliq, A., Bharti, P.K.: Influence of tool material on mechanical properties of AA6061-O during the friction stir welding process. IOSR J. Mech. Civ. Eng., e-ISSN: 2278–1684, **12**(5), Ver. I. Oct. 2015, 31–36 (2015)
6. Mohammed, M.H., Ishak, M., Rejab, M.R.M.: Effect of pin tool design on the material flow of dissimilar AA7075-AA6061 friction stir welds. In: 4th International Conference on Mechanical Engineering Research (ICMER2017) IOP Conference Series: Materials Science and Engineering 257 (2017) 012022. https://doi.org/10.1088/1757-899x/257/1/012022
7. Singarapu, U., Adepu K., Arumalle, S.R.: Influence of tool material and rotational speed on mechanical properties of friction stir welded AZ31B magnesium alloy. J. Magnes. Alloy. **3**, 335–344 (2015)
8. Richmire S., Hall, K., Haghshenas, M.: Design of experiment study on hardness variations in friction stir welding of AM60 Mg alloy. J. Magnes. Alloy. **6**, 215–228 (2018)
9. Ilangovan, M., RajendraBoopathy, S., Balasubramanian, V.: Effect of tool pin profile on microstructure and tensile properties of friction stir welded dissimilar AA 6061eAA 5086 aluminium alloy joints. Def. Technol. **11**, 174–184 (2015)
10. Bozkurta, Y., Boumerzoug, Z.: Tool material effect on the friction stir butt welding of AA2124-T4 Alloy Matrix MMC. J. Mater. Res. Technol. **7**(1) 29–38 (2018)
11. Karimi, N., Nourouzi, S., Shakeri, M., Habibnia, M., Dehghani, A.: Effect of tool material and offset on friction stir welding of Al alloy to carbon steel. Adv. Mater. Res. **445**, 747–752 (2012)

Experimental Investigations of Glycerin/Al_2O_3 Nanofluid in the Hydrodynamically Developing Region for Automotive Cooling Applications

Kondru Gnana Sundari, Lazarus Godson Asirvatham, Joseph John Marshal, T. Michael N. Kumar and Mona Sahu

Abstract The research work presented in this paper is about the experimental investigations of the convective heat-transfer behavior of glycerin/Al_2O_3 nanofluids at the entry regions (hydrodynamically and thermally developing) analyzed for a boundary condition having heat flux as constant. Different concentrations of Al_2O_3 nanoparticles of 0.05, 0.1, and 0.15 vol.% are mixed with glycerin and water at 50:50 ratio. The mass flow rate is kept under laminar flow condition by varying the Reynolds number between 500 and 2000. The testing condition of the heater section has a diameter of 25.4 mm and a length of 500 mm is tightly wound with coil representing a heater. The thermophysical properties and the variations of Nusselt numbers are experimentally studied. The results show an enhancement of 42% of the heat-transfer coefficient at a Reynolds number–2000.

Keywords Glycerin · Alumina · Radiator · Heat transfer

1 Introduction

The essential study of heat-transfer propagation of enhancement of various fluids had become a significant aspect of concern in automobile and electronic industry. The extensive review of the thermal properties has become essential parameters of innovative research. As the energy consumption has become a concerned parameter to be reduced and at the same verge, the system which improves the efficiency of heat transfer has always been a demand for new methods of heat-transfer techniques [1]. The first time colloidal mixture of nanoparticles (1–100 nm) in a base liquid was called as nanoparticle fluid suspensions [2, 3]. The dispersion of nanosized particles

K. G. Sundari · L. G. Asirvatham (✉) · J. J. Marshal · M. Sahu
Department of Mechanical Engineering, Karunya Institute of Technology and Science, Coimbatore 641114, India
e-mail: godson@karunya.edu

T. M. N. Kumar
Department of Mechanical Engineering, Bharathiyar College of Engineering, Karaikal 605609, India

L. Li et al. (eds.), *Advances in Materials and Manufacturing Engineering*, Lecture Notes in Mechanical Engineering, https://doi.org/10.1007/978-981-15-1307-7_61

in the base fluid significantly improves the flow of mixing and enhanced properties in thermal conductivity when compared to the working base fluid. In the past, many fluids like water, oil, ethylene glycol, etc., were used for improving the heat transfer [4]. Many new techniques are developed to enhance the heat absorption rate of conventional fluids to improve the thermal efficiency. However, the efficiency is very low for the conventional fluids when applied in the heating and cooling industries. Many automobile cooling mechanisms have working fluid as water, ethylene glycol and sometimes glycerol has been used as conventional working fluids called as coolants in automobile radiator for years [4]. However, the low thermal conductivity of the working fluids really has drawn attention of many researchers, to find liquids that provide higher thermal conductivity compared to that of conventional coolants [5, 6]. Researchers have worked on enormous investigations on thermal conductivity, particle size, and shape by suspending the nanoparticles in different aqueous solutions [7, 8]. Many metallic particles such as aluminum oxide, copper oxide, carbides, and CNTs, metals (Ag, Au, nanotubes) are used in preparing the nanofluids for experimental purposes [9, 10]. The essential accessories for automobiles are a car radiator which is used as a cooling device [11, 12]. The engine's true size and life depend on the working condition and heat-transfer performance of the radiator. The radiators with significant heat-transfer performance will sustain different parameters of higher efficiency engine, which leads to a smaller engine size as well as effective fuel economy with less emission of gases. The redesign of the thermal fluid with suspending nanosize particles in conventional fluids has been an innovative approach [13, 14]. The ASTM engine coolant grade specifications for heavy-duty vehicles are environmentally safe as they are neutral in their corrosive action on the engine parts than ethylene glycol, glycerin-based coolants are cost-effective than ethylene glycol and a helpful supportive of the renewable fuels industry. Glycerin is considered as a greener alternative for the atmospheric conditions than that of ethylene glycol. So, glycerin-based coolants are promising coolants when nanoparticles are suspended.

2 Experimental Work

The glycerin-based coolant-G13 is taken as the working fluid in the entire experimental work and the setup is shown in Fig. 1.

The Al_2O_3 nanosize particles at dispersion rate of 50:50 ratio of G13/water are sonicated for 20 min before sent through the experimental setup. The temperatures in the thermocouples are noted at sixteen different points at ambient conditions in the data logger which is connected to a laptop. To arrest every leak in the experimental setup, the water is continuously pumped throughout the setup for half an hour. The figure clearly represents the real-time engine setup which is wound with a coil. The radiator, which has 49 tubes and cross flow in a function having a forced convection fan behind, is attached to know the performance of the heat carried by the nanofluid. The input heat which is 6919 W/m^2 is given as a constant heat flux throughout the experimental conditions. The readings are taken at ambient temperature to check

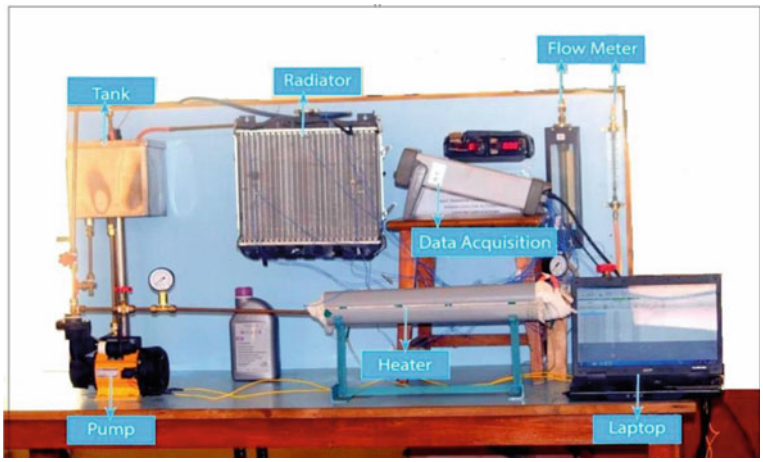

Fig. 1 Photographic view of the experimental setup

the thermocouples reading in the sixteen thermocouples as the flow rate increases at a particular heat flux which is constant throughout and the readings are noted for different volume concentrations. The steady-state readings are taken at the end of every flow rate. The errors of the measured parameters are and the uncertainty values are recorded.

3 Results and Discussion

3.1 Thermophysical Properties

The thermal properties are measured for glycerin/Al_2O_3 nanofluid at various temperature and different volume concentrations. The average values are recorded to know the enhancement and accuracy of the derived parameters. Figure 2 clearly shows the variations of the thermal properties as the volume concentration increases. The addition of nanoparticles in base fluid increases, the thermal conductivity property rises from 4.76 to 38.47% at the initial increase of temperature. Due to the random motion of the nanoparticles which are solid particles in the base fluid results in the enhancement of the thermal conductivity. The size of the nanoparticles helps in the improvement of the thermal property when mixing in the base fluids. When the temperature rises from 30 to 50 °C and volume concentration varies from 0.05 to 0.15 vol.% an average increase of 10.36–46.15% enhancement is observed in glycerin/Al_2O_3 nanofluid. The viscosity of the nanofluid raises as the nanoparticles concentration raises when the solid particles are dispersed in the G13 coolant. It is noticed as the volume concentration increases, the viscosity of the base fluid is

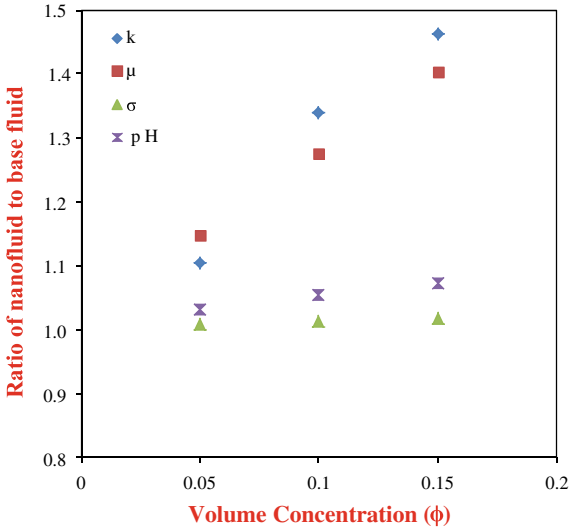

Fig. 2 Thermophysical properties variation with volume concentration

lower than the nanofluid but reduces as the temperatures raise from 30 to 50 °C. It is observed the increase of viscosity is 1.11–1.36 due to the suspension of low concentration of nanoparticles.

3.2 Axial Profile of Nusselt Number at Re–1000

Figure 3 shows at the distance of 7.48 length on the axial profile which is at the second local point the Nusselt number increases from 15 to 32 as the concentration solid particles varies from 0.05 to 0.15 vol.%. It is observed that 62% of local heat-transfer enhancement for 0.15 vol.% of nanoparticles is dispersed in the coolant for a Reynolds number-1000.

The figure shows that the flow is a developing flow. The Nusselt number variations indicate that the amount of heat absorbed at the entry length is higher in the heater section. The thickness of the boundary-layer development signifies that the properties causing for the increase in the thermal properties is due to the shear action and Brownian motion of particles dispersed. The increase in the Nusselt number at the entry length is because of the larger velocity gradient.

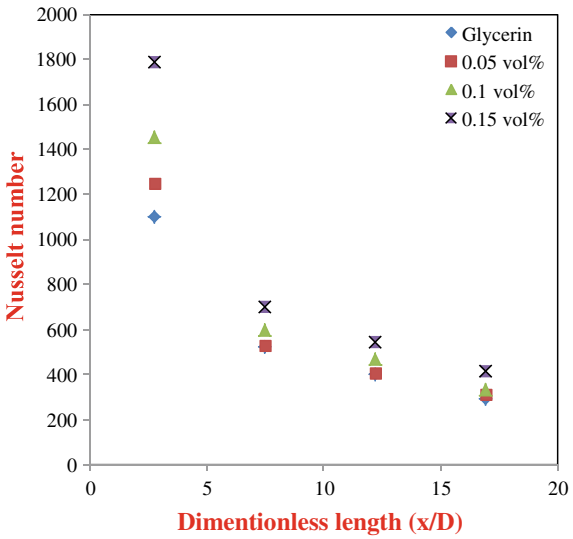

Fig. 3 Effect of Nusselt number on local points

3.3 *Effect of Nusselt Number as Colburn J Factor Varies with Reynolds Number*

The variation of Nu number as Colburn J factor varies with Reynolds number is shown in Fig. 4. This Colburn J factor includes the changes of Prandtl number as the Reynolds number varies. The development of the thermal boundary layer is effected

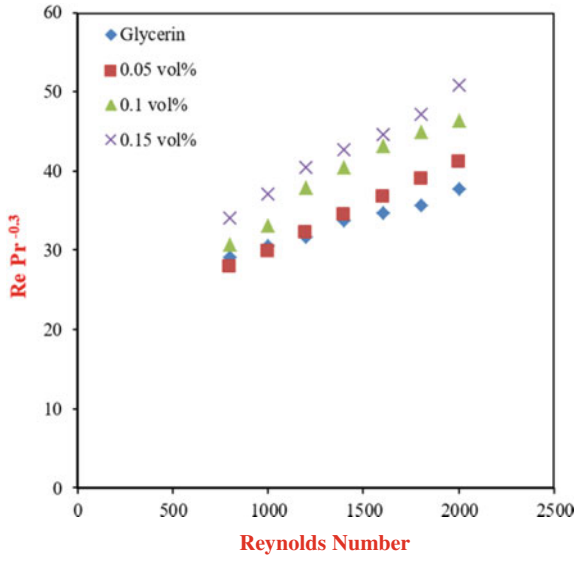

Fig. 4 Variation of Nusselt number as Colburn J factor with respect to the Reynolds number

as the nanoparticles are dispersed and the heat-transfer enhancement is observed. The heat transfer is tremendously increasing due to the addition of nanoparticles and also effects the development of boundary layer. The addition of particular amount of volume concentration of nanoparticles in the base fluid effects the boundary-layer development which increases the heat-transfer rate.

4 Conclusions

- When the glycerin-based coolant is dispersed with Al_2O_3 nanoparticles, the thermal conductivity increases as the temperature varies from 30 to 50 °C. The viscosity of the nanofluid decreases as the temperature ranges from 30 to 50 °C when the nanoparticles are dispersed in the coolant
- At a particular Reynolds number 2000, the enhancement of heat-transfer coefficient increases from 28 to 42% which is a makeable enhancement.
- The results clearly show the Nusselt number at Reynolds number 1000 is higher at the entry length as the nanoparticles are added results in the heat-transfer enhancement.

References

1. Peyghambarzadeh, S.M., Hashemabadi, S.H., Hoseini, S.M., Jamnani, M.S: Experimental study of heat transfer enhancement using water/ethylene glycol based nanofluids as a new coolant for car radiators. Int. Commun. Heat Mass Transf. **38**, 1283–1290 (2011)
2. Choi, S.U.S., Eastman, J.A.: Enhancing thermal conductivity of fluids with nanoparticles. ASME Int. Mech. Eng. Congr. Expo. **66**, 99–105 (1995)
3. Godson, L.A., Lal, M.D., Wongwises, S.: Measurement of thermo physical properties of metallic nanofluids for high temperature applications. **153**, 152–173 (2010)
4. Mohammad, E.H., Karimipour, A., Yan, W., Akbari, M., Safari, M.R., Dahari, M.: Experimental study on thermal conductivity of ethylene glycol based nanofluids containing Al_2O_3 nanoparticles. Int. Commun. Heat Mass Transfer **88**, 728–734 (2015)
5. Adnan, M.H., Bakar, R.A., Kadirgama, K., Sharma, K.V.: Heat transfer enhancement using nanofluids in an automotive cooling system. Int. Commun. Heat Mass Transf. **53**, 195–202 (2014)
6. Xiake, L., Zou, C., Qi, A.: Experimental study on the thermo-physical properties of car engine coolant (water/ethylene glycol mixture type) based SiC nanofluids. Int. Commun. Heat Mass Transfer **77**, 159–164 (2016)
7. Fricke, H.: A mathematical treatment of the electric conductivity and capacity of disperse systems I. The electric conductivity of a suspension of homogeneous spheroids. Phys. Rev. **24**, 575–587 (1924)
8. Granqvist, C.G., Hunderi, O.: Optical properties of ultrafine gold particles. Phys. Rev. B **16**, 3513–3534 (1977)
9. Hamilton, R.L.: Thermal conductivity of heterogeneous two-component systems. Ind. Eng. Chem. Fundam. **1**, 187–191 (1962)

10. Godson, L., Raja, B., Mohan Lal, D., Wongwises, S.: Convective heat transfer characteristics of silver-water nanofluid under laminar and turbulent flow conditions. J. Therm. Sci. Eng. Appl. **4** (2012)
11. Jeffrey, D.J.: Conduction through a random suspension of spheres. Proc. R. Soc. A Math. Phys. Eng. Sci. **335**, 355–367 (1973)
12. Murshed, S.M.S., Leong, K.C., Yang, C.: Investigations of thermal conductivity and viscosity of nanofluids. J. Therm. Sci. **47**(5), 560–568 (2008)
13. Eastman, J.A., Choi, U.S., Li, S., Thompson, L.J., Lee, S.: Enhanced thermal conductivity through the development of nanofluids. Materials Research Society Symposium—Proceedings, pp. 3–11 (1997)
14. Siddiqui, F.A., Dasgupta, E.S., Fartai, A.: Experimental investigation of air side heat transfer and fluid flow performances of multi-port serpentine cross-flow mesochannel heat exchanger. Int. J. Heat Fluid Flow **33**, 207–219 (2012)

Experimental Investigation of Twin Elliptic Orifice at Different NPR Levels

S. Parameshwari, Pradeep Kumar, S. Thanigaiarasu and E. Rathakrishnan

Abstract Jet study lays the proper foundation for future aircraft ad rocket system design and development, for example, reduce jet noise in rocket, minimized nature of infrared signature in fighter airplanes, etc. Keeping these concerns, the present study is focused on the experimental investigation of twin elliptic orifice of aspect ratio two. The aluminum material is used for the twin orifice by rapid prototyping method. The total exit area of the orifice was maintained as equivalent diameter (Deq) of 7 mm. The test has been carried out at nozzle pressure ratios (NPRs) of two, three, and four by using high-speed jet facility. The proximity between the twin orifices was kept 1, 2, and 3 mm. Centerline pressure decay of jets was measured up to 20 Deq, and these results indicate that the mixing rate of jets was effective at lower nozzle pressure ratio compared to higher nozzle pressure ratio of two and three. In addition, the closest proximity of 1 mm of twin orifice enhances the faster mixing along its length of the jet field of the measured NPRs. The amplitude of pressure oscillations was high at 4 Deq than other locations. The jet mixing was started at 2 Deq and ends at 7, 8, and 9 Deq for 1, 2, and 3 mm proximity, respectively, of measured nozzle pressure ratio range. The reason of the above results depends on orifice geometry, aspect ratio, and nozzle pressure ratio of elliptic jet.

Keywords Centerline pressure decay · Twin elliptic jet · Pressure ratio

S. Parameshwari (✉) · P. Kumar
Department of Aerospace Engineering, Karunya Institute of Technology and Sciences, Coimbatore 641114, India
e-mail: paramaero29@gmail.com

S. Thanigaiarasu
Department of Aerospace Engineering, Madras Institute of Technology, Chennai 600044, India

E. Rathakrishnan
Department of Aerospace Engineering, Indian Institute of Technology, Kanpur 208016, India

L. Li et al. (eds.), *Advances in Materials and Manufacturing Engineering*, Lecture Notes in Mechanical Engineering, https://doi.org/10.1007/978-981-15-1307-7_62

1 Introduction

Jet study creates an impact toward the aerospace industries in the aircraft/rocket developments. This also met immense application in the non-aerospace field such as machine cutting, jet wiring, and metal deposition; the jet may be classified into free jet, impinging jet, and co-flow jet [1]. Based on the exit configuration of nozzle/orifice, the jet is further classified as circular jet [2], elliptic jet [3], triangular jet [4], and rectangular jet [5, 6]. Many researchers contributed their work on above-mentioned jets and came up with good results on jet spread and decay. Apart from that few researchers worked on the controlled jet by means of employing controls such as active control [7, 8] (micro jet, fluid injection) and passive control (tabs, wires, shifted tabs [9–11]). Apart from the controlled circular, triangular, and rectangular jet, the elliptic one gained the advantage with increased thrust and leads the future development of rocket nozzles. Because the elliptic jet resulted in highest mixing compared with circular component, the elliptic jet experiences better spread rate relative to rectangular jets, circular jets, and triangular jets in the supersonic flows [12]. The strength of axis switching gained as pressure ratio increases. The decay along the jet centerline was captured using stereoscopic particle image velocimetry that resulted in the nominal increase of entrainment rate of elliptic jet against the circular one. Also axis switching is a typical feature mainly depending on jets' initial conditions. Three-axis switching was found in the Ho and Gutmark [13] study. Quinn [14] also observed the axis switching of two along the jet spread direction that enables faster mixing. The elliptic jet may attain circular shape after 30 D (diameter of nozzle exit) along the jet spread. To reduce this jet spread, Bajpai and Rathakrishnan [15] introduced the concept of tabs (cross wire) which decreased the spread rate by fifty percent. Either passive or active control introduced in the jet studies will have associated penalty in terms of momentum deficit, which leads to thrust loss and surplus of aerodynamic drag.

Hence, the orifice (absence of boundary layer) jet was concentrated with twin nature of identical jet shape of elliptic. The edge-to-edge distance between the orifices is varied from 1, 2, and 3 mm, and pressure ratio was selected for the present study is 2, 3, and 4. The current study aims to focus on the impact of twinjet mixing of orifice within the field.

2 Model Description and Experimental Setup

The twin elliptic orifice is made up of aluminum material from rapid prototyping method. The aspect ratio of orifice is kept two and the proximity between the orifices is considered as 1, 2, and 3 mm. The equivalent diameter of elliptic model exit area is maintained with 7 mm in all proximity cases. For the current investigation, jets mixing was tested at the nozzle pressure ratio of 2, 3, and 4. This paper explains the experimental investigation of aerodynamic mixing process and associated shock

pattern of twin elliptic sonic jets with a variable proximity range. Schematic diagrams representing the geometrical details of the twin orifice facing minor axis is shown in Fig. 1.

The experimental work has been carried out using the MIT (Madras Institute of Technology) high-speed jet facility, in Fig. 2. An o-ring kept between the model holder and the face of the flange at the model inlet face ensures that the attachment

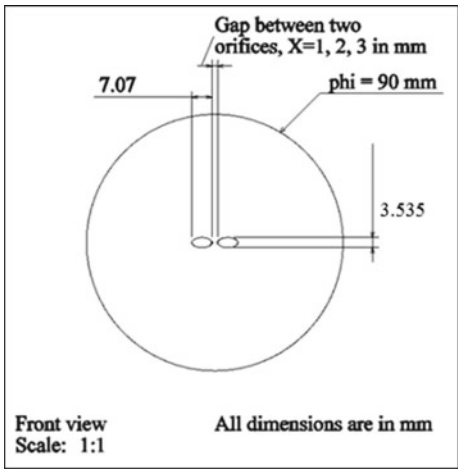

Fig. 1 Geometric configuration of AR2 twin elliptic orifice

Fig. 2 Photographic view of the high-speed jet facility

is leak-free. The high-pressure tank has a storing capacity of 15 bar which is interconnected with dryer, control valve, and settling chamber just before the open jet exit. The control valve helps to regulate the flow with the desired NPR level, and the shape of the settling chamber controls flow turbulence. To decrease the flow of non-uniformity, the two wire-mesh screens are kept inside the settling chamber with a distance apart from each other just before model entrance. The required pressure ratio is attained by controlling the chamber pressure.

2.1 Transducer and Pitot Probe Specifications

The pressure systems (16 channel of 9010 transducers) help to measure the total pitot pressure along the orifice centerline of designed elliptical orifice. The software connected with transducer helps the user to acquire data and displays the total pressure readings from all channels of a monitor which interconnected with computer. The number of samples to be averaged is selected with the help of transducer with its settings menu. The transducer accuracy is kept to be ±0.15% full scale (after the re-zero calibration).

The inner and outer diameters of pitot probe are maintained of 0.4–0.6 mm, respectively, for pitot pressure measurement of jet flow field. The twin elliptic orifice exit to the pitot probe area ratio was $(7/0.6)^2 = 136.11$, which is well above the limit of 64 regarding the probe blockage as negligible [16]. The pitot probe is connected with transducer with 1 mm silicon tube for all pressure readings [17]. The settling chamber pressure was maintained within ±2% during the experiments of the current investigation for the pressure ratio of 2, 3, and 4. The pitot probe movement is kept with a resolution of ±0.1 mm in the linear translation of three-dimensional traverse. The range of the pressure measurements was repeated within ±3%.

3 Results and Discussion

3.1 Centerline Pressure Decay Along Orifice Center

The jet issuing from orifice/nozzle propagates into the atmosphere toward downstream which increases the entrainment rate of jet. Further increase in entrainment that carries mass entraining vortices will become transporting vortices along spread path and this will be the initial step for jet characteristic decay [16]. However, potential core of subsonic jet is unaffected and flow velocity remains constant. Also for supersonic jet, this jet core prevails full of wakes. The elliptic jet follows the strict procedure that is ahead of potential core definition. The decay is different for elliptic jet unlike the circular jet is uniform. Thus, the core length of the jet represents the distance between the orifice exit and beginning point of the characteristic decay.

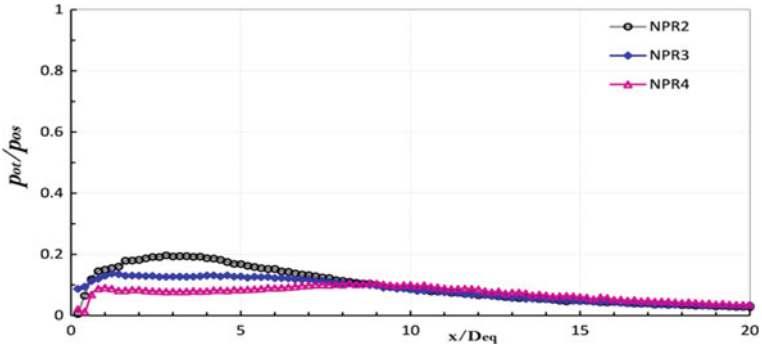

Fig. 3 Axis centerline pressure decay of AR2 elliptic orifice with 1 mm proximity

Faster jet mixing is a representation of the faster jet decay. Therefore, to study characteristics of twin elliptic orifice jet, the pitot pressure (Pot) is measured up to 20 Deq from the orifice exit along the jet axis direction which is non-dimensionalized with the settling chamber pressure (Pos) and this is plotted as a function of non-dimensionalized axial distance [17]. The distance between the orifices is kept 1, 2, and 3 mm. For all proximity, the axes centerline pressure decay was plotted at all measured NPRs.

From Fig. 3, the experimental results show that the total pressure oscillations decrease as pressure ratio increases from 2 to 4. The mixing begins at x/Deq = 0 and ends at 10 x/Deq. The decreased nature of centerline pressure decay plot indicates faster mixing at pressure ratio of 4. Similarly, from Fig. 5, the elliptic jet shows faster decay at NPR 4 than NPR 2 and 3.

Figure 5 also experiences similar nature as Figs. 3 and 4. From the results and discussion, it reveals that NPR 4 with 1 mm proximity level has highest mixing and this orifice is a better choice in the supersonic flow mixing than other studied orifices. In addition, this implicates that the distance between the orifices and pressure ratio controls the nature of jet flow [18].

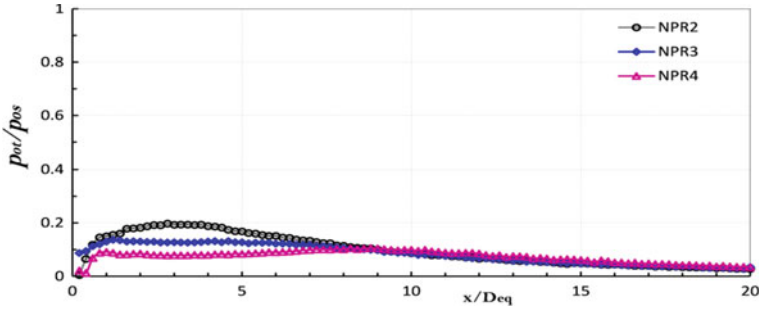

Fig. 4 Axis centerline pressure decay of AR2 elliptic orifice with 2 mm proximity

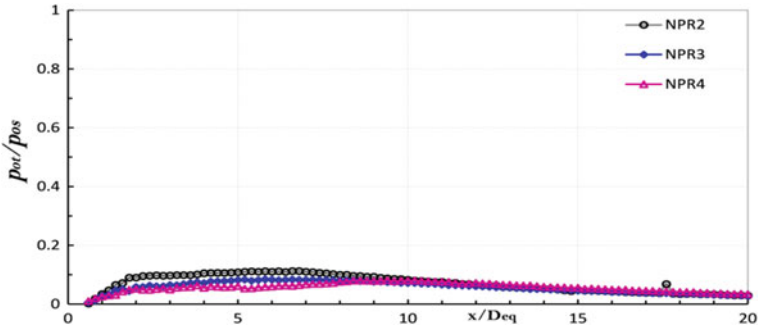

Fig. 5 Axis centerline pressure decay of AR2 elliptic orifice with 3 mm proximity

4 Conclusions

- The current study clearly focused that aerodynamics jet mixing is getting slow down at NPR 4 compared to NPR 2 and NPR 3.
- The amplitude of pressure oscillations may be the reason for the least mixing of twinjet. Therefore, orifice facing minor axis with 1 mm proximity at NPR 4 shows faster decay which implies faster mixing took placed in the close vicinity of closure of shocks.
- In addition to this, the jets mixing was initiated at 1x/Deq and ends with 10x/Deq along the jet axis direction at all proximity levels. Further study on flow visualization may support waves that prevailed in the core of jet.

References

1. Trumper, M.T., Behrouzi, P., McGuirk, J.J.: Influence of nozzle exit conditions on the near-field development of high subsonic and under expanded axisymmetric jets. Aerospace **5**, 35–45 (2018). https://doi.org/10.3390/aerospace5020035
2. Ho, C.M., Gutmark, E.: Vortex induction and mass entrainment in a small-aspect-ratio elliptic jet. J. Fluid Mech. **179**, 383–405 (1987). https://doi.org/10.1017/S0022112087001587
3. Morris, P.J., Miller, D.J.: Wavelike structures in elliptic jets. A*I*AA 22nd Aerospace Sciences Meeting 1984, Reno, Nevada, USA, paper no. AIAA8-84-0399. AIAA (1984). https://doi.org/10.2514/6.1984-399
4. Miller, D.: The stability of an elliptic jet. AIAA 22nd Aerospace Sciences Meeting-1984, Reno, Nevada, USA, paper no. AIAA-84-0068, AIAA (1984). https://doi.org/10.2514/6.1984-68
5. Zaman, K.B.M.Q.: Effect of 'delta tabs' on mixing and axis switching in jets from asymmetric nozzles. 32nd Aerospace Science Meeting and Exhibit 1994, Reno, NV, USA, paper no. AIAA-94-0186.AIAA (1994). https://doi.org/10.2514/6.1994-186
6. Ahuja, K.K., Brown, W.H.: Shear flow control by mechanical tabs. AIAA 2nd Shear Flow Confernce 1989, Tempe, AZ, USA. Paper no. AIAA-89-0994. AIAA (1989). https://doi.org/10.2514/6.1989-994

7. Ramesh, G.,Venkatakrishnan, L., Prabhu, A.: PIV studies of large scale structures in the near field of small aspect ratio elliptic Jets. J. Vis. **9**(1), 23–30 (2006). https://doi.org/10.1007/bf03181565
8. Lovaraju, P., Paparao, K.P.V., Rathakrishnan, E.: Shifted cross-wire for supersonic jet control. 40th AIAA/ASME/SAE/ASEE Joint Propulsion Conference and Exhibit 2004, Fort Lauderdale, Florida, paper no. AIAA 2004–4080. AIAA (2004). https://doi.org/10.2514/6.2004-4080
9. Maruthupandiyan, K., Rathakrishnan, E.: Supersonic jet control with shifted tabs. Proc. Inst. Mech. Eng. Part G: J. Aerosp. Eng. **232**(3), 1–17 (2016). https://doi.org/10.1177/09544.10016679197
10. Munday, D., Mihaescu, M., Gutmark, E.: Experimental and numerical study of jets from elliptic nozzles with conic plug. AIAA J. **49**(3), 554–564 (2011). https://doi.org/10.2514/1.J050587
11. Khan, A., Kumar, R., Verma, S.B., Manishankar, C.: Effect of cross wire tab orientation on twin jet mixing charcteristics. Exp. Therm. Fluid Sci. **99**, 344–356 (2018). https://doi.org/10.1016/j.expthermflusci.2018.08.005
12. Gutmark, E., Schadow, K.C., Bicker, C.J.: Mode switching in supersonic circular jets. AIAA Conference 1988, 1st National Weapons Center, Cincinnati, OH, USA, paper no. 88–3610-CP. AIAA (1988). https://doi.org/10.2514/6.1988-3610
13. Bradbury, L.J.S., Khadem, A.H.: The distortion of a jet by tabs. J. Fluid Mech. **70**(4), 801–813 (1975). https://doi.org/10.1017/S0022112075002352
14. Quinn, W.R.: On mixing in an elliptic turbulent free jet. Phys. Fluids **11**(10), 1716–1722 (1989). https://doi.org/10.1063/1.857536
15. Bajpai, A., Rathakrishnan, E.: Control Supersonic Elliptical Jet **114**, 1–17 (2017). https://doi.org/10.1017/aer.2017.114
16. Rathakrishnan, E.: Instrumentation, measurements and experiments in fluids 2nd edn. CRC Press, Taylor and Francis Group, Singapore (2016). ISBN:978-1-315-39486-2
17. Rathakrishnan, E.: AR4 elliptic jet control with limiting tab. Fluid Dyn. Res. **50**(2), 1–20 (2017). https://doi.org/10.1088/1873-7005/aa9b96
18. Chauhan, V., Kumar, S.M.A., Rathakrishnan, E.: Mixing characteristics of underexpanded elliptic sonic jets from orifice and nozzle. J. Propuls. Power **31**(2), 496–504 (2015). https://doi.org/10.2514/1.b35451

Experimental Investigations on the Effect of Wheel Size on an Industrial Trolley

Wilson Kumar Masepogu, Mona Sahu and Santhiyagu Joseph Vijay

Abstract Manual material handling using push–pull trolleys in small- and medium-scale enterprises (SMEs) has become an inevitable activity. A study was carried out to find the best wheel size in pushing a newly developed industrial trolley. Three various wheels of sizes 100, 125 and 150 mm diameters were used in this study. The results present the best wheel size and comfortable handle height of the trolley for five subjects of different stature at five varying loads. Experiments were conducted in a laboratory for a selected population of five subjects with a varying stature 1650, 1740, 1780, 1790 and 1820 mm, with five different loads 75, 156, 188, 219 and 250 kg and with five different handle heights 900, 950, 1000, 1100 and 1150 mm. Handle height of 1100 mm and a 150 mm diameter wheel size was found to be better in reducing the effort required in pushing the trolley and in reducing the discomfort experienced by the subjects.

Keywords Manual material handling · Wheel size · Heart rate (HR) · EMG · Industrial trolley

1 Introduction

Industrial trolleys are widely used by the workers in all types of manufacturing industries for material handling. During the material handling operations, the risk factors lead to severe musculoskeletal disorders (MSDs). The workers should be able to manoeuvre the trolleys with ease. Trolleys should be light in weight with optimum handle heights and the wheel sizes [1]. The most influential factors were found to be the cart weight and external load. Hence, workplaces involving pushing and pulling should be checked for best practices in handling to reduce musculoskeletal problems [2]. The guidelines for pushing and pulling task by considering shoulder physical capacity are based on gender, handle height, exertion type (push or pull) and handle orientation for these tasks. [3]. For 70–80% of users, shoulder height

W. K. Masepogu (✉) · M. Sahu · S. J. Vijay
Department of Mechanical Engineering, Karunya Institute of Technology and Science, Coimbatore, Tamil Nadu 641114, India
e-mail: wilson@karunya.edu

L. Li et al. (eds.), *Advances in Materials and Manufacturing Engineering*, Lecture Notes in Mechanical Engineering, https://doi.org/10.1007/978-981-15-1307-7_63

is the recommended handle height. Handles falling in this range reduce the strain on the wrists and hands and reduce compression load at L5-S1 (lower back) [4]. Inadequate assistive devices, improper workstations and awkward postures can lead to musculoskeletal disorders among workers. They can be reduced by ergonomic interventions [5]. The pushing and pulling force at 1150 mm handle height would be less compared to 1010 and 880 mm handle heights. The exerted initial pushing forces were less when 150 mm diameter wheels were used and more when 100 and 125 mm diameter wheels were used [6]. The push or pull forces are often distinguished as initial forces sustained forces and ending forces which are required to move and stop the object from a stationary position [7]. There is much importance to be given during MMH tasks that need to be converted from lifting to pushing and pulling [8]. Electro-goniometry of the wrist is a feasible method for studying wrist movements and limits of the human body joint angles. It helps in deciding the ergonomic design aspects of MMH devices [9]. The use of the specialized design of experiments (DOE) software is less time consuming, more efficient, insightful, comprehensive and less error-prone than generating the same design by manual methods [10]. The purpose of this study was to find the effect of wheel size on the performance of the trolley. Push forces were measured using a force gauge, and heart rate of the subject was measured using a Polar heart rate meter.

2 Materials and Methods

2.1 Test Subjects

Prior permissions were obtained from the Institution Human Ethics Committee, Coimbatore, Tamil Nadu, for conducting laboratory experiments on human beings. Five male students volunteered and actively participated as subjects. The age, height and weight details of the students are given in Table 1. Written statements were taken from these subjects confirming that they do not have any past records of any type of MSDs.

Table 1 Age, height and weight of the subjects

Subject. no	Age (years)	Stature (mm)	Weight (kg)
1	19	1650	68
2	19	1730	59
3	18	1740	61
4	19	1750	85
5	19	1820	58

2.2 Experimental Set-Up

Laboratory experiments were conducted on a push–pull trolley with four wheels and a height-adjustable handle ranging from 900 to 1100 mm. Polypropylene caster wheels of 100, 125 and 150 mm diameter with a uniform wheel width of 38 mm were used. All the wheels were oriented towards forwarding direction before the start of each experimental trial. The horizontal push bar was firmly welded to the base structure of the trolley at 110° angle. A no-objection statement was obtained from all the subjects for publication in revealing the human identity. The trolley with the subject is shown in Fig. 1. The Polar RS100 h monitor was used to measure the continuous heart rate of the subject during the experimental trials. The heart rate would be detected by the transmitter utilizing the rear area of the electrode and displayed in the wrist unit. It has an accuracy of ±1% or 1 bpm, and the measurement ranges between 15 and 240 beats/min (bpm) at the temperature 25 °C/77 °F.

EMG sensor SX230 (Bipolar Precision, Biometrics Ltd. London, UK) has integral electrodes with a fixed electrode distance of 20 mm. The EMG electrode was placed by the following method described by Lin et al. [6]. These sensors were fixed parallel to the longitudinal axis on each subject's bulk muscles, viz. flexor digitorum, deltoid and upper trapezius. An ultra-high-quality signal was obtained using SX230 with very little skin preparation. Every single data sample was squared first, and then, a moving average was calculated. The real-time EMG signals were acquired and saved into the micro-SD card. DataLOG unit was synchronized to Biometrics analysis software v8.51 to acquire the data in real time and then saved to the laptop/PC for further analysis. A high-pass filter was applied to eliminate the DC offsets due to membrane

Fig. 1 Side view of the test set-up

potentials, and a low-pass filter was applied to filter out the undesirable frequencies above 450 Hz. RMS filter was used for better amplitude values and using the vertical markers.

2.3 Experimental Design

Design-Expert DX9 software was used to formulate the design of experiments. Response surface methodology (RSM) was used for finding the effect of input variables inducing the output responses by varying them at the same time and carrying out a finite number of trials. A three factorial with five-level central composite design (CCD) matrix was framed to design the experiments to predict the effects of the load in the trolley, wheel size and handle height on push force exerted by the subjects. The twenty experimental combinations as shown in Table 2 were conducted to record the push force. Equation 1 shows the second-order quadratic equation, where the coded factors are quantitative and they are denoted by $x_1, x_2, \ldots, x_k$, where, β_0 is the offset

Table 2 Design matrix coded factors with corresponding values

Run no.	Design matrix coded factors			Subject height (mm)	Handle height (mm)	Trolley load (kg)
	Factor 1	Factor 2	Factor 3			
1	1	−1	1	1780	950	169
2	1	−1	−1	1780	950	106
3	−1	1	1	1690	1050	169
4	0	2	0	1740	1100	138
5	−1	1	−1	1690	1050	106
6	0	0	0	1740	1000	138
7	0	0	0	1740	1000	138
8	−1	−1	1	1690	950	169
9	0	0	0	1740	1000	138
10	1	1	−1	1780	1050	106
11	2	0	0	1820	1000	138
12	0	0	0	1740	1000	138
13	0	0	−2	1740	1000	75
14	−2	0	0	1650	1000	138
15	−1	−1	−1	1690	950	106
16	0	−2	0	1740	900	138
17	0	0	0	1740	1000	138
18	1	1	1	1780	1050	169
19	0	0	2	1740	1000	200
20	0	0	0	1740	1000	138

term, β_i are the linear main effects, β_{ii} are the quadratic main effects, β_{ij} are the linear-by-linear interactions, i and j are the index numbers for factors and ε is the residual error term.

$$y = \beta_0 + \sum_{i=1}^{k} \beta_i x_i + \sum_{i=1}^{k} \beta_{ii} x_i^2 + \sum_i \sum_j \beta_{ij} x_i x_j + \varepsilon \quad (1)$$

2.4 Task and Procedure

Procedural instructions were given to all subjects about the tasks and experimental trials. Three trials were conducted for each subject on all the three different wheels for each set of run/combination, and the average was taken as the input data into the CCD matrix of the DOE software. Each subject was allowed to push the trolley at his normal walking speed for a distance of 15 m. Initial pushing forces were recorded using positive peak button on force gauge.

3 Results and Discussions

Figure 2 shows the heart rates of a subject when the trolley was pushed with a handle height of 1100 mm and loads varying from 125 to 250 kg. In general, heart rates increase with an increase in the load of the trolley. Heart rates differ for different wheel diameters, but at loads ranging from 156 to 219 kg, there is minimal difference in heart rates for wheel diameters 100 and 125 mm. Heart rates decrease with the use of bigger diameter wheels indicating that the discomfort can be reduced. Figure 3 shows the effect of wheel diameter on heart rate for all five subjects. The values of heart rates are almost the same for most of the subjects when wheel diameters of 100 and 125 mm are used. But the heart rates were lowest when the 150 mm wheel diameter was used. The effect of wheel diameter is shown on the initial push force

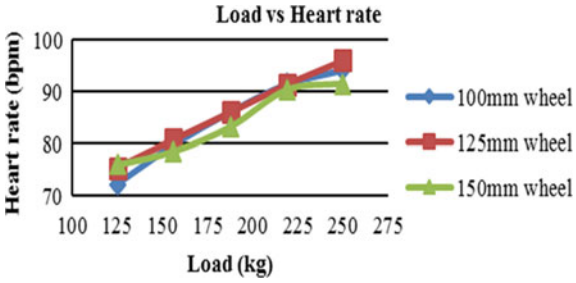

Fig. 2 Load versus heart rate at 110 mm handle height for subject 2

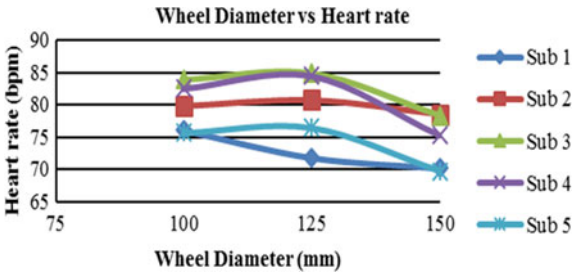

Fig. 3 Wheel diameter versus heart rate at 1100 mm handle height for all five subjects

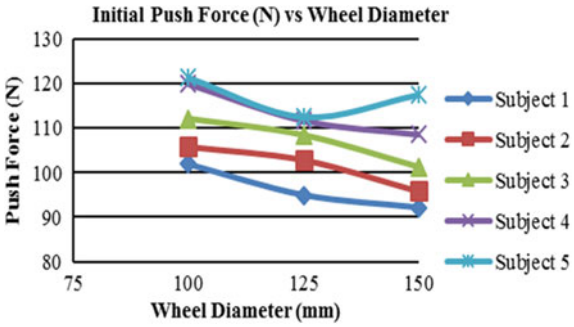

Fig. 4 Wheel diameter versus push force (N) at 1100 mm handle height for all five subjects

for all five subjects as in Fig. 4. It can be noted that the initial push forces were least when the wheel diameter is 150 mm for most of the subjects. Figure 5 shows the effect of wheel diameter on muscle activity. The % MVC is the least at the wheel diameter of 150 mm for all subjects.

Appropriate permissions were obtained from the Managing Director of the gear manufacturing company in Coimbatore, Tamil Nadu, South India, to carry out an observational study. Workers in the company have expressed their difficulties in using the existing trolleys. The newly developed trolley shown in Fig. 1 was used for finding out the wheel size which would reduce the force required to push the trolley which would give a lower heart rate. It was found that the usage of handle height of 1100 mm reduced 25–35% of the pushing efforts (including force and heart rate)

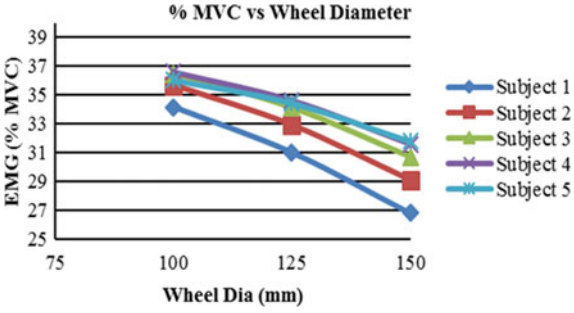

Fig. 5 Wheel diameter versus EMG (%MVC) at 1100 mm handle height for all five subjects

exerted by the subjects when compared to 900 mm handle height. It can be taken as the most comfortable height for the population selected with the anthropometric data (subject's height/stature) ranges from 1650 to 1820 mm. The forces exerted, the heart rate experienced, the muscle activity generated and the wrist extensions were considerably low at a handle height of 1100 mm when compared to the other handle heights. Ergonomical evaluations can be carried out for pushing and pulling tasks at the workplace to assess the degree of forces exerted on the trolley by the subject/worker. The push/pull forces are frequently distinguished as initial forces required to move an object from a stationary position. Heart rate methodology was generally considered a cost-effective method in ergonomics intervention to decrease workload and to create favourable working conditions. Unlike the energy expenditure technique, this can be used as a simple practical approach in natural settings. Therefore, the economic problems involved in ergonomics interventions can be solved with much ease. Surface electromyography (sEMG) can be utilized as the best data acquisition tool for ergonomic interventions to emphasize the possibilities of the assessment of muscle activities. The results of the present study have shown that there is a gradual decrease in the heart rate and the push force by using of the new trolley with wheels having 150 mm diameter and a handle height of 1100 mm for the selected population. EMG results confirm the results.

4 Conclusions

The outcome of this research is useful in selecting industrial trolleys for reducing the discomfort experienced by industrial workers whose stature is in the range of 1650–1820 mm. A 150 mm wheel diameter was found to be better than the wheels having 100 mm or 125 mm diameter. This study concludes that a handle height of 1100 and a 150 mm wheel diameter will help the industrial workers to work comfortably and eliminate WMSDs resulting in better occupational health and increased productivity.

References

1. Kumar, P., Maiti, J.: Ergonomic design of products and work systems. 21st Century perspectives of Asia, Springer ISBN 978-981-10-5457-0 (2018)
2. Argubi-Wollesen, A., Wollesen, B., Leitner, M., Mattes, K.: Human body mechanics of pushing and pulling: analyzing the factors of the task-related strain on the Musculoskeletal system. Saf. Health Work. **8**, 11–18 (2017)
3. Chow, A.Y., Dickerson, C.R.: Determinants and magnitudes of manual force strengths and joint moments during two-handed standing maximal horizontal pushing and pulling. Ergonomics **59**(4), 534–544 (2016)
4. Halloran, R.O., Tedja, I.: Reducing manual handling injury risk through trolley design in anatomy teaching laboratory. Australian Universities Safety Association Conference, Queenstown (2015)

5. Somnath, G., Dev, S.: Design and evaluation of ergonomic interventions for the prevention of musculoskeletal disorders in India. Ann. Occup. Environ. Medicine **26**, 18. https://doi.org/10.1186/2052-4374-26-18, 2014
6. Lin, C.L., Chen, M.S., Wei, Y.L., Wang, M.J.J.: The evaluation of force exertions and muscle activities when operating a manual-guided vehicle. Appl. Ergon. **41**, 313–318 (2009)
7. Douglas, C.: Montgomery, Design and Analysis of Experiments, 8th Edn. Wiley Inc., ISBN 978-1-118-14692-7 (2013)
8. Jansen, J.P., Hoozemans, M.J., van der Beek, A.J., Frings-Dresen, M.H.: Evaluation of ergonomic adjustments of catering carts to reduce external pushing forces. Appl. Ergon. **33**, 117–127 (2002)
9. Bedny, Gregory Z., Karwowski, Waldemar, Seglin, Mark H.: A heart rate evaluation approach to determine the cost-effectiveness of an ergonomics intervention. Int. J. Occup. Saf. Ergon. **7**(2), 121–133 (2001)
10. Balogh, I., Ohlsson, K., Nordander, C., Skerfving, S., Hansson, G.A.: Precision of measurements of physical workload during standardized manual handling Part III: goniometry of wrists. J. Electromyogr. Kinesiol. **19**(5), 1005–1012 (2009)

Multiobjective Scheduling in Flexible Manufacturing System by Modified Cuckoos Search Algorithm

B. Satish Kumar, G. Janardhana Raju and G. Ranga Janardhana

Abstract In this present work, an attempt is made to solve FMS scheduling problem by considering the multiobjective using Modified Cuckoos Search Algorithm. Combined Objective Function (COF) is formulated by considering two objectives with equal weightage i.e., minimizing the machine idle time and minimizing the penalty cost. The problem considered is 43 jobs need to be manufactured by processing on 16 machines is taken from literature. Matlab program is written to calculate COF value and for finding best sequence, COF value MCS algorithm is implemented. Best sequence and COF values obtained by MCS algorithm are compared with values obtained by other Algorithms like SPT, LPT, PSO, GA & CS. It is observed that sequence obtained by Modified Cuckoos Search Algorithm is giving better COF values.

Keywords Flexible Manufacturing Systems · Combined Objective Function · Modified Cuckoo Search Algorithm · Multi Objective Scheduling

1 Introduction

Manufacturing scheduling is very important in FMS. In today's highly competitive world, FMS is important because of its need to accommodate fluctuation in demands and fulfilling customer's requirements with immediate effects. So, researchers are trying to find solutions for FMS scheduling problem by developing the algorithms to optimize the scheduling.

B. Satish Kumar (✉)
Department of Mechanical Engineering, Vignana Bharathi Institute of Technology, Hyderabad, India
e-mail: satishbk91@gmail.com

G. Janardhana Raju
Dean-School of Engineering, Nalla Narasimha Reddy Education Society's Group of Institutions, Hyderabad, India

G. Ranga Janardhana
Department of Mechanical Engineering, JNTU, University College of Engineering, Anantapur, India

L. Li et al. (eds.), *Advances in Materials and Manufacturing Engineering*, Lecture Notes in Mechanical Engineering, https://doi.org/10.1007/978-981-15-1307-7_64

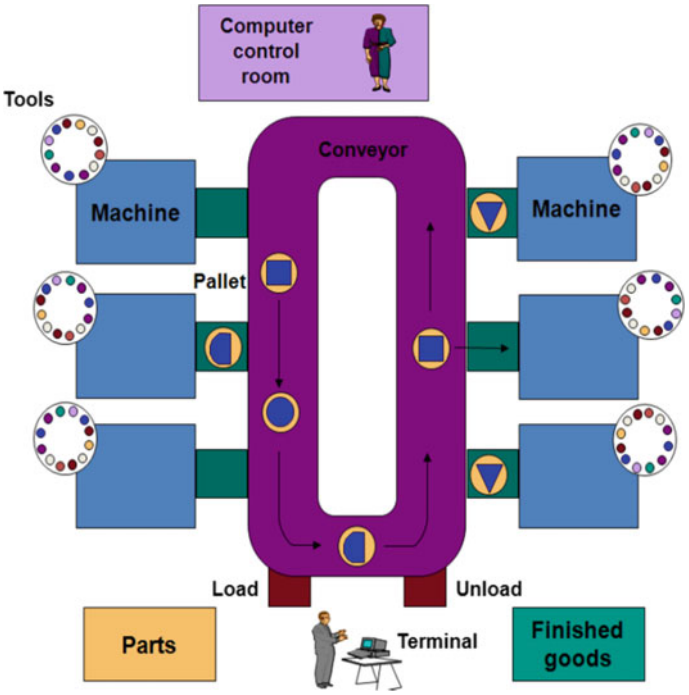

Fig. 1 Typical view of FMS

FMS consists a group of machines which are coordinated and controlled by a common control center. The scope for flexibility in the manufacturing systems is an advantage; it is a very complex task when it comes to scheduling of parts in a changing environment. In this work, MCS algorithm is used to find the better sequence to get better COF values (Fig. 1).

In FMS, most important objectives are:

- Machine idle time minimization
- Penalty cost minimization
- Increasing the production
- In-process inventories minimization
- Setup and tool changes time minimization
- Minimization of total elapsed time

In the present work, we have considered two objectives, i.e. Machine idle time Minimization and penalty cost minimization, equal weightage is given for both the objectives. It is emphasized to calculate the penalty cost and COF value for the sequences obtained by using the various Algorithms for the COF.

2 Literature Survey

Researchers gave importance for the FMS scheduling problem because of global completion in manufacturing industry. Effective scheduling plays a main function to face the competition in the market.

Burnwal et al. used CS Algorithm for optimization of scheduling in FMS [1]. Deb and Yang proposed a new met heuristic algorithm CS to find optimum solution for Scheduling Problem [2]. Farzad Khorsandi used Multiobjective uniform diversity Genetic Algorithm for optimization of economic benefits for organizations [3]. Gopikrishna and Nagabrahmam applied scatter search algorithm for optimizing the schedules in FMS [4]. Jerald et al. used different Algorithms like GA, SA, MA & PSOA for solving the Multi Objective Scheduling problem with the objectives of minimizing the machine idle time and penalty cost for not meeting the due dates. Results obtained by different algorithms are compared [5]. Kazim and Syed developed codes in C++ for getting optimum sequence of operation to reduce waiting time of machine and maximize the machine utilization for FMS scheduling problems [6]. Lal and Waiker proposed scheduling by priority rules [7, 8]. Murthy et al. developed an algorithm for optimizing the manufacture plans in FMS [9]. Persi and Walter solved the problem of maximization of machine utilization [10]. Sankar and Solberg applied MOGA for scheduling of 16 machines and 43 jobs problem and obtained better results compared to other Algorithms [11]. Stecke and Solberg have carried out modeling and simulation studies of FMS [12]. Udhayakumar and Kumanan proposed PSO for integration between manufacturing schedule and MHS in FMS [13–15]. Srinivas et al. proposed an efficient backbone-based quick link failure recovery multicast routing protocol [16]. Srinivas et al. developed L2R protocol to generate an alternate path for link failures in backbone networks [17]. Mahesh concluded that integration of MRP and CRP will be helpful to generate a near to optimal production schedule [18]. Proposed methodology for scheduling optimization of FMS Modified Cuckoos Search Algorithm.

CS is an optimization algorithm developed by Yang and Deb in 2009 [2]. The original CS algorithm was usually used to solve benchmark or real-world problems over continuous search space. Nowaday's many researchers are using CSA to find the optimum solution for different problems. MCSA [19] focuses to enhance the standard CSA through replacing the random selection with the tournament selection as shown in algorithm Fig. 2. MCSA has two modifications from the standard Cuckoos Search Algorithm. The two modifications that are made to the CS with the aim of increasing converging rate for implementing in more wider applications.

2.1 Problem Definition

Considered two sample problems: problem number one is considered randomly shown in Table 1 and problem number two taken from literature, i.e. from the papers

Objective function *f(X);*
Generate Intial population of n host next;
Evaluate fitness and Rank eggs;
While t< Max iterations or (stop criterion) do
Get a cuckoo (say i) randomly by Levy flights *Fi;*
Evaluate its quality fitness *Fi;*
Call the tournament selection to get *Fj*
If *Fj>Fi* then
Replace the current solution with new solution;
end if
New egg is laid by host bird via levy Levy flights with mutation fraction of *Pα*
Evaluate its quality fitness *Fxnew*
If Fx new < Fx then
Replace the current solution with new solution
end if
Rank the solution and find current best
end while
Post process results and visualization

Fig. 2 Modified Cuckoos Search Algorithm

Table 1 Sample problem number 1 data

Part no.	M/c no. (processing time in min)	Due date (days)	Batch size	Penalty cost (Rs./unit/day)
1	5 (4)–6 (5)–7 (1)	40	8	2
2	4 (2)–5 (3)–6 (2)–7 (5)	60	5	1
3	2 (1)–8 (1)–9 (2)	15	6	3
4	8 (2)–10 (2)	20	5	2
5	8 (1)–11 (3)–13 (4)	50	8	4

by Jerald and Sankar et al. [5] shown in Table 2 provides all the information required for individual jobs.

The assumptions made in this work are as follows:

- There are 43 varieties of products to be manufactured
- Each type/variety has a particular processing sequences, batch size, deadline, and penalty cost for not meeting the deadline.
- Each processing step has a processing time with a specific machine.
- Forty-three jobs have been taken and processing sequence on different machines has been decided.
- One job will be processed on one machine at a time based on the sequence of parts as per the required batch size.

Combined Objective Function (COF) is formulated by cosidering the two objectives with equal weightage.

$$\text{COF} = W_1 \times \left(\frac{\text{PC}}{\text{MP}}\right) + W_2 \times \left(\frac{X_q}{\text{TE}}\right) \tag{1}$$

Table 2 Sample problem number 2 data

Part no.	M/c no. (processing time in min)	Due date (days)	Batch size	Penalty cost (Rs./unit/day)
1	6 (1)–7 (1)–8 (1)–10 (2)	17	150	1
2	2 (1)–6 (1)–8 (2)–9 (2)–14 (4)–16 (2)	17	200	1
3	8 (1)–11 (3)–13 (4)	14	800	1
4	9 (4)	26	700	2
5	4 (5)–5 (3)–15 (4)	11	150	1
6	6 (5)–14 (1)	16	700	1
7	3 (5)–6 (3)–16 (5)	26	250	2
8	5 (4)–6 (5)–8 (1)	26	850	2
9	4 (1)–5 (5)–8 (1)–11 (1)	1	100	0
10	2 (2)–9 (1)–16 (4)	20	150	2
11	8 (4)–12 (2)	1	250	1
12	6 (2)–8 (4)–10 (1)	19	1000	3
13	6 (1)–7 (5)–10 (4)	25	700	4
14	4 (2)–5 (3)–6 (2)–15 (2)	22	1000	4
15	5 (4)–8 (3)	15	700	5
16	5 (3)	27	750	3
17	3 (1)–6 (4)–14 (1)	20	650	4
18	9 (2)–16 (3)	24	250	5
19	4 (1)–5 (5)–6 (2)–8 (2)–15 (5)	5	450	1
20	8 (2)–11 (4)	11	50	5
21	4 (5)–5 (5)–8 (4)–15 (4)	16	850	3
22	12 (5)	24	200	5
23	4 (2)–5 (1)–6 (5)–8 (4)	14	50	4
24	8 (4)–11 (4)–12 (5)–13 (4)	7	200	5
25	7 (3)–10 (2)	24	350	1
26	10 (2)	27	450	0
27	8 (5)–11 (5)–12 (4)	22	400	1
28	2 (1)–8 (1)–9 (2)	3	950	5
29	4 (1)–5 (5)	7	700	1
30	11 (3)–12 (5)	18	1000	1
31	8 (2)–10 (2)	2	800	2
32	2 (3)–6 (4)–9 (3)	15	800	1
33	5 (4)–6 (5)–15 (3)	27	500	4

(continued)

Table 2 (continued)

Part no.	M/c no. (processing time in min)	Due date (days)	Batch size	Penalty cost (Rs./unit/day)
34	3 (2)–6 (2)	12	300	4
35	3 (4)–14 (1)	9	900	2
36	3 (2)	20	700	2
37	1 (5)–2 (2)–6 (3)–8 (3)–9 (2)–16 (4)	22	250	4
38	2 (4)–8 (3)–9 (2)–16 (5)	8	50	1
39	6 (5)–10 (5)	9	500	1
40	2 (2)–6 (4)–9 (4)	7	250	5
41	5 (1)–8 (2)–15 (1)	22	800	4
42	2 (5)–6 (4)–9 (3)–16 (1)	19	400	2
43	1 (3)–5 (2)–6 (2)–8 (2)–15 (3)	15	550	3

Table 3 COF values for sample problem one

	Sequence 1	Sequence 2	Sequence 3	Sequence 4	Sequence 5
Sequence	1,2,3,4,5	2,3,4,5,1	3,4,5,1,2	4,5,1,2,3	5,1,2,3,4
COF	0.3931	0.3923	0.4061	0.4833	0.382

W_1 Weightage factor for minimizing the total penalty cost
W_2 Weightage factor for minimizing the total elapsed time
PC Total penalty cost
MP Maximum penalty
X_q Total machines idle time
TE Total elapsed time.

3 Calculations and Results

For problem number one shown in Table 1, there are 120 possible sequences are possible and code was written in MATLAB for calculating COF values by using Eq. 1. Manual calculations were made for randomly selected sequence to find COF Value and same were compared by writing the program in MATLAB, both the values were got same. For problem number two shown in Table 2, applied Modified Cuckoos Search Algorithm [1] to find the best sequence which gives the best COF value. MATLAB program run for 10 iterations, 20 iterations, 30 iterations, 40 iterations, 60 iterations and finally, for 100 iterations. It has been found that for less number of iterations, results are not good as we increase the iteration number, it started giving

Table 4 COF values obtained for sample problem two by different algorithms

Algorithm	SPT [11]	PSO [5]	CS [1]	MCS
	20,23,38,19	27,30,38,10,	8,14,28,31,	19,21,28,31,
	26,22,10	18,15,34,42,	3,42,26,33,	32,24,30,3,
	34,18,36,11	5,33,8,37	22,20,5,24,	39,11,14,15,
	25, 5, 16,2,	23,25,9,2,	12,41,18,7,	41,12,13,17,
	40,4,41, 31	35,43,20,6,	10,19,23,38,	16,33,35,8,
Sequence	7,24,28,17	4,36,19,17,	4,35,40,37,	43,4,36,18,
	6, 9, 35,37	24,39,31,12,	21,15,17,39,	40,34,22,37,
	37,15,39,42	28,32,26,16,	6,2,34,1,	42,6,29,7,
	27, 33,3,43	14,22,3,1,	29,27,16,36,	27,25,10,20,
	19,13, 12,32,	11,41,29,40,	30,25,32,13,	2,23,1,5,
	30, 8,14,21	21,13, 7	43,11, 9	38,9,26
CoF	0.3240	0.2983	0.2646	0.1419

better results, but after 40 iterations the value and sequences obtained were same therefore, we have stopped at 100 iterations. For 100 iterations, we have run the code for 5 times and at 100 iterations, every time we have good best sequence and CoF value as same, and we got COF = 0.1419. COF values obtained by other researchers using different algorithms are tabulated and compared shown in Table 4. Results shows that for first problem, Sequence 5 is giving the better COF value shown in Table 3. For problem number 2, MCS Algorithm is giving better COF value.

4 Conclusion

Many researchers are made an attempt to solve multiobjective scheduling problem by implementing the different algorithm like SPT, PSO, CS. In the present work, we have written program in MATLAB for calculating combined objective function value which is the combination of two objectives, i.e. minimization of machine idle time and minimization of penalty cost. Equal weightages are assumed for the both the objectives. We have implemented MCSA for obtaining better sequence which gives optimum COF value for the scheduling problem taken from literature, i.e. 43 parts to be processed on sixteen machines. It is observed that MCS is giving better COF values. Finally, it is concluded that MCS is giving the better results than other algorithms like CS, PSO, and SPT. In the future, we are planning to implement this MCS Algorithm for much bigger size problem.

References

1. Burnwal, S., Deb, S.: Scheduling optimization of flexible manufacturing system using cuckoo search-based approach. Int. J. Adv. Manuf. Technol. **2**(64), 951–959 (2013)
2. Deb, S, Yang, X.S.: Engineering optimization by cuckoo search. Int. J. Math. Model. Numer. Optim. **1**(4), 330–343 (2010)
3. Shahrestani, F.K., Mahbobi, H., Mohebi, E., Mosaffa, H.B.: Optimization of scheduling flexible manufacturing systems by using multi-objective Genetic algorithm. Inter. Discipl. J. Contemp. Res. Bus. **5**(1), 1015–1023 (2013)
4. Gopikrishna, N., Nagabrahmam, P.: Review of flexible manufacturing systems on rational exploration of flexible manufacturing systems. Int. Res. J. Eng. Technol. **3**(2), 625–629 (2016)
5. Jerald, J., Asokan, P., Prabaharan, G., Saravanan, R.: Scheduling optimization of flexible manufacturing systems using particle swarm optimization algorithm. Int. J. Adv. Manuf. Technol. **25**(9), 964–971 (2005)
6. Kazim, S.M., Singh, A.K., Jayswal, S.C.: Scheduling optimization in FMS using genetic algorithm with make span criterion. Int. J. Technol. Res. Eng. **1**(12), 1532–1536 (2014)
7. Waikar, A.M., Sarker, B.R., Lal, A.M.: A comparative study of some priority dispatching rules under different shop loads. J. Prod. Plan. Control. **6**(4), 301–310 (2007)
8. Lee, D.H, Kim, Y.D.: Scheduling algorithm for flexible manufacturing systems with partially grouped machines. J. Manuf. Syst. **18**(4), 301–309 (1999)
9. Murthy, A.N.N., Chandrasekhara, K., Vijay Kumar, M.: Dynamic scheduling of flexible manufacturing system using heuristic approach. Opsearch **48**, 1–19 (2011)
10. Piero, P., Walter, U.: A hierarchic approach to production planning and scheduling of a flexible manufacturing system. Robot. Comput. Integr. Manuf. **15**, 373–385 (1999)
11. Sankar, S., et al.: A multi objective genetic algorithm for scheduling a flexible manufacturing system. Int. J. Adv. Manuf. Technol. **15**(22), 229–236 (2003)
12. Stecke, K.E., Solberg, J.J.: Loading and control policies for flexible manufacturing system. Int. J. Prod. Res. **19**(5), 481–490 (1981)
13. Udhayakumar, P., Kumanan, S.: Integrated scheduling of flexible manufacturing system using evolutionary algorithms. Int. J. Adv. Manuf. Technol. **61**(5–8), 621–635 (2012)
14. Mahmudy, W.F.: Optimization of part type selection and machine loading problems in flexible manufacturing system using variable neighborhood search. Int. J. Comput. Sci. **42**(3), 1–11 (2015)
15. Kumar, M.S., Kumar, B.S.: Performance analysis of material handling systems for a layout with different speeds. Int. J. Mech. Prod. Eng. Res. Dev. **8**(5), 1–16 (2018)
16. Vodnala, D., Kumar, S.P., Aluvala, S.: An Efficient backbone based quick link failure recovery multicast Routing protocol. Elsevier-Perspectives in science, **8**(1):135–137(2016)
17. Vodnala, D., Kumar, S.P., Aluvala, S.: L2R: multicast routing protocol for effective localized route recovery in backbone networks. Int. J. Control. Theory Appl. **33**(9), 79–87 (2016)
18. Mahesh, V.: Integrated model for machine scheduling and inventory management under finite capacity settings. Int. J. Mech. Eng. Technol. **9**(10), 1021–1032 (2018)
19. Shehab, M., Khader, A.T., Laouchedi, M.: Modified Cuckoos search algorithm for solving global optimization problem. In: Proceedings of the 2nd International Conference of Reliable Information and Communication Technology (IRICT-2017), pp. 561–570, Springer in nature, Malaysia (2017)

Hidden Markov Modelling of High-Speed Milling (HSM) Process Using Acoustic Emission (AE) Signature for Predicting Tool Conditions

P. Sachin Krishnan, K. Rameshkumar and P. Krishnakumar

Abstract Tool condition monitoring is an important activity to monitor and maintain the quality of products manufactured in any machining process without any manual intervention. Hidden Markov models (HMM) are developed in this study for predicting tool conditions in a High-Speed Milling of titanium alloy using a carbide tool. Tool conditions are predicted using AE signatures captured during the metal cutting operation. A correlation between AE features and tool conditions were established using Baum-Welch and Viterbi algorithms. HMM models proposed in this study are integrated with the *K*-means clustering algorithm. The clustered data has been represented as an integer sequence and is divided into 3 tool states such as 'sharp', 'intermediate' and 'worn-out'. Three HMM models are created for each state of the tool. Two AE features namely 'Root Mean Square (RMS)' and 'Rise' were used for developing HMMs. The performance of the HMMs is evaluated using log-likelihood measure.

Keywords Condition monitoring · Acoustic emission (AE) · High-speed milling · Hidden markov model (HMM)

1 Introduction

Acoustic emission (AE) sensors are used to detect high-frequency elastic waves that are generated during the metal cutting process. AE will happen in the higher frequency range from 100 to 1 MHz [1]. The main advantage of AE-based tool-condition monitoring is that AE signal will not interfere with the cutting process. The frequency range of the AE emissions is much higher compared to other sensors such as vibration.

Hidden Markov model is a doubly stochastic mathematical model, which can predict conditions of the cutting tool dealing with dynamic and probabilistic events occur in machining operations [2].

P. Sachin Krishnan · K. Rameshkumar (✉) · P. Krishnakumar
Department of Mechanical Engineering, Amrita School of Engineering, Amrita Vishwa Vidyapeetham, Coimbatore 641112, India
e-mail: k_rameshkumar@cb.amrita.edu

L. Li et al. (eds.), *Advances in Materials and Manufacturing Engineering*, Lecture Notes in Mechanical Engineering, https://doi.org/10.1007/978-981-15-1307-7_65

HMM is initially used in the speech recognition process by Rabiner and Juang [3]. Hidden Markov models are used for diagnosis and prognostics of tool states in metal cutting operation using AE signature by Geramifard et al. [4]. Yu et al. [5] proposed Hidden Markov models using AE and vibration sensors in a CNC milling process. An intelligent fuzzy neural network approach was implemented by Jahromi et al. [6] in a high-speed milling environment using AE signatures. Wear process in the milling of titanium alloy was studied by Harris et al. [7]. Off late, Krishnakumar et al. [8–10] studied the ultra-precision high-speed milling of titanium alloys using the signals captured by AE and vibration sensor. A comprehensive review focusing on sensors, signal-processing techniques applied for tool-condition monitoring were reviewed by the researchers in the recent past [11–14].

From the literature review, it is observed that tool-condition monitoring systems are vital in an automated manufacturing environment to predict the tool condition or process. The decision can be taken for maintenance or replacement of tools/components of a machine/mechanical system without the intervention of a human. In precision milling operations, better correlations with tool wear were achieved using AE sensors. Only a few implementations of doubly stochastic methods like Hidden Markov models exist for predicting the tool conditions.

2 Methodology and Experimental Set-up

In this paper, tool conditions of a carbide tool in ultra-precision high-speed milling are predicted using Hidden Markov models. AE signals representing tool conditions were captured and dominant features are extracted in the time domain. *K*-means clustering algorithm is used for representing the tool-condition data as an integer sequence for developing HMM models for each tool state. Log-likelihood measures are used to predict the tool conditions. Methodology and experimental set-up are shown in Fig. 1.

The AE sensor used in this study is 'Micro 30 D' supplied by M/s Physical Acoustic Corporation (USA) and the operating frequency range is 100–350 kHz. Experiments were conducted with optimum parameters. The tool flank wear right from sharp state to worn-out state was recorded and plotted by conducting experiments. This exercise is carried out to identify the tool conditions using surface roughness plot. Using the surface roughness plot, tool conditions are identified and shown in Fig. 2.

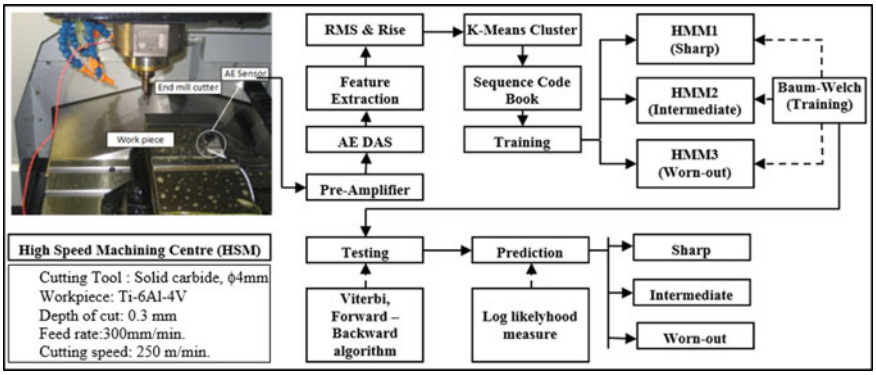

Fig. 1 Methodology and experimental set-up

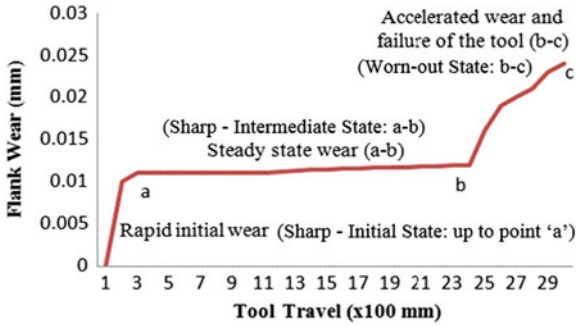

Fig. 2 Surface roughness plot

2.1 *Hidden Markov Model for Tool-Condition Monitoring (TCM)*

Hidden Markov model is an extension of the concept of Markov chain [3]. It means that the input and output of the model are probabilistic. There are basically two types of HMM, discrete HMM and continuous HMM. In this paper, discrete HMM is used to represent the tool conditions. Figure 3 shows the first-order three states HMM.

(a) The number of hidden states in the model which is denoted by '*N*'. Hidden states are interconnected and transition can occur from one state to another. The three hidden states are sharp-initial, sharp-intermediate and worn-out.
(b) The number of distinct observation symbol which is used to define a hidden state which is denoted by '*M*' is denoted as $V = \{v_1, v_2, v_3, \ldots, v_M\}$.
(c) State transition probability matrix $[A]$ is an $N \times N$ matrix, which gives the probability values of transition from one hidden state to another.

It is denoted by $[A] = a_{ij}$, where $a_{ij} = P\left(q_t = S_j \middle| q_{t-1} = S_i\right), 1 \leq i, j \leq 1$

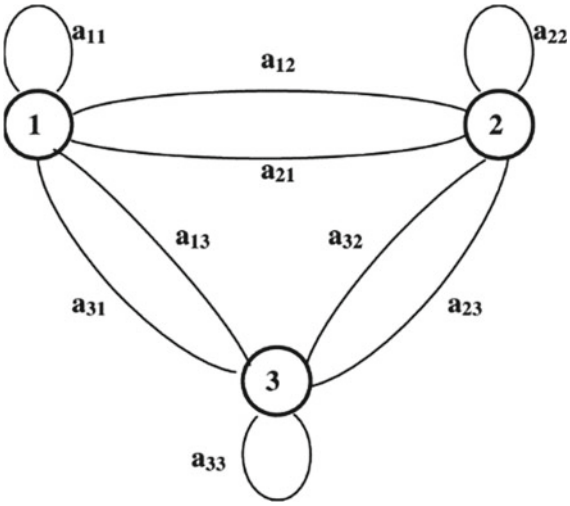

Fig. 3 1st order three state HMM [3]

(d) Observation symbols are connected with the model by the observation symbol probability matrix $[B]$. It gives the probability that the observation symbol represents a particular hidden state. This connects the observation with the hidden states. It is denoted by $[B] = b_{jm}$, where $b_{jm} = P\left(o_t = v_m | q_t = S_j\right)$, $1 \leq m \leq M$

(e) Initial state distribution which defines the initial state of the model. It is denoted by the symbol, π where, $\pi = [\pi_i]$ in which $\pi_i = P(q_i = S_i)$, $1 \leq i \leq N$

(f) A basic HMM is denoted by the symbol λ (Parameters of HMM) and is defined as: $\lambda = (A, B, \pi)$.

3 HMM Implementation

3.1 HMM Training and Testing

HMM tool box in MATLAB developed by Murphy [15] is utilized in this study for building the HMM for tool-condition monitoring. The observation sequence got from the *k*-means clustering algorithm is provided as an input to HMM for training. A total of 8177 data points were used for training and testing of HMMs. For training, 80% of the data from each state is selected. The remaining 20% is kept for testing of the model. Training is carried out using the Baum–Welch algorithm [16]. For the given AE observation sequence input, the Baum–Welch algorithm provides the final transition, emission and state probabilities. Testing of HMMs is done with Viterbi

and forward–backward algorithms [16]. The HMM which is having maximum log-likelihood value will provide the index of the tool for that particular signal, i.e. ($P(O|\lambda)$).

3.2 Results and Discussions

State transition probability matrix [A], emission probability matrix [B] and the initial probability matrix [π] were computed using the Baum–Welch algorithm using the training sequences generated by the k-means algorithm. K-means algorithm is used to generate sequences for 'RMS' and 'Rise' AE features. Baum–Welch algorithm is used for training each state of the HMM. A state represents the condition of the cutting tool. State parameters viz. λ_1, λ_2, and λ_3 are computed using the Baum–Welch algorithm. The state transition probabilities and emission probabilities are shown in Table 1. The maximum probability is represented in the diagonal of the transition probability matrix [A]. Maximum probability is the indication of the system tends to remain in the same state most of the time.

Testing of the HMM model is carried out using Viterbi and forward–backward algorithms. Testing is carried out using 20% of the AE data from each state of the tool. The log-likelihood measure is used to identify the condition of the cutting tool. It is to be noted that the observation sequence, say, 'sharp-initial' is correctly

Table 1 State transition and emission probabilities of AE-RMS and AE-Rise data

State transition probability, [A]—RMS								
HMM1 (sharp–initial state)			HMM1 (sharp–intermediate state)			HMM1 (worn-out state)		
0.9880	0.0120	0	0	0	0	0	0	0
0	0.9943	0.0057	0	0.9987	0.0013	0	0	0
0	0	1	0	0	1	0	0	1
State transition probability, [A]—*Rise*								
0.5690	0.2777	0.1533	0	0	0	0	0	0
0	0.6608	0.3392	0	0.4375	0.5625	0	0	0
0	0	1	0	0	1	0	0	1
Emission probability, [B]—*RMS*								
1	0	1.6e−114	0	0	0	0	0	0
9.5e−10	0.9939	0.0061	0.9382	0	0.0618	0	0	0
0.8835	6.35e−16	0.1145	0.2046	0.3539	0.4415	0.2284	0.6379	0.1337
Emission probability, [B]—*Rise*								
0.1811	0.5727	0.2462	0.0011	0.5527	0.4462	0	0	0
0.6564	0.1901	0.1535	0.3523	0.1379	0.5098	0.0065	0.9519	0.0416
0.1772	0.6477	0.1750	0.3772	0.1852	0.4376	0.3771	0.2264	0.3966

Table 2 Log-likelihood values of test data (RMS and rise)

Log-likelihood values	HMM1 (sharp-initial)	HMM2 (sharp-intermediate)	HMM3 (worn-out)
RMS data			
Testdata1 (sharp)	**−7.8640**	−13.2406	−236.7144
Testdata2 (intermediate)	−800.8292	**−792.0994**	−2.1468e+3
Testdata3 (worn-out)	−676.1572	-inf	**−217.0855**
Rise data			
Testdata1 (sharp)	−176.516	**−174.0160**	−175.5962
Testdata2 (intermediate)	−1.5981e+03	**−1.5924e+03**	−1.60e+03
Testdata3 (worn-out)	−406.542	−417.602	**−403.325**

classified if the log-likelihood value of HMM of 'sharp-initial' is higher compared to the other two states of the tool. Similarly, for the other two states, log-likelihood values are computed and compared with all the HMM's. For all the states of test data, the corresponding HMM model is providing maximum log-likelihood value for AE-RMS data. This means, the proposed HMM model with AE-RMS feature is predicting the tool conditions accurately. The log-likelihood values for testcases extracted from 'RMS' and 'Rise' data for all the HMMs are given in Table 2.

In the case of HMM model using 'Rise' feature data, the log-likelihood values of 'sharp-initial' condition are misclassified as 'sharp-intermediate'. The misclassification is evident from the log-likelihood values shown in Table 2. The log-likelihood value for HMM1 is supposed to be higher than the log-likelihood value of HMM2 in 'sharp-initial' condition for 'Rise data'. The other two test data sets belonging to 'sharp-intermediate', and 'worn-out' are classified correctly by the HMM for 'Rise data'. The misclassification is due to the AE data collected from the narrow region of 'initial-sharp' state of the tool, where 'sharp' and 'sharp-intermediate' conditions of the tool are difficult to distinguish. It is concluded that 'AE-RMS' feature has good correlation with carbide tool conditions in high-speed machining of titanium alloys compared to 'AE-Rise' feature.

4 Conclusions

Tool-condition monitoring of solid carbide tool in high-speed machining of titanium alloy is proposed in this paper using AE signature. An experimental set-up was established to study the ability of discrete Hidden Markov models to predict the tool conditions by extracting AE features in time domain. Three tool states, namely 'sharp-initial', 'sharp-intermediate' and 'worn-out' were identified by experimental results using surface roughness plot. Discrete observation sequences (Code-book)

were created using the *k*-means clustering algorithm. Three different HMM models were developed corresponding to three different states of the tools.

HMMs were trained with AE features of 'RMS' and 'Rise' using the Baum–Welch algorithm. Tool states are defined using transition and emission probabilities. Testing of the HMMs is carried out using 20% of the total data which are not used for the training purpose. Viterbi and forward–backward algorithms were used for training. HMM models are evaluated using log-likelihood measures.

The present study shows, among AE features of 'RMS' and 'Rise', HMM model with 'RMS' AE feature is able to predict the tool states accurately. All the tool states were predicted correctly by the HMM using the 'RMS' feature. HMM with 'Rise' feature misclassifies the 'Sharp-initial' observation sequences as 'Sharp-intermediate' state.

It is concluded that HMMs are able to classify the tool conditions accurately in precision high-speed machining of Titanium alloys. AE feature, 'RMS' is having good correlation with tool wear. Further, HMM models can be extended for predicting the tool conditions in real-time. Remaining useful life predictions using HMMs can be taken up in future.

Acknowledgements This research is supported by Directorate of Extramural Research and Intellectual Property Rights (ER and IPR), Defence Research and Development Organization (DRDO), ERIP/ER/0803740/M/01/1194, 13 January 2010.

References

1. Dornfeld, D.A., Lee, Y., Chang, A.: Monitoring of ultra-precision machining processes. Int. J. Adv. Manuf. Technol. **21**(8), 571–578 (2003)
2. Wang, L., Mehrabi, M.G., Kannatey-Asibu Jr, E.: Hidden Markov model-based tool wear monitoring in turning. J. Manuf. Sci. Eng. **124**(3), 651–658 (2002)
3. Rabiner, L.R., Juang, B.H.: An introduction to hidden Markov models. ieee assp magazine **3**(1), 4–16 (1986)
4. Geramifard, O., Xu, J., Zhou, J., Li, X.: A physically segmented hidden markov model approach for continuous tool condition monitoring: diagnostics and prognostics. IEEE Trans. Ind. Inf. **8**(4), 964–973 (2012)
5. Yu, J., Liang, S., Tang, D., Liu, H.: A weighted hidden markov model approach for continuous-state tool wear monitoring and tool life prediction. Int. J. Adv. Manuf. Technol. **91**(1–4), 111–201 (2016)
6. Jahromi, A., Meng, J., Li, X., Lim, B.: Sequential fuzzy clustering based dynamic fuzzy neural network for fault diagnosis and prognosis. Neurocomputing **196**, 31–41 (2016)
7. Harris, K., Triantafyllopoulos, K., Stillman, E., Mcleay, T.: A multivariate control chart for auto correlated tool wear processes. Qual. Reliab. Eng. Int. **32**(6), 2093–2106 (2016)
8. Krishnakumar, P., Rameshkumar, K., Ramachandran, K.I.: Feature level fusion of vibration and acoustic emission signals in tool condition monitoring using machine learning classifiers. Int. J. Progn. Health Manag. **9**, 1–15 (2018)
9. Krishnakumar, P., Rameshkumar, K., Ramachandran, K.I.: Acoustic emission-based tool condition classification in a precision high-speed machining of titanium alloy: a machine learning approach. Int. J. Comput. Intell. Appl. **17**(03), 1850017 (2018)

10. Krishnakumar, P., Rameshkumar, K., Ramachandran, K.I.: Machine learning based tool condition classification using acoustic emission and vibration data in high speed milling process using wavelet features. Intell. Decis. Technol. **12**(2), 265–282
11. Teti, R., Jemielniak, K., O'Donnell, G., Dornfeld, D.: Advanced monitoring of machining operations. CIRP Ann. Manuf. Technol. **59**(2), 717–739 (2010)
12. Roth, J.T., Djurdjanovic, D., Yang, X., Mears, L., Kurfess, T.: Quality and inspection of machining operations: tool condition monitoring. J. Manuf. Sci. Eng. **132**(4), 041015 (2010)
13. Bhuiyan, M.S.H., Choudhury, I.A., Dahari, M., Nukman, Y., Dawal, S.Z.: Application of acoustic emission sensor to investigate the frequency of tool wear and plastic deformation in tool condition monitoring. Measurement **92**, 208–217 (2016)
14. Zhou, Y., Xue, W.: A multisensor fusion method for tool condition monitoring in milling. Sensors **18**(11), 3866 (2018)
15. https://www.cs.ubc.ca/~murphyk/Software/HMM/hmm.html (2018)
16. Rabiner, L.R., Juang, B.H.: Fundamentals of speech recognition. Englewood Cliffs: PTR Prentice Hall. **14** (1993)

Effects of the Activating Fluxes on the Properties of the Tungsten Inert Gas Welded Structural Steel

R. S. Vidyarthy, R. Bhattacharjee, S. Mohapatra and B. B. Nayak

Abstract Tungsten inert gas (TIG) welding process is a frequently recommended welding process for joining and repairing of the structural steels. However, its limitation towards the lesser depth of penetration decreases its productivity. Activating flux tungsten inert gas (A-TIG) welding is an innovative solution to the lesser depth of penetration without compromising the weld quality. In the current work, three different oxides SiO_2, TiO_2 and Cr_2O_3 are used as a single-component activating flux to develop the bead on plate-type welds on structural steel. Significant increase in depth of penetration was registered in the A-TIG weldments as compared conventionally TIG-welded samples. Weld bead geometry was studied through different aspects such as penetration depth, width, depth to width ratio and area of weld-fusion zone.

Keywords A-TIG welding · Activating flux · Bead geometry · Microstructure · Microhardness

1 Introduction

Mild steel is a multipurpose engineering material frequently used in girders, nuts, bolts, screws and structural steel are all manufactured using mild steel, owing to its affordability and mechanical property. It is also used in the manufacturing of various tools and equipment, for rail track, transmission towers and industrial building. Tungsten inert gas (TIG) welding is widely used in the industries for joining of structural steels. However, due to the lesser depth of penetration, the productivity of the TIG welding process is a major issue during welding of thicker sections. Multiple weld passes required for welding the thick sections (>3 mm) [1, 2]. This

R. S. Vidyarthy (✉)
Department of Mechanical Engineering, BITS-Pilani, Hyderabad Campus, Hyderabad 500078, India
e-mail: ravi.vidyarthyfme@hyderabad.bits-pilani.ac.in

R. Bhattacharjee · S. Mohapatra · B. B. Nayak
School of Mechanical Engineering, Kalinga Institute of Industrial Technology, Deemed to be University, Bhubaneswar, India

L. Li et al. (eds.), *Advances in Materials and Manufacturing Engineering*, Lecture Notes in Mechanical Engineering, https://doi.org/10.1007/978-981-15-1307-7_66

leads to other problems like angular distortion, corrosion sensitization and residual stresses [3, 4]. To tackle these issues, nowadays, Tungsten Inert Gas welding with flux (A-TIG) process is widely referred. Deep and narrow weld bead may obtain with A-TIG welding. However, the study of activating fluxes during A-TIG welding is limited to some of the materials like austenitic stainless steels, ferritic/martensitic steel and duplex stainless steel only [5–7]. After an exhaustive literature survey, it was observed that, significant works have not been reported on interaction of A-TIG welding with mild steel. It is expected that, better understanding of mild steel's response to various activating fluxes could lead to drastic increase in productivity of fabrication industries.

2 Materials and Method

In the current study, mild steel was used as the base metal. Optical emission spectroscope (OES) was used to analyse the chemical composition of the base metal (0.1068% C, 0.9216% Mn, and 0.1661% Si). The ultimate tensile strength of the base metal was 440 ± 5 MPa. The hardness of the as received base metal was found 131 ± 4 HV. Metal strips of specimen size 150 mm $\times$ 30 mm $\times$ 8 mm were prepared for the welding purpose. SiO_2, TiO_2 and Cr_2O_3 were used as single-component activating fluxes.

The "bead on plate" welds were prepared using A-TIG welding process. Welding was done manually to check the feasibility of the A-TIG welding process during manual welding. Direct current straight polarity was used. Weld quality was inspected through visual and macroscopic study. For macroscopic and microscopic study, samples were prepared by typical metallographic procedures including flattening using belt grinder, abrasive paper and cloth polishing, followed by etching. Abrasive papers containing SiC of 80–2000 grit number are used for mechanical polishing. After paper polishing, samples were cloth-polished using alumina powder. Villela's reagent for about 55–60 s was applied for etching.

3 Results and Discussions

Microstructure of the base metal Optical microstructure of the as received base metal is shown in Fig. 1a. Ferritic grains structure along with pearlite grains were observed during the microstructure study. Lighter as well as darker brown ferrite grains were observed. Black pearlite grains were also observed. Pearlites were generally seen as unidirectional colony wise formation in the base metal microstructure. Similar kind of microstructure was also observed by Lakshminarayanan et al. [8].

Visual Inspection of weldments

Figure 2 shows the weldments welded at welding speed (WS) of about 120 mm/min

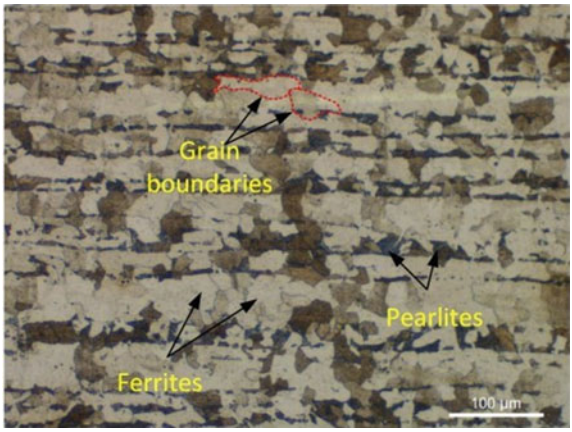

Fig. 1 Optical microstructure of the as received substrate material

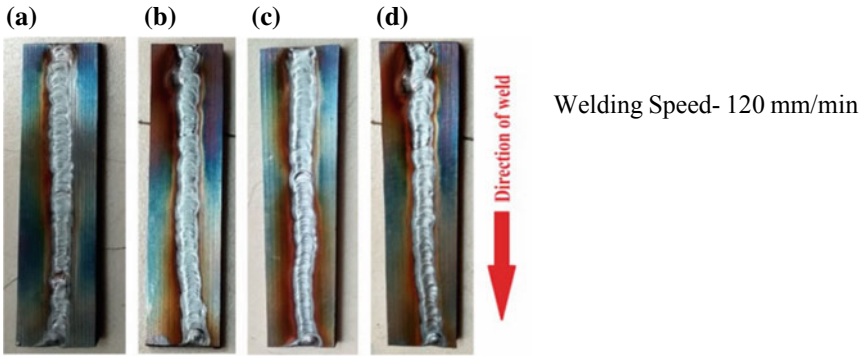

Fig. 2 Appearance of without flux specimen after weld at welding current of **a** 120 A, **b** 140 A, **c** 160 A, **d** 180 A

and at four different welding current (WC) values (a) 120 A, (b) 140 A, (c) 140 A and (d) 160 A. Welding defects like spatter, surface porosity, discontinuity and weld crater were not observed on the weld surface of any of the weldments (Fig. 2a–d). Weld surfaces were also found free from the slag residue.

Figure 3 shows the coated plate before and after welding ("welding current 120 mm/min and welding speed-180 A"). The sequence of the coating starts from the uncoated region was (a) TiO_2, (b) Cr_2O_3 and (c) SiO_2, respectively. The weld bead was found slightly differ in TiO_2, Cr_2O_3 and SiO_2 coated regions. Welding defects like spatter, surface porosity, discontinuity and weld crater were not observed on the weld surface of any of the A-TIG weldments (Fig. 4a–c). However, flux residue was observed on the A-TIG weldments. The flux residue was later removed by simple cleaning.

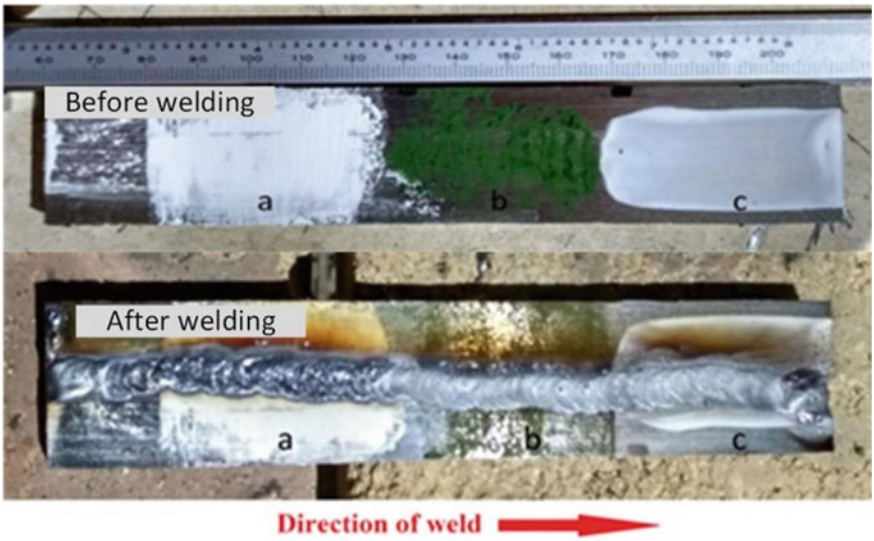

Fig. 3 Figure shows the plate before and after welding (coated with various fluxes **a** TiO_2, **b** Cr_2O_3, **c** SiO_2)

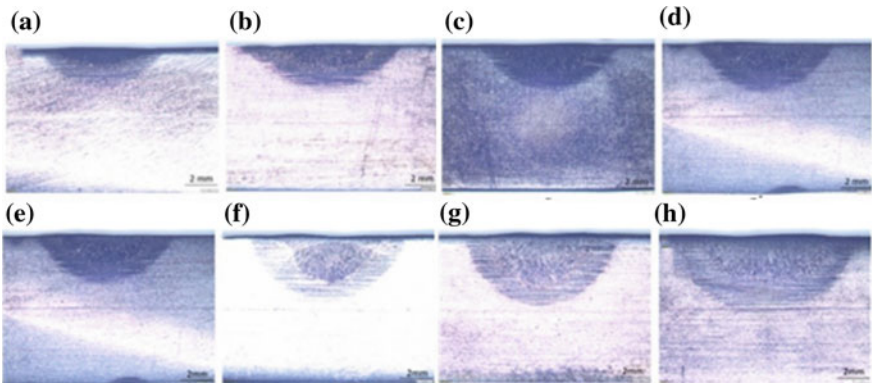

Fig. 4 Macrostructures of the weld cross section of the weldments welded at "welding speed-120 mm/min and welding current **a** 120 A, **b** 140 A, **c** 160 A, **d** 180 A without flux"; and "welding current of 180 A and welding speed of 120 mm/min **e** without flux, **f** with flux TiO_2, **g** with flux Cr_2O_3, **h** with flux SiO_2"

4 Macroscopic Analysis

The macrostructure of the weld bead cross section of the conventional TIG weldments and A-TIG weldments are given in Fig. 4a–h. Different weld zones, namely weld-fusion zone, heat-affected zones and unaffected base metal were observed in the weld cross-sectional macrostructure. Welding defects like gas inclusion or welding cracks

were not found during macrostructure study. However, significant change in depth of penetration as well as in bead width was observed with varying welding current (Fig. 4a–d) and with activating fluxes (Fig. 4e–h). With the increase in welding current from 120 to 180 A, the DOP was found to have increased from 1.32 to 2.43 mm (Fig. 5a). Vasudevan et al. [9] also stated that the depth of penetration of conventional TIG weldments increases with increase of current up to certain limit, after that irrespective of current depth of penetration does not increases. The BW was found to have increased from 6.39 to 7.46 mm for currents value at 120 and 160 A, respectively (Fig. 5b). A similar trend was observed for WA as it increased from 4.97 to 11.81 mm^2 for welding current values of 120 and 180 A, respectively (Fig. 5d). The increase in weld-fusion zone area could be attributed to increase in heat input by increasing welding current [10, 11]. The D/W Ratio was observed to have increased from 0.20 to 0.32 with the increase in welding current values of 120–180 A (Fig. 5c). It is also proposed that the arc pressure is more effective at higher welding current, and thus, it also help to increase in depth of penetration.

Significant increase in penetration depth was observed during welding with TiO_2 (3.01 mm), SiO_2 (2.81 mm) and Cr_2O_3 (3.35 mm) as compared to the TIG welding without flux (2.43 mm) at a same process parameter "welding current of 180 A and welding speed of 120 mm/min" (Fig. 5e). The weld bead width has shown different behaviour with different fluxes. The bead width was found decreasing with

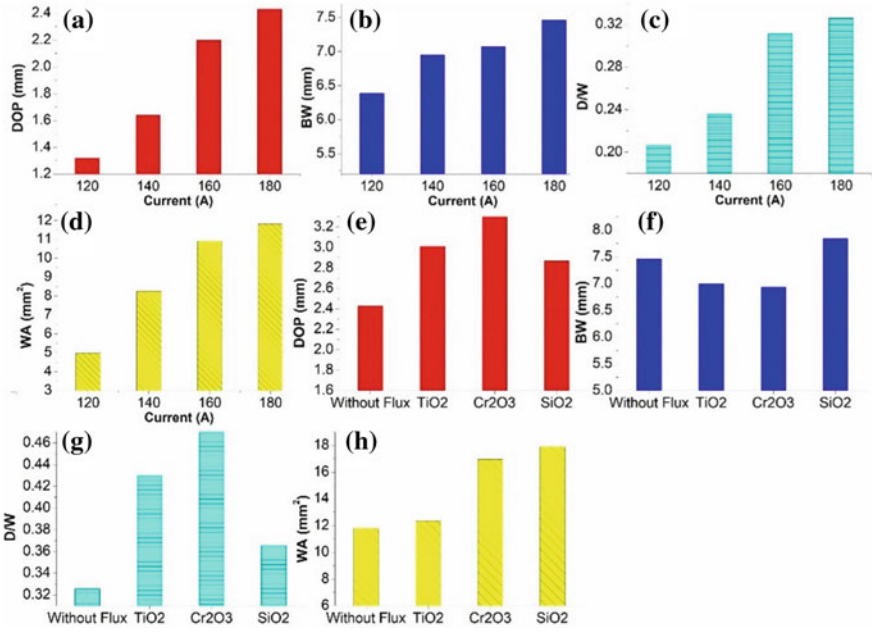

Fig. 5 Impact of process parameters on weld bead geometry "(**a**–**d**) at a welding speed of 120 mm/min" and "(**e**–**h**) at a welding speed of 120 mm/min and welding current of 180 A"

Cr_2O_3 (6.94 mm) and TiO_2 (7 mm) as compared to the conventional TIG weldments (7.46 mm) (Fig. 5f). However, bead width was found more in case of SiO_2 (7.85 mm) as compared to the without flux weldments (Fig. 5f). D/W was found maximum in weldments obtained with SiO_2 (0.48) followed by Cr_2O_3 (0.43) and then, TiO_2 (0.36). Almost 48% increase in D/W was observed in SiO_2 (0.48) weldments as compared to without weldments (0.32) (Fig. 5g). Weld-fusion zone area was found higher in case of the A-TIG weldments as compared to conventional TIG weldments (11.81 mm^2). Maximum weld-fusion zone was found maximum in SiO_2 (17.89 mm^2) followed by Cr_2O_3 (16.95 mm^2) and minimum in TiO_2 (12.34 mm^2) (Fig. 5h). Increase in penetration depth in presence of activating flux may be attributed to the reversal in Marangoni convection. However, decrease in weld bead width could be due to the arc constriction [12]. The activating flux used during the A-TIG welding, is used to dissociate and mixed to the molten metal pool. This results in change in the surface tension-temperature gradient from negative to positive. Surface tension–temperature gradient change leads to deep and narrow weld bead [13, 14]. It is also stated that a part of the activating flux is used to evaporate. The evaporated activating flux captured the electron from the arc column outer peripheral. This results in constricted arc column and thus narrow weld bead [15, 16]. Impact of different activating flux on the weld bead depends on the interaction properties between the base metal and activating flux used [17].

5 Conclusions

1. Depth of penetration, bead width, weld-fusion zone area and depth to width ratio increased with increase of welding current during TIG welding.
2. Depth of penetration, depth to width ratio and weld-fusion zone area were found more in A-TIG weldments as compared to TIG weldments. However, bead width decreased by applying the activating flux.
3. Activating fluxes influenced the weld bead geometry significantly during manual TIG welding process.
4. Cr_2O_3 was found best among all three fluxes used to enhance the depth of penetration and reduce the bead width.

References

1. Vidyarthy, R.S., Dwivedi, D.K., Vasudevan, M.: J. Mater. Eng. Perform. **26**, 1391–1403 (2017)
2. Vasantharaja, P., Vasudevan, M.: J. Nucl. Mater. **421**, 117–123 (2012)
3. Nayee, S.G., Badheka, V.J.: J. Manuf. Process. **16**, 137–143 (2014)
4. Vidyarthy, R.S., Dwivedi, D.K.: J. Mater. Eng. Perform. **26**, 5375–5384 (2017)
5. Sakthivel, T., Vasudevan, M., Laha, K., Parameswaran, P., Chandravathi, K.S.S., Mathew, M.D.D., Bhaduri, K.K.: Mater. Sci. Eng. A **528**, 6971–6980 (2011)

6. Maduraimuthu, V., Vasudevan, M., Parameswaran, P.: Trans. Indian Inst. Met. **68**, 181–189 (2015)
7. Ramkumar, K.D., Goutham, P.S., Radhakrishna, V.S., Tiwari, A., Anirudh, S.: J. Manuf. Process. **23**, 231–241 (2016)
8. Lakshminarayanan, A., Balasubramanian, V., Salahuddin, M.: J. Iron. Steel Res. Int. **17**, 68–74 (2010)
9. Vasudevan, M.: J. Mater. Eng. Perform. **26**, 1325–1336 (2017)
10. Vidyarthy, R.S., Dwivedi, D.K., Muthukumaran, V.: Mater. Manuf. Process. **33**, 709–717 (2017)
11. Tanaka, M., Lowke, J.J.: J. Phys. D. Appl. Phys. **40** (2007)
12. Vidyarthy, R.S., Dwivedi, D.K.: J. Manuf. Process. **22**, 211–228 (2016)
13. Sándor, T., Mekler, C., Dobránszky, J., Kaptay, G.: Metall. Mater. Trans. A **44**, 351–361 (2013)
14. Mills, K.C., Keene, B.J., Brooks, R.F., Shirali, A.: Philos. Trans. R. Soc. A Math. Phys. Eng. Sci. **356**, 911–925 (1998)
15. Vora, J.J., Badheka, V.J.: Trans. Indian Inst. Met. **69**, 1755–1764 (2016)
16. D.S. Howse, Improved Productivity in Fusion Welding, university of Warwick, 2002
17. Vidyarthy, R.S., Dwivedi, D.K.: J. Manuf. Process. **31**, 523–535 (2018)

Powder Metallurgy Processing of Rapidly Solidified Alloyed Cast Iron Powders for Machine Components

S. K. Khuntia and B. B. Pani

Abstract Cast iron powders containing little amount of Al, Cr, and Si were produced via water atomization technique and then got annealed at 900 °C for removing oxygen in hydrogen atmosphere. The advantages of rapid solidification remained undisturbed in spite of high temperature. The powders after pre-compaction studies were cold compacted up to 700 MPa pressure and then sintered at different temperatures like 720, 850, and 1000 °C. Growth like dimensional changes was observed in all the samples. The sample which was compacted at 700 MPa and sintered at 1000 °C showed 48 HRC hardness. High hardness values could enable these materials for manufacturing high-strength machine components.

Keywords Water atomization · Cast iron powders · Compaction · Sintering

1 Introduction

In search of low and high performance powdered materials, rapid solidification techniques can be adapted to produce ferrous-based structurally modified materials with excellent properties. From Serby and others work [1–7], it is already found that high carbon content alloyed steel and cast iron materials can be processed both in conventional metallurgy and powder metallurgy processes to obtain very fine-grained ferrite-carbide structure in the range of 0.2–5 μm by adopting proper thermal and mechanical processing. By super-plastic deformation at ambient temperature, different high-strength and high-hardness machine components can be manufactured from such fine-grained structurally modified materials [8, 9].

In the present investigation, an attempt has been made to manufacture rapidly solidified cast iron powders. After proper characteristic studies, such powders have been consolidated in cold compaction and sintering techniques to manufacture high-performance machine components.

S. K. Khuntia (✉)
College of Engineering Bhubaneswar, Bhubaneswar, Odisha, India
e-mail: sujit_khuntia@yahoo.com

B. B. Pani
Veer Surendra Sai University of Technology, Burla, Odisha, India

L. Li et al. (eds.), *Advances in Materials and Manufacturing Engineering*, Lecture Notes in Mechanical Engineering, https://doi.org/10.1007/978-981-15-1307-7_67

Table 1 Chemical characteristics of rapidly solidified cast iron powders in wt%

C	Al	Si	S	Cr	P	Fe
3.49	2.1	1.3	0.012	1.6	0.03	Balance

Table 2 Physical characteristics of rapidly solidified cast iron powders

Apparent density (gm/cm^3)	2.63
Flow rate (s/50 gm)	23
True density (pycnometric) (gm/cm^3)	7.3

2 Experimental Procedure

Wrought iron was manufactured using arc furnace, and then, this wrought iron was used as feedstock to produce water atomized cast iron powders using a high-frequency induction furnace. During melting, requisite amount of additives was added to obtain nearly 2 wt% Al, 1–2 wt% Cr, and 1–2 wt% Si in the cast iron powders. After sieving, powders above 100 mesh size were discarded and powders below 100 mesh size were taken for annealing. Some powders were annealed at 700 °C for two hours and the rest were annealed at 900 °C for one hour.

2.1 Powder Characteristic Studies

The 900 °C annealed powders were characterized in various ways. The chemical characteristic study is presented in Table 1, and the physical characteristic study is presented in Table 2.

2.2 Powder Consolidation

The annealed powders were blended with 1% zinc stearate for better surface lubrication. The powders were cold consolidated using a 50-ton capacity universal testing machine. Double action die set-up was used for compaction of powders. The 700 °C annealed powders showed very poor compressibility. However, the 900 °C annealed powders, when compacted within 300–700 MPa pressure, showed very good compressibility. These were considered for further processing. The green densities, which were recorded in metric method, are presented in Tables 3, 4, and 5.

Table 3 Green density, Sintered density, and % Growth in volume data for compacts sintered at 720 °C

Compaction pressure (MPa)	Green density (gm/cm^3)	Sintered density (gm/cm^3)	% Growth in volume
300	4.62	4.35	6.2
400	4.73	4.47	5.81
500	4.88	4.62	5.62
600	5.17	4.92	5.08
700	5.24	5.05	3.76

Table 4 Green density, Sintered density, and %Growth in volume data for compacts sintered at 850 °C

Compaction pressure (MPa)	Green density (gm/cm^3)	Sintered density (gm/cm^3)	% Growth in volume
300	4.63	4.32	7.17
400	4.71	4.42	6.56
500	4.84	4.55	6.42
600	5.19	4.88	6.27
700	5.23	4.95	5.65

Table 5 Green density, Sintered density, and %Growth in volume data for compacts sintered at 1000 °C

Compaction pressure (MPa)	Green density (gm/cm^3)	Sintered density (gm/cm^3)	% Growth in volume
300	4.42	4.3	7.44
400	4.72	4.4	7.27
500	4.85	4.53	7.06
600	5.19	4.86	6.79
700	5.22	4.93	5.88

2.3 Sintering Studies

Three different temperatures like 720 °C, 850 °C, and 1000 °C were selected for sintering studies. A Therelek make sintering furnace was used for this case. The cold compacted samples were sintered for one hour in hydrogen atmosphere. The sintered densities along with % growth in volume are also presented in Tables 3, 4, and 5.

2.4 Microstructural and Hardness Analysis

SEM analysis of 700 MPa compacted and 1000 °C sintered materials was done using a scanning electron microscope which is presented in Fig. 2.

The hardness test was done using a Rockwell hardness tester for 700 MPa compacted samples which were sintered at 720 °C, 850 °C, and 1000 °C, respectively. The hardness data are presented in Fig. 3.

3 Results and Discussions

3.1 Powder Characteristic Analysis

It is observed from Table 1 that there are 2.1% Al, 1.6% Cr, and 1.3% Si present in the cast iron powders. The presence of Aluminum helps in grain refinement in powders. Chromium acts as a carbide stabilizer, and silicon enhances the A1 transformation temperature up to 1000 °C. Table 2 shows that the flow-ability of the powders is 23 s/gm, which is a very good value for using the powders in automatic pressing system for making PM components. The calculated apparent density can be effectively utilized for die and punch design. Apparent density (2.63 gm/cm^3) is quite good for such kind of powders for component manufacturing.

3.2 Cold Compaction and Sintering Studies

Cold compaction study is a very important study for making use of such materials for component making. When 700 °C annealed powders were cold compacted, the powders showed very poor compressibility. This was so happened because here, nearly 50% volume of the materials were either iron carbides or complex carbides, which made the powders quite brittle and that is why these could not be compacted well. When the powders were annealed at 900 °C, carbon from the powder surfaces were removed due to surface decarburization, and thus, the surface of the powders became ductile. That is why such powders were compacted well. Figure 1 shows that no grain growth has taken place in the internal parts of the powders. Here, the cold compacts are quite strong for further sintering studies.

From the sintering studies (Tables 3, 4 and 5), it is observed that green densities are higher than sintered densities for different compaction pressures. The main reason for such growth is attributed to pearlitic transformation of some of the iron carbides during sintering. Hence, higher is the sintering temperature, higher is the pearlitic transformation as well as the growth. From the same tables, it is also observed that the growth amount is higher for lesser compaction pressures.

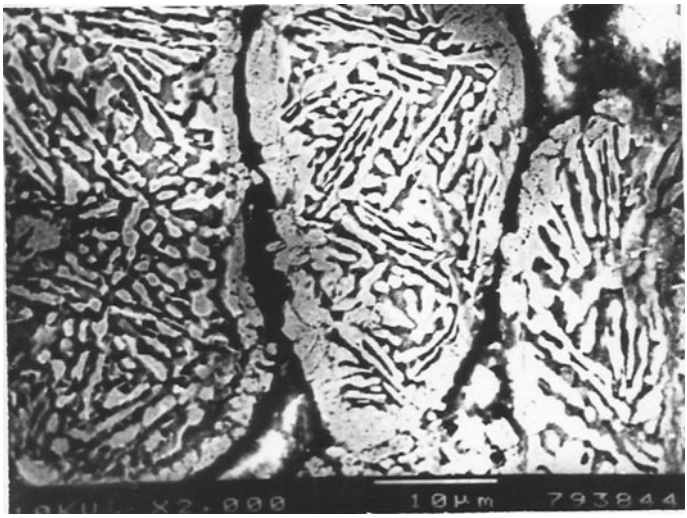

Fig. 1 SEM micrograph of surface decarburized rapidly solidified alloyed cast iron powders

3.3 Microstructural and Hardness Studies

From Fig. 2, it is noticed that very fine-grained (2–3 µm) ferrite-carbide structures are present in fine-grained ferrite matrix in sintered compacts. These fine-grained ferrite-carbide structures can provide very high hardness and wear-resistant properties in the

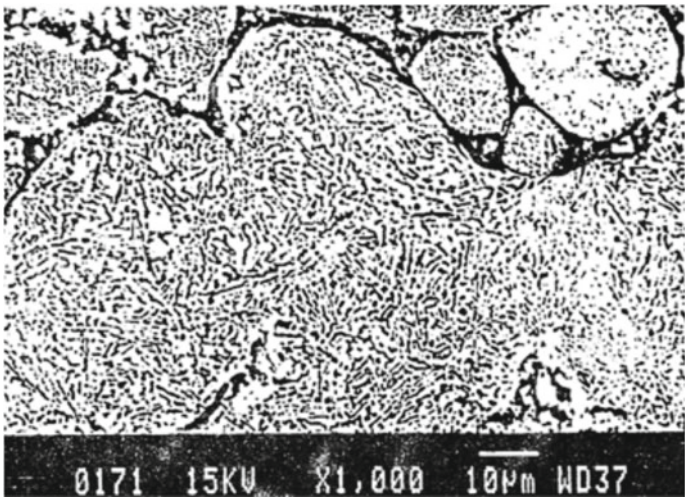

Fig. 2 SEM micrograph showing bonding among powder particles compacted at 700 MPa and sintered at 1000 °C for one hour

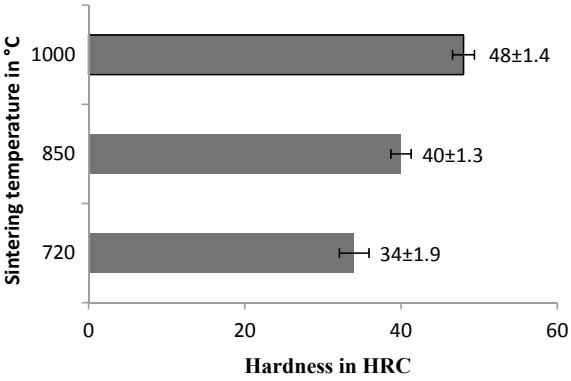

Fig. 3 Hardness values for compacts sintered at 1000 °C, 850 °C, and 720 °C

compacts. From hardness studies, it was observed that 48HRC, 40 HRC, and 34 HRC hardness values were found for samples sintered at temperatures like 1000 °C, 850 °C, and 720 °C, respectively. The hardness values are presented in Fig. 3 with error bars. This increase in hardness with temperature is probably due to increased diffusion among powder particles at increased temperatures.

4 Conclusion

1. Surface decarburization at 900 °C annealing temperature helped in better compaction of rapidly solidified alloyed cast iron powders.
2. Growth was observed in all samples after sintering. It increased with increase in sintering temperature. Growth enhances porosity of the material and enables it to be used as a self-lubricating bearing.
3. Fine-grained ferrite-carbide structures, in the range of 2–3 μm, were found in ferrite matrix for samples compacted at 700 MPa and sintered at 1000 °C. The presence of these structures increases the strength and wear resistance of the processed material.

References

1. Sherby, O.D.: Ultra high carbon steels and ancient blacksmiths. Iron Steel Inst. Jpn. Int. **39**(7), 637–648 (1999)
2. Serby, O.D.: Superplastic ultra high carbon steel. Scr. Metall. **9**, 569–574 (1975)
3. Mordike, B.L., Kainer, K.U.: Consolidation of rapidly solidified powders. Solid State Phenom. **8, 9**, 135–148 (1989)
4. Lesuer, D.R., Syn, C.K., Goldberg, A., Wadsworth, J., Serby, O.D.: The case for ultra high carbon steels as structural materials. JOM **45**, 40–46 (1993)

5. Mohanty, O.N.: Rapid solidification of cast iron-some new observations. Trans. Tech. Publ. **18, 19**, 65–82 (1989)
6. Pani, B.B.: Studies on production of water atomised white cast iron and iron powders from sponge iron fines and composite manufacturing. Ph.D. thesis. IIT, Kharagpur (2001)
7. Pani, B.B., Mukunda, P.G., Mohanty, O.N.: Processing and microstructural analysis of rapidly solidified white cast iron powders. Trans. Powder Metall. Assoc. India **28**, 1–4 (2002)
8. Walser, B., Kayali, E.S., Serby, O.D.: Warm working and superelasticity in plain ultra high carbon steels. In: 4th International Conference on the Strength of Metals and Alloys, vol. 1(8), pp. 266–270 (1976)
9. Serby, O.D.: Superplastic boarding of ferrous laminates. Scr. Metall. **13**(10), 941–946 (1979)

Effect of Debond and Randomness on Thermal Conductivities of Hollow Fiber Composites

G. Srivalli, G. Jamuna Rani and V. Balakrishna Murthy

Abstract A hollow fiber composite provides more flexibility to tailor the required material properties when compared to solid fiber composite. In the present work, an attempt has been made to steady the micromechanical thermal behavior of a hollow fiber composite using a finite element software ANSYS, and the thermal conductivities of the composite material are determined. The inner and outer diameters of hollow fiber are selected for the volume fractions of void, fiber and matrix equal to 0.2, 0.44 and 0.36, respectively. Finite element models are validated with rule of mixtures for longitudinal conductivity and further extended for the prediction of transverse thermal conductivity. Effect of fiber–matrix interface debond and fiber randomness on thermal conductivity of the composite is studied for a range of values of conductivity ratio of fiber to matrix. From the present study, it is observed that transverse thermal conductivity is influenced by debond and randomness, and deviation in this property from that of a regular model is more with more mismatch in the properties of constituents.

Keywords FEM · Thermal conductivity · Hollow random fiber · Interface debond

1 Introduction

Other than the structural analysis with micromechanical behavior, thermal analysis also plays a vital role in various applications like electronics and aerospace sectors. In order to improve the importance of thermal behavior, there is a need to concentrate on every phase of material like fiber, matrix and at interfacial points. The study of micro-mechanics is useful in obtaining the aggregate property of a composite from properties its constituents, so that in the macro-analysis, a composite lamina can be treated as a homogenous material with orthotropic properties. The properties of a lamina are greatly influenced by the defects such as voids and debond at the fiber–matrix interface and also on the randomness of fibers in the matrix.

G. Srivalli (✉) · G. Jamuna Rani · V. Balakrishna Murthy
Mechanical Engineering Department, V. R. Siddhartha Engineering College, Vijayawada, India
e-mail: valliadusumilli@gmail.com

L. Li et al. (eds.), *Advances in Materials and Manufacturing Engineering*, Lecture Notes in Mechanical Engineering, https://doi.org/10.1007/978-981-15-1307-7_68

Benveniste [1] discussed the effective thermal conductivities of composites at interfaces where thermal resistance at boundary exists based on the usage of harmonics of spheroidal shape in oblate and prolate configurations. Wang [2] studied a particular composite named aluminum nitride powder-filled polyimide (AIN/PI) for finding thermal conductivity with effect to shape of particle and resistance of thermal barrier at interface which showed positive effect and negative effect on thermal conductivity, respectively. Lee [3] discussed a method by name generalized self-consistent method (GSCM) to obtain the thermal conductivity effectiveness of composites and observed a considerable effect on thermal conductivity with respect to contact conductance and volume fraction. Hasselman [4] observed that because of thermal barrier resistance at interface, the composite systems thermal conductivity effect rely on dispersed phase and dispersion size of volume fraction. Lu [5] studied interfacial characteristic effect on effective thermal conductivity of randomly distributed fiber composites and found an increase in thermal interaction between the matrix and inclusion than of regular arrays. Sihn [6] considered laminated composites of regular and randomly distributed fibers for analyzing the transverse thermal conductivity using micromechanical analysis and observed positive effect for randomness at higher volume fractions. Hande [7] considered hollow glass microspheres which are filled with polypropylene composites to find out tensile properties and thermal conductivities by considering surface treatment and by not considering also. He observed that by considering surface treatment, there is no significant effect on thermal conductivity. Srinivasa Rao [8] considered hollow fiber composite to find transverse thermal conductivity where he showed positive effect for fiber-dominated and negative effect for matrix-dominated composites to increase transverse thermal conductivity. Wang [9] studied carbon fiber composites with 3D numerical model to find effective thermal conductivity and obtained good validation with experimental data.

2 Problem Modeling

One-fourth portion of a square unit cell is considered for developing a finite element model of a hollow fiber composite as shown in Fig. 1. Dimensions 'a,' 'b,' R_i and R_o are selected so that volume fractions of void, fiber and matrix are equal to 0.2, 0.44 and 0.36, respectively. In a regular arrangement of fibers, θ is equal to 45°. This value oscillates about 45° for randomly placed fibers. For this model, longitudinal thermal conductivity (KL) and transverse thermal conductivity (KT) are calculated for a range of conductivity ratios (Kf/Km).

Eight-node three-dimensional linear brick element [10] of length 2 units for 'a' value of 100 units is considered for the generation of finite element mesh. The thermal properties of fiber and matrix are selected to maintain the conductivity ratios as listed in Table 1. Temperatures along the faces of FE model are applied to allow a unidirectional flow of heat in the required direction with a temperature gradient equal to unity.

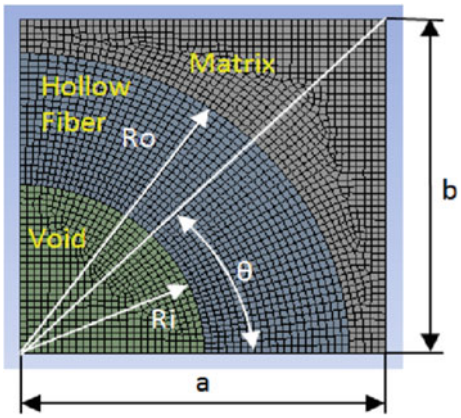

Fig. 1 Geometry and FE model

Table 1 Conductivity ratios for different cases

Case	Fiber dominant	Matrix dominant
Kf/Km (or) CR	2	1/200
	5	1/100
	10	1/50
	25	1/25
	50	1/10
	100	1/5
	200	1/2

3 Solution

The finite element model is validated for longitudinal thermal conductivity using rule of mixtures. Figure 2 shows the temperature contour for longitudinal heat flow with CR = 2. Heat flow value from the FE solution is obtained as 12,362 W.

Rule of mixtures equation is given by

$$\mathrm{KL} = \mathrm{Kf}^{*} V_{\mathrm{f}} + \mathrm{Km}^{*} V_{\mathrm{m}} + \mathrm{Kv}^{*} V_{\mathrm{v}}$$

where V_{f}, V_{m} and V_{v} are volume fractions of fiber, matrix and void, respectively.

$$\text{KL-Theoretical} = 2^{*}0.44 + 1^{*}0.36 + 0^{*}0.2 = 1.24\,\mathrm{W/mm\,K}$$

KL-FEM = Reaction heat/(100 * 100) = 12,362/10,000 = 1.236 W/mm K. Further, this model is used to determine transverse thermal conductivity by changing the

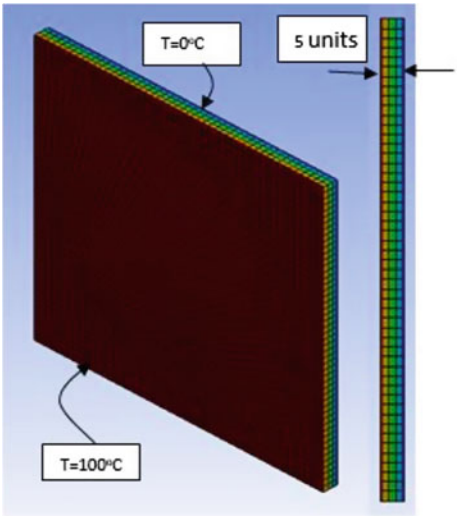

Fig. 2 Temperature in longitudinal flow

heat flow direction. Figure 3 shows the temperature contour for transverse heat flow in the model with CR = 2. The transverse thermal conductivity is calculated using the formula,

$$\text{KT-FEM} = \text{Reaction heat}/\left(5^{*}100\right) = 513.63/500 = 1.02726\,\text{W/mm K}.$$

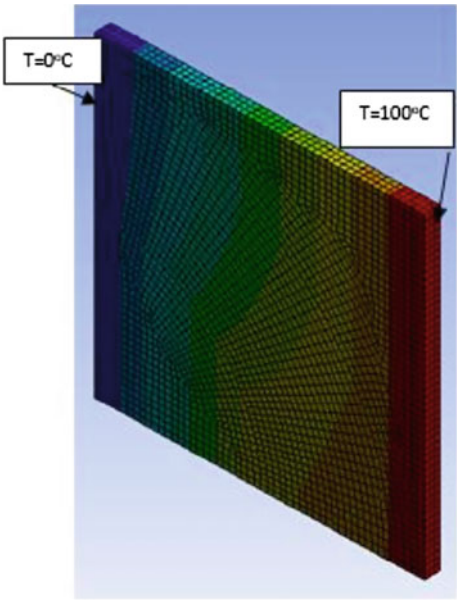

Fig. 3 Temperature in transverse flow

4 Results

Figures 4 and 5 represent the debond effect on the longitudinal thermal conductivity of fiber-dominated case and matrix-dominated case, respectively. In both fiber- and matrix-dominated cases, longitudinal thermal conductivity of the composite is not affected by debond since there is no deviation of flow. Figures 6 and 7 represent the randomness of composites for longitudinal thermal conductivity in fiber-dominated case and matrix-dominated case, respectively. In case of random fiber, the property obtained for any value of θ is normalized with property of regular fiber composite

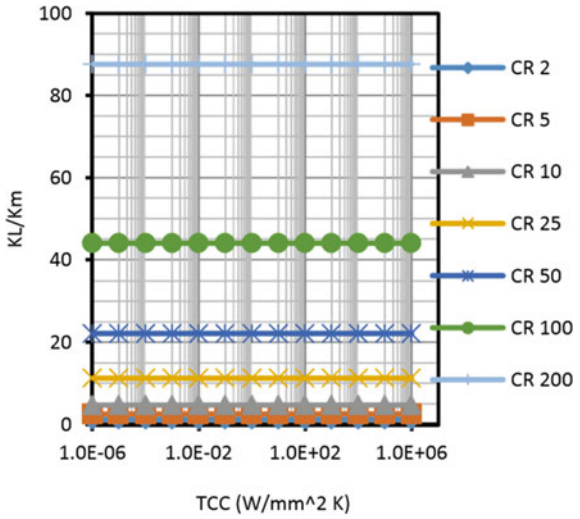

Fig. 4 Variation of KL/Km with TCC and CRR in fiber-dominated case

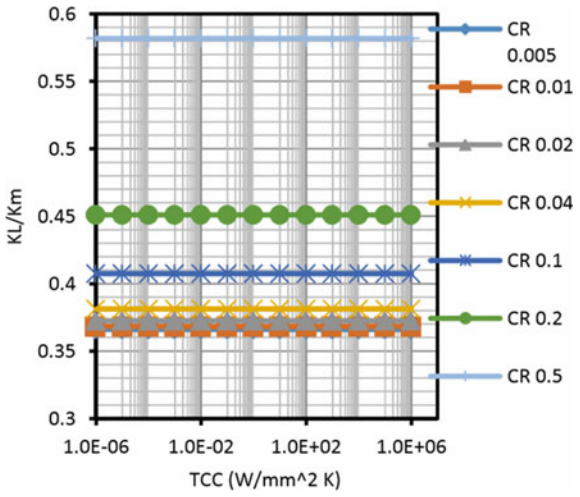

Fig. 5 Variation of KL/Km with TCC and CRR in matrix-dominated case

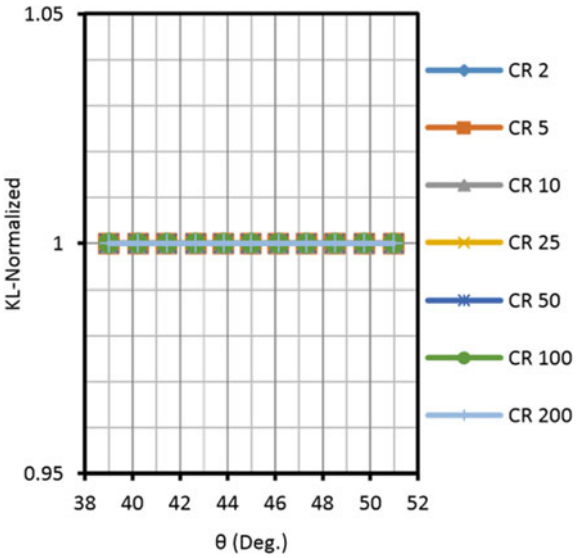

Fig. 6 Variation of KL-normalized with θ and CR in fiber dominated case

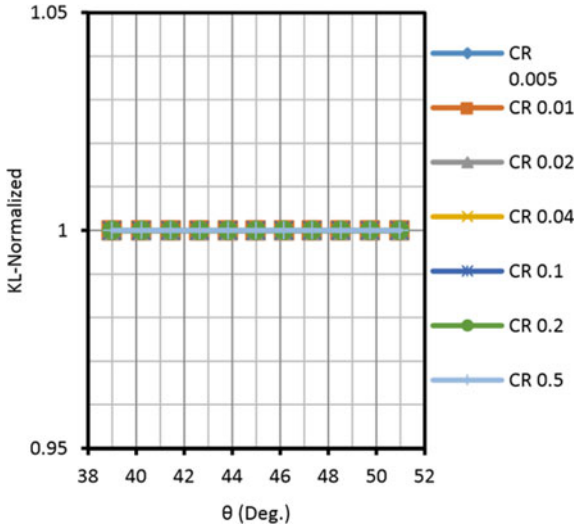

Fig. 7 Variation of KL-normalized with θ and CR in fiber dominated case

with same CR. Similar to the case of debond, in random fiber arrangement case also the longitudinal thermal conductivity of the composite is not affected. In continuous fiber-reinforced composites, the longitudinal conductivity is governed by rule of mixtures and which is independent of the presence of randomness and debond

Figures 8 and 9 represent the debond effect on the transverse thermal conductivity of fiber-dominated cases and matrix-dominated cases, respectively. In fiber-dominated cases, debond effect shows its significance in the range of 1e−3 to 1e+1

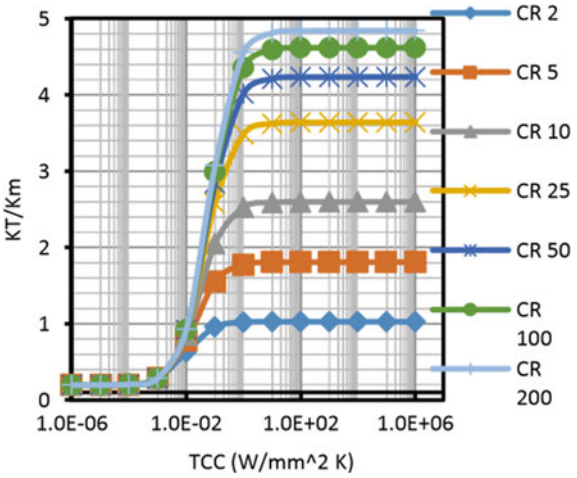

Fig. 8 Variation of KT/Km with TCC and CR in fiber dominated cases

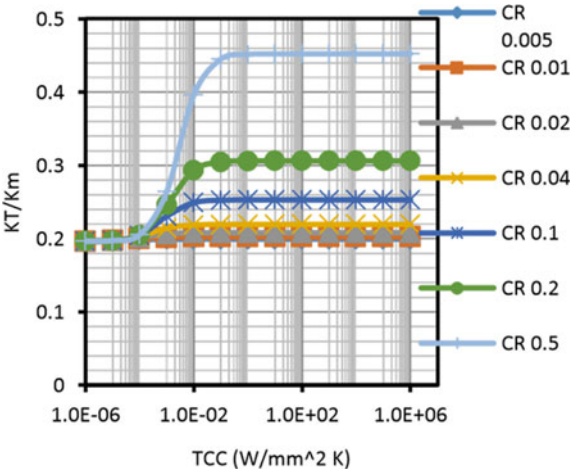

Fig. 9 Variation of KT/Km with TCC and CR in matrix dominated cases

and in matrix-dominated cases in the range of 1e−4 to 1 of TCC. In both the cases, with the increase in CR there is an increase in KT/Km in partially or completely bonded interfaces. Figures 10 and 11 represent the randomness effect of composites on transverse thermal conductivity in fiber-dominated cases and matrix-dominated cases, respectively. At extreme values of θ, though not practically exist, it is observed that a maximum variation of 7.5 times on the higher side and 0.75 times on the lower side in KT when compared with regular composite for CR = 200. In matrix-dominated case, deviations from regular model are observed to be 1.4 on the higher side and 0.5 on the lower side when CR = 1/200. If the randomness is considered as a deviation of θ about 6.6% from regular model (i.e., $\pm 3°$), KT is increased by 30% in fiber-dominated cases at CR = 200 and 20% in matrix-dominated for CR = 1/200.

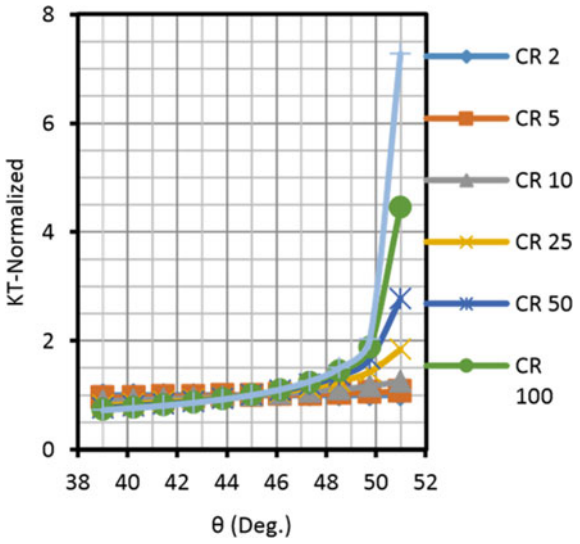

Fig. 10 Variation of KT-normalized with θ and CR in fiber-dominated case

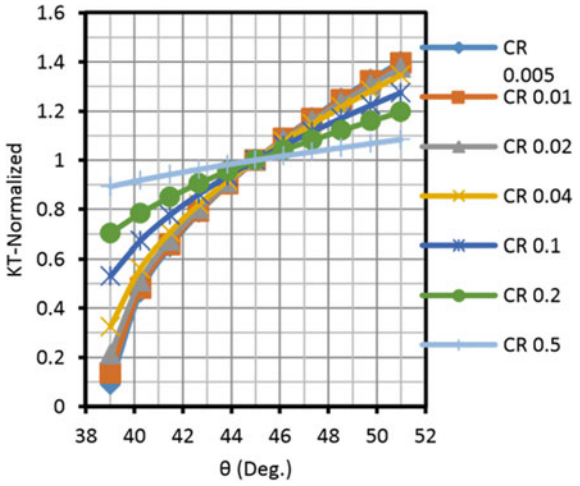

Fig. 11 Variation of KT-normalized with θ and CR in matrix-dominated case

Increase in θ means increase in the b/a ratio as can be seen from Fig. 1 and decreases overall conduction resistance for x-directional flow resulting in an increase in KT. At the same time, resistance in y-directional flow increases, causing for reduction in through thickness conductivity.

5 Conclusion

The effect of fiber–matrix interface debond and fiber randomness in the cross-sectional plane on thermal conductivities of continuous hollow fiber composites is studied by applying the finite element method using three-dimensional micromechanical models. No variation in the longitudinal thermal conductivity is observed either due to debond or due to fiber randomness. Transverse thermal conductivity is greatly affected by the interface debond, and this intensity is observed to be more at higher CR values. Extreme values of CR, i.e., 200 in fiber-dominated case and 1/200 in matrix-dominated case can exhibit maximum variation due to randomness.

References

1. Benveniste, Y.: The effective conductivity of composites with imperfect thermal contact at constituent interfaces. Int. J. Eng. Sci. **24**(9), 1537–1552 (1986)
2. Wang, J.: Effects of interfacial thermal barrier resistance and particle size and shape on the thermal conductivity of AIN/PI composites. Comput. Sci. Technol. **64**, 1623–1628 (2004)
3. Lee, Y.-M.: A generalised self-consistent method for calculation of effective thermal conductivity of composites with interfacial contact conductance. Int. Commun. Heat Mass Transfer **33**, 142–150 (2006)
4. Hasselman, D.P.H.: Effective thermal conductivity of composites with interfacial thermal Barrier resistance. J. Compos. Mater. **21**, 508–514 (1987)
5. Lu, S.-Y.: Effect of interfacial characteristics on effective conductivities of composites containing randomly distributed aligned long fibers. Chem. Eng. Sci. **15**(19), 4393–4404 (1996)
6. Sihn, S.: Micromechanical analysis for transverse thermal conductivity of composites. J. Compos. Mater. 1–11 (2010)
7. Huang, Z.M.: Simulation of the mechanical properties of fibrous composites by the bridging micromechanics model. Composites **32**, 143–173 (2001)
8. Srinivasa Rao, T.: Transverse thermal conductivity of hollow fiber composites. Int. J. Eng. Technol. Sci. Res. **5**(5), 389–394 (2018)
9. Wang, M.: Thermal conductivity enhancement of carbon fiber composites. Science Direct **29**(2), 418–421 (2009)
10. ANSYS reference manuals from Internet

Study of Mechanical Property of Cenosphere and Clamshell as Filler Material in Jute Epoxy Composite

Manoj Kumar, Hemalata Jena, B. Surekha and Sanjukta Sahoo

Abstract This study is involved with the comparative analysis of mechanical properties of jute epoxy composites with cenosphere filler and jute epoxy composites with clamshell filler. The composites are prepared using hand-lay-up method with a different weight percentage of fillers (0 wt%, 5 wt% and 10 wt%). 5 wt% cenosphere-filled jute epoxy composites show improved and higher values for tensile strength, flexural strength and inter-laminar shear strength than jute epoxy composite and 5 wt% clamshell-filled jute epoxy composites, respectively. Composite with 10 wt% cenosphere filler shows the highest value for hardness. There is a decrease in impact strength with increase in filler content for both the fillers in the jute epoxy composites.

Keywords Jute fibre · Epoxy resin · Cenosphere · Clamshell · Mechanical properties

1 Introduction

Natural fibre-reinforced composites have become an alternative to many of the synthetic fibre-reinforced composites since few decades [1, 2]. Eco-friendly nature of natural fibres, especially bio-degradability, makes them an exceptional replacement for synthetic fibres. Out of several natural fibres available, jute is one of the most commonly used fibres, but its hydrophilic nature, dimensional instability and variable qualities limit its uses [3]. Most of the limitations have been overcome by introducing secondary reinforcement, i.e. particulate filler into natural fibre-reinforced polymer composites which mainly improved the adhesion between the fibre and the matrix material [4, 5].

M. Kumar (✉)
Department of Mechanical Engineering, RTC Institute of Technology, Ormanjhi, Ranchi 835219, India
e-mail: mk803505@gmail.com

H. Jena · B. Surekha
School of Mechanical Engineering, KIIT Deemed to be University, Bhubaneswar 751024, India

S. Sahoo
Department of Civil Engineering, KIIT Polytechnic, Bhubaneswar 751024, India

L. Li et al. (eds.), *Advances in Materials and Manufacturing Engineering*, Lecture Notes in Mechanical Engineering, https://doi.org/10.1007/978-981-15-1307-7_69

Micro- and nano-sized rigid spherical fillers have been already used to improve surface quality and strength of polymer composites [6]. Ceramic or metallic spherical fillers have higher cost. Cenosphere is a hollow micro-spherical industrial waste found in fly ash, which is easily available and also cost-effective [7]. Cenosphere is generally composed of alumina-silicate. These days cenosphere is being used in polymer matrix composites due to its lower density, homogeneity, good dispersion and inertness. Addition of cenosphere reduces the requirement of matrix material, enhances properties of composites and also reduces the cost of the composite in addition to enhanced thermal insulation and higher specific strength [8].

Day-by-day addition of new filler materials in fibre-reinforced polymer matrix composite is an emerging trend to get the best properties in the composites and clamshell is one of them. Clamshell belonging to the class of Bivalvia is composed of calcium carbonate (95%) and organic material (5%) [9]. Addition of this filler is a cost-effective option to replace filler material like calcium carbonate in the polymer matrix composite [10].

In the present study, a comparative analysis has been performed over the mechanical properties of jute epoxy composite with cenosphere filler and jute epoxy composite with clamshell filler.

2 Materials and Method

2.1 Materials

Jute Fibre Mat. Jute fibres have been locally procured in the form of a bidirectional woven mat having yarn count 95 tex as shown in Fig. 1. The fibres are washed

Fig. 1 Jute fibre mat

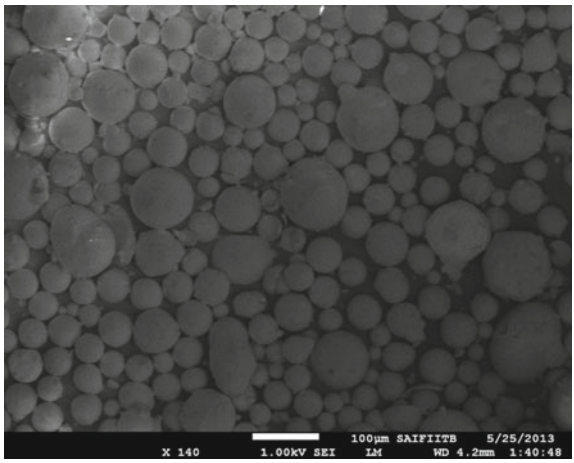

Fig. 2 SEM image of cenosphere

thoroughly using water to remove unwanted particles. After washing the mat, it is dried under sunlight for 3 days. The density of jute fibre is 1.5 gm/cc.

Matrix Material. An epoxy resin of L12 grade consisting of Diglycidyl Ether of Bisphenol-A (DGEBA) is collected from HARIPA India Limited, Kolkata. Its corresponding hardener is also procured from same.

Cenosphere. Ash cenosphere of particle size 60–90 µm procured from Micro Minechem Pvt. Ltd., Delhi, has been used for the cenosphere-filled jute epoxy composite. Its particle density ranges from 0.5 to 0.8 gm/cc and has a melting temperature of 1300–1500 °C. The main components of cenosphere are SiO_2 (50–65 wt%), Al_2O_3 (20–36 wt%) and Fe_2O_3 (2–10 wt%) [7]. Cenosphere has very fine assimilation and dispersion in epoxy resin along with chemical inertness and stability. It is also insoluble in water. The SEM image for cenosphere is shown in Fig. 2.

Clamshell. The clamshell (Fig. 3) has been collected from the Bay of Bengal sea coast at Chandipur Sea Beach, Odisha. Firstly, the clamshell is cleaned up using a brush to remove the dust particles and then washed thoroughly using water. After the cleaning process, it is dried under sunlight for 3 days. Clamshell particles of sizes 60–90 µm are prepared by ball milling for the present investigation. It is in powder form of white colour.

2.2 Composite Fabrication

The composites are prepared using jute fibre as reinforcement, epoxy as matrix material and cenosphere and clamshell as filler material. A mixture of epoxy resin and hardener is prepared in a ratio of 10:1 by weight. In the present work, traditional hand-lay-up technique is used to prepare different composites with dimensions 250 × 200 × 6 mm^3. Cenosphere and clamshell with different weight percentages (0 wt%,

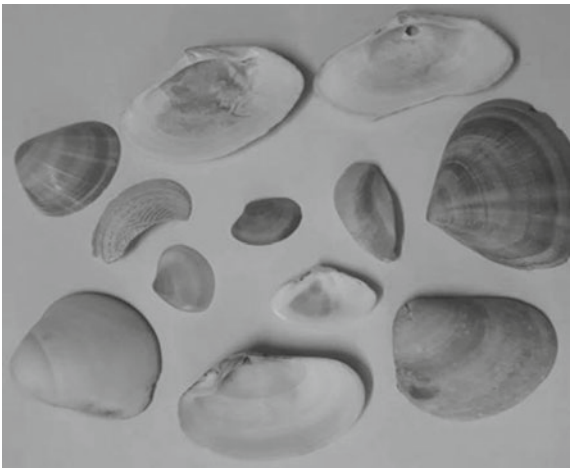

Fig. 3 Clamshell

Table 1 Composition of the composite materials

Composites	Jute (wt%)	Epoxy (wt%)	Cenosphere (wt%)	Clamshell (wt%)
JE	38	62	–	–
JEC_1	38	57	5	–
JEC_2	38	52	10	–
$JECS_1$	38	57	–	5
$JECS_2$	38	52	–	10

5 wt% and 10 wt%) are used to produce the composites JE, JEC_1, JEC_2, $JECS_1$ and $JECS_2$. The composition of these composites is shown in Table 1.

3 Mechanical Test

The tensile test is performed using an Instron 3369 Universal Testing Machine (UTM) at a cross-head speed of 3 mm/min. Flat specimens of 250 × 25.4 mm^2 are tested according to ASTM 3039. Five specimens for each composition are used to get the mean value of the tensile strength. The 3-point bending test is performed according to ASTM 790 using the same UTM in order to measure flexural and inter-laminar shear strength (ILSS) of specimens with dimensions 130 mm × 25.4 mm. For the test, gauge length for the specimens is maintained at 100 mm and a cross-head speed of 3 mm/min.

In the present work, the hardness value is measured using a Barcol hardness tester. Minimum four indentations are made to obtain the average value of hardness value. Reading for Barcol hardness number is taken directly from the display panel.

Impact tests are performed according to ASTM D256 in an impact tester which is a low-velocity impact test machine. Composite samples with dimensions 65 × 12.7 × 3 mm^3 with a '*V*' notch of 2 mm and angle 45° are prepared. Five samples for each composite are taken for the analysis of impact strength.

4 Results and Discussion

Tests are performed under controlled laboratory conditions to study the various mechanical characteristics of the different composites.

4.1 Tensile Strength

Figure 4 shows the results for the tensile strength of jute epoxy composites with different wt% of fillers. From the graph, it can be observed that the addition of cenosphere results in increase in tensile strength of the composite by 39.44% up to 5 wt%, but beyond this, tensile strength is reduced. Similarly, there is also an increase in tensile strength of the composite with addition of clamshell by 5.72% up to 5 wt%. After that, there is a decrease in the tensile strength. The reason for the increase in tensile strength for JEC_1 and $JECS_1$ may be because of good assimilation and dispersion of cenosphere and clamshell fillers. Comparatively, it can be stated that JEC_1 and JEC_2 show higher values for tensile strength than $JECS_1$ and $JECS_2$ by 31.89% and 32.12%, respectively. Due to the spherical nature of cenosphere, it gives better dispersion in the matrix which improves the mechanical strength. The agglomeration of filler due to the higher amount of filler may be responsible for decrease in tensile strength for JEC_2 and $JECS_2$. Figure 5 shows the SEM image of composite where it indicates the nature of failure as breakage of fibre and debonding of fibre from the matrix during the tensile test.

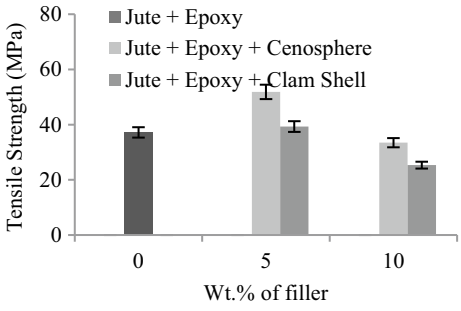

Fig. 4 Variation of tensile strength with filler content

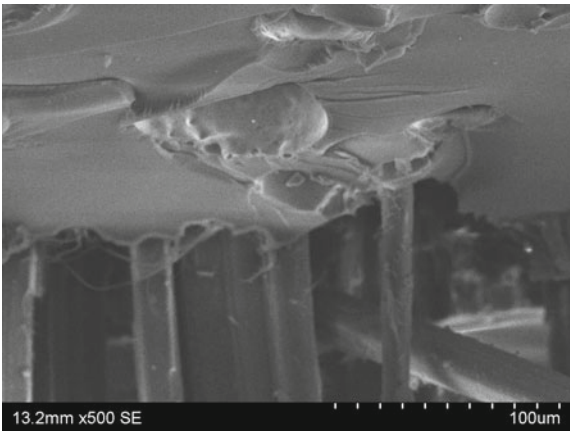

Fig. 5 SEM image of jute epoxy composite with cenosphere

4.2 Flexural and Inter-laminar Shear Strength

The values for flexural strength and ILSS for the different composites are shown in Figs. 6 and 7, respectively. Flexural and ILSS for both cenosphere- and clamshell-filled composites are increasing up to 5 wt% of filler, but after that, it decreases. The flexural strength and the ILSS for the JEC_1 increase by 87.62% and 211.92%, respectively. For $JECS_1$, the ILSS increases by 59.33%. The JEC_1 shows higher values for flexural strength and ILSS than $JECS_1$ by 44.78% and 94.83%, respectively. Proper bonding between jute and epoxy along with filler content leads to the improvement in ILSS for JEC_1 and $JECS_1$.

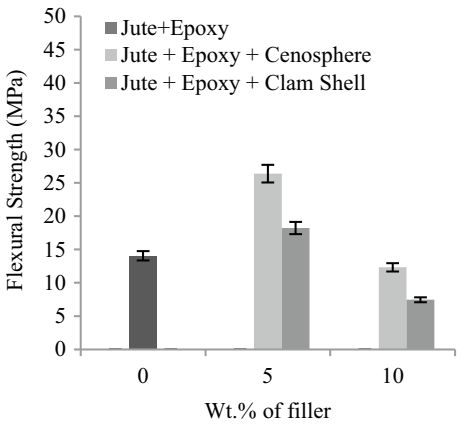

Fig. 6 Variation of flexural strength with filler content

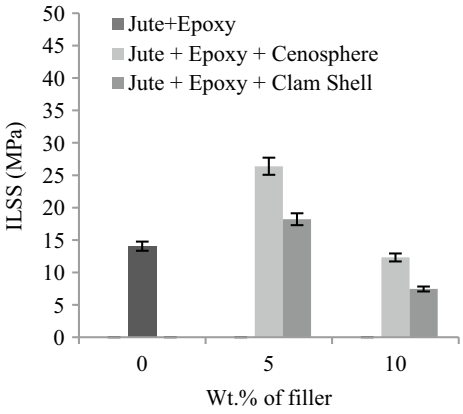

Fig. 7 Variation of ILSS with filler content

4.3 Hardness

Test results shown in Fig. 8 indicate that there is a continuous improvement in hardness value for jute epoxy composite with cenosphere filler and the maximum value is obtained for JEC_2 which is 77.26% greater than JE. Similar trend is observed in hardness for clamshell-filled jute epoxy composite. In comparison with $JECS_1$ and $JECS_2$, JEC_1 and JEC_2 show higher values for hardness by 19.30% and 32.10%. The increase in strength of composites may be because of the higher fracture strength and rigidness of cenosphere, and for clamshell, it may be because of its hardness.

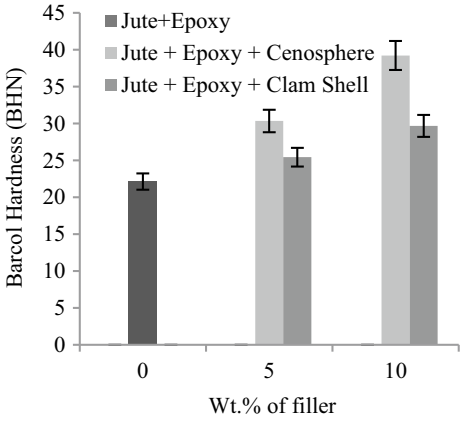

Fig. 8 Variation of hardness with filler content

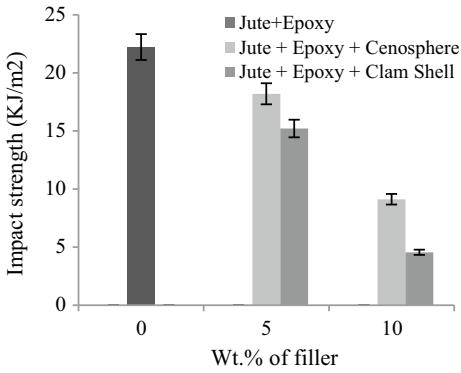

Fig. 9 Variation of impact strength with filler content

4.4 Impact Strength

The test results for the impact tests for different composites are shown in Fig. 9. There is a continuous decrement in the impact strength with increase in filler content for both cenosphere- and clamshell-filled composites. The decrement of impact strength for 10 wt% cenosphere is 58.97%, where it is 79.48% for the clamshell-filled jute epoxy composites. The decrease in crystallinity and increase in amorphous content in the composites with the increase in filler content leads to the decrease in impact strength.

5 Conclusions

Based on the experimental investigations, the following observations are made:

- 5 wt% filler gives higher values for tensile strength, flexural strength and ILSS.
- The hardness value of the composite increases with the addition of fillers.
- The impact strength is observed to be decreased with increase in filler content.
- More improvement in mechanical property is observed with the addition of cenosphere than clamshell filler.

References

1. Gon, D., Das, K., Paul, P., Maity, S.: Jute composites as wood substitute. Int. J. Text. Sci. **1**, 84–93 (2012)
2. Shanmugam, D., Thiruchitrambalam, M.: Static and dynamic mechanical properties of alkali treated unidirectional continuous palmyra leaf stalk fibre/jute fibre reinforced hybrid polyester composites. Mater. Des. **50**, 533–542 (2013)

3. Stark, N.: Influence of moisture absorption on mechanical properties of wood flour-polypropylene composites. J. Thermoplast. Compos. Mater. **14**, 421–432 (2001)
4. Dalbehera, S., Acharya, S.K.: Effect of cenosphere addition on the mechanical properties of jute-glass filler hybrid epoxy composites. J. Ind. Text. **46**, 177–188 (2015)
5. Biswas, S., Satapathy, A., Patnaik, A.: Effect of ceramic fillers on mechanical properties of bamboo fiber reinforced epoxy composites: a comparative study. Adv. Mater. Res. **123**, 1031–1034 (2010)
6. Nayak, R.K., Mahato, K.K., Ray, B.C.: Water absorption behavior, mechanical and thermal properties of nano TiO_2 enhanced glass fiber reinforced polymer composites. Compos. Part A **90**, 736–747 (2016)
7. Raask, E.: Hollow and spherical particles in pulverised-fuel ash. J. Inst. Fuel **41**, 339–344 (1968)
8. Jena, H., Pandit, M.K., Pradhan, A.K.: Effect of cenosphere on mechanical properties of bamboo-epoxy composites. J. Reinf. Plast. Compos. **32**(11), 794–801 (2013)
9. Yao, Z., Xia, M., Li, H., Chen, T., Ye, Y., Zheng, H.: Bivalve shell: not an abundant useless waste but a functional and versatile biomaterial. Crit. Rev. Env. Sci. Technol. **44**(22), 2502–2530 (2014)
10. Li, H.Y., Chen, T., Zhang, H.Y., Yao, Z.T., Zhang, L., Pan, L., Ye, Y., Xia, M.S.: Preparation of bio-filler from pearl oyster shell and its surface properties. J. China Ceram. Soc. **40**, 1671–1679 (2012)

Fuzzy C-means Clustering-Based ANFIS Regression Modeling of Hybrid Laser-TIG Fabrication

Sanjib Jaypuria, Trupti Ranjan Mahapatra, Sushanta Tripathy, Swaraj Nakhale and Santosh Kumar Gupta

Abstract Hybrid laser-TIG welding is performed on austenitic stainless steel under mutual action of both laser and TIG heat source on weld pool. The process parameters were considered as the TIG current, laser power, pulse frequency and duration whereas the weld bead penetration was taken as the output of the system. Experimentation was conducted based on central composite design matrix. To test the suggested model, five test cases experiments were also performed by creating some random input combinations by keeping the range of each input variables intact. Multiple regression was conducted to establish the correlation between process and output parameters of hybrid laser-TIG welding. An adaptive neuro-fuzzy inference system (ANFIS) architecture had also been developed based on fuzzy c-means clustering (FCM) to conduct the regression analysis. The performance of both regression models was evaluated based on root-mean-square error and mean absolute percentage error. FCM-ANFIS regression was found to be more accurate in conducting prediction of response variable based on the value of both RMSE and MAPE in training as well as test cases. FCM-ANFIS-based regression seemed to be an advanced version of multiple statistical regression models in terms of an accurate control module design and subsequently for automation of the process.

Keywords FCM · ANFIS · Regression · Hybrid laser-TIG welding

1 Introduction

The industrial use of austenitic stainless steel is very wide, and the austenitic steel 316LN is one of the primary structural materials in both fusion and fission nuclear

S. Jaypuria · S. K. Gupta
Indian Institute of Technology Kharagpur, Kharagpur 721302, India

T. R. Mahapatra (✉)
Veer Surendra Sai University of Technology (VSSUT), Burla 768018, India
e-mail: trmahapatra_pe@vssut.ac.in

S. Tripathy · S. Nakhale
Kalinga Institute of Industrial Technology (KIIT), Bhubaneswar 751024, India

L. Li et al. (eds.), *Advances in Materials and Manufacturing Engineering*, Lecture Notes in Mechanical Engineering, https://doi.org/10.1007/978-981-15-1307-7_70

industries [1]. Therefore, a suitable welding technology is the requirement of the large and heavy nuclear structural components. Also, the demand for distortion-free, minimization of residual stress and capital cost gave rise to hybrid welding, where both processes complement each other and fulfill the industrial requirement. Here, the laser welding with a high density of energy and scanning speed leads to higher production rates, less distortion and residual stress as compared to that of traditional welding process [2, 3]. Furthermore, hybrid welding utilizes the arc heat source, which has a large gap bridgeability as wine cup shape bead profile (keyhole shape) is generally obtained with the use of this type of hybrid welding. It also enhances the bead penetration without any filler. However, laser-arc interaction with steel plate gives rise to various thermos-physical processes in the weld pool that altogether affect the final weld bead geometry [3]. Therefore, the bead penetration in this hybrid welding is a function of process parameters, which is dynamic and needs an accurate model to correlate input and output. The interdependency among input variables and the involvement of multiple variables create difficulties for traditional statistical approaches to model the input–output of a manufacturing process. Regression is such a conventional approach, where input–output modeling of a given system can be established with much ease. However, their inability to model complex nonlinear process is quite disappointing. The error in prediction of response using a regression model is becoming a problem for the automation module of the process [4].

Many attempts have already been made to improve the performance of the regression model by modifications and introducing various soft computing tools in a model and subsequently comparing those results with experimental data [5, 6]. The fuzzy regression model [7] and machine-learning techniques, namely neural network and neuro-fuzzy model [8], are used in past for predicting bead geometry parameters, residual stresses, etc. Xue et al. [9] employed fuzzy linear regression approach in welding to predict the bead width. They also pointed out that fuzzy regression could be applied to any model that deals with the high degree of fuzziness. However, ANFIS model was found to be superior based on accuracy in prediction because of their better local interpolation capabilities.

We note that many studies have been reported regarding linear and nonlinear regression of various manufacturing processes that have become the basis of their input–output modeling. The need for alternative tools like neural network and neuro-fuzzy network for modeling of the process is also pointed out. Therefore, a fuzzy c-means-based neuro-fuzzy modeling of hybrid welding is attempted in this work. The developed approach is justified by their prediction accuracy of test data and is measured through root-mean-square error and mean absolute percentage error in prediction.

Table 1 Input parameters of hybrid laser-TIG welding along their range [3]

Welding parameters/level	Pulse peak power (PP) (W)	Pulse frequency (PF) (Hz)	Pulse duration (PD) (ms)	TIG current (CT) (A)
Level 1	2000	4	5	100
Level 1	2220	5	5.63	102.5
Level 1	2875	8	7.5	110
Level 1	3530	11	9.38	117.5
Level 1	3750	12	10	120

Table 2 Test cases along with responses with different approaches

Test cases	PP	PF	PD	CT	Experimental BP	Regression BP	FCM-ANFIS BP
1	3664	11.98	9.97	118	5.676	5.584	5.572
2	3682	11.75	9.98	119	5.662	5.614	5.616
3	3704	11.82	9.99	114	5.667	5.474	5.487
4	3729	11.98	9.98	104	5.657	5.552	5.554
5	3750	12	10	120	5.822	5.428	5.539

2 Experimentation and Data Collection

For the present experimentation, austenitic stainless steel 316LN plate (300 mm × 125 mm × 5.6 mm) is considered. Bead-on-plate welding experiments were performed based on the design matrix compiled with the central composite design. Totally, 30 numbers of bead-on-plate (BOP) welds were prepared, and depth of penetration of the weld was evaluated by an optical microscope. Welding speed was taken as 20 cm/min, and defocusing distance was maintained at −2 mm. The gas flow rate and torch angle were kept 10 lt/min and 450, respectively. The range for input parameters was decided by conducting free tail runs, and five levels of these input variables are presented in Table 1 [3]. Also, five test cases with their experimental and predicted results are shown in Table 2. Regression results of the test cases were also collected from the available literature [3].

3 Tools and Techniques

3.1 Fuzzy C-means Clustering

Clustering technique is one of the effective methods to recognize natural grouping if a dataset. In general, there are two classes of clustering techniques, namely supervised (has known reference) and unsupervised (devoid of the reference vectors that are

pre-defined). Fuzzification is the technique to outdo the uncertainties in forming of data groups. Data form a part one group, and the disjoint of traditional clustering is the hard clustering. Initialization of the fuzzy system is assisted by unsupervised clustering in the absence of reference in the triage data. Fuzzy subtractive and fuzzy c-means are the clustering techniques used to determine the rules from the available dataset. The number of rules is equal to the number of clusters.

Fuzzy c-means clustering algorithm [10] helps to generate the number of clusters. The following equation helps in calculating the number of clusters in the model.

$$J = \sum_{i=1}^{I} \sum_{j=1}^{J} u_{ij}^{m} \left\| X_j - V_i \right\|^2 \tag{1}$$

Details of I, J, V_i, X_j, u_{ij} and m (generally equal to 2) can be seen in [10].
The degree of membership u_{ij} is defined as:

$$u_{ij} = \left[\sum_{k=1}^{I} \left\| \frac{X_j - V_i}{X_j - V_k} \right\|^{2/m-1} \right] \tag{2}$$

The comparison between two generated values of membership is done by the algorithm. Cluster generation by algorithm is stopped as soon as it finds insignificant difference between these values.

3.2 Adaptive Neuro-Fuzzy Inference System (ANFIS)

It is a combination of both fuzzy logic and neural network, where both methods complement each other to minimize the drawbacks of the individual approach. A simplified ANFIS structure considered (Fig. 1) contains five layers, and each layer represents a different function. To each node, the input data (x and y) are presented, and output is calculated using Gaussian membership function $\mu(x)$ in the first layer and is represented as below [11, 12].

$$O_{1i} = \mu_{A_i}(x), \quad i = 1, 2; \quad O_{1i} = \mu_{B_{i-2}}(y), \quad i = 3, 4; \quad \mu(x) = e^{-((x-v_i)/\sigma_i)^2} \tag{3}$$

where x is the input to the node i. A_i and B_i represent membership values of μ_A and μ_B, respectively. v_i and σ_i are mean and standard deviation of provided dataset, respectively. Each node's output in the first layer is then fed to the second layer for computing the firing strength of each rule (w_i) via multiplication as follows to attain the output of the second layer.

$$O_{2i} = w_{2i} = \mu_{A_i}(x) x \mu_{B_{i-2}}(y) \tag{4}$$

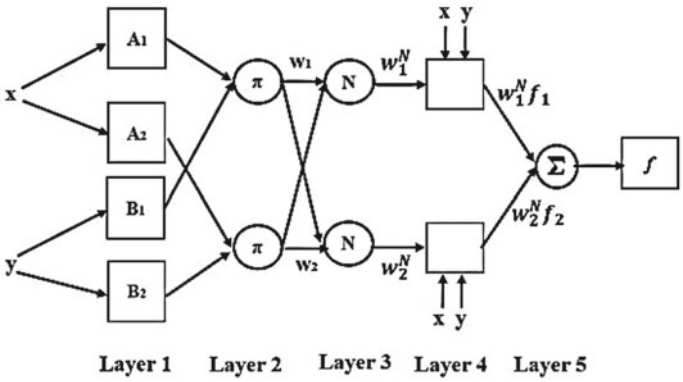

Fig. 1 ANFIS schematic architecture

Then, the normalized firing strength ($\overline{w_i}$) is computed for each node in the third layer. The formula for calculation is given below.

$$O_{3i} = \overline{w_i} = w_i / \left(\sum_{i=1}^{2} w_i \right), \tag{5}$$

The output of each node in the fourth layer (adaptive layer) is calculated as the product of its normalized firing strength ($\overline{w_i}$) and output of the corresponding fired rule (f). The output is shown below.

$$O_{4i} = \overline{w_i} f_i = \overline{w_i}(p_i x + q_i y + r_i) \tag{6}$$

where p_i, q_i and r_i are the coefficients of Sugeno FLC or resultant parameters of the node. There is a single node in the fifth layer whose output is the overall output of the model, and it is expressed as follows:

$$O_5 = \sum_i \overline{w_i} f_i \tag{7}$$

4 Results and Discussion

The proposed ANFIS-FCM model was used to develop the input–output model for prediction of bead penetration in hybrid laser-TIG welding. Here, 30 datasets were used as training pairs and another five data pairs as the testing dataset. ANFIS-FCM model was developed using MATLAB environment.

Table 3 Test cases along with responses with different approaches

Parameters	Description
Input membership function	Gaussian
Output membership function	Linear
Number of nodes	157
Number of linear parameters	75
Number of nonlinear parameters	120
Total number of parameters	195
Number of training data pairs	30
Number of checking data pairs	5
Number of fuzzy rules	15

The membership function parameters of a single output were identified via a hybrid-learning algorithm. Takagi-Sugeno type fuzzy inference system was considered for building ANFIS-FCM model. Gaussian and linear membership functions were used for input and output, respectively. A step size 0.01 with the maximum epoch of 500 was set to initialize the model. The RMS was used to assess the model accuracy. The specification of the ANFIS-FCM model is presented in Table 3.

In addition to this, the hybrid-learning algorithm was used to optimize membership function parameters. It was seen from the result that minimum mean absolute percentage error (MAPE) and root-mean-square error (RMSE) achieved with the FCM-ANFIS approach. The RSME value of test cases was found to be 0.207 and 0.050 for regression and FCM-ANFIS, respectively. It signifies the model accuracy and scope for input–output modeling of any complex manufacturing process. The experimental results along with predicted results are shown in Fig. 2. The mean absolute percentage error was found to be 0.513 for FCM-based ANFIS approach and 3.248 for conventional regression approach. The percentage deviation of FCM-based

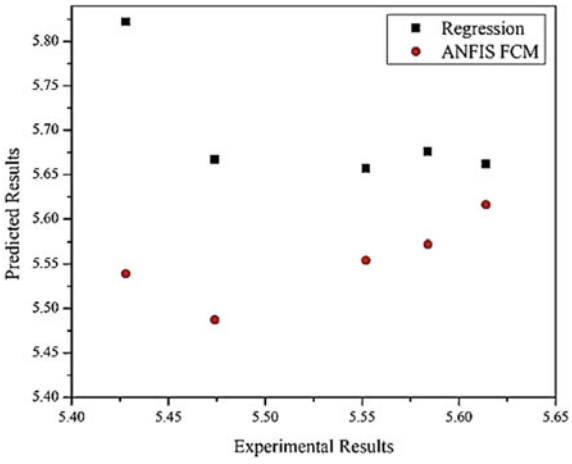

Fig. 2 Experimental versus predicted result

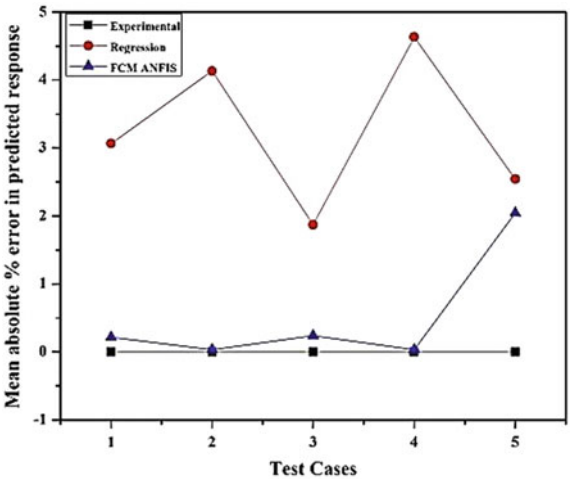

Fig. 3 Percentage deviation in predicted results

approach was also found to be much smaller than that of regression. It could be evident from Fig. 3 that FCM-based results are closer to experimental results. The use of FCM in ANFIS helps to achieve better accuracy because the generation of fewer rules and help to reduce computational complexity. Hybrid-learning algorithm also helped to refine the membership function parameters and to improve the prediction capability.

5 Conclusion

Hybrid laser-TIG welding was conducted considering austenitic stainless steel as work material and bead penetration as response of the system. Fuzzy c-means clustering-based adaptive neuro-fuzzy inference system (FCM-ANFIS) model was developed to perform the prediction of responses. The statistical performance of the model was examined with RMSE and mean absolute percentage error (MAPE). The better prediction capability of FCM-ANFIS was evident from the result of RMSE (0.050) and MAPE (0.513) for the validation data. The prediction accuracy might be because the fuzzy set can handle the uncertainty of parameter belongingness for a particular response. It could also be concluded that the prediction accuracy of the FCM-ANFIS is higher than that of conventional regression for a complex nonlinear process.

References

1. Dalle, F., et al.: Conventional austenitic steels as out-of-core materials for Generation IV nuclear reactors. In: Structural Materials for Generation IV Nuclear Reactors, pp. 595–633 (2017)
2. Li, X., et al.: Effect of post weld heat treatment on the microstructure and properties of Laser-TIG hybrid welded joints for CLAM steel. Fusion Eng. Des. **128**, 175–181 (2018)
3. Ragavendran, M., et al.: Optimization of hybrid laser–TIG welding of 316LN steel using response surface methodology (RSM). Opt. Lasers Eng. **94**, 27–36 (2017)
4. Weron, R.: Electricity price forecasting: a review of the state-of-the-art with a look into the future. Int. J. Forecast. **30**(4), 1030–1081 (2014)
5. Zhao, D., et al.: Modeling and process analysis of resistance spot welded DP600 joints based on regression analysis. Mater. Des. **110**, 676–684 (2016)
6. Vedrtnam, A., et al.: Optimizing submerged arc welding using response surface methodology, regression analysis, and genetic algorithm. Def. Technol. **14**(3), 204–212 (2018)
7. Sung, B.S., et al.: Fuzzy regression model to predict the bead geometry in the robotic welding process. Acta Metall. Sin. (Engl. Lett.) **20**(6), 391–397 (2017)
8. Mathew, J., et al.: Prediction of welding residual stresses using machine learning: comparison between neural networks and neuro-fuzzy systems. Appl. Soft Comput. **70**, 131–146 (2018)
9. Xue, Y., et al.: Fuzzy regression method for prediction and control the bead width in the robotic arc-welding process. J. Mater. Process. Technol. **164**, 1134–1139 (2005)
10. Jang, J.S.: ANFIS: adaptive-network-based fuzzy inference system. IEEE Trans. Syst. Man Cybern. **23**(3), 665–685 (1993)
11. Maji, K., Pratihar, D.K., Nath, A.K.: Analysis and synthesis of laser forming process using neural networks and neuro-fuzzy inference system. Soft. Comput. **17**(5), 849–865 (2013)
12. Pratihar, D.K.: Soft Computing: Fundamentals and Applications. Narosa Publishing House, New Delhi, India (2013)

Transverse Vibration and Stability of a Cracked Functionally Graded Rotating Shaft System

Debabrata Gayen, Debabrata Chakraborty and Rajiv Tiwari

Abstract Transverse vibration and stability of functionally graded (FG) shafts containing a transverse surface crack are studied considering material nonlinearity. Based on Timoshenko beam theory (TBT), a finite element (FE) model is developed for an FG shaft. Under thermal environment, material properties of radially graded FG shafts are considered using power law of material gradation. Stainless steel (SS), alumina (Al_2O_3) and zirconia (ZrO_2) are used as constituent materials of FGM I (SS/Al_2O_3) and FGM II (SS/ZrO_2). Local flexibility coefficients (LFCs) are computed as functions of temperature, size of crack and material gradient index based on linear elastic fracture mechanics. Influences of FGM type, material gradient, temperature gradient and crack size on dynamics of cracked FG rotors system are studied. Results show that beside the crack and geometric parameters, the choice of gradient index has importance on dynamics of the FG shaft for high-temperature applications.

Keywords FG cracked shaft · Power law gradient index · Temperature dependency material property · Natural whirling frequency · Stability threshold speed

1 Introduction

Functionally graded materials (FGMs) are identified as advanced composite materials for increasing applications ranging from engineering to industrial areas due to their continuous and smooth gradation to achieve superior thermo-mechanical properties over laminated composite materials. Reddy and Chin [1] presented the dynamics of FG structures subjected to thermo-mechanical load. Using TBT, Gayen and Roy [2] carried out the dynamic behavior of an FG shaft. Nelson and Mcvaugh [3] studied the

D. Gayen (✉) · D. Chakraborty · R. Tiwari
Department of Mechanical Engineering, Indian Institute of Technology Guwahati, Guwahati 781039, India
e-mail: d.gayen@iitg.ac.in

D. Chakraborty
e-mail: chakra@iitg.ac.in

R. Tiwari
e-mail: rtiwari@iitg.ac.in

L. Li et al. (eds.), *Advances in Materials and Manufacturing Engineering*, Lecture Notes in Mechanical Engineering, https://doi.org/10.1007/978-981-15-1307-7_71

analysis of rotating shafts using TBT. Zorzi and Nelson [4] studied the same work [3] with inclusions of both internal dampings. Chen and Ku [5] discussed the stability of a cracked shaft subjected to axial periodic load. Sekhar and Dey [6] reported the influences of depth and location of cracks, slenderness and internal damping on the instability speed of a cracked homogeneous rotor. Yang and Chen [7] presented a theoretical investigation on free vibration and elastic buckling for an edge cracked FG beam. Gayen et al. [8] discussed the free vibration of a non-spinning cracked shaft made of FGM. Gayen et al. [9, 10] analyzed the dynamics of cracked shaft made of FGM and reported the importance of material gradient.

However, there are a large number of works stated for free vibration analysis of FG cracked beam, and very few works are reported in the open literatures for transverse vibration of cracked shaft made of FGM, under thermal environment. Hence, the objective of this study is to examine the importance of FGM type, material gradient, temperature, slenderness and size and location of crack on dynamics of a two-disk cracked FG shaft system.

Thermo-Mechanical Material Properties

Temperature-related material properties P (Young's modulus E, thermal conductivity K and Poisson's ratio ν) for radially graded FG shaft are considered the same as work of Touloukian [11]. In addition, for the FG shaft P is given in the work of Reddy and Chin [1]

$$\mathsf{P}(y,T) = \mathsf{P}_m(T) + \{\mathsf{P}_c(T) - \mathsf{P}_m(T)\}\left\{\frac{(y-R_m)}{(R_c-R_m)}\right\}^k, \quad R_c \le y \le R_m, \quad 0 \le k \le \infty \tag{1}$$

where y is radial direction, T is temperature and R is radius. Power law gradient index is k. Following power law of material gradation, temperature distributions in the FG shaft are obtained using $\mathrm{d}/\mathrm{d}y[K(y)\mathrm{d}T/\mathrm{d}y]$ with thermal boundary conditions.

FE Formulation

The FE discretization of a cracked shafts made of FGM is shown in Fig. 1a, where L is total length, L_e is elementary length and D is diameter of the shaft and at a distance of L_c from the left-end support, the depth of crack is considered α. Figure 1b shows that P_1, P_2, P_5 and P_6 are the shear forces and P_3, P_4, P_7 and P_8 are the bending moments, translation displacements are v and w and rotational displacements are β and Γ and Ω is the rotating speed; Fig. 1c shows cracked geometry for fully open crack.

The additional displacement u_i^c due to crack is given

$$u_i^c = \frac{\partial}{\partial P_i}\int_0^{\alpha_x} \frac{1}{E(y,T)}\left[\left(\sum_{i=1}^{4} K_{\mathrm{I}i}\right)^2 + \left(\sum_{i=1}^{4} K_{\mathrm{II}i}\right)^2\right.$$

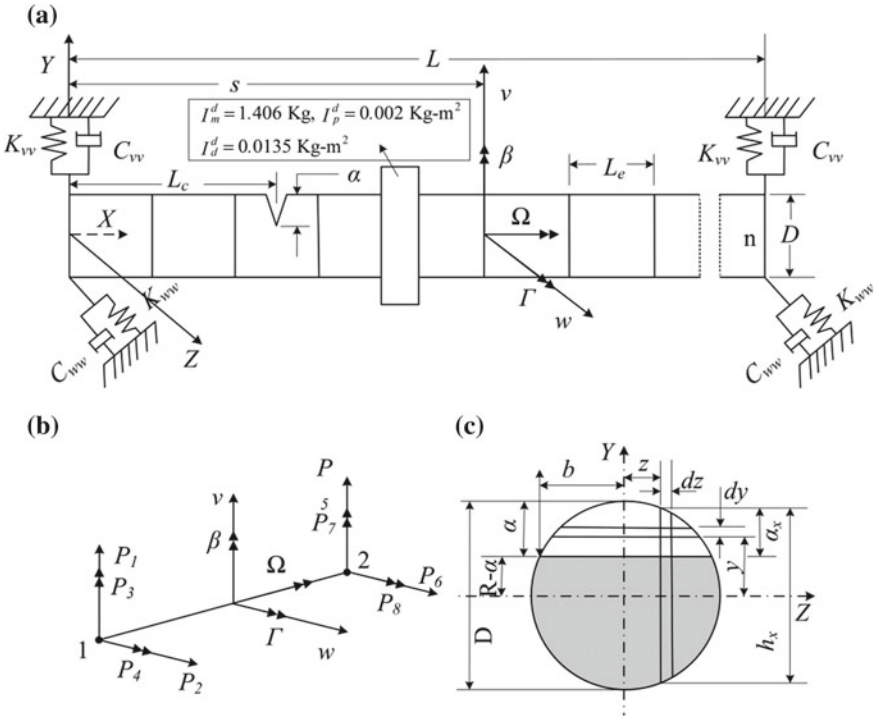

Fig. 1 FG cracked rotor system: **a** FE discretization with coordinate. **b** Loads. **c** Geometry of cracked cross section

$$+\{1+\nu(y,T)\}\left(\sum_{i=1}^{4} K_{\mathrm{III}i}\right)^2\Bigg]\mathrm{d}y \tag{2}$$

where the details of K_{I}, K_{II} and K_{III} were reported in Refs. [9, 10].

Here, LFCs are computed using Castigliano's theorem and Paris's equations [12] along with expressions of SIFs, and LFCs for fully open crack are expressed as (refer Fig. 1c)

$$C_{ij}^c = \frac{\partial u_i^c}{\partial P_j} = \frac{\partial^2}{\partial P_i\,\partial P_j}\int_{-b}^{b}\int_{0}^{\alpha_x}\frac{1}{E(y,T)}\Bigg[\left(\sum_{i=1}^{4} K_{\mathrm{I}i}\right)^2+\left(\sum_{i=1}^{4} K_{\mathrm{II}i}\right)^2$$
$$+\{1+\nu(y,T)\}\left(\sum_{i=1}^{4} K_{\mathrm{III}i}\right)^2\Bigg]\mathrm{d}y\mathrm{d}z \tag{3}$$

Using Eq. (3), LFCs for fully open crack are computed and corresponding flexibility matrix, and corresponding cracked stiffness matrix is given in details in Refs. [9, 10].

For a fully open cracked shaft made of FGMs, the equations of motion are given

$$\left(\mathbf{M}_t^s + \mathbf{M}_r^s\right)\ddot{\mathbf{q}}^s(t) - \boldsymbol{\Omega}\mathbf{G}^s\,\dot{\mathbf{q}}^s(t) + \mathbf{K}^s\,\mathbf{q}^s(t) = \mathrm{f}^s(t) \tag{4}$$

The elementary matrices of Eq. (4) reported in the works [3, 9, 10].

The resultant system equations of motion are given along with shaft's internal damping and are given

$$\begin{aligned}&\mathbf{M}\ddot{\mathbf{q}}(t) + (\eta_v\mathbf{K} - \boldsymbol{\Omega}\mathbf{G} + \mathbf{C})\dot{\mathbf{q}}(t)\\ &+ \left[\left\{\left(1+\eta_h\right)\mathbf{K}/\sqrt{1+\eta_h^2}\right\} + \left(\boldsymbol{\Omega}\eta_v + \eta_h/\sqrt{1+\eta_h^2}\right)\mathbf{K}_c\right]\mathbf{q}(t) = \mathbf{F}(t)\end{aligned} \tag{5}$$

where η_v and η_h are viscous and hysteretic damping. Considering $\mathbf{F}(t) = 0$, the solution of Eq. (5) is $\lambda_n(\Omega) = \xi_n(\Omega) \pm \mathrm{i}\omega_n(\Omega)$, logarithmic decrement is $\delta_n = -2\pi\xi_n/\omega_n$.

2 Results and Discussions

Based on FE formulation and developed FE code, the dynamic responses are computed for the FG shaft systems. Shaft's length $L = 1.25$ m, diameter $D = 0.1$ m, simply supported and flexible end bearings ($K_{vv}^b = K_{ww}^b = 17.513$ MN/m, $K_{vw}^b = K_{wv}^b = 0$, $C_{vv}^b = C_{ww}^b = 1$ KNs/m and $C_{vw}^b = C_{wv}^b = 0$) are considered, and twenty-five (25) FEs are used to model the FG shaft as shown in Fig. 1a. In the present FE model, a disk (located at a distance of 0.6 m from left-end support) is considered with $I_{\mathrm{p}}^{\mathrm{s}}$ is 0.002 kg-m^2 and I_d^{s} is 0.0135 kg-m^2, weight 1.406 kg, respectively. A FE code is developed using MATLAB for validating the FE cracked FG formulation to confirm the correctness of the FE formulation and its accuracy, and different analysis for transverse vibration analysis of the cracked FG rotor system is studied.

Validation

The FE cracked formulation of FG component is validated. For this, a cracked beam made of FGM with end conditions and for $L/D = 10.0$, $E_1 = 70$ GPa, $\nu = 0.33$, $\rho_1 = 2780\,\mathrm{kg/m^3}$, $\alpha/R = 0.4$, and $k = 2.0$ similar to those used by Yang and Chen [7]. Dimensionless natural frequencies are computed using the present FE code and compared with Yang and Chen [7], and Table 1 shows a very good agreement, thus validating the FE formulation of FG cracked.

Influences of k, α/R, ΔT and FGM Types on Natural Frequency

Figure 2a–b shows the importance of k, ΔT and crack size α/R of natural frequency of a centrally located cracked FG shaft ($L/D = 12.5$) with simply supports at both

Table 1 Variation of ϖ_n with end conditions for an FG cracked beam

$\frac{E_2}{E_1}$	Cantilever		Simply supported		Fixed-Fixed	
	Present	Yang and Chen [7]	Present	Yang and Chen [7]	Present	Yang and Chen [7]
0.2	0.9748	0.9811	0.9376	0.9535	0.9867	0.9871
1.0	0.9956	0.9951	0.9890	0.9912	0.9971	0.9966
5.0	0.9983	0.9986	0.9956	0.9992	0.9988	0.9990

ends, and the percentage reduction of natural frequency ($\%\,\varpi_n = (1 - \omega_n^{\mathrm{c}}/\omega_n^{\mathrm{uc}}) \times 100$, superscripts c and uc denote crack and un-cracked, respectively) is presented. Figure 2a shows that percentage reduction of ϖ_{1V} decreases with the decrease in gradient index k as ceramic content increase and also the reduction decreases with decrease in ΔT as the material becomes harder at lower temperature. Figure 2b shows that % reduction of ϖ_{1V} increases with the decrease in α/R as stiffness degradation is lower. It is also observed from Fig. 2a–b that reduction of ϖ_{1V} is more for FGM I (SS/Al_2O_3) than the FGM II (SS/ZrO_2).

Influences of k and ΔT on Stability Analysis

Figure 3 shows the importance of k and ΔT on reduction of stability threshold speed and critical speed $\left(\%\,\overline{\Omega}_{\mathrm{th,cr}} = \left(1 - \overline{\Omega}^{c}_{\mathrm{th,cr}}/\overline{\Omega}^{\mathrm{uc}}_{\mathrm{th,cr}}\right) \times 100\right)$ of a FG (SS/Al_2O_3) rotor disk-bearing system for $\eta_v = 0.0002$ s and $\eta_h = 0.0$. It shows that % reduction in $\overline{\Omega}_{\mathrm{th}}$ increases with the decrease in ΔT and k, but $\overline{\Omega}_{\mathrm{cr}}$ increases with the increase in k and ΔT. This is the facts that due to increase in metallic content with k and materials become rises softer for higher values of ΔT.

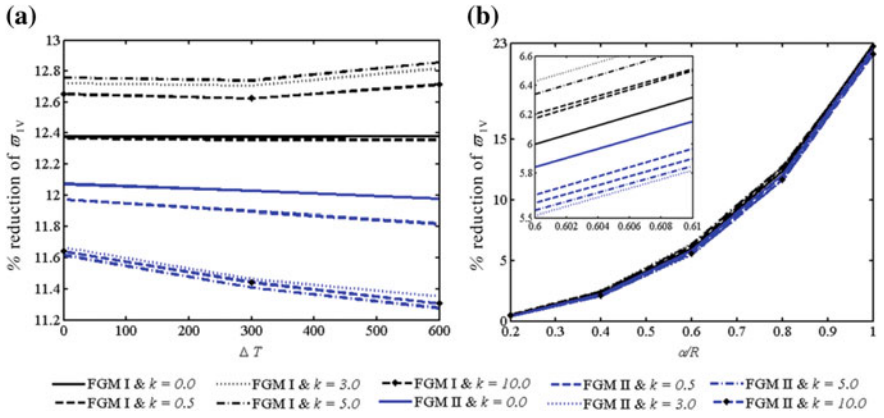

Fig. 2 Percentage reduction of ϖ_{1V} for different FGM of a cracked shaft with **a** k and ΔT for $\alpha/R = 0.8$. **b** k and α/R for $\Delta T = 0\,\mathrm{K}$

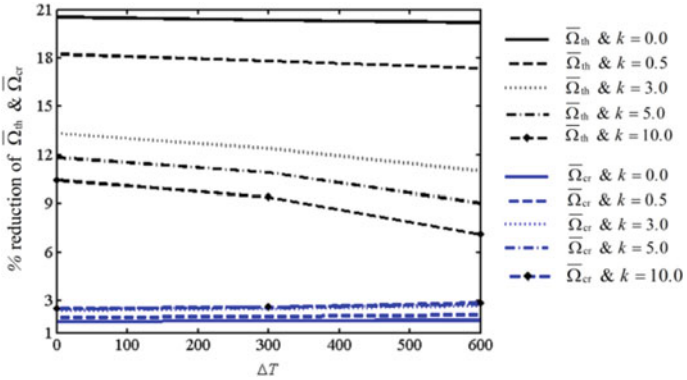

Fig. 3 Percentage reduction of $\overline{\Omega}_{th}$ and $\overline{\Omega}_{cr}$ for various k and ΔT for SS/Al_2O_3 shaft

3 Conclusions

The present work enables us to arrive at the following important conclusion

- A parametric study has been conducted for better understanding the importance of gradient index, temperature, crack size and end conditions on dynamics of cracked FG shafts.
- Both the gradient index and temperature have a huge influence to reduce natural frequencies, whirling speeds and to increase stability speeds of the cracked shafts made of FGMs. Hence, designing shafts made of FGMs for large temperature gradients with high operating speeds in service, gradient index along with temperature has important role.
- For reduction in natural frequency for using FGM I (SS/Al_2O_3) and FGM II (SS/ZrO_2), FGM I show a better choice in using higher operating speed than FGM II.

References

1. Reddy, J.N., Chin, C.D.: Thermoelastical analysis of functionally graded cylinders and plates. J. Therm. Stresses **21**, 593–626 (1998)
2. Gayen, D., Roy, T.: Finite element based vibration analysis of functionally graded spinning shaft system. Proc. Inst. Mech. Eng. Part C J. Mech. Eng. Sci. **228**(18), 3306–3321 (2014)
3. Nelson, H.D., Mcvaugh, J.M.: The dynamics of rotor bearing systems using finite elements. ASME Trans. J. Eng. Ind. **98**, 593–600 (1976)
4. Zorzi, E.S., Nelson, H.D.: Finite element simulation of rotor-bearing systems with internal damping. ASME Trans. J. Eng. Power **99**(1), 71–76 (1977)
5. Chen, L.W., Ku, D.M.: Finite element analysis of natural whirl speeds of rotating shafts. Comput. Struct. **40**(3), 741–747 (1991)
6. Sekhar, A.S., Dey, J.K.: Effects of cracks on rotor system instability. Mech. Mach. Theory **35**(12), 1657–1674 (2000)

7. Yang, J., Chen, Y.: Free vibration and buckling analyses of functionally graded beams with edge cracks. Compos. Struct. **83**(1), 48–60 (2008)
8. Gayen, D., Chakraborty, D., Tiwari, R.: Free vibration analysis of functionally graded shaft system with a surface crack. J. Vib. Eng. Technol. **6**, 483–494 (2018)
9. Gayen, D., Chakraborty, D., Tiwari, R.: Whirl frequencies and critical speeds of a rotor-bearing system with a cracked functionally graded shaft—finite element analysis. Eur. J. Mech. A Solids **61**, 47–58 (2017)
10. Gayen, D., Chakraborty, D., Tiwari, R.: Finite element analysis for a functionally graded rotating shaft with multiple breathing cracks. Int. J. Mech. Sci. **134**, 411–423 (2017)
11. Touloukian, Y.S.: Thermophysical Properties of High Temperature Solid Materials. McMillan, New York (1967)
12. Tada, H., Paris, P.C., Irwin, G.R.: The Stress Analysis of Cracks Handbook. Del Research Corporation, USA (1973)

Influence of Treated Titania Nanoparticle on Mechanical Properties of Dental Nano-Composites: Manufacturing Method and Experimental Results

Smita Rani Panda, B. C. Routara, Shanta Chakrabarty and Aswini Kumar Kar

Abstract This paper presents the experimental results on influence of nanoparticle size on the mechanical performance of dental nano-composites that comprised of a common dental acrylic resin matrix and different sized treated Titania nanoparticles. The experimental dental nano-composite as manufactured by incorporating treated Titania nanoparticles of size 100 nm as fillers into a common acrylic resin matrix (UDMA). To improve the dispersion ability, the Titania nanoparticles were treated before mixing via high-energy ball milling procedure. The nano-composite properties such as wear rate, modulus of rupture and surface hardness were measured and evaluated. The stability of nanoparticles in the solution was enhanced by adding three (3, 12 and 48 wt%) concentration of silane (A 174), i.e. 3-methacryloxypropyltrimithoxysilane. Dental nano-composite with 3 wt% shown better wear resistance, modulus of rupture and surface hardness as compared to other samples.

Keywords Dental nano-composite · Titania nanoparticle · Acrylic resin matrix · Wear rate · Modulus of rupture · Hardness

1 Introduction

In the recent years, nanotechnology has transmuted in all directions of medical applications covering the dentistry. Nanotechnology, being the molecular engineering, is the manufacturing of ultra-practical materials and structures in the scale of 0.1–100 nm by numerous physical or chemical procedures [1]. There is a significant difference in material properties at nanoscale and at an individual atomic/molecular and bulk level [2]. In recent times, although there are lots of developments in physical and chemical properties of materials, no material is found suitable for any dental application [1]. For instance, mercury toxicity from amalgam restorations [3–7],

S. R. Panda · B. C. Routara (✉) · S. Chakrabarty
School of Mechanical Engineering, KIIT Deemed to be University, Bhubaneswar, India
e-mail: bcroutray@gmail.com

A. K. Kar
Department of Prosthodontics, Kalinga Institute of Dental Sciences, Bhubaneswar, India

L. Li et al. (eds.), *Advances in Materials and Manufacturing Engineering*, Lecture Notes in Mechanical Engineering, https://doi.org/10.1007/978-981-15-1307-7_72

amalgam colour for aesthetics [8–10] and imperfect properties of composite restorative materials [11]. To overcome these problems, nano-materials have been advanced in the forms of metals, polymers, ceramics and composites for the healthcare purposes [12]. Because of its exclusive properties, nano-materials continue as a focal topic among biomaterials researchers to achieve benefits in improved life. Nano-materials developed by earlier researchers are being utilized essentially for a limited range of health sector like sustained release formulations, gene delivery, optical systems and analysis techniques of biological markers in an individual's genome and proteome [2, 13, 14].

In recent years, nano-materials have taken a lead role in applications as dental materials without much understanding on their manufacturing procedures, properties and usage. Therefore, a rigorous research is necessary on these aspects for the appropriate employment of materials in dentistry. The production of smart materials for dental applications in different routes such as achieving synthetic materials matching morphology and properties similar to natural dental tissues, getting biomaterials resembling their properties very closely to the replacing tissues via biomimetic methods and regeneration of lost tissues are completely dependent on involvement of nanotechnology [15].The requirement of nanodentistry is to achieve the near-net shape through the application of nano-materials [16]. Earlier researchers presented several approaches used for variety of feasible applications in dentistry [17, 18] as depicted in Fig. 1.

Open literature revealed that there has been impressive research on the applications of nano-materials particularly in modernistic dentistry such as restorative [19], regenerative and tissue [20], periodontics [21], preventive [22], orthodontics [23], prosthodontics [24], implantation [25] and endodontic [26]. In recent years, the progress of research has attained its importance from theoretical analysis to clinical practice. The objective of this investigation was to manufacture dental nano-filled

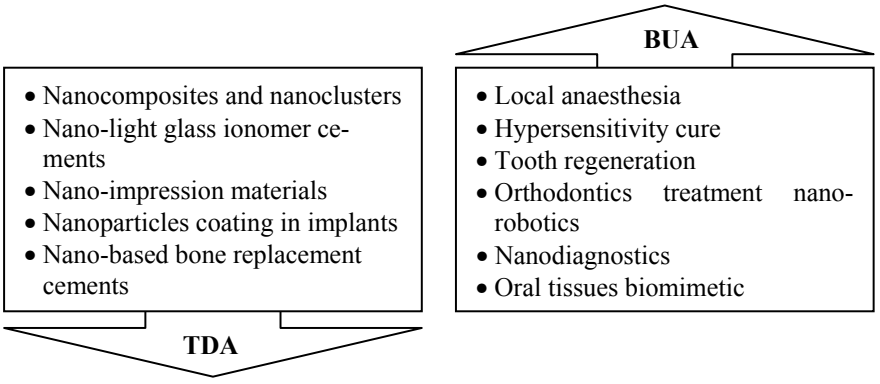

Fig. 1 Advanced nanotechnology methods and their dental applications

composites with different sizes, treated, nano-TiO_2 particles in urethane dimethacrylate (UDMA) and evaluate their mechanical properties for potential applications in dentistry.

2 Materials and Methods

In this section, the raw materials, sample preparation, manufacturing technique and testing methods of nano-filled dental composite are elaborated. The raw materials used were nano-TiO_2 particles of size 100 nm obtained by means of high-energy ball milling, monomers of urethane dimethacrylate (UDMA) as matrix. Silane (A 174), i.e. 3-methacryloxypropyltrimethoxysilane in three (3, 12 and 48 wt%) different concentrations are used as additives to improve the stability of nanoparticles in the solution. The experimental conditions and materials selected are listed in Table 1. To compare the performance of the nano-composites at different combinations of matrix and reinforcement materials, the mechanical properties such as wear rate, modulus of rupture and surface hardness were measured and materials were characterized by using SEM, TEM and EDX.

Titanium oxide nanoparticle found in form of hexagonal crystal of black colour has density 4.23 g/cm^3 and molar mass 79.9378 g/mol. It has very high melting point temperature of 1843 °C and boiling temperature 2972 °C and thermal conductivity is 11.7 W/m.K. Pure titanium dioxide is derived from limonite or leucoxene ores. It is also derived from rutile beach sand in its purest form. The thermo-physical properties of the nanoparticles are listed in Table 2.

The process of high-energy ball milling (HEBM) for synthesis of nano-sized particles from various powder materials uses a unique procedure of making alloys and composites, which is not possible to be synthesized by traditional techniques. HEBM is widely used in order to get the uniform particle size of the material in nano scale. Figure 2a shows the image of high-energy ball milling machine (planetary

Table 1 Material design considerations

Sl. no.	Materials	Unit	Levels
1	**Matrix**: Urethane dimethacrylate (UDMA)	%	10
2	**Reinforcement**: TiO_2 nanoparticles size	nm	10, 25 and 100
3	**Additive**: Silane (A 174)	wt%	3, 12 and 48

Table 2 Thermo-physical properties of TiO_2 nanoparticles

Physical properties	Value
Mass density (kg/m^3)	686.2
Specific heat (J/kg K)	4250
Thermal conductivity (W/m K)	8.9538

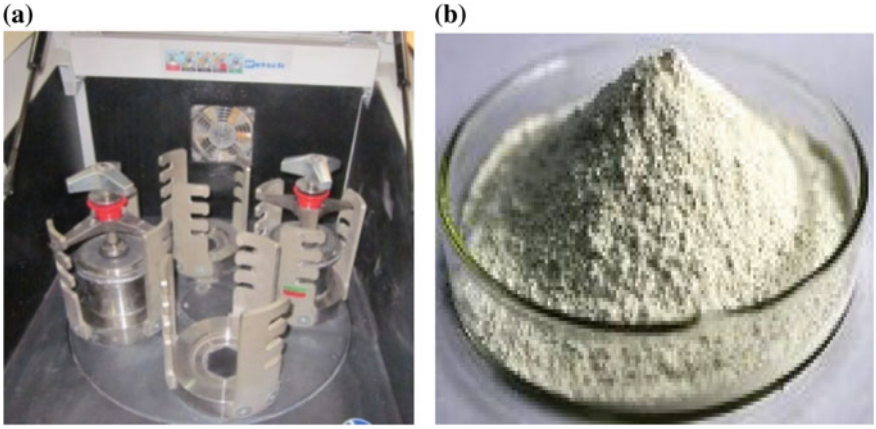

Fig. 2 **a** Image of HEBM (planetary type) machine and **b** image of prepared TiO_2 nanoparticles

type) with its components that consists of one turn disc and two or four bowls and a number of grinding balls.

A couple of parameters included in HEBM which on transforming, we can deliver an extensive variety of fine particle with different sizes and at the same time with diverse physical properties.

These parameters are (a) type of mill, (b) milling atmosphere, (c) milling media, (d) intensity of processing, (e) ball-to-powder weight ratio (BPR), (f) milling time and (g) milling temperature. TiO_2 nanoparticles were prepared by milling bulk micro-size powder of TiO_2 for period of 10 h at 10:1 ball-to-powder ratio. Periodic intervals were given to rest the machine and to cool down the bowls. The image of prepared TiO_2 nanoparticles contained in glass containers is depicted Fig. 2b.The characterization of the prepared nanoparticles was done by transmission electron microscopy (TEM), scanning electron microscopy (SEM), model: JEOL 6480 LV) and energy dispersive X-ray (EDX) detector of Oxford data reference system analysis. The illustrative SEM and TEM micrographs and EDX analysis in Fig. 3a–c show the typical morphology of the TiO_2 powders, respectively, where the particle size estimated from the micrographs is 100 nm. Elemental mapping of Titania was performed by EDX on the silicon layers. During measurements in TEM, a drop of suspended sample was positioned on a carbon-coated grid. The ethanol was gradually evaporated at room temperature, leaving the nano-TiO_2 on the grid.

The sample preparation procedure is depicted in Fig. 4.

Once the nano-composite samples prepared were cured by using WEIBER batch oven for solidification. This oven is essentially heated box with insulated doors and microprocessor-based temperature control up to 850 °C that process products one at a time or in a group. To assess the effectiveness of fabricated nano-composites under dry sliding condition, wear tests were performed on a pin-on-plate type machine (TR201LE) under ambient conditions. The test specimens having the size of 8 mm

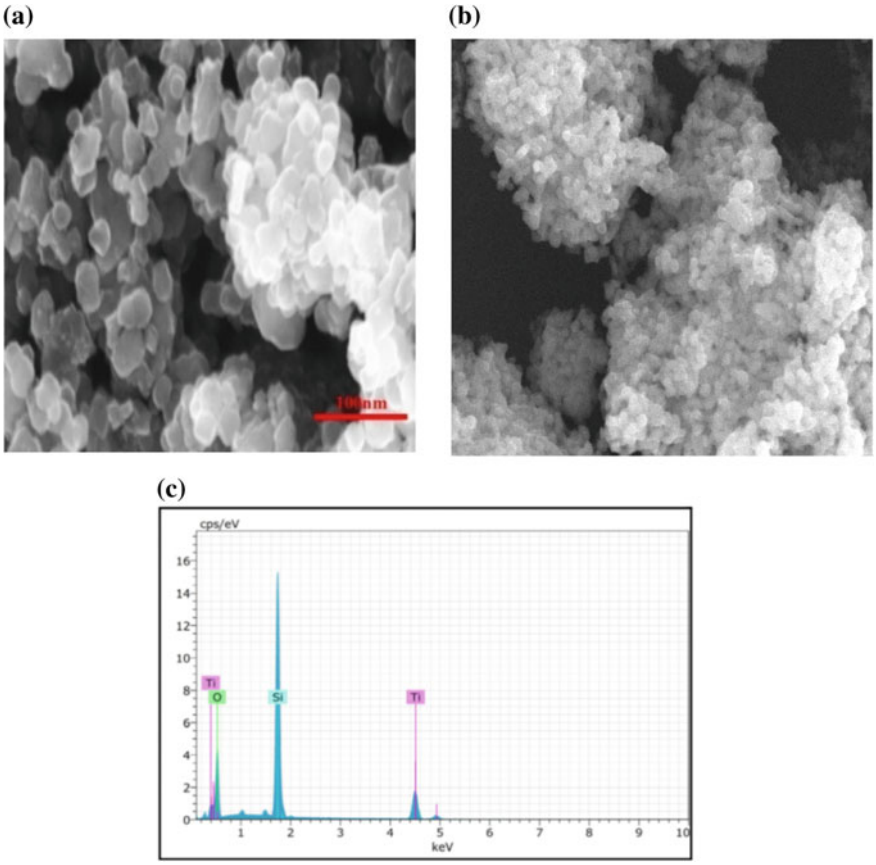

Fig. 3 **a** SEM micrograph. **b** TEM micrograph and **c** EDX analysis of TiO_2 nanoparticles

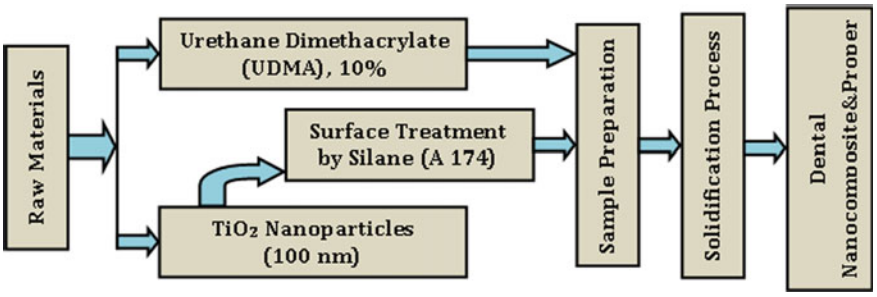

Fig. 4 The schematic of sample preparation route

diameter and 40 m length were slide against the low alloy steel disc (material: EN-31-HRS 60 W 61 equivalent to 4340) of diameter 215 mm and hardness R_c 62. A progression of tests is directed with three sliding speeds of 1, 2 and 3 m/s under three diverse typical loadings of 10, 30 and 50 N and length of time of sliding time of 1000, 2000 and 3000 s. The material loss from the composite surface is measured utilizing an electronic balance with precision ±0.1 mg. Coefficient of grinding and wear are measured consistently with an electric sensor connected to the machine and are recorded. Traditional three-point bending tests were performed to find out the modulus of rupture by using a universal testing machine (model: TUF-C-1000KN). The tests were performed at a fixed speed of 6 mm/s with an initial load of 5 KN improved up to the specimen failure. To confirm the wear resistance capabilities of the fabricated nano-composites, the surface hardness was measured by means of a micro Vickers hardness tester (model: HVS-1000) with a measuring range: 5–3000 HV.

3 Results and Discussion

Due to the deliquescent nature and agglomeration prone, the stability of Titania nanoparticles has been a serious problem while applied in any purposes. The large surface area Titania nanoparticles once agglomerated forms a size beyond nanoscale. Because of the vigorous agglomeration tendency, in fabrication nano-composites, these nanoparticles used as composite material reinforcements tend to be non-uniform distribution and provide very low mechanical performance. Therefore, the stability of Titania nanoparticles needs to be explored before mixing in a non-aqueous solvent. Thus, the grafted coupling agent silane (A 174), i.e. 3-methacryloxypropyltrimithoxysilane was used as additives for the treatment of nanoparticles in three concentrations 3 wt%, 12 wt% and 48 wt%, respectively, to improve the stability in the solution. Once the nano-composite samples were produced, the mechanical properties (wear loss, modulus of rupture and surface hardness) were measured via appropriate instruments as discussed in previous section. The mechanical properties of nano-composites with normal and treated Titania nanoparticles were compared. The influence of nanoparticle treatment was investigated from the plots generated out of experimental data as depicted in Fig. 5.

The influence of silane (A 174) treated to the matrix containing 100 nm Titania on the wear behaviour of nano-composites is depicted in Fig. 5a. Each of the tests was repeated for three times for the statistical calculations. Values from Fig. 5a confirmed that the nano-composite with Titania nanoparticle treated at 3% silane (A 174) gave lower wear loss compared to other nano-composites. The maximum and minimum wear losses achieved with this nano-composite were 10.22 and 7.84%. The mean wear loss was found higher in case of the nano-composite with nanoparticles treated at 12% silane. Compared to the normal nano-composite, it was observed that the addition of A 174 silane improved the wear resistance might be due to the superior bonding. The moduli of rupture (MPa) of the normal and treated nano-composites were measured in three repetitive tests. The mean, maximum and minimum values

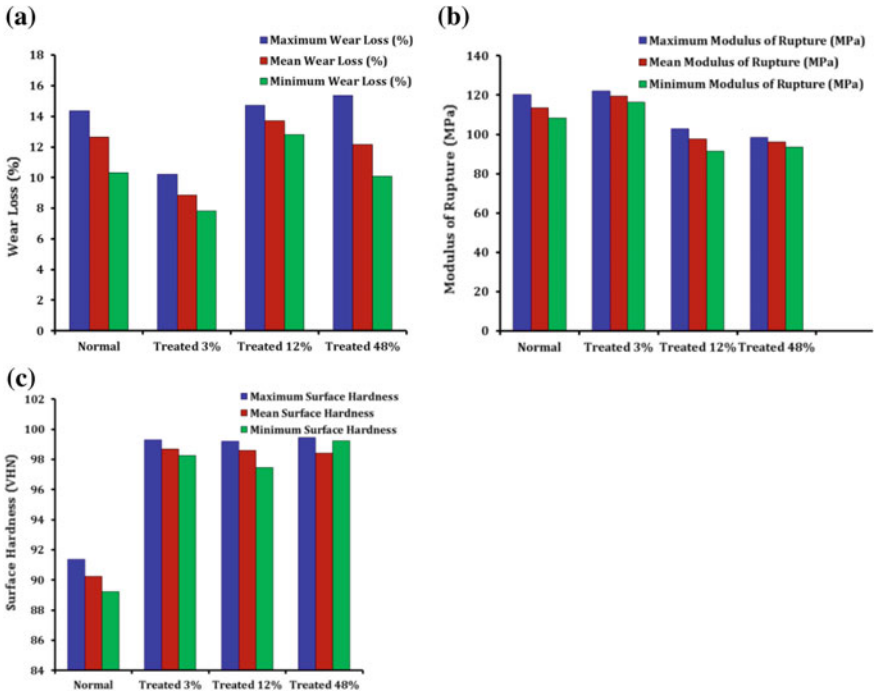

Fig. 5 **a** Wear loss (%), **b** modulus of rupture (MPa) and **c** surface hardness (VHN) of nano-composite reinforced with normal and treated 100 nm TiO_2 nanoparticles

were calculated and plotted as shown in Fig. 5b. As observed from Fig. 5b, the modulus of rupture was significantly higher for the nano-composite samples with treated TiO_2 particles at 3% silane compared with other samples. In the other hand, the modulus of rupture is improved due to grafting of TiO_2 particles with silane, might be because of strong bondage between the treated TiO_2 particles and UDMA matrix. The microhardness of nano-composite surfaces was measured and plotted as depicted in Fig. 5c. From the figure, it can be predicted that the mean hardness values of the treated TiO_2 nano-composite with 3% of silane were slightly higher as compared to other nano-composites. Compared to the normal nano-composites, the hardness was improved significantly in case of nano-composites with treated TiO_2 nanoparticles. This improvement might be due to strong bonding and uniform distribution of TiO_2 nanoparticles in the UDMA matrix.

4 Conclusions

The experimental results on the evaluation of mechanical properties for the fabricated dental nano-composites indicated that addition of treated TiO_2 nanoparticles in the UDMA matrix improved the dispersion and resulted good mechanical properties as

compared to those for addition of normal TiO_2 nanoparticles. Some of the conclusions are as follows:

- Nano-TiO_2 particles up to size 100 nm was successfully synthesized via HEBM route.
- Addition of silane (A 174) dramatically improved the bonding between the reinforcement (nano-TiO_2 particles) and matrix (UDMA) reducing the clusters in the dental nano-composite fabrication.
- Nano-composites with treated nano-TiO_2 particles have shown reduced wear loss and improved modulus of rupture and surface hardness as compared to those for nano-composites with normal nano-TiO_2 particles.

References

1. Mitra, S.B., Wu, D., Holmes, B.N.: An application of nanotechnology in advanced dental materials. J. Am. Dent. Assoc. **134**(10), 1382–1390 (2003)
2. Roco, M.C.: Nanotechnology: convergence with modern biology and medicine. Curr. Opin. Biotechnol. **14**(3), 337–346 (2003)
3. Eley, B.M.: The future of dental amalgam: a review of the literature. Part 2: mercury exposure in dental practice. Br. Dent. J. **182**(8), 293 (1997)
4. Eley, B.M.: The future of dental amalgam: a review of the literature. Part 4: mercury exposure hazards and risk assessment. Br. Dent. J. **182**(10), 373 (1997)
5. Jones, D.W.: A Canadian perspective on the dental amalgam issue. Br. Dent. J. **184**(12), 581 (1998)
6. Warfvinge, K.: Mercury exposure of a female dentist before pregnancy. Br. Dent. J. **178**(4), 149 (1995)
7. Smart, E.R., Macleod, R.I., Lawrence, C.M.: Resolution of lichen planus following removal of amalgam restorations in patients with proven allergy to mercury salts: a pilot study. Br. Dent. J. **178**(3), 108 (1995)
8. Eley, B.M.: The future of dental amalgam: a review of the literature. Part 7: possible alternative materials to amalgam for the restoration of posterior teeth. Br. Dent. J. **183**(1), 11 (1997)
9. Bharti, R., Wadhwani, K.K., Tikku, A.P., Chandra, A.: Dental amalgam: an update. J. Conserv. Dent. JCD **13**(4), 204 (2010)
10. Khurshid, Z., Zafar, M., Qasim, S., Shahab, S., Naseem, M., AbuReqaiba, A.: Advances in nanotechnology for restorative dentistry. Materials **8**(2), 717–731 (2015)
11. Saunders, S.A.: Current practicality of nanotechnology in dentistry. Part 1: focus on nanocomposite restoratives and biomimetics. Clin. Cosmet. Invest. Dent. **1**, 47 (2009)
12. Silva, G.A.: Introduction to nanotechnology and its applications to medicine. Surg. Neurol. **61**(3), 216–220 (2004)
13. McLean, J.W.: Alternatives to amalgam alloys: 1. Br. Dent. J. **157**, 432–433 (1984)
14. Yardley, R.M.: Alternatives to amalgam alloys: 2. Br. Dent. J. **157**(12), 434 (1984)
15. Zhang, L., Webster, T.J.: Nanotechnology and nanomaterials: promises for improved tissue regeneration. Nano Today **4**(1), 66–80 (2009)
16. Gupta, J.: Nanotechnology applications in medicine and dentistry. J. Investig. Clin. Dent. **2**(2), 81–88 (2011)
17. Subramani, K., Ahmed, W. (eds.): Emerging Nanotechnologies in Dentistry: Processes, Materials and Applications. William Andrew, Amsterdam, The Netherlands (2011)
18. Mikkilineni, M., Rao, A.S., Tummala, M., Elkanti, S.: Nanodentistry: new buzz in dentistry. Eur. J. Gen. Dent. **2**(2), 109 (2013)

19. Melo, M.A., Guedes, S.F., Xu, H.H., Rodrigues, L.K.: Nanotechnology-based restorative materials for dental caries management. Trends Biotechnol. **31**(8), 459–467 (2013)
20. Mitsiadis, T.A., Woloszyk, A., Jiménez-Rojo, L.: Nanodentistry: combining nanostructured materials and stem cells for dental tissue regeneration. Nanomed. **7**(11), 1743–1753 (2012)
21. Bartold, P.M.: Future directions in clinical periodontics. In: Research Advances and Clinical Practice in Periodontics: Bridging the Gap, p. 103 (2006)
22. Neel, E.A.A., Bozec, L., Perez, R.A., Kim, H.W., Knowles, J.C.: Nanotechnology in dentistry: prevention, diagnosis, and therapy. Int. J. Nanomed. **10**, 6371 (2015)
23. Maheshwari, S., Verma, S.K., Tariq, M., Gaur, A.: Nano-orthodontics revolutionizing oral health care. Indian J. Oral Sci. **5**(3), 109 (2014)
24. Wang, W., Liao, S., Zhu, Y., Liu, M., Zhao, Q., Fu, Y.: Recent applications of nanomaterials in prosthodontics. J. Nanomater. **2015**, 3 (2015)
25. Najeeb, S., Zafar, M.S., Khurshid, Z., Siddiqui, F.: Applications of polyetheretherketone (PEEK) in oral implantology and prosthodontics. J. Prosthodont. Res. **60**(1), 12–19 (2016)
26. Akbarianrad, N., Mohammadian, F., Alhuyi Nazari, M., Rahbani Nobar, B.: Applications of nanotechnology in endodontic: a review. Nanomed. J. **5**(3), 121–126 (2018)

Quality Management in Producing Engineering Graduates by the Premier Technical Institutions: A Case Analysis

Papiya Chatterjee, Deepanjali Mishra, Mangal Sain and Purna Chandra Mishra

Abstract Governments in central and state levels issue orders to establish new IITs and IIMs every year which generates opportunities to students across the country to take admission and build their future. The statistical data revealed by IIT Kanpur, India, the organiser of 2018 JEE (Advanced) indicated that there has been an increase of total of 11,279 seats offered in the IITs in the year 2018 which is 291 seats more from 2017. The Joint Admission Board (JAB) has proposed an additional 1000 seats in IITs and a 14% supernumerary increase in admission for women, though several IITs doubt existing campuses can accommodate more students. The situation gets precarious when a student is unable to get through in the campus placement. Earlier, it was taken for granted situation that if a student graduates from any IIT, there is 100% job security which has indeed changed in the present-day context. This paper analyses the issues of technical institutions facing in producing quality engineers, establishes a relation between the mushrooming of IITs and job security of the student and the suggested reform policies to be undertaken by the technical institutes in manufacturing quality engineers. It would propose to highlight on the risk factor of admitting students by these premier institutions on its brand image.

Keywords Premier institutions · Graduates · Quality · Management · Engineering colleges

P. Chatterjee · D. Mishra (✉)
School of Humanities, KIIT Deemed to be University, Bhubaneswar, Odisha 751024, India
e-mail: deepanjali.mishrafhu@kiit.ac.in

M. Sain
Department of Information Engineering, Dongseo University, 47 Jurye-ro, Sasang-gu, Busan 47011, Republic of Korea

P. C. Mishra
School of Mechanical Engineering, KIIT Deemed to be University, Bhubaneswar, Odisha 751024, India

L. Li et al. (eds.), *Advances in Materials and Manufacturing Engineering*, Lecture Notes in Mechanical Engineering, https://doi.org/10.1007/978-981-15-1307-7_73

1 Introduction

It is a widely known fact that India is faced with the problem of substandard engineering education. Many engineering institutions with the exception of IIT's and NIT's fail to cater to the needs of the students' education and training which would facilitate them in getting a good job. The situation is so grim that now parents are shying away from getting their children admitted in premier state government engineering colleges. This situation is due to the fact that every year there is mushrooming of low standard technical institutions all over the country. As a result of which the students passing from these institutions fail to get placement. This ultimately results in the decline in the number of students taking admissions in these institutions even if they create hype through advertisements. When there is no enrolment, the colleges are forced to shut down. This will lead to a decrease in about 80,000 seats less in engineering stream from this year which would account to nearly 3.1 lakh seats less in four years. As per the reports of All India Council for Technical Education (AICTE), the number of technical institutions who have applied for closure is about 200 which are considered to be "substandard". The trend of decline in the number of seats in engineering colleges started in 2016. As per the reports of AICTE, it would amount to 75,000 seats per year; whereas, the intake of students in 2016–17, total intake capacity at undergraduate level was 15, 71, 220, of which total enrolment was very less compared to the previous years. The stringent rules of AICTE force the colleges voluntarily every year [1]. One of them is the lack of infrastructure. AICTE has categorically mentioned that those colleges who have lack of proper infrastructure and account to 30% less admission than the previous years would likely to be shut down. More than 410 technical colleges all over India were approved to be shut down by the AICTE in 2014–15 to 2017–18. When the then government formed a committee under the leadership of Prof. UR Rao in 2003 in order to access the performance of the engineering colleges all over the country and an analysis of the future of engineering graduates, committee came up with a conclusion that there is a huge expansion of the number of engineering colleges but fail to sustain in the long run because the supply exceeded the demand of the engineering graduates. Now even after 15 years, the committee report is unchallenged and completely justified.

The placement scenario is even worse. As per AICTE reports, out of the eight lakh students who graduated last year, less than 50% of the students succeeded in getting jobs through campus selection. As per the reports of national daily, Indian Express, in their report, the Rao's committee recommended a suspension of five years on providing approval to the undergraduate technical institutions in those states where the intake of the student is more than the national average standing at 150 seats per million populations. Unfortunately, this recommendation given by the Rao's committee was not implemented. The year 2008–09 saw the rise of joining 30% more students in engineering colleges compared to the previous which was ironically was the highest rise compared to 2001. As per the data given by AICTE and last year itself, approximately 700 new colleges got approval, and in the year 2016–17, there was a vacancy of about 50% of the 15.5 lakh bachelors in engineering seats all over India [2].

Therefore, the crisis of Indian education is quite prominent, and numerable studies have emphasised that employability situation is very low of the graduates in engineering. At the same time, a recently conducted study analysed that the engineering graduates of Russia and China perform better than the engineering graduates of India. Students who are from India make remarkable in subjects like mathematics and critical thinking skills while they are in their first two years while studying as compared to those students who are from countries like China or Russia. On the other hand, Chinese and Russian students excel in overall higher-order thinking skills according to a research that was conducted jointly by Stanford University and the World Bank to find the learning outcome assessment of undergraduate technical students, which makes the scene clear that the ambition of the students is not to achieve success in life which is probably another factor for creating a barrier in their academic enhancement.

1.1 Issues Faced by the Technical Institutions to Produce Quality Engineers

As per the latest trend, many IIT graduates have shown interest in pursuing management courses after the completion of their graduation even though the premier institutions have succeeded in producing quality engineers, researchers and academicians. Many reputed institutions have IIT aluminous heading the department or the whole institutions. Yet, the students are keen to pursue further education. There are many reasons which could be responsible for it. One of them is the lack of basic science education and communication skills provision in these institutes which is more important. Certain institutions have very much outdated syllabus, non-existent laboratories and incompetent faculty members because many institutions do not want to spend more in the salary of the faculties of non-technical backgrounds. IITs need to address these basic issues because faculties who join IITs are reputed researchers and academicians since they have considerable amount of funds to set up laboratories and generate facility in facilitating the best education to the students who join the course.

1.2 Relationship Between Massive Rise in the Number of IITs and Job Security

A shocking revelation was made by a New Delhi-based employment solutions company, “Aspiring Minds” in 2013 who conducted a study on employability-focused skills taking huge sample of 150,000 students of 2013 passed engineering students. It found that approximately 97% of graduating engineers inspire jobs that are related to software engineering or core companies. And 3% of students possess requisite skills

eligible to get employment in core companies and software firms, and 7% of the graduate engineers could handle the jobs of the core companies. As per the reports of the HRD ministry, there are about 6214 engineering and technology institutions who enrol approximately 2.9 million students every year, and they manufacture about 1.5 million engineers who get ready to go to the job market each year. It is because of the very poor situation of the Indian technical education which is responsible and indicates that the students fail to possess the requisite skills that is required to get placed. Bharwani states "The ability to apply the concepts learnt to constantly develop innovative things and find solutions to complex problems are main factors working behind the employability of an engineer". He further adds, "The state of the economy also plays a major role for employment generation. Industry insiders say that in a strained economic condition, companies do not want to spend much on training and would prefer candidates with some skill sets who can be made billable soon" [3]. Location factor: As per the reports of the Aspiring Minds, cities which are in Tier-1, like Mumbai, Delhi, Bangalore and Hyderabad, 18.26% of technical graduates are suitably skilled; whereas, in cities which are Tier-2 cities such as Pune, Nagpur and Surat, about 14.17% engineers are proficient.

(i) Problems in fluency in speaking English

It is considered to be one of the major concerns of the engineering students. Many students come from vernacular medium which results in their inability to speak English fluently. English being a global language is widely acceptable and used as a means of communication during interviews which makes it difficult to get placed in companies.

(ii) Syllabus not updated regularly

One glance at the syllabus of the engineering course content points out that it does not thrust on those subjects that would be beneficial in getting a job in industry. The course fails to cater to the needs of the industry as the gap between the needs of a market and the syllabus. The primary reason for this issue is irregular update in the syllabus. Sometimes, the new branches are added keeping an eye on the needs of the industry but it fails because the faculties of the existing stream take classes and the management does not bother to maintain the quality.

(iii) Lack of quality teachers

Unavailability of good researchers and academicians to teach the students is a major concern for the engineering institution which might be due to the fact that the graduates or the post graduates aspire to go abroad and earn their bread and butter instead of staying here in India. And some good toppers prefer to stay in software engineering companies instead of coming and taking classes because of less financial gains in the teaching jobs.

(iv) Absence of innovativeness and research skills

Students much build the capability of critical thinking and making critical analysis of their own. In one of the public address, the HRD minister Prakash Javadekar said,

"Why do we lack innovation in India? Because, we don't allow questioning. We don't promote inquisitiveness. If a child asks questions in school, he is asked to sit down. This should not go on. We need to promote inquisitiveness, children should ask questions" [1]. Therefore, the students should get ample opportunities to think for himself/herself, innovate things on their own and must be ready with solutions to any problem. This should starts from the school so that when a student gets admitted in the engineering courses and start education, he/she is ready with all these skills because the job market is only concerned with innovating new techniques of viewing a problem that may arise and handling such crises and ultimately finding solution to these problems.

(v) Faulty education system

Due to the semester system of education, the students get bored with the continuous learning process due to which they do not concentrate on attending classes. They are bothered with getting good marks by using all possible means to impress the faculties and resorting to other means. So, when these students graduate, they hardly know anything about the subject matter and fail to qualify in the competitive exams.

(vi) Lack of skill-based education

Skill-based education is very important for the engineering students because they require undertaking rigorous training in order to enter into the companies for which they are selected. These trainings are given for making them ready in handling crisis in the company, problem solving, critical thinking, etc. Therefore, skill-based training should start during their four years of engineering. Bharwani has emphasised, **"**One of the major problems facing the fresh graduates is their insufficient understanding of basic concepts. The lack of in-depth understanding of technical information, lack of client-handling skills and insufficient knowledge across domains are the major skill gaps in the area" [1]. It is a common tendency of a student to get the notes from the teachers, do last minute study and write what they have memorised in the exam. They succeed in getting good grades. But, they are completely incompetent when they enter the job market because they lack practical knowledge.

(vii) The IT "employability"

The Aspiring Minds report again reveals that even though various IT sectors which conduct maximum number of placement interviews by visiting campus of the IITs and taking students for their companies through pool campus, a dismal 18.43% engineers are competently qualified for the jobs, and on the other hand, a miserable 3.21% of graduates are competent for IT product roles. Due to the fact that it is comparatively easier to get through IT sector, students who are from other branches of engineering too sit for IT sector. This creates problem when non-IT students work in IT firms as they are unaware of the system, and they have not studied it in their core branch.

(viii) Disregard of essential soft skills

As communication skills are important, in the same way soft skills are equally important for a student aspiring for placement. Bharwani says, "This is perhaps the trickiest issue," "The lack of ability of the individual to deliver his views effectively at the interview leads to rejection of even the most brilliant candidate. This is because training institutes do not make an effort to ensure that the candidates develop their skills in a wholesome manner which can contribute towards client-handling and team communication skills". The student should be equipped with emotional intelligence, leadership skills and team spirit among other qualities that are needed to sustain in a job [1].

(ix) Risk factor of admitting students by the premier institutions

In order to maintain quality, the IITs face challenges most of the time. The recent expulsion of 73 students by the administration of IIT Roorkee for their underperformance is one the best example. Ironically, it is forced to lower the criteria for admitting students from the weaker sections. The IITs also intend to admit students having scores of meagre 31 out of total 504. It may also admit student with lesser score even in order to fill up the vacant seats which was 8.8% in the year 2014. Subsequently, the quality in the IITs was bound to decrease the criteria for getting admitted in the general category was decreased from 35% to 24.5%. It was further lowered from 35 to 24.5% for the reserved categories. To add to this, even the cut-offs plus the qualifying marks for the students coming under reserved categories are proposed to be reduced so that a third category of students would be created, and they would be sent for a preparatory course provided if they could get minimum 6.1%.

2 Gender Diversity in Technological Institutions

Gender diversity in engineering colleges has been gradually improving over the past few years, due to various reasons. The greater educated mass, awareness of women education and current scenario of job facilities providing equal opportunities to both the sectors of society have immensely contributed to the improvement of gender ratio of male and female in all the notable sectors. With an aim to improve the gender ratio at the engineering colleges to at least 20% or one woman in every five students by 2020, the Indian Institutes of Technology initiated to create at least 550 extra seats exclusively for women in the batches starting in 2018 and 2019. Considerably, an abysmally small number of women join Indian Institute of Technology which is one woman in every ten admissions till 2017, irrespective of the fact that women perform and secure better result than men at higher secondary level. Despite the better performance, it is considered by many that competitively men progress farther than women. To bring a cure to this problem, the Ministry of Human Resource Development directed all the IITs to ensure that at least 14% of their seats went to women in 2018 batch. To quote the words of Aditya Mittal, Chairman of Joint

Entrance Examination (Advanced) at IIT Delhi: "Considering approximately 10% of the students enrolled at IITs, last year were women, about 550 supernumerary seats would be needed to bring up the woman percentage to 14% in 2018" [1].

Presenting a data of 2017 admission in IITs, nearly 11,000 students were admitted, where the percentage of women at some of the institutes fill even below 10%. IIT Kanpur had only 54 women among 826 it admitted in 2017, a percentage of 65% while IIT Guwahati had only 6.3% women among 643 students. This resulted in an initiation of seat allocation for the incoming batch of 2018 to 14% of admission to women candidates [4]. Complying the decision, in 2018, IIT Kanpur, the centre for JEE Advanced 2018 had proposed the introduction of 800 supernumerary seats at various IITs for girls. This is in accordance with the gender diversity plan by Ministry of Human Resource Development which said firstly, at least 8% more seats will be added to IITs this year to accommodate more girls, and secondly, this will enhance female representation in popular streams like computer science and electrical engineering.

The government's initiative of improving the percentage of girls at IIT is a great step; this will develop the shortfall of ratio between girls and boys, thereby striking a better gender balance. Eventually, these steps would not only improve the gender ratio but also would bring considerable amount of empowerment in the womenfolk, making them lead in almost all the fields. The praiseworthy move of government is not bereft of its pitfalls. The statistics from Indian Institute of Technology's entrance test JEE (Advanced) shows only 38% of female candidates eligible for IITs actually opted or accepted for a seat in IITs. The JEE (Advanced) data reveals that women opt for limited choices during counselling and also target engineering institutes close to their hometown/staying place due to safety issues. Female candidates made limited choices, opting only for computer science or electrical engineering and targeted institutions for study in their preferred geographical area, basing on where their hometowns were.

Quality management in producing better engineers by the premier technical institutions is one of the major steps in brand boosting of these institutions, which the IITs have been undoubtedly trying to achieve. The lesser number of women joining the IITs, despite the reservation of seats has been a major concern of the IITs. They have been trying to take every possible measure in this regard. Help desks and web-based portals have been launched to attract more number of women in the elite institutions. The web portals have been providing easy access to information on academics and life in the IITs. The informed choices and preferences about admissions are conveyed to the parents through mails, phone calls and special pages on social networking sites. Help desks provide information about the counselling process and subject choices a candidate can opt for. Structural and customised mails are sent to individuals securing position, by congratulating them and urging them to fill up variety of choices. Even branch changing options were kept open till the end of first year for the convenience of the study choices. Professor Timothy A Gonsalves, director of IIT Mandi and chair of the subcommittee on improving the gender ratio in IITs, remarked on the quality management in terms of gender ratio as: "To help such students make an informed decision while filling in their choice of institutes

during counselling, we have set up teams of volunteers, women faculty members, students and alumni, who will reach out to these female candidates and their parents on making IITs their first option. The candidates need to know that they should not worry too much about the IIT branch they are assigned. It is better to take up another IIT branch than to join another institute" [5].

3 Impact of Brain Drain in Quality Maintenance

The term Brain Drain has come into existence and limelight with the growing trend of skilled and educated workforce, and people emigrate from one country to another for better job prospects, career gains, research and opportunities of higher education. The depletion of talent from the native which nurtures their talents may need the talent of the skilled mass for its prosperity and development. It is the migration of country's intellect which on the contrary would have served the motherland by contributing to its progress if provided with equally considerable opportunities. Brain Drain or "Human Capital Fight" as it is also termed leads to threats of the progression and growth of countries, thereby making it lose its valuable human resource enriched in technical knowledge and skills. This even leads to disparity in the social and economic status of the countries as the rich nations provide better monetary gains and job prospects, thus grow richer and more developed. On the other hand, the poorer nations stay underdeveloped and backward.

India has seen considerable amount of increase in the emigration of skilled human resource from the country. Better career options, lucrative remunerations security of life and health are few noteworthy reasons for which India has been facing the flood of Brain Drain. The issues with which India has been struggling are corrupt political system, unemployment, unsystematic work culture in private companies, unsafe work and social life, poor compensation and appreciation of work, etc., equally remain major factors for India suffering loss of great talents. To further note, few more reasons of the issue include lack of opportunity of scientific technological courses and research prospects offered in the developed nations. India loses around 3% of its skilled engineers, teachers, doctors and scientists to the developed nations like the USA, out of which the most number of emigrating workforces consists of engineers, either for job opportunities or better prospects of higher education. About 20% of the brightest minds of premium engineering and technological institutes leave country for job or for research purpose. Even it is conceded that, unlike the undergraduate programmes at IITs, PhDs are considered less prestigious. This leads to the fact that very few students from the premier institutes prefer to do PhDs at IITs while most prefer to go abroad for better exposure and academic experience.

Government's commitment in support of research and permission of freely conducting experiments would curb the issue to a great extent. For attracting highly skilled researchers and scientists to pursue their research and development interests in Indian Institutions government, it has taken several initiatives such as Faculty Recharge Programme, CV Raman Post-Doctoral Fellowship Scheme by University

Grants Commission (UGC), Ramanujan Fellowship, JC Bose Fellowship are to name a few. One of the best and recent moves by the Government of India is to provide students of premier institutions, better research prospects by further making them not to choose foreign universities for the same purpose. The Government of India approved the scheme "Prime Minister's Research Fellowship (PMRF)" at a total cost of Rs. 1650 crore for a period of seven years beginning 2018–19. Under the Scheme, the best students who have completed (in last five years) or are in the final year of B. Tech or Integrated M. Tech or M. Sc. In science and technology streams from ISC/IITs/NITs/IISERs/IIITs, with 8 CGPA will be offered a fellowship with a considerable amount of stipend. Government has also vowed to provide necessary budgetary support to all institutions including IITs and IISc for up gradation of research programmes [6]. The qualitative approach in improvement of the standard policies of job placement in Indian companies rather than foreign companies with the help of government initiatives of educational aspects and job opportunities would definitely deter the students seeking for job or education in other countries.

4 Conclusion

It is no doubt a fact that candidates aspiring to become engineers by taking up a course in engineering have an objective to get placed in companies, and it will not be wrong to say that mushrooming of IITs does create an impact in determining the quality of students. However, if these premier institutions take measures of improvisation as mentioned in the paper, it would lead to placement opportunities which would ultimately lead to quality maintenance.

References

1. https://economictimes.indiatimes.com/industry/services/education/india-is-in-the-middle-of-an-engineeringeducation-crisis/articleshow/. Last accessed 17 Jan 2019
2. Singh, H., et al.: Qualitative assessment for improvement of technical education using total quality management: a survey. IRJET **2**(6), 888–899 (2015)
3. Chakraborty, R.: Only 7 per cent engineering graduates employable: what's wrong with India's engineers? India Today Help Desk, 13 July 2016
4. https://www.businesstoday.in/opinion/deep-dive/a.-k.-sarkar-s.k.-choudhury-on-engineering-studentsemployment/story/205041.html/. Last accessed 17 Jan 2019
5. https://economictimes.indiatimes.com/jobs/only-6-of-those-passing-out-of-indias-engineering-colleges-arefit-for-a-job/articleshow/64446292.cms/. Last accessed 15 Jan 2019
6. https://www.theweek.in/content/archival/news/india/nits-have-better-gender-diversity-than-iits.html/last. Accessed 16 Jan 2019

Network Repair Algorithms for Wireless Sensors and Actuators Based on Graph Theory

Ju Jinquan, Mohammed Abdulhakim Al-Absi and Hoon Jae Lee

Abstract In view of the shortcomings of traditional wireless sensor and actuator networks, such as low speed and high consumption, this paper studies the repair algorithm of wireless sensor and actuator networks based on graph theory. Firstly, the concept of wireless sensor and actuator network is analyzed, then the cooperative algorithm of wireless sensor and actuator network is elaborated, and a SA cooperative algorithm with low energy consumption and low latency is proposed. Finally, the algorithm of cut-point detection is summarized. The algorithm is mainly based on simulation model NS2 and topological repair of cut point. The simulation results show that the real-time performance and energy consumption of the proposed algorithm are better than those of K-IDS algorithm and RCR algorithm.

Keywords Cut-point detection · WSAN · Wireless sensor · Actuator network · Repair algorithm · Cooperative algorithm

1 Introduction

Wireless sensor has been applied in many fields, including environmental monitoring, health care, and other aspects of deployment, but in the application process, the demand for the combination of actuator and sensor is increasing. In this context, the network system needs to interact with the physical environment through the reactor in order to collect the corresponding information. From the engineering point of view, the actuator also belongs to the converter, which can accept the signal and transform the corresponding signal. In the use of traditional sensor and actuator networks, some mature research theories have been gradually formed. Some small, intelligent, and

J. Jinquan · M. A. Al-Absi · H. J. Lee (✉)
Division of Information and Communication Engineering, Dongseo University, 47 Jurye-ro, Sasang-gu, Busan 47011, Republic of Korea
e-mail: hjlee@dongseo.ac.kr

J. Jinquan
e-mail: Jujinquan351939917@gmail.com

M. A. Al-Absi
e-mail: Mohammed.a.absi@gmail.com

L. Li et al. (eds.), *Advances in Materials and Manufacturing Engineering*, Lecture Notes in Mechanical Engineering, https://doi.org/10.1007/978-981-15-1307-7_74

low-cost wireless sensing execution devices are gradually coming out. Under this background, the application of sensor-actuator network has been extended.

WSAN belongs to the extension of WSN. The difference between WSAN and WSAN is that WSAN can change the environment and physical world. At the same time, wireless sensor and actuator networks can be applied in disaster relief, intelligent construction, biology, chemistry, and other detection fields in the future.

Wireless sensor-actuator network can be self-organized and has the ability to work intelligently and independently. Users can also connect to the network remotely and send some basic instructions.

In WSAN applications, sensors belong to static state and actuators belong to motion state. In some specific environments, sensor nodes can also move freely. For example, in the problem of sensor location, sensor nodes can move to the location of failed sensor nodes to ensure the continuous coverage of signals in the region. Therefore, sensors and actuators can be integrated into robots to enable the robot to perform perception, while also having mobile functions.

2 Collaboration Algorithms for Wireless Sensor and Actuator Networks

2.1 Distributed Framework Algorithms

Distributed framework algorithm is proposed by relevant scholars. In this kind of algorithm, event-driven problem model is taken as different level problem model, and linear programming is adopted. Multi-state distributed algorithm is mainly used to realize arbitrary switching of start-up, acceleration, idle, and aggregation states in each sensor. After sending the corresponding data, the original node can calculate the arrival time of the corresponding data on the packet actuator node. The data transmission speed that has been achieved is expressed by r, and the corresponding data is propagated by virtue of the periodicity of the actuator node. If the value of R decreases, the transmission power of sensor nodes will also be reduced, thus reducing the energy consumption in transmission, so as to realize the effective utilization of resources.

Because the reliable upper limit and lower limit cannot be calculated accurately under this algorithm, it is impossible to summarize the relevant formulas when the network changes, which is also the main reason why this kind of algorithm stays at the design stage. This kind of algorithm can transform the AA-based collaboration problem into a mixed non-linear integer programming model. In the area where an accident occurs, the divine domain energy of the actuator node can be maximized within the constraints of task time. Therefore, this kind of algorithm focuses on the energy consumption of collaboration within the actuator node.

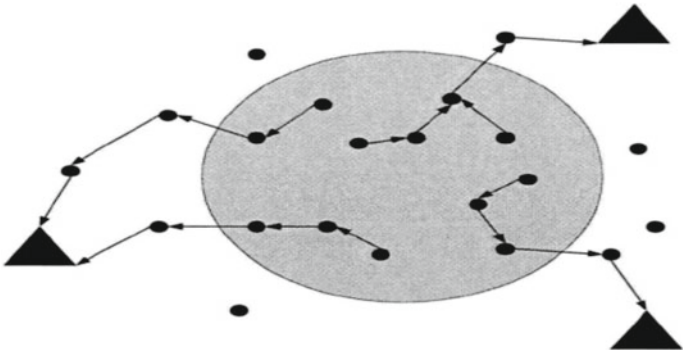

Fig. 1 Clustering schematic

2.2 Real-Time Collaboration and Routing Framework Algorithms

As shown in Fig. 1, it configures the corresponding sensor nodes in the dynamic hierarchical structure, in which the energy is the clustering protocol. DEAR belongs to energy-aware routing algorithm. It integrates forward tracking and backtracking routing technologies and establishes a routing between nodes and routers in a specific time.

Because of the existence of SINK nodes, in the semi-automatic architecture, it is necessary to use centralized DEAR algorithm to coordinate sensor nodes and actuator nodes. In the absence of SINK nodes, SA collaboration needs to be achieved by means of distributed D-DEAR. In multi-path selection, the most efficient way is to be chosen, and data transmission is realized on this path to meet the delay constraints.

2.3 Topology Maintenance Algorithms

Topology maintenance algorithm is mainly used to repair the network with the help of the adjacent nodes of the time-sensitive nodes, which can effectively repair the network and ensure the coherence of the network when the amount of information exchange and the moving distance are the smallest. In the process of repairing the algorithm, the nodes around the aging node need to be relocated, and the distance between the node and the failure node needs to be kept $r/2$. In this kind of algorithm, r belongs to the communication radius of nodes. If there is a problem of network coherence after the adjacent nodes move, cascade mobility is needed to repair the network. Topology maintenance algorithm belongs to the network of sensors. As long as the failure nodes have problems, the neighboring nodes can repair the network. At the same time, in the process of running, topology repair is the basic condition without cooperative communication between nodes.

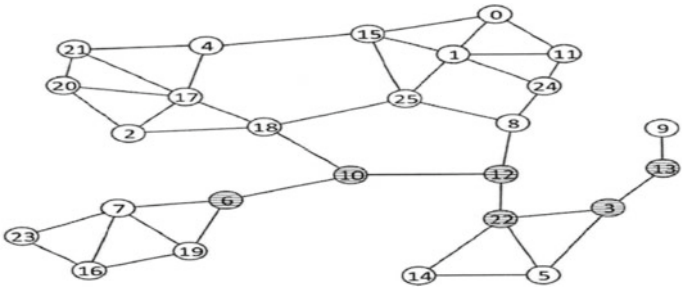

Fig. 2 Topology schematic

A network repair algorithm between actuators does not need to consider the cut points of the failed nodes, and its repair method is similar to that of the topology maintenance algorithm. The main purpose is to locate the failure-proximity node in the direction of the failure node and guide the distance between the two nodes to be $r/2$. However, under such failures, various impacts caused by node movement are repaired by sending information to find the best node (Fig. 2).

2.4 Improved Network SA Collaboration Algorithms

On the basis of the above research, this paper proposes a low energy consumption and low delay cooperative algorithm, which is divided into four stages as follows.

Step 1. With the goal of network energy consumption optimization, the ideal number of actuator nodes and the communication radius between sensor nodes are determined according to the area of events, the number of sensor nodes, the energy consumption of receiving and sending nodes, the frequency of events, and other factors, taking into account the constraints of network connectivity and delay.

Step 2. Random and uniform deployment of sensor nodes and actuator nodes in the network, using clustering method, dividing the network into several clusters, clustering can effectively reduce the communication load, while avoiding too many actuator nodes to participate in the same event, each cluster has only one actuator node, because the energy and computing power of the actuator node is much higher than that of the sensor node. So it is simpler and more real-time to select actuator nodes as cluster heads and other sensor nodes as cluster members. Sensor nodes in clusters detect physical quantities and send them only to cluster heads, which decide how to execute and take corresponding actions.

Step 3. After clustering, it is necessary for the actuator node to receive the event information as soon as possible and respond to the event in a timely manner. By minimizing the distance between the sensor node farthest from the actuator node in the cluster and the actuator node, the actuator node can receive the information from all the cluster members as soon as possible and find the event as early as possible

and then respond in time. Therefore, the actuator node needs to find the appropriate location in its cluster and redeploy it.

Step 4. After the deployment of sensor nodes and actuator nodes, they begin to communicate with each other. Sensor nodes choose the optimal path to transmit data information to actuator nodes to ensure low energy consumption and high real time. In this paper, a single-hop and multi-hop hybrid communication mode is adopted. Within the communication radius of sensor nodes, sensor nodes communicate directly with the actuator nodes. When the distance exceeds this distance, the sensor nodes communicate with the actuator nodes according to the shortest path algorithm (searching for the next hop relay node, using multi-hop mode to transmit to the actuator nodes).

Network energy consumption is composed of actuator node energy consumption and sensor node energy consumption. In this paper, the network structure is assumed to be a hybrid of periodic acquisition and event-driven. Under this assumption, the total energy consumption of an actuator node can be obtained as shown in formula:

$$E_{\text{actor}} = T_{\text{com}} E_{rx}\left(\frac{N_{\text{sensor}} * l}{N_{\text{actor}}}\right) + E_{\text{agger}}\left(\frac{N_{\text{sensor}} * l}{N_{\text{actor}}}, l\right) + \chi\left(\frac{N_{\text{sensor}}}{N_{\text{actor}}}\right) E_{tx}(d, l) + T_{\text{event}} E_{\text{action}}(t) t_{\text{event}} \quad (1)$$

Among them, the frequency of events is the number of rounds of periodic data acquisition, which is the energy consumption of an actuator node. In this paper, Karush-Kuhn-Tucker (KKT) condition [1] is used as the first-order necessary condition to obtain the local optimal solution.

2.5 *Clustering Algorithm*

In wireless sensor networks, some clustering-based protocols have been proposed. The multi-hop mode and data fusion method within a specific cluster can effectively reduce the energy consumption of the network. For example, LEACH is a clustering-based routing protocol applied to WSN. In LEACH algorithm, in order to save energy, sensor nodes are clustered automatically according to the received signal strength. Cluster members send data to cluster heads, and then the cluster heads are transmitted to SINK nodes [2].

Because of the simultaneous existence of actuator nodes and sensor nodes, there are some obvious differences between WSAN and traditional WSN: heterogeneity of nodes, deployment of nodes, coordination of nodes, etc. Therefore, the protocol proposed for WSN cannot be well used in WSAN application requirements and characteristics.

This paper considers that the actuator node has sufficient energy, strong function, and mission to accomplish tasks, so the actuator node is usually fixed as cluster head.

A clustering algorithm based on Voronoi graph of actuator nodes is proposed. The clustering algorithm is described in detail below.

The concept of Voronoi structure was discovered by Russian mathematician M. G. Voronoi in 1908 and named after him. In essence, it is a universal structure in which macroscopic and microscopic entities interact with each other by distance in nature. The basic definition [3] is described below.

From the computational geometry obtained by Voronoi structure, V-graph is for N discrete points in a plane. It divides the plane into several zones, each of which includes a point. The area where the point is located is a set of nearest points to the point.

Firstly, assuming that sensor nodes and actuator nodes have been deployed, sensor nodes and actuator nodes are known their own locations (by equipping with GPS receivers), the whole network is divided into several clusters based on the Voronoi graph of actuator nodes, each cluster includes one actuator node and several sensor nodes. Each cluster is considered to be a different subnet. The clustering stage is as follows: As the cluster head of the subnet, the actuator node broadcasts its own information (including location coordinates, node type, residual energy), the sensor node receives all the letters sent by the actuator node, the sensor node automatically joins the subnet of the nearest actuator node, and then the sensor node sends ACK confirmation information to the actuator node.

In order to ensure the real-time performance of the network, sensor nodes need to monitor events in time and send them to the actuator, which can perform tasks as soon as possible. According to the analysis of real-time performance in Ref. [4], once the sensor node monitors the event, it usually needs to send the information to the nearest actuator node, which guarantees both real-time and low energy consumption.

3 Simulation Result and Analysis

It is assumed that the simulation experiment (NS2) is carried out in a square area of 200 m * 200 m, in which 100 sensor nodes are deployed randomly and evenly. Temperature and humidity sensors are used to collect physical signals, that is, soil temperature and humidity, which are powered by batteries. Sensor nodes are static and have definite locations. According to the analysis results of the ideal number of actuator nodes, there are 9 actuator nodes and the actuator nodes are mobile.

In order to facilitate the analysis of nodes, the actuator nodes and sensor nodes are labeled and displayed in the cluster. The triangle represents the actuator and the black dot represents the sensor. As shown in Fig. 3.

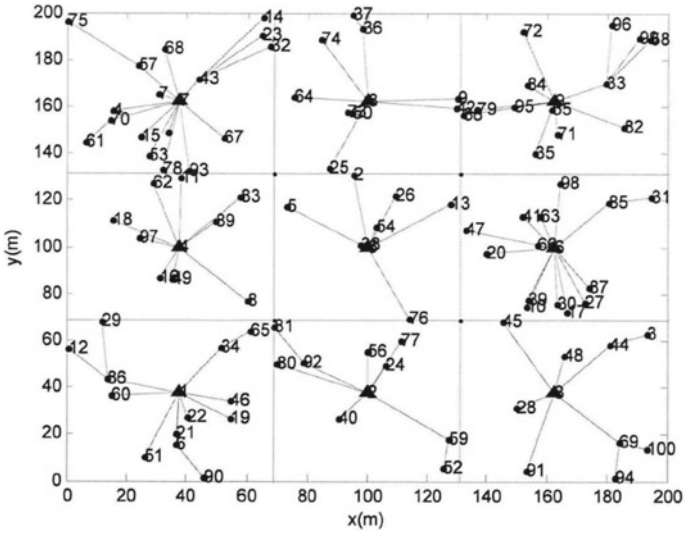

Fig. 3 Data transfer model based on Voronoi diagram

4 Conclusion

In this paper, a graph-based wireless sensor and actuator network (WSAN) repair algorithm is proposed to overcome the shortcomings of traditional wireless sensor and actuator networks, such as low speed and high consumption. Firstly, the concepts of wireless sensor and actuator networks are analyzed, and then the cooperative algorithms of wireless sensor and actuator networks are elaborated. At the same time, a SA cooperative algorithm with low energy consumption and low latency is proposed. Finally, the analysis of cut-point detection algorithm is summarized. The algorithm is mainly based on the simulation model NS2 and the topological repair of cut point.

Acknowledgements This work was supported by Institute for Information and Communications Technology Promotion (IITP) grant funded by the Korean government (MSIT) (No. 2018-0-00245), and it was also supported by the Basic Science Research Program through the National Research Foundation of Korea (NRF) funded by the Ministry of Education, Science, and Technology (grant number: NRF2016R1D1A1B01011908).

References

1. Fukushima, M.: Basis of Nonlinear Optimization, pp. 76–78. Science Press, Beijing (2011)
2. Tianshuang, Q., Hong, T., Ting, L., Yanghua, Yi, J.: Wireless Sensor Network Protocol and Architecture, pp. 67–68. Electronic Industry Press, Beijing (2018)

3. Qiang, C.: The Theory and Application of Limited Voronoi Mesh Generation. Beijing University of Posts and Telecommunications Press, Beijing (2010)
4. Nan, G., Zhijun, L., Shouxu, J.: Actor deployment strategies in WSANs. First Int. Conf. Perv. Comput. Sig. Process. Appl. **8**(10), 150–154 (2010)

Cryptography Survey of DSS and DSA

Mohammed Abdulhakim Al-Absi, Azamjon Abdullaev, Ahmed Abdulhakim Al-Absi, Mangal Sain and Hoon Jae Lee

Abstract Digital signatures are the basis for identifying who sends file identities in modern society today. Digital signatures are a way to provide integrity and reliability for digital data signatures. Signatures use a set of principles and parameters that allow a computer to verify the identity and authentication of data. There are three algorithms for digital signature generation in the DSS. The first one is the RSA, the second is the ElGamal algorithm, and the third is the elliptic curve digital signature algorithm (ECDSA). This paper discusses the cryptography including different types of digital signatures based on the key type and some algorithms of digital signature, RSA, ElGamal, and ECDSA.

Keywords Digital signature · Digital signature algorithm · DSA · ECDSA · RSA · DSS

1 Introduction

The signature is always created using the private key, where the user only knows the private key. It also verifies that the signature uses a public key that matches the private key. Each user has a public key and a special key pair. The public key is known to

M. A. Al-Absi · A. Abdullaev · M. Sain · H. J. Lee (✉)
Division of Information and Communication Engineering, Dongseo University, 47 Jurye-ro, Sasang-gu, Busan 47011, Republic of Korea
e-mail: hjlee@dongseo.ac.kr

M. A. Al-Absi
e-mail: Mohammed.a.absi@gmail.com

A. Abdullaev
e-mail: Azamjon.a.sobirovich@gmail.com

M. Sain
e-mail: mangalsain1@gmail.com

A. A. Al-Absi
Department of Smart Computing, Kyungdong University, 46 4-gil, Bongpo, Gosung, Gangwon-do 24764, Republic of Korea
e-mail: absiahmed@kduniv.ac.kr

L. Li et al. (eds.), *Advances in Materials and Manufacturing Engineering*, Lecture Notes in Mechanical Engineering, https://doi.org/10.1007/978-981-15-1307-7_75

all and can be used to verify user signature. However, the private key is not shared, and the private key is used to create the signature, which is only by the user [1].

They [2] proposed an effective framework for user authentication of wireless sensor networks based on passwords and smart cards and the use of one-way hash functions. This scenario provides mutual authentication and allows users to change passwords when needed. The problem is that it does not provide a noticeable internal attack because the password is sent to the base station in plain text. It also encounters synchronization issues because it uses timestamps to avoid replay attacks.

Digital signatures are used to detect unauthorized data modifications. However, the recipient of the third-party digital signature file proves that the document has been signed by the signer. This is undeniable because the person signing the document cannot refuse to sign it later. We can use digital signature algorithms in electronic money transfer, email, data storage, electronic data exchange, software distribution, and any application that actually needs to ensure data integrity and originality [3].

Digital signature algorithm (DSA): Set the Digital signature standard (DSS). The standard includes creating domain parameters, creating private and public key pairs, and verifying and generating digital signatures.
Digital signature algorithm (RSA): The public key is set in the USS Encryption Standard (ANS). FIPS documentation 186-4 uses one or both of these criteria and specifies other requirements.
Elliptic curve digital signature algorithm (ECDSA): Set in ANS X9.62.

The public key is applied during the signature verification process. However, you do not need to keep secret keys to maintain integrity. Anyone can verify the correct signature of the message using the public key [4, 5].

During the signature and construction validation process, the message is converted to a fixed-length analysis of the message by the specified hash function. Both digital signature and original message are ready to use (Fig. 1).

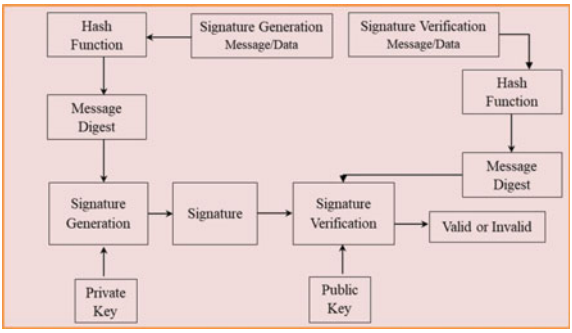

Fig. 1 Digital signature processes

2 Applications of Digital Signatures

Electronic signatures can be provided by sites [6, 7] with source, identity, and status of electronic sources and informed consent of the site.

Integrity: There is status where is a need for dependability where the message has not been changed during transmission. Nonetheless, if the message has a digital signature, the digital signature is discarded because the message is modified after the signature.
Confidentiality: It protects information only and obtains information from authorized users.
Authentication: To authenticate the origin of message, we can use digital signatures. For instance, Alice will send Bob the encrypted message digest. In order to authenticate Bob on signing, he must apply the same defragmentation function that Alice carries to the message you sent him. Alice will also be used to decrypt the encrypted message and compare the two. If the two are similar, he has successfully verified the signature. If the two do not match, a transmission error occurs or someone tries to impersonate Alice. However, a valid signature indicates that a property user sent a message when the property's digital signature is restricted to a specific user.
Non-repudiation: Here, the information that we may have received can be definitely attributed to somebody, and there is no way that they can take it back. They definitely said what is that we have in this message right here.

3 Comparison of RSA with ECDSA

ECDSA and RSA are suitable for data protection within the network. For security, RSA and ECDSA equip the same security level with the short and large keys. Using encryption technology, data transmission, verification, less power consumption, faster signature generation, the minimal size key of ECDSA probably allows for minimum estimation fit lightweight wireless systems and devices (Table 1).

Table 1 Comparison of RSA and ECDSA

Domain		Key generation	Execution time	Verification time	Signature time	Complexity	Security
ECDSA	Light weight devices	Faster	Fast	Slow	Slow	Discrete logarithm	High
RSA	Super computers laptops, PC	Fast	Slow	Fast	Fast	Integer factorization	High

Key generation: Key generation differences are faster than RSA due to different key lengths [8]. RSA creates and generates utilizing two big prime numbers, so it takes so much time than the minimum ECDSA keys which is generated.
Verification time: RSA verification time is so fast because it is simpler in terms of cryptographic computations as only a lower of modular multiplications is needful.
Execution time: Considering the RSA keys which are significantly bigger than the ECDSA keys, RSA takes longer time to generate the key compared to ECDSA.
Signature time: The time needed for ECDSA operations to generate signatures is so mash slower because of the convergence among the key sizes. The time needed for RSA operations to generate signatures so fast increases because of its big keys which are not reasonable and keep delay packets from being transferred.

4 Comparison of RSA with ECC

The ECC has full exponential time where the RSA takes sub-exponential time. For instance, the ECC for 160-bit key size takes 9.6×1011 MIP years [9] where the RSA of 1024 bits for key size takes 3×1011 MIP years. With the smaller key size, the ECC offers same security level. The size of data in the RSA is smaller than the ECC, and the power computational is smaller for ECC compared to the RSA.

5 Different Types of Digital Signatures

Digital signature with attachment: A key message is required as confirmation input, for instance, DSS, ElGamal, and DSA.

Message recovery with digital signatures: It verifies that the predefined key message is not required, as the underlying message can be retrieved by the signature itself, for instance, Rabin, RSA, and Rueppel.

RSA-based digital signature: It includes digital signature with extension and digital signature with retrieving messages.

Blind signature technique [10]: It keeps anonymous senders anonymous to prevent monitoring of consumption patterns.

6 Simple Digital Signature Algorithm

The public key is used to verify the signature. You do not need to keep the public key secret, but you should keep it. Anyone can correctly verify the signed message using the public key.

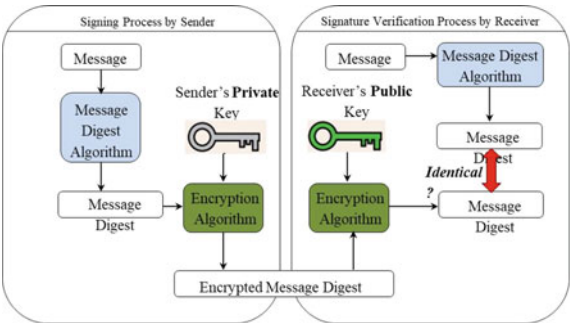

Fig. 2 Simple digital signature algorithm

Sender action: Create a message summary (MD). The message summary is "Summary of messages to be sent" created by a hash group approved by two users. The integrity algorithm ensures message integrity by creating completely different hashing values when one part of the message is changed. The encrypted message digest is generated when the message digest is encrypted using the sender's private key, which is called the digital signature (DS). The DS is compiled with the message and sent to the recipient (Fig. 2).

Recipient signature verification process: The recipient decrypts the digital signature using the public key of the sender to obtain the message digest generated by the sender. The receiver uses the same segmentation algorithm for the MD account of the received message. The MD value obtained is compared with the sender's MD value. If they match, the message remains the same and authenticity is guaranteed. At this point, decrypting the message using the public key of the sender results in an invalid message aggregation and changing the message so that it cannot be trusted. However, it is clear that the integrity of the message is maintained, but personal information is not retained because the message is sent explicitly.

This can be applied in situations where confidentiality is not an issue. Messages must be encrypted to ensure the confidentiality of communications. By default, the digital signature scheme typically consists of three algorithms: key generation algorithms, signatures, and signature verification. Techniques vary, and this system is classified according to mathematical problems. Public key systems are typically based on integers (RSA), separate algebraic numbers (such as DSA), and elliptic curve algorithms (ECDSA) and fall into three main categories. The safety score of all skills depends on the severity of the sport problem.

6.1 Digital Signature Algorithm (RSA)

RSA is a public key cryptosystem developed by inventors Ronald Reveset, Adi Shamir, and Leonard Adelman in 1977 [6]. He has done extensive blade analysis for many years. It is used for e-commerce and many other secure online connections. RSA uses one-way function for additional complex properties [11]. RSA is a block

encoding in which plain text and encoded text are integers between 0 and $e - 1$ of the integer e. RSA provides security features to address a large number of security problems [12].

Working of RSA: Choose two large random numbers r and q about the same length. Compute their product $e = rq$. Euler's totient function $\phi(e)$ is computed, i.e., $\phi(e) = (r - 1)\ (q - 1)$. Next, we select the keys *a and b* such that $a.b \equiv 1\ (mod\ \phi(e))$. One key says that the public key is a, and the other keys are kept private b. At this point, we no longer need r, q, and $\phi(e)$. We can ignore these values. If there is an H message, the encryption of H is $C = Ha\ mod\ e$, *and* C is the encrypted text. C decryption is done by $H' = Cb\ mod\ e$.

With considering $H' = Mab\ mod\ e = Hk\phi(e) + 1\ mod\ e$ (where $a.b \equiv 1\ (mod\ \phi(e))) \Rightarrow H' = H.\ Hk\phi(e)\ mod\ e = H\ mod\ e$ (this can be demonstrated that $x\phi(e) \equiv 1\ (mod\ e)$).

Therefore, we can see $H = H$. Thus, RSA is used to perform encryption and decryption.

Elliptic curve digital signature algorithm (ECDSA)
ECDSA was originally proposed by Scott Vanstone in 1992 [13].
Elliptic curve digital signature algorithm (ECDSA) key generation [14, 15].
User A has these steps where r is a large prime:
Select a random integer $d \in [1, e - 1]$.
Compute $Q = d \times R$.
The private and public keys of the users A are Q and d, respectively.
The other users can check if the public key is valid by;
Check it out $Q \neq 0$.
Check it out xQ and yQ are properly represented elements of Fq.
Check it out Q is on the elliptic curve defined by *a and b*.
Check it out $eQ = Q$.
If any of these checks fail, the public key Q is invalid; otherwise, Q is valid. The following procedure describes how to generate the signature.
ECDSA signature generation
Select a pseudorandom integer $k \in [1, e - 1]$.
Check it out $k \times R = (x1, y1)$ and $r = x1$ mod e.
If $x1 \in, GF(2\ k)$, it is assumed that $x1$ is represented as a binary number.
If $r = 0$, then go to Step 1. Compute $k - 1\ mod\ e$.
Compute $s = k - 1(H(h) + d \cdot r)\ mod\ e$.
Here, H is the secure hash algorithm SHA-1.
If $s = 0$, *then go to Step* 1.
The signature for the message h is the pair of integers (r, s).
ECDSA signature verification
Verify that *r and s* are integers in the interval $[1, e - 1]$.
Compute $c = s - 1\ mod\ e$ *and* $H(h)$.
Compute $u1 = H(h) \bullet c\ mod\ e$ *and* $u2 = r \bullet c\ mod\ e$.
Compute $u1 \times R + u2 \times Q = (x0, y0)$ *and* $v = x0\ mod\ e$
Accept the signature *if* $v = r$.

ElGamal digital signature
ElGamal key generation
The prime r, a generator g of field Z_r^*, $A's$ private key dA is a random integer from the interval [1; $r-1$] and her public key is $yA = g^{d_A}.mod\, r$.
ElGamal signature generation
Select a random integer k from interval [1; $r-1$], satisfying $gcd(k; r-1) = 1$ [16, 17].
Compute $k-1\ mod\ (r-1)$; *Compute* $r = gk\ mod\ r$;
Compute $s = k-1\{h\,(h) - dAr\}\ mod\ (r-1)$. h is the hash function: $\{0; 1\} \rightarrow Zr$. $(r; s)$ *is A's signature of message h.*
ElGamal signature verification
Verify that $1 \leq r \leq r-1$;
Compute $v1 = y_A^r gkmod\, r$;
Compute $h\,(h)$ *and* $v2 = gh(h)$;
Accept if and only if $v1 = v2$.
Schnorr digital signature; Schnorr key generation
Primes q, r, satisfying $q \mid (r-1)$, the generator α of the unique cyclic subgroup of Z_r^* (satisfying $\exists\ u\ Z_r^*$, $\alpha = u(r-1)/q\ mod\ r$, *but* $\alpha \neq 1$). $A's$ private key dA is a random integer from the interval [1; $q-1$], and her public key is $yA = \alpha^{d_A} mod\, r$.
Schnorr signature generation
Select a random integer k from interval [1; $q-1$];
Compute $r = \alpha kmod\, r$, $e = h(h \mid r)$ *and* $s = dAe + k\ mod\ q$. h is the hash function $\{0; 1\} \rightarrow Zq$. $(s; e)$ *is A's signature of message h.*
Schnorr signature verification
Compute $v = \alpha s\ y_A^{-e}\ mod\ r$ *and* $e' = h(h \mid v)$;
Accept if and only if $e = e'$;

7 Comparison of Security Levels

The elliptic curve with the modulus a prime r is a solution (x, y) to an equation of the form:

$y2 = x3 + ax + b\ (mod\ r)$
For two numbers *a and b.*
If (x, y) satisfies the above equation,
Then $R = (x, y)$ is a point on the elliptic curve.

In fact, an elliptic curve can also be defined over the finite field consisting of 2 h elements. Such a representation offers extra efficiency in the operation of the ECC.

Using some particularly deep mathematics, it is possible to define the "addition" of two points on the elliptic curve.

Suppose *R and Q* are both points on the curve, then $R + Q$ will always be deferent point on the curve. The elliptic curve discrete logarithm problem can be stated as

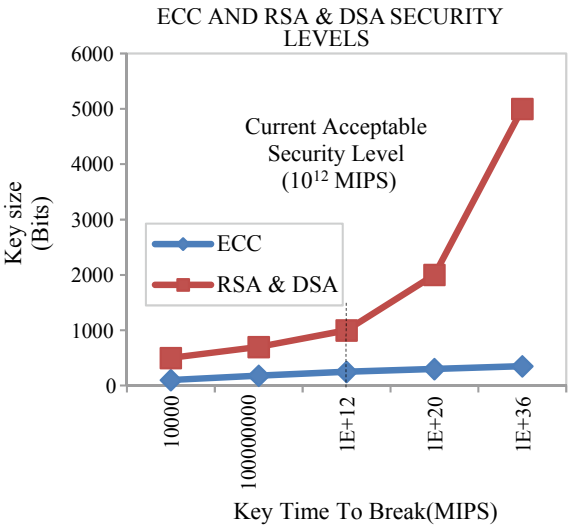

Fig. 3 Security levels of ECC and RSA & DSA

follows. Fix a prime p and an elliptic curve. xR represents the point R added to itself x times. Suppose Q is a multiple of R, so that $Q = xR$ for some x. Then the elliptic curve discrete logarithm problem is to determine x given R *and* Q.

Figure 3 checks the required time to break RSA or DSA of various measured sizes using the most famous general-purpose algorithm and the time required to interrupt ECC. This value is calculated in MIPS years. MIPS year represents a system computing time of one year and can process 1 million instructions per second. As a benchmark, it is widely believed that the 1012 MIPS solution at this time provides reasonable security because it requires a lot of computing power on the planet.

However, in order to obtain reasonable security in Fig. 3, we can see that DSA and RSA must use 1024-bit modules and 160-bit modules should be sufficient for elliptic curve cryptography (ECC). ECC and security niche require smaller modules than RSA or DSA and grow on systems with increased key sizes. For example, a 300-bit ECC is more secure than a 2000 DSA or RSA [7, 18].

8 Conclusion

Digital signatures are the foundation of today's modern world and are used to identify the sender of the document. In this paper, we explore the concept of encryption by including several types of digital signatures based on key types. First RSA algorithm, the second algorithm is the Elgatic algorithm, and fatigue is the elliptic curve digital signature algorithm (ECDSA). Electronic digital signature (EDS) eliminates most of the issues inherent in signing paper documents, but future work takes into account the identity of the sender of the document and the authenticity of the document.

Acknowledgements This work was supported by Institute for Information and Communications Technology Promotion (IITP) grant funded by the Korean government (MSIT) (No. 2018-0-00245), and it was also supported by the Basic Science Research Program through the National Research Foundation of Korea (NRF) funded by the Ministry of Education, Science, and Technology (grant number: NRF2016R1D1A1B01011908).

References

1. Hai-peng, C., Xuan-jing, S., Wei, W.: Digital signature algorithm based on hash round function and self-certified public key system. In: First International Workshop on Education Technology and Computer Science (2009)
2. Kumar, P., Sain, M., Lee, H.J.: An efficient two-factor user authentication framework for wireless senor networks. In: ICACT (2011)
3. Agnew, G., Mullin, R., Vanstone, S.: An implementation of elliptic curve cryptosystems over 2155. IEEE J. Sel. Areas Commun. **11**, 804–813 (1993)
4. Romney, W.: Digital signature signing engine to protect the integrity of digital assets by Gordon, 1-4244-0406-1/06/$20.00 ©2006 IEEE (2006)
5. Abdullaev, A., Al-Absi, M.A., Al-Absi, A.A., Sain, M., Lee, H.J.: Survey on digital signature algorithms. In: International Conference on Culture Technology (ICCT), pp. 408–411. Zhijiang College of Zhejiang University of Technology Shaoxing, China, 15–18 Nov 2018 (2018)
6. Kuppuswamy, P. Appa, P.M., Al-Khalidi, D.S.Q.: A new efficient digital signature scheme algorithm based on block cipher. IOSR J. Comput. Eng. (IOSRJCE) **7**(1), 47–52 (2012). ISSN: 2278-0661, ISBN: 2278-8727
7. Baral, S.: An efficient blind digital signature protocol based on elliptic curve. Int. J. Technol. Enhanc. Emerg. Eng. Res. **2**(9). ISSN 2347–4289
8. Ali, A.I.: Comparison and evaluation of digital signature schemes employed in NDN network. Int. J. Embed. Syst. Appl. (IJESA) 5(2) (2015)
9. Raju, G.V.S., Akbani, R.: Elliptic curve cryptosystem and its application. In: Proceedings of the IEEE International Conference on Systems Man and Cybernetics (IEEE-SMC), pp. 1540–1543 (2003)
10. http://www.iet.unipi.it/g.dini/Teaching/sanna/lecturenotes/applied-cryptography-digital-signature.pdf
11. Flinn, P.J., Jordan, J.M.: Using the RSA Algorithm for Encryption and Digital Signatures: Can You Encrypt, Decrypt, Sign and Verify without Infringing the RSA Patent? Alston & Bird LLP, 9 July 1997 (1997)
12. Rivest, R.L., Shamir, A., Adleman, L.: A method of obtaining digital signatures and public key cryptosystems. Comm. ACM **21** (1978)
13. Vanstone, S.A.: Responses to NIST's proposal. Commun. ACM **35**, 50–52 (1992)
14. Khalique, A., Singh, K., Sood, S.: Implementation of elliptic curve digital signature algorithm. Int. J. Comput. Appl. (0975-8887) **2**(2) (2010)
15. Aqeel, K., Kuldip, S., Sandeep, S.: Implementation of elliptic curve digital signature algorithm. Int. J. Comput. Appl. (0975-8887) **2**(2) (2010)
16. Stinson, D.: Cryptography Theory and Practice. CRC Press (1995)
17. El Gamal, T., A public key cryptosystem and a signature scheme based on discrete logarithms. In: Advances in Cryptology: Proceedings of CRYPTO'84, vol. 196. Lecture Notes in Computer Science, pp. 10–18. Springer (1985)
18. Abdullaev, A., Al-Absi, M.A., Al-Absi, A.A., Sain, M., Lee, H.J.: General study of digital signature schemes. In: International Conference on Culture Technology, Zhijiang College of Zhejiang University of Technology Shaoxing, China, ICCT, 15–18 Nov 2018, pp. 412–415 (2018)

Author Index

L. Li et al. (eds.), *Advances in Materials and Manufacturing Engineering*, Lecture Notes in Mechanical Engineering, https://doi.org/10.1007/978-981-15-1307-7